NOVA SCHOOL OF SCIENCE & TECHNOLOGY

DEPARTAMENT OF MATERIALS SCIENCE

MICROWAVE-ASSISTED SYNTHESES OF SUSTAINABLE TiO_2-BASED PLATFORMS FOR WATER REMEDIATION

MARIA LEONOR JOAQUIM DO NASCIMENTO MATIAS

Master in Micro and Nanotechnology Engineering

DOCTORATE IN NANOTECHNOLOGIES AND NANOSCIENCES

NOVA University Lisbon

April, 2025

NOVA SCHOOL OF SCIENCE & TECHNOLOGY

DEPARTAMENT OF MATERIALS SCIENCE

MICROWAVE-ASSISTED SYNTHESES OF SUSTAINABLE TiO_2-BASED PLATFORMS FOR WATER REMEDIATION

MARIA LEONOR JOAQUIM DO NASCIMENTO MATIAS

Master in Micro and Nanotechnology Engineering

Adviser: Daniela da Silva Nunes Gomes
Assistant Professor, NOVA University Lisbon

Co-advisers: Joana Catarina Ferreira Rodrigues
Assistant Researcher, University of Aveiro

Ana Maria Staack Reis Machado
Senior Researcher, NOVA University Lisbon

Examination Committee:

Chair: Elvira Maria Correia Fortunato
Full Professor, NOVA University Lisbon

Rapporteurs: Clara Isabel Barbosa Rodrigues Pereira
Assistant Professor, University of Porto

Ana Violeta Oliveira Morais de Sousa Girão
Researcher, CICECO - University of Aveiro

Adviser: Daniela da Silva Nunes Gomes
Assistant Professor, NOVA University Lisbon

Members: Elvira Maria Correia Fortunato
Full Professor, NOVA University Lisbon

Pedro Miguel Cândido Barquinha
Associate Professor, NOVA University Lisbon

DOCTORATE IN NANOTECHNOLOGIES AND NANOSCIENCES

NOVA University Lisbon
April, 2025

Microwave-assisted syntheses of sustainable TiO_2-based platforms for water remediation

To all who are curious about science

AGRADECIMENTOS

Em primeiro lugar quero agradecer à prof. Daniela Gomes. O seu apoio incondicional, conhecimento e amizade foram fundamentais para me motivar, para melhorar o meu espírito crítico e ajudar a superar os desafios. À sua disponibilidade, empatia e por acreditar sempre que iriamos conseguir fazer trabalhos excelentes. Sinto-me profundamente grata por ter tido esta oportunidade de realizar a tese de doutoramento sob a sua orientação, por tudo aquilo que me ensinou e postura exemplar em diversas situações. Sem dúvida foram a chave para o sucesso alcançado! Agradeço também às minhas coorientadoras, Ana Machado e Joana Rodrigues, pela rapidez na comunicação com ambas, por todos os conselhos/correções e pela confiança no trabalho. O vosso feedback contribuiu bastante para melhorar o meu trabalho e aprender convosco. Quero agradecer também aos professores do Departamento de Ciência dos Materiais da FCT, em especial à prof. Joana Pinto por tudo o que aprendi no XRD e pelas sugestões/ideias, ao prof. Pedro Barquinha e à prof. Rita Branquinho. À Dra. Diana Gaspar pelas sugestões, ajuda com as membranas de celulose e por ter conseguido participar na escola para alunos de doutoramento/workshop em Brno, onde tive a oportunidade de partilhar e discutir ideias com outros alunos de doutoramento, bem como contactar com empresas na área da microscopia. Foi uma experiência única! Agradeço também ao resto da equipa AlmaScience, ao Dr. Jonas Deurmeier pela ajuda no XPS, ao Tomás Calmeiro pela ajuda no AFM, ao prof. Henrique Almeida por todo o apoio e confiança no trabalho desenvolvido, à prof. Teresa Monteiro pelas correções, ao Dr. Auguste Fernandes pelas medidas de BET no IST, à prof. Patrícia Carvalho pela ajuda no STEM/DRX e correções, à prof. Catarina Reis e à aluna de doutoramento Mariana Amaral pelos ensaios de ecotoxicidade e por tudo o que aprendi na Faculdade de Farmácia. Ao Emanuel Carlos, à Ugur Deneb, ao Suman Nandy, ao Santanu Jana, à Shrabani Panigrahi e à Cláudia Pereira pelo trabalho em equipa para o paper da MXene, ao David Carvalho e Mariana Cortinhal pela ajuda nos ensaios de condutividade, ao Daniel Gouveia

pelas simulações de DFT e à Ana Pimentel. Agradeço ainda à Dra. Conceição Oliveira do IST pelos ensaios de LC-HRMS. Sem a sua persistência e ajuda não conseguiria obter estes resultados! Agradeço por tudo!

Agradeço ainda a alguns alunos/ex-alunos e investigadores: Maria Morais, Rita Xue, Teresa Rosa, David Bento, Beatriz Coelho, João Coelho, João Marcelino, Inês Cunha, Tiago Carvalho, Ana Rovisco, Raquel Barras, Raquel Martins, Tiago Paiva, Jenny Boane, Sofia Pádua e Ana Metelo.

Este trabalho não seria possível sem a bolsa que me foi atribuída pela FCT - Fundação para a Ciência e Tecnologia, I.P., à qual agradeço, com a referência UI/BD/151292/2021. Os trabalhos nesta tese foram financiados pela FCT no âmbito dos projetos LA/P/0037/2020, UIDP/50025/2020-2023 E UIDB/50025/2020-2023 do Laboratório Associado Instituto de Nanoestruturas, Nanomodelação e Nanofabricação (i3N), e pelo projeto CO2RED (DOI 10.54499/PTDC/EQU-EPQ/2195/2021). Os agradecimentos estendem-se ao projeto SYNERGY H2020-WIDESPREAD-2020-5, CSA, proposta número 952169 e EMERGE-2020-INFRAIA-2020-1, proposta número 101008701. Agradeço também ao apoio do projeto Sustainable Stone by Portugal - Valorization of Natural Stone for a digital, sustainable, and qualified future, número 40, proposta número C644943391-00000051, co-financiado pelo PRR (Recovery and Resilience Plan (Next Generation EU)).

Agradeço também ao centro que me acolheu (CENIMAT i3N), bem como ao CEMOP, à Alexandra Gonçalves, à prof. Elvira Fortunato por todo o interesse que demonstrou pelo meu trabalho e por todas as sugestões e correções e ainda ao prof. Rodrigo Martins.

Agradeço também a todo o pessoal do secretariado e da gestão do CENIMAT/CEMOP.

Por último, gostaria de agradecer à minha família, aos meus melhores amigos Tiago Gonçalves, Miguel Ângelo e Miguel Pita pelas tardes bem passadas em sessões de jogos de tabuleiro/PS/Nintendo, lanches, escape rooms, viagens… (não me vou esquecer da viagem ao "Japão" em Viseu (Ryokan), pena o Pita não ter ido também, talvez um dia possamos ir juntos ao Japão). Ao Tito, Maria, David, Nuno, Tairine e Márcio. Ao Diogo Coelho pela paciência, companheirismo, amor, por tudo o que já vivemos ao longo de mais de 10 anos e pelo que ainda espero vivermos!

Sem vocês isto não seria possível, muito obrigada!

”Σα βγεις στον πηγαιμό για την Ιθάκη,
να εύχεσαι να ’ναι μακρύς ο δρόμος,
γεμάτος περιπέτειες, γεμάτος γνώσεις.
Τους Λαιστρυγόνας και τους Κύκλωπας,
τον θυμωμένο Ποσειδώνα μη φοβάσαι,
τέτοια στον δρόμο σου ποτέ σου δεν θα βρεις,
αν μέν’ η σκέψις σου υψηλή, αν εκλεκτή
συγκίνησις το πνεύμα και το σώμα σου αγγίζει.
Τους Λαιστρυγόνας και τους Κύκλωπας,
τον άγριο Ποσειδώνα δεν θα συναντήσεις,
αν δεν τους κουβανείς μες στην ψυχή σου,
αν η ψυχή σου δεν τους στήνει εμπρός σου.
[…]
Πάντα στον νου σου να ’χεις την Ιθάκη.
Το φθάσιμον εκεί είν’ ο προορισμός σου.
Αλλά μη βιάζεις το ταξίδι διόλου.
Καλύτερα χρόνια πολλά να διαρκέσει·
και γέρος πια ν’ αράξεις στο νησί,
πλούσιος με όσα κέρδισες στον δρόμο,
μη προσδοκώντας πλούτη να σε δώσει η Ιθάκη.
Η Ιθάκη σ’ έδωσε τ’ ωραίο ταξίδι.
Χωρίς αυτήν δεν θα ’βγαινες στον δρόμο.
Άλλα δεν έχει να σε δώσει πια.
Κι αν πτωχική την βρεις, η Ιθάκη δεν σε γέλασε.
Έτσι σοφός που έγινες, με τόση πείρα,
ήδη θα το κατάλαβες η Ιθάκες τί σημαίνουν.”

Κ. Καβάφης (1911)

ABSTRACT

The widespread contamination of aquatic ecosystems poses critical environmental challenges, spurring intensive global research into advanced sustainable water remediation technologies. Titanium dioxide (TiO_2) nanostructures have emerged as prominent photocatalysts due to their physical/chemical stabilities, cost-effectiveness, and catalytic efficiency. However, TiO_2 has a wide band gap, restricting its utilization to the ultraviolet region. To enhance spectral responsiveness under visible light, various strategies were explored, including the creation of a heterostructure (graphitic carbon nitride/TiO_2), multi-dimensional defect engineering, as well as doping with two abundant elements: Fe and Ca. To overcome the limitations associated with the recovery and recyclability of nanopowders, TiO_2-based nanostructures synthesized under microwave irradiation were either incorporated into or directly synthesized onto green substrates, floating and non-floating. These substrates included cork, cellulose-based materials, resin, and polyurethane foams. The TiO_2-based nanopowders and platforms demonstrated excellent performance, achieving up to ~85 % combined adsorption and degradation of methyl orange and rhodamine B, and ~80 % for tetracycline, within 180–240 min, depending on the substrate type and synthesis conditions. These breakthroughs show that TiO_2-based nanostructures can be synthesized at mild temperatures (90–230 °C) using microwave-assisted methods and be easily integrated into eco-friendly substrates while enabling sustainable water purification. Moreover, this PhD thesis aligns with the United Nations Sustainable Development Goals by promoting circular economy principles through the development of reusable and eco-friendly materials, fine-tuned to improve water quality.

Keywords: TiO_2 nanostructures, Sustainable water remediation, Microwave-assisted syntheses, Eco-friendly platforms, Photocatalysis

RESUMO

A vasta contaminação dos ecossistemas aquáticos apresenta desafios ambientais urgentes, impulsionando uma investigação intensiva em tecnologias avançadas para a remediação sustentável da água. As nanoestruturas de dióxido de titânio (TiO_2) têm-se destacado devido às suas estabilidades físico-químicas, relação custo-benefício e eficiência catalítica. No entanto, o TiO_2 possui um hiato energético largo, o que restringe a sua utilização à região do ultravioleta. Para melhorar a sua capacidade de absorção à luz visível, várias estratégias foram exploradas, incluindo o fabrico heteroestruturas (nitreto de carbono grafítico/TiO_2), engenharia de defeitos, bem como dopagem com 2 elementos abundantes: Fe e Ca. Para ultrapassar as limitações associadas à recuperação e reciclabilidade dos nanopós, as nanoestruturas à base de TiO_2 sintetizadas por irradiação micro-ondas foram incorporadas ou sintetizadas diretamente em substratos ecológicos, flutuantes e não flutuantes. Estes substratos incluíram a cortiça, materiais à base de celulose, resina e esponjas de poliuretano. Os nanopós à base de TiO_2 e as plataformas demonstraram um desempenho excelente, alcançando até cerca de 85 % de adsorção e degradação de laranja de metileno e rodamina B, e aproximadamente 80 % para a tetraciclina, em 180 a 240 minutos, dependendo do tipo de substrato e das condições de síntese. Estes avanços provam que as nanoestruturas à base de TiO_2 podem ser sintetizadas a temperaturas moderadas (entre os 90 e os 230 °C) utilizando métodos assistidos por micro-ondas e facilmente integradas em substratos amigos do ambiente, ao mesmo tempo que possibilitam a purificação sustentável da água. Além disso, esta tese de doutoramento está alinhada com os Objetivos de Desenvolvimento Sustentável das Nações Unidas ao promover os princípios de economia circular através do desenvolvimento de materiais reutilizáveis e ecológicos, otimizados para melhorar a qualidade da água.

Keywords: Nanoestruturas de TiO_2, Remediação sustentável da água, Sínteses assistidas por micro-ondas, Plataformas ecológicas, Fotocatálise

CONTENTS

LIST OF FIGURES

LIST OF TABLES

ABBREVIATIONS AND ACRONYMS

0D	Zero-Dimensional
1D	One-Dimensional
2D	Two-Dimensional
3D	Three-Dimensional
AB1	Acid Black 1
ABF	Atomic-resolution annular Bright-Field
AFM	Atomic Force Microscopy
AM	Additive Manufacturing
AM0	Air Mass 0 Spectrum
AM1.5	Air Mass 1.5 Spectrum
AOPs	Advanced Oxidation Processes
ASTM	American Society for Testing and Materials
ATR	Attenuated Total Reflection
BET	Brunauer-Emmett-Teller
BF	Bright-Field
BiNFi-s	Biomass Cellulose Nanofibers
BNC	Bacterial Nanocellulose
BOD	Biological Oxygen Demand

BPA	Bisphenol A
BQ	p-benzoquinone
CB	Conduction Band
COD	Chemical Oxygen Demand
DFT	Density-Functional Theory
DG97	Direct Green 97
DIW	Direct Ink Writing
DMF	N,N-Dimethylformamide
DMSO	Dimethyl Sulfoxide
DRS	Diffuse Reflectance Data
EDS	Energy Dispersive X-ray Spectroscopy
EDTA	Ethylene Diamine Tetra Acid
EG	Ethylene Glycol
EP	European Pharmacopoeia
EPR	Electron Paramagnetic Resonance
ESI	Electronspray Ionization
FDM	Fused Deposition Modeling
FEG	Field Emission Gun
FFT	Fast Fourier Transform
FIB	Focused Ion Beam
FTIR	Fourier Transform Infrared Spectroscopy
FWHM	Full-Width at Half Maximum
GL 30	Gaussian (70 %)–Lorentzian (30 %) components
HAADF	High-Angle Annular Dark-Field
HCBPR	Horizontal Circulating Bed Photocatalytic Reactor

HRMS	High-resolution Mass Spectrometry
ICDD	International Centre for Diffraction Data
IPA	Isopropanol
IPMA	Instituto Português do Mar e da Atmosfera
IR	Infrared Radiation
ITO	Indium Tin Oxide
IUPAC	International Union of Pure and Applied Chemistry
LC	Liquid Chromatography
LED	Light-Emitting Diode
L-H	Langmuir-Hinshelwood
MB	Methylene Blue
MCE	Mixed Cellulose Esters
MO	Methyl Orange
MOS	Metal Oxide Semiconductors
MS	Mass Spectrometry
M-S	Mott-Schottky
M_w	Molecular Weight
MW/MWs	Microwave(s)
NHE	Normal Hydrogen Electrode
NS	No Scavengers
PAA	Polyacrylic Acid
PANI	Polyaniline
PEG	Polyethylene Glycol
PL	Photoluminescence
PLE	Photoluminescence Excitation

PU	Polyurethane
PVA	Polyvinyl Alcohol
rGO	Reduced Graphene Oxide
RhB	Rhodamine B
ROS	Reactive Oxygen Species
RT	Room Temperature
SA	Sodium Azide
SDG	Sustainable Development Goal
SE	Secondary Electrons
SEM	Scanning Electron Microscopy
SLA	Stereolithography
SLS	Selective Laser Sintering
STE	Self-Trapped Excitons
STEM	Scanning Transmission Electron Microscopy
STP	Standard Temperature and Pressure
TC	Tetracycline
TCPP	Tetra(4-carboxyphenyl)porphine
TEM	Transmission Electron Microscopy
TOC	Total Organic Carbon
TP/TPs	Transformation product(s)
TSS	Total Suspended Solid
TTIP	Titanium Isopropoxide
UHPLC	Ultra-High Performance Liquid Chromatography
US	Ultrasonic
UV	Ultraviolet

UV-VIS	Ultraviolet-Visible
UV-VIS-NIR	Ultraviolet-Visible-Near Infra Red
VASP	Vienna Ab initio Simulation Package
VB	Valence Band
XPS	X-ray Photoelectron Spectroscopy
XRD	X-ray Diffraction

SYMBOLS

h_0	Thickness
$\mathbf{V_0}$	Oxygen vacancies
λ_{max}	The wavelength at which a substance has its most substantial absorption
A_0	Initial absorbance
A_t	Absorbance of pollutant solution after a certain exposure time
B_t	Boyd parameter
C_0	Initial concentration
C^1	Value of the intercept of the 1st stage (intraparticle equation)
C^2	Values of the intercept of the 2nd stage (intraparticle equation)
C^3	Value of the intercept of the 3rd stage (intraparticle equation)
C_e	Equilibrium concentration
C_{int}^2	Interfacial capacitance
$C_{intraparticle}$	Boundary layer effect in the intraparticle diffusion equation
C_{TC}	Concentration of tetracycline
$Dead_{24\ h}$	Number of dead *A.Salina* nauplii 24 h after incubation
$Dead_{Total}$	Total number of dead *A.Salina* nauplii
$E^{\circ}_{Ag/AgCl}$	Reference potential measured against Ag/AgCl (0.1976 V *vs.* NHE at 25 °C)
E_{added}	Energies of the atoms added to form the defect (DFT calculations)
$E_{Ag/AgCl}$	Potential measured against Ag/AgCl
E_{CB}	Conduction band potential

E_{defect}	Total energy of a supercell of defective TiO_2 (DFT calculations)
E_F	Fermi energy
$E_{FB\ (NHE)}$	Flat band potential converted into NHE potential
E_{FB}	Flat band potential
E_{form}	Formation energies (DFT calculations)
$E_{pristine}$	Total energy of a supercell of pristine TiO_2 (DFT calculations)
$E_{removed}$	Energies of the atoms removed to form the defect (DFT calculations)
E_{VB}	Valence band potential
K_{ad}	Adsorption equilibrium constant
$M_{perlitre}$	Weight of the adsorbent used per litre of solution (Bangham's model equation)
N_d	Electron donor density
R^2	Statistical symbol that refers to the correlation coefficient
R_B^2	Statistical symbol that refers to the correlation coefficient for the Bangham or Boyd model
$V_{solution}$	Volume of solution
a_B	Constant in Bangham's model equation
a_e	Initial adsorption rate constant in Elovich equation
b_e	Extent of surface coverage and activation energy for chemisorption in Elovich equation
f_0	Resonance frequency of an isolated tip-cantilever system
k_1	Pseudo-first-order rate constant of adsorption
k_2	Pseudo-second-order rate constant of adsorption
k_{ap}	Apparent rate constant
k_b	Constant in Bangham's model equation
k_{id}	Intraparticle diffusion rate constant
k_{id}^1	Intraparticle diffusion rate constant of the 1st stage
k_{id}^2	Intraparticle diffusion rate constant of the 2nd stage

k_{id}^{3}	Intraparticle diffusion rate constant of the 3rd stage
k_r	Rate constant
n_a	Apparent or pseudo-reaction order
p_0	Saturation vapour pressure of the adsorptive (analysis gas) at a given temperature
q_e	Adsorption capacity uptake at the equilibrium
q_e^{cal}	Calculated quantity of pollutant adsorbed at the equilibrium time
q_e^{exp}	Experimental quantity of pollutant adsorbed at the equilibrium time
q_{max}	Maximum adsorption capacity
ε'	Dielectric constant (dielectric loss tangent equation)
ε''	Dielectric loss fator (dielectric loss tangent equation)
ε_0	Vacuum permittivity
ε_r	Dielectric constant
μ'	Microwave permeability (indicates the magnetic energy stored within the material)
μ''	Microwave permeability (represents the magnetic energy that can be converted into thermal energy)
h	Planck constant
k	Spring constant of the cantilever
ℓ	Length
pKa	Acid dissociation constant at logarithmic scale
v	Velocity
θ	Angle
λ	Wavelength
A	Absorbance
B	Energy-independent constant (Tauc equation)
C	Concentration of the organic pollutant at a given time
D	Penetration depth
E	Energy (DFT calculations)

F	Fraction of contaminant adsorbed at any time (Boyd model)
I	Current
K	Boltzmann constant
M	Mortality (%) of *A. Salina* nauplii
R	Reflectance
T	Temperature
V	Electric potential or voltage
W	Mass of adsorbent/catalyst
a	Lattice parameter
b	Lattice parameter
c	Lattice parameter
c	Speed of light
e	Electron charge
f	Ordinary frequency
k	Absorption coefficient (K-M function)
m	Constant that depends on the nature of the electronic transition (Tauc equation)
p	Absolute pressure
q	Adsorption capacity uptake at any time
r	Degradation rate
s	Scattering coefficient
t	Time
v	Photon's frequency
α	Absorption coefficient (Tauc equation)
ρ	Density
ω	Angular frequency

1 INTRODUCTION

1.1 Structure of the thesis

Chapter 1 presents the motivation, state-of-the-art and objectives of this thesis. Chapter 2 describes in detail the employed experiments, models and simulations. The next 6 chapters are divided into two main sections:

1. Development and characterization of pure TiO_2 nanostructures
   1.1. Incorporated on cork (Chapter 3)
   1.2. Incorporated on three-dimensional (3D)-printed macro-architectures (Chapter 4)
2. Development and characterization of modified TiO_2 nanostructures. The strategies employed to enhance the visible-light absorption of TiO_2 were:
   2.1. The construction of a heterostructure (graphitic carbon nitride (g-C_3N_4)/TiO_2) (Chapter 5)
   2.2. The introduction of surface defects by microwave irradiation using different solvents (ethanol, isopropanol (IPA) and water) (Chapter 6)
   2.3. Doping
      2.3.1. With iron (Fe^{2+}) ions (Chapter 7)
      2.3.2. With calcium (Ca^{2+}) ions (Chapter 8)

Chapter 9 provides the final remarks and outlines future perspectives. Lastly, Chapter 10 presents the outputs of this PhD thesis.

1.2 Motivation

This work is motivated by rising concerns over environmental pollution caused by organic pollutants in water streams worldwide, making their degradation an urgent priority [1]. Simultaneously, multiple challenges threaten progress toward achieving Sustainable Development Goal (SDG) 6 set by the United Nations (UN) ("Ensure access to water and sanitation for all") by 2030. The main obstacles include water scarcity and pollution [2].

To accomplish the ambitious objective of ensuring clean water for everyone, it is crucial to conduct research that monitors the amount of pollutants in water and to develop effective water treatment solutions that can purify wastewater [3]. To overcome this last issue, over the last few years, the development of novel and advanced nanotechnology-based solutions for the treatment of polluted effluents has been gaining increasing awareness [4]. Typical factors of interest in these nanotechnology-based solutions include efficacy, efficiency, cost, product

lifetime, and environmental and social impacts [4]. If current technologies are insufficient and/or inappropriate for effective wastewater treatment, novel, sustainable and low-cost materials and technologies that can offer several advantages such as efficiency and appropriateness need to be developed [4].

Photocatalysis is an eco-friendly technology with great potential for the total mineralization of organic water pollutants. Photocatalytic experiments also enable the use of solar energy, which makes the catalytic processes economically viable for large-scale applications while adding environmental value and supporting the achievement of SDG 6 [3,5,6].

Among the various photocatalysts studied, nanoscale TiO_2 structures have garnered significant attention for their ability to degrade various organic pollutants. Even though visible light constitutes a significant portion of the solar spectrum, TiO_2 has a wide band gap and, thus, mainly absorbs in the ultraviolet (UV) region. Moreover, it suffers from a high recombination rate between the photo-generated electron-hole pairs, and it possesses low adsorption ability for organic impurities due to its polar and non-porous surface, as well as for hydrophobic contaminants [7]. Another major drawback concerns the recyclability and recoverability of nano-sized TiO_2 from treated water. To avoid the limitations and costs associated with the recovery of nanometer-sized particles and to enable easy recovery and recycling of photocatalysts in practical photocatalytic applications, the functionalization of TiO_2-based nanostructures on different sustainable substrates is an excellent alternative [8–10].

One advantage of TiO_2-based nanostructures is the flexibility in the production routes, including sol–gel, atomic layer deposition, spray pyrolysis, sputtering, electrospinning, and hydrothermal/solvothermal production methods assisted by microwave irradiation [5,9]. Compared with conventional energy-intensive processes, TiO_2-based nanomaterials can be rapidly produced using microwave-assisted methods. These methods are also straightforward, safe, and environmentally friendly, especially when water is used as the solvent. Furthermore, they allow the operation at low temperatures, facilitating the direct integration of nanostructures onto various eco-friendly substrates [11] while guaranteeing high photocatalytic performance of the synthesized platforms [12]. Despite being an attractive method to synthesize nanostructures, more focus should be given to the fabrication of these nanostructures by using simple and fast microwave approaches without the need to calcinate the samples [18,27].

Considering these challenges, this PhD research aims to fabricate and characterize TiO_2-based nanopowders, as well as their integration on sustainable platforms using microwave-

assisted syntheses. The novelty of this work lies in the development of sustainable TiO_2-based materials and platforms through simple and less energy-consuming microwave-assisted approaches for water remediation.

1.3 Water pollution and organic pollutants

Liquid surface water comprises more than 97 % of the Earth's hydrosphere, with 96 % being saltwater from the oceans and 1.1 % as fresh liquid water. Of this 1.1 %, 99 % corresponds to groundwater, leaving only 1 % as fresh surface water. Despite its small percentage, fresh surface water is essential for human society's development and basic needs, having a major influence on the quality of human life and ecosystems [13,14]. Climate change, population growth, development of industrialization coupled with water mismanagement and overconsumption have led to a deterioration of the available water resources [15]. The United Nations (2024) projects that by 2030, 2 billion people will still lack access to adequate drinking water services, 3 billion to safely manage sanitation, and 1.4 billion to basic hygiene services [16]. Moreover, according to data from early February 2025 on the European Commission website, southern and eastern Europe, particularly the Mediterranean, Middle East, and Black Sea regions, are experiencing severe, prolonged, and critical drought conditions. Some areas of the Mediterranean, such as southeastern Spain, remain under persistent alert status with substantial effects on the vegetation [17]. Therefore, enhanced water management, together with surface water quality monitoring should be implemented to ensure safe and hygienic water use [13,18].

Although several water quality parameters are targeted in sewage treatment plants, such as turbidity, color, pH, alkalinity, chemical oxygen demand (COD - corresponds to the amount of oxygen required to oxidize an organic compound to carbon dioxide (CO_2) [19]), total organic carbon (TOC- corresponds to the total amount of carbon atoms covalently bonded in organic molecules in a water sample [20]) and total fecal coliforms [21], multiple toxic and recalcitrant organic contaminants (such as alkanes, aliphatic, alcohols and aromatic compounds [22]), as well as inorganic (such as alkaline compounds, nitrate or nitrite, sulphate and heavy metal ions [22]) are constantly being released to aquatic systems, making the wastewater treatment of effluents an ecological challenge [23,24].

Dyes, which are widely used in the textile, pharmaceutical, food, cosmetics, plastics, photographic and paper industries are a significant polluter of the environment [25]. Since these

contaminants do not bind tightly to fabric, they end up being released into aquatic systems and, without prior treatment, pose serious ecotoxicological threats and toxic effects on living organisms, including mutagenicity and carcinogenicity [26]. Although no recent data is available on worldwide dye production, it is estimated that around 700 thousand tonnes are produced annually, among which around 10-15 % of the total production is estimated to be discharged into the environment. In numerous European and Asian countries growing concerns about textile effluent disposal have prompted industries to implement effective wastewater treatment measures [27]. Consequently, the scientific output on dye removal from water sources has grown over the last few years [26,28].

Dyes can be divided into different groups according to their chemical structure and type of application, and they can also be separated into anionic (e.g. methyl orange (MO) [29] model dye), cationic (e.g. rhodamine B (RhB) [30] or methylene blue (MB) [31] model dyes) and non-ionic dyes (e.g. direct green 97 (DG97) [32]). For instance, RhB (N-[9-(2-carboxyphenyl)-6-(diethylamino)-3H-xanthen-3-ylidene]-N-ethylethanaminium [33]) finds applications across several sectors (e.g. paper, paint, and textile). It is a water-soluble and amphoteric dye classified as a xanthene dye. Owing to its recalcitrant nature, this dye endangers animals, plants, and humans, since it is highly toxic and carcinogenic, being often present in wastewater [33–36]. The largest and most important group of organic dyes is the azo dyes class, representing nearly 70 % of the total textile dye manufacturing [15,25]. Due to the low coloring rate on textiles, anionic dyes are discharged into the environment. MO dye is a common and stable azo dye. Its molecular structure contains aromatic bonds (–N = N–) and sulfonic (SO^{3-}) bonds attached to different functional groups such as amino, hydroxyl, methyl, nitro, carboxyl and sulfoxyl [37]. It is primarily used in the textile industry and as an acid-base indicator. Simultaneously, its environmental impact is of great concern, since it is resistant to biodegradation and can induce severe effects on animals and humans, such as gene mutation and cancer [15,38].

Pharmaceutical substances are also commonly present in effluents [39], emerging from pharmaceutical wastewater, human and veterinary antibiotics that are not completely metabolized, and out-of-date or unused antibiotics [40]. As a result, antibiotics accumulate in soils and reach aquatic environments, threatening aquatic and terrestrial organisms, as well as humans [40,41]. Although these pollutants are found at low concentrations in wastewater, surface, underground, and drinking water, they are recalcitrant, and their toxicity constitutes a significant risk to the well-being of ecosystems [42]. Moreover, the long-term existence of antibiotics in the environment may induce antibiotic-resistant bacteria and antibiotic-resistance

genes, leading to the spread of antibiotic resistance [40,43,44]. For this reason, it is essential to remove these pollutants from the environment, encompassing water and soil, to mitigate their environmental impact [45].

Among these pharmaceutical substances, tetracyclines represent the second-largest class of antibiotics globally, widely used to treat various bacterial infections and other pathological conditions. This class is frequently administered to both humans and animals and is also used as a feed additive in the agricultural sector [46–48]. A study involving 16 countries revealed that about 70 % of the world's antibiotic consumption occurs in Asia, with China accounting for a significant portion. Although research has shown that tetracycline concentrations are below the quantification limit in surface and groundwater, as well as in wastewater effluents in several European countries, even low concentrations (with an average of 0 to 20 ng. L^{-1}) pose environmental risks. Therefore, there is a need to develop new analytical methods for their detection [49,50].

These antibiotics can be categorized into three groups according to the production method. They can be produced by strains of *Streptomyces* bacteria or by biosynthesis (e.g. tetracycline (TC), chlortetracycline, oxytetracycline, demeclocycline), through semi-synthetic methods (e.g. doxycycline, lymecycline, meclocycline) or completely synthesized (e.g. tigecycline) [51–54]. Tetracycline molecules comprise a hydronaphtacene framework with four linearly condensed benzene rings. The main differences between the tetracycline analogues are the substituents at the carbons in the positions 5, 6, 7 and 9 [55]. They contain two different chromophore regions and possess three p*K*a values: pK_{a1} (protonation of oxygen bound at the carbon position 3), pK_{a2} (protonation of oxygen bound at the carbon positions 10 and 12) and pK_{a3} (protonation of dimethyl functional group at the carbon position 4) at pHs of 3.3, 7.7 and 9.7, respectively. Therefore, at pH values below pK_{a1}, they have a cationic form, at pH between pK_{a1} and pK_{a2} they are neutral (zwitterionic state) and above pK_{a3} they are anionic [46,53,56]. Table 1.1 provides a summary of the main physicochemical properties of the three organic pollutants previously mentioned (RhB, MO, and TC) and studied in this thesis.

Table 1.1: The main physicochemical properties of RhB, MO and TC.

Pollutant	Chemical formula	Chemical structure	Molecular weight (MW) ($g.mol^{-1}$)	Solubility in water ($g.L^{-1}$) @ 20 °C	Appear-ance	λ_{max} (nm)
RhB	$C_{28}H_{31}ClN_2O_3$ [57]	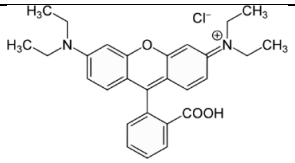 [58]	479.02 [57]	50 [57,59]	Reddish-violet powder [60]	554 [35]
MO	$C_{14}H_{14}N_3NaO_3S$ [61]	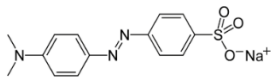 [61]	327.34 [61]	0.5 [62]	Orange powder [63]	464 [15]
TC	$C_{22}H_{24}N_2O_8$ [64]	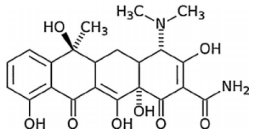 Requested with permission from [65]	444.4 [64]	0.231 (Very slightly soluble in water) [64]	Yellow powder [64]	360 [66]

1.4 Wastewater treatment processes and technologies

When water becomes contaminated and requires purification, the optimal treatment method should be chosen according to the decontamination standards established by each country [67]. There are five phases from which wastewater goes through to be converted into different products, according to the desired use. These phases consist of preliminary, primary, secondary, tertiary treatments, and a final stage to treat the sludge formed. The preliminary treatment eliminates the (floating) solid particles from the effluent by mechanical or physical means. Then, in the primary treatment, physicochemical and chemical methods are used, such as coagulation, precipitation and flocculation to remove the total suspended solid (TSS) load and turbidity. During the secondary treatment, which involves chemical and biological methods, aerobic organisms decompose the solid waste. The aim is to reduce organic matter in the form of biological oxygen demand (BOD - a measure of the amount of oxygen required to remove organic matter from water in the process of decomposition by aerobic bacteria)/COD, and other pollutants, such as ammoniacal nitrogen. The tertiary treatment (physical and

chemical methods) ensures that the final product is free from any impurities or chemicals that could harm the ecosystem by using techniques such as filtration and disinfection. The last step involves sludge treatment, including supervised tipping, recycling, or incineration [68–71].

Wastewater treatment supports the circular economy by serving as a source of energy, clean water, fertilizers, and nutrients. Nevertheless, it is challenging to extract its full potential, due to the need for more efficient and advanced sustainable approaches [72]. A broad selection of techniques can be used to treat wastewater, with the most frequent methods involving physical, chemical, and biological processes. Physical treatments such as adsorption, membrane filtration and reverse osmosis consist in the removal of pollutants by physical means [22]. These treatments have proved to be efficient in treating industrial pollutants from effluents [15]. However, their major drawbacks are the increased sludge formation volume and the high maintenance costs [15]. On the other hand, biological treatment methods use microorganisms to break down organic compounds being eco-friendly and generally inexpensive methods [15]. These processes commonly include biological adsorption, accumulation, and biodegradation [73]. However, achieving complete mineralization of contaminants becomes difficult when more complex molecules are involved [15]. Additionally, these biological methods are limited by strict environmental regulations, operate at a slow degradation rate, and carry the potential risk of introducing species that could cause harmful long-term effects [73]. Chemical treatments, such as advanced oxidation processes, electrochemical, Fenton reactions, oxidation and ozonation consist in the degradation of pollutants in the presence of powerful oxidizing agents [74], mainly hydroxyl radicals ($^{\bullet}OH$) [73]. These hydroxyl radicals can attack organic molecules through hydrogen abstraction, combination or addition of radicals, and electron transfer [75] while possessing a high redox potential (2.8 eV) and non-selective properties [75]. However, beyond the advantages and disadvantages of each treatment method, choosing the right technology also involves considering factors like affordability and suitability from economic, social and environmental perspectives [76].

1.5 Advanced oxidation processes

Advanced oxidation processes (AOPs) are becoming an increasingly important area of research for the oxidation of various water contaminants [77]. These processes enable the complete mineralization of hazardous organic chemicals into carbon dioxide (CO_2), water (H_2O), and mineral acids. Moreover, they are easy to use, provide fast reaction rates and can eliminate

dissolved organic contaminants present in aqueous systems at low concentrations that are difficult to remove [78,79]. The list of advanced oxidation technologies is extensive. Nevertheless, in most systems the formation of hydroxyl radicals is frequently achieved by a combination of strong oxidants, such as hydrogen peroxide (H_2O_2), ozone (O_3), or a combination of catalysts with irradiation (e.g UV or ultrasonic (US)). AOPs can be divided into several groups: photocatalysis, Fenton-based reactions (through a combination of H_2O_2 with ferrous ions), sonolysis (using US), ozone-based reactions, electrochemical oxidation, among others, like wet oxidation and supercritical water oxidation. It is also possible to combine these technologies [77,80].

Photocatalysis, in particular, is a "green" advanced oxidation process that holds great promise, since it can utilize solar energy to its fullest extent into value-added products, such as fuels or chemicals [81]. Photocatalytic experiments are simple to conduct, they can be performed at normal ambient conditions (temperature and pressure) and pollutants can be efficiently degraded at a reduced cost [9,15,82,83].

1.5.1 Heterogeneous photocatalysis

Photocatalysis is characterized by the acceleration of chemical reactions in the presence of a catalyst, under light irradiation. Photocatalysis can be homogeneous or heterogeneous. For homogeneous photocatalysis, both reactant and catalyst are in the same phase, whereas in heterogeneous they are in different phases [6,84]. In the first type of photocatalysis, transition-metal complexes are commonly employed as homogeneous photocatalysts owing to their stability and appropriate electronic band gaps. Frequent processes for homogeneous photocatalysis include the ozone process and the photo-Fenton reaction (Fe^+ and Fe^+/H_2O_2) [85]. However, heterogeneous systems offer more efficient and environmentally friendly post-reaction operations, such as easier separation of the catalyst from the reaction medium and catalyst reusability, thus being the most explored approach [86,87]. Since 1972 with the discovery of UV light-induced water splitting into hydrogen and oxygen at the TiO_2 anode by Fujishima and Honda [88,89], significant efforts have been devoted toward heterogeneous photocatalysis, particularly to degrade organic pollutants from air and water [90].

Heterogeneous photocatalysis typically employs inorganic semiconductor oxides as photocatalysts [90]. The entire photocatalytic process can be divided into 5 steps [91]:

1. Mass transfer of reactants (organic molecules) from the fluid to the catalyst surface
2. Adsorption of organic molecules on the photocatalyst surface
3. Photocatalytic reaction:

- Photon absorption by the catalyst
- Photogeneration of electron-hole pairs
- The charges are transferred to the catalyst surface and induce the redox reactions

4. Desorption of the product from the reaction
5. Mass transfer of the products from the interfacial region to the fluid.

In step 3, when the semiconductor photocatalyst is irradiated with light of higher energy than its band gap, the photons' energy is absorbed, electrons from the valence band (VB) are excited to the conduction band (CB) and electron-hole pairs are created equation (1.1). If the recombination of electrons and holes does not occur, electrons and holes can migrate to the surface of the photocatalysts and participate in redox reactions. Holes will oxidize water molecules and form superoxide radical species ($^{\bullet}O_2^-$), equation (1.2), while electrons will reduce oxygen molecules and generate $^{\bullet}OH$, equation (1.3). The superoxide radicals will be further protonated to harvest hydro-peroxyl radicals ($HOO^{\bullet}$) and subsequently hydrogen peroxide (H_2O_2) and hydroxyl radicals are formed, equations (1.4), (1.5), (1.6), (1.7) and (1.8). These hydroxyl radical species will be further responsible for the decomposition of organic compounds [84,92], equation (1.9). The reactions that occur can be written as follows [93]:

$$\text{Semiconductor} + h\nu \rightarrow e_{CB}^- + h_{VB}^+ \quad (1.1)$$

$$H_2O + h_{VB}^+ \rightarrow H^+ + {}^{\bullet}OH \quad (1.2)$$

$$O_2 + e_{CB}^- \rightarrow {}^{\bullet}O_2^- \quad (1.3)$$

$${}^{\bullet}O_2^- + H^+ \rightarrow HO_2^{\bullet} \quad (1.4)$$

$$HO_2^{\bullet} + HO_2^{\bullet} \rightarrow H_2O_2 + O_2 \quad (1.5)$$

$$H_2O_2 + e_{CB}^- \rightarrow OH^- + {}^{\bullet}OH \quad (1.6)$$

$$H_2O_2 + {}^{\bullet}O_2^- \rightarrow {}^{\bullet}OH + OH^- + O_2 \quad (1.7)$$

$$H_2O_2 + h\nu \rightarrow 2{}^{\bullet}OH \quad (1.8)$$

$$\text{Organic compounds} + {}^{\bullet}OH \rightarrow \text{Reaction intermediates} \rightarrow CO_2 + H_2O \quad (1.9)$$

Since the last decade, photocatalysis has been used due to its sustainable character, and employed in a wide range of applications, including water/wastewater treatment [94], air purification [95], antibacterial [96], self-cleaning treatments [97], among others.

In heterogeneous photocatalysis, the common reaction mechanisms include the Langmuir–Hinshelwood (L-H), Eley–Rideal (for gas-phase reactions), and Mars–van Krevelen mechanisms (for gas-phase reactions) [98]. In liquid-phase photocatalytic reactions, most systems follow the Langmuir–Hinshelwood (L-H) model [90].

1.5.1.1 Langmuir-Hinshelwood (L-H) kinetic model

The most frequently used kinetic model to explain the kinetics of the heterogeneous photocatalytic reactions is the L-H model, equation (1.10).

$$r = -\frac{dC}{dt} = \frac{k_r K_{ad} C}{1 + K_{ad} C} \tag{1.10}$$

in which r represents the degradation rate (mg. (L. min)$^{-1}$), C is the concentration of the organic pollutant (mg. L^{-1}) at a given time (t), k_r is the rate constant of reaction and K_{ad} the adsorption equilibrium constant (L. mg^{-1}) [9,99]. After integration in the interval [C, C_0], it is simplified to the pseudo-first-order-kinetics equation with an apparent rate constant (k_{ap}= $k_r K_{ad}$) and if we consider that the adsorption is weak, as well as the concentration of organic pollutants, the factor $K_{ad}C$ can be negligible and thus equation (1.11) is obtained [9]:

$$\ln\left(\frac{C}{C_0}\right) = -k_{ap} t \tag{1.11}$$

Based on equation (1.11), the rate constants k_{ap} (min^{-1}) can be determined by plotting $\ln\left(\frac{C}{C_0}\right)$ *vs.* time (t), in which the slope of the linear regression is the apparent rate constant [9,99].

This model assumes that reactants initially adsorb onto the catalytic surface, where the reaction occurs with the subsequent desorption of the reaction products [98]. The photodegradation rate of organic molecules in the presence of photocatalysts also follows the Langmuir-Hinshelwood model considering four possible scenarios: the reaction occurs between two adsorbed substances, the reaction occurs between a radical in solution and an adsorbed molecule, a radical in solution reacts with an adsorbed pollutant molecule, a surface-bounded radical on the photocatalyst reacts with a pollutant molecule in solution, or the reaction occurs between a radical and pollutant molecule present in solution [99].

1.6 Semiconductor photocatalysts

The photocatalytic activity is directly related to the photocatalysts, and it is well known that as the size of a material decreases down to the nanometer scale, new properties in it may emerge when compared to their bulk counterparts, particularly due to a higher surface area and surface-to-volume ratio. Additionally, nanomaterials may also exhibit quantum effects at the nanoscale. These properties, among others, might facilitate the reactions/interactions of a photocatalyst with the water pollutant for efficient photocatalytic degradation [100].

Nanostructures are materials with at least one dimension in the nanometer scale (between 1 and 100 nm). Such nanostructures can possess a zero-dimensional (0D), one-dimensional (1D), two-dimensional (2D) or 3D structure. A 0D material contains a nanometer scale in each of the three directions (x, y, z), a 1D material has a nanometer scale only in two directions, while a 2D structure has a nanometer scale only in one direction. For 3D nanostructures, although their dimensions are higher than 100 nm, their construction is a hierarchical architecture that grows in all directions using 0D, 1D, and 2D nanostructures [101]. Examples of 0D nanostructures include quantum dots, nanoparticles, fullerenes, and clusters, among others [101]. 1D structures are nanotubes, nanorods, nanowires and nanoribbons [101–103]. 2D nanostructures are for instance nanosheets [15,104], whereas 3D nanomaterials include metallic-organic frameworks and aerogels [101]. Examples of 0D, 1D, 2D and 3D nanostructures are illustrated in Figure 1.1.

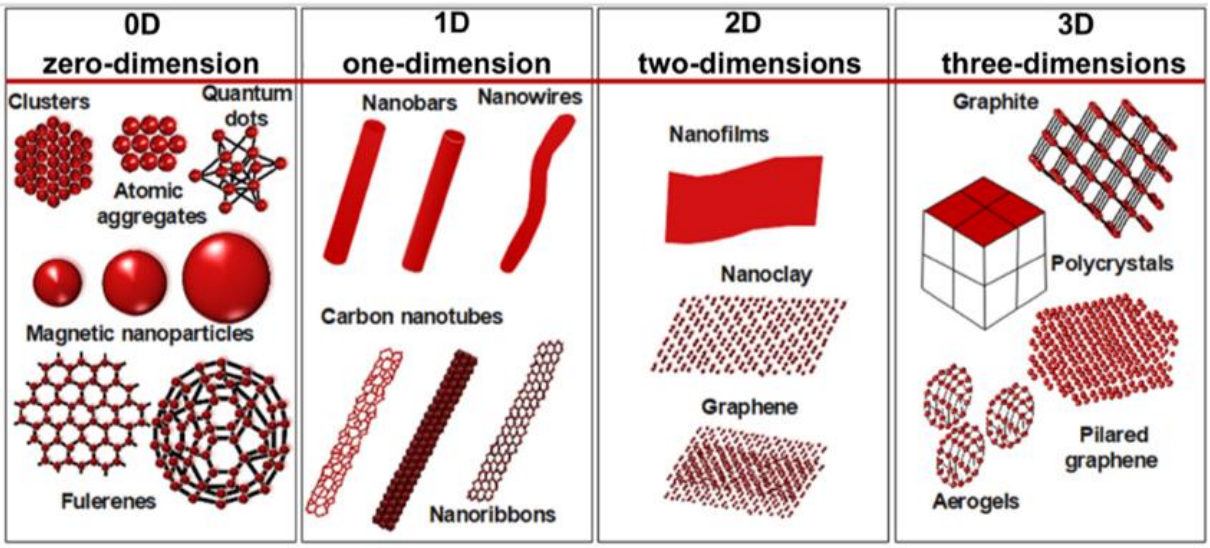

Figure 1.1: Schematic illustration with examples of 0D, 1D, 2D and 3D nanostructures. Reproduced from Ref. [105].

Extensive research has been conducted on nanomaterials as adsorbents and catalysts for water remediation owing to their unique physicochemical properties [106–108]. Indeed, depending on the material's dimensions (0D, 1D, 2D or 3D), the size and morphology of the final nanostructures will influence the final properties of the material (physical, chemical, electrical, optical, magnetic, mechanical and consequently adsorbing and catalytic) [109,110]. Other factors that determine the photocatalytic properties are, for instance, the crystallinity, band gap, preferential growth orientation, porosity and surface chemical properties [111,112], which depend greatly on the processing variables, such as applied temperature, precursors used, reactant concentrations, addition of surfactants or other chemicals and solution pH value [11,113].

Additionally, the material should be non-toxic, stable and manufactured through easy and low-cost methods [85].

For an efficient degradation of pollutants, the VB and CB edge position of the semiconductor must be more positive and negative than the potential of −OH/•OH (2.3 V *vs.* normal hydrogen electrode (NHE)) and $O_2/^{\bullet}O_2^-$ (−0.33 V *vs.* NHE) pairs, respectively [114]. Several semiconductors have suitable band gap energies, such as TiO_2, zinc oxide (ZnO), tungsten oxide (WO_3), iron (III) oxide (Fe_2O_3), and strontium titanate ($SrTiO_3$) [114], as depicted in Figure 1.2.

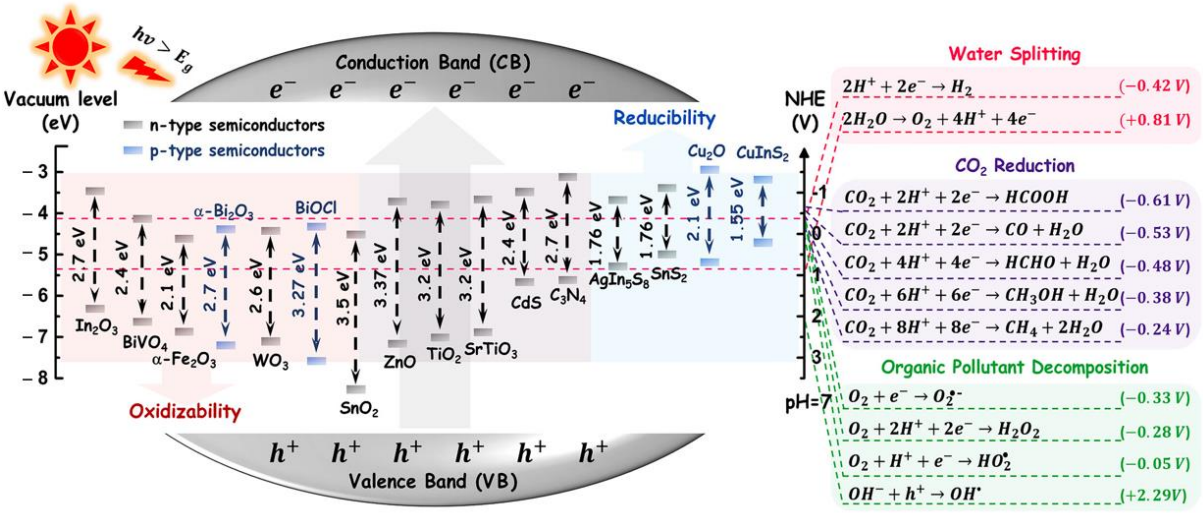

Figure 1.2: Band structures of several typical n-type and p-type semiconductors, separated into semiconductors with strong oxidation (red box, also including tin (IV) oxide (SnO_2), ZnO, TiO_2 and $SrTiO_3$ compounds) and reduction abilities (blue box, including cadmium sulfide (CdS) and graphitic carbon nitride (C_3N_4) compounds). The redox potentials (*vs.* NHE at pH = 7) for organic pollutant decomposition are illustrated in the green box. Reprinted with permission from Ref. [115].

Moreover, beyond suitable band-edge potentials, these semiconductors should exhibit low charge carrier recombination and high solar light absorption, both desirable properties in a photocatalyst [85]. There are two types of semiconductor photocatalysts: organic and inorganic [116]. These two types will be further explained in the next sections.

1.6.1 Organic semiconductors

Organic semiconductors are a class of semiconductors that exist as molecular structures and are composed of abundant elements like carbon, hydrogen, oxygen, and nitrogen [117,118]. Besides, these materials allow cost-effective processing (they can be solution-processed at low temperatures [119]) [117,120]. These materials possess several highly desirable

properties for optoelectronic device fabrication, including isomeric characteristics (e.g., stereoisomerism), optical attributes (e.g., tunable emission and lifetime), and an adjustable electronic structure that enhances their responsiveness to a broader spectrum of solar light, also making them excellent candidates for photocatalysis. Additionally, their diverse bonding modes, interaction types, and stacking patterns contribute to a wide range of electrical and optical behaviors, enabling the identification of relationships between organic molecular structure and photocatalytic efficiency [121–124]. Most organic molecules contain π conjugated core and side chains. The conjugated length of their π-core and the affinity between molecules can be tailored resulting in a variety of bonding modes, interaction types, and stacking patterns by introducing, for instance, unsaturated groups to the π-core, or hydroxyl, amine, carboxyl groups to the side chains. The molecular packing frequently relies on weak non-covalent interactions, such as π-π stacking, van der Waals forces, and hydrogen bonding. Through the optimization of their molecular structure and packing, various electrical and optical properties can be achieved. Moreover, organic semiconductors often strongly absorb visible light, allowing it to be harvested during photocatalytic experiments [125]. Nevertheless, they exhibit a low dielectric constant (ε_r = 3-5, meaning a high exciton binding energy [126]), resulting in a low charge carrier mobility. In addition, due to their molecular bonds and structural disorder, organic semiconductors are susceptible to exciton trapping. Consequently, a significant portion of charge carriers undergo recombination, limiting the overall photocatalytic efficiency under visible light [124,127–130]. Nevertheless, numerous strategies have been proposed to address this inherent limitation, including crystal engineering, modulation of molecular interactions and interface engineering (e.g. 2D organic-inorganic heterostructures [131]) to achieve varied electron-transporting behavior and enhance their responsiveness to a wider range of solar spectrum [124,130].

1.6.2 Inorganic semiconductors

Compared to organic semiconductors, inorganic semiconductors are composed of inorganic elements such as silicon (Si) or germanium (Ge) from IV and VI groups of the periodic table, or compound semiconductors like gallium arsenide (GaAs) [132,133]. The atoms are covalently bonded and the materials possess higher charge carrier mobility and better stability under mechanical, electrical, and environmental stress [119,134].

1.6.2.1 Metal oxides and metal oxide semiconductors (MOS)

Metal oxides are a class of materials largely explored in photocatalysis. They are composed of positive metallic and negative oxygen ions [135], in contrast to conventional covalent semiconductors such as Si [136]. These materials can exhibit insulator, semiconductor, or metallic characteristics [137,138]. The metals used can be transition metals or main-group metals (the metals in groups 1, 2, and 13-15 of the periodic table [139]) [140]. In terms of electronic structure, the d-orbitals in most transition metals are partially filled. An important feature of transition metal ions is their capability to exhibit several oxidation states, meaning that in some cases, two or more types of oxides can be obtained from one type of transition metal [141,142].

Specifically, MOS have been widely used in heterogeneous photocatalysis for the photodegradation of organic pollutants in water and air since most of them are low-cost, non-toxic and exhibit photo/chemical stabilities [143,144]. A great number of MOS are characterized by a large band gap (>3.0 eV) [74] and depending on the nature of the majority carriers (electron or holes), metal oxides can be categorized into two types: n-type and p-type. In n-type semiconductors, the majority carriers are electrons [145]. Examples of n-type semiconductors include TiO_2, WO_3, ZnO, Fe_2O_3, CdS, and bismuth tungstate (Bi_2WO_6) [146], while for p-type semiconductors, the majority carriers are holes [145], such as in bismuth oxide (Bi_2O_3), vanadium pentoxide (V_2O_5), and copper oxide (CuO or Cu_2O) [146]. Despite the ongoing search for more efficient photoactive materials under solar irradiation, TiO_2 is probably the most largely explored in heterogeneous photocatalysis, especially at the nanometer scale, and remains a benchmark photocatalyst [9,147,148].

1.6.2.1.1 TiO_2

TiO_2 is a versatile material and can be found in numerous applications (e.g. paint industry, self-cleaning, catalysis and biomedicine) [147,149–151]. Over the last years, this material has been garnering tremendous scientific and technological interest in environmental applications [147,152,153]. Due to its reduced toxicity, cost, and enhanced physical and chemical stabilities, TiO_2 is highly appealing for photocatalytic applications [135,154].

1.6.2.1.2 TiO_2 properties

TiO_2, an n-type semiconductor [155], has three naturally occurring polymorphs: anatase, brookite, and rutile. TiO_2 rutile and anatase forms present a tetragonal lattice, while brookite has an orthorhombic system. Rutile is the most stable form at higher temperatures,

whereas anatase and brookite are metastable and are easily transformed to rutile when heated. The band gap energies also vary according to the crystalline phase: 3.0 eV for rutile, 3.2 eV for anatase and ranging from 3.1 to 3.4 eV for brookite, at room temperature [92,156]. Brookite is difficult to synthesize, hence it is the least explored TiO_2 phase in photocatalytic applications when compared to rutile and anatase phases [156,157]. Despite that, the brookite phase has been observed as a by-product when the synthesis is carried out in an acidic medium at relatively low temperatures [156]. The synthesis parameters will determine the nucleation and growth of the different TiO_2 polymorphs, and consequently the physical, optical, electrical and chemical properties of TiO_2 [158].

The crystal structure of these TiO_2 polymorphs is related to the different spatial arrangements of TiO_6 octahedra, where each Ti^{4+} ion is surrounded by six O^{2-} ions (see the structure geometries in Table 1.2. In the tetragonal structure of anatase, each octahedron shares corners to form (001) planes, while in the rutile tetragonal structure, the (001) planes are formed by edge-sharing octahedrons. The orthorhombic structure of brookite consists of corner and edge-sharing octahedra [159]. Table 1.2 shows a summary of the most important properties of each naturally occurring TiO_2 polymorphs (anatase, rutile and brookite).

Table 1.2: Summary of the most important properties of the naturally occurring TiO_2 polymorphs (anatase, rutile and brookite).

	Anatase	Rutile	Brookite
Crystal structure	Tetragonal [160]	Tetragonal [160]	Orthorhombic [160]
Lattice constant (Å)	a = 3.79 [161] c = 9.51 [161]	a = 4.59 [161] c = 2.96 [161]	a = 9.17 [161] b = 5.46 [161] c = 5.14 [161]
Space group	$I4_1/amd$ [160]	$P4_2/mnm$ [160]	Pbca [160]
Density (ρ) (g/cm^3)	3.894 [160]	4.25 [160]	4.12 [160]
Refractive index	2.5688 [162]	2.9467 [162]	2.8090 [162]
Band gap (eV)	3.2 [32]	3.0 [32]	3.1−3.4 [32]
Structure geometry	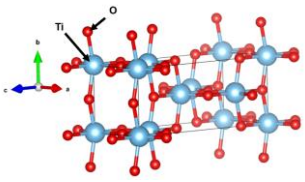 Source: Crystallography Open Database (7206075.cif)	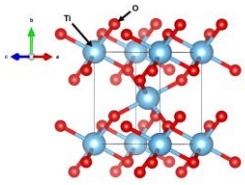 Source: Crystallography Open Database (9015662.cif)	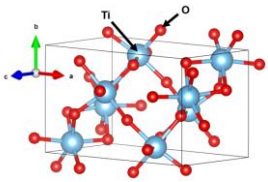 Source: Crystallography Open Database (9004139.cif)

Beyond the three common polymorphs of TiO_2 (anatase, rutile, and brookite), several additional phases are known, including high-pressure metastable structures such as TiO_2-B (a monoclinic crystal system), TiO_2-II (columbite-type, orthorhombic system), TiO_2-III (baddeleyite-type, orthorhombic system), TiO_2-R (a ramsdellite-like form, orthorhombic system) [163], TiO_2-H (hollandite-like form, orthorhombic system) [164], cubic TiO_2 (cubic system) [165],

TiO_2-OI (orthorhombic system) and TiO_2-OII (cotunnite ($PbCl_2$) structure-like, orthorhombic system) [166]. These phases are typically stabilized under high-pressure conditions, which limits their practical applicability. However, they remain the subject of active theoretical and experimental research. Studies have highlighted their potential in applications such as energy storage and photocatalysis [167–169].

Other phases were observed such as the Magnéli TiO_2 phases. These phases are sub-stoichiometric forms of TiO_2 and are characterized by the general formula Ti_nO_{2n-1} (where n ranges from 4 to 10). They are also notable for their excellent high conductivity, comparable to graphene, and chemical resistance, making them well-suited for electronic and catalytic applications. Their synthesis typically involves the reduction of TiO_2 in controlled environments, often employing high temperatures ranging between 850 and 1300 °C [170].

TiO_2 can also be found in an amorphous phase. However, the photocatalytic activity of this phase is negligible compared to TiO_2 crystalline phases [155]. In terms of photocatalytic activity, anatase TiO_2 (as a single phase) has shown superior photocatalytic activity to rutile or brookite. It has been reported that anatase exhibits a longer lifetime of photogenerated electrons and holes than rutile and brookite. Additionally, the average effective mass of electrons and holes in anatase is smaller than that of rutile and brookite, which favors a faster migration of photogenerated charge carriers from the interior to the surface of anatase; thus, reducing the recombination rate and improving the photocatalytic activity [35].

Although TiO_2 presents several advantages, the main drawbacks of using its pure form in photocatalytic applications are related to the wide band gap and high recombination of photogenerated electron/hole pairs [35]. Consequently, it only exhibits high photocatalytic efficiency under UV irradiation [171]. The UV contribution to the total solar spectrum (Figure 1.3) represents about 5 % [172]. Therefore, approaches for turning TiO_2 photocatalytic active under solar irradiation are imperative.

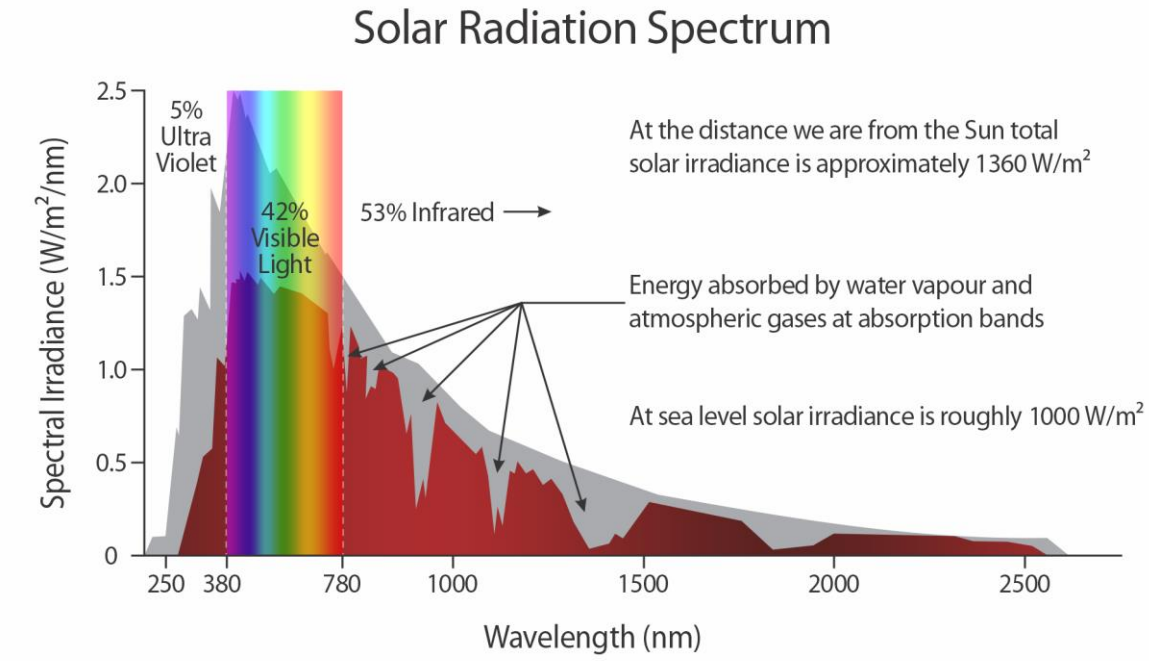

Figure 1.3: The air mass 0 spectrum (AM0) (grey area) and the air mass 1.5 spectrum (AM1.5) (red area) solar irradiation spectra show the solar energy distribution outside of the Earth's atmosphere and at the Earth's surface, respectively [173]. The AM 1.5 solar spectrum has a total radiation of 1000 $W.m^{-2}$ [174]. Reproduced from Ref. [174].

The development of photocatalysts driven by visible light and capable of harnessing the maximum possible solar energy, including visible light, is thus a key factor in improving their photocatalytic performance under solar light irradiation [175].

1.6.2.1.3 Synthesis of TiO_2-based nanostructures

The synthesis of metal oxides can be carried out through top-down or bottom-up approaches. In the first approach, the bulk material is broken down into nanoscale particles via physical methods, such as milling, exfoliation, sputtering and pulsed laser ablation techniques. The resulting nanomaterials are generally of excellent quality and display high crystallinity. Conversely, in the bottom-up approach, atomic nuclei are combined through self-assembly to form nanoparticles through techniques like chemical vapor deposition, sol–gel, hydrothermal and solvothermal methods, among others. The bottom-up approach has attracted attention since it allows control over the composition, morphology, and size of the nanostructures [176,177].

Various chemical and physical methods have been developed for the synthesis of TiO_2-based nanomaterials, including sol–gel [178,179], atomic layer deposition [180],

electrospinning, anodization [181], sputtering [182], ultrasonic irradiation [183], flame synthesis [183], hydrothermal/solvothermal production methods, including hydrothermal/solvothermal assisted by microwave irradiation [5,9,157,184].

Hydrothermal/solvothermal synthesis

Among these methods, hydrothermal/solvothermal synthesis is one of the most popular production routes for preparing nanomaterials and a broad range of nanostructures have already been produced through this approach [185–187]. In this technique, chemical reactions occur for the synthesis of inorganic compounds in the presence of organic solvents (in solvothermal syntheses) or water (in hydrothermal syntheses) [138]. A sealed reaction vessel is used, frequently made of stainless-steel autoclave, and the temperature of solvents can be brought to around their critical points via heating and at the same time with autogenous pressures. Highly crystalline materials can be obtained without additional annealing treatments [113,188]. The nanostructures with desired particle sizes, morphologies, crystallinity, and surface functionalities depend greatly on the processing variables, such as applied temperature, precursors used, reactant concentrations, addition of surfactants or other chemicals and solution pH value [11,113]. Even though this technique is simple, safe, environmentally friendly (when water is used as solvent), and mild synthesis temperatures can be applied, essential for the integration of nanostructures on innumerous types of substrates (e.g. plastics [11], textiles [11], paper [5,184], among others), in recent years microwave irradiation has proven to be a promising alternative [35,188].

Microwave heating *versus* conventional "autoclave" method

Compared with the conventional “autoclave” method, which relies on a conduction approach, microwave irradiation has a penetration characteristic, enabling a homogeneous heat-up of the reaction solution. This results in uniform nucleation and rapid crystal growth [188,189]. Additionally, higher yields/high product purity can be obtained with a reduced processing time, the reactions are reproducible due to the presence of a uniform microwave field around the mixture and upon optimization of the microwave parameters, there is the possibility of scale-up for industrial applications [9,190]. A comparison between conventional and microwave irradiation heating can be seen in Table 1.3.

Table 1.3: Comparison between conventional and microwave heating [9,190–192].

Conventional heating	Microwave heating
Conduction heating and convection currents	Heating by microwaves
Superficial/wall heating	Coupling at molecular level (volumetric heating)
Low heating rate	High heating rate
Non-uniform heating	Uniform heating
Higher energy consumption	Lower energy consumption
Long processing time (several hours [193,194])	Short processing time (a few minutes [193,194])
Product quality and quantity can be affected	Higher product quality and quantity
Material independent	Material dependent

Numerous studies have reported the production of visible-light-activated TiO_2 nanostructures using microwave synthesis methods, like other physical and chemical techniques mentioned earlier [15,35,195,196]. In the next section the most studied and effective strategies developed to enhance the visible light absorption of TiO_2 will be discussed.

1.7 Strategies to enhance the visible light absorption of TiO_2

Several attempts have been made to extend the light-harvesting capacity of TiO_2 to the visible range, such as doping, the fabrication of heterostructures and surface defect engineering [15,197].

1.7.1 Doping

Doping is the process of intentionally introducing impurities to any intrinsic material to modify the optical, electronic, and physical properties of the material [198]. The doping mechanism can be interstitial or substitutional. In interstitial doping, the impurities are added between the host atoms without replacing them. On the contrary, in substitutional doping the impurities replace some of the host atoms in the crystal lattice of the material [199]. The introduction of dopants into the TiO_2 lattice can lead to the formation of new defect states within the band gap that could absorb photons with energies lower than the energy of the band gap, thus extending the absorption of the material to the visible light spectrum, boosting the photocatalytic efficiency under solar light [200,201].

Regarding TiO_2 doping, dopants owing comparable radii with Ti^{4+} are segregated at the substitutional position, whereas dopants with smaller radii might occupy the interstitial

sites of TiO_2 [202]. The doping of TiO_2 crystals can be achieved by either self-doping, non-metal doping, metal doping, or co-doping. Self-doping refers to a process of introducing a charged cation of the same species of the crystal structure, co-doping occurs when there are two or more dopant elements introduced into the TiO_2 lattice structure, whereas non-metal and metal doping involve respectively doping of non-metals, such as boron (B), nitrogen (N), and carbon (C), and metals, such as manganese (Mn), vanadium (V), copper (Cu), silver (Ag) and Fe [198]. The type of dopant, along with precise control over its amount and distribution within the TiO_2 structure, can be used to adjust the material's optical, electronic, and mechanical properties, broadening its potential applications [198].

The most common doping elements are transition metals, such as Sc, Ti, V, Cr, Mn, Fe, Co, Ni, Cu and Zn [203]. These elements possess partially filled d-orbitals and they have been reported to facilitate the formation of Ti^{3+} states which increases the number of oxygen defects, thus promoting the adsorption of oxygen on the titania surface. Additionally, they introduce intraband states close to the CB or VB edge, which might induce visible light absorption at sub-band gap energies. Previous calculations revealed that there is a delocalization of the 3d or 4d states of the transition metals, and frequently these states hybridize with the Ti's 3d and O's 2p states, hence modifying the TiO_2 electronic structure and improving its visible light absorption ability [35,171,204].

Surface defects, such as oxygen vacancies may also be induced due to doping, which contributes to enhancing the photocatalytic activity of nanomaterials [205]. Doping subsequently not only improves photocatalytic performance, but also leads to changes in the nanomaterials' optical, electronic, and physical properties [198]. Nonetheless, an excessive concentration of dopant may induce the creation of multiple trappings of charge carriers, which in consequence increases the electron–hole recombination and decreases the number of active charge carriers [35,205].

Doping with iron is a cost-effective strategy due to its abundance on Earth and the ease with which iron atoms can substitute titanium (Ti) atoms. Moreover, iron doping is responsible for extending the photoexcitation response of TiO_2 to the visible absorption range and enhancing the catalyst's lifetime during the photocatalytic processes [35,206,207]. With the introduction of iron atoms, new electronic states emerge within the forbidden band of the semiconductor, leading to an extension in the light absorption range [208]. Similar to iron, Ca is an inexpensive metal with promising potential in photocatalysis. Despite the limited research

available, this scarcity encourages further investigation [209,210]. The literature review on the use of these two dopants in TiO_2 will be presented below.

1.7.1.1 Doping TiO_2 with Fe^{3+} ions

Amongst the different metal ions that have been successfully incorporated, Fe (a transition metal ion) appears as an excellent candidate for doping TiO_2 due to its half-filled d-electronic configuration and the similar atomic radius of Fe^{3+} ion (0.69 Å) and Ti^{4+} ion (0.75 Å). The titanium positions in the TiO_2 lattice can be easily substituted by the cation Fe^{3+}, which is reported to provide trap centers for photogenerated electrons and holes since the energy level of Fe^{2+}/Fe^{3+} is located near Ti^{3+}/Ti^{4+}; thus, enhancing the charge separation [35]. Several studies have reported that Fe doping enhanced the photocatalytic performance of TiO_2 compared to other metals or intrinsic TiO_2. For instance, Crişan *et al.* studied the effect of three transition metal ion dopants: Fe, cobalt (Co), and nickel (Ni) on TiO_2 for the degradation of nitrobenzene in water. The best photocatalytic activity results were achieved with Fe-doped TiO_2 nanopowder in 120 min under UV-VIS light irradiation (λ = 300–500 nm). The material reached ~85% degradation for a concentration of 0.5 wt. % Fe [211]. Sahoo and his team synthesized various metal ion-doped TiO_2 microstructures using a 1 mol. % concentration of different metal ion precursors, including silver nitrate, ferrous sulfate, and ferric nitrate solutions. TiO_2 was doped with Ag^{2+}, Fe^{2+}, and Fe^{3+} ions, and the resulting materials were evaluated for their photocatalytic efficiency in degrading MB and Acid Blue 93. Under visible light, Fe^{3+}-doped TiO_2 emerged as the most effective photocatalyst, achieving around 96% and 90% decolorization of MB and Acid Blue 93, respectively, within 180 minutes of light exposure [212]. Afonso *et al.* also demonstrated the outstanding performance of Fe-doped TiO_2 photocatalysts. The material with a TiO_2:$FeCl_3$ weight ratio of 1:1.6 exhibited the highest photocatalytic activity, achieving a RhB degradation efficiency of 93.8 % after 3 h of simulated solar light irradiation [213]. Another study showed that a TiO_2 catalyst doped with 0.5 mol. % Fe achieved a 92 % removal efficiency of bisphenol A (BPA) under simulated solar light [214]. Moreover, Sood *et al.* developed Fe-doped TiO_2 nanoparticles with improved performance in degrading p-nitrophenol, obtaining a degradation value of 92 % in 5 h when the Fe^{3+} molar concentration was 0.05 mol. %, under visible light irradiation and without the addition of oxidizing reagents [215]. Nevertheless, in terms of increasing TiO_2 photocatalytic activity with iron doping, some studies reported the opposite behavior. Multiple factors can contribute to the inconsistencies reported in the literature, including disparities in synthesis methods, annealing temperatures,

the organic compounds used for the photocatalytic tests, and the concentration of the iron dopant [35].

1.7.1.2 Doping TiO_2 with Ca^{2+} ions

In contrast with transition metals and rare earth metals, doping TiO_2 with alkaline earth metals, in particular with Ca, has been scarcely reported in the literature [216]. Moreover, calcium is cost-effective, abundant, and green [217]. Based on the limited studies available on water remediation employing Ca-doped TiO_2 nanomaterials, Michi *et al.* reported the synthesis of Ca-doped TiO_2 nanofibers by the sol-gel electrospinning method. The best RhB degradation rate was obtained with the 5 wt. % Ca-doped TiO_2 nanofibers reaching 95 % degradation after 100 min of UV light exposure, compared to 73 % with the undoped TiO_2 nanofibers. Both intrinsic and doped materials were composed of a mixture of anatase/rutile. The improved photocatalytic activity was attributed to the addition of calcium impurities into the TiO_2 lattice, which also led to a reduction of the rutile phase [210]. Another study by Liu *et al.* demonstrated the production of Ca-doped TiO_2 mesoporous anatase nanomaterials through a solid-state reaction route. The photocatalyst with the ratio of Ca:Ti=1:7 achieved a thiophene degradation of 90.2 % *vs.* 19.1 % with pure TiO_2, under visible light irradiation for 50 min of reaction. The degradation capacity of thiophene was attributed to the distribution, quantity and vibration intensity of hydroxyl groups at the surface of the Ca-doped TiO_2 materials. Furthermore, in these materials, some defects originated at the shallow surface. These defects could have acted as electron/hole traps, thereby improving the separation of photogenerated electrons and holes, resulting in improved photocatalytic activity of these materials [218].

1.7.2 Construction of heterostructures

The development of heterostructures based on TiO_2 could be an efficient alternative to improve the photoactivation of TiO_2 under visible light irradiation [146]. A heterostructure or junction is the interfacial union of two or more components with distinct electronic properties. This junction is typically composed of a semiconductor with one or more materials, such as metals or semiconductors [146].

Semiconductor/metal heterostructures are based on the deposition of metallic nanoparticles on semiconductors. In such a union, the recombination of electron-hole pairs can be minimized due to the flow of photoelectrons from the conduction band of the semiconductor

to the surface of the metallic nanoparticles and the creation of the Schottky barrier that prevents the return of these charges to the conduction band of the semiconductor [146,219].

Semiconductor/semiconductor heterostructures can be classified either as anisotype—a p-n junction—, or isotype heterojunctions, in which both coupled semiconductors are n-type (n-n junction) or p-type (p–p junction). Depending on the band position, 3 possible band alignments in semiconductor/semiconductor heterostructures are possible: straddling gap band alignment (type I), staggered gap (type-II), and the broken gap (type-III) [146,220].

As illustrated in Figure 1.4 (a), upon light irradiation, in a type-I heterostructure, the VB potential of semiconductor B is more positive than that of semiconductor A, whereas the potential of the CB of semiconductor A is more negative than that of semiconductor B. Consequently, both electrons and holes are transferred from A to B, resulting in the accumulation of charge carriers in B [146]. This accumulation in the semiconductor with a smaller band gap facilitates the recombination rate, which in turn decreases the photocatalytic activity.

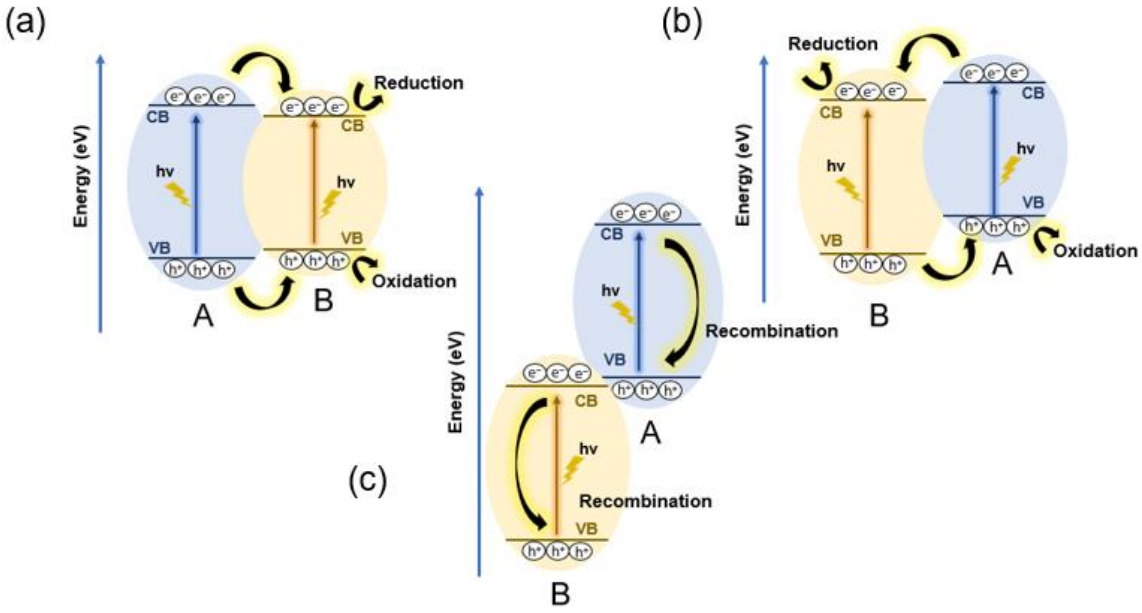

Figure 1.4: Schemes of the types of band diagrams in semiconductor junctions, (a) straddling gap or type-I, (b) staggered gap or type-II, and (c) broken gap or type-III. The band bending mechanisms were omitted. Adapted from [221,222].

In a type-II heterojunction, after illumination, the VB potential of semiconductor B is more negative than that of semiconductor A, and the CB potential of semiconductor A is more positive than that of semiconductor B (Figure 1.4 (b)). As a result, the photogenerated electrons and holes migrate to the CB of semiconductor B and VB of semiconductor A, respectively. This donor-acceptor interface can efficiently promote the separation of electrons and holes at the

interface [15,146]. However, the redox efficiencies in type-I and type-II are low, since oxidation and reduction reactions occur on the VB and CB with weaker redox potentials [114]. Meanwhile, in a type-III heterojunction, the charge carrier's separation is limited, once there is no overlap between the band gaps of two semiconductors A and B [114,223].

Unlike the traditional type-I, II and III heterostructures, Z-scheme heterojunctions retain stronger redox ability. According to the transport media, Z-scheme heterojunctions are divided into traditional Z-scheme/redox pair mediator Z-scheme, all-solid-state Z-scheme and direct Z-scheme or S-scheme (Figure 1.5) [224–226].

In a traditional Z-scheme or redox pair mediator Z-scheme, ion pairs are incorporated that contain an electron donor and an electron acceptor as the mediator. Upon light irradiation, electrons and holes are generated on both semiconductors A and B. Afterwards, the photogenerated electrons of semiconductor B and photogenerated holes of semiconductor A are consumed by an electron acceptor and donor, respectively. Then, the strong redox power of ion pairs separates electrons in the CB of semiconductor A and holes at the VB of semiconductor B. The electron donor is oxidized by the holes on semiconductor A and turns back to the electron acceptor, forming a circular process in which electron donors and acceptors are consumed by the photogenerated electron-hole pairs of the weaker redox potentials of semiconductors A and B. At the same time, redox ion pairs separate electrons on semiconductor A (CB) and holes on semiconductor B (VB) of higher redox potentials (Figure 1.5 (a)) [225].

Solid-state Z-scheme heterojunctions have the purpose of eliminating the use of redox pairs and replacing them with nanoconductors, hence extending the range of applications. A solid-state electron mediator (usually metals, such as Au, Ag, or Pt) is in contact with two semiconductors and promotes interfacial charge carrier transfer. The photogenerated electrons with weak reduction potential migrate from the CB of B and can recombine with the photogenerated holes with a weak oxidation potential induced from the VB of A, assisted by the electron mediator (Figure 1.5 (b)) [114,224]. In contrast to the traditional Z-scheme heterojunction, this configuration is compatible with liquid and gas phases [227]. Nevertheless, the utilization of expensive and photo-corrosive noble metals restricts their utilization as photocatalysts and suffer from light-shielding effects [114,227].

The photocatalysts in which carriers are directly transported through the interface between the two semiconductors present a direct Z-scheme. The photogenerated electrons in the CB of semiconductor B will be transferred to the interface and recombine with the holes in the VB of semiconductor A due to the electrostatic attraction. Therefore, holes and electrons with

stronger oxidative and reductive abilities can be preserved in the VB of semiconductor B and the CB of semiconductor A, respectively (Figure 1.5 (c)). Contrary to solid-state Z-scheme heterojunctions, this configuration can reduce the cost and eliminate the light-shielding effect [227].

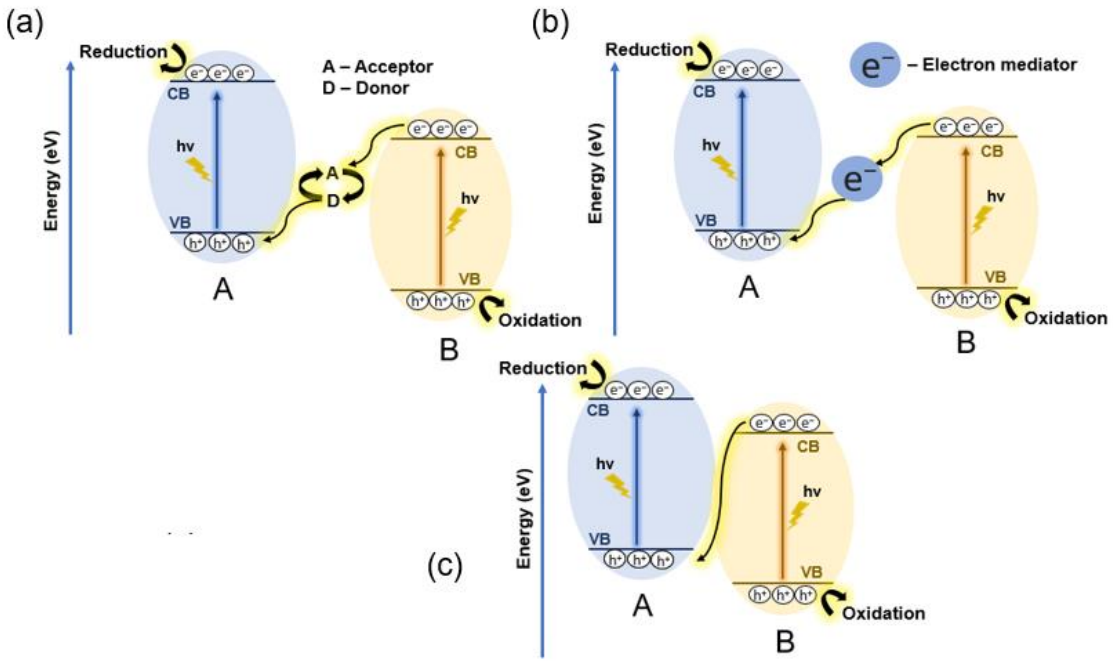

Figure 1.5: Schemes of the types of band diagrams in (a) traditional Z-scheme, (b) all-solid-state Z-scheme, and (c) direct Z-scheme photocatalysts. The band bending mechanisms were omitted. Adapted from [221,228].

1.7.2.1 g-C_3N_4/TiO_2 heterostructure

To improve solar light energy harvesting, TiO_2 has been coupled with several materials, such as molybdenum disulfide (MoS_2) [229], niobium(V) oxide (Nb_2O_5) [230], cerium vanadium oxide ($CeVO_4$) [231] and g-C_3N_4 [15,232]. In particular, g-C_3N_4, an organic semiconductor, has garnered significant interest, primarily due to its "earth-abundant" nature, reduced toxicity, facile synthesis, appealing electronic band structure and high physicochemical stability [15,233]. g-C_3N_4 is considered the most stable among the several carbon nitride allotropic forms (α-C_3N_4, β-C_3N_4, g-h triazine, cubic C_3N_4, pseudocubic C_3N_4), under ambient conditions [234]. Moreover, it has the lowest band gap attributed to the sp^2-hybridized carbon and nitrogen atoms, forming a 2D π-conjugated electronic system [15,235]. This material is composed of layers of triazine or tri-s-triazine ring structures (the tri-s-triazine-structure (Figure 1.6) is the most thermodynamically stable [235]), connected by N atoms, wherein van der Waals forces hold its layered stacking [15]. This semiconductor also exhibits electron-rich

properties, basic surface functionalities and H-bonding motifs, making it suitable for catalytic applications (Figure 1.6) [236].

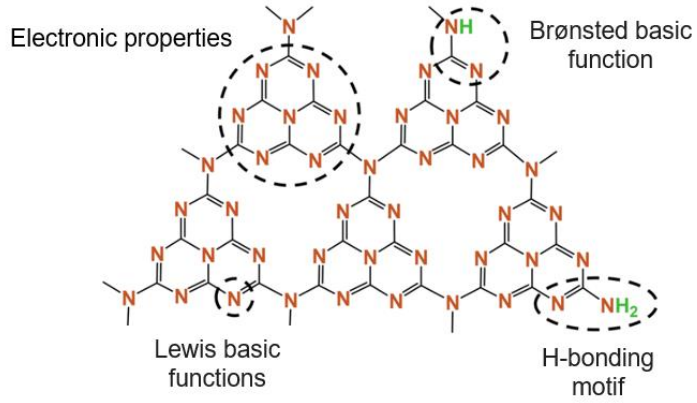

Figure 1.6: Tri-s-triazine-based structure of g-C_3N_4 and its multiple functional surface properties. Reproduced from Ref. [237].

Other characteristics of this material include high thermal stability (up to 600 °C in air) and hydrothermal stability (it is insoluble in acidic, neutral or basic medium). Furthermore, bulk g-C_3N_4 has a small surface area (10 $m^2.g^{-1}$), however, the fabrication of multi-layer or single-layer g-C_3N_4 nanosheets can significantly increase the specific surface area [238]. For example, monolayer g-C_3N_4 can achieve a specific surface area of up to 2500 $m^2.g^{-1}$ [239]. Larger specific surface area offer more active sites for the adsorption of pollutants during the photocatalytic experiments [240].

Regarding the fabrication methods, the thermal polymerization of low-cost precursors (between 500 and 600 °C in air or inert atmosphere) is the most popular approach, owing to its simplicity, high yield and cost-effectiveness [15,241]. The material's precursors are carbon- and nitrogen-rich organic compounds, typically dicyandiamide, melamine, urea and thiourea [15,235].

The band gap energy of g-C_3N_4 is between 2.7 and 2.8 eV, corresponding to a wavelength of 450–460 nm, which allows the absorption of visible light. Moreover, it presents a strong photoreduction capability, which is strongly promoted by the high redox potential of −1.3 V (*vs*. NHE at pH = 7 compared to the potential of −0.5 V for pure TiO_2) [2]. Nevertheless, since its top energy level of the VB is 1.4 V (*vs*. NHE at pH = 7 compared to 2.7 V for pure TiO_2), it has a weak oxidative capability for water oxidation, leading to insufficient hydroxyl radicals' production. In addition, the hybridization of the N 2p and C 2p states in the CB results in a fast recombination rate of photogenerated charge carriers. Besides that, it is difficult to

separate from water, which may cause secondary pollution, restricting its use in photocatalytic applications [2]. Yet, the effective coupling of g-C_3N_4 with other semiconductors has previously been shown to be advantageous in charge separation and enhanced absorption in the visible light region [2].

1.7.3 Surface defect engineering

Three types of defects can be introduced into semiconductor materials, potentially enhancing their effectiveness in photocatalysis: surface, bulk, and interfacial defects. These defects can be generated through various techniques, such as high-temperature treatment, rapid heating, chemical reduction, vacuum activation, ball milling, and plasma etching. Surface defects are irregularities that occur on the exterior of the material [242]. Common surface defects include vacancies (missing lattice atoms at the surface [243]), adatoms (extra atoms adsorbed onto the surface [244]), steps and kinks [245]. Bulk defects correspond to the ones that can be found within the interior (bulk) of the material and may encompass vacancies, interstitial/substitutional defects, dislocations and grain boundaries [246]. Interfacial defects, meanwhile, typically comprise grain, phase, twin boundaries and stacking faults that connect different regions within the material [247–250].

Defects in a semiconductor can be classified into 0D, 1D, 2D and 3D types. 0D defects (point defects) are defects that occur only at or around a single lattice point and can be introduced through doping or by removing a lattice atom (vacancy). 1D defects (line defects) arise from the misalignment of atoms in a crystal lattice and include two types: edge dislocation and screw dislocation. 2D defects (planar defects) involve the formation of planes that divide the structure into regions with identical crystal structures but different orientations. Examples include stacking faults, grain boundaries, and twin boundaries. Another type consists of 3D defects (volume defects), which can occur when two or more chemical species occupy one or more crystal sites, leading to voids or several types of disorder within the crystal lattice [243]. Most of the time, defects arise naturally, without deliberate engineering, occurring during the crystal growth process [243,251,252].

Studies have shown that microwave-assisted techniques can induce a higher density of defects, compared to conventional heating methods like water bath heating [253]. The defects will influence the optical, structural, electronic, and hence catalytic properties of the produced metal oxide semiconductor [254,255]. Thus, further detailed studies are essential to

characterize the defects induced by microwave synthesis and to understand their influence on the catalytic performance [256].

1.8 Immobilization of TiO_2-based materials onto substrates

Various strategies to extend the light absorption of TiO_2 have been developed, often in combination with the production of TiO_2-based materials immobilized onto substrates to enhance their practical application and reusability [15,35,257].

The effective utilization of photoactive materials in heterogeneous photocatalysis commonly requires powdered materials, due to the higher surface-to-volume ratios and mass transfer rates [258]. Nonetheless, the reuse and recovery of these materials are difficult and costly to implement at large-scale processes, making the immobilization of photocatalysts on substrates an excellent alternative to avoid these issues [8,259,260]. Furthermore, it avoids the aggregation and leaching of the nanopowders, thereby minimizing the exposure of toxic compounds to the environment [261,262]. Examples of those substrates include glass, polymers, textiles, cork [9], cellulose-based substrates [35], and perlite, among others [263,264]. In addition, the utilization of green and inexpensive substrates has attracted a lot of interest in photocatalytic applications [92]. It is important to note that the procedure used to fabricate the supported photocatalyst and the type of substrate significantly influence the photocatalytic activity of TiO_2 [265,266].

1.8.1 Floating/non-floating substrates

1.8.1.1 Cork

Over the last few years, a new category of photocatalysts, the so-called "floating photocatalysts", has emerged with the potential to overcome the issues of recovery and recyclability of nanopowders. Their use allows the maximization of the utilization of light as well as the oxygenation of the photocatalyst due to the proximity of the air/water interface. Moreover, their lightness makes them easy to collect from water, while no special equipment or stirring is needed during the photocatalytic reaction. Concerning sustainable and natural floating materials, cork presents several advantages, making it suitable for photocatalytic experiments.

Cork is extracted from the bark of the cork oak tree (*Quercus suber L.*), Figure 1.7, it flourishes in the specific regions of the Western Mediterranean (Portugal, Spain, Southern France, part of Italy, and North Africa) and it is renewable, hydrophobic and sustainable. As

a clear evidence of its sustainability, each time the bark is harvested from cork trees, the latter can absorb up to 5 times more CO_2 (to generate their bark) than a non-harvested tree [267]. Moreover, cork contributes to the circular economy, being extracted without damaging the tree and being regenerated over the years, and it serves as the base for several products, some of which are produced by recycled cork [9]. In terms of chemical composition, suberin represents almost 50 % of its chemical composition and it is mainly responsible for the elasticity and compressibility of cork. In a lower percentage, lignin and cellulose are present and extractives/polysaccharides appear in minor percentages, followed by hemicelluloses and ash [268]. Portugal is the world's largest producer of cork and around 100.000 tonnes of cork are estimated to be produced each year. The cork industry, despite being one of the most profitable markets in this country, generates a large amount of cork waste with no commercial value, being usually burned to generate energy. Hence, instead of being wasted, one can take advantage of its unique properties, making cork a platform in photocatalytic experiments for the treatment of contaminated effluents, which would benefit both industries [9,267].

Figure 1.7: Extraction of cork from a cork oak tree. Adapted from [269] and [270].

Studies focused on the production of TiO_2-based materials by a relatively fast and low-temperature microwave approach on cork and the investigation of their photocatalytic efficiency are scarce. From the previous studies, Sboui *et al.* reported, for instance, the preparation of TiO_2-PANI nanocomposites for the degradation of MO dye by using a sol–gel method for the synthesis of TiO_2 nanostructures and heating treatment 350 °C for 6 h, followed by an impregnation method to immobilize the nanocomposite on cork surface [271]. In another study by Idris *et al.*, TiO_2/polyvinyl alcohol (PVA)/cork nanocomposites were prepared through the immobilization of TiO_2 nanoparticles on cork and by employing PVA as a binder to anchor TiO_2 nanoparticles on the surface of the floating catalyst for the degradation of MB. For the photocatalyst preparation, several steps were involved, and higher temperatures were required to calcinate the TiO_2 nanostructures [272].

1.8.1.2 Polyurethane (PU) foams

PU is a thermoplastic polymer, easily adaptable to several industrial applications: tubing, footwear, industrial machinery, elastic fibers, insulators, medical devices, paints, and coatings, among others. This versatile material presents outstanding abrasion resistance, low density, flexibility at reduced temperatures and suitable properties (chemical, mechanical and physical) [260,273]. It is composed of repeated urethane (−NHCOO−) basic units and fabricated through the exothermic reaction involving diisocyanate (O = C = N − R′ − N = C = O) and either a polyester or a polyether polyol (HO–R–OH) [258]. The utilization of nanoparticles to modify the chemical and mechanical properties of PU has proved to be effective in their enhancement.

Although PU recycling presents some challenges, primarily due to the chemically cross-linked structure of most PUs in the market (thermosets) and the diverse compositions of PUs mixed during waste disposal [274], it has been demonstrated that polyurethanes can undergo chemical recycling, reverting to their constituent monomers or segments, and be utilized to generate new ones [275]. In this regard, research work is still in progress, but results indicate potential circular economy solutions for PU [276]. Therefore, the combination of nanoparticles with this polymer extends its applicability across an extensive range of research fields, for instance, photocatalysis, sensors, solar/fuel cells, biomedical materials, and self-cleaning coatings [273]. PU foams, besides having a floating character, present a large surface area, high adsorption ability and excellent reusability [260,277,278].

Various studies have been performed with PU sponges as oil adsorbents [277,279,280], but few works have reported the photodegradation of water pollutants using reusable polyurethane foams immobilized with nano TiO_2-based photocatalysts. To compare the performance of different TiO_2-based photocatalysts on PU supports for the decomposition of water contaminants, Table 1.4 presents the studies found in the literature. Studies with missing data were not included in Table 1.4.

Table 1.4: Performance of several TiO_2-based photocatalyst systems on PU supports for the degradation of water pollutants.

Photocatalyst	Immobilization in situ?	Light source	Photocatalytic conditions	Optimal degradation efficiency	k_{ap} (min^{-1})	References
Silicon dioxide-titanium dioxide (SiO_2/TiO_2)	No	UV light source <400 nm	• Pollutant: Acid Black 1 (AB 1) • Solution's concentration: 10 ppm • The total weight of the PU-SiO_2/TiO_2 film photocatalyst was 160 mg.	100 % of degradation in 60 min with the PU-40 % SiO_2/TiO_2 composite film	Not calculated	[281]
Iron-tetra(4-carboxyphenyl)porphine-sulphur-titanium dioxide-reduced graphene oxide (Fe-TCPP-S-TiO_2-rGO)	No	Solar light	• Pollutant: Cyanide • Volume: 50 mL • Solution's concentration: 100 ppm • Quantity of photocatalyst: 100 mg	91 % degradation as well as 88 % toxicity removal in 2 h	0.0196	[282]
Silver-titanium dioxide-graphene (Ag-commercial TiO_2 Aeroxide P25-graphene)	No	Visible light	• Pollutant: Diesel • Solution's concentration: 15000 ppm • Quantity of photocatalyst: 300 mg	76 % of degradation in 16 h	0.0017 (deduced based on the experimental data)	[260]
Commercial TiO_2 Aeroxide P25	No	UV light irradiation (λ = 254 nm, 18 mW cm^{-2})	• Pollutant: BPA • Solution's concentration: 10 ppm • Experiments were carried out in a self-designed horizontal circulating bed photocatalytic reactor (HCBPR) • The optimum ratio of the volume of PU foam to the effective reaction volume of HCBPR was 1 %	97 % degradation in 6 h (95 % removal of TOC)	0.003 (deduced based on the experimental data)	[8]

1.8.1.3 Cellulose-based materials

Among the various sustainable substrates available, cellulose is known as being the most abundant biopolymer on Earth. It is flexible, lightweight, inexpensive and compatible with wet-chemical synthesis routes (such as microwave synthesis). This material is ubiquitous and can be extracted from cotton, wood, hemp, rice, algae, bacteria, and several other natural sources. All these unique properties make it highly attractive for photocatalytic applications [5,6,92]. Cellulose is made of repeating glucose monomers, where the polysaccharide with a molecular structure of $(C_6H_{10}O_5)_n$ is linked together through β-1,4-glycosidic bonds by a condensation reaction [1,3]. Cellulose has three hydroxyl groups in each glucose unit with a degree of polymerization based on glucose units, ranging from 1000 to 15.000, depending on the cellulose origin and treatments [283]. These hydroxyl (OH) groups will confer some important characteristics, such as hydrophilicity, chirality, and biodegradability. In addition, the native cellulose OH groups can be substituted by functional groups, resulting in cellulose derivatives [284]. Furthermore, depending on the synthesis method and chemical modifications, cellulose-based materials can either float on the water surface or sink [285].

Microwave-synthesized TiO_2 nanostructures have already been fabricated on cellulose-based substrates. For instance, Zhang *et al.* produced nano-TiO_2/cellulose composites by a low-temperature (90 °C) and one-pot microwave-assisted synthesis approach. Cellulose fibres were used as substrates and the composite material showed a rapid lead (Pb^{2+}) adsorption from wastewater with a maximum capacity of 42.5 mg. g^{-1} [286]. A similar research study was conducted by Cardoso *et al.*, which demonstrated that the fabrication of TiO_2–cellulose nanocomposites is possible by the decomposition of titanium isopropoxide (TTIP) in ethanol media together with wood cellulose fibers into the microwave-assisted solvothermal system under mild conditions [287]. D. Nunes *et al.* also synthesized TiO_2 nanostructured films on bacterial nanocellulose (BNC) and tracing paper using microwave synthesis at low temperature (80 °C). This study demonstrated that flexible and reusable photocatalysts can be produced with minimal production stages under microwave irradiation [157]. Regarding this topic, research studies are still scarce. Other studies were found in the literature, but microwave irradiation was not the chosen synthesis method [288–290].

1.9 Combination of 3D printing and catalysis

The search for highly effective water remediation photocatalysts has led to intensive research and advancements in the field of photocatalysis, recently combined with 3D printing technologies. Additive manufacturing (AM) or 3D printing context has revolutionized design, prototyping, and manufacturing due to its operation simplicity, precision, free design, low-cost, rapid prototyping, and low energy consumption, apart from being able to produce complex structures. It is also considered a low-waste production alternative [10,291–294].

A noteworthy advantage of using a 3D structure instead of nanopowders is in the removal stage at the end of the photocatalytic treatment, since the 3D structure is easy to recycle and reuse [295,296]. Moreover, some important parameters, namely channel geometry, diameter, porosity, and surface-to-volume ratio can be optimized to boost the photocatalytic degradation of water pollutants [293]. These properties open up new possibilities for designing not only catalysts but also adsorbents that can be easily scaled up for industrial production [297].

3D printing technologies can be categorized into solid, liquid, and powder-based systems. In solid-based systems, 3D structures are fabricated by processing plastic wire materials, layers of adhesive-coated paper, plastic, or metal laminates. In liquid-based systems, a photosensitive resin is typically used as raw material, while powder-based materials normally consist of metal, ceramic or polymers in powder form [298].

Among the different approaches to 3D printing materials, the stereolithography (SLA) technique, which is a polymer-based system, is a well-established technique in several industries, since it offers precision and high-resolution [299] to fabricate intricate 3D objects from macro-to microscale [297]. The main advantages and disadvantages of this technique are summarized in Table 1.5:

Table 1.5: Main advantages and disadvantages of the SLA technique [300–302].

Advantages	Disadvantages
Affordability	Slower printing rate (depends on the model size)
User friendly	The printing resolution depends on the wavelength of the laser beam
Low maintenance	Maintenance cost
Rapid prototyping	Price of photosensitive resin
Large-size models can be printed	
High precision to print objects with complex structures and fine size.	

Some research groups have already demonstrated the potential of AM techniques to obtain 3D photoactive architectures based on metal oxide nanostructures for wastewater treatment. Sopha *et al.* produced large 3D Ti meshes fabricated by direct ink writing (DIW) with TiO_2 nanotube layers by using wireless anodization. The TiO_2 nanotube layers-modified 3D Ti meshes showed a superior performance for the photocatalytic degradation of MB dye in comparison to TiO_2-nanoparticle-decorated and non-anodized Ti meshes (with a thermal oxide layer), which led to multiple increases in the dye degradation rate [303]. In another study by Bansiddhi *et al.*, 3D-printed TiO_2/SiO_2/polymer scaffolds were fabricated by SLA technique, using TiO_2 synthesized via a solution combustion process, silica adsorbent prepared from sugarcane leaves, and photocurable resin as feedstock. The TiO_2/SiO_2/polymer scaffolds demonstrated potential in dye removal against MB and RhB dyes. The degradation percentages of MB and RhB in the presence of the TiO_2/SiO_2/polymer scaffolds were 81.9 % and 60 %, respectively. The 3D structures also revealed reusability characteristics after a hydrogen peroxide treatment [304]. Fu *et al.* also reported the fabrication of a Pd-decorated TiO_2 hierarchical vertical array by an extrusion-based 3D printer for the photocatalytic degradation of nitrophenol. The array demonstrated rapid and efficient photo-assisted catalytic reduction of high concentrations of 4-nitrophenol wastewater (2 g. L^{-1}, *ca.* 14.38 mmol. L^{-1}) and its feasibility for continuous flow wastewater treatment [305]. All these studies showed that 3D printing technologies enable the construction of highly efficient photocatalytic systems adaptable to different chemical reactions, providing a promising and scalable strategy for the treatment of polluted effluents.

1.10 Main objective and tasks to be developed

Driven by the motivation for this PhD research and insights gained from the state-of-the-art review, the main objective was established.

Main objective: Contribute to sustainability in the wastewater treatment field through the microwave-assisted synthesis of TiO_2-based materials, active under solar light and efficient for the removal and degradation of organic water pollutants. The novelty of this PhD thesis lies in creating these materials without employing energy-intensive processes, prolonged synthesis times and additional high-temperature treatments such as calcinations. Unlike previous adsorptive and photocatalytic studies that rely on unsustainable methods and use powdered materials, this work will unlock the potential of microwave irradiation by reporting straightforward approaches to produce eco-friendly TiO_2-based platforms using microwave irradiation exhibiting dual-functional adsorptive and photocatalytic properties, thereby eliminating the need to use materials in powder form. Their efficiency in recycling experiments will also be explored. In addition, various strategies for modifying TiO_2 will be investigated using microwave irradiation, with sustainability principles integrated throughout all processes. Furthermore, the proposed fabrication approaches aim to be easily scalable.

To achieve this, the main objective was divided into several tasks:

1st task: Improve the visible light harvesting of TiO_2 and achieve maximum performance in the photocatalytic experiments.

2nd task: Incorporation of the synthesized nanostructures on different cheap and eco-friendly substrates.

3rd task: Evaluate the removal and degradation efficiencies of organic pollutants in aqueous systems to simulate real-life environments over microwave-assisted-synthesized pristine and/or modified TiO_2 nanomaterials and/or TiO_2-based platforms. Their degradation will be assessed under simulated sunlight irradiation and/or natural sunlight irradiation. The adsorptive and photocatalytic behavior of the produced materials will be further understood through extensive characterization.

4th task: Perform reusability tests with the produced nanopowders and platforms to ensure their integrity for practical applications.

5th task: Examine the potential environmental impact of the produced materials by performing toxicity assays with aquatic species.

1.11 References

1. Wen, Y.; Schoups, G.; Van De Giesen, N. Organic pollution of rivers: Combined threats of urbanization, livestock farming and global climate change. *Scientific Reports* **2017**, *7*, 1–9, doi:10.1038/srep43289.
2. Water and Sanitation - United Nations Sustainable Development Available online: https://www.un.org/sustainabledevelopment/water-and-sanitation/ (accessed on Aug 21, 2024).
3. Mulay, M. R.; Martsinovich, N. TiO_2 Photocatalysts for Degradation of Micropollutants in Water. In *Clean Water and Sanitation*; Filho, W. L., Azul, A. M., Brandli, L., Salvia, A. L., Wall, T., Eds.; Springer, Cham, 2021; pp. 1–19 ISBN 978-3-319-70061-8.
4. Falinski, M. M.; Turley, R. S.; Kidd, J.; Lounsbury, A. W.; Lanzarini-Lopes, M.; Backhaus, A.; Rudel, H. E.; Lane, M. K. M.; Fausey, C. L.; Barrios, A. C.; Loyo-Rosales, J. E.; Perreault, F.; Walker, W. S.; Stadler, L. B.; Elimelech, M.; Gardea-Torresdey, J. L.; Westerhoff, P.; Zimmerman, J. B. Doing nano-enabled water treatment right: sustainability considerations from design and research through development and implementation. *Environmental Science: Nano* **2020**, *7*, 3255–3278, doi:10.1039/D0EN00584C.
5. Freire, T.; Fragoso, A. R.; Matias, M.; Vaz Pinto, J.; Marques, A. C.; Pimentel, A.; Barquinha, P.; Huertas, R.; Fortunato, E.; Martins, R.; Nunes, D. Enhanced solar photocatalysis of TiO_2 nanoparticles and nanostructured thin films grown on paper. *Nano Express* **2021**, *2,4*, 1–20.
6. Nunes, D.; Pimentel, A.; Branquinho, R.; Fortunato, E.; Martins, R. Metal oxide-based photocatalytic paper: A green alternative for environmental remediation. *Catalysts* **2021**, *11(4)*, 1–30, doi:10.3390/catal11040504.
7. Khan, H.; Shah, M. U. H. Modification strategies of TiO_2 based photocatalysts for enhanced visible light activity and energy storage ability: A review. *Journal of Environmental Chemical Engineering* **2023**, *11*, 111532, doi:10.1016/J.JECE.2023.111532.
8. Wang, R.; Ren, D.; Xia, S.; Zhang, Y.; Zhao, J. Photocatalytic degradation of Bisphenol A (BPA) using immobilized TiO_2 and UV illumination in a horizontal circulating bed photocatalytic reactor (HCBPR). *Journal of Hazardous Materials* **2009**, *169*, 926–932, doi:10.1016/j.jhazmat.2009.04.036.
9. Matias, M. L.; Morais, M.; Pimentel, A.; Vasconcelos, F. X.; Reis Machado, A. S.; Rodrigues, J.; Fortunato, E.; Martins, R.; Nunes, D. Floating TiO_2-Cork Nano-Photocatalysts for Water Purification Using Sunlight. *Sustainability* **2022**, *14(15)*, 9645, doi:10.3390/SU14159645/S1.
10. Xue, R.; Matias, M. L.; Pimentel, A.; Pinto, J. V.; Fortunato, E.; Martins, R. Photocatalytic Activity of 3D Printed TiO_2 Architectures Under Solar Radiation. In *Photocatalysis for Environmental Remediation and Energy Production*; Green Chemistry and Sustainable Technology; Springer International Publishing, 2023; pp. 79–100 ISBN 978-3-031-27706-1.
11. Yan Y. Xi; Yan F. Hsu; Wai K. Chan Hydrothermal Synthesis of Nanostructures. *Recent Patents on Nanotechnology* **2008**, *1*, 121–128, doi:10.2174/187221007780859591.
12. Kubiak, A.; Zalas, M.; Cegłowski, M. Innovative microwave in situ approach for

crystallizing TiO_2 nanoparticles with enhanced activity in photocatalytic and photovoltaic applications. *Scientific Reports* **2024**, *14*, 1–14, doi:10.1038/s41598-024-63614-7.

13. Syeed, M. M. M.; Hossain, M. S.; Karim, M. R.; Uddin, M. F.; Hasan, M.; Khan, R. H. Surface water quality profiling using the water quality index, pollution index and statistical methods: A critical review. *Environmental and Sustainability Indicators* **2023**, *18*, 100247, doi:10.1016/J.INDIC.2023.100247.
14. Rodrigues, V. Avaliação de Desempenho do Tratamento de Água, com a utilização da Ferramenta PAStool e dados das ETA de Tavira e de Beliche, Master's thesis, University of Algarve, 2017.
15. Matias, M. L.; Reis-Machado, A. S.; Rodrigues, J.; Calmeiro, T.; Deuermeier, J.; Pimentel, A.; Fortunato, E.; Martins, R.; Nunes, D. Microwave Synthesis of Visible-Light-Activated g-C_3N_4/TiO_2 Photocatalysts. *Nanomaterials* **2023**, *13(6)*, doi:10.3390/NANO13061090/S1.
16. Nations, U. Clean water and sanitation Available online: https://unstats.un.org/sdgs/report/2024/Goal-06/ (accessed on Oct 20, 2024).
17. Current drought situation in Europe, European Comission. Available online: https://joint-research-centre.ec.europa.eu/european-and-global-drought-observatories/current-drought-situation-europe_en (accessed on Feb 24, 2025).
18. UNESCO The United Nations world water development report 2019: leaving no one behind Available online: https://unesdoc.unesco.org/ark:/48223/pf0000367306 (accessed on Oct 20, 2024).
19. Li, D.; Liu, S. Water Quality Detection for Lakes. *Water Quality Monitoring and Management* **2019**, 221–231, doi:10.1016/B978-0-12-811330-1.00008-9.
20. Panczak, B.; Alt, H.; Van Wychen, S.; Sowell, A.; Lesco, K.; Laurens, L. M. L. Determination of Total, Organic, and Inorganic Carbon in Biological Cultures and Liquid Fraction Process Samples. *Technical Report NREL/TP-2700-78622* **2020**, 1–17.
21. Patel, A.; Arkatkar, A.; Singh, S.; Rabbani, A.; Solorza Medina, J. D.; Ong, E. S.; Habashy, M. M.; Jadhav, D. A.; Rene, E. R.; Mungray, A. A.; Mungray, A. K. Physico-chemical and biological treatment strategies for converting municipal wastewater and its residue to resources. *Chemosphere* **2021**, *282*, 130881, doi:10.1016/J.CHEMOSPHERE.2021.130881.
22. Abbas, K. Development of a Hybrid Multi-Functional Adsorbent-Solar- Photocatalyst for Detecting and Removing Toxic Heavy Metals and Refractory Pollutants from Water/Wastewater, PhD thesis, Curtin University, 2018.
23. Lin, L.; Yang, H.; Xu, X. Effects of Water Pollution on Human Health and Disease Heterogeneity: A Review. *Frontiers in Environmental Science* **2022**, *10*, 880246, doi:10.3389/fenvs.2022.880246.
24. Ghime, D.; Ghosh, P.; Ghime, D.; Ghosh, P. Advanced Oxidation Processes: A Powerful Treatment Option for the Removal of Recalcitrant Organic Compounds. In *Advanced Oxidation Processes - Applications, Trends, and Prospects*; Ciro Bustillo-Lecompte, Ed.; IntechOpen, 2020 ISBN 978-1-78984-891-5.
25. Manzoor, J.; Sharma, M. Impact of textile dyes on human health and environment. In *Impact of Textile Dyes on Public Health and the Environment*; Jangid, D. N. K., Ed.; IGI

Global, 2019; pp. 162–169 ISBN 9781799803133.
26. Samsami, S.; Mohamadi, M.; Sarrafzadeh, M. H.; Rene, E. R.; Firoozbahr, M. Recent advances in the treatment of dye-containing wastewater from textile industries: Overview and perspectives. *Process Safety and Environmental Protection* **2020**, *143 (10)*, 138–163, doi:10.1016/J.PSEP.2020.05.034.
27. Jorge, A. M. S.; Athira, K. K.; Alves, M. B.; Gardas, R. L.; Pereira, J. F. B. Textile dyes effluents: A current scenario and the use of aqueous biphasic systems for the recovery of dyes. *Journal of Water Process Engineering* **2023**, *55*, 104125, doi:10.1016/J.JWPE.2023.104125.
28. Moussavi, G.; Mahmoudi, M. Removal of azo and anthraquinone reactive dyes from industrial wastewaters using MgO nanoparticles. *Journal of Hazardous Materials* **2009**, *168*, *2–3*, 806–812, doi:10.1016/J.JHAZMAT.2009.02.097.
29. Sha, Y.; Mathew, I.; Cui, Q.; Clay, M.; Gao, F.; Zhang, X. J.; Gu, Z. Rapid degradation of azo dye methyl orange using hollow cobalt nanoparticles. *Chemosphere* **2016**, *144*, 1530–1535, doi:10.1016/J.CHEMOSPHERE.2015.10.040.
30. Utami, M.; Wang, S.; Fajarwati, F. I.; Salsabilla, S. N.; Dewi, T. A.; Fitri, M. Enhanced Photodegradation of Rhodamine B Using Visible-Light Sensitive N-TiO_2/rGO Composite. *Crystals* **2023**, *13*, 588, doi:10.3390/CRYST13040588.
31. Al-Ghouti, M. A.; Al-Absi, R. S. Mechanistic understanding of the adsorption and thermodynamic aspects of cationic methylene blue dye onto cellulosic olive stones biomass from wastewater. *Scientific Reports* **2020**, *10*, 1–18, doi:10.1038/s41598-020-72996-3.
32. Konicki, W.; Cendrowski, K.; Bazarko, G.; Mijowska, E. Study on efficient removal of anionic, cationic and nonionic dyes from aqueous solutions by means of mesoporous carbon nanospheres with empty cavity. *Chemical Engineering Research and Design* **2015**, *94*, 242–253, doi:10.1016/J.CHERD.2014.08.006.
33. Oladoye, P. O.; Kadhom, M.; Khan, I.; Hama Aziz, K. H.; Alli, Y. A. Advancements in adsorption and photodegradation technologies for Rhodamine B dye wastewater treatment: fundamentals, applications, and future directions. *Green Chemical Engineering* **2024**, *5*, 440–460, doi:10.1016/J.GCE.2023.12.004.
34. Kuśmierek, K.; Fronczyk, J.; Świątkowski, A. Adsorptive Removal of Rhodamine B Dye from Aqueous Solutions Using Mineral Materials as Low-Cost Adsorbents. *Water, Air, and Soil Pollution* **2023**, *234*, *531*, 1–14, doi:10.1007/s11270-023-06511-5.
35. Matias, M. L.; Pimentel, A.; Reis-Machado, A. S.; Rodrigues, J.; Deuermeier, J.; Fortunato, E.; Martins, R.; Nunes, D. Enhanced Fe-TiO_2 Solar Photocatalysts on Porous Platforms for Water Purification. *Nanomaterials* **2022**, *12*, 1005, doi:10.3390/nano12061005.
36. Rovisco, A.; Morais, M.; Branquinho, R.; Fortunato, E.; Martins, R.; Barquinha, P. Microwave-Assisted Synthesis of Zn_2SnO_4 Nanostructures for Photodegradation of Rhodamine B under UV and Sunlight. *Nanomaterials* **2022**, *12*, 2119, doi:10.3390/NANO12122119/S1.
37. Kishor, R.; Purchase, D.; Saratale, G. D.; Romanholo Ferreira, L. F.; Hussain, C. M.; Mulla, S. I.; Bharagava, R. N. Degradation mechanism and toxicity reduction of methyl orange dye by a newly isolated bacterium *Pseudomonas aeruginosa* MZ520730. *Journal of*

Water Process Engineering **2021**, *43*, 102300, doi:10.1016/J.JWPE.2021.102300.
38. Wu, L.; Liu, X.; Lv, G.; Zhu, R.; Tian, L.; Liu, M.; Li, Y.; Rao, W.; Liu, T.; Liao, L. Study on the adsorption properties of methyl orange by natural one-dimensional nano-mineral materials with different structures. *Scientific Reports* **2021**, *11(10640)*, 1–11, doi:10.1038/s41598-021-90235-1.
39. Kimosop, S. J.; Getenga, Z. M.; Orata, F.; Okello, V. A.; Cheruiyot, J. K. Residue levels and discharge loads of antibiotics in wastewater treatment plants (WWTPs), hospital lagoons, and rivers within Lake Victoria Basin, Kenya. *Environmental monitoring and assessment* **2016**, *188*, doi:10.1007/S10661-016-5534-6.
40. Zheng, S.; Wang, Y.; Chen, C.; Zhou, X.; Liu, Y.; Yang, J.; Geng, Q.; Chen, G.; Ding, Y.; Yang, F. Current Progress in Natural Degradation and Enhanced Removal Techniques of Antibiotics in the Environment: A Review. *International journal of environmental research and public health* **2022**, *19(17)*, 1–31, doi:10.3390/IJERPH191710919.
41. di Cerbo, A.; Pezzuto, F.; Guidetti, G.; Canello, S.; Corsi, L. Tetracyclines: Insights and Updates of their Use in Human and Animal Pathology and their Potential Toxicity. *The Open Biochemistry Journal* **2019**, *13*, 1–12, doi:10.2174/1874091X01913010001.
42. Castañeda, C.; Martínez, J. J.; Santos, L.; Rojas, H.; Osman, S. M.; Gómez, R.; Luque, R. Caffeine photocatalytic degradation using composites of NiO/TiO_2–F and CuO/TiO_2–F under UV irradiation. *Chemosphere* **2022**, *288*, 132506, doi:10.1016/J.CHEMOSPHERE.2021.132506.
43. Baaloudj, O.; Assadi, I.; Nasrallah, N.; El Jery, A.; Khezami, L.; Assadi, A. A. Simultaneous removal of antibiotics and inactivation of antibiotic-resistant bacteria by photocatalysis: A review. *Journal of Water Process Engineering* **2021**, *42*, 1–11, doi:10.1016/J.JWPE.2021.102089.
44. O'Dowd, K.; Nair, K. M.; Pillai, S. C. Photocatalytic degradation of antibiotic-resistant genes and bacteria using 2D nanomaterials: What is known and what are the challenges? *Current Opinion in Green and Sustainable Chemistry* **2021**, *30*, 1–7, doi:10.1016/J.COGSC.2021.100471.
45. Malakotian, M.; Asadzadeh, S. N.; Khatami, M.; Ahmadian, M.; Heidari, M. R.; Karimi, P.; Firouzeh, N.; Varma, R. S. Protocol encompassing ultrasound/Fe_3O_4 nanoparticles/persulfate for the removal of tetracycline antibiotics from aqueous environments. *Clean Technologies and Environmental Policy* **2019**, *21*, 1665–1674, doi:https://doi.org/10.1007/s10098-019-01733-w.
46. Gopal, G.; Alex, S. A.; Chandrasekaran, N.; Mukherjee, A. A review on tetracycline removal from aqueous systems by advanced treatment techniques. *RSC Advances* **2020**, *10*, *45*, 27081–27095, doi:10.1039/D0RA04264A.
47. Fiaz, A.; Zhu, D.; Sun, J. Environmental fate of tetracycline antibiotics: degradation pathway mechanisms, challenges, and perspectives. *Environmental Sciences Europe* **2021**, *33*, *64*, 1–17, doi:10.1186/S12302-021-00505-Y.
48. Zhu, H.; Li, M.; Zou, L.; Hu, Y.; Hao, H.; Dou, J.; Mao, J. A study on singlet oxygen generation for tetracycline degradation via modulating the size of α-Fe_2O_3 nanoparticle anchored on g-C_3N_4 nanotube photocatalyst. *Nano Research* **2023**, *16(2)*, 2236–2244, doi:10.1007/S12274-022-5015-X.
49. Antos, J.; Piosik, M.; Ginter-Kramarczyk, D.; Zembrzuska, J.; Kruszelnicka, I.

Tetracyclines contamination in European aquatic environments: A comprehensive review of occurrence, fate, and removal techniques. *Chemosphere* **2024**, *353*, 141519, doi:10.1016/J.CHEMOSPHERE.2024.141519.

50. Zhang, X.; Cai, T.; Zhang, S.; Hou, J.; Cheng, L.; Chen, W.; Zhang, Q. Contamination distribution and non-biological removal pathways of typical tetracycline antibiotics in the environment: A review. *Journal of Hazardous Materials* **2024**, *463*, 132862, doi:10.1016/J.JHAZMAT.2023.132862.
51. Bortolanza, M.; Santos-Lobato, B. L.; Nascimento, G. C.; Del-Bel, E. Chapter 29 - Management with antibiotics in Parkinson's disease. In *Diagnosis and Management in Parkinson's Disease: The Neuroscience of Parkinson's Disease*; Martin, C. R., R. Preedy, V., Eds.; Academic Press, 2020; Vol. 1, pp. 491–510 ISBN 9780128159460.
52. Tariq, S.; Rizvi, S. F. A.; Anwar, U. Tetracycline: Classification, Structure Activity Relationship and Mechanism of Action as a Theranostic Agent for Infectious Lesions-A Mini Review. *Biomedical Journal of Scientific & Technical Research* **2018**, *7*, 1–10, doi:10.26717/BJSTR.2018.07.001475.
53. Janser, I. Tetracycline Amide Antibiotics. In *Bioactive Carboxylic Compound Classes: Pharmaceuticals and Agrochemicals*; Lamberth, C., Dinges, J., Eds.; John Wiley & Sons, Ltd, 2016; pp. 115–131.
54. Chopra, I.; Roberts, M. Tetracycline Antibiotics: Mode of Action, Applications, Molecular Biology, and Epidemiology of Bacterial Resistance. *Microbiology and Molecular Biology Reviews* **2001**, *65*, 232, doi:10.1128/MMBR.65.2.232-260.2001.
55. Rusu, A.; Buta, E. L. The development of third-generation tetracycline antibiotics and new perspectives. *Pharmaceutics* **2021**, *13*, 2085, doi:10.3390/PHARMACEUTICS13122085/S1.
56. Chico, J.; van Holthoon, F.; Zuidema, T. Ion Suppression Study for Tetracyclines in Feed. *Chromatography Research International* **2012**, *2012*, 1–9, doi:10.1155/2012/135854.
57. Topare, N. S.; Surangea, S.; Chaudharia, A.; Raut-Jadhavc, S.; Khedkard, S. V.; Bokil, S. A. Adsorption of Rhodamine-B by using Citrus peel powder: Influence of operating parameters. *Journal of Indian Chemical Society* **2020**, *97*, 2188–2194.
58. Luaibi, H. M.; Al-Taweel, S. S.; Gaaz, T. S.; Kadhum, A. A. H.; Takriff, M. S.; Al-Amiery, A. A. Removal of rhodamine dye from water using erbium oxide nanoparticles. *Korean Journal of Materials Research* **2019**, *29*, 747–752, doi:10.3740/MRSK.2019.29.12.747.
59. Kumar, A. Adsorptive removal of Rhodamine B (dye) using low cost adsorbents, Master thesis, National Institute of Technology, 2013.
60. Rhodamine B | $C_{28}H_{31}ClN_2O_3$ | CID 6694 - PubChem Available online: https://pubchem.ncbi.nlm.nih.gov/compound/Rhodamine-B (accessed on Nov 6, 2024).
61. Samarghandi, M.; Hadi, M.; Moayedi, S.; Askari, F. Two-parameter isotherms of methyl orange sorption by pinecone derived activated carbon. *Iranian Journal of Environmental Health Science & Engineering* **2009**, *6*, 285–294.
62. Song, S.; Hao, C.; Zhang, X.; Zhang, Q.; Sun, R. Sonocatalytic degradation of methyl orange in aqueous solution using Fe-doped TiO_2 nanoparticles under mechanical agitation. *Open Chemistry* **2018**, *16*, 1283–1296, doi:10.1515/CHEM-2018-0137.
63. Methyl orange | $C_{14}H_{14}N_3NaO_3S$ | CID 23673835 - PubChem Available online: https://pubchem.ncbi.nlm.nih.gov/compound/Methyl-orange (accessed on Nov 6,

2024).
64. Tetracycline | $C_{22}H_{24}N_2O_8$ | CID 54675776 - PubChem Available online: https://pubchem.ncbi.nlm.nih.gov/compound/54675776 (accessed on Nov 6, 2024).
65. De Cazes, M.; Belleville, M. P.; Petit, E.; Llorca, M.; Rodríguez-Mozaz, S.; De Gunzburg, J.; Barceló, D.; Sanchez-Marcano, J. Design and optimization of an enzymatic membrane reactor for tetracycline degradation. *Catalysis Today* **2014**, *236*, 146–152, doi:10.1016/J.CATTOD.2014.02.051.
66. Singla, S.; Devi, P.; Basu, S. Highly Effectual Photocatalytic Remediation of Tetracycline under the Broad Spectrum of Sunlight by Novel $BiVO_4/Sb_2S_3$ Nanocomposite. *Catalysts* **2023**, *13(4)*, 731, doi:10.3390/CATAL13040731/S1.
67. Xiaoxin, Z.; Jin, H.; Ling, L.; Shuming, L.; Yueping, W.; Xinheng, Z. Research on standards and regulations of the operation of wastewater treatment plants. *IOP Conference Series: Earth and Environmental Science* **2019**, *267*, doi:10.1088/1755-1315/267/3/032028.
68. Mareddy, A. R. Technology in EIA. In *Environmental Impact Assessment*; Mareddy, A. R., Ed.; Butterworth-Heinemann: 12, 2017; pp. 421–490 ISBN 978-0-12-811139-0.
69. Silva, J. A. Wastewater Treatment and Reuse for Sustainable Water Resources Management: A Systematic Literature Review. *Sustainability (Switzerland)* **2023**, *15*, 10940, doi:10.3390/SU151410940.
70. Crini, G.; Lichtfouse, E. Wastewater Treatment: An Overview. In *Green Adsorbents for Pollutant Removal*; Crini, G., Lichtfouse, E., Eds.; Springer, 2018; pp. 1–21.
71. Ahirrao, S. Zero Liquid Discharge Solutions. In *Industrial Wastewater Treatment, Recycling and Reuse*; Ranade, V., Bhandari, V., Eds.; Butterworth-Heinemann, 2014; pp. 489–520 ISBN 978-0-08-099968-5.
72. Ren, G.; Han, H.; Wang, Y.; Liu, S.; Zhao, J.; Meng, X.; Li, Z. Recent Advances of Photocatalytic Application in Water Treatment: A Review. *Nanomaterials* **2021**, *11*, 1804, doi:10.3390/NANO11071804.
73. Iyyappan, J.; Gaddala, B.; Gnanasekaran, R.; Gopinath, M.; Yuvaraj, D.; Kumar, V. Critical review on wastewater treatment using photo catalytic advanced oxidation process: Role of photocatalytic materials, reactor design and kinetics. *Case Studies in Chemical and Environmental Engineering* **2024**, *9*, 100599, doi:10.1016/J.CSCEE.2023.100599.
74. Saratale, R. G.; Saratale, G. D.; Chang, J. S.; Govindwar, S. P. Bacterial decolorization and degradation of azo dyes: A review. *Journal of the Taiwan Institute of Chemical Engineers* **2011**, *42*, *1*, 138–157, doi:10.1016/J.JTICE.2010.06.006.
75. Garrido-Cardenas, J. A.; Esteban-García, B.; Agüera, A.; Sánchez-Pérez, J. A.; Manzano-Agugliaro, F. Wastewater Treatment by Advanced Oxidation Process and Their Worldwide Research Trends. *International Journal of Environmental Research and Public Health* **2019**, *17*, 170, doi:10.3390/IJERPH17010170.
76. Sharma, M. K.; Tyagi, V. K.; Singh, N. K.; Singh, S. P.; Kazmi, A. A. Sustainable technologies for on-site domestic wastewater treatment: a review with technical approach. *Environment, Development and Sustainability* **2022**, *24*, 3039–3090, doi:10.1007/S10668-021-01599-3.
77. Hübner, U.; Spahr, S.; Lutze, H.; Wieland, A.; Rüting, S.; Gernjak, W.; Wenk, J.

Advanced oxidation processes for water and wastewater treatment – Guidance for systematic future research. *Heliyon* **2024**, *10*, e30402, doi:10.1016/J.HELIYON.2024.E30402.

78. Mikhak, Y.; Torabi, M. M. A.; Fouladitajar, A. Chapter 3 - Refinery and petrochemical wastewater treatment. In *Sustainable Water and Wastewater Processing*; Galanakis, C. M., Agrafioti, E., Eds.; Elsevier, 2019; pp. 55–91 ISBN 9780128161708.
79. Abd El-Monaem, E. M.; Elshishini, H. M.; Bakr, S. S.; El-Aqapa, H. G.; Hosny, M.; Andaluri, G.; El-Subruiti, G. M.; Omer, A. M.; Eltaweil, A. S. A comprehensive review on LDH-based catalysts to activate persulfates for the degradation of organic pollutants. *npj Clean Water* **2023**, *6*, 1–24, doi:10.1038/s41545-023-00245-x.
80. Divyapriya, G.; Nambi, I. M.; Senthilnathan, J. Nanocatalysts in Fenton based advanced oxidation process for water and wastewater treatment. *Journal of Bionanoscience* **2016**, *10*, 356–368, doi:10.1166/JBNS.2016.1387.
81. Li, D.; Xu, H. Q.; Jiao, L.; Jiang, H. L. Metal-organic frameworks for catalysis: State of the art, challenges, and opportunities. *EnergyChem* **2019**, *1*, 100005, doi:10.1016/J.ENCHEM.2019.100005.
82. Liu, H.; Wang, C.; Wang, G. Photocatalytic Advanced Oxidation Processes for Water Treatment: Recent Advances and Perspective. *Chem Asian J* **2020**, *15*, 3239–3253, doi:10.1002/asia.202000895.
83. Guo, D.; Wu, Z.; Hu, Y.; Shu, X.; Che, J.; Yan, F.; Peng, B.; Zhu, G.; Jia, Y. Magnetically-induced enhancement of photocatalytic dye decomposition in ferroelectric $Hf_{0.5}Zr_2O_2$ films. *Ceramics International* **2024**, *50*, 33077–33084, doi:10.1016/J.CERAMINT.2024.06.016.
84. Ameta, R.; Solanki, M. S.; Benjamin, S.; Ameta, S. C. Chapter 6 - Photocatalysis. In *Advanced Oxidation Processes for Wastewater Treatment: Emerging Green Chemical Technology*; Ameta, Suresh C.; Ameta, R., Ed.; Elsevier Inc., 2018; pp. 135–175 ISBN 9780128105252.
85. Tahir, M. B.; Iqbal, T.; Rafique, M.; Rafique, M. S.; Nawaz, T.; Sagir, M. Chapter 5 - Nanomaterials for photocatalysis. In *Nanotechnology and Photocatalysis for Environmental Applications*; Tahir, M., Rafique, M., Shahid Rafique, M., Eds.; Elsevier, 2020; pp. 65–76.
86. Orege, J. I.; Oderinde, O.; Kifle, G. A.; Ibikunle, A. A.; Raheem, S. A.; Ejeromedoghene, O.; Okeke, E. S.; Olukowi, O. M.; Orege, O. B.; Fagbohun, E. O.; Ogundipe, T. O.; Avor, E. P.; Ajayi, O. O.; Daramola, M. O. Recent advances in heterogeneous catalysis for green biodiesel production by transesterification. *Energy Conversion and Management* **2022**, *258*, 115406, doi:10.1016/J.ENCONMAN.2022.115406.
87. Ayodhya, D.; Veerabhadram, G. A review on recent advances in photodegradation of dyes using doped and heterojunction based semiconductor metal sulfide nanostructures for environmental protection. *Materials Today Energy* **2018**, *9*, 83–113, doi:10.1016/J.MTENER.2018.05.007.
88. Fujishima, A.; Honda, K. Electrochemical Photolysis of Water at a Semiconductor Electrode. *Nature* **1972**, *238*, *5358*, 37–38, doi:10.1038/238037a0.
89. Ibhadon, A. O.; Fitzpatrick, P. Heterogeneous Photocatalysis: Recent Advances and Applications. *Catalysts* **2013**, *3*, 189–218, doi:10.3390/CATAL3010189.
90. Loddo, V.; Bellardita, M.; Camera-Roda, G.; Parrino, F.; Palmisano, L. Chapter 1 -

Heterogeneous Photocatalysis: A Promising Advanced Oxidation Process. In *Current Trends and Future Developments on (Bio-) Membranes: Photocatalytic Membranes and Photocatalytic Membrane Reactors*; Basile, A., Mozia, S., Molinari, R., Eds.; Elsevier, 2018; pp. 1–43 ISBN 9780128135495.

91. Herrmann, J. M. Heterogeneous photocatalysis: fundamentals and applications to the removal of various types of aqueous pollutants. *Catalysis Today* **1999**, *53*, 115–129, doi:10.1016/S0920-5861(99)00107-8.
92. Matias, M. L.; Nunes, D.; Pimentel, A.; Ferreira, S. H.; Borda D'Agua, R.; Duarte, M. P.; Fortunato, E.; Martins, R. Paper-based nanoplatforms for multifunctional applications. *Journal of Nanomaterials* **2019**, *2019*, doi:10.1155/2019/6501923.
93. Abebe, B.; Murthy, H. C. A.; Amare, E. Summary on Adsorption and Photocatalysis for Pollutant Remediation: Mini Review. *Journal of Encapsulation and Adsorption Sciences* **2018**, *8*, 225–255, doi:10.4236/jeas.2018.84012.
94. Nan Chong, M.; Jin, B.; Chow, C. W.; Saint, C. Recent developments in photocatalytic water treatment technology: A review. *Water Research* **2010**, *44,10*, 2997–3027, doi:10.1016/J.WATRES.2010.02.039.
95. He, F.; Jeon, W.; Choi, W. Photocatalytic air purification mimicking the self-cleaning process of the atmosphere. *Nature Communications* **2021**, *12*, *2528*, 1–4, doi:10.1038/s41467-021-22839-0.
96. Zhou, Z.; Li, B.; Liu, X.; Li, Z.; Zhu, S.; Liang, Y.; Cui, Z.; Wu, S. Recent Progress in Photocatalytic Antibacterial. *ACS Applied Bio Materials* **2021**, *4*, *5*, 3909–3936, doi:10.1021/acsabm.0c01335.
97. Mittal, T. Self-cleaning smart photocatalytic coatings for water treatment. *Materials Today: Proceedings* **2023**, *78*, 891–894, doi:10.1016/J.MATPR.2022.12.094.
98. Loddo, V.; Roda, G. C.; Parrino, F. Kinetic aspects of heterogeneous catalytic versus photocatalytic reactions. In *Heterogeneous Photocatalysis: Relationships with Heterogeneous Catalysis and Perspectives*; Marcì, G., Palmisano, L., Eds.; Elsevier, 2019; pp. 215–233 ISBN 9780444640154.
99. Szczepanik, B. Photocatalytic degradation of organic contaminants over clay-TiO_2 nanocomposites: A review. *Applied Clay Science* **2017**, *141*, 227–239, doi:10.1016/J.CLAY.2017.02.029.
100. Chen, X.; Mao, S. S. Titanium dioxide nanomaterials: Synthesis, properties, modifications and applications. *Chemical Reviews* **2007**, *107*, *7*, 2891–2959, doi:10.1021/CR0500535.
101. García-Betancourt, M. L.; Jiménez, S. I. R.; González-Hodges, A.; Salazar, Z. E. N.; Escalante-García, I. L.; Aparicio, J. R.; García-Betancourt, M. L.; Jiménez, S. I. R.; González-Hodges, A.; Salazar, Z. E. N.; Escalante-García, I. L.; Aparicio, J. R. Low Dimensional Nanostructures: Measurement and Remediation Technologies Applied to Trace Heavy Metals in Water. In *Trace Metals in the Environment - New Approaches and Recent Advances*; IntechOpen, 2020 ISBN 978-1-83880-332-2.
102. Chen, R.; Wang, Z.; Zhou, Q.; Lu, J.; Zheng, M. A Template-Free Microwave Synthesis of One-Dimensional Cu_2O Nanowires with Desired Photocatalytic Property. *Materials* **2018**, *11(10)*, 1843, doi:10.3390/MA11101843.
103. Machín, A.; Fontánez, K.; Arango, J. C.; Ortiz, D.; De León, J.; Pinilla, S.; Nicolosi, V.;

Petrescu, F. I.; Morant, C.; Márquez, F. One-Dimensional (1D) Nanostructured Materials for Energy Applications. *Materials* **2021**, *14(10)*, 2609, doi:10.3390/MA14102609.

104. Chen, L.; Ye, X.; Chen, S.; Ma, L.; Wang, Z.; Wang, Q.; Hua, N.; Xiao, X.; Cai, S.; Liu, X. Ti_3C_2 MXene nanosheet/TiO_2 composites for efficient visible light photocatalytic activity. *Ceramics International* **2020**, *46*, 25895–25904, doi:10.1016/J.CERAMINT.2020.07.074.
105. Asghar, N.; Hussain, A.; Nguyen, D. A.; Ali, S.; Hussain, I.; Junejo, A.; Ali, A. Advancement in nanomaterials for environmental pollutants remediation: a systematic review on bibliometrics analysis, material types, synthesis pathways, and related mechanisms. *Journal of Nanobiotechnology* **2024**, *22*, 1–28, doi:10.1186/S12951-023-02151-3.
106. Bodzek, M.; Konieczny, K.; Kwiecińska-Mydlak, A. Nano-photocatalysis in water and wastewater treatment. *Desalination and Water Treatment* **2021**, *243*, 51–74, doi:10.5004/DWT.2021.27867.
107. Yadav, K. K.; Cabral-Pinto, M. M. S.; Gacem, A.; Fallatah, A. M.; Ravindran, B.; Rezania, S.; Algethami, J. S.; Bashier Eltayeb, L.; Abbas, M.; Hassan Al-shareef, T.; Vinayak, V.; Truong Son, C.; Awjan Alreshidi, M.; Manuel Rodríguez-Díaz, J.; Homod, R. Z. Recent advances in the application of nanoparticle-based strategies for water remediation as a novel clean technology–A comprehensive review. *Materials Today Chemistry* **2024**, *40*, 102226, doi:10.1016/J.MTCHEM.2024.102226.
108. Tripathy, J.; Mishra, A.; Pandey, M.; Thakur, R. R.; Chand, S.; Rout, P. R.; Shahid, M. K. Advances in Nanoparticles and Nanocomposites for Water and Wastewater Treatment: A Review. *Water* **2024**, *16*, 1481, doi:10.3390/W16111481.
109. Mekuye, B.; Abera, B. Nanomaterials: An overview of synthesis, classification, characterization, and applications. *Nano Select* **2023**, *4*, 486–501, doi:10.1002/NANO.202300038.
110. Qin, Z. Nanostructure Design of Catalysts: Latest Advances and Prospects. *Nanomaterials* **2023**, *13*, 1980, doi:10.3390/NANO13131980.
111. Neaţu, Ş.; Maciá-Agulló, J. A.; Garcia, H. Solar light photocatalytic CO_2 reduction: General considerations and selected bench-mark photocatalysts. *International Journal of Molecular Sciences* **2014**, *15*, 5246–5262, doi:10.3390/IJMS15045246.
112. Zhou, Y.; Zhang, L.; Tao, S. Porous TiO_2 with large surface area is an efficient catalyst carrier for the recovery of wastewater containing an ultrahigh concentration of dye. *RSC Advances* **2018**, *8*, 3433–3442, doi:10.1039/C7RA11985B.
113. Li, J.; Wu, Q.; Wu, J. Synthesis of Nanoparticles via Solvothermal and Hydrothermal Methods. In *Handbook of Nanoparticles*; Springer International Publishing, 2015; pp. 1–28.
114. Goodarzi, N.; Ashrafi-Peyman, Z.; Khani, E.; Moshfegh, A. Z. Recent Progress on Semiconductor Heterogeneous Photocatalysts in Clean Energy Production and Environmental Remediation. *Catalysts 2023, Vol. 13, Page 1102* **2023**, *13*, 1102, doi:10.3390/CATAL13071102.
115. Lu, N.; Zhang, M.; Jing, X.; Zhang, P.; Zhu, Y.; Zhang, Z. Electrospun Semiconductor-Based Nano-Heterostructures for Photocatalytic Energy Conversion and

Environmental Remediation: Opportunities and Challenges. *Energy & Environmental Materials* **2023**, *6*, e12338, doi:10.1002/EEM2.12338.
116. Morab, S.; Sundaram, M. M.; Pivrikas, A. Review on Charge Carrier Transport in Inorganic and Organic Semiconductors. *Coatings* **2023**, *13*, 1657, doi:10.3390/COATINGS13091657.
117. Yan, C.; Li, Q.; Gong, Z.; Chen, Y.; Wang, L. Organic Semiconductor Nanostructured Photocatalysts. *Progress in Chemistry* **2020**, *33*, 1917–1934, doi:10.7536/PC200945.
118. Guo, Y.; Zhou, Q.; Zhu, B.; Tang, C. Y.; Zhu, Y. Advances in organic semiconductors for photocatalytic hydrogen evolution reaction. *EES Catalysis* **2023**, *1*, 333–352, doi:10.1039/D3EY00047H.
119. Eslamian, M. Inorganic and Organic Solution-Processed Thin Film Devices. *Nano-Micro Letters* **2016**, *9*, 1–23, doi:10.1007/S40820-016-0106-4.
120. Sivula, K. Are Organic Semiconductors Viable for Robust, High-Efficiency Artificial Photosynthesis? *ACS Energy Letters* **2020**, *5*, 1970–1973, doi:10.1021/ACSENERGYLETT.0C01084/.
121. Qin, Z.; Gao, C.; Gao, H.; Wang, T.; Dong, H.; Hu, W. Molecular doped, color-tunable, high-mobility, emissive, organic semiconductors for light-emitting transistors. *Science Advances* **2022**, *8*, 1–8, doi:10.1126/SCIADV.ABP8775.
122. Cao, J.; Shan, T.; Wang, J. K.; Xu, Y. X.; Ren, X.; Zhong, H. Stereoisomerism of ladder-type acceptor molecules and its effect on photovoltaic properties. *Dyes and Pigments* **2019**, *165*, 354–360, doi:10.1016/J.DYEPIG.2019.02.046.
123. Pohl, U. W. Electronic Properties of Organic Semiconductors. In *Epitaxy of Semiconductors*; Springer, Cham, 2020; pp. 177–205 ISBN 978-3-030-43869-2.
124. Wang, L.; Zhu, W. Organic Donor-Acceptor Systems for Photocatalysis. *Advanced Science* **2024**, *11*, 2307227, doi:10.1002/ADVS.202307227.
125. Conjugated aromatic systems. *Nature Synthesis* **2023**, *2*, 799–799, doi:10.1038/s44160-023-00404-5.
126. Tahir, M. H.; Ibrahim, M. A. A.; Sayed, S. R. M.; Magero, D.; Pembere, A. Dielectric constant prediction of polymers for organic solar cells and generation of library of new organic compounds. *Journal of Solid State Chemistry* **2025**, *345*, 125213, doi:10.1016/J.JSSC.2025.125213.
127. Nguyen, T. P. Defect analysis in organic semiconductors. *Materials Science in Semiconductor Processing* **2006**, *9*, 198–203, doi:10.1016/J.MSSP.2006.01.060.
128. Abd Nasir, F. H.; Woon, K. L. Charge carrier trapping in organic semiconductors: Origins, impact and strategies for mitigation. *Synthetic Metals* **2024**, *307*, 117661, doi:10.1016/J.SYNTHMET.2024.117661.
129. Chen, Z.; Chong, B.; Wells, N.; Yang, G.; Wang, L. Constructing a coplanar heterojunction through enhanced π-π conjugation in g-C_3N_4 for efficient solar-driven water splitting. *Chinese Chemical Letters* **2022**, *33*, 2579–2584, doi:10.1016/J.CCLET.2021.08.118.
130. Dong, J.; Yan, C.; Chen, Y.; Zhou, W.; Peng, Y.; Zhang, Y.; Wang, L. N.; Huang, Z. H. Organic semiconductor nanostructures: optoelectronic properties, modification strategies, and photocatalytic applications. *Journal of Materials Science & Technology* **2022**, *113*, 175–198, doi:10.1016/J.JMST.2021.09.002.

131. Khan, J.; Ahmad, R. T. M.; Tan, J.; Zhang, R.; Khan, U.; Liu, B. Recent advances in 2D organic–inorganic heterostructures for electronics and optoelectronics. *SmartMat* **2023**, *4*, e1156, doi:10.1002/SMM2.1156.
132. Wang, L.; Zhang, J.; Zhang, Y.; Yu, H.; Qu, Y.; Yu, J. Inorganic Metal-Oxide Photocatalyst for H_2O_2 Production. *Small* **2022**, *18*, 2104561, doi:10.1002/SMLL.202104561.
133. Huseynova, G. Inorganic versus organic semiconductors. *Material Science & Engineering International Journal* **2020**, *4*, 166–167, doi:10.15406/MSEIJ.2020.04.00145.
134. Jurchescu, O. D.; Baas, J.; Palstra, T. T. M. Effect of impurities on the mobility of single crystal pentacene. *Applied Physics Letters* **2004**, *84*, 3061–3063, doi:10.1063/1.1704874.
135. Nunes, D.; Pimentel, A.; Gonçalves, A.; Pereira, S.; Branquinho, R.; Barquinha, P.; Martins, R. Metal Oxide Nanostructures for Sensor Applications. *Semicond. Sci. Technol* **2019**, *34,4*, 1–178, doi:10.1088/1361-6641/ab011e.
136. He, H. Metal oxide semiconductors and conductors. In *Solution Processed Metal Oxide Thin Films for Electronic Applications*; Cui, Z., Korotcenkov, G., Eds.; Elsevier, 2020; pp. 7–30 ISBN 9780128149300.
137. Naseem, T.; Durrani, T. The role of some important metal oxide nanoparticles for wastewater and antibacterial applications: A review. *Environmental Chemistry and Ecotoxicology* **2021**, *3(3)*, 59–75, doi:10.1016/J.ENCECO.2020.12.001.
138. Branquinho, R.; Carlos, E.; Nunes, D.; Fortunato, E.; Martins, R. Sustainable Synthesis of Oxides for Electronics and Photocatalysis. In *Synthesis and Applications in Chemistry and Materials*; Pombeiro, A., Mahmudov, K. T., Silva, M. F., Eds.; World Scientific, 2024; Vol. 14, pp. 443–482 ISBN 978-981-127-993-5.
139. McQuarrie, D. A.; Rock, P. A.; Gallogly, E. B. INTERCHAPTER I: The Main-Group Metals. In *General Chemistry*; McClain, J., Ed.; University Science Books, 2011; p. 11 ISBN 1891389602.
140. Mabate, T. P.; Maqunga, N. P.; Ntshibongo, S.; Maumela, M.; Bingwa, N. Metal oxides and their roles in heterogeneous catalysis: special emphasis on synthesis protocols, intrinsic properties, and their influence in transfer hydrogenation reactions. *SN Applied Sciences* **2023**, *5*, *196*, 1–25, doi:10.1007/S42452-023-05416-6.
141. Sun, Y.; Chen, G.; Xi, S.; Xu, Z. J. Catalytically Influential Features in Transition Metal Oxides. *ACS Catalysis* **2021**, *11*, *22*, 13947–13954, doi:10.1021/acscatal.1c04393.
142. Niu, X.; Lei, Z. Copper doped manganese oxides to produce enhanced catalytic performance for CO oxidation. *Journal of Environmental Chemical Engineering* **2019**, *7*, *3*, 103055, doi:10.1016/J.JECE.2019.103055.
143. Zhang, H.; Zhang, Y.; Song, H.; Cui, Y.; Xue, Y.; Wu, C. E.; Pan, C.; Xu, J.; Qiu, J.; Xu, L.; Chen, M. Transition Metal (Fe_2O_3, Co_3O_4 and NiO)-Promoted CuO-Based α-MnO_2 Nanowire Catalysts for Low-Temperature CO Oxidation. *Catalysts* **2023**, *13(3)*, 588, doi:10.3390/CATAL13030588.
144. Riente, P.; Noël, T. Application of metal oxide semiconductors in light-driven organic transformations. *Catalysis Science & Technology* **2019**, *9*, 5186–5232, doi:10.1039/C9CY01170F.
145. Moumen, A.; Kumarage, G. C. W.; Comini, E. P-Type Metal Oxide Semiconductor Thin Films: Synthesis and Chemical Sensor Applications. *Sensors* **2022**, *22(4)*, 1359,

doi:10.3390/S22041359.
146. Angel, Raquel Del; Durán-Álvarez, Juan C.; and Zanella, R. TiO_2-Low Band Gap Semiconductor Heterostructures for Water Treatment Using Sunlight-Driven Photocatalysis. In *Titanium Dioxide - Material for a Sustainable Environment*; Yang, D., Ed.; IntechOpen, 2018; pp. 1–518 ISBN 978-1-78923-327-8.
147. Coronado, J. M., & Hernández-Alonso, M. D. The Keys of Success: TiO_2 as a Benchmark Photocatalyst. In *Design of Advanced Photocatalytic Materials for Energy and Environmental applications*; Coronado, Juan M.;Fresno, Fernando;Hernández-Alonso, María D.;Portela, R., Ed.; SpringerLink: London, 2013; pp. 85–101 ISBN 978-1-4471-5061-9.
148. Bagheri, S.; Muhd Julkapli, N.; Bee Abd Hamid, S. Titanium Dioxide as a Catalyst Support in Heterogeneous Catalysis. *The Scientific World Journal* **2014**, *2014*, 727496, doi:10.1155/2014/727496.
149. Padmanabhan, N. T.; John, H. Titanium dioxide based self-cleaning smart surfaces: A short review. *Journal of Environmental Chemical Engineering* **2020**, *8(5)*, 104211, doi:10.1016/J.JECE.2020.104211.
150. Wei, J.; Zhu, P.; Chen, P. Degradation of Tetracycline on SiO_2-TiO_2-C Aerogel Photocatalysts under Visible Light. *Materials* **2022**, *15(5)*, 1963, doi:10.3390/MA15051963.
151. Ahn, T. K.; Lee, D. H.; Kim, T. sup; Jang, G. chol; Choi, S. J.; Oh, J. B.; Ye, G.; Lee, S. Modification of Titanium Implant and Titanium Dioxide for Bone Tissue Engineering. *Advances in experimental medicine and biology 1077*, 355–368, doi:10.1007/978-981-13-0947-2_19.
152. Fujishima, A.; Zhang, X. Titanium dioxide photocatalysis: present situation and future approaches. *Comptes Rendus Chimie* **2006**, *9(5–6)*, 750–760, doi:10.1016/J.CRCI.2005.02.055.
153. Zhou, X.; Schmuki, P. One-dimensional TiO_2 nanotube–based photocatalysts: enhanced performance by site-selective decoration. In *Interface Science and Technology*; Elsevier, 2020; Vol. 31, pp. 231–264.
154. Nunes, D.; Pimentel, A.; Santos, L.; Barquinha, P.; Pereira, L.; Fortunato, E.; Martins, R.; Pimentel, A.; Barquinha, P.; Pereira, L.; Fortunato, E.; Martins, R. *Metal oxide nanostructures: Synthesis, properties and applications*; Korotcenkov, G., Ed.; 1st ed.; Elsevier, 2018; ISBN 9780128115121.
155. Etacheri, V.; Di Valentin, C.; Schneider, J.; Bahnemann, D.; Pillai, S. C. Visible-light activation of TiO_2 photocatalysts: Advances in theory and experiments. *Journal of Photochemistry and Photobiology C: Photochemistry Reviews* **2015**, *25*, 1–29, doi:10.1016/J.JPHOTOCHEMREV.2015.08.003.
156. Di Paola, A.; Bellardita, M.; Palmisano, L. Brookite, the Least Known TiO_2 Photocatalyst. *Catalysts* **2013**, *3*, 36–73, doi:10.3390/catal3010036.
157. Nunes, D.; Pimentel, A.; Araujo, A.; Calmeiro, T. R.; Panigrahi, S.; Pinto, J. V.; Barquinha, P.; Gama, M.; Fortunato, E.; Martins, R. Enhanced UV Flexible Photodetectors and Photocatalysts Based on TiO_2 Nanoplatforms. *Springer Nature* **2018**, *61*, 1591–1606.
158. Stephen, L. Titanium Dioxide Versatile Solid Crystalline: An Overview. In *Assorted Dimensional Reconfigurable Materials*; Dongre, R., Peshwe, D. R., Eds.; IntechOpen, 2020 ISBN 978-1-78985-514-2.

159. Nguyen, T. T.; Edalati, K. Brookite TiO_2 as an active photocatalyst for photoconversion of plastic wastes to acetic acid and simultaneous hydrogen production: Comparison with anatase and rutile. *Chemosphere* **2024**, *355*, 141785, doi:10.1016/J.CHEMOSPHERE.2024.141785.
160. Kong, E. D. H.; Chau, J. H. F.; Lai, C. W.; Khe, C. S.; Sharma, G.; Kumar, A.; Siengchin, S.; Sanjay, M. R. GO/TiO_2-Related Nanocomposites as Photocatalysts for Pollutant Removal in Wastewater Treatment. *Nanomaterials* **2022**, *12*, 1–26, doi:10.3390/NANO12193536.
161. Yan, X.; Chen, X. Titanium Dioxide Nanomaterials. In *Encyclopedia of Inorganic and Bioinorganic Chemistry*; R.A. Scott, Ed.; John Wiley & Sons, Ltd, 2015; pp. 1–38 ISBN 9781605113296.
162. Ola, O.; Maroto-Valer, M. M. Review of material design and reactor engineering on TiO_2 photocatalysis for CO_2 reduction. *Journal of Photochemistry and Photobiology C: Photochemistry Reviews* **2015**, *24*, 16–42, doi:10.1016/J.JPHOTOCHEMREV.2015.06.001.
163. Akimoto, J.; Gotoh, Y.; Oosawa, Y.; Nonose, N.; Kumagai, T.; Aoki, K.; Takei, H. Topotactic Oxidation of Ramsdellite-Type $Li_{0.5}TiO_2$, a New Polymorph of Titanium Dioxide: TiO_2(R). *Journal of Solid State Chemistry* **1994**, *113*, 27–36, doi:10.1006/JSSC.1994.1337.
164. Gatou, M. A.; Syrrakou, A.; Lagopati, N.; Pavlatou, E. A. Photocatalytic TiO_2-Based Nanostructures as a Promising Material for Diverse Environmental Applications: A Review. *Reactions* **2024**, *5*, 135–194, doi:10.3390/REACTIONS5010007.
165. Dash, D.; Pandey, C. K.; Chaudhury, S.; Tripathy, S. K. Structural, electronic, and mechanical properties of cubic TiO_2: A first-principles study. *Chinese Physics B* **2018**, *27*, 017102, doi:10.1088/1674-1056/27/1/017102.
166. Dubrovinskaia, N. A.; Dubrovinsky, L. S.; Ahuja, R.; Prokopenko, V. B.; Dmitriev, V.; Weber, H. P.; Osorio-Guillen, J. M.; Johansson, B. Experimental and Theoretical Identification of a New High-Pressure TiO_2 Polymorph. *Physical Review Letters* **2001**, *87*, 275501, doi:10.1103/PhysRevLett.87.275501.
167. Nagakawa, H.; Ochiai, T.; Ma, H.; Wang, C.; Zhang, X.; Shen, Y.; Takashima, M.; Ohtani, B.; Nagata, M. Elucidation of the electron energy structure of TiO_2(B) and anatase photocatalysts through analysis of electron trap density. *RSC Advances* **2020**, *10*, 18496–18501, doi:10.1039/D0RA02587A.
168. Akrami, S.; Watanabe, M.; Ling, T. H.; Ishihara, T.; Arita, M.; Fuji, M.; Edalati, K. High-pressure TiO_2-II polymorph as an active photocatalyst for CO_2 to CO conversion. *Applied Catalysis B: Environmental* **2021**, *298*, 120566, doi:10.1016/J.APCATB.2021.120566.
169. Lee, J. G.; Pickard, C. J.; Cheng, B. High-pressure phase behaviors of titanium dioxide revealed by a Δ-learning potential. *Journal of Chemical Physics* **2022**, *156*, doi:10.1063/5.0079844.
170. Vargas-Galvis, F.; Holguín-Villa, J. D.; Arias Gómez, J. A.; Mejía, A. F.; Velásquez, A. A.; Arroyave, M.; Palacio Espinosa, C. C. Formation, Transformation, and Electrical Performance of Magnéli Phases Obtained by Flame Spraying from TiO_2 Particles. *Journal of Materials Engineering and Performance* **2024**, *33*, 2562–2571, doi:10.1007/S11665-023-08887-1.
171. Kumar, S. G.; Devi, L. G. Review on modified TiO_2 photocatalysis under UV/visible

light: Selected results and related mechanisms on interfacial charge carrier transfer dynamics. *Journal of Physical Chemistry A* **2011**, *115*, *46*, 13211–13241, doi:10.1021/jp204364a.

172. Wang, X.; Wang, F.; Sang, Y.; Liu, H.; Wang, X.; Wang, F.; Sang, Y.; Liu, H. Full-Spectrum Solar-Light-Activated Photocatalysts for Light–Chemical Energy Conversion. *Advanced Energy Materials* **2017**, *7*, 1700473, doi:10.1002/AENM.201700473.
173. Kruse, O.; Rupprecht, J.; Mussgnug, J. H.; Dismukes, G. C.; Hankamer, B. Photosynthesis: A blueprint for solar energy capture and biohydrogen production technologies. *Photochemical and Photobiological Sciences* **2005**, *4*, 957–970, doi:10.1039/B506923H.
174. Solar Radiation Spectrum • SunWind Solar Available online: https://sunwindsolar.com/blog/solar-radiation-spectrum/ (accessed on Nov 5, 2024).
175. Han, Y. X.; Yang, C. L.; Wang, M. S.; Ma, X. G.; Wang, L. Z. Enhancing the visible-light absorption of TiO_2 with the use of key N, Co, and Na dopant concentrations. *Solar Energy Materials and Solar Cells* **2015**, *132*, 94–100, doi:10.1016/J.SOLMAT.2014.08.027.
176. Das, A.; Peu, S. D.; Hossain, M. S.; Akanda, M. A. M.; Salah, M. M.; Akanda, M. M. H.; Rahman, M.; Das, B. K. Metal Oxide Nanosheet: Synthesis Approaches and Applications in Energy Storage Devices (Batteries, Fuel Cells, and Supercapacitors). *Nanomaterials* **2023**, *13*, 1066, doi:10.3390/NANO13061066.
177. Pathak, J.; Pandey, B.; Singh, P.; Kumar, R.; Kaushik, S.; Sahu, I. P.; Thakur, T. K.; Kumar, A. Exploring the Paradigm of Phyto-Nanofabricated Metal Oxide Nanoparticles: Recent Advancements, Applications, and Challenges. *Molecular Biotechnology* **2023**, 1–21, doi:10.1007/S12033-023-00799-8.
178. Dubey, R. S.; Krishnamurthy, K. V.; Singh, S. Experimental studies of TiO_2 nanoparticles synthesized by sol-gel and solvothermal routes for DSSCs application. *Results in Physics* **2019**, *14,102390*, 1–6.
179. Khairy, M.; Zakaria, W. Effect of metal-doping of TiO_2 nanoparticles on their photocatalytic activities toward removal of organic dyes. *Egyptian Journal of Petroleum* **2014**, *23,4*, 419–426.
180. Scuderi, V.; Impellizzeri, G.; Romano, L.; Scuderi, M.; Nicotra, G.; Bergum, K.; Irrera, A.; Svensson, B. G.; Privitera, V. TiO_2-coated nanostructures for dye photo-degradation in water. *Nanoscale research letters* **2014**, *9,1*, 1–7.
181. Maragatha, J.; Rajendran, S.; Endo, T.; Karuppuchamy, S. Microwave synthesis of metal doped TiO_2 for photocatalytic applications. *Journal of Materials Science: Materials in Electronics* **2017**, *28,7*, 5281–5287.
182. Boyadzhiev, S.; Georgieva, V.; Rassovska, M. Characterization of reactive sputtered TiO_2 thin films for gas sensor applications. *Journal of Physics: Conference Series* **2010**, *253,012040*, 1–7.
183. Fang, F.; Kennedy, J.; Manikandan, E.; Futter, J.; Markwitz, A. Morphology and characterization of TiO_2 nanoparticles synthesized by arc discharge. *Chemical Physics Letters* **2012**, *521*, 86–90, doi:10.1016/J.CPLETT.2011.11.046.
184. Nunes, D.; Freire, T.; Barranger, A.; Vieira, J.; Matias, M.; Pereira, S.; Pimentel, A.; Cordeiro, N. J. A.; Fortunato, E.; Martins, R. TiO_2 Nanostructured Films for Electrochromic Paper Based-Devices. *Applied Sciences* **2020**, *10(4)*, 1200,

doi:10.3390/APP10041200.
185. Schäf, O.; Ghobarkar, H.; Knauth, P. Hydrothermal Synthesis of Nanomaterials, volume 8. In *Nanostructured Materials*; Springer, Boston, MA, 2004; pp. 23–41 ISBN 978-0-306-47722-5.
186. Gan, Y. X.; Jayatissa, A. H.; Yu, Z.; Chen, X.; Li, M. Hydrothermal Synthesis of Nanomaterials. *Journal of Nanomaterials* **2020**, *2020*, 1–3, doi:10.1155/2020/8917013.
187. Nunes, D.; Pimentel, A.; Santos, L.; Barquinha, P.; Pereira, L.; Fortunato, E.; Martins, R. Synthesis, design, and morphology of metal oxide nanostructures. In *Metal Oxide Nanostructures*; Elsevier, 2019; pp. 21–57 ISBN 978-0-12-811512-1.
188. Yang, G.; Park, S. J. Conventional and Microwave Hydrothermal Synthesis and Application of Functional Materials: A Review. *Materials* **2019**, *12(7)*, 1177, doi:10.3390/MA12071177.
189. Onwudiwe, D. C. Microwave-assisted synthesis of PbS nanostructures. *Heliyon* **2019**, *5(3)*, e01413, doi:10.1016/J.HELIYON.2019.E01413.
190. Kumar, A.; Kuang, Y.; Liang, Z.; Sun, X. Microwave chemistry, recent advancements, and eco-friendly microwave-assisted synthesis of nanoarchitectures and their applications: a review. *Materials Today Nano* **2020**, *11*, 100076, doi:10.1016/J.MTNANO.2020.100076.
191. Gude, V. G.; Martinez-Guerra, E. Green Chemistry of Microwave-Enhanced Biodiesel Production. In *Production of Biofuels and Chemicals with Microwave*; Fang, Z., Richard L. Smith, J., Qi, X., Eds.; Springer Nature, 2015; Vol. 3, pp. 225–250.
192. Bilecka, I.; Niederberger, M. Microwave chemistry for inorganic nanomaterials synthesis. *Nanoscale* **2010**, *2*, 1358–1374, doi:10.1039/B9NR00377K.
193. Rajasekhar, K. K.; Ananth, V. S.; Nithiyananthan, T. S.; Hareesh, G.; Kumar, P. N.; Siva, R.; Reddy, P. COMPARATIVE STUDY OF CONVENTIONAL AND MICROWAVE INDUCED SYNTHESIS OF SELECTED HETEROCYCLIC MOLECULES. *International Journal of ChemTech Research CODEN* **2010**, *2*, 592–597.
194. Grewal, A. S.; Kumar, K.; Redhu, S.; Bhardwa, S. Microwave assisted synthesis: a green chemistry approach. *International Research Journal of Pharmaceutical and Applied Sciences* **2013**, *3*, 278–285.
195. Wu, M. C.; Chang, I. C.; Hsiao, K. C.; Huang, W. K. Highly visible-light absorbing black TiO_2 nanocrystals synthesized by sol–gel method and subsequent heat treatment in low partial pressure H_2. *Journal of the Taiwan Institute of Chemical Engineers* **2016**, *63*, 430–435, doi:10.1016/J.JTICE.2016.02.026.
196. Dave, D. P.; Chauhan, K. V. Synthesis of visible spectrum-active TiO_2 thin film induced by RF magnetron sputtering. *Materials Today: Proceedings* **2022**, *62*, 4254–4259, doi:10.1016/J.MATPR.2022.04.755.
197. Vilas Vilela, L.; Ruiz-Rubio, L.; Wang, H.; Armakovi´carmakovi´c, S. J.; Savanovi´csavanovi´c, M. M.; Armakovi´c, S. A. Titanium Dioxide as the Most Used Photocatalyst for Water Purification: An Overview. *Catalysts* **2022**, *13(1)*, 26, doi:10.3390/CATAL13010026.
198. Sukrey, N. A.; Bushroa, A. R.; Rizwan, M. Dopant incorporation into TiO_2 semiconductor materials for optical, electronic, and physical property enhancement: doping strategy and trend analysis. *Journal of the Australian Ceramic Society 2023* **2023**, *1*,

1–27, doi:10.1007/S41779-023-00958-9.
199. Wach, A.; Zou, X.; Wojtaszek, K.; Kayser, Y.; Garlisi, C.; Palmisano, G.; Jacinto, S.; Szlachetko, J. Towards understanding the TiO_2 doping at the surface and bulk. *X-Ray Spectrometry* **2023**, *52*, 261–268, doi:10.1002/XRS.3363.
200. Bhat, A. P.; Jadhav, A. J.; Holkar, C. R.; Pinjari, D. V. Doped-TiO_2 and doped-mixed metal oxide-based nanocomposite for photocatalysis. In *Handbook of Nanomaterials for Wastewater Treatment: Fundamentals and Scale up Issues*; Bhanvase, B., Sonawane, S., Pawade, V., Pandit, A., Eds.; Elsevier, 2021; pp. 155–180 ISBN 9780128214961.
201. Juárez-Cortazar, D. E.; Torres-Torres, J. G.; Hernandez-Ramirez, A.; Arévalo-Pérez, J. C.; Cervantes-Uribe, A.; Godavarthi, S.; de los Monteros, A. E. E.; Silahua-Pavón, A. A.; Cordero-Garcia, A. Doping of TiO_2 Using Metal Waste (Door Key) to Improve Its Photocatalytic Efficiency in the Mineralization of an Emerging Contaminant in an Aqueous Environment. *Water* **2022**, *14(9)*, 1389, doi:10.3390/W14091389.
202. Xiang, D.; Gong, Y.; Chen, C.; Sun, R.; Zhao, S.; Liu, Y.; Jian, Q.; Li, Y.; Dou, W.; Li, D.; Ying, P.; Tang, G. Orbital Splitting and Interstitial Doping Lead to High Thermoelectric Performance in *n*-type PbSe. *Small* **2025**, *21*, 2412833, doi:10.1002/SMLL.202412833.
203. Zou, J.; Park, J.; Yoon, H.; Mark Sammes, N.; Chung, J. Effects of transition metal ion dopants on the performance of $Ca_{2.9}Bi_{0.1}Co_4O_{9-\delta}$ cathode. *Journal of Alloys and Compounds* **2013**, *558*, 188–194, doi:10.1016/J.JALLCOM.2012.10.043.
204. Clyde, E.; Lopez, R. Rational Selection of Transition Metal Co-Dopant in Sulfur-Doped Titanium Dioxide. *Engineering Proceedings* **2023**, *37(1)*, 15, doi:10.3390/ECP2023-14699.
205. Medhi, R.; Marquez, M. D.; Lee, T. R. Visible-Light-Active Doped Metal Oxide Nanoparticles: Review of their Synthesis, Properties, and Applications. *ACS Applied Nano Materials* **2020**, *3*, *7*, 6156–6185, doi:10.1021/acsanm.0c01035.
206. Frey, P. A.; Reed, G. H. The ubiquity of iron. *ACS Chemical Biology* **2012**, *7*, 1477–1481, doi:10.1021/CB300323Q.
207. Rosa, D.; D'Agostino, F.; Bavasso, I.; Bracciale, M. P.; Di Palma, L. Easy way to produce iron-doped titania nanoparticles via the solid-state method and investigation their photocatalytic activity. *Journal of Materials Research* **2023**, *38*, 1282–1292, doi:10.1557/S43578-022-00885-8.
208. Ochoa Rodríguez, P. A.; Pecchi, G. A.; Casuscelli, S. G.; Elías, V. R.; Eimer, G. A. A simple synthesis way to obtain iron-doped TiO_2 nanoparticles as photocatalytic surfaces. *Chemical Physics Letters* **2019**, *732*, 1–6.
209. Shelhammer, D.; Cao, X. A.; Liu, N.; Wang, H. J.; Zhou, Y. M. Doping effects and stability of calcium in organic electron-transport materials. *Organic Electronics* **2020**, *84*, 105799, doi:10.1016/J.ORGEL.2020.105799.
210. Minchi, L.; Cao, F.; Xinni, Z.; Youqiang, C.; Xuhua, L. Photocatalytic activity of Ca-TiO_2 nanofibers with different concentrations of calcium. *Chemical Physics Letters* **2019**, *736*, 136807, doi:10.1016/J.CPLETT.2019.136807.
211. Crişan, M.; Drăgan, N.; Crişan, D.; Ianculescu, A.; Niţoi, I.; Oancea, P.; Todan, L.; Stan, C.; Stănică, N. The effects of Fe, Co and Ni dopants on TiO_2 structure of sol–gel nanopowders used as photocatalysts for environmental protection: A comparative study. *Ceramics International* **2016**, *42*, 3088–3095, doi:10.1016/J.CERAMINT.2015.10.097.
212. Sahoo, C.; Gupta, A. K. Characterization and photocatalytic performance evaluation of

various metal ion-doped microstructured TiO_2 under UV and visible light. *Journal of Environmental Science and Health, Part A* **2015**, *50*, 659–668, doi:10.1080/10934529.2015.1011958.

213. Afonso, C.; Lima, O.; Segundo, I. R.; Landi, S.; Margalho, É.; Homem, N.; Pereira, M.; Costa, M. F. M.; Freitas, E.; Carneiro, J. Effect of Iron-Doping on the Structure and Photocatalytic Activity of TiO_2 Nanoparticles. *Catalysts* **2022**, *13*, 58, doi:10.3390/CATAL13010058.
214. Le, P.-N.-M.; Tran, H.-T.; Huynh, N.-D.-T.; Ngo, T.-H.; Truong, V.-T.; Le, M.-V. The Role Of Iron Dopant On The Photocatalytic Performance Of Anatase TiO_2: Synthesis, Characterization, And Removal Of Bisphenol-A Under Simulated Natural Light. *Journal of Applied Science and Engineering* **2023**, *27*, 2675–2685, doi:10.6180/jase.202406_27(6).0008.
215. Sood, S.; Umar, A.; Mehta, S. K.; Kansal, S. K. Highly effective Fe-doped TiO_2 nanoparticles photocatalysts for visible-light driven photocatalytic degradation of toxic organic compounds. *Journal of Colloid and Interface Science* **2015**, *450*, 213–223, doi:10.1016/J.JCIS.2015.03.018.
216. Fu, W.; Ding, S.; Wang, Y.; Wu, L.; Zhang, D.; Pan, Z.; Wang, R.; Zhang, Z.; Qiu, S. F, Ca co-doped TiO_2 nanocrystals with enhanced photocatalytic activity. *Dalton Transactions* **2014**, *43*, 16160–16163, doi:https://doi.org/10.1039/C4DT01908C.
217. Guo, S.; Wang, H.; Yang, W.; Fida, H.; You, L.; Zhou, K. Scalable synthesis of Ca-doped α-Fe_2O_3 with abundant oxygen vacancies for enhanced degradation of organic pollutants through peroxymonosulfate activation. *Applied Catalysis B: Environmental* **2020**, *262*, 118250, doi:10.1016/J.APCATB.2019.118250.
218. Liu, S.; Min, Z.; Hu, D.; Liu, Y. Synthesis of Calcium Doped TiO_2 Nanomaterials and Their Visible Light Degradation Property. *Proceedings of the International Conference on Material and Environmental Engineering (ICMAEE 2014)* **2014**, *57*, doi:10.2991/ICMAEE-14.2014.12.
219. Zhang, Z.; Yates, J. T. Band bending in semiconductors: Chemical and physical consequences at surfaces and interfaces. *Chemical Reviews* **2012**, *112(10)*, 5520–5551, doi:10.1021/CR3000626.
220. Di Liberto, G.; Cipriano, L. A.; Tosoni, S.; Pacchioni, G. Rational Design of Semiconductor Heterojunctions for Photocatalysis. *Chemistry – A European Journal* **2021**, *27*, *53*, 13306–13317, doi:10.1002/CHEM.202101764.
221. Zhang, Y.; Yu, H.; Zhai, R.; Zhang, J.; Gao, C.; Qi, K.; Yang, L.; Ma, Q. Recent Progress in Photocatalytic Degradation of Water Pollution by Bismuth Tungstate. *Molecules* **2023**, *28(24)*, 8011, doi:10.3390/MOLECULES28248011.
222. Sharma, K.; Raizada, P.; Hasija, V.; Singh, P.; Bajpai, A.; Nguyen, V. H.; Rangabhashiyam, S.; Kumar, P.; Nadda, A. K.; Kim, S. Y.; Varma, R. S.; Le, T. T. N.; Le, Q. Van ZnS-based quantum dots as photocatalysts for water purification. *Journal of Water Process Engineering* **2021**, *43(12)*, 102217, doi:10.1016/J.JWPE.2021.102217.
223. Schumacher, L.; Marschall, R. Recent Advances in Semiconductor Heterojunctions and Z-Schemes for Photocatalytic Hydrogen Generation. *Topics in Current Chemistry* **2022**, *380*,*53*, 1–42, doi:10.1007/S41061-022-00406-5.
224. Li, J.; Yuan, H.; Zhang, W.; Jin, B.; Feng, Q.; Huang, J.; Jiao, Z. Advances in Z-scheme

semiconductor photocatalysts for the photoelectrochemical applications: A review. *Carbon Energy* **2022**, *4*, *3*, 294–331, doi:10.1002/CEY2.179.

225. Lai, Y. J.; Lee, D. J. Solid mediator Z-scheme heterojunction photocatalysis for pollutant oxidation in water: Principles and synthesis perspectives. *Journal of the Taiwan Institute of Chemical Engineers* **2021**, *125*, 88–114, doi:10.1016/J.JTICE.2021.05.049.
226. Li, F.; Yue, X.; Liao, Y.; Qiao, L.; Lv, K.; Xiang, Q. Understanding the unique S-scheme charge migration in triazine/heptazine crystalline carbon nitride homojunction. *Nature Communications* **2023**, *14*, *3901*, 1–10, doi:10.1038/s41467-023-39578-z.
227. Liu, D.; Chen, S.; Li, R.; Peng, T. Review of z-scheme heterojunctions for photocatalytic energy conversion. *Wuli Huaxue Xuebao/ Acta Physico - Chimica Sinica* **2021**, *37(6)*, 2010017, doi:10.3866/PKU.WHXB202010017.
228. Huang, D.; Chen, S.; Zeng, G.; Gong, X.; Zhou, C.; Cheng, M.; Xue, W.; Yan, X.; Li, J. Artificial Z-scheme photocatalytic system: What have been done and where to go? *Coordination Chemistry Reviews* **2019**, *385*, 44–80, doi:10.1016/J.CCR.2018.12.013.
229. Lin, Y.; Ren, P.; Wei, C. Fabrication of MoS_2/TiO_2 heterostructures with enhanced photocatalytic activity. *CrystEngComm* **2019**, *21*, *22*, 3439–3450, doi:10.1039/C9CE00056A.
230. Ücker, C. L.; Riemke, F.; Goetzke, V.; Moreira, M. L.; Raubach, C. W.; Longo, E.; Cava, S. Facile preparation of Nb_2O_5/TiO_2 heterostructures for photocatalytic application. *Chemical Physics Impact* **2022**, *4*, 100079, doi:10.1016/J.CHPHI.2022.100079.
231. Yao, L.; Li, X.; Liu, H.; Li, Z.; Lu, Q. One-dimensional hierarchical $CeVO_4/TiO_2$ heterostructures with enhanced photocatalytic performance. *Journal of Nanoparticle Research* **2019**, *21*, *140*, 1–13, doi:10.1007/s11051-019-4582-6.
232. Zhang, X.; Li, L.; Zeng, Y.; Liu, F.; Yuan, J.; Li, X.; Yu, Y.; Zhu, X.; Xiong, Z.; Yu, H.; Xie, Y. TiO_2/Graphitic Carbon Nitride Nanosheets for the Photocatalytic Degradation of Rhodamine B under Simulated Sunlight. *ACS Applied Nano Materials* **2019**, *2*, *11*, 7255–7265, doi:10.1021/ACSANM.9B01739.
233. Shen, L.; Xing, Z.; Zou, J.; Li, Z.; Wu, X.; Zhang, Y.; Zhu, Q.; Yang, S.; Zhou, W. Black TiO_2 nanobelts/g-C_3N_4 nanosheets Laminated Heterojunctions with Efficient Visible-Light-Driven Photocatalytic Performance. *Scientific Reports* **2017**, *7*, *41978*, 1–11, doi:10.1038/srep41978.
234. Ahmad, T.; Khan, S.; Rasheed, T.; Ullah, N. Graphitic carbon nitride nanosheets as promising candidates for the detection of hazardous contaminants of environmental and biological concern in aqueous matrices. *Microchimica Acta* **2022**, *189*, doi:10.1007/S00604-022-05516-X.
235. Ong, W. J.; Tan, L. L.; Ng, Y. H.; Yong, S. T.; Chai, S. P. Graphitic Carbon Nitride (g-C_3N_4)-Based Photocatalysts for Artificial Photosynthesis and Environmental Remediation: Are We a Step Closer to Achieving Sustainability? *Chemical Reviews* **2016**, *116*, 7159–7329, doi:10.1021/ACS.CHEMREV.6B00075.
236. Zhu, J.; Xiao, P.; Li, H.; Carabineiro, S. A. C. Graphitic carbon nitride: Synthesis, properties, and applications in catalysis. *ACS Applied Materials and Interfaces* **2014**, *6(19)*, 16449–16465, doi:10.1021/AM502925J.
237. Vuong, H.-T.; Nguyen, D.-V.; Phuong, L. P.; Minh, P. P. D.; Ho, B. N.; Nguyen, H. A. Nitrogen-rich graphitic carbon nitride (g-C_3N_5): Emerging low-bandgap materials for

photocatalysis. *Carbon Neutralization* **2023**, *2*, 425–457, doi:10.1002/CNL2.65.
238. Wang, Q.; Li, Y.; Huang, F.; Song, S.; Ai, G.; Xin, X.; Zhao, B.; Zheng, Y.; Zhang, Z. Recent Advances in g-C_3N_4-Based Materials and Their Application in Energy and Environmental Sustainability. *Molecules* **2023**, *28*, 432, doi:10.3390/MOLECULES28010432.
239. Sano, T.; Tsutsui, S.; Koike, K.; Hirakawa, T.; Teramoto, Y.; Negishi, N.; Takeuchi, K. Activation of graphitic carbon nitride (g-C_3N_4) by alkaline hydrothermal treatment for photocatalytic NO oxidation in gas phase. *Journal of Materials Chemistry A* **2013**, *1*, 6489–6496, doi:10.1039/C3TA10472A.
240. Luo, X.; Dong, Y.; Wang, D.; Duan, Y.; Lei, K.; Mao, L.; Li, Y.; Zhao, Q.; Sun, Y. Facile synthesis of g-C3N4 nanosheets for effective degradation of organic pollutants via ball milling. *Reviews on Advanced Materials Science* **2023**, *62*, doi:10.1515/RAMS-2023-0123.
241. Singh, P. P.; Srivastava, V. Recent advances in visible-light graphitic carbon nitride (g-C_3N_3) photocatalysts for chemical transformations. *Royal Society of Chemistry* **2022**, *12,18245*, 1–21, doi:10.1039/d2ra01797k.
242. Zhong, K.; Sun, P.; Xu, H. Advances in Defect Engineering of Metal Oxides for Photocatalytic CO_2 Reduction. *Small* **2024**, 1–29, doi:10.1002/SMLL.202310677.
243. Raizada, P.; Soni, V.; Kumar, A.; Singh, P.; Parwaz Khan, A. A.; Asiri, A. M.; Thakur, V. K.; Nguyen, V. H. Surface defect engineering of metal oxides photocatalyst for energy application and water treatment. *Journal of Materiomics* **2021**, *7*, 388–418, doi:10.1016/J.JMAT.2020.10.009.
244. Bernholc, J.; Buongiorno Nardelli, M.; Orlikowski, D.; Roland, C.; Zhao, Q. ATOMIC TRANSFORMATIONS, STRENGTH, PLASTICITY, AND ELECTRON TRANSPORT IN STRAINED CARBON NANOTUBES. *Fiber Fracture* **2002**, 357–376, doi:10.1016/B978-008044104-7/50016-2.
245. Kumar, V. Defects on surfaces. *Bulletin of Materials Science* **1988**, *10*, 161–172.
246. Liang, C.; Gu, H.; Xia, J.; Mei, S.; Pang, P.; Zhang, N.; Guo, J.; Guo, R.; Shen, Y.; Yang, S.; Wei, Z.; Shao, G.; Xing, G. Recent Progress in Perovskite-Based Reversible Photon–Electricity Conversion Devices. *Advanced Functional Materials* **2022**, *32*, 2108926, doi:10.1002/ADFM.202108926.
247. Bergamaschini, R.; Isa, F.; Falub, C. V.; Niedermann, P.; Müller, E.; Isella, G.; Von Känel, H.; Miglio, L. Self-aligned Ge and SiGe three-dimensional epitaxy on dense Si pillar arrays. *Surface Science Reports* **2013**, *68*, 390–417, doi:10.1016/J.SURFREP.2013.10.002.
248. Wang, M.; Duan, B. Materials and their biomedical applications. In *Encyclopedia of Biomedical Engineering*; Elsevier, 2019; Vol. 1–3, pp. 135–152 ISBN 9780128051443.
249. Williams, D. B.; Carter, C. B. Planar Defects. In *Transmission Electron Microscopy*; Springer, Boston, MA, 1996; pp. 379–399 ISBN 978-1-4757-2519-3.
250. Liu, X.; Wang, H.; Lu, H.; Liu, X.; Zhao, Z.; Hou, C.; Gu, L.; Song, X. Grain-interior planar defects induced by heteroatom monolayer. *Advanced Powder Materials* **2023**, *2*, 100130, doi:10.1016/J.APMATE.2023.100130.
251. Fang, Z.; Bueken, B.; De Vos, D. E.; Fischer, R. A. Defect-Engineered Metal-Organic Frameworks. *Angewandte Chemie - International Edition* **2015**, *54*, 7234–7254, doi:10.1002/ANIE.201411540.
252. Bai, S.; Zhang, N.; Gao, C.; Xiong, Y. Defect engineering in photocatalytic materials.

Nano Energy **2018**, *53*, 296–336, doi:10.1016/J.NANOEN.2018.08.058.
253. Chen, Q.; Luo, X.; Mu, G.; Mao, X.; Yin, H.; Lester, E. H.; Wu, T. Microwave-Assisted Synthesis of a Defect-Rich CuO Electrode for Selective Electrochemical CO_2 Reduction to C^{2+} Products. *ACS Sustainable Chemistry and Engineering* **2024**, *12*, 15134, doi:10.1021/ACSSUSCHEMENG.4C05008.
254. Flores Cantera, J.; Wang, J. A.; Paredes Carrea, S. P.; Chen, L. F.; Salmones, J.; González, J. A microwave-ultrasound assisted synthesis of defective TiO_2 and WO_3/TiO_2 nanoparticles for ultralow sulfur diesel production. *Materials Letters* **2024**, *360*, 136030, doi:10.1016/J.MATLET.2024.136030.
255. Herring, N. P.; Panda, A. B.; AbouZeid, K.; Almahoudi, S. H.; Olson, C. R.; Patel, A.; El-Shall, M. S. Microwave Synthesis of Metal Oxide Nanoparticles. In *Metal Oxide Nanomaterials for Chemical Sensors*; Carpenter, M. A., Mathur, S., Kolmakov, A., Eds.; Springer, New York, NY, 2013; pp. 245–284 ISBN 978-1-4614-5395-6.
256. Thundiyil, R.; Poornesh, P.; Ozga, K.; Jedryka, J. An insight in to microwave induced defects and its impact on nonlinear process in NiO nanostructures under femtosecond and continuous wave laser excitation. *RSC Advances* **2024**, *14*, 30011–30036, doi:10.1039/D4RA06056C.
257. Yang, Z.; Lin, Z.; Huang, J. Hierarchically Structured NH_2-MIL-125/TiO_2/Cellulose Composite Membranes With Enhanced Photocatalytic Performance. *ChemNanoMat* **2023**, *9*, e202200504, doi:10.1002/CNMA.202200504.
258. Kardeş, M.; Yatmaz, H. C.; Öztürk, K. ZnO Nanorods Grown on Flexible Polyurethane Foam Surfaces for Photocatalytic Azo Dye Treatment. *ACS Applied Nano Materials* **2023**, *6*, *8*, 6605–6613, doi:10.1021/acsanm.3c00210.
259. Rico-santacruz, M.; García-muñoz, P.; Keller, V.; Batail, N.; Pham, C.; Robert, D.; Keller, N. Alveolar TiO_2-β-SiC photocatalytic composite foams with tunable properties for water treatment. *Catalysis Today* **2019**, *328*, 235–242.
260. Ni, L.; Li, Y.; Zhang, C.; Li, L.; Zhang, W.; Wang, D. Novel floating photocatalysts based on polyurethane composite foams modified with silver/titanium dioxide/graphene ternary nanoparticles for the visible-light-mediated remediation of diesel-polluted surface water. *Journal of Applied Polymer Science* **2016**, *133*, *19*, 1–9, doi:10.1002/APP.43400.
261. Mohd Adnan, M. A.; Muhd Julkapli, N.; Amir, M. N. I.; Maamor, A. Effect on different TiO_2 photocatalyst supports on photodecolorization of synthetic dyes: a review. *International Journal of Environmental Science and Technology* **2018**, *16*, 547–566, doi:10.1007/S13762-018-1857-X.
262. Shan, A. Y.; Ghazi, T. I. M.; Rashid, S. A. Immobilisation of titanium dioxide onto supporting materials in heterogeneous photocatalysis: A review. *Applied Catalysis A: General* **2010**, *389*, 1–8, doi:10.1016/J.APCATA.2010.08.053.
263. Nasir, A. M.; Jaafar, J.; Aziz, F.; Yusof, N.; Salleh, W. N. W.; Ismail, A. F.; Aziz, M. A review on floating nanocomposite photocatalyst: Fabrication and applications for wastewater treatment. *Journal of Water Process Engineering* **2020**, *36*, 101300, doi:10.1016/J.JWPE.2020.101300.
264. Porley, V.; Robertson, N. Chapter 6 - Substrate and support materials for photocatalysis. In *Nanostructured Photocatalysts: From Materials to Applications in Solar Fuels and*

Environmental Remediation; Elsevier, 2020; pp. 129–171 ISBN 9780128178362.
265. Ma, Y.; Qiu, J. bin; Cao, Y. an; Guan, Z. shen; Yao, J. nian Photocatalytic activity of TiO_2 films grown on different substrates. *Chemosphere* **2001**, *44*, 1087–1092, doi:10.1016/S0045-6535(00)00360-X.
266. Samriti; Tyagi, R.; Ruzimuradov, O.; Prakash, J. Fabrication methods and mechanisms for designing highly-efficient photocatalysts for energy and environmental applications. *Materials Chemistry and Physics* **2023**, *307*, 128108, doi:10.1016/J.MATCHEMPHYS.2023.128108.
267. Alves, H. F. Cork as a raw material for antibacterial membranes and fibers, Master's thesis, FCT-UNL: Lisboa, 2019.
268. Branco, D. G.; Campos, J. R.; Cabrita, L.; Evtuguin, D. V. Structural features of macromolecular components of cork from Quercus suber L. *Holzforschung* **2020**, *74(6)*, 625–633, doi:10.1515/HF-2019-0271.
269. The cork harvest in Portugal- Jamie Goode's wine blog. Available online: https://www.wineanorak.com/wineblog/portugal/the-cork-harvest-in-portugal (accessed on Jan 21, 2024).
270. The cork oak - Portugal's magical tree. Available online: https://www.mimove.com/fr/ombudsblog/post/3652-the-cork-oak-portugals-magical-tree/es (accessed on Jan 21, 2024).
271. Sboui, M.; Nsib, M. F.; Rayes, A.; Swaminathan, M.; Houas, A. TiO_2–PANI/Cork composite: A new floating photocatalyst for the treatment of organic pollutants under sunlight irradiation. *Journal of Environmental Sciences* **2017**, *60*, 3–13.
272. Mohamad Idris, N. H.; Rajakumar, J.; Cheong, K. Y.; Kennedy, B. J.; Ohno, T.; Yamakata, A.; Lee, H. L. Titanium Dioxide/Polyvinyl Alcohol/Cork Nanocomposite: A Floating Photocatalyst for the Degradation of Methylene Blue under Irradiation of a Visible Light Source. *ACS Omega* **2021**, *6,22*, 14493–14503.
273. Alam, M.; Alandis, N. M.; Zafar, F.; Sharmin, E.; Al-Mohammadi, Y. M. Polyurethane-TiO_2 nanocomposite coatings from sunflower- oil-based amide diol as soft segment. *Journal of Macromolecular Science, Part A: Pure and Applied Chemistry* **2018**, *55*, 698–708, doi:10.1080/10601325.2018.1526638.
274. Polo Fonseca, L.; Duval, A.; Luna, E.; Ximenis, M.; De Meester, S.; Avérous, L.; Sardon, H. Reducing the carbon footprint of polyurethanes by chemical and biological depolymerization: Fact or fiction? *Current Opinion in Green and Sustainable Chemistry* **2023**, *41*, 100802, doi:10.1016/J.COGSC.2023.100802.
275. Mendiburu-Valor, E.; Calvo-Correas, T.; Martin, L.; Harismendy, I.; Peña-Rodriguez, C.; Eceiza, A. Synthesis and characterization of sustainable polyurethanes from renewable and recycled feedstocks. *Journal of Cleaner Production* **2023**, *400*, 136749, doi:10.1016/J.JCLEPRO.2023.136749.
276. Gausas, L.; Kristensen, S. K.; Sun, H.; Ahrens, A.; Donslund, B. S.; Lindhardt, A. T.; Skrydstrup, T. Catalytic Hydrogenation of Polyurethanes to Base Chemicals: From Model Systems to Commercial and End-of-Life Polyurethane Materials. *JACS Au* **2021**, *1*, *4*, 517–524, doi:https://doi.org/10.1021/jacsau.1c00050.
277. Li, B.; Liu, X.; Zhang, X.; Zou, J.; Chai, W.; Lou, Y. Rapid adsorption for oil using superhydrophobic and superoleophilic polyurethane sponge. *Journal of Chemical*

Technology & Biotechnology **2015**, *90*, *11*, 2106–2112, doi:10.1002/JCTB.4646.
278. Bouraie, M. El; Abdelghany, A. Sorption Features of Polyurethane Foam Functionalized with Salicylate for Chlorpyrifos: Equilibrium, Kinetic Models and Thermodynamic Studies. *Polymers* **2020**, *12(9)*, 2036, doi:10.3390/POLYM12092036.
279. Khandan Barani, A.; Roudini, G.; Barahuie, F.; Binti Masuri, S. U. Design of hydrophobic polyurethane–magnetite iron oxide-titanium dioxide nanocomposites for oil-water separation. *Heliyon* **2023**, *9*, *5*, e15580, doi:10.1016/J.HELIYON.2023.E15580.
280. Seah, M. Q.; Ng, Z. C.; Lau, W. J.; Gürsoy, M.; Karaman, M.; Wong, T. W.; Ismail, A. F. Development of surface modified PU foam with improved oil absorption and reusability via an environmentally friendly and rapid pathway. *Journal of Environmental Chemical Engineering* **2022**, *10*, *1*, 106817, doi:10.1016/J.JECE.2021.106817.
281. Mahesh, K. P. O.; Kuo, D.-H.; Huang, B.-R.; Ujihara, M.; Imae, T. Chemically modified polyurethane-SiO_2/TiO_2 hybrid composite film and its reusability for photocatalytic degradation of Acid Black 1 (AB 1) under UV light. *Applied Catalysis A: General* **2014**, *475*, 235–241, doi:10.1016/j.apcata.2014.01.044.
282. Pattanayak, D. S.; Mishra, J.; Nanda, J.; Sahoo, P. K.; Kumar, R.; Sahoo, N. K. Photocatalytic degradation of cyanide using polyurethane foam immobilized Fe-TCPP-S-TiO_2-rGO nano-composite. *Journal of Environmental Management* **2021**, *297*, 113312, doi:10.1016/J.JENVMAN.2021.113312.
283. Seddiqi, H.; Oliaei, E.; Honarkar, H.; Jin, J.; Geonzon, L. C.; Bacabac, R. G.; Klein-Nulend, J. Cellulose and its derivatives: towards biomedical applications. *Cellulose* **2021**, *28*, 1893–1931, doi:10.1007/S10570-020-03674-W.
284. Aziz, T.; Farid, A.; Haq, F.; Kiran, M.; Ullah, A.; Zhang, K.; Li, C.; Ghazanfar, S.; Sun, H.; Ullah, R.; Ali, A.; Muzammal, M.; Shah, M.; Akhtar, N.; Selim, S.; Hagagy, N.; Samy, M.; Al Jaouni, S. K. A Review on the Modification of Cellulose and Its Applications. *Polymers 2022, Vol. 14, Page 3206* **2022**, *14(15)*, 3206, doi:10.3390/POLYM14153206.
285. Jiang, Z.; To, N. Recent Advances in Chemically Modified Cellulose and Its Derivatives for Food Packaging Applications: A Review. *Polymers* **2022**, *14*, 1533, doi:10.3390/POLYM14081533.
286. Zhang, J.; Li, L.; Li, Y.; Yang, C. Microwave-assisted synthesis of hierarchical mesoporous nano-TiO_2/cellulose composites for rapid adsorption of Pb^{2+}. *Chemical Engineering Journal* **2017**, *313*, 1132–1141, doi:10.1016/J.CEJ.2016.11.007.
287. Cardoso, G. V.; Di Salvo Mello, L. R.; Zanatta, P.; Cava, S.; Raubach, C. W.; Moreira, M. L. Physico-chemical description of titanium dioxide–cellulose nanocomposite formation by microwave radiation with high thermal stability. *Cellulose* **2018**, *25*, *4*, 2331–2341, doi:10.1007/S10570-018-1734-2.
288. Matsudo, A.; Oliveira, L. V. F.; Martins, T. S.; Camilo, F. F. Eco-Friendly Photocatalytic Solutions: Synthesized TiO_2 Nanoparticles in Cellulose Membranes for Enhanced Degradation of Indigo Carmine Dye. *ACS Omega* **2024**, *9*, 43395–43405, doi:10.1021/ACSOMEGA.4C04017.
289. Marques, P. A. A. P.; Trindade, T.; Neto, C. P. Titanium dioxide/cellulose nanocomposites prepared by a controlled hydrolysis method. *Composites Science and Technology* **2006**, *66*, 1038–1044, doi:10.1016/J.COMPSCITECH.2005.07.029.
290. Kateshali, A. F.; Soleimannejad, J.; Tan, H. W.; Pang, Y. L.; Lim, S. Synthesis of Titanium

Dioxide/Cellulose Derived from Banana Peel for Sonocatalytic Degradation of Methylene Blue. *IOP Conference Series: Earth and Environmental Science* **2021**, *945*, 012008, doi:10.1088/1755-1315/945/1/012008.

291. Roy Barman, S.; Gavit, P.; Chowdhury, S.; Chatterjee, K.; Nain, A. 3D-Printed Materials for Wastewater Treatment. *JACS Au* **2023**, *3*, *11*, 2930–2947, doi:10.1021/jacsau.3c00409.
292. Chen, L.; Zhou, S.; Li, M.; Mo, F.; Yu, S.; Wei, J. Catalytic Materials by 3D Printing: A Mini Review. *Catalysts* **2022**, *12(10)*, 1081, doi:10.3390/CATAL12101081.
293. Elkoro, A.; Soler, L.; Llorca, J.; Casanova, I. 3D printed microstructured Au/TiO_2 catalyst for hydrogen photoproduction. *Applied Materials Today* **2019**, *16*, 265–272, doi:10.1016/J.APMT.2019.06.007.
294. Abdulhameed, O.; Al-Ahmari, A.; Ameen, W.; Mian, S. H. Achieving Sustainability in Manufacturing through Additive Manufacturing: An Analysis of Its Enablers. *Sustainability* **2023**, *15(12)*, 9504, doi:10.3390/SU15129504.
295. Xu, C.; Liu, T.; Guo, W.; Sun, Y.; Liang, C.; Cao, K.; Guan, T.; Liang, Z.; Jiang, L. 3D Printing of Powder-Based Inks into Functional Hierarchical Porous TiO_2 Materials. *Advanced Engineering Materials* **2020**, *22*, 1–8.
296. Sevastaki, M.; Suchea, M. P.; Kenanakis, G. 3D Printed Fully Recycled TiO_2-Polystyrene Nanocomposite Photocatalysts for Use Against Drug Residues. *Nanomaterials* **2020**, *10*, 1–11.
297. Wu, Y.; He, J.; Huang, W.; Chen, W.; Zhou, S.; She, X.; Zhu, W.; Huang, F.; Li, H.; Xu, H. Stereolithography 3D printed monolithic catalyst for highly efficient oxidative desulfurization of fuels. *Fuel* **2023**, *332*, 126021, doi:10.1016/J.FUEL.2022.126021.
298. Wang, Y.; Xu, Z.; Wu, D.; Bai, J. Current Status and Prospects of Polymer Powder 3D Printing Technologies. *Materials* **2020**, *13(10)*, 2406, doi:10.3390/MA13102406.
299. Lakkala, P.; Munnangi, S. R.; Bandari, S.; Repka, M. Additive manufacturing technologies with emphasis on stereolithography 3D printing in pharmaceutical and medical applications: A review. *International Journal of Pharmaceutics: X* **2023**, *5*, 100159, doi:10.1016/J.IJPX.2023.100159.
300. Quan, H.; Zhang, T.; Xu, H.; Luo, S.; Nie, J.; Zhu, X. Photo-curing 3D printing technique and its challenges. *Bioactive Materials* **2020**, *5*, 110–115, doi:10.1016/J.BIOACTMAT.2019.12.003.
301. Chen, J.; Wu, P.; Bu, F.; Gao, Y.; Liu, X.; Guan, C. 3D printing enhanced catalysis for energy conversion and environment treatment. *DeCarbon* **2023**, *2*, 100019, doi:10.1016/J.DECARB.2023.100019.
302. Formlabs The Ultimate Guide to Stereolithography (SLA) 3D Printing Available online: https://www.studocu.com/in/document/biju-patnaik-university-of-technology/basic-mechanical-engineering-basic-civil-engineering/resin-3d-printing-guide/85980969 (accessed on Nov 22, 2024).
303. Sopha, H.; Kashimbetova, A.; Hromadko, L.; Saldan, I.; Celko, L.; Montufar, E. B.; Macak, J. M. Anodic TiO_2 Nanotubes on 3D-Printed Titanium Meshes for Photocatalytic Applications. *Nano Letters* **2021**, *21*, *20*, 8701–8706, doi:10.1021/acs.nanolett.1c02815.
304. Bansiddhi, A.; Panomsuwan, G.; Hussakan, C.; Htet, T. L.; Kandasamy, B.; Janbooranapinij, K.; Choophun, N.; Techapiesancharoenkij, R.; Pant, H. R.; Ang, W. L.; Jongprateep, O. Ecofriendly 3D Printed TiO_2/SiO_2/Polymer Scaffolds for Dye Removal.

Topics in Catalysis **2023**, *66*, 1662–1673, doi:10.1007/s11244-023-01864-x.

305. Fu, C.; Li, D.; Zhang, J.; Guo, W.; Yang, H.; Zhao, B.; Chen, Z.; Fu, X.; Liang, Z.; Jiang, L. Vertical 3D Printed Pd/TiO_2 Arrays for High Efficiency Photo-assisted Catalytic Water Treatment. *Chemical Research in Chinese Universities* **2023**, *39*, 891–901, doi:10.1007/s40242-023-3182-2.

2

RESEARCH METHODOLOGIES

2.1 Synthesis methods and working principles

Unlike traditional hydrothermal/solvothermal methods, which require long processing times (from half a day to several days) and high energy consumption (over a thousand watts), hydrothermal/solvothermal methods assisted by microwave irradiation offer a more sustainable alternative. They enable the synthesis of materials in a shorter amount of time (from a few minutes to hours) while consuming less power (hundreds of watts) [1].

2.1.1 Microwave irradiation

Microwaves are a type of electromagnetic wave, consisting of two perpendicular components: electric and magnetic fields that travel at the speed of light in a vacuum. They occupy the electromagnetic spectrum between 300 MHz (λ = 1 m) and 300 GHz (λ = 1 mm), between radio wave and infrared regions of the spectrum [2,3]. In industrial, medical, and scientific applications, two primary microwave (MW) frequencies are commonly used: 0.915 GHz and 2.45 GHz. For example, domestic microwave ovens typically operate at a frequency of 2.45 GHz [4]. Although microwave reactors were initially introduced to the market as domestic appliances, they have also found applications for conducting syntheses of organic and inorganic materials at laboratory scale [5].

2.1.1.1 Microwave working principles and mechanisms

Microwave heating involves the use of electric and magnetic fields. The basis for the operation of a microwave is the dielectric heating of different materials by two mechanisms: dipole polarization and ion conduction. Microwaves can heat any material with mobile electric charges, such as polar units of reactants/solvents (dipoles) or conducting ions in a solvent/solid. In the first mechanism, upon microwave heating, the polar molecules, such as water molecules, try to orientate with the rapidly changing alternating electric field. As a result, heat is generated by the rotation, friction, and collision of molecules. In the second mechanism, ions present in the mixture will move based on the orientation of the electric field. The microwave energy field continuously changes, and so, the ions are always changing directions through the solution, causing a localized heating that rises due to friction and collision [6–9], Figure 2.1. The combination of electric and magnetic mechanisms is called interfacial polarization.

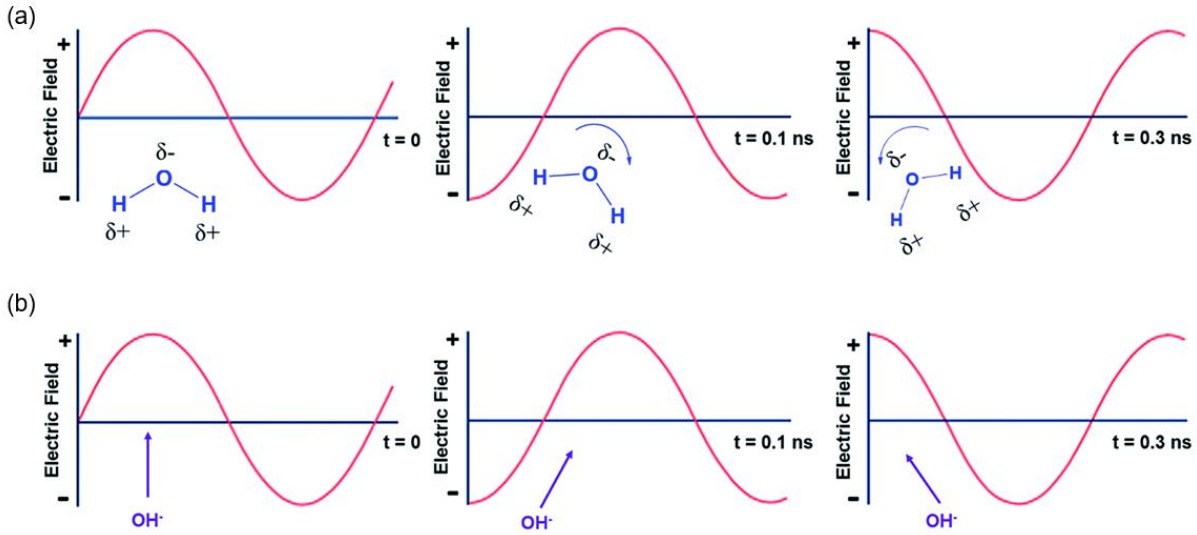

Figure 2.1: (a) Dipolar polarization mechanism. (b) Ion conduction mechanism. Reproduced from [3] and with permission from [10].

The polarity of a reaction mixture plays a crucial role in its ability to interact with microwave energy, directly influencing the heating efficiency. For instance, the higher the polarity of a reaction mixture, the better it couples with microwave energy, resulting in more efficient heating. For example, more polar solvents such as ethylene glycol (EG), ethanol and isopropanol (IPA), followed by water, are more efficient at converting microwave energy into heat compared to nonpolar solvents like acetone, toluene or hexane [5,11]. This polarity interaction is defined by the dielectric loss tangent (tan δ), which provides a measure for the ability of a solvent to absorb microwave radiation and to convert electromagnetic energy into heat at a given frequency and temperature [12,13]. The dielectric loss tangent can be determined by the following equation (2.1) [4]:

$$\tan \delta = \frac{\varepsilon''}{\varepsilon'} \tag{2.1}$$

where ε'' (the imaginary part) indicates the dielectric loss factor (the material's ability to dissipate electrical energy), while ε' (the real part) is the dielectric constant and describes the amount of electrical energy stored within the material [2,14]. For efficient absorption and rapid heating, a high tan δ is required [13]. Materials with a tan δ> 0.5 are considered good microwave absorbers, with 0.1< tan δ< 0.5 they are medium absorbers and when tan δ< 0.1 the materials are typically low absorbers.

From equation (2.1), it can also be inferred that higher absorbers exhibit large dielectric losses, allowing them to heat rapidly. Medium absorbers heat effectively but need more time

to reach the target temperature. On the other hand, low microwave-absorbing solvents can be heated well beyond their boiling points, though they require prolonged heating. The dielectric constants and corresponding dielectric loss tangents of thirteen common solvents are presented in descending order of tan δ (Table 2.1) [11,13].

Table 2.1: Dielectric constant and loss tangents of thirteen common solvents at 2.45 GHz and 20 °C [11,13,15].

Solvent	Dielectric constant ε'	tan δ
Ethylene glycol	37.0	1.350
Ethanol	24.3	0.941
Dimethyl sulfoxide (DMSO)	45.0	0.825
2-propanol	18.3	0.799
Methanol	32.6	0.659
2-methoxyethanol	16.9	0.410
Acetic acid	6.2	0.174
N,N-Dimethylformamide (DMF)	37.7	0.161
Water	80.4	0.123
Chloroform	4.8	0.091
Ethyl Acetate	6.0	0.059
Acetone	20.7	0.054
Toluene	2.4	0.040

For example, water has the highest dielectric constant (80.4) among all solvents, which might suggest it is the most polar. However, this is not the case, as its tan δ value is 0.123, which classifies it as a medium absorber [11].

For magnetic substances, the dielectric loss tangent (tan δ_μ) follows equation (2.2) [2]:

$$\tan \delta_\mu = \frac{\mu''}{\mu'} \tag{2.2}$$

where μ' (the real part) describes the amount of magnetic energy stored within the material, while μ'' (the imaginary part) represents the amount of magnetic energy that can be converted into thermal energy.

It is important to point out that the dielectric loss tangents of the substances greatly vary with temperature [16]. Other critical factors, including a substance's specific heat capacity, heat of vaporization, and penetration depth, significantly influence the heating rate [5]. The

penetration depth (D) quantifies how deeply light can enter a medium. It is defined as the distance within the medium where the absorbed electric field drops to e^{-1} of its initial value [17]. The penetration depth can be estimated by using equation (2.3) [2,18]:

$$D = \frac{c}{\omega\sqrt{2\varepsilon'}\left(\sqrt{1+\tan^2\delta}-1\right)^{1/2}} \tag{2.3}$$

in which ω is the angular frequency ($\omega = 2\pi f$) and c is the speed of light ($\mathrm{m.s^{-1}}$).

The penetration depth of the microwaves is deeper into most nonpolar solvents than into polar ones. However, in substances containing ions, the penetration depth can decrease significantly, preventing effective microwave heating. In such cases, vigorous magnetic stirring is required. Therefore, evaluating the heating efficiency and penetration depth of microwaves in a substance is essential for achieving optimal microwave heating [16].

2.1.1.2 Microwave components

The microwave apparatus is composed of the generator parts, transmission portion and applicator parts. The first typically comprises a transformer (produces the necessary high voltage), a magnetron (emits the microwaves), and a solenoid (which wraps the magnetron tube and creates a magnetic field to regulate the power of the microwaves). The transmission part has a waveguide made of metal to guide the microwaves from the transmitter to the applicator (the chamber used to place the samples) [4,14,16]. According to the frequency of the microwave radiation generated by the magnetron, the size of this waveguide varies [16]. The equipment is also equipped with protective and measuring elements (e.g. control unit), along with other integrated systems such as a cooling section [19].

2.1.1.3 Types of reactor systems

There are two types of reactor systems: multimode cavities, which allow multiple vessels to be irradiated simultaneously, and single-mode systems, where only one vial is irradiated at a time [20]. In the first mode when the microwaves enter the cavity (heating chamber), they will move around and reflect from the walls. High- and low-energy modes are created (hot and cold spots) as the waves interact, either reinforcing or canceling each other. This results in a non-uniform microwave field in the chamber. To better visualize the hot and cold spots, Figure 2.2 displays the simulated spatial temperature profile of a multi-component meal (nine chicken nuggets and mashed potatoes) alongside three experimental temperature profiles captured with a thermal imaging camera. Both experimental and simulated results indicate that most of the mashed potatoes (represented with a parallelepiped shape in the experimental

profile) remained at lower temperatures, except at the edges. Likewise, the center of the chicken nuggets (represented as cubes in the simulation and squares in the experimental profile) did not reach higher temperatures. Notably, the two nuggets in the center remained around 30 °C, while the nuggets on the edges, particularly their borders, reached approximately 75 °C, as observed in the experimental profiles [21]. To avoid a non-uniform microwave field, microwaves have rotating platforms to ensure that the sample is exposed to constant microwave energy. In the second mode, a more uniform microwave energy is irradiated to the sample since the only cavity has the width of a single wave. This enables efficient heating of small sample volumes, as small as 0.2 mL [5].

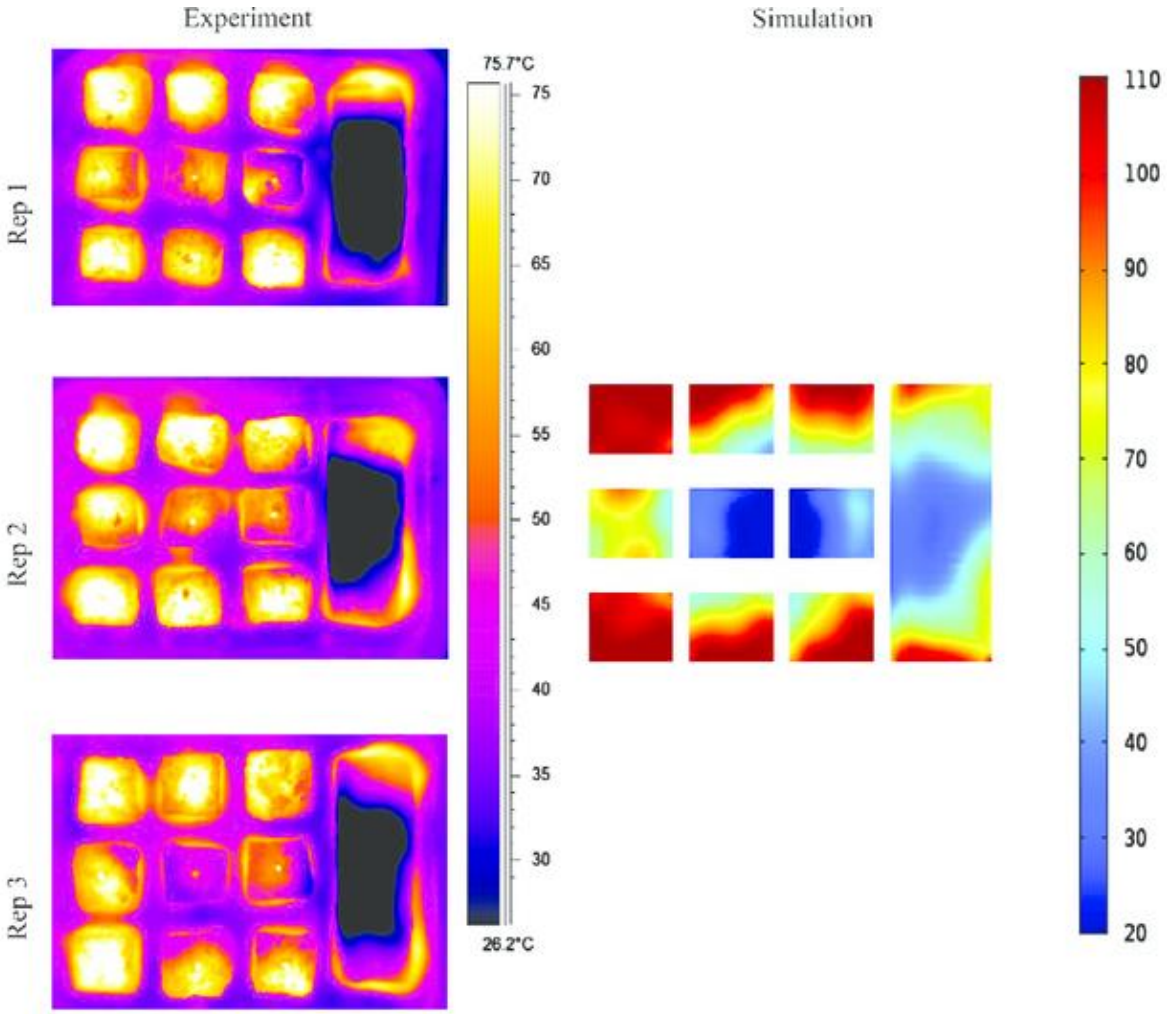

Figure 2.2: Comparison of the spatial temperature profiles of a multi-component meal after 90 seconds of heating in a 1200 W microwave oven: experiment in triplicate *vs.* simulation results. Reproduced from Ref. [21].

2.1.1.4 Laboratory microwave systems

For this PhD thesis, two microwaves were used: a CEM Discover SP (Matthews, CEM Corporation) and a MARS One digestion system (Matthews, CEM Corporation), Figure 2.3 (a)

and (b), respectively. Both systems operate with sealed vessels. The first system is a single-mode setup that uses a quartz vial for the reaction mixture with a maximum capacity of 35 mL (standard pressurized). The second system, in contrast, is a multi-mode setup that enables higher material synthesis capacity. It includes turntables capable of holding 12 Teflon tubes, each with a maximum reaction mixture capacity of 75 mL. The control is made through a contactless infrared radiation (IR) sensor. MW reaction vessels are frequently made of Teflon and quartz materials since these materials are transparent to the MWs [22]. The closed-vessel systems provide several advantages over open-vessel conditions, namely the possibility to work with higher temperatures and pressures, accelerated reaction kinetics, and reduction of the digestion time (in the case of digestion microwave systems) [23].

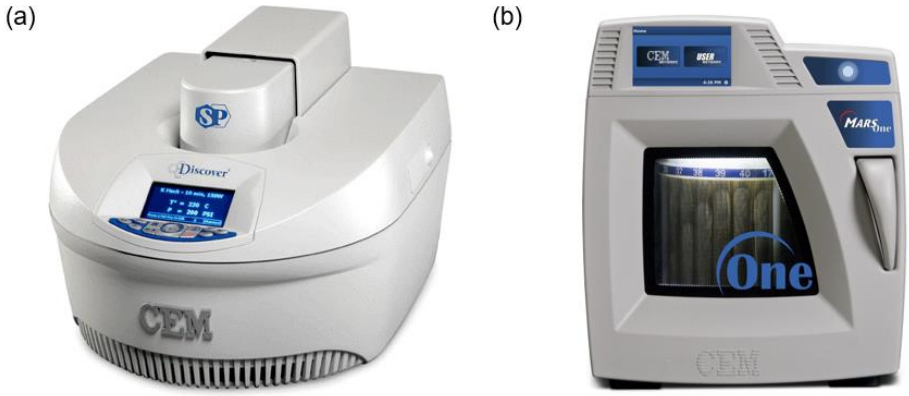

Figure 2.3: Available microwave systems in the laboratory. (a) CEM Discover SP and (b) MARS One digestion system.

2.1.1.5 Microwave parameters

Some process variables integrated in the microwave can be controlled by the user, namely [24]:

- Temperature (°C)
- Power (W)
- Time (min)
- Pressure (psi). This parameter must be programmed in the method of the CEM Discover SP system. The MARS One system does not have this option to be programmed.
- Magnetic stirring. This parameter must be programmed in the method of the CEM Discover SP system. The MARS One system does not have this option to be programmed.

A pressurized environment offers significant advantages by enabling the boiling point of most solvents to be reached and exceeded within seconds. The power applied to a

microwave reaction is also important as insufficient power may fail to reach the desired temperature, whereas excessive power can exceed it. Regardless of the solvent used, reactions often involve diverse reagents and catalysts that can enhance the coupling efficiency of the reaction mixture to microwave energy. Therefore, sometimes applying a lower power for a controlled duration at a specific temperature can yield more effective results. The applied temperature should be selected carefully to ensure the formation of the desired material, prior to its deterioration. Additionally, by applying continuous magnetic stirring, a homogeneous temperature distribution is promoted. Once the optimal temperature is determined, the reaction time can be adjusted to maximize product yield. If the reaction struggles to reach the target temperature, a gradual increase in the power may be necessary. Moreover, studies have demonstrated that simultaneously cooling the reaction vessel during a reaction helps maintain a constant high-power level for direct molecular heating, thus improving the reaction rates and percent yields of lower-yielding reactions. Simultaneous cooling is particularly beneficial in reactions involving heat-sensitive reagents and/or products. Introducing compressed air into the heating chamber while applying microwave irradiation prevents thermal heat from accumulating in the reaction mixture [24,25].

Other parameters, such as the selection of reagents (catalysts: acid/base, surfactants, solvents, etc.) influence the final product, namely size, shape, and crystallinity, and should be adjusted before the microwave synthesis [13,24,26,27]. Concerning the solvents, some reactions can be carried out in a solvent-free medium. This is applied, for instance, when all reagents are in liquid form, when solid reagents melt at a specific temperature, or when the reaction mixture efficiently absorbs microwave energy. Most of the solvent-free reactions that have been reported are conducted in an open vessel and usually require larger vessels and mechanical stirring. In solution-phase reactions, the choice of solvent can play a critical role in determining the outcome. As previously mentioned, the higher the polarity of a reaction mixture or solvent, the better it can couple with microwave energy, resulting in a faster increase in internal temperature. Temperature-sensitive reaction mixtures benefit significantly from this property, as a nonpolar solvent can help dissipate the thermal heat generated by the interaction between microwave irradiation and polar reagents. This ensures that while the reaction receives the necessary activation energy, the internal temperature remains low [24].

2.1.1.6 Specific experimental details

Synthesis of TiO_2 nanostructures on cork via microwave irradiation (study 1)

Titanium (IV) isopropoxide (TTIP) with 97 % purity from Sigma-Aldrich (CAS: 546-68-9) was used as the titanium dioxide precursor. To prepare a solution of 120 mL, 10 mL of a 1 M acid solution (oxalic acid anhydrous from Sigma-Aldrich (CAS: 144-62-7) was added to 110 mL of absolute anhydrous ethanol from Carlo Erba reagents (CAS: 64-17-5) and stirred for 10 min, until a homogeneous solution is obtained. Afterwards, 4 mL of TTIP was added dropwise to the previous solution. Then, the obtained solution was left to stir overnight. This process guarantees the complete homogenization of the solution. Microwave synthesis was performed using a CEM microwave digestion system (MARS one) at 1000 W, 120 ± 10 °C for 1 h. Solution volumes of 20 mL were transferred into Teflon vessels of 75 mL, which were kept sealed. To produce the TiO_2 cork platforms, cork sheets from Bi-Office (ref. RL044330 222468) were cut into pieces of 1.5 × 3.5 cm^2, fixed with Kapton tape to ordinary glass squares and each cork piece was transferred to one microwave vessel containing the solution. Each piece should be fully immersed in the solution. The functionalized cork platforms were afterwards cleaned in an ultrasonic bath, first with deionized water for 10 min and then with IPA for another 10 min. To eliminate excess solvents from the cork substrates, each piece was left to dry for a few minutes on top of lab paper and dried at 60 °C in a desiccator between 30 min and 2 hours. TiO_2 nanopowder was simultaneously formed during microwave synthesis. The nanopowder was washed repeatedly several times with deionized water followed by IPA using a centrifuge at 4500 rpm for 5 min each time. Finally, the nanopowder was kept overnight in a desiccator for drying at 80 °C in vacuum. A schematic of the experimental procedure is shown in Figure 2.4 [28].

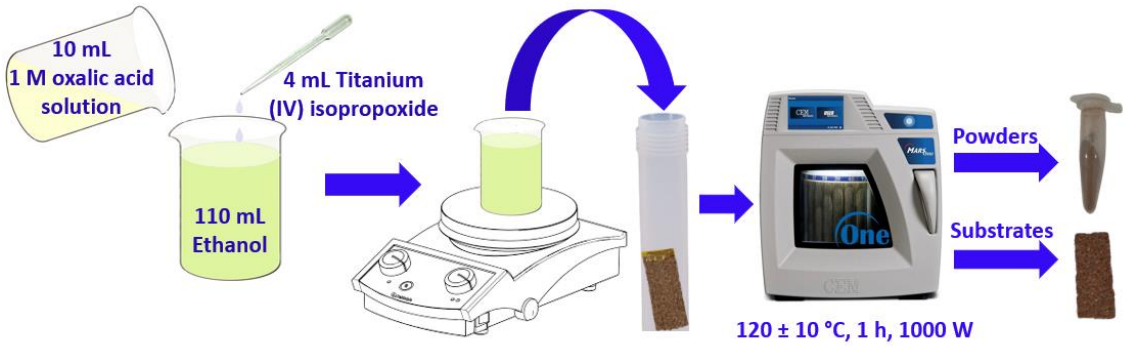

Figure 2.4: Schematic of the TiO_2 microwave synthesis procedure. The real images of the cork substrates before and after synthesis are shown together with the TiO_2 nanopowder simultaneously produced [28].

The final TiO_2 cork appeared slightly darker in color after microwave synthesis. This change has been previously reported, and it can be explained by the temperature increase, attributed

to the reactions involving cork components called the extractives, without any degradation occurring [28].

Synthesis of TiO_2 nanostructures via microwave irradiation for incorporation on 3D-printed architectures (study 2)

TiO_2 nanostructures were synthesized using a solvothermal method assisted by microwave irradiation. To prepare the solution, 2.5 mL of a 1 M solution of anhydrous oxalic acid (Sigma-Aldrich; CAS: 114-62-7) was added to 57.5 mL of absolute ethanol (Sigma-Aldrich; CAS: 64-17-5) and left to stir in a magnetic plate for 3 min. Afterwards, 2 mL of TTIP (Sigma-Aldrich; CAS: 546-68-9) was added to the solution and stirred for 1 h. For the microwave synthesis, 20 mL of the prepared solution was poured into a capped vessel and put into the microwave (CEM Focused Microwave Synthesis System Discover SP). The optimized parameters set for the TiO_2 nanostructures' synthesis were 90 °C, 2 h, 10 bars (145 psi) and 100 W. After the microwave synthesis, the nanopowder was filtered using the centrifuge (Neya 16 Remi Centrifuge). In total, 3 cycles of Milli-Q water and 1 cycle of IPA under the same condition of 4000 rpm for 5 min were conducted to wash the nanostructures. The nanopowder was then placed into a desiccator at 60 °C under a vacuum and left to dry for 3 h. In the end, the powder was ground and stored in a recipient for further use [29].

Synthesis of g-C_3N_4 by thermal polycondensation (study 3)

g-C_3N_4 in powder form was directly prepared by calcination of 20 g of urea (from Sigma-Aldrich CAS: 57-13-6), which was transferred into a ceramic crucible and heated in a muffle furnace at 550 °C for 2 h, with a heating ramp of 35 min. The crucible was sealed to avoid nanopowder loss. The reaction was carried out with the exhaustion system turned on since the thermal decomposition of urea releases toxic gases and vapors (such as ammonia). In the end, a pale-yellow powdered product was obtained [30].

Synthesis of TiO_2 nanostructures and g-C_3N_4/TiO_2 heterostructures via microwave irradiation (study 3)

For the synthesis of the g-C_3N_4/TiO_2 heterostructures, the obtained g-C_3N_4 nanopowder was dispersed in 23 mL of ethanol (96 %), and the solution was ultrasonically dispersed for 15 min to achieve homogeneity. Afterward, 0.3 mL of hydrochloric acid (HCl, 37 % purity from Merck) was added, followed by 0.8 mL of dropwise TTIP (97% purity from Sigma-Aldrich).

The solution was left to stir for 10 min. A volume of 20 mL of the prepared solution was then transferred to a 35 mL Pyrex vessel, which was placed in a CEM Discovery SP microwave. The synthesis was carried out for 1 h at 150 °C with a maximum power of 100 W and a maximum pressure of 17 bar (250 psi). The resulting g-C_3N_4/TiO_2 nanopowders were washed alternately with deionized water and IPA several times using a centrifuge at 5320 rpm for 5 min each time and dried in a desiccator at 80 °C, under a vacuum. Pure TiO_2 was also obtained by performing a microwave synthesis under the same experimental conditions, except for the addition of g-C_3N_4 nanopowder [30]. A schematic of the experimental procedure for the synthesis of g-C_3N_4/TiO_2 heterostructures by microwave is visible in Figure 2.5.

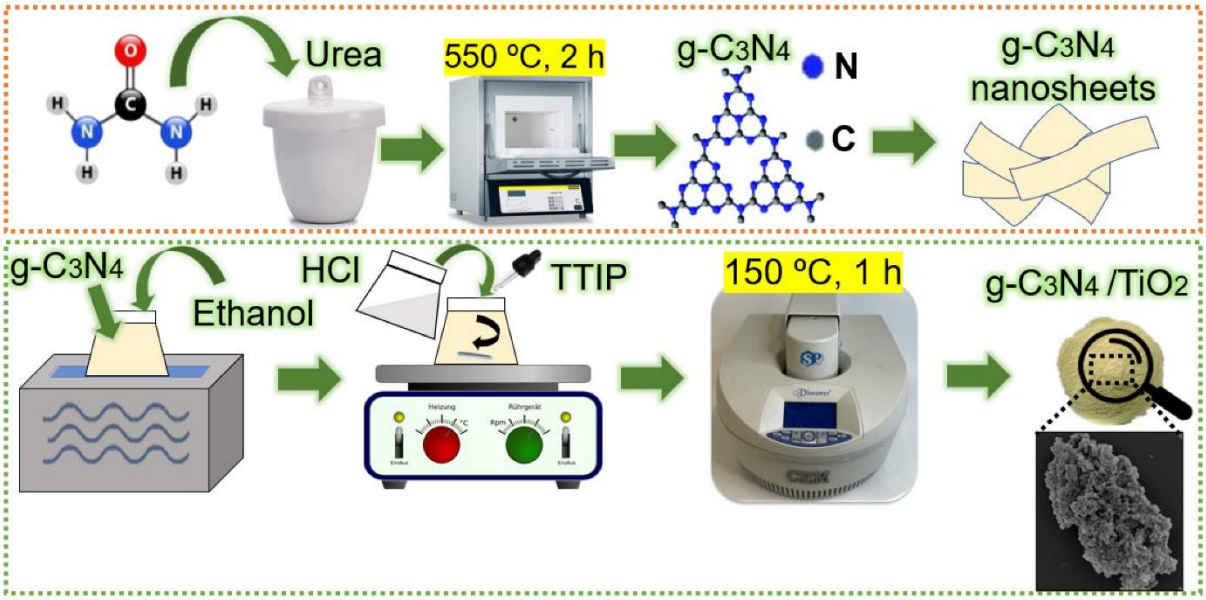

Figure 2.5: Schematic diagram for the MW synthesis of g-C_3N_4/TiO_2 heterostructures. The schematic in the orange box represents the first steps for the synthesis of g-C_3N_4/TiO_2 heterostructures, while the schematic in the green box represents the last steps [30].

Synthesis of TiO_2 nanostructures for incorporation on PU foams via microwave irradiation (study 4)

TiO_2 nanostructures were synthesized by a fast microwave approach. To prepare a solution of 50 mL, 4 mL of HCl (37 % purity from Merck) was added to 44.4 mL of different solvents (deionized water, ethanol, or IPA). Afterwards, 1.6 mL of TTIP with 97 % purity from Sigma-Aldrich was added dropwise to the previous solution and it was left to stir for 10-20 min, or until a homogeneous solution was obtained. Microwave synthesis was performed using a CEM microwave digestion system (MARS one) and was carried out at 1000 W, 200 ± 10 °C for 10 min. Solution volumes of 25 mL were transferred into Teflon vessels of 75 mL, which were kept sealed. The resultant TiO_2 nanopowders were washed with deionized water

and ethanol several times using a centrifuge at 5300 rpm for 5 min each time until the pH of the solution was 6-7. Finally, the nanopowders were kept in a desiccator for drying at 80 °C in a vacuum for 12 h. It is important to mention that the microwave-assisted syntheses are reproducible, and the obtained weights were 0.43 g (% yield = 100 %), 0.32 g (% yield ≈ 74 %), and 0.15 g (% yield ≈ 35 %) when ethanol, IPA and H_2O were used as solvents, respectively [31].

Synthesis of TiO_2 and Fe:TiO_2 nanostructures via surfactant-assisted microwave irradiation (study 5)

TTIP, 97 % purity from Sigma-Aldrich was dissolved in absolute anhydrous ethanol from Carlo Erba reagents (CAS: 64-17-5) and oxalic acid anhydrous from Sigma-Aldrich (CAS: 144-62-7). To prepare a solution of 120 mL, 5 mL of a 1 M oxalic acid solution was added to 115 mL of absolute ethanol and stirred for 10 min. Afterwards, 1 mL of polyethylene glycol (PEG) 400 from Sigma-Aldrich (CAS: 25322-68-3) was added, followed by a dropwise addition of 4 mL TTIP. Then the solution was stirred for 1 h. Microwave synthesis was performed using a CEM microwave digestion system (MARS one), which was carried out at 1000 W, 170 ± 10 °C for 1 h. Solution volumes of 40 mL were transferred into Teflon vessels of 75 mL, which were kept sealed. To prepare the Fe:TiO_2 nanoparticles, 1, 2, and 5 mol.% of iron (III) nitrate nonahydrate purchased from Sigma-Aldrich (CAS: 7782 81-8, 98 % purity) were added to the previous solution, before the addition of TTIP. The nominal ratios of Fe precursor: TTIP were 0.01, 0.02, and 0.05 for 1, 2, and 5 mol. % of Fe, respectively. The solution was stirred for 1 h, before transferring it to the microwave vessel. The as-synthesized TiO_2 nanopowders were cleaned using a centrifuge at 4000 rpm for 5 min. The powders were washed several times with deionized water, followed by IPA. Finally, the nanomaterials were kept overnight in a desiccator for drying at 80 °C under a vacuum [26].

Synthesis of TiO_2 and Ca:TiO_2 nanostructures via microwave irradiation (study 6)

A microwave-assisted solvothermal method was employed. To prepare the Ca:TiO_2 nanomaterials, 5 or 10 mol. % of calcium nitrate tetrahydrate ($Ca(NO_3)_2{\cdot}4H_2O$, purity: 99% from Sigma-Aldrich, CAS:13477-34-4) was dissolved in 48.4 mL of ethanol (purity: 96 %; CAS 64-17-5) until a homogeneous solution was obtained. Then, 1.6 mL of TTIP (purity: 97 % from Sigma-Aldrich) was added dropwise under fast magnetic stirring. The preparation of the solutions was conducted at RT. For comparison, a solution of pure TiO_2 was also prepared without calcium nitrate tetrahydrate. In this case, a milky solution was obtained, while the solutions with calcium precursor turned opaque. 20 mL of each mixture was then distributed into

two Teflon vessels of 75 mL. A CEM MARS one microwave digestion system was used for the syntheses with a power of 1000 W operating at 230 ± 10 °C for 30 min. After that, the nanopowder was alternately washed with deionized water and ethanol using a centrifuge for 3 min at 5250 rpm (4 cycles). The final product was dried in a desiccator at 80 °C overnight.

2.1.2 Incorporation of the nanomaterials on different substrates

2.1.2.1 3D printing using the SLA technique

3D printing or AM involves the deposition of material layer-by-layer to create three-dimensional structures or objects. It is not limited to prototyping, being also used for manufacturing, enabling large-scale customization, and transforming industries such as agriculture, healthcare, automotive, medicine, construction, and aerospace, as well as individual customers who have acquired additive manufacturing equipment [32,33]. This technology surpasses traditional manufacturing methods by reducing costs without the need for molds or casting patterns. It enables the creation of complex geometries, offers greater freedom to meet the desirable specifications, provides high-quality control over the manufacturing process, faster production speeds, and minimizes waste, thus contributing to sustainability [32,33]. 3D printing originated in the 1980s, initially using polymer materials with methods such as SLA, fused deposition modeling (FDM), and selective laser sintering (SLS) [33]. According to American Society for Testing and Materials (ASTM) Standard F2792, 3D printing technologies are divided into seven techniques: binder jetting, material extrusion, directed energy deposition, material jetting, powder bed fusion, sheet lamination, and vat photopolymerization. Each technique is tailored to specific applications [32,34]. Among the current AM techniques, SLA was the first 3D printing process available on the market and it remains one of the most frequently used techniques [32,34].

Stereolithography or vat photopolymerization is an AM process in which a light source solidifies liquid resin into 3D objects. As mentioned in Chapter 1, SLA has several advantages including precision, speed, cost-effectiveness, and versatility. These benefits make it an essential process for creating models and prototypes to be applied in various fields [35]. For the design of the 3D prototypes by using SLA, a 3D computer-aided design software (e.g. CAD or Sketch Up) is used. The models are then generated by converting the digital model file into a suitable format (e.g. STL). Then, the data can be transferred from computer-aided design software to the 3D printing device. For most 3D models, a support structure is required to attach

overhanging parts to the build platform, preventing deflection caused by gravity and preserving newly formed sections during the peeling process. This support structure is automatically generated by the 3D printer's software (PreForm software). The printer firmware interprets the data from the STL file. Afterwards, the 3D model is sliced into cross-sections of typically 100 microns (depending on the 3D printer), and several printing parameters such as printing speed and pressure, layer height (resolution), infill pattern, and infill density are optimized to change the accuracy of the printed object. Before the 3D printing starts, it is necessary to define the build parameters and prepare the loading of the material, placement, and leveling of the build platform. The printer checks if the liquid tank contains enough photosensitive resin, which is photopolymerized when exposed to UV laser irradiation. If not, it fills the tank with resin. There are two types of stereolithography processes: traditional (top-down) and inverted (bottom-up) [36]. An inverted stereolithography printer was used, where a transparent tank with a non-stick surface serves as a substrate for the liquid resin to cure against, allowing for easy detachment of newly formed layers. The build platform is submerged just below the resin surface by a distance equal to the thickness of one layer. A UV laser (λ = 355 nm) is directed at two mirror galvanometers, which guide the light to the correct coordinates through a series of mirrors. The focused light then passes upward through the tank's bottom, curing a layer of photopolymer resin. The vertical movement of the build platform, combined with the horizontal movement of the tank, separates the cured layer from the tank's bottom. The build platform then rises, allowing fresh resin to flow beneath. This process is repeated until the print is complete. In more advanced systems, the tank is heated to maintain a controlled environment, and a wiper moves across the tank between layers to circulate the resin and remove clusters of semi-cured material. Post-printing treatment steps are typically necessary to completely remove material in excess and stabilize the curing, such as UV treatment [37–43].

2.1.2.2 Composition of a photosensitive resin

A photocurable resin is composed of photoinitiators, monomers/oligomers, and additives (visual and functional supplements, like dyes). Resin is a polymer composed of short carbon chains from one to a few thousand carbons. The monomer and oligomer chains in the resin contain active groups at their ends. When the resin is exposed to UV light, the photoinitiator molecule splits into two parts, generating highly reactive radicals. These radicals are transferred to the active groups on the monomer and oligomer chains. While this process

forms longer chains and creates cross-links, the resin transitions from a liquid to a solid state. This transformation from liquid to a highly polymerized solid occurs within milliseconds [29].

2.1.2.3 Incorporation of TiO_2 nanostructures on 3D-printed architectures

In this study, the desktop Form2 (Formlabs) automated resin SLA system was used (see Figure 2.6). This is an inverted-stereolithography SLA printer, in which several types of resin can be employed depending on the final application [44].

Figure 2.6: Lab desktop SLA 3D printer Form2 (from FormLabs).

3D macro-architectures were designed on Onshape, a CAD software system. Two models of different sizes were produced: a large structure and a thin structure. The dimensions of both large and thin 3D-printed blocks are indicated in Figure 2.7. The resin used was the "Formlabs High Temp Resin", which was made for high-temperature resistance [29]. In this case, it was chosen to withstand the temperature of the microwave.

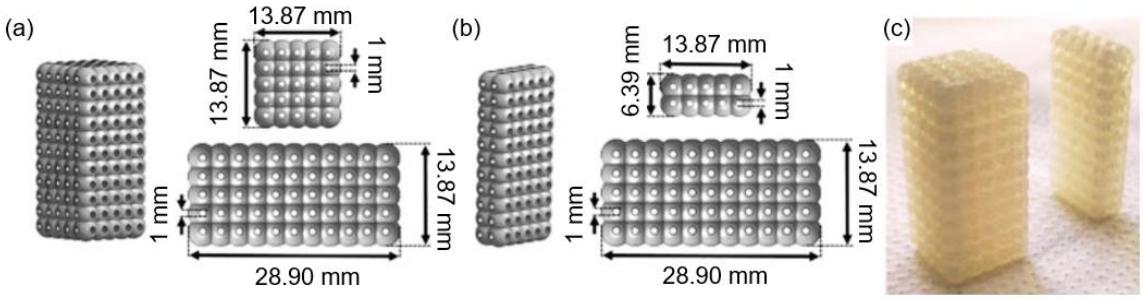

Figure 2.7: Design and dimensions of the 3D-printed TiO_2 architectures indicated as large structure in (a) and thin structure in (b). The real photographic image of the 3D-printed blocks is shown in (c). Reproduced with permission from [29].

The printed structures were removed from the 3D printer and cleaned using IPA to eliminate residual uncured resin. They were submerged in an IPA bath for 6 minutes. After cleaning, the uncured structures were dried and exposed to UV irradiation (PSD Pro Series Digital UV Ozone System, NOVASCAN) for 30 minutes at 60 °C to complete polymerization. Both large and thin structures have cavities with centered crossed channels along the x-, y-, and z-axes. The large structure features 5 × 5 × 11 holes with a calculated surface area of 20,217 mm², a calculated surface area to volume ratio of 0.0036 mm^{-1} and a calculated surface area to measured mass ratio of 4.238 $mm^2.g^{-1}$, while the thin structure comprises 2 × 5 × 11 holes with a surface area of 8,084 mm², a calculated surface area to volume ratio of 0.0032 mm^{-1} and a calculated surface area to measured mass ratio of 3.676 $mm^2.g^{-1}$ [29].

Before UV curing, both thin and large 3D-printed structures were impregnated with TiO_2 nanostructures produced via microwave irradiation. For this step, 0.1 g of TiO_2 nanopowder was added to a bottle containing the 3D-printed block. The nanostructures were distributed evenly over the block's surface by manually shaking the bottle for 5 minutes. The printed block was then subjected to the UV post-curing process [29].

Following UV curing, the impregnated blocks were washed in Milli-Q water for 10 minutes at RT using a Bandelin Sonorex ultrasonic bath to remove any non-adherent nanostructures. To enhance the photocatalytic activity of the 3D-printed architectures, the blocks were subjected to microwave synthesis after impregnation and UV curing. The 3D-printed block was placed in a MW vessel, and the solution used to produce TiO_2 nanostructures was added [29]. Details of the microwave parameters can be found in section 2.1.1.6. The entire process for fabricating the 3D-printed architectures is illustrated in Figure 2.8. Two fabrication conditions were investigated (see Figure 2.8): (a) impregnation only with the TiO_2

nanostructures and (b) impregnation with TiO_2 nanostructures followed by a subsequent MW synthesis step.

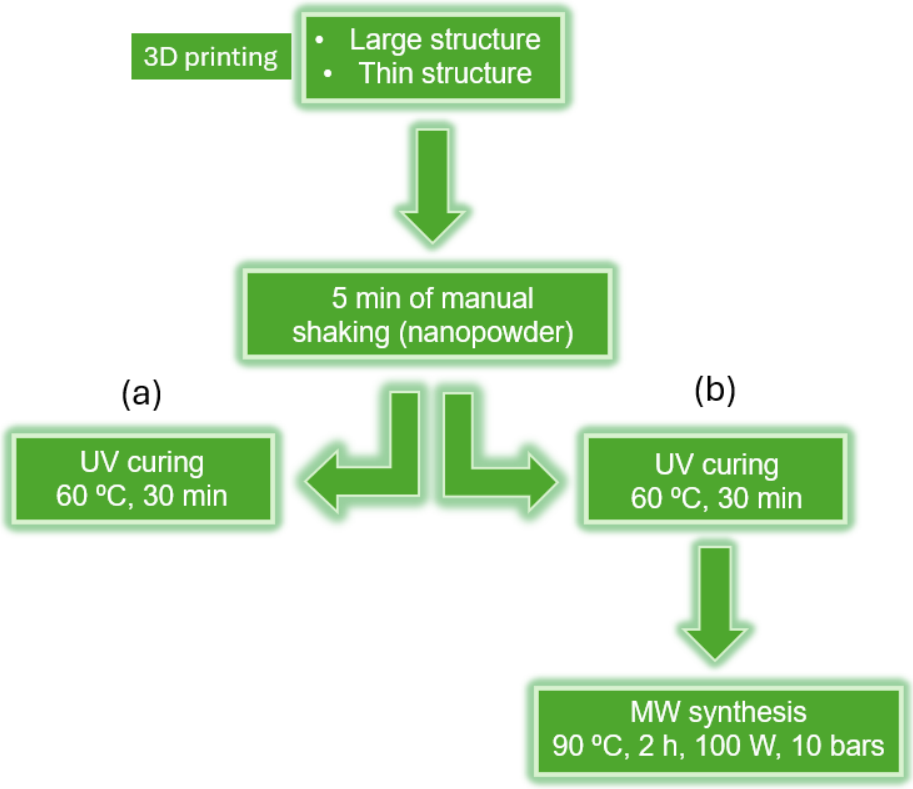

Figure 2.8: Schematic of the production of the 3D-printed architectures under the two investigated conditions: (a) impregnation only with the TiO_2 nanostructures and (b) impregnation with TiO_2 nanostructures followed by a subsequent MW synthesis step. Adapted from [29].

2.1.2.4 Dip-coating technique

Various methods are available for thin film coating, including dip-coating [45], drop-casting [46], spin-coating [47], spray-coating [48], blade-coating [49], and roll-coating [50], among others. Dip coating is a simple, waste-free, low energy consumption, and low-cost technique widely used to prepare films with a thickness generally below 1 μm [51] at both lab and industrial scales [45,51–53]. Dip-coating process begins by preparing a stable solution with dispersed nanoparticles and a volatile solvent. It is also frequently used to apply coatings from sol–gel solutions. This technique is also suitable for coating complex geometries and large surfaces. Its process can also be manual or automatic (the latter improves reproducibility, processing speed and allows a scale-up [54]), and it can be carried out in a batch or continuous mode. The substrate to be coated is immersed into the solution at a controlled speed followed by a dwell time. Afterwards, it is withdrawn at a steady rate and dried, allowing the

evaporation of the solvent (Figure 2.9). This process results in a uniform and thin layer of nanoparticles deposited on the substrate due to viscous drag and capillary action. The final step, solvent evaporation, can be conducted by drying the substrate either at RT or using a dryer [55,56].

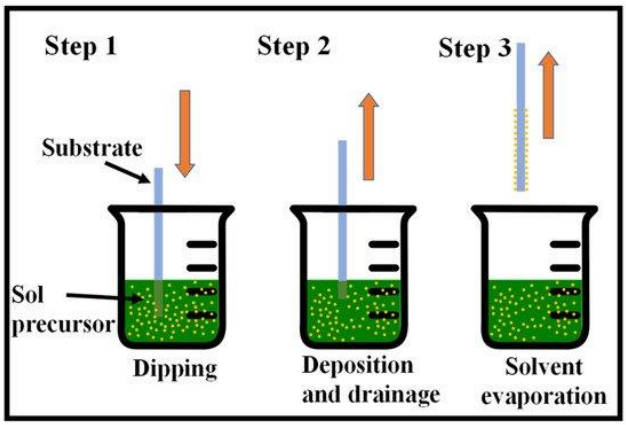

Figure 2.9: Sequential steps of the dip-coating process: step 1- dipping, step 2 - deposition and drainage, and step 3- solvent evaporation. Reproduced from ref. [45].

During the withdrawal stage, there are two main types of forces: draining and entraining forces. Draining forces pull the liquid away from the substrate and back into the bath, while entraining forces work to retain the fluid on the substrate. The balance between these forces determines the thickness of the film [57]. The formation of the film can also be divided into four regions ([57,58], see Figure 2.10):

- Static meniscus: this region is characterized by a balance between hydrostatic and capillary pressures, which dictates the meniscus shape.
- Dynamic meniscus: located around the stagnation point, where entraining and draining forces are in equilibrium. In this region, entraining forces gradually influence the solution flow until they become dominant.
- Constant thickness zone: in this region, the film achieves a uniform thickness (h_0).
- Wetting Zone: the region where the film started to be formed.

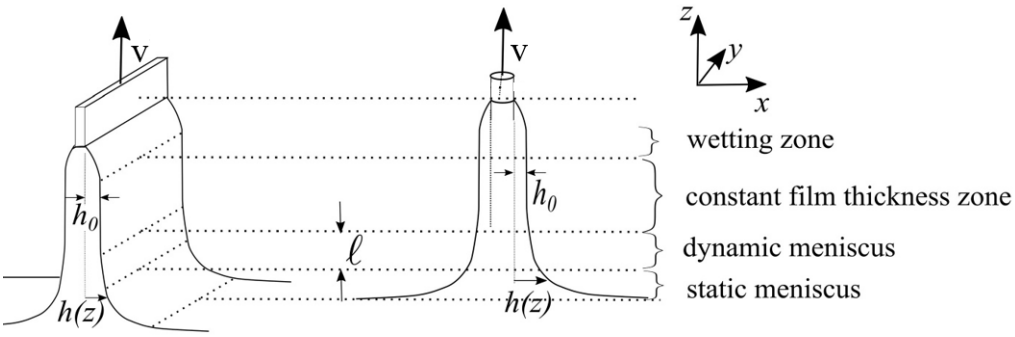

Figure 2.10: Coating occurs when a solid (a plate is represented on the left-hand side and a fiber is illustrated on the right-hand side) is withdrawn at a velocity (v) from a liquid solution. At the bottom, the static meniscus is visible. The liquid is sheared in the dynamic meniscus, which extends over a length (ℓ). A uniform film with a constant thickness (h_0) is formed between this dynamic meniscus and a wetting zone. Adapted from ref. [58].

Based on the dominant forces governing the coating behavior, three distinct coating regimes can be defined as (i) viscous flow, (ii) draining and (iii) capillary regimes. The first regime occurs at high velocities and with viscous solutions, where coating behavior is governed by viscous forces and gravitational attraction. In this regime, the entraining forces arise from viscous forces acting on the solution as the substrate is withdrawn. If the withdrawal speeds or solution viscosities are too low, viscous forces weaken. Consequently, the balance between entraining and draining forces becomes influenced by surface-tension-driven solution movement. Under these conditions, the coating is in the drainage regime. When the speed drops below approximately 0.1 $\mathrm{mm.\,s^{-1}}$, a third coating regime emerges, the capillary regime. In this regime, the solution is entrained onto the substrate through viscous flow at a rate slower than that of evaporation. At these coating speeds, a constant film thickness is never fully achieved. As a result, in the capillary regime, the final thickness depends on the withdrawal rate, the solution properties, and the solvent's evaporation rate [57].

Some critical parameters must be taken into account during the dip-coating process of nanoparticles [45,54,56,59,60]:

- Withdrawal speed
- Liquid properties (such as density, viscosity, surface tension and pH)
- Substrate properties
- Dwell time
- Number of dips
- Atmospheric conditions (like temperature and airflow)

The thickness and uniformity of the coating are highly influenced by the withdrawal speed. To produce thin films, a very slow pull-up speed is required, while thicker coatings demand a high rate of immersion, a faster pull-up speed, combined with rapid drying of highly volatile solvents [45,59,60]. Nevertheless, achieving a completely uniform substrate is challenging, particularly when using high-surface tension solvents like water. In addition, the thickness control is tough when preparing ultra-thin layers (< 20 nm) or ultra-thick layers (> 1000 nm) from highly diluted or highly viscous solutions [53].

Solvents should exhibit moderate volatility (boiling points between 50 °C to 120 °C) to allow enough time for the liquid film to level out while maintaining the drying time as short as possible. They should also have a low surface tension to ensure a complete wetting of the substrate and a homogeneous liquid flow. Solvents commonly employed include short-chained aliphatic alcohols (such as ethanol, n-propanol, isopropanol and n-butanol), though other solvents like esters or glycol ethers can be chosen. Mixing different solvents can help optimize deposition performance, but phase separation due to selective evaporation must be avoided, as it typically leads to flow instabilities and wetting issues [54]. Additives can be incorporated into the solution to control film formation and extend the lifetime of the coating, such as complexing agents or components with low vapor pressure (e.g., polyethylene glycol). However, it is important to keep in mind that additives can serve as potential sources of contamination, which may affect the coating properties.

Furthermore, atmospheric conditions such as airflow affect film formation, particularly by influencing solvent evaporation. Before starting the deposition, it is essential to thoroughly clean the substrate to ensure complete wetting and prevent surface contamination. An optimal dwell time can also minimize the turbulence caused by the substrate's immersion. Additionally, to increase film thickness or create stacks of different coating materials, a multiple dip-coating process can be applied [54].

Another relevant parameter concerns the substrate's properties. This technique is effective for coating nanopore networks, as the solution is rapidly filled within the pores due to the unidirectional movement of the linear meniscus upon withdrawal [56]. Moreover, the surface energy of a substrate plays a significant role in wettability, affecting the coating's spread and adhesion. A higher surface energy promotes better wetting, resulting in a more uniform film, whereas a low surface energy leads to poor wetting and uneven coatings. Surface treatments are an effective solution to enhance wettability and improve coating quality [57]. In addition, factors such as the substrate's roughness, chemistry and mechanical properties can be adjusted

for an excellent coating of substrates [61–63]. Although dip-coating is a simple process, multiple variables will dictate the final characteristics of the coating. When properly controlled, it could be a reliable and effective deposition technique [54].

2.1.2.4.1 Incorporation of TiO_2 nanostructures on PU foams by dip-coating

In this work, 30 mg of the microwave-synthesized TiO_2 nanopowder (see section 2.1.1.6) was dispersed in 20 mL of Milli-Q water and ultrasonic agitated for 30 min (solution A), step 1 in Figure 2.11. A second solution (solution B) was prepared by mixing 10 mg of polyacrylic acid (PAA) with 20 mL of Milli-Q water. Solution B was left to stir for 30 min, step 1 in Figure 2.11. After that, solution B was poured into solution A and stirred magnetically. Then, the pH was adjusted with NaOH to 7 [64], step 2 in Figure 2.11. Commercial porous polyurethane foam was cut into parallelepipeds of 1.5 cm^3 by volume (0.5 cm height × 1 cm width × 3 cm length). The previously cut PU foam pieces were cleaned for 15 min in Milli-Q water using an ultrasonic bath to remove possible dirt [31].

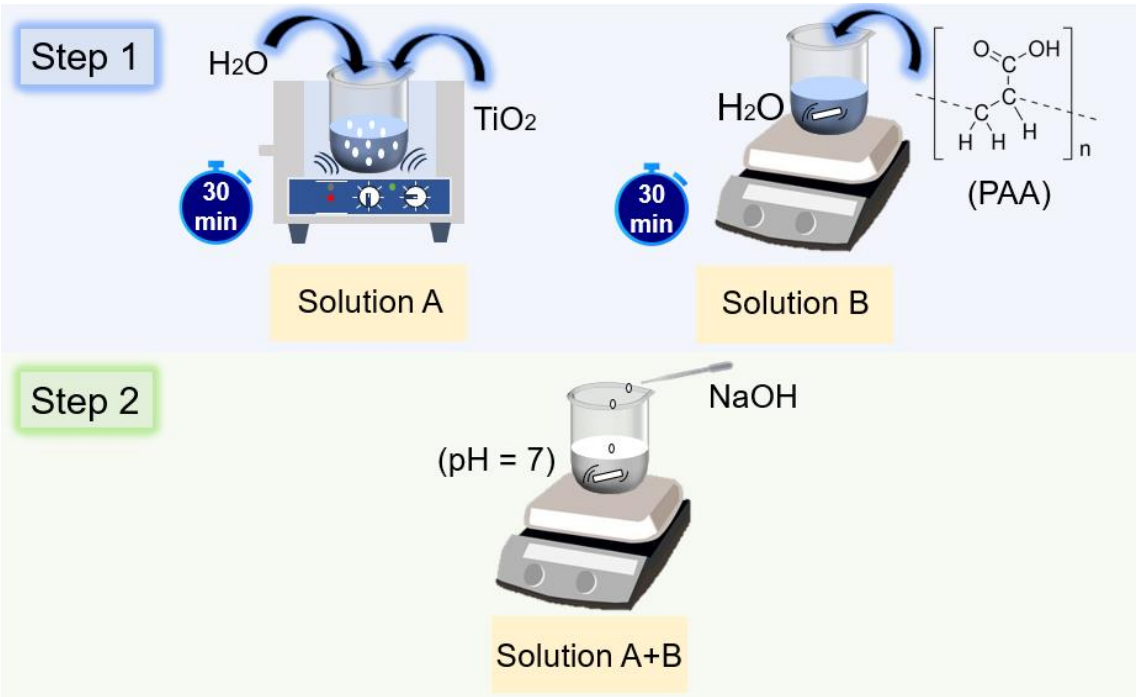

Figure 2.11: Diagram illustrating the process of preparing the dip-coating solution for the impregnation of PU foams with TiO_2 nanostructures. Steps 1 and 2 illustrate the preparation of solutions A, B and A+B, respectively [31].

Similarly to previous papers [59,65], to improve the hydrophilicity, PU foams were pre-treated in a 1 M aqueous (aq.) solution of NaOH at 60 °C for 20 min, under agitation. This solution will etch away part of the cell windows within the foam structure, exposing hydrophilic groups. To complete the pre-treatment, the sponges were rinsed many times with Milli-Q water and dried under a vacuum for 12 h at 80 °C [31].

The incorporation of TiO_2 nanostructures on PU was carried out by manually dipping the PU foams into the previously mixed solution (solution A+B). The immersion time was 5 s and a sequence of 5 dipping cycles was performed at RT (step 3 in Figure 2.12). Some bubbles were formed after each dip, and to remove them, the foams were squeezed several times with tweezers. A hairdryer was then used to dry the foams (the height of the foams was 22 cm and the distance between the hairdryer and the foam was around 7 cm). Between each dipping cycle, foams were dried for 10 min (Figure 2.12). Lastly, they were ultrasonically cleaned in Milli-Q water for 1 h to remove unbonded particles and dried at 80 °C overnight under a vacuum in a desiccator. The same foam was weighed before the TiO_2 impregnation (~0.066 g), after the TiO_2 impregnation (~0.071 g) and after the ultrasonic cleaning (~0.069 g). The final weight of the TiO_2 nanopowder on the foam substrate was around 3 mg and the foam maintained the same initial dimensions. Macrographs of the TiO_2-PU foam are visible in Figure 2.12, in which one of them shows that its flexibility is maintained after the impregnation and drying procedures. The technique employed proved to be simple and replicable [31].

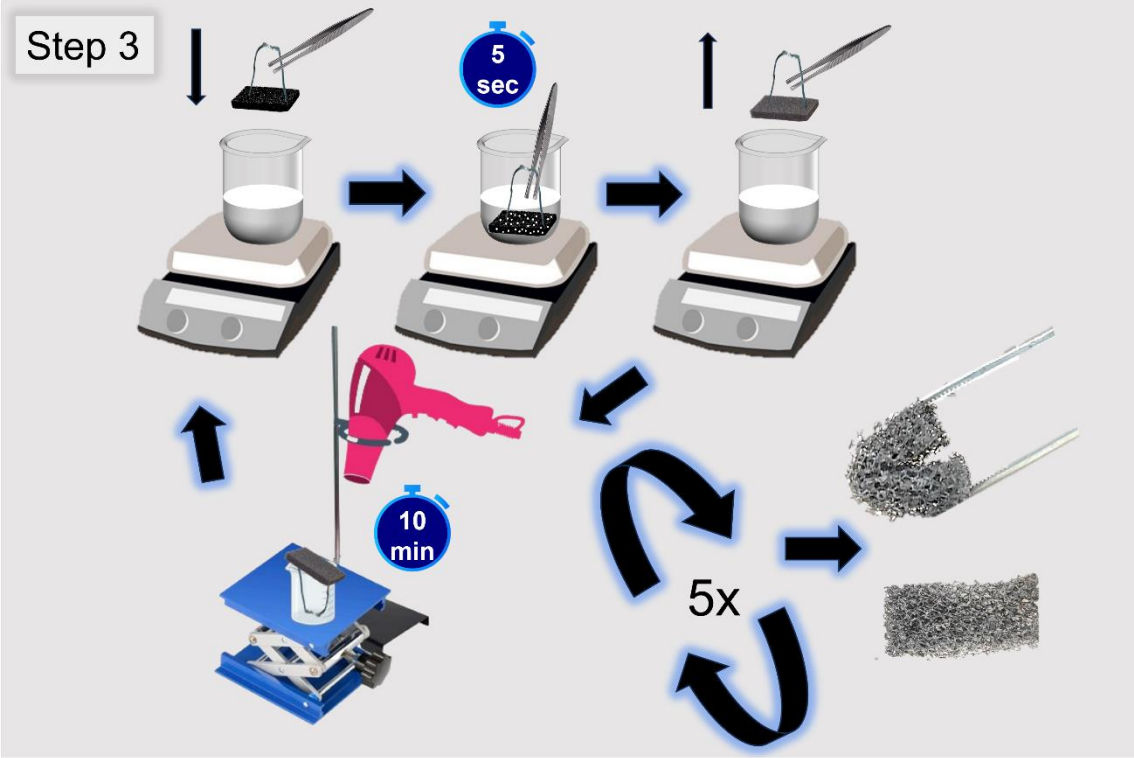

Figure 2.12: Diagram illustrating the dip-coating procedure. Step 3 represents the dip-coating and drying processes to obtain TiO_2-PU foams. Real photographic images of the produced TiO_2-PU foam are also visible [31].

2.1.2.5 Drop-casting technique

Drop-casting, similar to dip-coating, is a simple, fast and reduced-cost technique for producing thin films, though it is restricted to small areas [66,67]. Moreover, no material waste is generated [67]. A droplet of liquid with a suspension of particles is deposited onto the substrate and allowed to dry naturally or under a controlled atmosphere [68,69]. During the drop-casting process, the substrate can be heated to further accelerate the evaporation process [69]. However, the main challenges of this method lie in controlling film thickness and ensuring a uniform, continuous coating [69]. In fact, drop-casting suffers from the "coffee-ring effect". This phenomenon occurs due to solvent evaporation during film assembly, which induces capillary flows within the droplet. These capillary flows transport particles toward the three-phase contact line (where the solid, liquid, and gas phases converge [70]), causing the particles to accumulate at the film boundaries and form a ring pattern. The ring's width is typically in the micrometer range, leaving most of the area originally covered by the droplet largely unchanged [71]. This effect is primarily driven by two mechanisms: enhanced evaporation caused by the curvature at the droplet's edge and the pinning at the three-phase contact line. While pinning prevents the droplet from contracting, the increased evaporation at the edge

generates a flux flow within the droplet. However, this phenomenon can be mitigated by adjusting the liquid properties, such as viscosity and pH, surface properties, including surface roughness, as well as atmospheric conditions [26,71,72].

Key controllable parameters include [26,68,69,71–74]:

- Liquid properties (type of solvent(s) and its polarity, pH, viscosity,…)
- Substrate properties (surface roughness, temperature of the substrate,…)
- Atmospheric conditions

The volume of dispersion and particle concentration can be easily adjusted depending on the desired film thickness or structure. Higher concentrations typically produce thicker films but may result in defects and non-uniformities. Therefore, optimizing the concentration is essential to achieve the target film thickness and uniformity [74,75]. Regarding the type of solvent(s), volatile solvents that efficiently wet the substrate and resist thin film instabilities, such as de-wetting, are generally preferred. Water is rarely used due to its low vapor pressure and high surface tension, but it can be replaced by alcohols. Organic solvents such as hexane, toluene, and halogenated compounds are often more suitable for nanoparticles with hydrophobic capping ligands. These solvents enhance substrate wetting, and at the same time promote the formation of uniform films by avoiding de-wetting issues [74]. The polarity of the solvent can also influence the microstructure of the thin film. For example, a study showed that variations in the overall morphology and structural order of tetra(aniline)-surfactant thin film are closely linked to the solvent's polarity [73]. The substrate's temperature during deposition can also affect the evaporation rate of the solvent and the morphology of the film. A controlled heating temperature ensures uniform evaporation and minimizes the formation of film defects. In contrast, excessively high temperatures may cause rapid evaporation, creating non-uniform films [74,76]. The environment conditions such as humidity, temperature, and pressure are equally important since they can affect solvent evaporation rates and film formation [74,77]. By optimizing these process parameters, reproducible thin films can be achieved, potentially enabling large-scale production [67].

2.1.2.5.1 Incorporation of TiO_2 and Fe:TiO_2 nanostructures on polymeric substrates by drop-casting

Several circular polymeric filters made of MCE (mixed cellulose esters, composed of inert cellulose nitrate and cellulose acetate polymers) with a pore size of 0.22 μm and diameter of 47 mm were tested. The filters were attached to previously cut ordinary glass squares using Kapton tape. These glass squares were used to prevent the polymeric substrates from bending,

after complete drying of the droplets. In this study, 40 mg of nanoparticles was added to 9 mL of deionized water. Then, 1 mL of EG from Carlo Erba Reagents (CAS: 107-21-1, 99.5 % purity) was also added to the previous solution. It is reported that a small amount of EG (10–30 vol. %) in colloidal suspensions produces uniform layers. Before applying the droplets, and to mitigate the coffee-ring effect, the hydrophilic polymeric substrates were heated on a hot plate at 80 °C. Six layers of 1 mL of the aqueous solution were uniformly applied onto the substrates, leaving the necessary time for each layer to dry [26]. A schematic of the overall experimental procedure (sections 2.1.1.6 and 2.1.2.5.1) is visible in Figure 2.13.

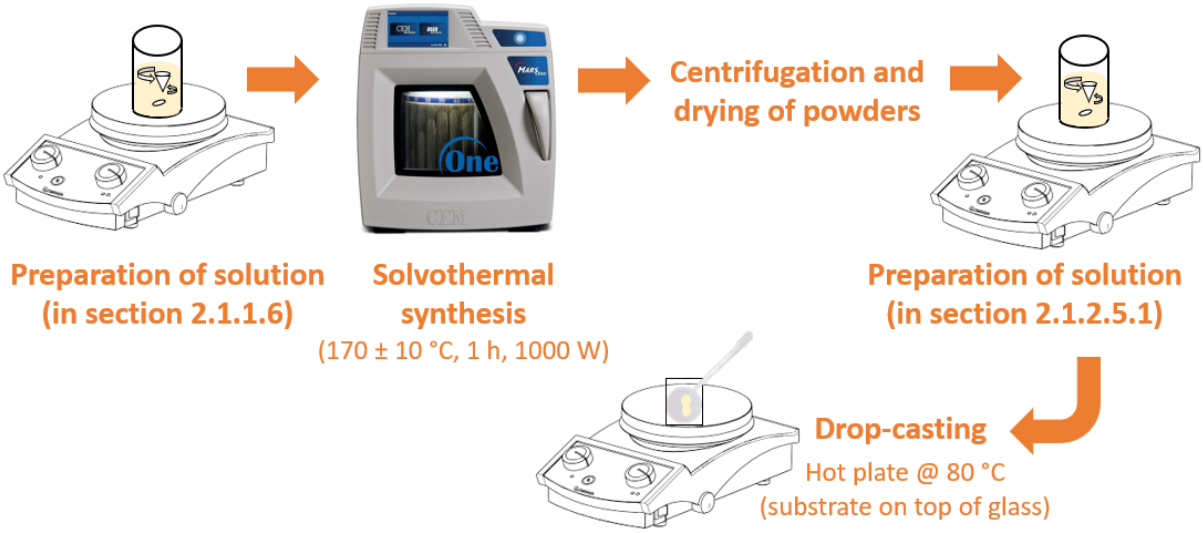

Figure 2.13: Schematic illustration of the synthesis of TiO_2 and Fe:TiO_2 nanostructures followed by the impregnation process on the filters [26].

2.1.2.6 Fabrication of TiO_2 and Ca:TiO_2 cellulose-based membranes

The pristine membrane was made using biomass cellulose nanofibers (BiNFi-s from Sugino Machine Ltd., Japan, average fiber width: 10-50 nm) with a solid content of 2 %. The nanofibers' gel was dispersed in deionized water and stirred for 30 min, followed by the addition of pure TiO_2 and Ca:TiO_2 nanopowders, and vigorously stirred for 30 min. Afterwards, TiO_2 and Ca:TiO_2 membranes were poured into a Petri dish and left to dry in a controlled environment (T = 25 °C with a relative humidity of 40 %). After drying, the membranes were peeled off the dishes. A pristine membrane (without nanopowder) was also fabricated under the same experimental conditions.

2.2 Optimization of the synthesis parameters and impregnation parameters

TiO_2 nanostructures were directly synthesized on cork and 3D-printed resin blocks using low-temperature solvothermal methods under microwave irradiation at 120 °C and 90 °C, respectively, with oxalic acid (one-step methods). These specific temperatures combined with oxalic acid were selected to prevent substrate damage under microwave irradiation, which would occur with higher temperatures or stronger acids. Although water is the most eco-friendly solvent, ethanol was chosen for all studies due to its crucial role in maintaining particle uniformity in size and shape. To achieve complete substrate coverage, microwave irradiation was applied for 60 min on the cork and 120 min on the resin substrates. While TiO_2 nanostructures can be synthesized in acidic, neutral, or basic environments, better control over their morphology and crystal structure is typically obtained under acidic or basic conditions. However, similarly to the study with the cork and 3D-printed substrates, oxalic acid was used to synthesize Fe-modified nanostructures, as extreme pH levels complicate the doping process. Additionally, it was found that temperatures above 150 °C facilitate the formation of defects, heterostructures, and doping. Therefore, in the case of defective TiO_2 nanostructures on PU foams, g-C_3N_4/TiO_2 heterostructures, Fe and Ca-modified TiO_2 nanostructures on cellulose-based substrates, the nanopowders were obtained at 200 °C, 150 °C, 170 °C and 230 °C, respectively. To prevent the substrates from being destroyed under microwave irradiation, defective TiO_2 nanostructures on PU foams and Fe-modified TiO_2 nanostructures on MCE water filters had alternative impregnation techniques (dip-coating and drop-casting, respectively, two-step methods). Both techniques were versatile, simple to implement, and cost-effective for impregnating TiO_2-based materials onto various substrates. Finally, using a simple mixing approach, Ca-modified TiO_2 cellulose-based substrates were developed, and the nanostructures appeared uniformly distributed throughout the membrane and fully embedded within the cellulose fiber matrix.

The initial syntheses were conducted using a single-mode microwave (CEM Discover SP), followed by upscaling with a multimode microwave (MARS 1) to enhance the yields. Upscaling was performed in almost all studies, except for those involving TiO_2 on 3D-printed architectures and g-C_3N_4/TiO_2 heterostructures, since in other studies, the results for both microwaves were compared and found to be similar after adjusting the parameters for each one [76,77].

2.3 Summary of the conditions used in each study

Table 2.2 presents a comparison of the various parameters used to produce TiO_2-based nanomaterials and the main differences between the studies. Despite variations in MW parameters across studies following optimization, TTIP and ethanol were always used as the Ti precursor and solvent, respectively.

Table 2.2: Comparison of the various parameters used to produce TiO_2-based nanomaterials and the main differences across the studies.

	MW used	MW parameters	Precursor	Solvent	Acid	Substrate	Strategies to enhance the visible light absorption
Study 1	MARS 1	120 °C 60 min 1000 W	TTIP (Ti precursor)	Ethanol	Oxalic acid	Cork (floating)	–
Study 2	CEM discover SP	90 °C 120 min 10 bars (145 psi) 100 W	TTIP (Ti precursor)	Ethanol	Oxalic acid	Resin (3D-printed blocks, non-floating)	–
Study 3	CEM discover SP	150 °C 60 min 17 bars (250 psi) 100 W	TTIP (Ti precursor) Urea (g-C_3N_4 synthesis)	Ethanol	HCl 37 %	None	Construction of heterostructures (g-C_3N_4/TIO_2)
Study 4	MARS 1	200 °C 10 min 1000 W	TTIP (Ti precursor)	Ethanol, IPA, or water	HCl 37 %	PU foams (floating)	Creation of surface defects
Study 5	MARS 1	170 °C 60 min 1000 W	TTIP (Ti precursor) Iron (III) nitrate (Fe precursor: 1, 2 and 5 mol. %)	Ethanol	Oxalic acid	MCE water filters (non-floating)	Doping (Fe^{3+} ions)
Study 6	MARS 1	230 °C 30 min 1000 W	TTIP (Ti precursor) Calcium nitrate tetrahydrate (Ca precursor: 5 and 10 mol. %)	Ethanol	No acid	Cellulose-based membranes (non-floating)	Doping (Ca^{2+} ions)

2.4 Characterization techniques

X-ray diffraction (XRD)

XRD measurements were carried out in an X'Pert PRO PANalytical powder (X'Pert diffractometer using Cu Kα line radiation (λ = 1.540598 Å), operated at 45 kV and 40 mA. Diffraction patterns were recorded from 20° to 80° (detector angle 2θ) with a step of 0.05° in a Bragg-Brentano configuration using the nanostructures in the form of powder. For the TiO_2 nanopowders that were integrated into 3D-printed blocks, the measurements were performed from 20° to 70° 2θ with a step size of 0.0334°. For the g-C_3N_4/TiO_2 heterostructures' study, the diffractograms were acquired from 10° to 90° (2θ) range with a step of 0.05°. For the research focused on TiO_2 nanostructures incorporated on PU foams and Ca:TiO_2 cellulose-based membranes, a different equipment was used: an Aeris Benchtop XRD System equipped with a PIXcel1D detector. In this case, the XRD diffractograms were acquired from 10° to 90° and 20° to 80° (2θ) range, considering a step of 0.02° and 0.0109° (spinning mode, rotation time: 4 s), respectively. The TiO_2 anatase, rutile and brookite simulated diffractograms were obtained from the International Centre for Diffraction Data (ICDD) with file numbers 00-021-1272, 00-021-1276, and 00-029-1360, respectively. The average crystallite size of the synthesized nanomaterials was estimated by the Debye–Scherrer equation, which can be seen in Ref. [78], using the software X'pert highscore plus (Almelo, The Netherlands, version 4.6a (4.6.1.23823)). The lattice parameters were estimated through X-pert highscore plus after the alignment with the reflections of standard silicon powder.

Electron microscopy

In the 3D-printed architectures, TiO_2 nanostructures on cork and Fe:TiO_2 nanostructures on water filters' studies, scanning electron microscopy (SEM) images were obtained using a Hitachi Regulus 8220 Scanning Electron Microscope (Mito, Japan), while for the energy dispersive X-ray spectroscopy (EDS) analyses, a Carl Zeiss AURIGA CrossBeam focused ion beam (FIB)-SEM workstation (Oberkochen, Germany) was used. For the other studies, SEM images were acquired with a Hitachi Regulus 8220 Scanning Electron Microscope (Mito, Japan) equipped with an Oxford EDS detector. The flat cross-sections of the cellulose membranes (pristine, with TiO_2 and 10 mol. % of Ca:TiO_2) were prepared by the liquid nitrogen

cryogenic fracture prior to SEM observations. The membrane thicknesses were measured using ImageJ software [79].

Scanning transmission electron microscopy (STEM), including high-angle annular dark-field (HAADF) imaging, and transmission electron microscopy (TEM) observations were carried out with a Hitachi HF5000 field-emission transmission electron microscope operated at 200 kV (Mito, Japan). This is a cold field emission gun (FEG) TEM/STEM with a spherical aberration corrector for the probe, and it is equipped with one 100 mm^2 EDS detector from Oxford Instruments. A drop of the sonicated dispersion was deposited onto lacey-carbon copper grids and allowed to dry before observation. The average particle size and standard deviation of the nanostructures were calculated based on the SEM and TEM images obtained from the dimensions of several particles using ImageJ software [79].

Atomic force microscopy (AFM)

AFM images were acquired with an Asylum Research MFP-3D Standalone system (Oxford Instruments, Abingdon, UK) operated under ambient conditions, in alternate contact mode, using commercially available silicon probes (Olympus AC160TS, f_0 = 300 kHz, k = 26 $N.m^{-1}$; Olympus Corporation, Tokyo, Japan). The images and height profiles were exported using Asylum Research's software packages after low-level plane fitting.

Raman spectroscopy

Raman spectroscopy measurements were obtained with an inVia Qontor confocal Raman microscope from Renishaw (Kingswood, UK). A 50 mW green diode pumped solid state laser operated at 532 nm was used as the excitation source, with a 10 s exposure time and settings of 3 or 5 accumulations. The Raman spectra were recorded as an extended scan in the range of 100–700 cm^{-1}. The laser beam was focused with a long working distance (8.2 mm) 50× Olympus objective. The results present are based on the average of several scans taken on the surface of the synthesized materials. The 521 cm^{-1} peak of a silicon wafer was used to calibrate the spectrograph for possible fluctuations in the Raman system. All measurements were performed at RT.

Reflectance/absorbance measurements

Total reflectance and absorbance measurements were recorded by using a double-beam ultraviolet-visible-near infrared (UV-VIS-NIR) Shimadzu spectrophotometer with an

integrating sphere in the range of 280–800 nm. The specular reflectance was also recorded in the same range to obtain the diffuse reflectance data (DRS) and estimate the band gap energies using the Kubelka-Munk function. $BaSO_4$ white powder was used as the reference. In some studies, a PerkinElmer Lambda 950 UV/VIS/NIR spectrophotometer was used to directly measure diffuse reflectance and absorbance. All measurements were carried out at RT.

Photoluminescence (PL)/Photoluminescence excitation (PLE) experiments

RT PL and PLE experiments were also conducted. A Fluorolog-3 set-up from Horiba Scientific was used with a double additive grating Gemini 180 monochromator (1200 gr. mm^{-1} and 2×180 mm) in the excitation and a triple grating iHR550 spectrometer in the emission (1200 gr. mm^{-1} and 550 mm). The excitation source used was a 450 W Xe lamp, exploring different excitation wavelengths. The PLE experiments were carried out by monitoring the observed emission maximum. For the g-C_3N_4/TiO_2 nanomaterials, RT PL measurements were performed using a PerkinElmer LS55 luminescence spectrometer (PerkinElmer, Waltham, MA, USA) equipped with a Xenon lamp as an excitation source. The PL data were acquired from 400 to 600 nm, using an excitation wavelength of 350 nm.

Brunauer-Emmett-Teller (BET) method

The determination of the specific surface area was achieved by nitrogen adsorption according to the BET method, in the determined p/p_0 range and following the methodology described in ISO-9277 [80]. The results were obtained at 77 K using the ASAP 2010 Micromeritics adsorption equipment. Before the experiments, an outgassed procedure was carried out overnight or for 6 h at 120 °C under a vacuum (5 °. min^{-1}) for the nanopowders (~0.2 g).

X-ray photoelectron spectroscopy (XPS)

The XPS experiments were performed using a Kratos Axis Supra with monochromatic Al Kα irradiation (1486.6 eV). The XPS scans were acquired using a 225 W X-ray power and 40 eV of pass energy. The peaks were adjusted to the C 1s binding energy at 284.8 eV, except for the analysis of Fe:TiO_2 nanomaterials, where the peaks were aligned to the O 1s binding energy at 530 eV. The XPS data were analyzed using CasaXPS software. For the study related to Ca:TiO_2 materials, the scans were obtained with an X-ray power of 150 W and a pass energy of 10 eV. In this case, the peaks were not adjusted to the binding energy of C 1s or O 1s.

Fourier transform infrared spectroscopy (FTIR)

RT FTIR transmittance spectrum of the produced powders was recorded on a PerkinElmer FT-IR Spectrometer Spectrum Two (Waltham, MA, USA), equipped with an attenuated total reflection (ATR) cell in the range of 400–4000 cm^{-1}.

2.5 Experimental methods

Adsorption and photocatalytic experiments under simulated solar light

The photocatalytic activity of the TiO_2-based platforms (including TiO_2 3D-printed architectures, TiO_2-based cork platforms, and both pure TiO_2 and Fe:TiO_2 nanostructures on water filters) was assessed at RT for the degradation of RhB ($C_{28}H_{31}ClN_2O_3$) from Sigma Aldrich under a simulated solar light source. All experiments followed the international standard ISO 10678 [81]. A 50 mL solution of RhB (5 mg. L^{-1}) in Millipore water was stirred under low magnetic stirring, with each platform positioned at the bottom of a reaction vessel. The TiO_2-based platforms were kept for a specific period in the dark (30 minutes for the TiO_2 3D-printed blocks/TiO_2-based nanostructures on water filters and 60 min for the TiO_2 cork-based materials) to achieve adsorption–desorption equilibrium. For floating photocatalysts, no stirring was applied during the reactions to prevent oxygenation of the solution and to simulate conditions for floating photocatalyst applications. A light-emitting diode (LED) solar simulator (LSH 7320) was used, providing an AM 1.5 spectrum with an intensity of 100 mW. cm^{-2}) (1000 mW. m^{-2} = 1 SUN). Absorbance spectra were recorded at various time intervals using a UV-VIS spectrophotometer (PerkinElmer), extending up to 360 min (6 h) for the TiO_2 3D-printed blocks, 300 min (5 h) for the TiO_2-based nanostructures on water filters and 720 minutes (12 h) for the TiO_2-based cork platforms. Measurements were conducted in the 400–700 nm wavelength range (maximum peak intensity of RhB occurs at 554 nm). Control experiments using blank RhB solution and pristine substrates were also performed under identical conditions [26,28,29].

Reusability tests were performed on the water filters that exhibited the best performance and consisted in recovering the water filters with further discarding of the total liquid. The recovered filters were dried in air, prior to the next exposure. For the 3D-printed architectures, after each cycle, the photocatalyst was washed with water, exposed under UV light for 15 min to clean the residues. All reusability tests were carried out by repeated solar radiation

exposure of the same sample in fresh solutions considering the same exposure times. Three and five cycles were performed for the 3D-printed architectures and water filters, respectively. For the cork substrates, the reusability tests (three cycles) followed the same procedure as mentioned for the water filters, except they were conducted under natural sunlight [26,28,29].

The photocatalytic activities of pure TiO_2, g-C_3N_4 and g-C_3N_4/TiO_2 nanopowders were evaluated at RT, considering the degradation of MO ($C_{14}H_{14}N_3NaO_3S$) from Sigma-Aldrich under simulated solar light source. For each experiment, 25 mg of each nanopowder was dispersed in 50 mL of the MO solution (12.5 mg. L^{-1}) and stirred for 30 min (under low magnetic stirring) in the dark to establish the absorption–desorption equilibrium. Solar light exposure was conducted by using a WAVELABS LS-2 LED solar simulator with AM 1.5 spectrum, at an intensity of 1 SUN. Absorption spectra were recorded using a UV-VIS spectrophotometer with different time intervals, up to a total of 240 min (4 h). The measurements were performed in the 300–600 nm range (MO maximum absorption peak is located at 464 nm). A blank experiment (photolysis) was also investigated by irradiating the MO solution without any photocatalyst (before and after light exposure).

For the reusability experiments, a procedure similar to that used for the water filters was followed. However, in this case, the catalysts were recovered by centrifugation at 6000 rpm for 5 min with further discarding of the supernatant. The nanopowders were then dried at 60 °C for 12 h, before the next exposure. Additional parallel photocatalytic experiments were performed to guarantee the same photocatalyst mass in each cycle (25 mg) [30].

TiO_2 nanopowders for further incorporation on PU foams were also tested for the photocatalytic degradation of water pollutants, this time targeting a different water pollutant: tetracycline (50 mL of the TC solution (~30 ppm)). The conditions were the same as for the g-C_3N_4/TiO_2 nanopowders, with the exception that the nanopowders were kept in the dark for 4 h. The decay of the maximum absorption peak of tetracycline (at λ = 360 nm) was monitored using a UV-VIS spectrophotometer at fixed time intervals in the 200–450 nm range. The standard curves of tetracycline were obtained by the absorption spectra with various concentrations of 5, 10, 15, 20 and 30 ppm [31]. The linear expression that relates TC concentration and absorbance could thus be obtained and it is given by the following equation (equation (2.4)):

$$A = 0.03705 \times C_{\mathrm{TC}} \tag{2.4}$$

where A is the absorbance and C_{TC} is the TC concentration in mg. L^{-1} [31].

The amount of adsorbed tetracycline per gram of adsorbent, and adsorption capacity (uptake, q (mg. g^{-1})) was calculated according to equation (2.5):

$$q = \frac{V_{\text{solution}} \cdot (C_0 - C_e)}{W} \times 100 \quad (2.5)$$

In equation (2.5), C_0 and C_e are the initial and equilibrium concentrations of tetracycline (mg. L^{-1}), respectively, V_{solution} is the volume of the solution (L), and W is the mass of the adsorbent (g) [82]. The percentage of pollutant uptake by the sorbent (sorption efficiency) was calculated using the following equation, equation (2.6) [82]:

$$\text{Sorption efficiency (\%)} = \frac{C_0 - C_e}{C_0} \times 100 \quad (2.6)$$

The pseudo-first-order model given by Lagergren is described by the following equation [82]:

$$\log(q_e - q) = \log q_e - k_1 t/2.303 \quad (2.7)$$

in which q_e and q represent the amounts of pollutant adsorbed (mg. g^{-1}) at the equilibrium time and time t (min) respectively, k_1 is the rate constant of adsorption (min^{-1}). The rate constant and the corresponding linear regression correlation coefficient values can be determined from the straight-line plots of $\log(q_e - q)$ as a function of t [82].

The pseudo-second-order model given by McKay and Ho is expressed by equation (2.8) [82]:

$$\frac{t}{q} = \frac{1}{k_2 q_e^2} + \frac{t}{q_e} \quad (2.8)$$

where q_e and q represent the amounts of pollutant adsorbed (mg. g^{-1}) at the equilibrium time and time t (min) respectively, k_2 is the pseudo-second-order rate constant (g. mg^{-1}. min^{-1}). The values of q_e and k_2 can be determined from the straight-line plots of $\frac{t}{q}$ as a function of t [82].

The linear form of the Elovich equation is represented by equation (2.9) [82]:

$$q = \frac{\ln(a_e b_e)}{b_e} + \frac{1}{b_e} \ln(t) \quad (2.9)$$

in which a_e is the initial adsorption rate constant (mg. g^{-1}. min^{-1}), b_e is the extent of surface coverage and the activation energy for chemisorption (g. mg^{-1}). The values of a_e and b_e can be obtained from the plot of q as a function of $\ln(t)$ [82].

The intraparticle diffusion (Weber-Morris) model is expressed as follows [82]:

$$q = k_{\mathrm{id}}\sqrt{t} + C_{\mathrm{intraparticle}} \tag{2.10}$$

where k_{id} is the intraparticle diffusion rate constant ($\mathrm{mg.g^{-1}.min^{-0.5}}$). If intraparticle diffusion occurs, then the plot of q against $\sqrt{t}$ is linear. The value of the intercept ($C_{\mathrm{intraparticle}}$) is related to the thickness of the boundary layer i.e., the larger the intercept the higher the boundary layer effect [82].

Bangham's model equation can be expressed by equation (2.11) [82,83]:

$$\mathrm{loglog}\left(\frac{C_0}{C_0 - qM}\right) = \log\left(\frac{k_{\mathrm{b}} M_{\mathrm{perlitre}}}{2.303 V_{\mathrm{solution}}}\right) + \alpha_{\mathrm{B}}.\log(t) \tag{2.11}$$

where C_0 is the initial concentration of the adsorbate in solution ($\mathrm{mg.L^{-1}}$), V_{solution} is the volume of solution (mL), M_{perlitre} is the weight of adsorbent used per litre of solution ($\mathrm{g.L^{-1}}$), q ($\mathrm{mg.g^{-1}}$) is the amount of adsorbate retained at time t, and α_{B} and k_{b} are constants [82]. Through the straight-line plot of $\mathrm{loglog}\left(\frac{C_0}{C_0 - qM}\right)$ as a function of $\log(t)$, the constants α_B and k_{b} can be determined from the slope and intercept, respectively. If the double logarithmic plots show a linear plot, then the diffusion of adsorbate into the pores of adsorbents is not the only rate-controlling step [83].

The Boyd kinetic model can be expressed by equations (2.12), (2.13), and (2.14) [82,84]:

$$F = \frac{q}{q_{\mathrm{e}}} = 1 - \frac{6}{\pi^2}\sum_{n=1}^{\infty}\frac{1}{n^2}\exp\left(-n^2 B_{\mathrm{t}}\right) \tag{2.12}$$

$$B_{\mathrm{t}} = \left(\sqrt{\pi} - \sqrt{\pi - \left(\frac{\pi^2 F}{3}\right)}\right) \text{ for } F < 0.85 \tag{2.13}$$

$$B_{\mathrm{t}} = -0.4977 - \ln(1 - F) \text{ for } F > 0.85 \tag{2.14}$$

where F is the fraction of contaminant adsorbed at any time compared with the equilibrium. The Boyd kinetic equation is applied to identify the rate-limiting step of the adsorption process. The limiting step is represented by plotting B_{t} (Boyd parameter) as a function of t. If the plot is linear and passes through the origin, the adsorption process is controlled by intraparticle diffusion [84]. Otherwise, the adsorption process is controlled by film diffusion or by both film and intraparticle diffusions [82,84,85].

The photocatalytic experiments were conducted up to a total of 30 min (0.5 h) and in triplicate for the TiO_2 nanopowders, before and after light exposure. For the reusability tests, the dried nanopowder with the best adsorptive and photocatalytic performance was evaluated under the same experimental conditions previously described in the g-C_3N_4/TiO_2 experimental procedure [31].

In this last study, regeneration + reutilization assays were conducted, in which 40 mg of the recovered catalyst (separated by centrifugation after the first photocatalytic cycle) was suspended in 150 mL of deionized water and irradiated by UV light using three mercury lamps (model HNSL from Osram Puritec) with a power of 95 W each, a wavelength of 254 nm, and a total UV light intensity of 35 $mW.cm^{-2}$.The solution vessel was placed at 27.5 cm from the UV light source for 240 min. After the irradiation process, the TiO_2 nanopowder was separated by centrifugation, washed with water, and dried under vacuum overnight. The dried material was used as the catalyst in the next catalytic cycle for adsorption and photocatalytic degradation of TC under the solar simulator [31,86].

For the photocatalytic activity of the TiO_2-based nanostructures on PU foams, each TiO_2 PU foam was added to 15 mL of tetracycline solution, and the experiments were conducted in the dark for 1 h to achieve the absorption–desorption equilibrium, followed by 180 min under simulated solar light. For the reusability tests (three runs), no centrifugation was required before the measurements in the spectrophotometer. The functionalized TiO_2 PU foam was only washed with deionized water and dried at RT prior to the following cycle while maintaining the same duration in the dark/light exposure times [31].

Following a similar procedure to that of the photocatalytic experiments with TiO_2 PU foams, the adsorption and degradation of TC over cellulose-based membranes (pristine, with pure TiO_2 and Ca:TiO_2 nanomaterials) were tested in the dark (until the adsorption-desorption equilibrium was reached), and then under a simulated solar light source. The only difference was that one quarter of each membrane was positioned at the bottom of a reaction beaker with 12.5 mL of a TC solution (30 $mg.L^{-1}$). Each piece of membrane was stirred for 120 min (under constant low magnetic stirring) in the dark. The spectra were recorded at different time intervals with a spectrophotometer from 200–700 nm. The light experiments were carried out for 60 min. The best-performing membrane was reused and after each cycle, the membrane was washed with deionized water and left to dry at RT before being subjected to a new cycle with a fresh solution (5 cycles) [31].

Photocatalytic activity under natural sunlight

RhB photocatalytic degradation tests under natural sunlight with the cork substrates were also conducted. The experiments started around midday in the city of Caparica and in the month of May. The total exposure time was 240 min (4 h) since after that time (at the end of the day) the solar intensity significantly decreased. Moreover, if the exposure was continued

on another day, the experimental conditions (solar intensity and UV level) would significantly differ, and for that reason, it has been considered 4 h of sunlight exposure for each photocatalytic experiment. The sunlight intensity was measured three times by using a solar power meter from Sciencetech (Sciencetech-Inc., London, ON, Canada): before light exposure, in the middle and at the end of the experiment. Before light exposure, the sunlight intensity was 810, 800 and 880 $W.m^{-2}$, respectively, for the first, second and third experiments. In the middle of the experiments (after 2 h of light exposure), the intensity decreased to 730, 750 and 810 $W.m^{-2}$, respectively, for the first, second and third experiments. At the end of the experiments (after 4 h of light exposure), the sunlight intensity was 400, 350 and 300 $W.m^{-2}$, respectively, for the first, second and third experiments. During the photocatalytic experiments, the temperatures ranged between 17–26 °C, 19–28 °C and 20–26 °C for the first, second and third experiments, respectively. The UV levels were 7 out of 11 in the first experiment and 8 out of 11 in the second and third experiments, according to the IPMA (Instituto Português do Mar e da Atmosfera) website [28].

The photocatalytic experiments for the degradation of TC with the cellulose-based membranes (without photocatalyst, with pure TiO_2 and 10-Ca:TiO_2) under natural sunlight started around midday in Caparica (Portugal) in July. The total light exposure time was 30 min since the solutions with Ca:TiO_2 nanopowders showed a tendency for stabilization after 15 to 30 min. Sunlight intensity was measured twice using the same solar power meter mentioned above, before light exposure and at the end of the experiment. In both measurements, the sunlight intensity was 85 $mW.cm^{-2}$. According to the IPMA website, the UV level was 8 out of 11.

Reactive oxygen species (ROS) scavengers' experiments

ROS scavengers were used to investigate the species and the mechanisms involved in the photocatalytic degradation of several water pollutants when exposed to light irradiation. In these assays, ethylene diamine tetra acetic acid (EDTA, $C_{10}H_{16}N_2O_8$, ≥ 98 % purity from Sigma-Aldrich, CAS: 60-00-4) was used as a hole (h^+) scavenger, hydrogen peroxide (HP, H_2O_2, > 30 % w/v, CAS: 7722-84-1 from PanReac AppliChem) as an electron scavenger (e^-), isopropanol (IPA, C_3H_8O, 99.8% purity from Sigma-Aldrich) as a hydroxyl radical (•OH) scavenger, p-benzoquinone (BQ, $C_6H_4O_2$, ≥ 98 % purity from Midland Scientific (Sigma-Aldrich), CAS: 106-51-4) as the superoxide radical ($•O_2^-$) scavenger, and sodium azide (SA, NaN_3, BioXtra, CAS: 26628-22-8 from Sigma-Aldrich) as a singlet oxygen ($^1O_2$) scavenger. The trapping

experiments were conducted under the same conditions as those to evaluate the adsorption and photocatalytic performance. After the dark phase, typically 5 mL of a 0.5 mM aq. solution of each scavenger is added to the pollutant's solution (50 mL) containing 25 mg of photocatalyst. A solution without a scavenger + photocatalyst + 5 mL of deionized water (or the same volume of the scavenger's solution) was also exposed to light for comparison (denoted as NS). For the Ca:TiO_2 membranes, since a quarter of each membrane was used (~6.25 mg of nanopowder), only 12.5 mL of the TC solution and 1.25 mL of a 0.5 mM aq. solution of each scavenger was added to this solution.

Liquid Chromatography-High Resolution Qq *Time-of-Flight Mass Spectrometry analysis*

The transformation products (TPs) formed during the photocatalytic degradation of TiO_2 PU foam solution were analyzed by LC-HRMS. Aliquots of 10 μL were analysed on an UHPLC Elute system interfaced with a QqTOF Impact II mass spectrometer equipped with an electrospray ionization (ESI) source, operating in the positive mode (Bruker Daltonics, Bremen, Germany). Internal calibration was achieved with an ammonium formate solution introduced to the ion source via a 20 μL loop at the beginning of each analysis, using a six-port valve. Acquisition was performed in a data-dependent MS/MS mode with an acquisition rate of 3 Hz using a dynamic method with a fixed cycle time of 3 s, and a *m*/*z* dependent isolation window of 0.03 Da. Data acquisition and processing were performed using Data Analysis 5.1 software. Chromatographic separation was achieved on a Kinetex C18 column 100 Å (150 x 2.1 mm, 3 μm particle size, Phenomenex) at 45 °C using a flow rate of 0.4 $mL.min^{-1}$. The mobile phase was 0.1 % of acid formic in water (v/v, eluent A) and in acetonitrile (eluent B), the elution gradient was as follows: 0-0.5 min linear gradient to 5 % B; 1-3 min linear gradient to 60 % B, 3-5 min linear gradient to 100 % B, 5-9 min isocratic 100 % B, 9-11 min linear gradient to 5 % B, and then the column was re-equilibrated with 5 % B for 4-min. The TPs were identified by HRMS based on their accurate *m*/*z* values released as protonated molecules ($[M + H]^+$), considering the accuracy and precision of the measurement parameters, such as error (ppm) and mSigma. The molecular formulas were validated by extracting the ionic chromatograms from the raw data, and accurate mass isotopic patterns were evaluated, supporting the respective proposed chemical structures.

Ecotoxicity assays

Artemia salina or brine shrimp is a zooplankton used to feed larval fish. This organism is reported to be a suitable test organism for toxicity studies in the presence of nanostructures [87,88]. For this reason, it was selected as a biological safety model test. Acute toxicities of PU foams with and without TiO_2 nanostructures on *A. salina* were investigated. To prepare Artemia's environment, artificial seawater was first prepared by mixing regular tap water with commercial seawater salt (JBL GmbH & Co.), according to supplier instructions. Then, dry *A. salina* cysts were added to the artificial seawater and were left to hatch under aeration and artificial light, for 48 h, at 25-30 °C. Afterwards, 900 µL of artificial seawater, containing 10-15 nauplii, pristine PU foams and pre-treated TiO_2 PU-foams with dimensions of 1.5 × 1.5 × 1.5 cm^3; 10 % DMSO as positive control; and artificial seawater as negative control were added to 24-well plates and incubated for 24 h, at 25–30 °C. After that, the dead nauplii were counted. To kill the remaining nauplii, 100 % DMSO was added to all the wells and left to incubate for 2 h, at 25–30 °C [89,90]. After counting the total *A. salina*, the mortality, *M* (%) was calculated according to equation (2.15).

$$M\ (\%) = \frac{Dead_{24\ \mathrm{h}}}{Dead_{\mathrm{Total}}} \times 100 \qquad (2.15)$$

where $Dead_{24\ \mathrm{h}}$ represents the number of dead *A. salina* nauplii 24 h after incubation and and $Dead_{\mathrm{Total}}$ represents the total of nauplii present in each well test. PU foams were tested with five replicates [31]

Electrochemical characterization

To evaluate the electrochemical performance of the produced materials, a solution was prepared with 2.5 mg of each nanopowder, 10 µL of Nafion perfluorinated resin (5 wt. % in lower aliphatic alcohols and water, containing 15–20% of water content, from Sigma-Aldrich, CAS: 31175-20-9) and 0.25 mL of DMF with ≥ 99 % purity from Sigma-Aldrich). Then, indium tin oxide (ITO) glass samples were cut with dimensions of 2 cm × 1 cm, and an appropriate amount of the solution was evenly coated on a sample area of around 1 cm^2. Each layer was left to dry at 50 °C before applying a new layer. The photoelectrochemical properties were assessed on a standard three-electrode system (Gamry Reference 600) by using a potentiostat model 600 from Gamry Instruments and with an electrochemical interface (Gamry Echem Analyst). ITO glass coated with the photocatalyst, platinum wire and the standard electrode

Ag/AgCl (3 M KCL) were used as the working electrode, the counter electrode and the reference electrode, respectively. The electrolyte was a solution with 0.5 M of Na_2SO_4 at pH = 6.3. The Mott–Schottky (M-S) curves were measured at 1 kHz. The potentials measured against the (Ag/AgCl) reference were converted into NHE potentials, following equation (2.16) [30]:

$$E_{\mathrm{FB\ (NHE)}} = E_{\mathrm{Ag/AgCl}} + E^{\circ}{}_{\mathrm{Ag/AgCl}} \qquad (2.16)$$

$$(E^{\circ}{}_{\mathrm{Ag/AgCl}} = 0.1976\ \mathrm{V}\ vs.\ \mathrm{NHE\ at\ 25\ °C})$$

Electrical characterization

TiO_2 and Ca:TiO_2 nanostructures were deposited onto the commercial interdigitated electrodes using a drop-casting technique, as described in [91]. Briefly, a Kapton mask was placed over the electrodes exposing only the finger area. A 50 μL drop of a solution composed of 1 mg of nanopowder in 1 mL of IPA was applied to the finger area (0.4 cm × 0.4 cm) with a micropipette. The solvent was then evaporated using a hot plate at 60 °C for 2 min, and the solution was homogeneously spread.

The electrical characterization of the devices was performed in a parameter analyzer (Agilent 4155C from Keysight Technologies) in combination with an Everbeing probe station (Everbeing Int'l Corp.). The measurements were performed for a voltage range of −10 to 10 V under 5 cycles at RT.

2.6 Computational methods

Density-functional theory (DFT)

DFT calculations were also performed for the study related to Ca:TiO_2 membranes using the Vienna Ab initio Simulation Package (VASP) code [92]. The hybrid exchange-correlation functional HSE06 [93] was chosen both for structure relaxations and electronic structure calculations due to its ability to predict considerably more accurate semiconductor band gaps when compared to standard local or semi-local functionals [94]. The exchanged fraction was fixed at 15 %, as this has been shown to describe the electronic structure of anatase TiO_2 with a band gap compatible with the one measured in the study of the Ca:TiO_2 membranes [95]. The defect-related simulations were run on periodic TiO_2 supercells, containing 3×3×1 unit

cells (i.e., a total of 108 atoms), to ensure a separation of around 10 Å between periodic replicas of the defects. The explicitly treated electrons were $3p^6\ 3d^3\ 4s^1$ for Ti, $2s^2\ 2p^4$ for O, and $3s^2\ 3p^6\ 4s^2$ for Ca, with the rest of the electrons included in the frozen core, handled by the projector augmented-wave method [96]. For the supercell calculations, Brillouin zone integration was done using the Γ point, the energy cutoff for the plane-wave basis set was 415 eV, and the energy and force convergence thresholds were 10^{-5} eV and 0.01 eV/Å, respectively.

2.7 References

1. Kharisov, B. I.; Kharissova, O. V.; Méndez, U. O.; Kharisov, B. I.; Kharissova, O. V.; Méndez, U. O. Microwave Hydrothermal and Solvothermal Processing of Materials and Compounds. In *The Development and Application of Microwave Heating*; Cao, W., Ed.; IntechOpen, 2012 ISBN 978-953-51-0835-1.
2. Palma, V.; Barba, D.; Cortese, M.; Martino, M.; Renda, S.; Meloni, E. Microwaves and Heterogeneous Catalysis: A Review on Selected Catalytic Processes. *Catalysts* **2020**, *10*, 246, doi:10.3390/CATAL10020246.
3. Zhang, X.; Rajagopalan, K.; Lei, H.; Ruan, R.; Sharma, B. K. An overview of a novel concept in biomass pyrolysis: microwave irradiation. *Sustainable Energy & Fuels* **2017**, *1*, 1664–1699, doi:10.1039/C7SE00254H.
4. Afolabi, O. O. D.; Sohail, M. Microwaving human faecal sludge as a viable sanitation technology option for treatment and value recovery – A critical review. *Journal of Environmental Management* **2017**, *187*, 401–415, doi:10.1016/J.JENVMAN.2016.10.067.
5. Leadbeater, N. E. 9.10 Organic Synthesis Using Microwave Heating. In *Comprehensive Organic Synthesis: Second Edition*; Knochel, P., Ed.; Elsevier, 2014; Vol. 9, pp. 234–286 ISBN 9780080977430.
6. Yang, G.; Park, S. J. Conventional and Microwave Hydrothermal Synthesis and Application of Functional Materials: A Review. *Materials* **2019**, *12(7)*, 1177, doi:10.3390/MA12071177.
7. Kumar, A.; Kuang, Y.; Liang, Z.; Sun, X. Microwave chemistry, recent advancements, and eco-friendly microwave-assisted synthesis of nanoarchitectures and their applications: a review. *Materials Today Nano* **2020**, *11*, 100076, doi:10.1016/J.MTNANO.2020.100076.
8. Zhu, Y. J.; Chen, F. Microwave-assisted preparation of inorganic nanostructures in liquid phase. *Chemical Reviews* **2014**, *114*, *12*, 6462–6555, doi:10.1021/cr400366s.
9. Branquinho, R.; Carlos, E.; Nunes, D.; Fortunato, E.; Martins, R. Sustainable Synthesis of Oxides for Electronics and Photocatalysis. In *Synthesis and Applications in Chemistry and Materials*; Pombeiro, A., Mahmudov, K. T., Silva, M. F., Eds.; World Scientific, 2024; Vol. 14, pp. 443–482 ISBN 978-981-127-993-5.
10. Kappe, C. O.; Dallinger, D.; Murphree, S. S. Microwave Theory. In *Practical Microwave Synthesis for Organic Chemists*; John Wiley & Sons, Ltd, 2008; pp. 11–44.
11. CEM Corporation Solvent Choice for Microwave Synthesis Available online: https://cem.com/microwave-chemistry/solvent-choice (accessed on Nov 21, 2024).

12. Bilecka, I.; Niederberger, M. Microwave chemistry for inorganic nanomaterials synthesis. *Nanoscale* **2010**, *2*, 1358–1374, doi:10.1039/B9NR00377K.
13. Pimentel, A.; Rodrigues, J.; Duarte, P.; Nunes, D.; Costa, F. M.; Monteiro, T.; Martins, R.; Fortunato, E. Effect of solvents on ZnO nanostructures synthesized by solvothermal method assisted by microwave radiation: a photocatalytic study. *Journal of Materials Science* **2015**, *50,17*, 5777–5787, doi:10.1007/s10853-015-9125-7.
14. Chia, S. R.; Nomanbhay, S.; Milano, J.; Chew, K. W.; Tan, C. H.; Khoo, K. S. Microwave-Absorbing Catalysts in Catalytic Reactions of Biofuel Production. *Energies* **2022**, *15*, 7984, doi:10.3390/EN15217984.
15. Gabriel, C.; Gabriel, S.; Grant, E. H.; Halstead, B. S. J.; Michael P Mingos, D. Dielectric parameters relevant to microwave dielectric heating. *Chemical Society Reviews* **1998**, *27*, 213–223, doi:10.1039/A827213Z.
16. Horikoshi, S.; Serpone, N. General Introduction to Microwave Chemistry. In *Microwaves in Catalysis*; Horikoshi, S., Serpone, N., Eds.; John Wiley & Sons, Ltd, 2015; pp. 1–28.
17. Douplik, A.; Saiko, G.; Schelkanova, I.; Tuchin, V. V. The response of tissue to laser light. In *Lasers for Medical Applications: Diagnostics, Therapy and Surgery*; Jelínková, H., Ed.; Woodhead Publishing, 2013; pp. 47–109 ISBN 9780857092373.
18. Zhao, Y.; Chen, J. Applications of microwaves in nuclear chemistry and engineering. *Progress in Nuclear Energy* **2008**, *50*, 1–6, doi:10.1016/J.PNUCENE.2007.08.009.
19. Nordh, U.; Carlsson, H.; Niklasson, O.; Hallgren, F. Methods of controlling cooling in a microwave heating apparatus and apparatus thereof 2021, 1–11.
20. Kremsner, J. M.; Stadler, A.; Kappe, C. O. The Scale-Up of Microwave-Assisted Organic Synthesis. In *Microwave Methods in Organic Synthesis*; Larhed, M., Olofssonq, K., Eds.; Springer Berlin Heidelberg: Berlin, Heidelberg, 2006; pp. 233–278 ISBN 978-3-540-36759-8.
21. Pitchai, K.; Chen, J.; Birla, S.; Gonzalez, R.; Jones, D.; Subbiah, J. A microwave heat transfer model for a rotating multi-component meal in a domestic oven: Development and validation. *Journal of Food Engineering* **2014**, *128*, 60–71, doi:10.1016/J.JFOODENG.2013.12.015.
22. Interaction of microwave radiation with other materials Available online: https://www.berghof-instruments.com/en/overview-of-digestion-techniques/microwaveheating/interaction-of-microwave-radiation-with-other-materials/ (accessed on Nov 21, 2024).
23. Open vs. closed Digestion Available online: https://www.berghof-instruments.com/en/overview-of-digestion-techniques/digestion-systems/open-vs-closed-digestion/ (accessed on Nov 21, 2024).
24. CEM Corporation Getting Started with Microwave Synthesis Available online: https://cem.com/microwave-chemistry/getting-started (accessed on Nov 21, 2024).
25. Obermayer, D.; Damm, M.; Kappe, C. O. Design and evaluation of improved magnetic stir bars for single-mode microwave reactors. *Organic & Biomolecular Chemistry* **2013**, *11*, 4949–4956, doi:10.1039/C3OB40790J.
26. Matias, M. L.; Pimentel, A.; Reis-Machado, A. S.; Rodrigues, J.; Deuermeier, J.; Fortunato, E.; Martins, R.; Nunes, D. Enhanced Fe-TiO_2 Solar Photocatalysts on Porous Platforms for Water Purification. *Nanomaterials* **2022**, *12*.

27. Sánchez-campos, D.; Valderrama, M. I. R.; López-ortíz, S.; Salado-leza, D.; Fernández-garcía, M. E.; Mendoza-anaya, D.; Salinas-rodríguez, E.; Rodríguez-lugo, V. Modulated Monoclinic Hydroxyapatite: The Effect of pH in the Microwave Assisted Method. *Minerals* **2021**, *11*, 314, doi:10.3390/MIN11030314.
28. Matias, M. L.; Morais, M.; Pimentel, A.; Vasconcelos, F. X.; Reis Machado, A. S.; Rodrigues, J.; Fortunato, E.; Martins, R.; Nunes, D. Floating TiO_2-Cork Nano-Photocatalysts for Water Purification Using Sunlight. *Sustainability* **2022**, *14(15)*, 9645, doi:10.3390/SU14159645/S1.
29. Xue, R.; Matias, M. L.; Pimentel, A.; Pinto, J. V.; Fortunato, E.; Martins, R. Photocatalytic Activity of 3D Printed TiO_2 Architectures Under Solar Radiation. In *Photocatalysis for Environmental Remediation and Energy Production*; Green Chemistry and Sustainable Technology; Springer International Publishing, 2023; pp. 79–100 ISBN 978-3-031-27706-1.
30. Matias, M. L.; Reis-Machado, A. S.; Rodrigues, J.; Calmeiro, T.; Deuermeier, J.; Pimentel, A.; Fortunato, E.; Martins, R.; Nunes, D. Microwave Synthesis of Visible-Light-Activated g-C_3N_4/TiO_2 Photocatalysts. *Nanomaterials* **2023**, *13(6)*, doi:10.3390/NANO13061090/S1.
31. Matias, M. L.; Pimentel, A.; Reis-Machado, A.; Rodrigues, J. C.; Fernandes, A.; Monteiro, T.; Almeida Carvalho, P.; Neves Amaral, M. N.; Reis, C. P.; Deuermeier, J.; Fortunato, E.; Martins, R.; Nunes, D. Functionalized 3D Polyurethane Foams with Microwave-synthesized TiO_2 Nanostructures for Solar Light-driven Degradation of Tetracycline. *Environmental Science: Advances* **2025**, 4, 713–738 doi:10.1039/D4VA00110A.
32. Shahrubudin, N.; Lee, T. C.; Ramlan, R. An Overview on 3D Printing Technology: Technological, Materials, and Applications. *Procedia Manufacturing* **2019**, *35*, 1286–1296, doi:10.1016/J.PROMFG.2019.06.089.
33. Matias, M. L.; Pereira, C.; Almeida, H. V.; Jana, S.; Panigrahi, S.; Menda, U. D.; Nunes, D.; Fortunato, E.; Martins, R.; Nandy, S. 3D printed MXene architectures for a plethora of smart applications. *Materials Today Advances* **2024**, *23*, 100512, doi:10.1016/J.MTADV.2024.100512.
34. Jadhav, A.; Jadhav, V. S. A review on 3D printing: An additive manufacturing technology. *Materials Today: Proceedings* **2022**, *62*, 2094–2099, doi:10.1016/J.MATPR.2022.02.558.
35. Husna, A.; Ashrafi, S.; Tomal, A. A.; Tuli, N. T.; Bin Rashid, A. Recent advancements in stereolithography (SLA) and their optimization of process parameters for sustainable manufacturing. *Hybrid Advances* **2024**, *7*, 100307, doi:10.1016/J.HYBADV.2024.100307.
36. Moritz, T.; Maleksaeedi, S. Additive manufacturing of ceramic components. In *Additive Manufacturing: Materials, Processes, Quantifications and Applications*; Zhang, J., Jung, Y.-G., Eds.; Elsevier, 2018; pp. 105–161 ISBN 9780128121559.
37. Roy Barman, S.; Gavit, P.; Chowdhury, S.; Chatterjee, K.; Nain, A. 3D-Printed Materials for Wastewater Treatment. *JACS Au* **2023**, *3*, *11*, 2930–2947, doi:10.1021/jacsau.3c00409.
38. Furman, M.; Corbel, S.; Wild, G.; Zahraa, O. Photocatalytic reaction intensification using monolithic supports designed by stereolithography. *Chemical Engineering and Processing: Process Intensification* **2010**, *49*, 35–41, doi:10.1016/j.cep.2009.11.002.
39. Fiedor, P.; Ortyl, J. A new approach to micromachining: High-precision and innovative

additive manufacturing solutions based on photopolymerization technology. *Materials* **2020**, *13*, 1–25, doi:10.3390/ma13132951.
40. Bogdan, E.; Michorczyk, P. 3D Printing in Heterogeneous Catalysis—the State of the Art. *Materials* **2020**, *13*, 1–23, doi:10.3390/ma13204534.
41. Quan, H.; Zhang, T.; Xu, H.; Luo, S.; Nie, J.; Zhu, X. Photo-curing 3D printing technique and its challenges. *Bioactive Materials* **2020**, *5*, 110–115, doi:10.1016/J.BIOACTMAT.2019.12.003.
42. Chen, J.; Wu, P.; Bu, F.; Gao, Y.; Liu, X.; Guan, C. 3D printing enhanced catalysis for energy conversion and environment treatment. *DeCarbon* **2023**, *2*, 100019, doi:10.1016/J.DECARB.2023.100019.
43. Formlabs The Ultimate Guide to Stereolithography (SLA) 3D Printing Available online: https://www.studocu.com/in/document/biju-patnaik-university-of-technology/basic-mechanical-engineering-basic-civil-engineering/resin-3d-printing-guide/85980969 (accessed on Nov 22, 2024).
44. Formlabs Guide to Stereolithography (SLA) 3D Printing | Formlabs Available online: https://formlabs.com/blog/ultimate-guide-to-stereolithography-sla-3d-printing/ (accessed on Nov 29, 2024).
45. Butt, M. A. Thin-Film Coating Methods: A Successful Marriage of High-Quality and Cost-Effectiveness—A Brief Exploration. *Coatings* **2022**, *12*, 1115, doi:10.3390/COATINGS12081115.
46. Dane, T. G.; Bartenstein, J. E.; Sironi, B.; Mills, B. M.; Alexander Bell, O.; Emyr MacDonald, J.; Arnold, T.; Faul, C. F. J.; Briscoe, W. H. Influence of solvent polarity on the structure of drop-cast electroactive tetra(aniline)-surfactant thin films. *Physical Chemistry Chemical Physics* **2016**, *18*, 24498–24505, doi:10.1039/C6CP05221E.
47. Tyona, M. D. A comprehensive study of spin coating as a thin film deposition technique and spin coating equipment. *Advances in materials Research* **2013**, *2*, 181–193, doi:10.12989/AMR.2013.2.4.181.
48. Lin, S.; Zhang, Y.; Shao, L.; Lau, C. H. Spray-assisted assembly of thin-film composite membranes in one process. *Advanced Membranes* **2024**, *4*, 100080, doi:10.1016/J.ADVMEM.2023.100080.
49. Siegrist, S.; Nandi, P.; Kothandaraman, R. K.; Abdessalem, A.; Tiwari, A. N.; Fu, F. Understanding Coating Thickness and Uniformity of Blade-Coated SnO_2 Electron Transport Layer for Scalable Perovskite Solar Cells. *Solar RRL* **2023**, *7*, 2300273, doi:10.1002/SOLR.202300273.
50. Ottesen, V.; Kumar, V.; Toivakka, M.; Chinga-Carrasco, G.; Syverud, K.; Gregersen, Ø. W. Viability and properties of roll-to-roll coating of cellulose nanofibrils on recycled paperboard. *Nordic Pulp and Paper Research Journal* **2017**, *32*, 179–188, doi:10.3183/NPPRJ-2017-32-02-P179-188.
51. Hedayat, N.; Du, Y.; Ilkhani, H. Review on fabrication techniques for porous electrodes of solid oxide fuel cells by sacrificial template methods. *Renewable and Sustainable Energy Reviews* **2017**, *77*, 1221–1239, doi:10.1016/J.RSER.2017.03.095.
52. Shukla, S. K.; Kushwaha, C. S.; Guner, T.; Demir, M. M. Chemically modified optical fibers in advanced technology: An overview. *Optics & Laser Technology* **2019**, *115*, 404–432, doi:10.1016/J.OPTLASTEC.2019.02.025.

53. Grosso, D. How to exploit the full potential of the dip-coating process to better control film formation. *Journal of Materials Chemistry* **2011**, *21*, 17033–17038, doi:10.1039/C1JM12837J.
54. Puetz, J.; Aegerter, M. A. Dip Coating Technique. In *Sol-Gel Technologies for Glass Producers and Users*; Aegerter, M. A., Mennig, M., Eds.; Springer US, 2004; pp. 37–48.
55. Suhag, R.; Kumar, N.; Petkoska, A. T.; Upadhyay, A. Film formation and deposition methods of edible coating on food products: A review. *Food Research International* **2020**, *136*, 109582, doi:10.1016/J.FOODRES.2020.109582.
56. Griffin, D. J.; O'Kane, D. M. Dip Coating: Practical Guide to Theory and Troubleshooting | Ossila Available online: https://www.ossila.com/pages/dip-coating (accessed on Feb 6, 2025).
57. Rio, E.; Boulogne, F. Withdrawing a solid from a bath: How much liquid is coated? *Advances in Colloid and Interface Science* **2017**, *247*, 100–114, doi:10.1016/J.CIS.2017.01.006.
58. Shakeel Ahmad, M.; Pandey, A. K.; Abd Rahim, N. Advancements in the development of TiO_2 photoanodes and its fabrication methods for dye sensitized solar cell (DSSC) applications. A review. *Renewable and Sustainable Energy Reviews* **2017**, *77*, 89–108, doi:10.1016/J.RSER.2017.03.129.
59. Ebnesajjad, S.; Landrock, A. H. Adhesive Applications and Bonding Processes. In *Adhesives Technology Handbook*; Elsevier, 2015; pp. 206–234.
60. Benkreira, H. The effect of substrate roughness on air entrainment in dip coating. *Chemical Engineering Science* **2004**, *59*, 2745–2751, doi:10.1016/J.CES.2004.03.024.
61. Noguchi, A.; Masuda, T.; Chen, C.; Yoshizawa, S.; Isu, N.; Takai, M. Hydrophilic surfaces from simple dip-coating method: amphiphilic block copolymers with zwitterionic group form antifouling coatings under atmospheric conditions. *Materials Advances* **2020**, *1*, 2737–2744, doi:10.1039/D0MA00184H.
62. Bertin, V.; Snoeijer, J.; Raphaël, E.; Salez, T. Enhanced Dip Coating on a Soft Substrate. *Physical Review Fluids* **2022**, *7*, 1–6, doi:10.1103/PhysRevFluids.7.L102002ï.
63. Swift, T.; Swanson, L.; Geoghegan, M.; Rimmer, S. The pH-responsive behaviour of poly(acrylic acid) in aqueous solution is dependent on molar mass. *Soft Matter* **2016**, *12*, 2542–2549, doi:10.1039/C5SM02693H.
64. Kardeş, M.; Yatmaz, H. C.; Öztürk, K. ZnO Nanorods Grown on Flexible Polyurethane Foam Surfaces for Photocatalytic Azo Dye Treatment. *ACS Applied Nano Materials* **2023**, *6*, *8*, 6605–6613, doi:10.1021/acsanm.3c00210.
65. Eslamian, M.; Soltani-Kordshuli, F. Development of multiple-droplet drop-casting method for the fabrication of coatings and thin solid films. *Journal of Coatings Technology and Research* **2018**, *15*, 271–280, doi:10.1007/S11998-017-9975-9.
66. Brian, D.; Eslamian, M. Design and development of a coating device: Multiple-droplet drop-casting (MDDC-Alpha). *Review of Scientific Instruments* **2020**, *91*, 33902, doi:10.1063/1.5129699/1031783.
67. Kaliyaraj Selva Kumar, A.; Zhang, Y.; Li, D.; Compton, R. G. A mini-review: How reliable is the drop casting technique? *Electrochemistry Communications* **2020**, *121*, 106867, doi:10.1016/J.ELECOM.2020.106867.
68. Yunus, Y.; Mahadzir, N. A.; Ansari, M. N. M.; Aziz, T. H. T. A.; Afdzaluddin, A. M.; Anwar, H.; Wang, M.; Ismail, A. G. Review of the Common Deposition Methods of

Thin-Film Pentacene, Its Derivatives, and Their Performance. *Polymers* **2022**, *14*, 1112, doi:10.3390/POLYM14061112.
69. Yildirim Erbil, H. Dependency of Contact Angles on Three-Phase Contact Line: A Review. *Colloids and Interfaces* **2021**, *5*, 8, doi:10.3390/COLLOIDS5010008.
70. Li, H.; Buesen, D.; Williams, R.; Henig, J.; Stapf, S.; Mukherjee, K.; Freier, E.; Lubitz, W.; Winkler, M.; Happe, T.; Plumeré, N. Preventing the coffee-ring effect and aggregate sedimentation by *in situ* gelation of monodisperse materials. *Chemical Science* **2018**, *9*, 7596–7605, doi:10.1039/C8SC03302A.
71. Yunker, P. J.; Still, T.; Lohr, M. A.; Yodh, A. G. Suppression of the coffee-ring effect by shape-dependent capillary interactions. *Nature* **2011**, *476*, 308–311, doi:10.1038/nature10344.
72. NanoComposix Drop-Casting Available online: https://nanocomposix.com/pages/depositing-monolayers-and-thin-films-of-nanoparticles?utm_source=chatgpt.com (accessed on Feb 6, 2025).
73. Liu, Y.; Zhao, X.; Cai, B.; Pei, T.; Tong, Y.; Tang, Q.; Liu, Y. Controllable fabrication of oriented micro/nanowire arrays of dibenzo-tetrathiafulvalene by a multiple drop-casting method. *Nanoscale* **2014**, *6*, 1323–1328, doi:10.1039/C3NR05680E.
74. Zuo, C.; Ding, L.; Zuo, [C; Ding, L. Drop-Casting to Make Efficient Perovskite Solar Cells under High Humidity. *Angewandte Chemie International Edition* **2021**, *60*, 11242–11246, doi:10.1002/ANIE.202101868.
75. Zuo, C.; Scully, A. D.; Gao, M. Drop-Casting Method to Screen Ruddlesden-Popper Perovskite Formulations for Use in Solar Cells. *ACS Applied Materials and Interfaces* **2021**, *13*, 56217–56225, doi:10.1021/ACSAMI.1C17475.
76. Schön, U.; Messinger, J.; Eichner, S.; Kirschning, A. Comparison of monomode and multimode microwave equipment in Suzuki–Miyaura reactions—*en route* to high throughput parallel synthesis under microwave conditions. *Tetrahedron Letters* **2008**, *49*, 3204–3207, doi:10.1016/J.TETLET.2008.03.094.
77. Hoz, A. D. La; Alcázar, J.; Carrillo, J.; Herrero, M. A.; Muñoz, J. D. M.; Prieto, P.; Cózar, A. De; Diaz-Ortiz, A.; Hoz, A. D. La; Alcázar, J.; Carrillo, J.; Herrero, M. A.; Muñoz, J. D. M.; Prieto, P.; Cózar, A. De; Diaz-Ortiz, A. Reproducibility and Scalability of Microwave-Assisted Reactions. In *Microwave Heating*; Chandra, U., Ed.; IntechOpen, 2011 ISBN 978-953-307-573-0.
78. Vinila, V. S.; Isac, J. Synthesis and structural studies of superconducting perovskite $GdBa_2Ca_3Cu_4O_{10.5+\delta}$ nanosystems. In *Design, Fabrication, and Characterization of Multifunctional Nanomaterials*; Sabu, T., Kalarikkal, N., Abraham, A., Eds.; Elsevier, 2022; pp. 319–341 ISBN 9780128205587.
79. Schneider, C. A.; Rasband, W. S.; Eliceiri, K. W. NIH Image to ImageJ: 25 years of image analysis. *Nature Methods* **2012**, *9(7)*, 671–675, doi:10.1038/NMETH.2089.
80. ISO 9277- Determination of the specific surface area of solids by gas adsorption — BET method, 2nd ed.; ISO–International Standardization Organization: Geneva, Switzerland. **2010**.
81. Nunes, D.; Pimentel, A.; Santos, L.; Barquinha, P.; Fortunato, E.; Martins, R. Photocatalytic TiO_2 Nanorod Spheres and Arrays Compatible with Flexible Applications. *Catalysts* **2017**, *7 (2)*, 1–18.

82. Matos, R.; Kuźniarska-Biernacka, I.; Rocha, M.; Belo, J. H.; Araújo, J. P.; Estrada, A. C.; Lopes, J. L.; Shah, T.; Korgel, B. A.; Pereira, C.; Trindade, T.; Freire, C. Design and photo-Fenton performance of Graphene/CuS/Fe_3O_4 tertiary nanocomposites for Rhodamine B degradation. *Catalysis Today* **2023**, *418*, 114132, doi:10.1016/J.CATTOD.2023.114132.
83. Sumanjit; Rani, S.; Mahajan, R. K. Equilibrium, kinetics and thermodynamic parameters for adsorptive removal of dye Basic Blue 9 by ground nut shells and Eichhornia. *Arabian Journal of Chemistry* **2016**, *9*, *2*, S1464–S1477, doi:10.1016/J.ARABJC.2012.03.013.
84. Zamora, F.; Sabio, E.; Román, S.; María González-García, C.; Ledesma, B. Modelling the Adsorption of p-Nitrophenol by the Boyd Method in Conjunction with the Finite Element Method †. *Adsorption Science and Technology* **2010**, *28(8)*, 671–687.
85. Yao, C.; Chen, T. A film-diffusion-based adsorption kinetic equation and its application. *Chemical Engineering Research and Design* **2017**, *119*, 87–92, doi:10.1016/J.CHERD.2017.01.004.
86. Dalto, F.; Kuźniarska-Biernacka, I.; Pereira, C.; Mesquita, E.; Soares, O. S. G. P.; Pereira, M. F. R.; Rosa, M. J.; Mestre, A. S.; Carvalho, A. P.; Freire, C. Solar light-induced methylene blue removal over TiO_2/AC composites and photocatalytic regeneration. *Nanomaterials* **2021**, *11(11)*, 1–24, doi:10.3390/NANO11113016.
87. Ozkan, Y.; Altinok, I.; Ilhan, H.; Sokmen, M. Determination of TiO_2 and $AgTiO_2$ Nanoparticles in Artemia salina: Toxicity, Morphological Changes, Uptake and Depuration. *Bulletin of Environmental Contamination and Toxicology* **2016**, *96*, *1*, 36–42, doi:https://doi.org/10.1007/s00128-015-1634-1.
88. Ates, M.; Daniels, J.; Arslan, Z.; Farah, I. O. Effects of aqueous suspensions of titanium dioxide nanoparticles on Artemia salina: assessment of nanoparticle aggregation, accumulation, and toxicity. *Environ Monit Assess* **2013**, *185(4)*, 3339–48, doi:10.1007/s10661-012-2794-7.
89. Ferreira-Gonçalves, T.; Iglesias-Mejuto, A.; Linhares, T.; Coelho, J. M. P.; Vieira, P.; Faísca, P.; Catarino, J.; Pinto, P.; Ferreira, D.; Ferreira, H. A.; Gaspar, M. M.; Durães, L.; García-González, C. A.; Reis, C. P. Biological Thermal Performance of Organic and Inorganic Aerogels as Patches for Photothermal Therapy. *Gels* **2022**, *8(8)*, 485, doi:10.3390/GELS8080485/S1.
90. Lopes, J.; Ferreira-Gonçalves, T.; Ascensão, L.; Viana, A. S.; Carvalho, L.; Catarino, J.; Faísca, P.; Oliva, A.; de Barros, D. P. C.; Rodrigues, C. M. P.; Gaspar, M. M.; Reis, C. P. Safety of Gold Nanoparticles: From In Vitro to In Vivo Testing Array Checklist. *Pharmaceutics* **2023**, *15(4)*, 1120, doi:10.3390/PHARMACEUTICS15041120/S1.
91. Manuel, D.; De Carvalho, S. Fabrication of ultraviolet sensors based on ZTO and ZnO nanowires, NOVA School of Science and Technology, 2023.
92. Kresse, G.; Furthmüller, J. Efficient iterative schemes for *ab initio* total-energy calculations using a plane-wave basis set. *Physical Review B* **1996**, *54*, 11169, doi:10.1103/PhysRevB.54.11169.
93. Krukau, A. V.; Vydrov, O. A.; Izmaylov, A. F.; Scuseria, G. E. Influence of the exchange screening parameter on the performance of screened hybrid functionals. *The Journal of Chemical Physics* **2006**, *125*, 224106, doi:10.1063/1.2404663.
94. Gouveia, J. D.; Coutinho, J. Can we rely on hybrid-DFT energies of solid-state problems with local-DFT geometries? *Electronic Structure* **2019**, *1*, 015008, doi:10.1088/2516-

1075/AAFC4B.
95. S B, S. L.; Murali, M. D.; Posselt, M.; Sasikala Devi, A. A.; Sharan, A. Modified HSE06 functional applied to anatase TiO_2: influence of exchange fraction on the quasiparticle electronic structure and optical response. *Electronic Structure* **2022**, *4*, 045001, doi:10.1088/2516-1075/AC8F03.
96. Blöchl, P. E. Projector augmented-wave method. *Physical review. B, Condensed matter* **1994**, *50*, 17953–17979, doi:10.1103/PHYSREVB.50.17953.

3

DEVELOPMENT AND CHARACTERIZATION OF TiO_2 ON CORK

The next section was adapted from the publication: Matias, M. L.; Morais, M.; Pimentel, A.; Vasconcelos, F. X.; Reis Machado, A. S.; Rodrigues, J.; Fortunato, E.; Martins, R.; Nunes, D. Floating TiO_2-Cork Nano-Photocatalysts for Water Purification Using Sunlight. *Sustainability* **2022**, *14(15)*,9645. doi: 10.3390/su14159645.

3.1 Introduction

Cork, as a renewable resource and biodegradable material, exemplifies sustainability by offering a natural and eco-friendly alternative that supports environmental conservation and reduces carbon footprints [1,2]. Given that approximately 22 wt. % of cork production is wasted annually and typically burned for energy, repurposing it for photocatalytic applications presents a valuable and sustainable solution. Therefore, cork was selected as a substrate for photocatalytic applications [2].

In this study, TiO_2 nanomaterials were simultaneously produced in powder form and deposited directly onto cork substrates via MW-assisted approaches. The syntheses were carried out using oxalic acid at low temperatures (120 °C) for 1 h and without any seed layer or preliminary preparation steps (see section 2.1.1.6). The produced TiO_2 nanopowder was analysed through XRD, Raman spectroscopy, TEM, FTIR, and UV–VIS absorption measurements, while the TiO_2-cork substrates were characterized using XRD and SEM. These substrates were evaluated as floating photocatalysts for the degradation of RhB under simulated solar light and natural light sources. Reusability tests were also conducted under natural sunlight.

3.2 Results and discussion

3.2.1 Structural and optical characterization of the TiO_2 nanopowder

3.2.1.1 XRD

Figure 3.1 shows the experimental XRD diffractogram of the TiO_2 nanopowder. All experimental peaks are fully assigned to TiO_2 tetragonal anatase phase (ICDD file No. 00-021-1272), and correspond to the reflections (101), (004), (200), (105), (211), (204), (116), (220) and (215) at 2θ = 25.3°, 37.8°, 48.0°, 53.8°, 54.9°, 62.8°, 68.9° and 75.0°, respectively. No peaks related to other TiO_2 crystalline phases (brookite or rutile) were observed. Moreover, no impurities were detected, such as $Ti(OH)_4$ [3,4]. The XRD results also demonstrate that the materials are

well crystallized and the broad diffraction peaks suggest the presence of very small crystallites [3,4]. Some contribution from the cork's chemical components released during synthesis, especially due to the brown color of the resulting powders, was expected. However, it was not confirmed by the XRD results, possibly because the material is amorphous or not well-crystallized. The average crystallite size of the synthesized TiO_2 nanomaterials was estimated using the Debye–Scherrer equation with the software X'pert highscore plus. The calculated crystallite size value was found to be around 4.8 nm.

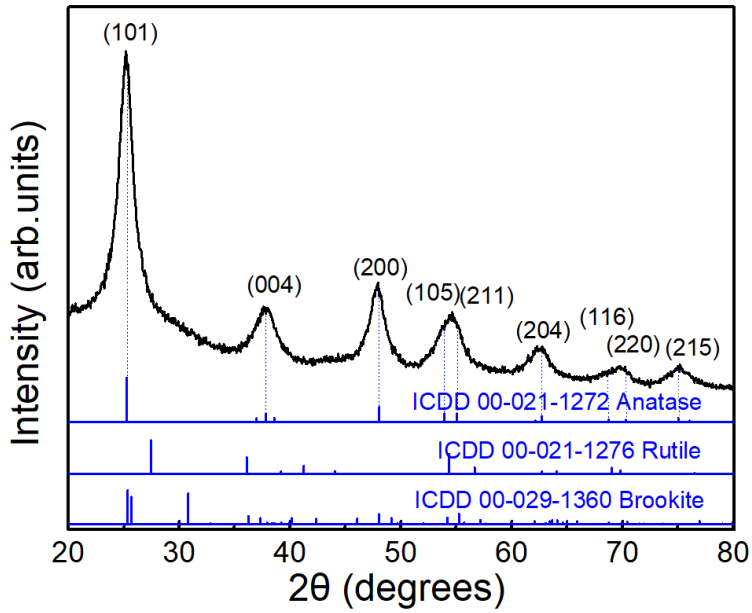

Figure 3.1: XRD diffractogram of the TiO_2 nanopowder simultaneously synthesized by MW irradiation. For comparison, the simulated TiO_2 anatase, rutile and brookite structures are also presented.

3.2.1.2 Raman spectroscopy measurements

Raman spectroscopy measurements were performed to confirm the purity of the synthesized materials. Since the cork substrates obscured the signal of the TiO_2 nanomaterials (Figure A.1), probably due to the high penetration depth of the laser's light (in this case with a wavelength of 532 nm), only the materials in powder form were investigated. Six Raman active modes ($A_{1g} + 2B_{1g} + 3E_g$) are predicted for anatase [4–6]. As observed from the Raman spectrum in Figure 3.2, among those, five TiO_2 anatase bands were identified at 144 cm^{-1} (E_g), 198 cm^{-1} (E_g), 393 cm^{-1} (B_{1g}), 515 cm^{-1} ($B_{1g} + A_{1g}$) and 636 cm^{-1} (E_g). The purity of the synthesized TiO_2 nanopowder is confirmed and aligns with the XRD results.

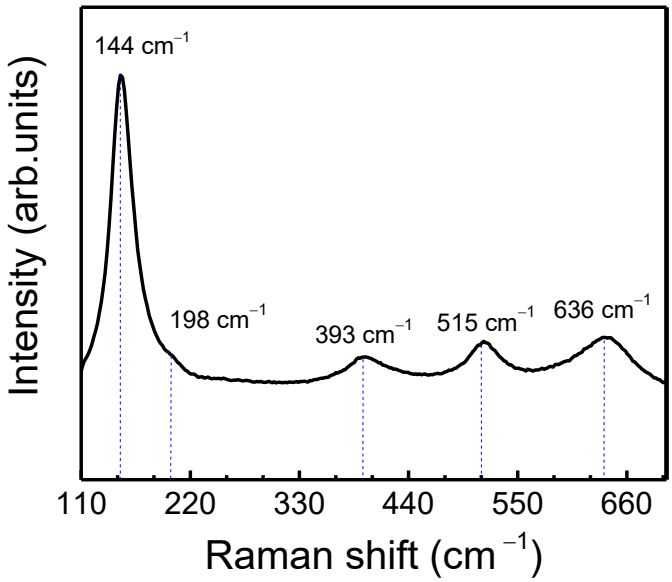

Figure 3.2: Raman spectrum of the synthesized TiO_2 nanopowder. The vertical dot lines represent the TiO_2 anatase Raman bands.

Nevertheless, the anatase TiO_2 phase was obtained, as seen previously from the XRD and Raman spectroscopy results, indicating the successful conversion of the TiO_2 precursors under MW irradiation, which is based on the following equations (3.1) and (3.2) [7]:

$$Ti(OCH(CH)_3)_2)_4 + H_2C_2O_4 + 2H_2O \rightarrow Ti(OH)_2\,C_2O_4 \downarrow + 4C_3H_7OH \qquad (3.1)$$

$$Ti(OH)_2\,C_2O_4 \rightarrow TiO_2 + H_2O \uparrow + CO_2 \uparrow + CO \uparrow \qquad (3.2)$$

3.2.1.3 FTIR

The TiO_2 nanopowder was also investigated using FTIR and the result is presented in Figure 3.3. The presence of hydroxyl groups is indicated by the appearance of a broad band between 3000 and 3600 cm^{-1} and a band at 1680 cm^{-1} due to the adsorption of water from the surrounding environment [8–11]. For the lower wavenumber region, a peak located at around 1111 cm^{-1} is visible and attributed to the stretching vibration of the Ti-OH bond [11], whereas the peaks located at 438 cm^{-1} and 1396 cm^{-1} are attributed to Ti–O bending [12] and Ti-O-Ti stretching modes [13], respectively. Other peaks corresponding to vibrational modes of residual organic species were also observed. FTIR stretching band at 1680 cm^{-1} is likely related to C=O groups [14,15], while the broad and small peak that appears at 1260 cm^{-1} is probably

ascribed to C–O stretching mode from groups such as ethers (common linkages in lignin [16]), alcohols, esters, lactones, phenols or carboxylic acids [17], all present in cork's chemical composition [18–20]. The brown nanopowder obtained from MW synthesis may indicate the presence of traces of organic species coming from the cork substrates (see Figure 2.4, Chapter 2), as revealed by FTIR, which were not detected by XRD and Raman spectroscopy techniques.

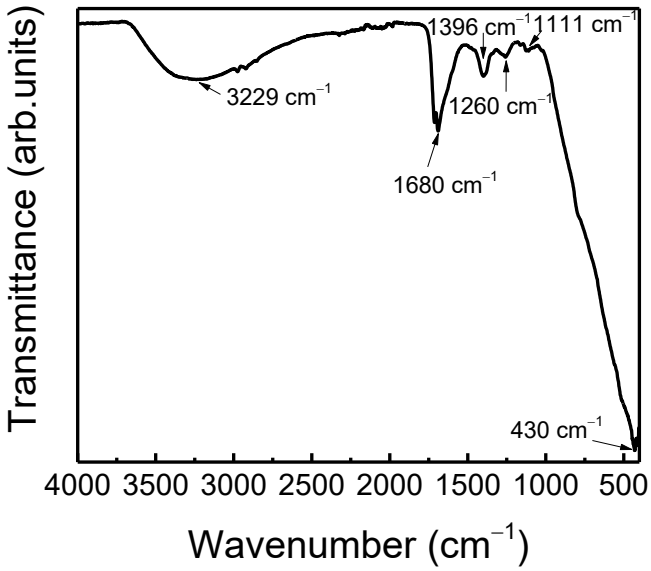

Figure 3.3: FTIR spectrum of the TiO_2 nanopowder.

3.2.1.4 Electron microscopy

Figure 3.4 shows the SEM and TEM images of the TiO_2 nanopowder synthesized under MW irradiation. From the SEM image (Figure 3.4 (a)), the formation of nano-sized particles largely agglomerated can be observed. Nevertheless, from TEM, it could be perceived that these agglomerates are formed by very fine nanoparticles, displaying a nearly spherical shape (Figure 3.4 (c) and (d)). The average particle size was found to be 4.86 ± 1.31 nm. The inset in Figure 3.4 (b) also shows the particle size distribution, revealing that small particles in the 4–6 nm range are more likely to be found. The ring diffraction pattern in Figure 3.4 (b) attested that these particles are solely from the anatase phase. Moreover, the fast Fourier transform (FFT) images and the lattice spacing (~ 0.35 nm) correspond to the (101) planes of anatase TiO_2 nanocrystals, Figure 3.4 (c) and (d). From the FFT image in Figure 3.4 (c), taken in the area indicated as A in the black square, it can be observed that two sets of lattices are present and that they are not perpendicular to each other with an equal lattice spacing of ~ 0.35 nm, corresponding to the (101) and (011) planes of the anatase phase. Observed through the $[11\bar{1}]$ zone

axis, the angle inferred between both (101) and (011) is 82° consistent with the theoretical value reported for pure TiO_2 anatase (ICDD file number 00-021-1272).

The TiO_2 nanopowder synthesized without cork substrates (Figure A.2) also revealed similar characteristics to those observed in the TiO_2 nanopowder synthesized with cork substrates. The MW synthesis resulted in very fine nanoparticles, in agreement with the findings from an analogous study [21].

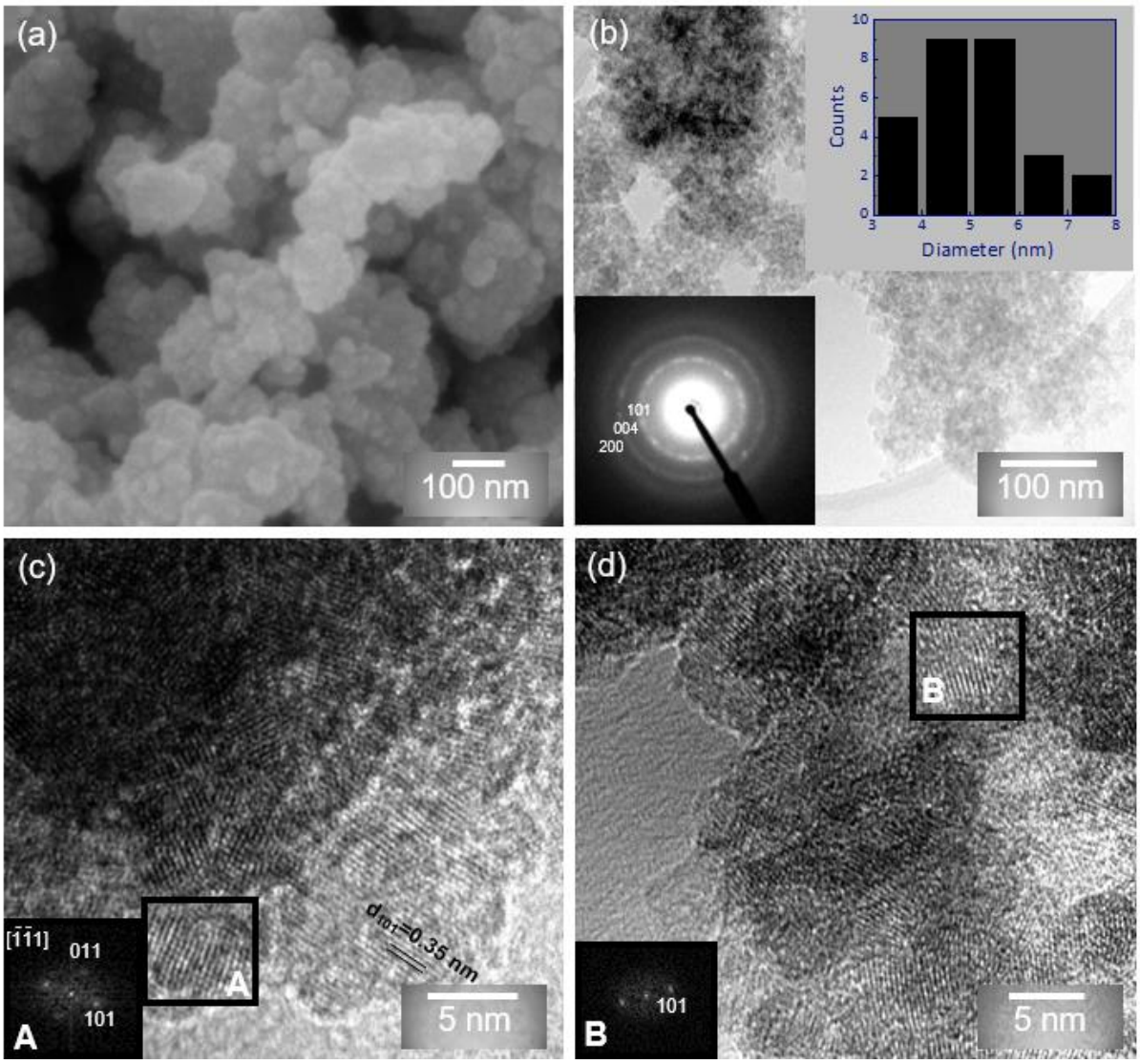

Figure 3.4: (a) SEM image of the TiO_2 nanopowder synthesized under MW irradiation (120 °C for 1 h). TEM images of the TiO_2 nanopowder: (b) bright-field (BF) image of the TiO_2 nanopowder, (c) and (d) high-resolution TEM image of the nanocrystals. The inset in (b) depicts the electron diffraction pattern of TiO_2 nanoparticles with the anatase phase together with the particle size distribution, and (c) and (d) show the FFT images of the areas indicated as A and B, respectively (black squares).

3.2.1.5 Optical characterization

The optical properties of the produced TiO_2 nanopowder (in the presence of the cork substrates) were investigated by recording the UV-VIS absorption spectrum (see Figure 3.5). As observed in Figure 3.5, an absorption maximum is obtained in the UV region, around 306 nm (~ 4.1 eV), and the absorption is seen to extend through all the visible region.

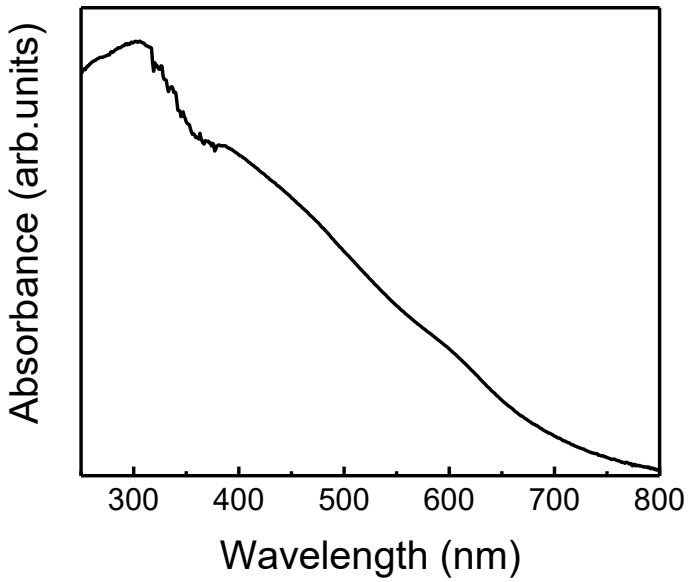

Figure 3.5: Absorption curve of the TiO_2 nanopowder synthesized in the presence of the cork substrates.

For comparison, the absorption spectrum of the TiO_2 nanopowder synthesized in the absence of the cork substrates was also recorded (Figure 3.6). In this last case, even though the absorption maximum is placed at the same value as in Figure 3.6, no absorption occurs beyond 400 nm as expected (Figure 3.6), since pure TiO_2 presents a wide band gap value (around 3.2 eV for pure TiO_2 anatase nanoparticles [3,22,23]).

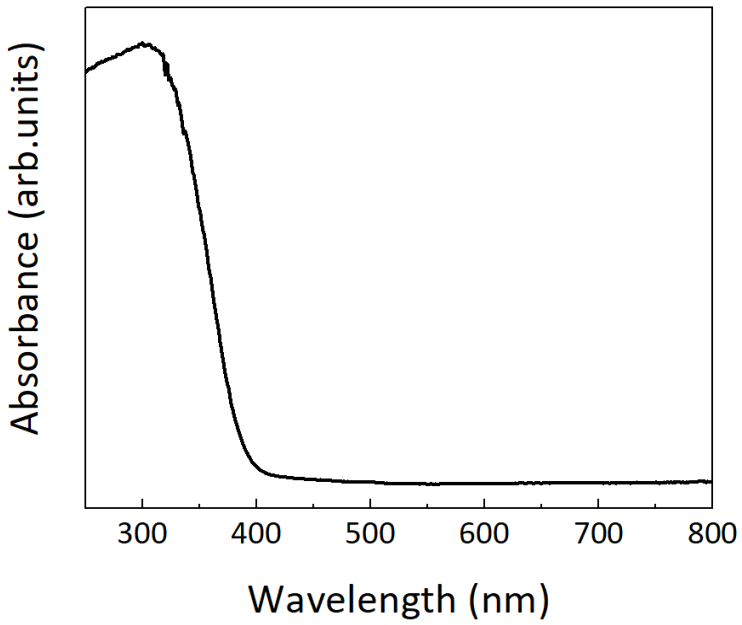

Figure 3.6: Absorption curve of the TiO_2 nanopowder synthesized in the absence of the cork substrates.

It can thus be concluded that the visible light absorption in Figure 3.6 may be attributed to the presence of the binders that were transferred to the TiO_2 nanopowder from the cork during the MW synthesis that resulted in its brown color. Additionally, the introduction of defects, including surface defects, in TiO_2 crystals during synthesis should also be considered, as these defects can enhance visible light absorption [24,25]. In fact, several studies have reported the impact of different binders on the TiO_2 nanostructures, with these extractives interacting with the nanostructures and modifying their morphology, size and optical properties [26–28].

3.2.2 Structural characterization and photocatalytic performance of the TiO_2-cork substrates

3.2.2.1 XRD

XRD analyses were also carried out for pristine cork and TiO_2-cork substrates (Figure 3.7). It can be observed that the pristine cork substrate shows a broad peak centered at around $2\theta = 21°$, indicating its amorphous nature [29,30]. When it comes to the cork substrate, five weak and broad peaks were detected, which can be associated with the presence of anatase. The XRD peaks observed at 25.3°, 37.8°, 48.0°, 53.8°, and 54.9°, correspond to the (101), (004), (200), (105), (211) reflections of the TiO_2 anatase phase. The results corroborate with the XRD data obtained for the TiO_2 nanopowder (Figure 3.1), confirming the presence of TiO_2 anatase nanostructures at the surface of the cork.

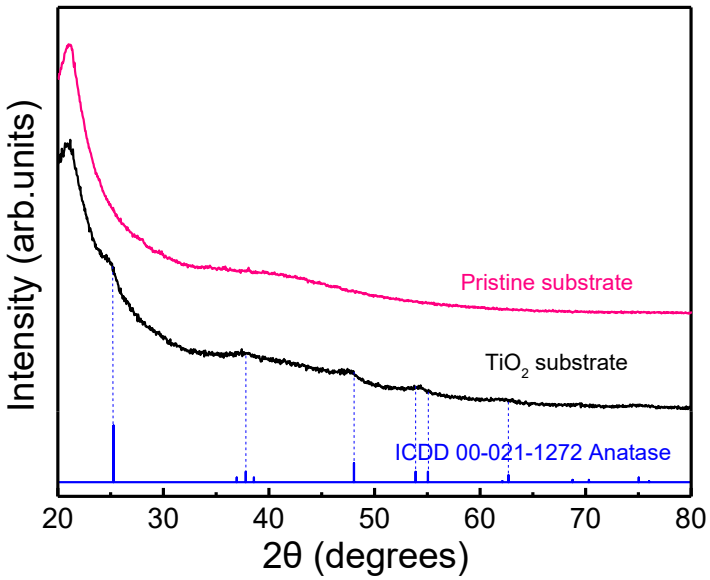

Figure 3.7: XRD diffractograms of the pristine and TiO_2-cork substrates. For comparison, the simulated TiO_2 anatase is presented.

3.2.2.2 Electron microscopy

SEM images of the pristine cork substrates together with the TiO_2 ones are shown in Figure 3.8. In Figure 3.8 (a) to (c), the pristine cork is shown, which displays several closed and air-hollow unit cells, forming polygons in a regular honeycomb arrangement and the number of sides in these polygons varies. As reported for *Quercus suber L*, hexagonal, pentagonal and heptagonal cells are the most frequent, representing around 95 % of the total forms [31]. The diameter of the cork cells is around 15–20 μm (see Figure 3.8 (a)) and their size depends on the season in which they are formed [31]. For instance, early cork cells (cells formed in the main growth period) are greater in height and have thinner cell walls, while late cork cells (cells formed at the end of the growth period) are smaller and have thicker walls [32,33]. In the specific case of *Quercus suber L.*, for early cork cells, prism height ranges from 30–40 μm, prism base edges from 13–15 μm, the average base area from $4–6\times10^{-6}$ cm^2, and the cell wall thickness between 1 and 1.5 μm. Late cork cells have a reduced prism height, nearly 10 μm, and the cell wall thickness almost doubles. The number of cells per cm^3 fluctuates from 4 to 7×10^7 for early cork and late cork from 10 to 20×10^7 [31]. Another important characteristic is the non-uniform undulations of the cell walls, which vary from cell to cell, as well as the roughness of their surface [34]. Some corrugated cells are observed, together with a few collapsed cells (see Figure 3.8 (a)). Concerning the irregularities on the surface of the cells, granulates and small deposits are visible with no defined shape (Figure 3.8 (c)) [32]. It is also visible that the interior

of these cork cells is closed, without internal porosity. After the MW synthesis (Figure 3.8 (d) to (f)), it is possible to observe that the honeycomb arrangement of the cork cells is preserved. Additionally, the TiO_2 agglomerates of nanoparticles are discernible at the surface of the cork, filling the cork cells and entirely covering the substrate Figure 3.8 (f)).

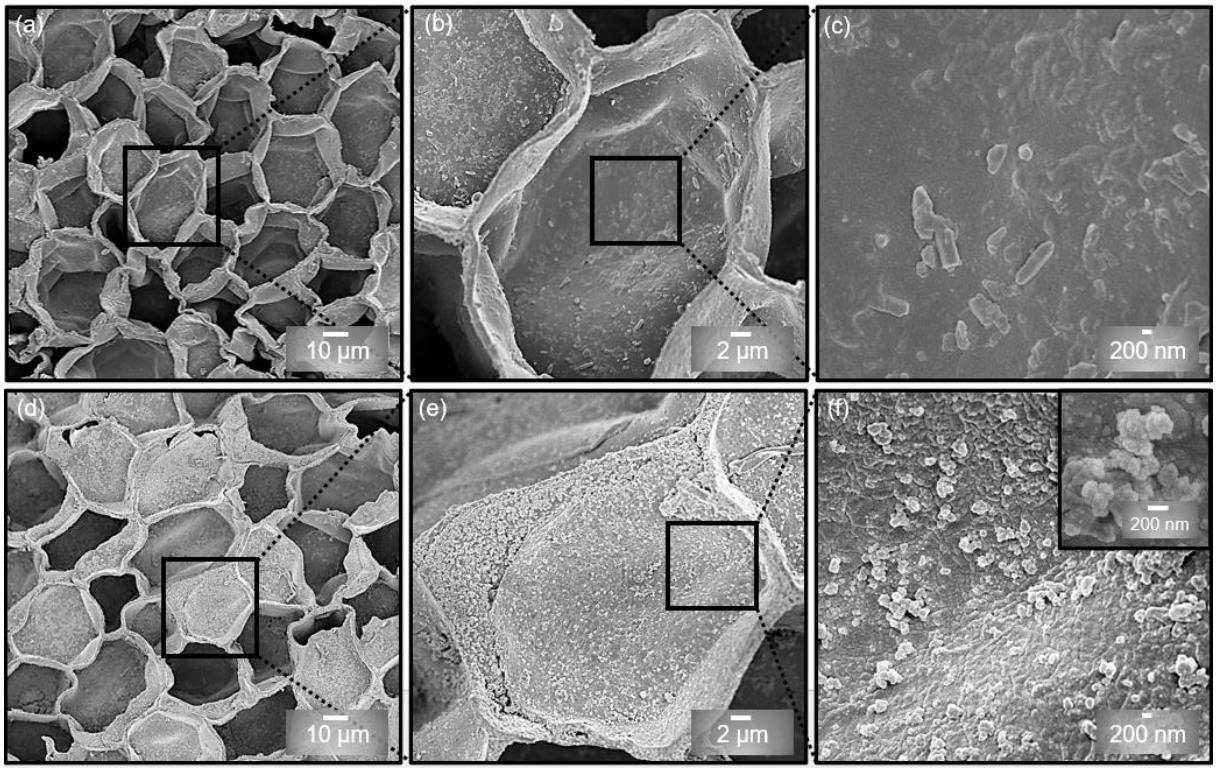

Figure 3.8: SEM images of the pristine cork substrates (a) to (c) together with the TiO_2 ones (d) to (e). The inset in (f) shows a TiO_2 nanoparticles' agglomerate at the interior of a cork's cell.

The chemical composition of the substrates before (pristine cork) and after the MW synthesis (TiO_2-cork substrates) was analyzed by EDS (Figure A.3). The pristine cork substrates ($C_{123}H_{182}O_{56}N$ for *Quercus suber L.* [35]) were mainly composed of C and O, consistent with its chemical composition [29]. For the TiO_2-cork substrates, a uniform distribution of Ti, together with C and O was observed. This indicates the homogeneous distribution of all elements on the surface of the cork.

3.2.2.3 Photocatalytic activity of the TiO_2-cork substrates

3.2.2.3.1 RhB photocatalytic degradation under simulated solar light

The RhB decolorization in the presence of the cork substrates (pristine and with TiO_2) was evaluated under simulated solar light for a total of 12 h. The aliquots of the dye were taken after 1 h (up to 4 h) and, after that time, every 2 h using the UV-VIS spectrophotometer. A

gradual decrease in the absorption peak of RhB (at 554 nm [36,37]) was observed over time. The decolorization rate (%) of the RhB dye was calculated according to equation (3.3):

$$\text{Decolorization (\%)} = \frac{A_0 - A_t}{A_0} \times 100 \quad (3.3)$$

where A_0 is the initial absorbance of the pollutant solution before irradiation and A_t is the absorbance of pollutant solution after a certain exposure time (t) [21,38]. Blank experiments (only RhB solution) were also carried out under simulated solar light and natural sunlight (Figure 3.9 (c) and Figure 3.10 (c)). Although a slight increase in the RhB concentration is observed for both cases, possibly due to the evaporation of the solvent over time [4], no degradation of the RhB dye was observed in both cases, as reported in other studies [39,40].

Figure 3.9 (a) shows a RhB decolorization of 44 % without any catalyst on the surface of the cork after 12 h. The uptake of RhB molecules by the pristine cork stems from its honeycomb structure and cork cells' surface roughness, increasing the RhB adsorption capacity during the first few hours. However, after 8 h of light exposure, a tendency for stabilization is visible (Figure 3.9 (c)). After that time, fewer trap sites on the cork surface could be available leading to a decrease in the absorption rate. According to the literature, the adsorption kinetics model of organic pollutants on cork presents a convex initial curvature, indicating that the adsorption rate decreases with time: it becomes more difficult for the adsorbate to find free sites to adsorb since the main sites are gradually occupied [41]. This overall significant adsorption of RhB molecules by the pristine cork, which is visible with and without irradiation in Figure 3.9 (a), has also been previously reported [42].

It is also well established that suberin, the main chemical component of cork, is hydrophobic due to the existence of aliphatic substances bound to the aromatic domain as triacylglycerol esters. Lignin, the second most abundant chemical component of cork, is characterized by the presence of aromatic alcohol monolignols and acids (in particular, cinnamic and ferulic acid) [43–45]. It is reported that the aromatic domain of both suberin and lignin will determine the interaction between cork and the organic compounds, like RhB [46], which are essentially hydrophobic [43,47]. As a result, these hydrophobic regions in the cork will confer it special affinity to organic pollutants, and hence it is expected that an increase in the diffusion of hydrophobic dye molecules into the cork will occur [47,48].

Meanwhile, with the TiO_2-cork substrate (Figure 3.9 (b)), the decolorization efficiency was substantially increased to 76 %, for the same exposure time. This indicates that the synthesized TiO_2 nanomaterials effectively contributed to the degradation of RhB.

It is well known that different factors may influence the photocatalytic activity of TiO_2, such as the phase structure, crystallite size, specific surface area and exposed crystal facets [49,50]. As confirmed by TEM and SEM, particles in the nanometer range were formed with an average size of 5 nm. Smaller nanoparticles possess a high specific surface area and surface-to-volume ratio [51]. As a consequence, more active sites on the catalyst are available to interact with the pollutant molecules [4]. Moreover, if the particle size is decreased, the distance that photogenerated electron-hole pairs need to travel is reduced, thus reducing the probability of their recombination [52]. It was also observed by TEM and SEM that these particles formed agglomerates. Such agglomerates influence the specific surface area of the nanoparticles and consequently their photocatalytic activity [21,53,54]. Several approaches and synthesis parameters can be used to minimize their formation including a variation of the solution's pH and the addition of surfactants, among others. Nevertheless, the synthesized TiO_2 nanoparticles enhanced the cork's performance in the removal of RhB molecules from water (Figure 3.9 (a) and (b)).

The (101) anatase surface is found to dominate the structure of nanosized anatase crystallites due to its energetic preference and higher stability, being labeled as the majority surface [55]. As observed in Figure 3.4, (101) anatase near-spherical nanocrystals without a specific facet on the crystal surface are largely present in the nanopowder produced. Therefore, no contribution to RhB degradation from active anatase facets has been considered.

Moreover, in general, it is accepted that for pure TiO_2 phases, anatase exhibits superior photocatalytic activity than the other two crystalline phases: rutile and brookite. Rutile and brookite are direct band gap semiconductors, while anatase presents an indirect band gap. Therefore, anatase TiO_2 has a longer lifetime of photogenerated electrons and holes. Additionally, the average effective mass of photogenerated electrons is the lightest compared to rutile and brookite and, as a result, it exhibits the fastest migration of photogenerated electrons and holes from the interior to the surface of anatase particles. Hence, a lower recombination rate is expected with pure TiO_2 anatase, thus showing a better photocatalytic performance [49,56].

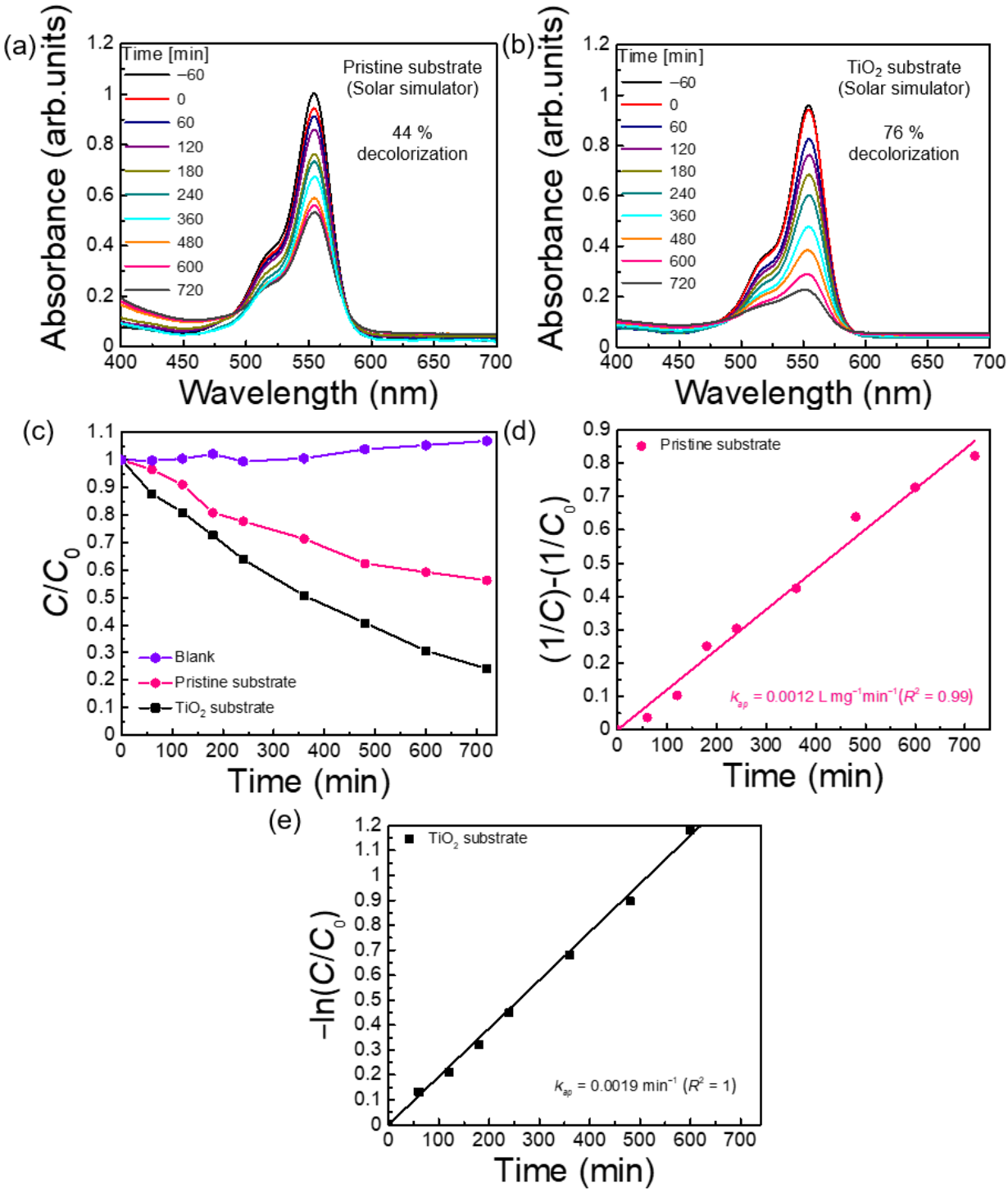

Figure 3.9: RhB absorbance spectra under simulated solar light radiation (LED simulator with AM 1.5 Spectrum) up to 12 h (720 min) for cork substrates: (a) pristine substrate and (b) TiO_2 substrate. (c) Decolorization ratio (C/C_0) of RhB dye without any substrate (blank), with the pristine and TiO_2-cork substrates, (d) pseudo-second-order kinetics for RhB decolorization in the presence of the pristine substrate, and (e) pseudo-first-order kinetics for RhB decolorization in the presence of the TiO_2 substrate.

The RhB degradation process in the presence of TiO_2-cork substrates was investigated by using the Langmuir-Hinshelwood model (equation (1.11, see Chapter 1)). Based on this equation, the rate constants k_{ap} (min^{-1}) can be determined by plotting $-\ln\left(\frac{C}{C_0}\right)$ *vs.* t [57], where the slope of the linear regressions are the apparent rate constants [21].

The obtained photodegradation apparent rate constant was found to be 0.0019 min^{-1} with the TiO_2 substrate (Figure 3.9 (e)), and it can be concluded that the photocatalytic dye degradation follows the pseudo-first-order kinetics, since a good correlation for the fitted line was obtained (R^2 above 0.95 [58]). In contrast with the TiO_2 substrate, the pristine cork substrate (Figure 3.9 (d)) did not show a satisfactory fitting for the pseudo-first-order equation (which has also already been reported [42]), but fitted well (R^2 = 0.99) the pseudo-second-order equation, described with the following equation:

$$\frac{1}{C} - \frac{1}{C_0} = k_{ap}t \qquad (3.4)$$

Based on equation (3.4), the rate constant can be obtained by a linear fit, through the plot of $\frac{1}{C} - \frac{1}{C_0}$ *vs.* time [59], and a value of 0.0012 $L.mg^{-1}.min^{-1}$ was obtained. As mentioned before, this trend can be explained by a fast adsorption of RhB molecules in the first 8 h (480 min), followed by a slower uptake and a subsequent stabilization, since fewer adsorption sites are available.

3.2.2.3.2 RhB photocatalytic degradation under natural sunlight

RhB decolorization under natural sunlight was also monitored with the cork substrates (pristine and with TiO_2) within 4 h (240 min) (Figure 3.10). For comparison, the degree of RhB decolorization under simulated solar light up to 4 h, in the presence of both cork substrates, was also calculated and it is summarized in Table 3.1. As indicated before, no stirring nor oxygenation were needed during the reactions. Due to the floating characteristic of cork during the photocatalytic experiments under natural sunlight, the substrates can thus be easily collected from the solution (Figure A.4).

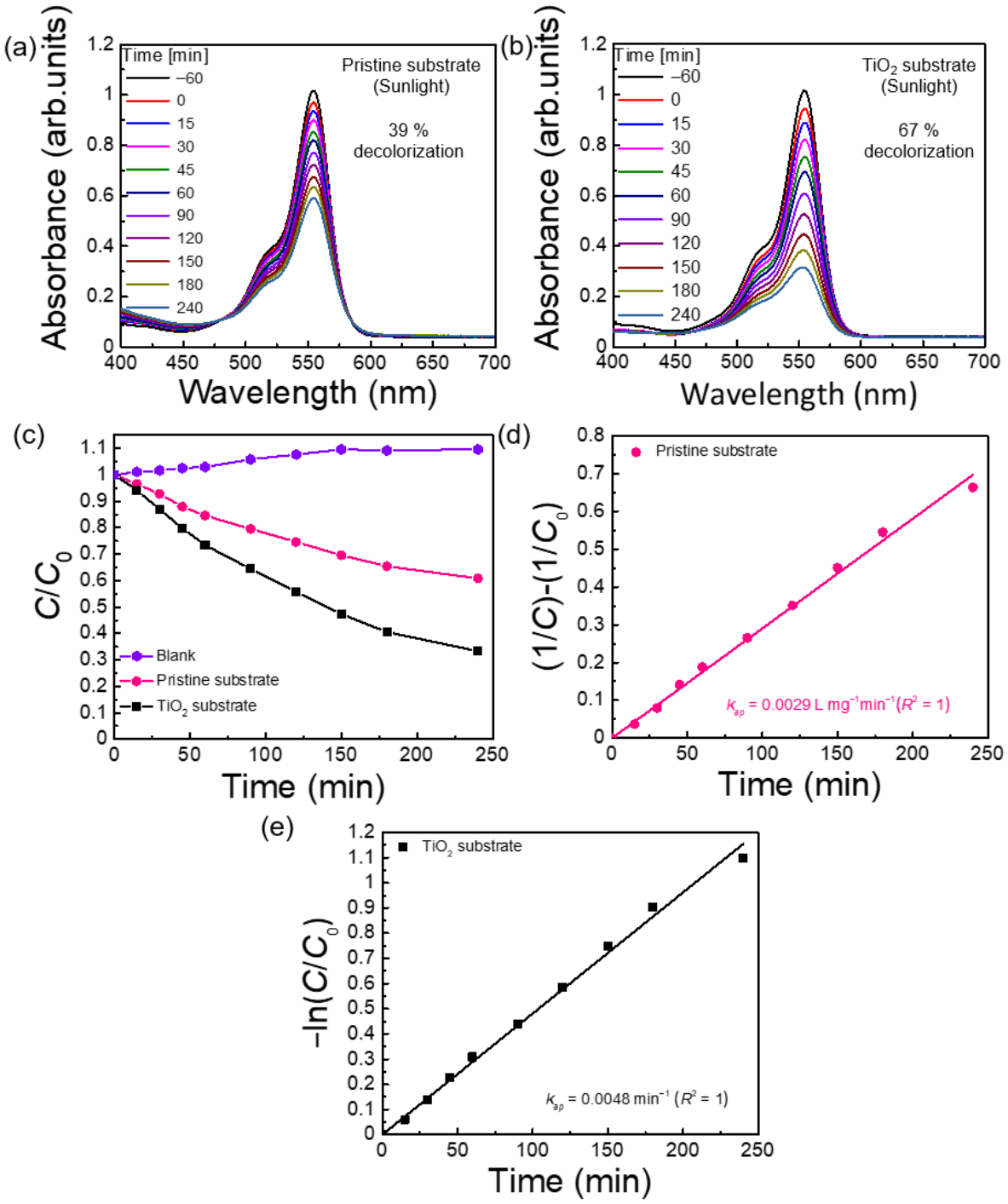

Figure 3.10: RhB absorbance spectra under natural sunlight up to 4 h (240 min) for cork substrates: (a) pristine substrate and (b) TiO_2 substrate. (c) Decolorization ratio (C/C_0) of RhB dye without any substrate (blank), with the pristine and TiO_2-cork substrates, (d) pseudo-second-order kinetics for RhB decolorization in the presence of the pristine substrate, and (e) pseudo-first-order kinetics for RhB decolorization in the presence of the TiO_2 substrate.

Table 3.1: RhB decolorization percentages under simulated solar light and natural sunlight exposure up to 4 h.

		RhB decolorization (%)
Simulated solar light	Pristine substrate	22
	TiO_2 substrate	36
Natural sunlight exposure	Pristine substrate	39
	TiO_2 substrate	67

Table 3.1 shows that in the presence of the pristine substrate, a difference in the RhB decolorization is observed, 22 % *vs*. 39 % of degradation under simulated solar light and natural sunlight, respectively. Cork's chemical components may degrade upon prolonged UV light irradiation [60]. In fact, the absorption of UV light by pristine cork under natural sunlight might lead to the photooxidation of cellulose, hemicellulose, and degradation of some lignin content present in cork, which could generate chromophore groups, such as carboxylic acids, quinones and hydroperoxide radicals. As a result, these chromophore groups could trigger photochemical reactions on the cork surface, thus promoting a faster decolorization of RhB, in comparison with simulated solar light exposure [61–63]. For the TiO_2-cork substrates, as observed, an increase of decolorization efficiency by 31 % was obtained under natural sunlight when compared to simulated solar light during 4 h. In contrast with the solar spectrum, which is composed of around 5 % UV light, 43 % visible light and 50 % IR light [64], the LED solar simulator used in the photocatalytic experiments mainly provides visible light (the irradiance is cut for shorter wavelengths (high UV energy)), see Figure A.5. Since TiO_2 anatase has a wide band gap value (~ 3.2 eV), it is mostly photoactive in the UV region [65], and so the difference may be due to the UV light contribution of natural sunlight. This is also supported by the obtained apparent rate constants with the TiO_2 substrate under natural sunlight, as visible in Figure 3.10 and under simulated solar light (Figure 3.9 (e)). The reaction was 2.5 times faster under natural sunlight (k_{ap} = 0.0048 min^{-1}) than under simulated solar light (0.0019 min^{-1}) in a third of the time (12 h under simulated solar light compared to 4 h under natural sunlight).

3.2.2.3.3 Reusability tests under natural sunlight

Reusability tests are of great importance to evaluate the stability of the photocatalyst [66]. Since the best results were obtained under natural sunlight, reusability tests with the TiO_2 cork substrate were performed under 3 consecutive cycles within 4 h (240 min) under natural sunlight. Figure 3.11 shows the decolorization ratio (C/C_0) of the RhB dye, the pseudo-first-order model fitting for RhB decolorization under 3 cycles and a column chart of RhB

decolorization efficiency with the number of uses. A summary of the obtained results is also presented in Table 3.2.

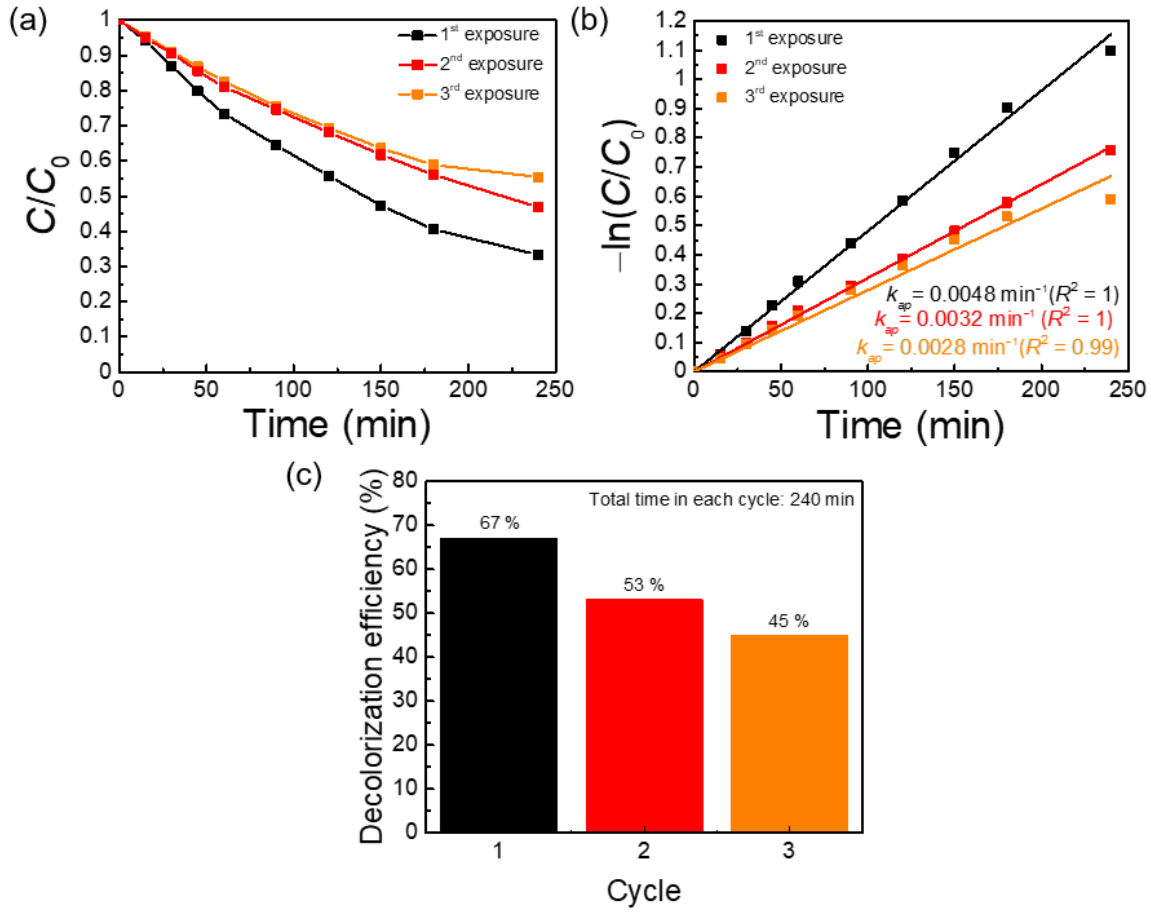

Figure 3.11: Three consecutive reusability tests under natural sunlight with the TiO_2-cork substrate: (a) decolorization ratio (C/C_0) of the RhB dye, (b) pseudo-first-order kinetics for the RhB decolorization and (c) decolorization efficiency (%) *vs.* the number of cycles.

Table 3.2: Kinetic parameters (rate constants k_{ap} and linear regression coefficients R^2) for the RhB decolorization under natural sunlight (1st, 2nd and 3rd exposures) up to 4 h with the TiO_2-cork substrate.

		k_{ap} (min^{-1})	R^2
1st sunlight exp.	Pseudo-first-order-kinetics reaction	0.005	1
2nd sunlight exp.		0.003	1
3rd sunlight exp.		0.003	0.99

In Table 3.2 and Figure 3.11, a decrease in photocatalytic activity was observed with the number of exposures. The reaction rate decreased from 0.005 min^{-1} in the first cycle to 0.003 min^{-1} in the third cycle. After performing 3 consecutive cycles, a decolorization efficiency loss of around 22 % was obtained. Since neither heat/UV treatments nor rinsing were

applied to the substrate between cycles, a high percentage of RhB molecules could have remained from the previous cycle adsorbed on the photocatalyst surface, hindering the available pore sites on the TiO_2-cork substrate for reaction [67,68], thus decreasing its overall cycling efficiency. This effect has been previously reported in different studies [21,67–69]. It is worth mentioning that this work demonstrates the real contribution of the RhB molecules' adsorption on pristine cork substrates, with a direct effect on the overall photocatalytic activity of the floating photocatalysts.

3.3 Summary

TiO_2 nanomaterials were directly synthesized on cork substrates by a fast and low-temperature solvothermal method under MW irradiation (120 °C for 1 h) without any preliminary process by using oxalic acid. These nanomaterials were characterized in powder form, as well as on cork substrates. The characterization of TiO_2 nanopowder by XRD, Raman spectroscopy and TEM revealed the presence of the TiO_2 anatase structure. Although some FTIR bands indicated the presence of cork's organic species in the TiO_2 nanopowder, crystalline TiO_2 anatase nanoparticles were formed on the cork, as proved by XRD data. The obtained brown powdered TiO_2 material showed a broad absorption band peaked at ~306 nm, which extended through the visible range up to 800 nm. SEM and EDS analyses of the TiO_2 substrates showed the formation of nearly spherical TiO_2 nanoparticles that uniformly covered the honeycomb cells of the cork. The best RhB decolorization efficiency was obtained with the TiO_2-cork substrate under natural sunlight, and a RhB degradation of 67 % was obtained compared to 39 % with the pristine cork substrate in 4 h of natural light exposure. In the presence of the TiO_2 substrates, the photocatalytic reaction was 2.5 times faster under natural sunlight than under simulated solar light, in a third of the time (12 h under solar simulating light compared to 4 h under natural sunlight). In summary, the results presented show that by using a simple MW approach, cork floating catalysts based on TiO_2 materials can be employed for removing organic pollutants from water under natural sunlight.

3.4 References

1. Yadav, M.; Singhal, I. Sustainable construction: the use of cork material in the building industry. *Materials for Renewable and Sustainable Energy* **2024**, *13*, 1–9, doi:10.1007/S40243-024-00270-X.

2. Alves, H. F. Cork as a raw material for antibacterial membranes and fibers, Master's thesis, FCT-UNL: Lisboa, 2019.
3. Nunes, D.; Pimentel, A.; Santos, L.; Barquinha, P.; Fortunato, E.; Martins, R. Photocatalytic TiO_2 Nanorod Spheres and Arrays Compatible with Flexible Applications. *Catalysts* **2017**, *7 (2)*, 1–18.
4. Freire, T.; Fragoso, A. R.; Matias, M.; Vaz Pinto, J.; Marques, A. C.; Pimentel, A.; Barquinha, P.; Huertas, R.; Fortunato, E.; Martins, R.; Nunes, D. Enhanced solar photocatalysis of TiO_2 nanoparticles and nanostructured thin films grown on paper. *Nano Express* **2021**, *2,4*, 1–20.
5. Ohsaka, T.; Fujiki, I.; Fujiki, Y. Raman Spectrum of Anatase, TiO_2. *Journal of Raman Spectroscopy* **1978**, *7,6*, 321–324.
6. El-Deen, S. S.; Hashem, A. M.; Abdel Ghany, A. E.; Indris, S.; Ehrenberg, H.; Mauger, A.; Julien, C. M. Anatase TiO_2 nanoparticles for lithium-ion batteries. *Ionics* **2018**, *24,10*, 2925–2934.
7. Deng, D.; Martin, S. T.; Ramanathan, S. Synthesis of hollow porous nanospheres of hydroxyl titanium oxalate and their topotactic conversion to anatase titania. *Journal of Materials Research* **2011**, *26,12*, 1545–1551.
8. Shyniya, C. R.; Bhabu, K. A.; Rajasekaran, T. R. Enhanced electrochemical behavior of novel acceptor doped titanium dioxide catalysts for photocatalytic applications. *Journal of Materials Science: Materials in Electronics* **2017**, *28,9*, 6959–6970.
9. Maragatha, J.; Rajendran, S.; Endo, T.; Karuppuchamy, S. Microwave synthesis of metal doped TiO_2 for photocatalytic applications. *Journal of Materials Science: Materials in Electronics* **2017**, *28,7*, 5281–5287.
10. Praveen, P.; Viruthagiri, G.; Mugundan, S.; Shanmugam, N. Structural, optical and morphological analyses of pristine titanium di-oxide nanoparticles - Synthesized via sol-gel route. *Spectrochimica Acta - Part A: Molecular and Biomolecular Spectroscopy* **2014**, *117*, 622–629.
11. Sboui, M.; Nsib, M. F.; Rayes, A.; Swaminathan, M.; Houas, A. TiO_2–PANI/Cork composite: A new floating photocatalyst for the treatment of organic pollutants under sunlight irradiation. *Journal of Environmental Sciences* **2017**, *60*, 3–13.
12. Chougala, L. S.; Yatnatti, M. S.; Linganagoudar, R. K.; Kamble, R. R.; Kadadevarmath, J. S. A simple approach on synthesis of TiO_2 nanoparticles and its application in dye sensitized solar cells. *Journal of Nano- and Electronic Physics* **2017**, *9,4*, 1–6.
13. Alsharaeh, E. H.; Bora, T.; Soliman, A.; Ahmed, F.; Bharath, G.; Ghoniem, M. G.; Abu-Salah, K. M.; Dutta, J. Sol-Gel-Assisted Microwave-Derived Synthesis of Anatase Ag/TiO_2/GO Nanohybrids toward Efficient Visible Light Phenol Degradation. *Catalysts* **2017**, *7 (5), 133*, 1–11.
14. Tan, C.; Tirri, T.; Wilen, C.-E. Investigation on the Influence of Chain Extenders on the Performance of One-Component Moisture-Curable Polyurethane Adhesives. *Polymers* **2017**, *9*, *184*, 1–19.
15. Dietz, J. 5 Functionalization and Characterization of Isocyanate Modified Lignins. In *Synthesis and characterization of novel functional lignins - towards Bio-based Polyurethane Materials.*; Apprimus Wissenschaftsverlag: Germany, 2015; Vol. 1, p. 75 ISBN 3863593758.

16. Nishimura, H.; Kamiya, A.; Nagata, T.; Katahira, M.; Watanabe, T. Direct evidence for α ether linkage between lignin and carbohydrates in wood cell walls. *Scientific Reports* **2018**, *8,6538*, 1–11.
17. Novais, R. M.; Caetano, A. P. F.; Seabra, M. P.; Labrincha, J. A.; Pullar, R. C. Extremely fast and efficient methylene blue adsorption using eco-friendly cork and paper waste-based activated carbon adsorbents. *Journal of Cleaner Production* **2018**, *197,1*, 1137–1147.
18. Mislata, A. M.; Puxeu, M.; Ferrer-Gallego, R. Aromatic Potential and Bioactivity of Cork Stoppers and Cork By-Products. *Foods* **2020**, *9(2)*, 133.
19. Graça, J.; Santos, S. Glycerol-derived ester oligomers from cork suberin. *Chemistry and Physics of Lipids* **2006**, *144,1*, 96–107.
20. Barros-Timmons, A.; Lopes, M. H.; Pascoal Neto, C.; Dhanabalan, A.; Oliveira, O. N. Langmuir monolayers of fractions of cork suberin extract. *Colloids and Surfaces B: Biointerfaces* **2010**, *79,2*, 516–520.
21. Matias, M. L.; Pimentel, A.; Reis-Machado, A. S.; Rodrigues, J.; Deuermeier, J.; Fortunato, E.; Martins, R.; Nunes, D. Enhanced Fe-TiO_2 Solar Photocatalysts on Porous Platforms for Water Purification. *Nanomaterials* **2022**, *12*.
22. Li, K.; Wang, H.; Pan, C.; Wei, J.; Xiong, R.; Shi, J. Enhanced photoactivity of Fe + N Codoped anatase-rutile TiO_2 nanowire film under visible light irradiation. *International Journal of Photoenergy* **2012**, *1,398508*, 1–8.
23. Damkale, S. R.; Arbuj, S. S.; Umarji, G. G.; Rane, S. B.; Kale, B. B. Highly crystalline anatase TiO_2 nanocuboids as an efficient photocatalyst for hydrogen generation. *RSC Advances* **2021**, *11*, 7587–7599.
24. Krishna, V.; Bai, W.; Han, Z.; Yano, A.; Thakur, A.; Georgieva, A.; Tolley, K.; Navarro, J.; Koopman, B.; Moudgil, B. Contaminant-Activated Visible Light Photocatalysis. *Scientific Reports* **2018**, *8*, 1894, doi:10.1038/S41598-018-19972-0.
25. Li, Z.; Wang, S.; Wu, J.; Zhou, W. Recent progress in defective TiO_2 photocatalysts for energy and environmental applications. *Renewable and Sustainable Energy Reviews* **2022**, *156*, 111980, doi:10.1016/J.RSER.2021.111980.
26. Masjedi, M.; Mir, N.; Noori, E.; Gholami, T.; Salavati-Niasari, M. Effect of Schiff base ligand on the size and the optical properties of TiO_2 nanoparticles. *Superlattices and Microstructures* **2013**, *62*, 30–38.
27. Gholami, T.; Bazarganipour, M.; Salavati-Niasari, M.; Mir, N.; Hamadanian, M.; Bagheri, S. Considering the effect of a ligand as new complexing agent in the characteristics of TiO_2 nanoparticles. *Journal of Molecular Liquids* **2016**, *215*, 467–471.
28. Hidalgo, M. C.; Aguilar, M.; Maicu, M.; Navío, J. A.; Colón, G. Hydrothermal preparation of highly photoactive TiO_2 nanoparticles. *Catalysis Today* **2007**, *129,1*, 50–58.
29. Abenojar, J.; López de Armentia, S.; Barbosa, A. Q.; Martínez, M. A.; Velasco, F.; da Silva, L. F. M.; del Real Romero, J. C. Coating cork particles with iron oxide: effect on magnetic properties. *Wood Science and Technology* **2020**, *54,1*, 869–889.
30. Filipe-Ribeiro, L.; Cosme, F.; Nunes, F. M. Cork powder as a new natural and sustainable fining agent to reduce negative volatile phenols in red wine. *BIO Web of Conferences* **2019**, *15,02017*, 1–6.
31. Pereira, H.; Rosa, M. E.; Fortes, M. A. The Cellular Structure of Cork from *Quercus Suber L. IAWA Journal* **1987**, *8,3*, 213–218.

32. Miranda, I.; Gominho, J.; Pereira, H. Cellular structure and chemical composition of cork from the Chinese cork oak (*Quercus variabilis*). *Journal of Wood Science* **2013**, *59,1*, 1–9.
33. Oliveira, V. Cork Structural Characteristics And Their Influence On The Oxygen Ingress Through Wine Stoppers, PhD thesis, Insituto Superior de Agronomia - Lisbon University, 2016.
34. Pereira, H. The rationale behind cork properties: A review of structure and chemistry. *BioResources* **2015**, *10,3*, 1–23.
35. Serra, P. Corticeira Amorim: Uncorking the future. Master's thesis, Católica Lisbon, 2016.
36. Luisa, M.; Gioia, D.; Martins, L. M.; Pastor, I. M.; Khanam, S.; Rout, S. K. Enhanced Photocatalytic Oxidation of RhB and MB Using Plasmonic Performance of Ag Deposited on Bi_2WO_6. *Chemistry* **2022**, *4(2)*, 272–296.
37. Zhao, J.; Wu, T.; Wu, K.; Oikawa, K.; Hidaka, H.; Serpone, N. Photoassisted degradation of dye pollutants.3.Degradation of the cationic dye rhodamine B in aqueous anionic surfactant/TiO_2 dispersions under visible light irradiation: Evidence for the Need of Substrate Adsorption on TiO_2 Particles. *Environ. Sci. Technol.* **1998**, *32,16*, 2394–2400.
38. Maeno, K.; Patel, B. R.; Endo, T.; Kerman, K. Angle-sensitive photonic crystals for simultaneous detection and photocatalytic degradation of hazardous diazo compounds. *Micromachines* **2020**, *11(1)*, 1–12.
39. Ferreira, S. H.; Morais, M.; Nunes, D.; Oliveira, M. J.; Rovisco, A.; Pimentel, A.; Águas, H.; Fortunato, E.; Martins, R. High UV and Sunlight Photocatalytic Performance of Porous ZnO Nanostructures Synthesized by a Facile and Fast Microwave Hydrothermal Method. *Materials* **2021**, *14(9)*, 1–17.
40. Rovisco, A. Solution-based Zinc-Tin Oxide nanostructures : from synthesis to applications, PhD thesis, FCT-UNL, 2019.
41. Pintor, A. M. A.; Ferreira, C. I. A.; Pereira, J. C.; Correia, P.; Silva, S. P.; Vilar, V. J. P.; Botelho, C. M. S.; Boaventura, R. A. R. Use of cork powder and granules for the adsorption of pollutants: A review. *Water Research* **2012**, *46,10*, 3152–3166.
42. Bíbová, H.; Hykrdová, L.; Hoang, H.; Eliáš, M.; Jirkovský, J. SiO_2/TiO_2 composite coating on light substrates for photocatalytic decontamination of water. *Journal of Chemistry* **2019**, *2019*, 1–12.
43. Pirozzi, C.; Pontoni, L.; Fabbricino, M.; Bogush, A.; Campos, L. C. Effect of organic matter release from natural cork used on bisphenol a removal from aqueous solution. *Journal of Cleaner Production* **2020**, *244,118675*.
44. Marques, A. V.; Rencoret, J.; Gutiérrez, A.; Del Río, J. C.; Pereira, H. Ferulates and lignin structural composition in cork. *Holzforschung* **2016**, *70,4*, 275–289.
45. Graça, J. Suberin: The biopolyester at the frontier of plants. *Frontiers in Chemistry* **2015**, *3*, 1–11.
46. Andree, F.; Ludwigshafen; Burkhardt, H.; Limburgerhof; Riedel, G. Rhodamine dyes which are sparingly soluble or insoluble in water, U.S. Patent, 1970, 1–2.
47. Pintor, A. M. A.; Silvestre-Albero, A. M.; Ferreira, C. I. A.; Pereira, J. P. C.; Vilar, V. J. P.; Botelho, C. M. S.; Rodríguez-Reinoso, F.; Boaventura, R. A. R. Textural and surface characterization of cork-based sorbents for the removal of oil from water. *Industrial and*

Engineering Chemistry Research **2013**, *52,46*, 16427–16435.
48. R. de Aguiar, T.; Guimarães Neto, J. O. A.; Şen, U.; Pereira, H. Study of two cork species as natural biosorbents for five selected pesticides in water. *Heliyon* **2019**, *5,1*, e01189,1-15.
49. Zhang, J.; Zhou, P.; Liu, J.; Yu, J. New understanding of the difference of photocatalytic activity among anatase, rutile and brookite TiO_2. *Physical Chemistry Chemical Physics* **2014**, *16*, *38*, 20382–20386, doi:10.1039/C4CP02201G.
50. Lu, Y.; Zang, Y.; Zhang, H.; Zhang, Y.; Wang, G.; Zhao, H. Meaningful comparison of photocatalytic properties of {001} and {101} faceted anatase TiO_2 nanocrystals. *Science Bulletin* **2016**, *61,13*, 1003–1012.
51. Nunes, D.; Pimentel, A.; Gonçalves, A.; Pereira, S.; Branquinho, R.; Barquinha, P.; Martins, R. Metal Oxide Nanostructures for Sensor Applications. *Semicond. Sci. Technol* **2019**, *34,4*, 1–178, doi:10.1088/1361-6641/ab011e.
52. Bakbolat, B.; Daulbayev, C.; Sultanov, F.; Beissenov, R.; Umirzakov, A.; Mereke, A.; Bekbaev, A.; Chuprakov, I. Recent Developments of TiO_2-Based Photocatalysis in the Hydrogen Evolution and Photodegradation: A Review. *Nanomaterials* **2020**, *10(9)*, 1–16.
53. Avilés-García, O.; Espino-Valencia, J.; Romero, R.; Rico-Cerda, J. L.; Natividad, R. Oxidation of 4-chlorophenol by mesoporous titania: Effect of surface morphological characteristics. *International Journal of Photoenergy* **2014**, *2014*, 1–11.
54. Li, G.; Lv, L.; Fan, H.; Ma, J.; Li, Y.; Wan, Y.; Zhao, X. S. Effect of the agglomeration of TiO_2 nanoparticles on their photocatalytic performance in the aqueous phase. *Journal of Colloid and Interface Science* **2010**, *348*, 342–347.
55. Wang, H.; Lewis, J. P. The reactive sites in faceted anatase nanoparticles. *physica status solidi (b)* **2011**, *248,9*, 2037–2043.
56. Luttrell, T.; Halpegamage, S.; Tao, J.; Kramer, A.; Sutter, E.; Batzill, M. Why is anatase a better photocatalyst than rutile? - Model studies on epitaxial TiO_2 films. *Scientific Reports* **2014**, *4*, *4043*, 1–8, doi:10.1038/srep04043.
57. Colina-Márquez, J.; Machuca-Martínez, F.; Puma, G. L.; Mueses, M. . Photocatalysis: Fundamentals, Materials and Potential. In *Molecules*; Pierre Pichat, Ed.; MDPI: Basel: Switzerland, 2016; pp. 1–664.
58. Alkaykh, S.; Mbarek, A.; Ali-Shattle, E. E. Photocatalytic degradation of methylene blue dye in aqueous solution by $MnTiO_3$ nanoparticles under sunlight irradiation. *Heliyon* **2020**, *6,4*, e03663,1-6, doi:10.1016/j.heliyon.2020.e03663.
59. Gao, W.; Ran, C.; Wang, M.; Li, L.; Sun, Z.; Yao, X. The role of reduction extent of graphene oxide in the photocatalytic performance of Ag/AgX (X = Cl, Br)/rGO composites and the pseudo-second-order kinetics reaction nature of the Ag/AgBr system. *Physical Chemistry Chemical Physics* **2016**, *18,27*, 18219–18226.
60. Cogulet, A.; Blanchet, P.; Landry, V. Wood degradation under UV irradiation: A lignin characterization. *Journal of Photochemistry and Photobiology B: Biology* **2016**, *158*, 184–191.
61. De Vasconcelos, G. C. M. S.; De Carvalho, L. H.; Barbosa, R.; De Cássia De Lima Idalino, R.; Alves, T. S. Effects of weathering on mechanical and morphological properties cork filled green polyethylene eco-composites. *Polímeros* **2020**, *30 (1)*.
62. Badji, C.; Soccalingame, L.; Garay, H.; Bergeret, A.; Bénézet, J. C. Influence of weathering on visual and surface aspect of wood plastic composites: Correlation

approach with mechanical properties and microstructure. *Polymer Degradation and Stability* **2017**, *137*, 162–172.
63. Pandey, K. K. Study of the effect of photo-irradiation on the surface chemistry of wood. *Polymer Degradation and Stability* **2005**, *90*, 9–20.
64. Molinari, R.; Lavorato, C.; Argurio, P. Visible-Light Photocatalysts and Their Perspectives for Building Photocatalytic Membrane Reactors for Various Liquid Phase Chemical Conversions. *Catalysts* **2020**, *10,1334*, 1–38.
65. Angel, Raquel Del; Durán-Álvarez, Juan C.; and Zanella, R. TiO_2-Low Band Gap Semiconductor Heterostructures for Water Treatment Using Sunlight-Driven Photocatalysis. In *Titanium Dioxide - Material for a Sustainable Environment*; Yang, D., Ed.; IntechOpen, 2018; pp. 1–518 ISBN 978-1-78923-327-8.
66. Lee, Y. J.; Lee, H. S.; Lee, C. G.; Park, S. J.; Lee, J.; Jung, S.; Shin, G. A. Application of PANI/TiO_2 Composite for Photocatalytic Degradation of Contaminants from Aqueous Solution. *Applied Sciences* **2020**, *10,19*, 1–12.
67. Nunes, D.; Fragoso, A. R.; Freire, T.; Matias, M.; Marques, A. C.; Martins, R.; Fortunato, E.; Pimentel, A. Ultrafast Microwave Synthesis of WO_3 Nanostructured Films for Solar Photocatalysis. *physica status solidi (RRL) – Rapid Research Letters* **2021**, *15,9*, 2100196.
68. Moulai, F.; Fellahi, O.; Messaoudi, B.; Hadjersi, T.; Zerroual, L. Electrodeposition of nanostructured γ-MnO_2 film for photodegradation of Rhodamine B. *Ionics* **2018**, *24,7*, 2099–2109.
69. Zhang, K.; Yang, Y.; Xu, M.; Cheng, T.; Zhou, G. Synthesis of Mackinawite (FeSm) and its heterogeneous Fenton-like catalytic degradation performance of rhodamine B. *Water Science and Technology* **2022**, *85,3*, 354–366.

4

DEVELOPMENT AND CHARACTERIZATION OF TiO_2 ON 3D-PRINTED ARCHITECTURES

The next section was adapted from the publication: Xue, R.; Matias, M. L.; Pimentel, A.; Pinto, J. V.; Fortunato, E.; Martins, R. Photocatalytic Activity of 3D Printed TiO_2 Architectures Under Solar Radiation. In *Photocatalysis for Environmental Remediation and Energy Production*; Green Chemistry and Sustainable Technology; Springer International Publishing, 2023; pp. 79–100 ISBN 978-3-031-27706-1.

4.1 Introduction

This study reports the fabrication of 3D-printed TiO_2 macro-architectures for evaluation as photocatalysts in water purification under solar radiation. The 3D structures, designed as blocks, were manufactured using an SLA 3D printer. TiO_2 nanopowder synthesized through MW irradiation was subsequently impregnated onto the printed block using a simple mixing approach before the UV curing of the resin. MW synthesis was also employed to directly produce TiO_2 thin films on the macro-architectures, after impregnation and without the need for a seed layer. 3D structures with two different sizes, different numbers of holes, and crossed channels were fabricated (see section 2.1.2.3). The 3D materials were designed to increase the reaction/exposed area, with strong adsorption capacity and high catalytic activity for pollutant degradation under solar radiation. The structural characterization of the nanopowders and 3D-printed materials, after impregnation or MW synthesis, was carried out by XRD and SEM coupled with EDS. The optical properties were assessed for the TiO_2 nanostructures through DRS studies. The photocatalytic activities of the 3D-printed architectures were evaluated for RhB degradation under solar radiation. Additionally, the reusability of the most effective photocatalyst was examined.

The materials will hereafter be referred to as (see table below, Table 4.1):

Table 4.1: Assigned names and description of the synthesized materials.

Assigned names	Description of the synthesized materials
L-TiO_2	Large structure with just the impregnation of TiO_2 nanostructures
T-TiO_2	Thin structure with just the impregnation of TiO_2 nanostructures
L-TiO_2:MW	Large structure with the impregnation of TiO_2 nanostructures that was further subjected to MW synthesis
T-TiO_2:MW	Thin structure with the impregnation of TiO_2 nanostructures that was further subjected to MW synthesis

4.2 Results and discussion

4.2.1 Structural and optical characterization of the TiO_2 nanopowder

4.2.1.1 XRD

The TiO_2 nanopowder produced under MW irradiation was analysed by XRD, and the obtained results are shown in Figure 4.1. The TiO_2 crystalline phase present in the nanopowder is anatase with tetragonal crystallographic structure and no other secondary phases were detected. The characteristic reflections of the TiO_2 anatase phase positioned at $2\theta = 25.25°$, 37.71° and 48.01° are assigned to (101), (004), and (200), respectively [1]. Moreover, no other peaks associated with impurities, such as $Ti(OH)_4$ were found. The mean particle size calculated from Scherrer's equation [2] was 10 nm.

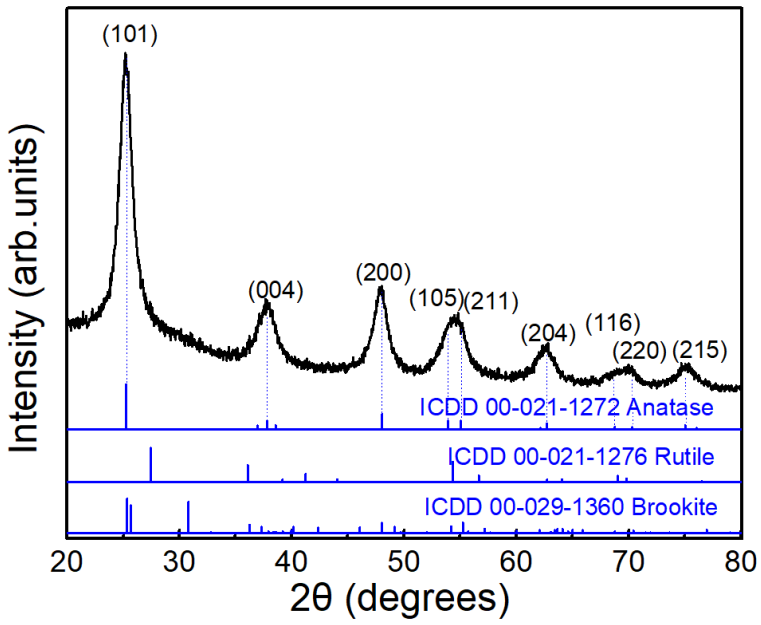

Figure 4.1: XRD diffractogram of the produced TiO_2 nanopowder. The simulated TiO_2 anatase, rutile and brookite structures are also presented for comparison.

4.2.1.2 Electron microscopy and optical measurements

Figure 4.2 (a) shows the SEM image of the TiO_2 nanostructures synthesized under MW irradiation. The MW synthesis resulted in very fine particles, with a morphology resembling nanospheres. The average sphere diameter calculated was 17.05 ± 3.45 nm. DRS studies were carried out for the TiO_2 nanopowder. Its optical band gap value (E_g) value was determined through the Tauc method. The Tauc equation (4.1) is described as follows [3]:

$$(\alpha h\nu)^{1/m} = B(h\nu - E_g) \quad (4.1)$$

where α is the absorption coefficient, h is the Planck constant, ν is the photon's frequency, B is an energy-independent constant, and m is a constant that depends on the nature of the electron transition and is equal to ½ for allowed direct transitions and 2 for allowed indirect transitions [4]. Additionally, the corresponding absorption spectra (α) can be substituted by the measured reflectance, R, through the application of the Kubelka−Munk function ($F(R)$, equation (4.2)) [5,6]:

$$F(R) = \frac{(1-R)^2}{2R} = \frac{k}{s} \quad (4.2)$$

in which k represents the absorption coefficient and s is the scattering coefficient. The optical band gap values can be obtained by extrapolating the linear part of the plots relating $(F(R)h\nu)^{1/m}$ and $(h\nu)$ to $(F(R)h\nu)^{1/m} = 0$, Figure 4.2 (b) [7]. This approach is frequently used in the literature for estimating the band gap energy values. However, in the case of nanoparticles, their high surface area may contribute to absorption, potentially leading to inaccuracies in the calculated band gap values. Nevertheless, for comparison purposes with the literature, this was the method employed [8–10]. The direct band gap value estimated was 3.22 eV, which is within the reported values for the TiO_2 anatase phase [11,12]. A direct band gap was considered since it was previously reported that for very fine TiO_2 anatase nanoparticles, the direct transition is more favorable [13].

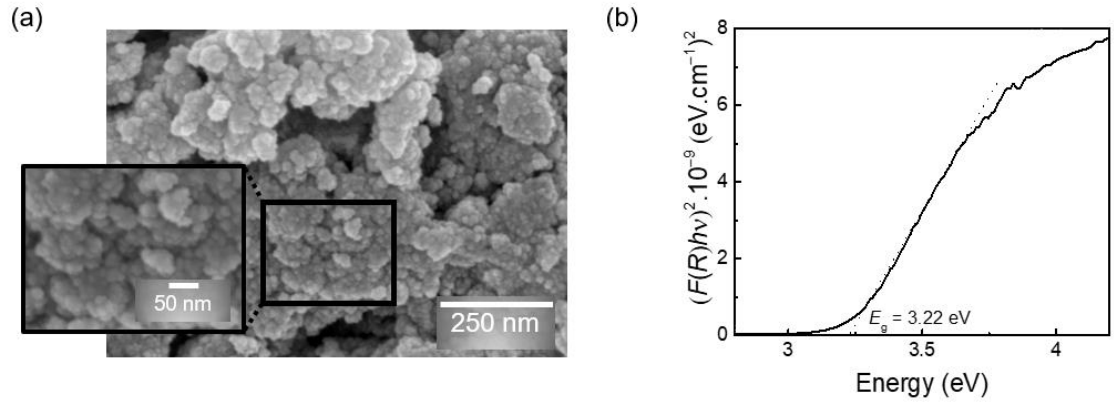

Figure 4.2: (a) SEM image of the TiO_2 nanostructures, and (b) displays the $(F(R)hv)^{1/m}$ *vs.* (hv) plots to estimate the optical band gap of the TiO_2 nanostructures.

4.2.2 Structural characterization and photocatalytic performance of the 3D-printed architectures

4.2.2.1 Electron microscopy

Figure 4.3 shows the SEM images of the 3D-printed architectures following the impregnation with TiO_2 nanostructures and subsequent MW synthesis. Since both large and thin structures were fabricated under identical conditions and parameters, they exhibited the same characteristics. Therefore, only the results for the large structure are discussed in this section. Figure 4.3 (a) clearly demonstrates that MW irradiation does not compromise the integrity of the printed block structure or its cavities. Figure 4.3 (a) and (c) confirm the successful impregnation of TiO_2 nanopowder on the surface of 3D-printed blocks. Figure 4.3 (b) shows TiO_2 agglomerates in the micrometer size range, evenly distributed within the resin matrix. Nevertheless, using the mixing approach, the TiO_2 nanostructures remain as large agglomerates, without achieving a uniform coating on the surface of the printed blocks. SLA 3D printing techniques require a UV post-curing process after printing to transform monomers into highly crosslinked polymer networks [14]. During the curing process, the printed blocks undergo thermal expansion due to exposure to UV light and temperature exposure [15,16]. Consequently, the final block tends to shrink as it cools to room temperature, resulting in a reduction in size and an enhancement in mechanical properties compared to the raw printed material before UV curing [17,18]. Hence, impregnating TiO_2 nanostructures on the surface of the uncured printed block allows them to gradually adhere to the resin during the UV curing process, ensuring they remain attached to the surface after curing and cooling processes.

The 3D-printed architectures following impregnation were subjected to MW irradiation. As shown in Figure 4.3 (c), this process resulted in a complete coverage of the printed block, forming a continuous and uniform TiO_2 thin film composed of TiO_2 nanospheres. This continuous film effectively coated the exterior of the printed blocks, while the MW synthesis also provided coverage of the interior walls of both structures. Similar to other rough substrates, the formation of TiO_2 thin films without any seed layer or chemical treatment for adhesion is expected to be due to substrate roughness, which promotes nucleation and fixation of the TiO_2 structures [19,20]. Moreover, the thickness of this film could not be inferred precisely due to the roughness of the surface and observed heterogeneities since the micrometer-sized TiO_2 agglomerates from the previous impregnation remain visible even after MW synthesis.

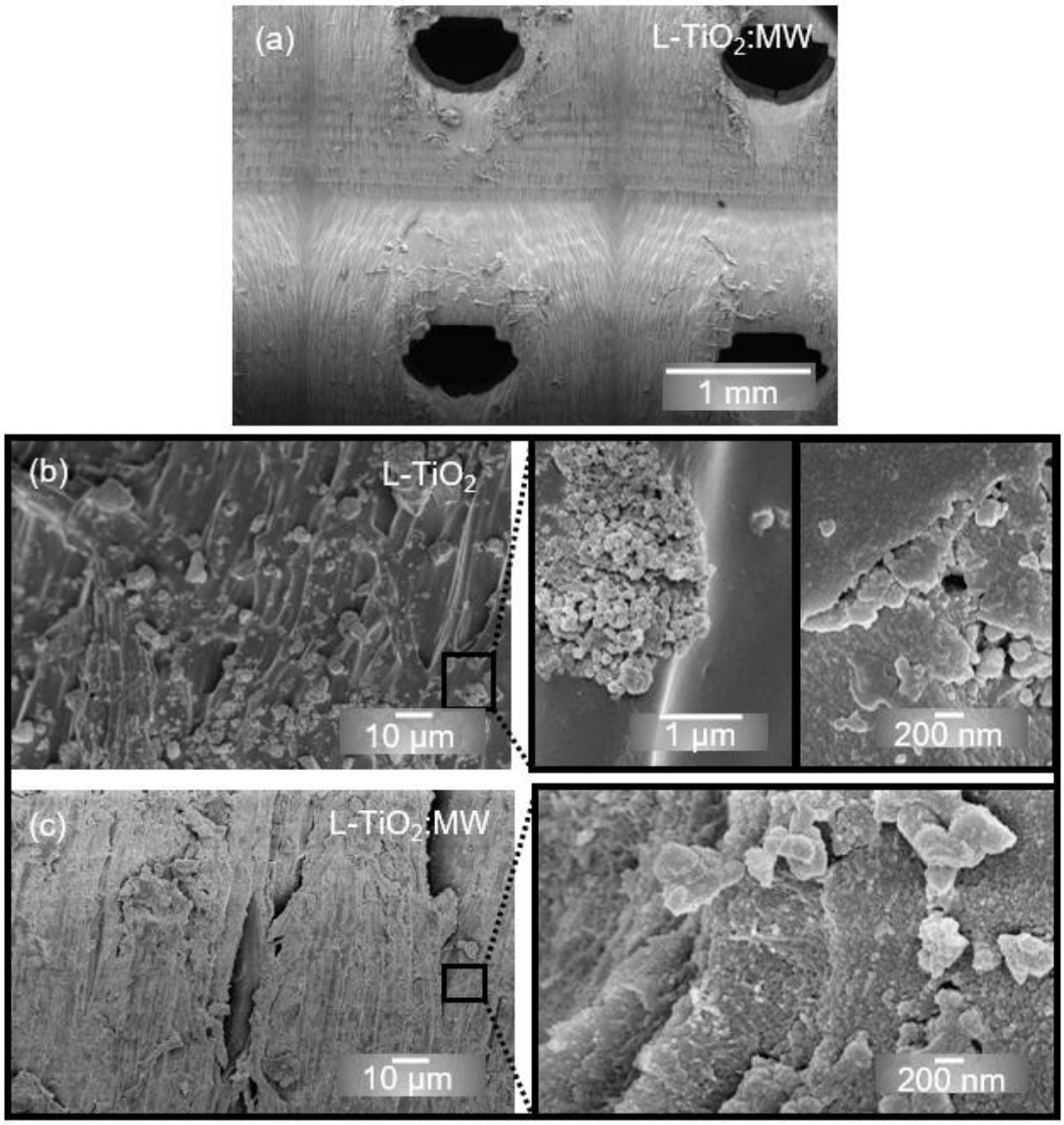

Figure 4.3: SEM images of a 3D-printed macro-architecture in (a) together with the surface of the printed block following the impregnation of TiO_2 nanostructures (L-TiO_2) in (b), and after the impregnation of TiO_2 followed by the MW synthesis (L-TiO_2:MW) in (c). The insets show the TiO_2 agglomerates in (b) and the formation of a TiO_2 thin film in (c).

EDS analyses were also carried out and are presented in Figure 4.4. The presence of C, O, and Ti was observed in both conditions studied. The prominent signal of C is attributed to the resin used for 3D printing. As expected from the SEM images in Figure 4.3 (b), Ti appears as micrometer-sized agglomerates in the L-TiO_2 printed block. In contrast, the L-TiO_2:MW material exhibits a more uniform distribution of Ti (Figure 4.4 (h)), with a stronger signal throughout the material, confirming the homogeneous covering of its surface. No impurities were detected.

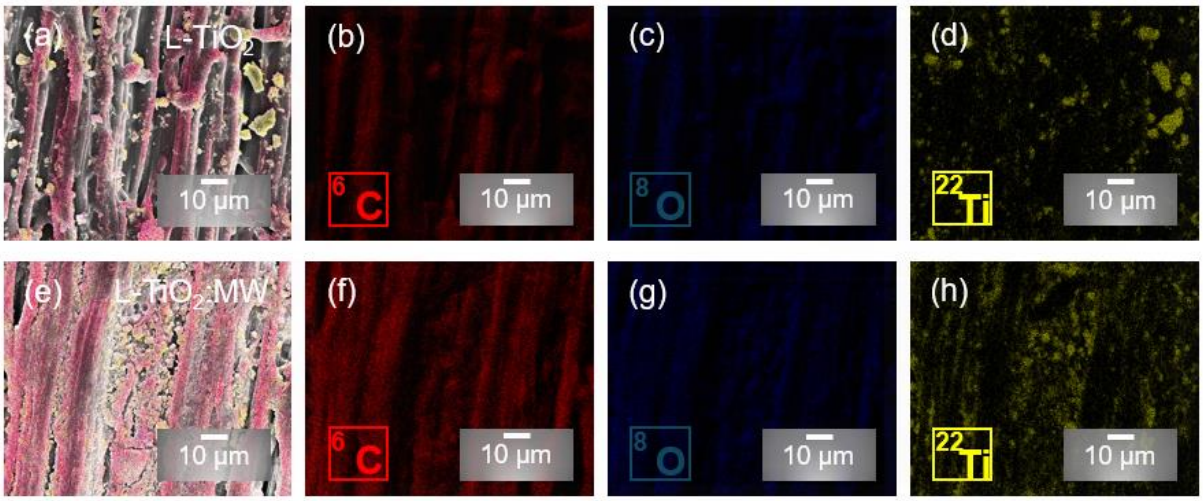

Figure 4.4: SEM and EDS analyses on the 3D-printed TiO_2 macro-architectures after the impregnation with TiO_2 nanostructures (L-TiO_2) in (a) and after impregnation + MW synthesis (L-TiO_2:MW) in (e). The corresponding EDS maps of C (b and f), O (c and g), and Ti (d and h) are also visible.

4.2.2.2 Photocatalytic activity of the 3D-printed TiO_2 architectures

The photocatalytic activity of the 3D-printed TiO_2 macro-architectures was evaluated through the degradation of RhB under solar radiation using a sun simulator. Both large and thin structures were considered with the TiO_2 impregnation, and they were compared to those impregnated and then subjected to MW synthesis. The contribution of the 3D-printed block without TiO_2 nanostructures to the RhB degradation was also studied.

Figure 4.5 (a) to (d) show the RhB absorbance spectra at various solar exposure times with the different 3D-printed TiO_2 architectures acting as photocatalytic agents. After the photocatalytic experiments, a pinkish coloration can be observed on the 3D-printed blocks. Figure 4.6 presents the degradation ratio (C/C_0) *vs.* exposure time, where C is the concentration of the pollutant at each exposure time and C_0 is the initial solution concentration [21]. The gradual RhB degradation under solar radiation could be inferred for all conditions up to 360 min. A 3D-printed block without TiO_2 nanostructures was also measured during the solar radiation exposure experiments and no significant RhB photodegradation was observed over time (Figure 4.6 (a)).

The limit of 360 min was imposed due to the first appearance of a hypsochromic shift. This shift is a consequence of self-photosensitization of the dye when exposed to visible light. This behavior is commonly observed when conducting visible light-assisted photocatalysis using dyes [22,23]. Apart from the decomposition of the dye through the destruction of chromophore structure in the photocatalytic process, RhB molecules can shift to an excited state

under visible light. During their excited state, they transfer electrons to the CB of the photocatalyst and RhB cation radicals ($RhB^{\bullet+}$) are formed, which are responsible for the successive N-deethylation reactions. This process is not governed by reactive oxygen species and involves the sequential removal of ethyl groups from the amino nitrogen atoms, leading to a hypsochromic shift in both the absorption and emission maxima [24–26]. N-deethylation of RhB is known to be a stepwise process, in which the N-deethylated products are responsible for the gradual hypsochromic shift in the absorbance peak [27,28] Hence, when hypsochromic shift starts to appear, it means that the degradation of RhB is no longer predominantly due to the action of the photocatalyst.

As shown in Figure 4.5 and Figure 4.6, the large structure condition (L) demonstrated a better performance compared to the thin structure (T). This behavior was expected due to the higher number of cavities (more channels for reaction) and larger reaction/exposed area. Moreover, the design of crossed channels is expected to maximize the contact between the solution and photocatalyst, increasing the photocatalytic efficiency of the printed blocks. Both L-TiO_2 and L-TiO_2:MW materials (Figure 4.5 (a) and (c)) reached RhB degradation values of 72 %. Nevertheless, the L-TiO_2:MW material was more effective regarding the RhB photodegradation under solar radiation, reaching the threshold/hypsochromic shift earlier than the L-TiO_2. The T-TiO_2 material reached 31 % of RhB degradation (Figure 4.5 (b)), while the T-TiO_2:MW degraded 44 % for the same exposure time (Figure 4.5 (d)). Comparing both large and thin 3D-printed structures subjected to MW synthesis, the larger structure was 28 % more efficient (Figure 4.5 (c) and (d)).

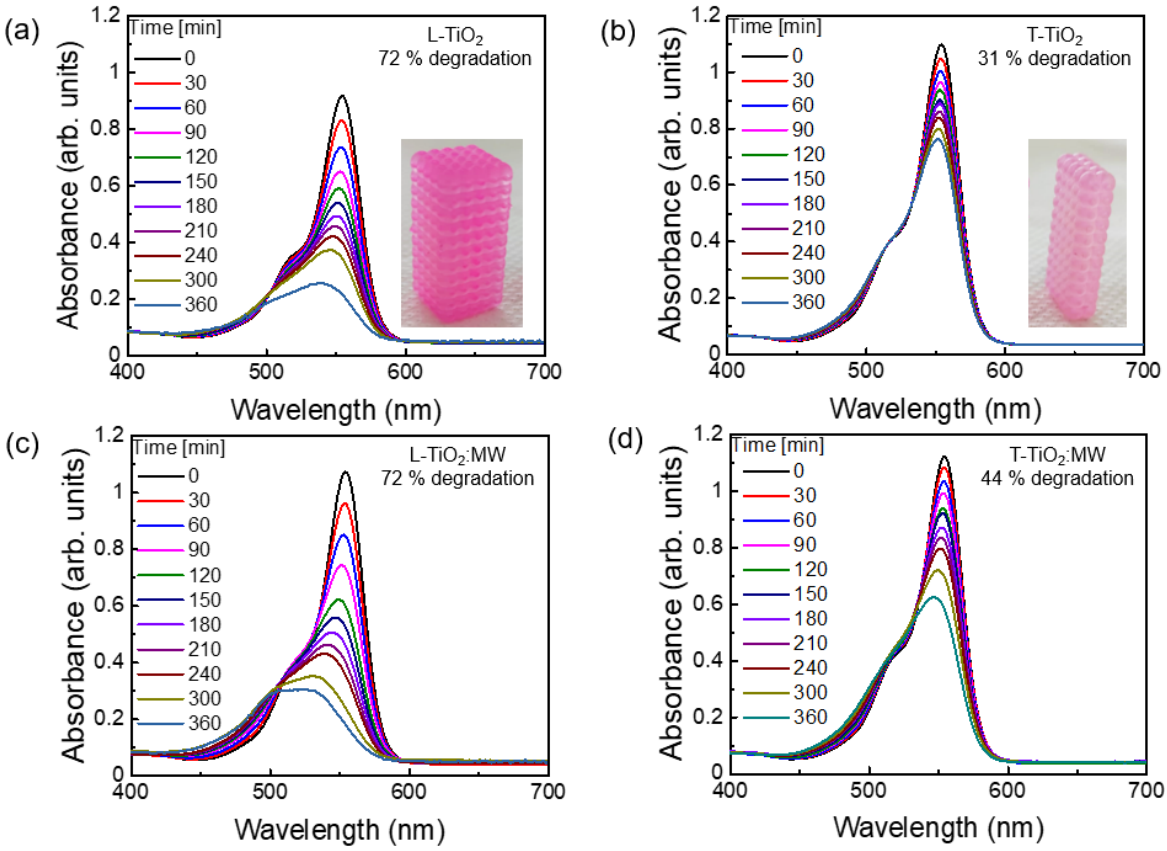

Figure 4.5: RhB absorbance spectra under solar radiation at RT with (a) the L-TiO_2 material, (b) T-TiO_2 material, (c) L-TiO_2:MW material and (d) T-TiO_2:MW material. The slight differences in the initial values (0 min) are related to different concentrations of RhB solutions used in the photocatalytic measurements. The insets show the photographic images of the 3D-printed blocks after photocatalysis in (a) and (b).

To enable quantitative comparison between the 3D-printed TiO_2 architectures, the photocatalytic reaction rates were determined (Figure 4.6). The calculated reaction rates were: 0.0038 min^{-1} for the L-TiO_2:MW, 0.0034 min^{-1} for the L-TiO_2, 0.0015 min^{-1} for the T-TiO_2:MW, 0.0011 min^{-1} for the T-TiO_2 and 0.000283 min^{-1} for the 3D-printed block without TiO_2 nanostructures. The pseudo-first-order rate constant was calculated from the slope of ln (C_0/C) *vs.* the solar radiation exposure time (t) [29]. The photocatalytic reaction rate was higher for the L-TiO_2:MW attesting its superior photocatalytic activity under solar radiation. The photocatalytic activity relies on several factors including the band gap energy, crystallite size, degree of crystallinity, specific surface area, and active facets, among others [30,31]. In this work, the impregnated TiO_2 nanostructures were investigated, revealing that MW synthesis resulted in very fine spherical particles (~17 nm as calculated from SEM images) with the TiO_2 anatase phase and an optical band gap value within the values reported for the anatase phase [11,32].

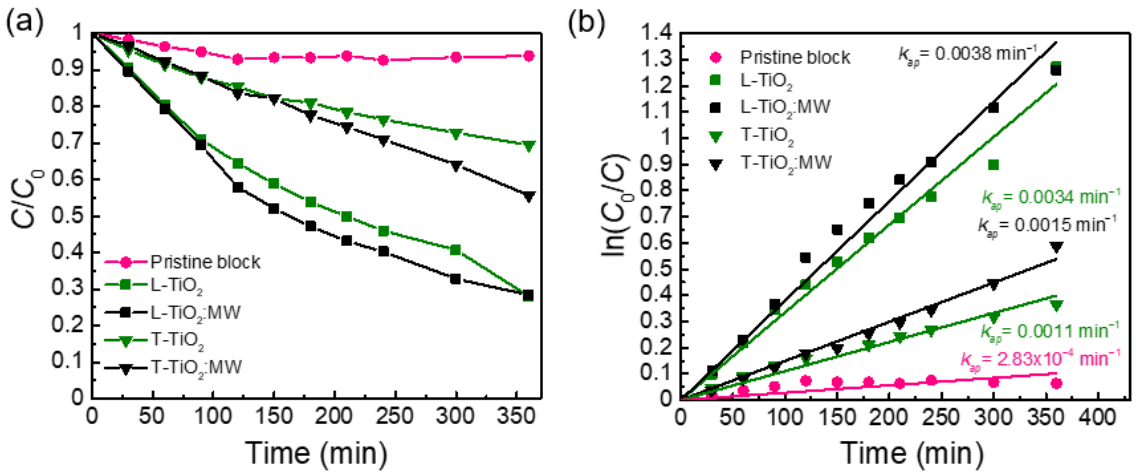

Figure 4.6: RhB degradation ratio (C/C_0) *vs.* exposure time for the 3D-printed TiO_2 architectures under solar radiation in (a) together with the corresponding photocatalytic reaction rates with the respective fitting curves in (b).

The nano-sized particles exhibit an enhanced redox capability, as they facilitate the migration of electrons and holes to their surface while suppressing electron–hole recombination, thereby improving the photocatalytic performance [33]. Therefore, for all conditions investigated, a significant contribution from the TiO_2 nanostructures is expected due to the typically higher specific surface area associated with smaller particles [34]. However, since all the 3D-printed TiO_2 macro-architectures were impregnated with TiO_2 nanostructures using the same approach, a similar contribution from these particles is anticipated across all the materials.

The printed design, including the size, number of holes, and crossed channels of the 3D-printed macro-architectures significantly influenced the overall photocatalytic activity. The larger structure exhibited a calculated surface/exposed area 2.5 times greater than that of the thinner structure, providing a higher number of holes and channels for reaction. Consequently, the improved photocatalytic efficiency is attributed to the design of the 3D-printed block. The correlation between the design of 3D-printed materials and their photocatalytic activity has been demonstrated in previous studies. Elkero *et al.* reported the production of 3D-printed Au/TiO_2 monoliths for the photogeneration of hydrogen from water/ethanol gaseous mixtures under dynamic conditions and UV radiation [35]. The influence of the microfilaments' diameter on the photocatalytic activity was demonstrated. It was found that the diameter of the microfilaments was a critical design parameter for the efficient photoproduction of hydrogen because it determined the total geometric exposed area. 3D-printed monoliths with filaments of 580, 410 and 200 µm in diameter were produced, and the 200 µm microfilament was more efficient since it had more channels for reaction. It can also be concluded that using MW synthesis to produce a TiO_2 thin film after the impregnation of TiO_2 nanostructures

enhanced the photocatalytic activity of the larger 3D blocks. The entire and even coverage of the printed block surface (exterior and interior walls) effectively accelerated RhB photodegradation under solar radiation, achieving the threshold/hypsochromic shift more quickly compared to the L-TiO_2 material (compare Figure 4.5 (a) with Figure 4.5 (c)). Moreover, as observed in Figure 4.3 (c), the thin film consists of nanospheres. Therefore, the improved photocatalytic efficiency of the L-TiO_2:MW can also be attributed to the presence of TiO_2 nanostructures composing the thin film [20,36].

Regarding the photocatalytic stability of the 3D-printed macro-architectures, cycling tests were carried out with the best photocatalyst, i.e., L-TiO_2:MW. Before the next cycle, the photocatalyst was washed with water, subjected to UV light for 15 min, and then reintroduced into a container with a fresh RhB solution. The results reveal its reusability over time (Figure 4.7 (a) and (b)). Figure 4.7 (a) demonstrates that the 3D-printed block can be reused multiple times without any significant loss in its photocatalytic efficiency. The reaction rates were 0.0038, 0.0035 and 0.0037 min^{-1} (Figure 4.7 (b)) for the first, second and third cycles, respectively, attesting the consistent RhB degradation under solar radiation after several cycling tests.

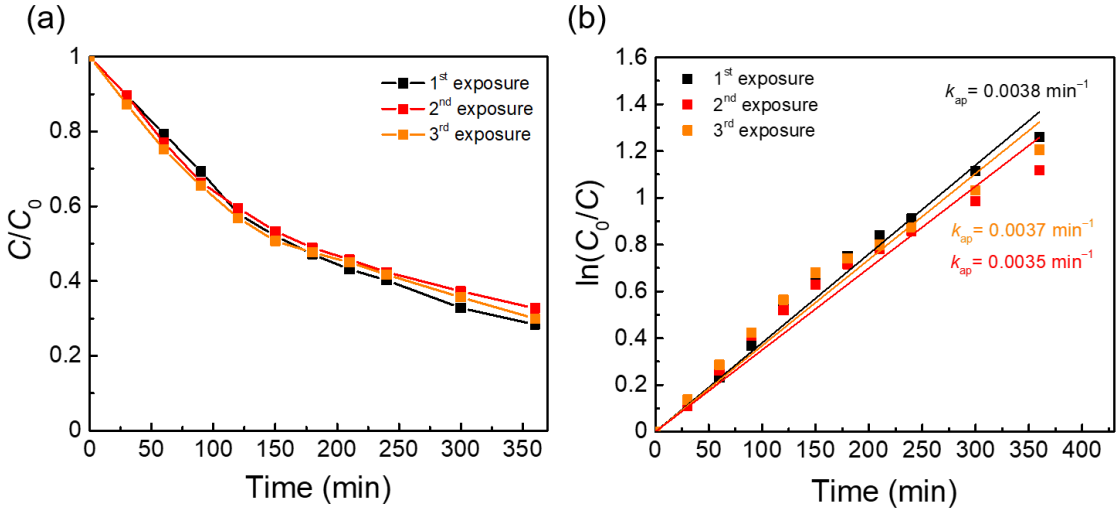

Figure 4.7: (a) Three different cycles of RhB degradation ratio (C/C_0) *vs.* exposure time for the L-TiO_2:MW material under solar radiation. (b) Photocatalytic reaction rates with the respective fitting curves.

The photocatalytic experiments showed that combining 3D printing with the simple mixing of TiO_2 nanostructures produced under MW irradiation, followed by MW synthesis to create uniform TiO_2 thin films, allowed the fabrication of enhanced photocatalysts with excellent stability and superior reusability when exposed to solar radiation. The produced materials

also eliminate the need for recovering powder, particularly nanopowder, which represents a huge drawback in wastewater cleaning treatments.

4.3 Summary

3D-printed macro-architectures were successfully produced using the SLA 3D printing technique by exploring two distinct sizes with a different number of holes and crossed channels. A novel method was demonstrated by impregnating the photocatalyst onto the printed block. In this approach, the TiO_2 nanostructures produced under MW irradiation were incorporated into the resin before UV curing by directly mixing the powder. This eliminated the need for pre- or post-processing steps, thereby reducing additional costs and avoiding time-consuming techniques. To improve the photocatalytic activity of the printed blocks, MW synthesis was used to produce TiO_2 thin films without a seed layer, after the impregnation of TiO_2 nanostructures. The TiO_2 nanostructures synthesized under MW irradiation resulted in the formation of very fine TiO_2 anatase particles that appeared as spheres, as well as in the thin film. The photocatalytic activity of the 3D-printed architectures was assessed by evaluating the degradation of RhB under solar radiation, with the best photocatalyst achieving a degradation of 72 %. The larger structure exhibited higher degradation rates than the thin structure, owing to the greater number of holes/channels for reaction and a larger reaction/exposed area. Therefore, the design of the structures was crucial in determining the final photocatalytic performance. Moreover, the presence of the MW-synthesized TiO_2 thin film, along with the TiO_2 impregnated agglomerates, accounted for the improved photocatalytic performance observed in the materials studied. The best photocatalyst (L-TiO_2:MW) also displayed stability and reusability over time. The 3D-printed blocks developed in this study, combined with the MW-synthesized TiO_2 nanostructures resulted in stable and reusable photocatalysts. These provide an alternative to powdered photocatalysts and can be produced using simple, fast, and less energy-consuming methods that are easily scalable for real-world applications.

4.4 References

1. Thamaphat, K.; Limsuwan, P.; Ngotawornchai, B. Phase Characterization of TiO_2 Powder by XRD and TEM. *Agriculture and Natural Resources* **2008**, *42*, 357–361.
2. Cullity, B. D.; Stock, S. R. *Elements of X-Ray Diffraction*; 3rd ed.; Pearson: USA, 2014; ISBN 1269374508.

3. Aydın, C.; Benhaliliba, M.; Al-Ghamdi, A. A.; Gafer, Z. H.; El-Tantawy, F.; Yakuphanoglu, F. Determination of optical band gap of ZnO:$ZnAl_2O_4$ composite semiconductor nanopowder materials by optical reflectance method. *Journal of Electroceramics* **2013**, *31*, 265–270, doi:10.1007/S10832-013-9829-5.
4. Haryński, Ł.; Olejnik, A.; Grochowska, K.; Siuzdak, K. A facile method for Tauc exponent and corresponding electronic transitions determination in semiconductors directly from UV–Vis spectroscopy data. *Optical Materials* **2022**, *127*, 112205, doi:10.1016/J.OPTMAT.2022.112205.
5. Yang, L.; Kruse, B. Revised Kubelka–Munk theory. I. Theory and application. *Journal of the Optical Society America A* **2004**, *21*, 1933–1941, doi:10.1364/JOSAA.21.001933.
6. Landi, S.; Rocha Segundo, I.; Freitas, E.; Vasilevskiy, M.; Carneiro, J.; Tavares, C. J. Use and misuse of the Kubelka-Munk function to obtain the band gap energy from diffuse reflectance measurements. *Solid State Communications* **2022**, *341*, 1–7.
7. Gu, Y. e.; Su, X.; Du, Y.; Wang, C. Preparation of flower-like Cu_2O nanoparticles by pulse electrodeposition and their electrocatalytic application. *Applied Surface Science* **2010**, *256*, 5862–5866, doi:10.1016/J.APSUSC.2010.03.065.
8. Gholizadeh, Z.; Aliannezhadi, M.; Ghominejad, M.; Tehrani, F. S. High specific surface area γ-Al_2O_3 nanoparticles synthesized by facile and low-cost co-precipitation method. *Scientific Reports* **2023**, *13*, 1–14, doi:10.1038/s41598-023-33266-0.
9. Abdullah, B. J. Size effect of band gap in semiconductor nanocrystals and nanostructures from density functional theory within HSE06. *Materials Science in Semiconductor Processing* **2022**, *137*, 1–10, doi:10.1016/J.MSSP.2021.106214.
10. Makuła, P.; Pacia, M.; Macyk, W. How To Correctly Determine the Band Gap Energy of Modified Semiconductor Photocatalysts Based on UV-Vis Spectra. *Journal of Physical Chemistry Letters* **2018**, *9*, 6814–6817.
11. Reyes-Coronado, D.; Rodríguez-Gattorno, G.; Espinosa-Pesqueira, M. E.; Cab, C.; De Coss, R.; Oskam, G. Phase-pure TiO_2 nanoparticles: anatase, brookite and rutile. *Nanotechnology* **2008**, *19*, 145605, doi:10.1088/0957-4484/19/14/145605.
12. Dette, C.; Pérez-Osorio, M. A.; Kley, C. S.; Punke, P.; Patrick, C. E.; Jacobson, P.; Giustino, F.; Jung, S. J.; Kern, K. TiO_2 anatase with a bandgap in the visible region. *Nano Letters* **2014**, *14*, 6533–6538, doi:10.1021/NL503131S.
13. Reddy, K. M.; Manorama, S. V.; Reddy, A. R. Bandgap studies on anatase titanium dioxide nanoparticles. *Materials Chemistry and Physics* **2003**, *78*, 239–245, doi:10.1016/S0254-0584(02)00343-7.
14. Decker, C. UV-radiation curing chemistry. *Pigment & Resin Technology* **2001**, *30*, 278–286, doi:10.1108/03699420110404593.
15. Park, J. K.; Hur, B.; Ko, C. C.; García-Godoy, F.; Kim, H. I. L.; Kwon, Y. H. Effect of light-curing units on the thermal expansion of resin nanocomposites. *American Journal of Dentistry* **2010**, *23*, 331.
16. Shardakov, I. N.; Trufanov, A. N. Identification of the Temperature Dependence of the Thermal Expansion Coefficient of Polymers. *Polymers* **2021**, *13*, 3035, doi:10.3390/POLYM13183035.
17. Uzcategui, A. C.; Muralidharan, A.; Ferguson, V. L.; Bryant, S. J.; McLeod, R. R. Understanding and Improving Mechanical Properties in 3D printed Parts Using a Dual-

Cure Acrylate-Based Resin for Stereolithography. *Advanced Engineering Materials* **2018**, *20*, 1800876, doi:10.1002/ADEM.201800876.
18. Martín-Montal, J.; Pernas-Sánchez, J.; Varas, D. Experimental Characterization Framework for SLA Additive Manufacturing Materials. *Polymers* **2021**, *13*, 1147, doi:10.3390/POLYM13071147.
19. Nunes, D.; Pimentel, A.; Araujo, A.; Calmeiro, T. R.; Panigrahi, S.; Pinto, J. V.; Barquinha, P.; Gama, M.; Fortunato, E.; Martins, R. Enhanced UV Flexible Photodetectors and Photocatalysts Based on TiO_2 Nanoplatforms. *Springer Nature* **2018**, *61*, 1591–1606.
20. Freire, T.; Fragoso, A. R.; Matias, M.; Vaz Pinto, J.; Marques, A. C.; Pimentel, A.; Barquinha, P.; Huertas, R.; Fortunato, E.; Martins, R.; Nunes, D. Enhanced solar photocatalysis of TiO_2 nanoparticles and nanostructured thin films grown on paper. *Nano Express* **2021**, *2,4*, 1–20.
21. Zhou, N.; Polavarapu, L.; Gao, N.; Pan, Y.; Yuan, P.; Wang, Q.; Xu, Q. H. TiO_2 coated Au/Ag nanorods with enhanced photocatalytic activity under visible light irradiation. *Nanoscale* **2013**, *5*, 4236–4241, doi:10.1039/C3NR00517H.
22. Zhang, Y.; Zhou, J.; Li, Z.; Feng, Q. Photodegradation pathway of rhodamine B with novel Au nanorods @ ZnO microspheres driven by visible light irradiation. *Journal of Materials Science* **2018**, *53*, 3149–3162, doi:10.1007/S10853-017-1779-X.
23. Chen, F.; Zhao, J.; Hidaka, H. Highly selective deethylation of rhodamine B: Adsorption and photooxidation pathways of the dye on the TiO_2/SiO_2 composite photocatalyst. *International Journal of Photoenergy* **2003**, *5*, 209–217, doi:10.1155/S1110662X03000345.
24. He, Z.; Sun, C.; Yang, S.; Ding, Y.; He, H.; Wang, Z. Photocatalytic degradation of rhodamine B by Bi_2WO_6 with electron accepting agent under microwave irradiation: Mechanism and pathway. *Journal of Hazardous Materials* **2009**, *162*, 1477–1486, doi:10.1016/J.JHAZMAT.2008.06.047.
25. Nunes, D.; Fragoso, A. R.; Freire, T.; Matias, M.; Marques, A. C.; Martins, R.; Fortunato, E.; Pimentel, A. Ultrafast Microwave Synthesis of WO_3 Nanostructured Films for Solar Photocatalysis. *physica status solidi (RRL) – Rapid Research Letters* **2021**, *15,9*, 2100196.
26. Jakimińska, A.; Pawlicki, M.; Macyk, W. Photocatalytic transformation of Rhodamine B to Rhodamine-110 – The mechanism revisited. *Journal of Photochemistry and Photobiology A: Chemistry* **2022**, *433*, 114176, doi:10.1016/J.JPHOTOCHEM.2022.114176.
27. Ferreira, S. H.; Morais, M.; Nunes, D.; Oliveira, M. J.; Rovisco, A.; Pimentel, A.; Águas, H.; Fortunato, E.; Martins, R. High UV and Sunlight Photocatalytic Performance of Porous ZnO Nanostructures Synthesized by a Facile and Fast Microwave Hydrothermal Method. *Materials* **2021**, *14(9)*, 1–17.
28. Rochkind, M.; Pasternak, S.; Paz, Y. Using Dyes for Evaluating Photocatalytic Properties: A Critical Review. *Molecules* **2014**, *20*, 88–110, doi:10.3390/MOLECULES20010088.
29. Thorat, J. H.; Chaudhari, P. D.; Tamboli, M. S.; Arbuj, S. S.; Patil, D. B.; Kale, B. B. Architecture of ZnO nanosheets and nanochips via zinc oxalato-hydrazinate complex. *Journal of Nanoparticle Research* **2014**, *16*, doi:10.1007/S11051-014-2450-Y.
30. Guo, Y.; Li, H.; Chen, J.; Wu, X.; Zhou, L. TiO_2 mesocrystals built of nanocrystals with exposed {001} facets: facile synthesis and superior photocatalytic ability. *Journal of*

Materials Chemistry A **2014**, *2*, 19589–19593, doi:10.1039/C4TA05068A.
31. Nunes, D.; Pimentel, A.; Pinto, J. V.; Calmeiro, T. R.; Nandy, S.; Barquinha, P.; Pereira, L.; Carvalho, P. A.; Fortunato, E.; Martins, R. Photocatalytic behavior of TiO_2 films synthesized by microwave irradiation. *Catalysis Today* **2016**, *278*, 262–270.
32. Fu, W.; Li, G.; Wang, Y.; Zeng, S.; Yan, Z.; Wang, J.; Xin, S.; Zhang, L.; Wu, S.; Zhang, Z. Facile formation of mesoporous structured mixed-phase (anatase/rutile) TiO_2 with enhanced visible light photocatalytic activity. *Chemical Communications* **2017**, *54*, 58–61, doi:10.1039/C7CC05750D.
33. Suttiponparnit, K.; Jiang, J.; Sahu, M.; Suvachittanont, S.; Charinpanitkul, T.; Biswas, P. Role of Surface Area, Primary Particle Size, and Crystal Phase on Titanium Dioxide Nanoparticle Dispersion Properties. *Nanoscale Research Letters* **2011**, *6*, 1–8, doi:10.1007/S11671-010-9772-1.
34. Elkoro, A.; Soler, L.; Llorca, J.; Casanova, I. 3D printed microstructured Au/TiO_2 catalyst for hydrogen photoproduction. *Applied Materials Today* **2019**, *16*, 265–272, doi:10.1016/J.APMT.2019.06.007.
35. Huang, J.; He, Y.; Wang, L.; Huang, Y.; Jiang, B. Bifunctional $Au@TiO_2$ core–shell nanoparticle films for clean water generation by photocatalysis and solar evaporation. *Energy Conversion and Management* **2017**, *132*, 452–459.

5

DEVELOPMENT AND CHARACTERIZATION OF G-C_3N_4/TiO_2 NANOPOWDERS

The next section was adapted from the publication: Matias, M. L.; Reis-Machado, A. S.; Rodrigues, J.; Calmeiro, T.; Deuermeier, J.; Pimentel, A.; Fortunato, E.; Martins, R.; Nunes, D. Microwave Synthesis of Visible-Light-Activated g-C_3N_4/TiO_2 Photocatalysts. *Nanomaterials* **2023**, *13(6)*, doi:10.3390/NANO13061090.

5.1 Introduction

The development of visible-light-driven photocatalysts has become highly appealing for environmental remediation through simple, fast and green chemical methods. A simple, seed-layer-free and fast (1 h) MW-assisted approach is demonstrated to produce g-C_3N_4/TiO_2 heterostructures for the degradation of MO under visible light. The structural, optical and electrochemical characterizations were performed by XRD, SEM and STEM (the last two equipped with EDS detectors), AFM, XPS, UV-VIS absorption, PL spectroscopies, and M–S plots. Different g-C_3N_4 amounts mixed with TiO_2 (15, 30 and 45 wt. %) were investigated for the photocatalytic degradation of MO dye using a solar simulator for up to 240 min (4 h). The materials produced will hereafter be called 15-GCN-T, 30-GCN-T and 45-GCN-T for the 15, 30 and 45 wt. % of g-C_3N_4 in TiO_2, respectively. For a better understanding of the species involved in the photocatalytic degradation process, experiments were performed with reactive oxygen species scavengers. Reusability tests were also carried out up to five consecutive cycles.

5.2 Results and discussion

5.2.1 Structural and optical characterization of the g-C_3N_4/TiO_2 nanopowders

5.2.1.1 XRD

The produced nanopowders, i.e. TiO_2, g-C_3N_4, 15-GCN-T, 30-GCN-T and 45-GCN-T were investigated by XRD. As seen in Figure 5.1, after heat-treating urea at 550 °C for 2 h, two diffraction maxima at 13.2° and 27° (2θ) appear, indexed to the planes (100) and (002) of g-C_3N_4, respectively [1]. According to previous studies, the broad diffraction maximum detected at 13.2° is ascribed to the in-planar structure of repeated N-bridged tri-s-triazine units, whereas the maximum at 27° is attributed to the stacking of the conjugated aromatic systems [2]. A slight shift could be observed in the diffractogram of the produced g-C_3N_4 nanopowder when

compared to the database and, for that reason, the simulated g-C_3N_4 was not present. Nevertheless, the XRD data is consistent with the literature for this material [1–4]. For the pure TiO_2 nanopowder, the experimental XRD diffractograms could be fully ascribed to the anatase TiO_2 phase (ICDD file number 00-021-1272). When it comes to the heterostructures, for all conditions, the TiO_2 anatase diffractograms are also present. On the other hand, when g-C_3N_4 content is increased with respect to TiO_2, a diffraction maximum at 27° appears, indicating the presence of graphitic carbon nitride. This can be observed in the 30-GCN-T and 45-GCN-T nanopowders (identified with black arrows in Figure 5.1), confirming the co-existence of both materials (TiO_2 and g-C_3N_4). The absence of graphitic carbon nitride patterns in the 15-GCN-T nanopowder is likely due to the low percentage present in this material. No further XRD maxima or impurities were detected for all the materials produced.

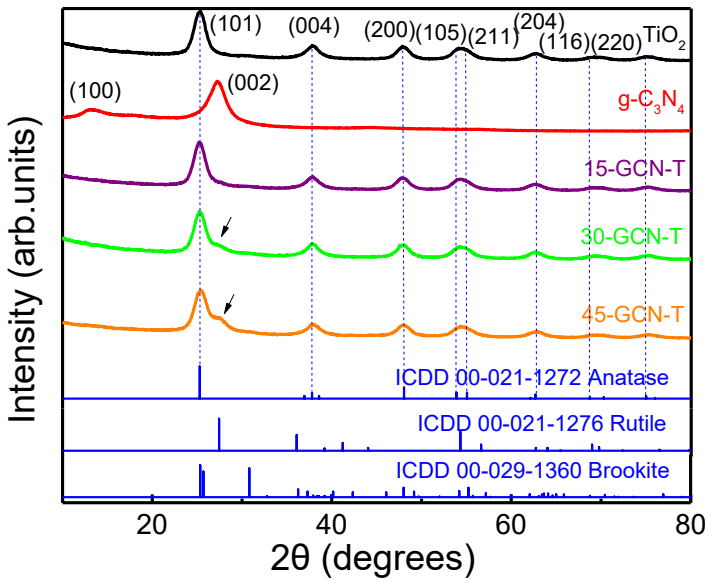

Figure 5.1: XRD diffractograms of TiO_2, g-C_3N_4 and heterostructures composed by TiO_2 with different weight loading percentages of g-C_3N_4 (15-GCN-T, 30-GCN-T and 45-GCN-T). The simulated anatase, rutile and brookite TiO_2 are also shown for comparison. Black arrows indicate the diffraction maximum at 27°, likely associated with the presence of graphitic carbon nitride.

5.2.1.2 Electron microscopy

Figure 5.2 displays the SEM images of TiO_2, g-C_3N_4 and g-C_3N_4/TiO_2 heterostructures. As can be seen in Figure 5.2 (a), the microwave synthesis in the presence of ethanol as solvent resulted in several irregularly shaped particles with an average particle size of 543 ± 135 nm (Figure 5.2 (b)). Figure 5.2 (b) clearly shows that the larger particles are composed of

aggregates of TiO_2 nanocrystals, with the inset highlighting the presence of a hollow sphere. SEM images of g-C_3N_4 are displayed in Figure 5.2 (c) and (d). Graphitic carbon nitride produced by direct calcination resulted in a 2D structure composed of a stack of thin sheets with wrinkles and irregular shapes. Some micro-holes are also perceptible at the surface of the sheets, which were probably formed due to the escape of gases, such as NH_3, during the high-temperature synthesis of g-C_3N_4. Consequently, the gas release could have etched the s-triazine network structure [5]. Figure 5.2 (e)–(j) show the SEM images of the g-C_3N_4/TiO_2 heterostructures. The similar shape and size of the TiO_2 particles observed previously in Figure 5.2 (a) are present in the 15-GCN-T material, covering some areas of the g-C_3N_4 sheets. A TiO_2 film was also formed at the surface of the sheets (Figure 5.2 (f)). Nevertheless, this film did not completely cover the g-C_3N_4 sheets for the 15-GCN-T material. Interestingly, when g-C_3N_4 content was further increased, as shown in Figure 5.2 (g)–(j), the larger TiO_2 particles reduced in size, and smaller TiO_2 agglomerates were formed, composing a film that was expressively thick for the 45-GCN-T material (Figure 5.2 (j)). The close contact between the two materials is thus essential to improve the charge separation and strengthen the photocatalytic activity [6].

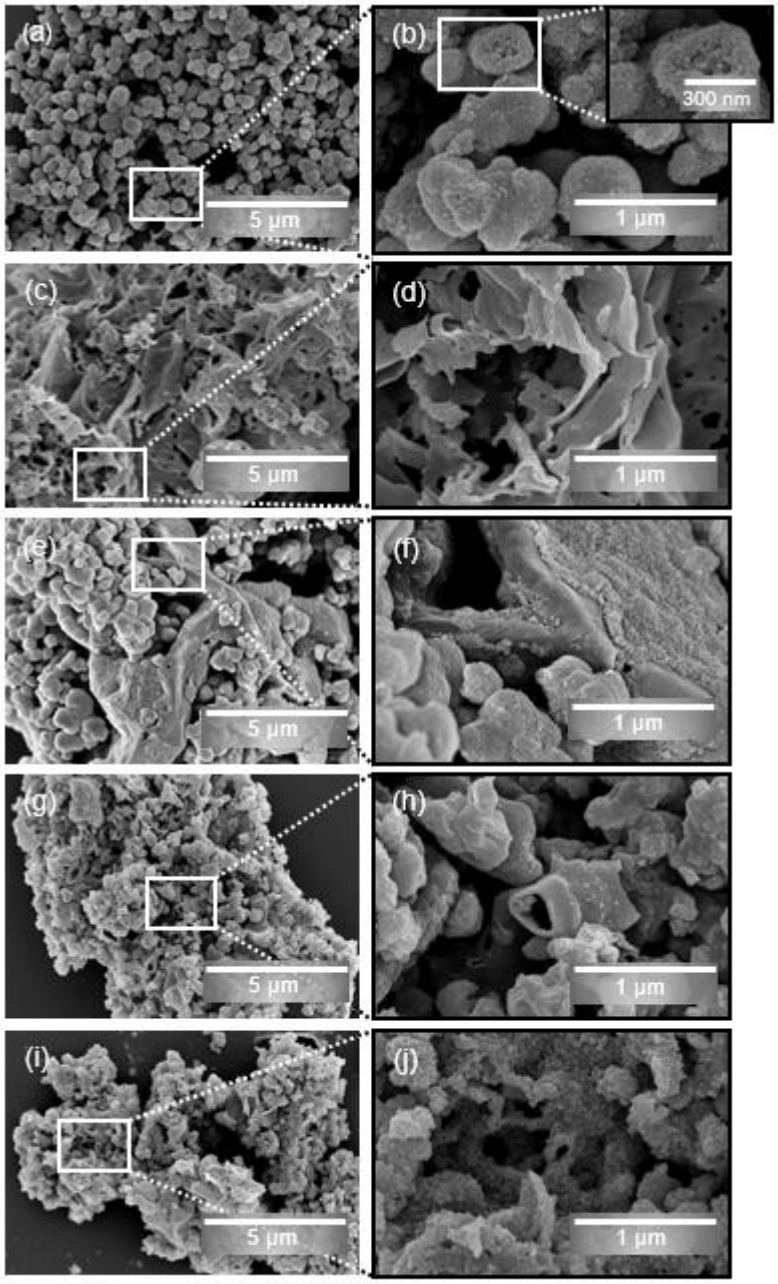

Figure 5.2: SEM images of the produced materials (a) TiO_2, (c) g-C_3N_4, (e) 15-GCN-T, (g) 30-GCT and (i) 45-GCN-T. The respective high-magnification SEM images are shown in ((b),(d),(f),(h),(j)), and (b) also displays an amplified SEM image of a hollow TiO_2 sphere.

Due to the high amount of g-C_3N_4 on the 45-GCN-T material, some g-C_3N_4 nanosheets were not covered by TiO_2, which could result in a faster recombination rate of photogenerated charge carriers and, lastly, a decrease in the photocatalytic activity. For this reason, the 30-GCN-T material was selected to be further investigated. The 30-GCN-T material was investigated using STEM (Figure 5.3). In both STEM and bright-field TEM images (Figure 5.3 (a)–(d)),

the presence of a thin 2D nanostructure with a sheet-like structure is clear. The TiO_2 nanostructures are also clearly discernible in the STEM and TEM images (Figure 5.3 (a)–(g)). The ring diffraction pattern in Figure 5.3 (d) attested that these particles are solely in the anatase TiO_2 phase.

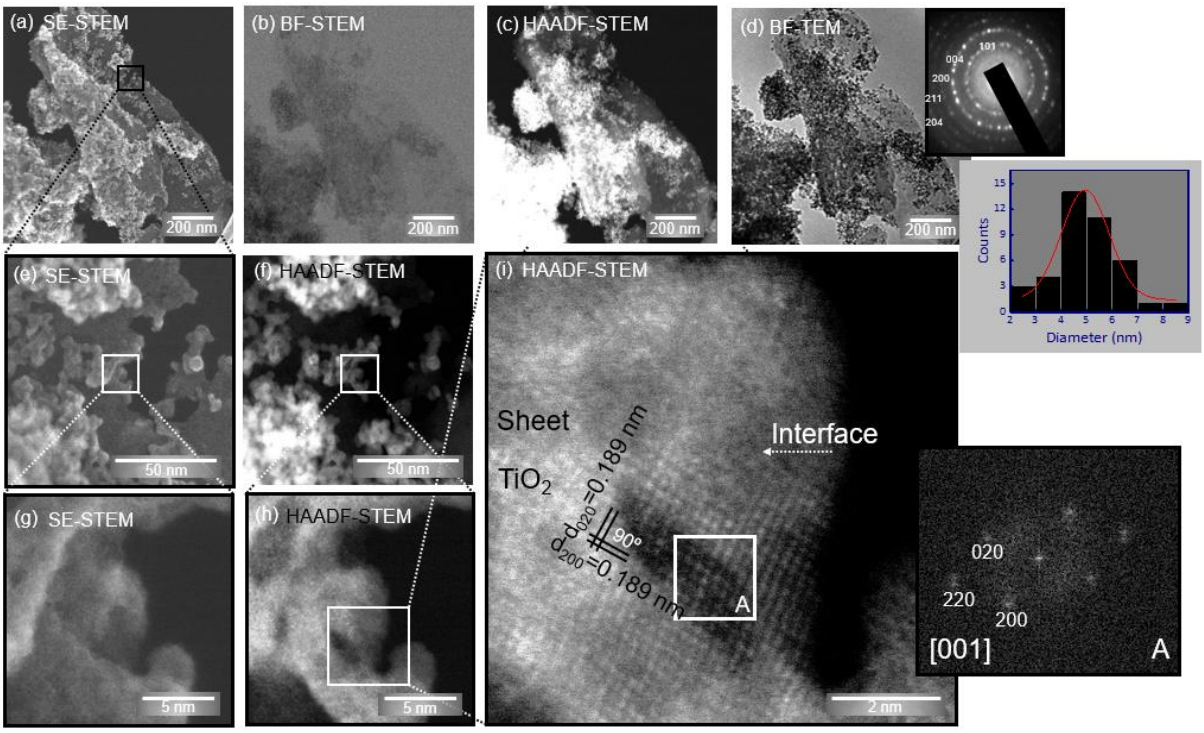

Figure 5.3: (a) Secondary electrons (SE) STEM image of the 30-GCN-T material, (b) BF STEM image of the same area of (a), (c) HAADF-STEM image of the area in (a), (d) BF TEM image of the area in (a). The insets in (d) depict the electron diffraction pattern of TiO_2 nanoparticles with the anatase phase and the particle size distribution of the TiO_2 nanoparticles measured by TEM analyses. (e) and (f) Magnified SE-STEM and HAADF-STEM images of the area analyzed in (a), respectively. (g) SE-STEM and (h) HAADF-STEM image of a TiO_2 nanocrystal attached to the g-C_3N_4 sheet, and (i) atomic-resolution HAADF-STEM image of the area in (g) and (h), where the interface between the TiO_2 nanocrystal and the g-C_3N_4 sheet is clear. The inset in (i) shows the FFT image of the area indicated as A (white square).

Consistent with the SEM results, it can be observed that g-C_3N_4 sheets are covered with TiO_2 nanostructures, though they do not form a continuous film. Larger agglomerates are also perceptible (Figure 5.3 (a)–(f)), but, as observed previously, these are significantly smaller than those found in the pure TiO_2 material. As reported in an analogous study [7], it can be seen that these agglomerates are formed by very fine TiO_2 nanoparticles with irregular shapes, where near spherical nanocrystals and more elongated ones can be observed (Figure 5.3 (g)–(i)). The average TiO_2 particle size was found to be 5.17 ± 1.37 nm, and it can be seen from the

particle size distribution (inset of Figure 5.3 (d)) that smaller particles in the range of 4–7 nm are more likely to be found.

The STEM images (Figure 5.3 (g)–(i)) confirm the close contact between the g-C_3N_4 sheets and the TiO_2 nanocrystals, where the in-depth analysis conducted using detailed HAADF imaging (Figure 5.3 (i)) revealed a clear interface between the TiO_2 nanocrystal and the g-C_3N_4 sheet. As reported earlier in the literature [8], low crystallinity of g-C_3N_4 sheets was detected in the TEM measurements. The atomic-resolution HAADF-STEM image in Figure 5.3 (i) clearly reveals the atomic columns. Based on the Z-contrast, the visible spots are assumed to correspond to Ti atoms [9]. These Ti atomic columns are perpendicular to each other, and a lattice spacing of ≈ 0.189 nm was measured, which perfectly matches the (200) and (020) atomic planes of anatase [10]. Two other distinct TiO_2 nanocrystals were investigated in Figure 5.4 (a) and (b), revealing the (100) and (010) atomic planes of anatase with a lattice spacing of ≈ 0.378 nm [9]. The insets in Figure 5.3 (i) and Figure 5.4 (a) and (b) represent the FFT images generated from areas indicated as A, B, and C, respectively. As observed in the [001] zone axis, it is evident from the FFT patterns that the angles between (200) and (020), as well as between (100) and (010) are 90°, in accordance with the theoretical value reported for pure crystalline anatase TiO_2 (ICDD file number 00-021-1272). Based on the atomic-resolution HAADF images and FFT patterns, the tetragonal atomic arrangement on the (001) surface of the TiO_2 nanocrystals can be inferred [10].

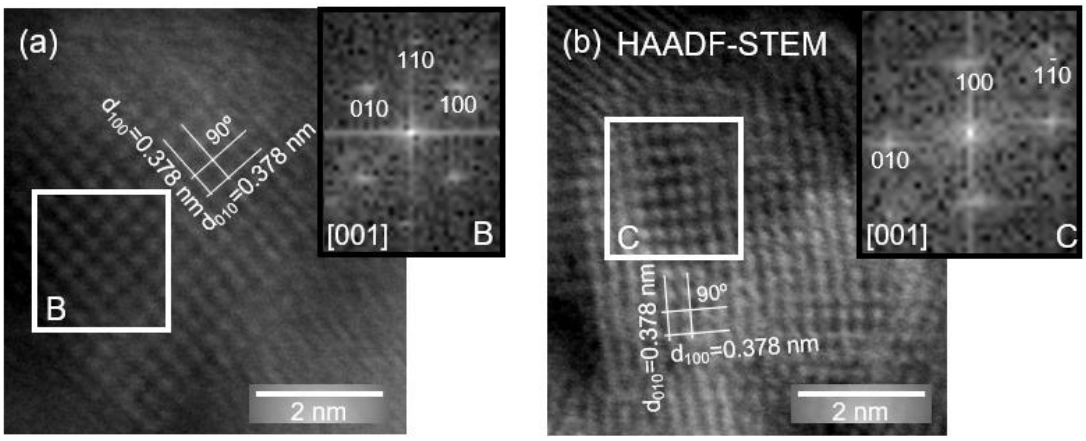

Figure 5.4: (a), (b) Atomic-resolution HAADF-STEM images of two distinct TiO_2 nanocrystals. The insets in (a) and (b) show the FFT images of areas indicated as B and C, respectively (white squares).

EDS analyses were also carried out for the 30-GCN-T material. Figure 5.5 (a) shows a magnified SE-STEM image of a g-C_3N_4 sheet with TiO_2 agglomerates on its surface. EDS

analyses confirmed that the sheet is mainly composed of C (Figure 5.5 (b)), N (Figure 5.5 (c)) and O (Figure 5.5 (d)), while Ti was detected in the agglomerates, revealing a uniform distribution of this element (Figure 5.5 (e)).

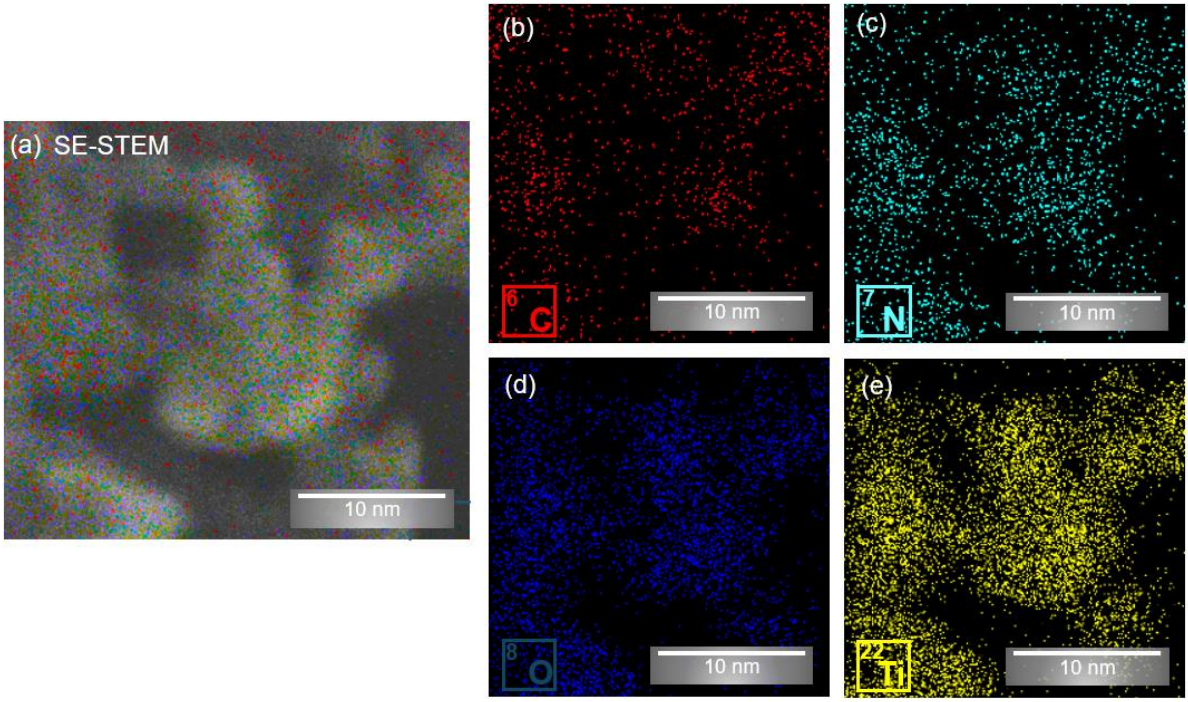

Figure 5.5: Artificially colored (mixed) SE-STEM image of the 30-GCN-T material (a), together with the corresponding EDS maps of C (b), N (c), O (d) and Ti (e).

5.2.1.3 AFM

AFM measurements were performed to determine the average height/thickness of the produced g-C_3N_4 nanosheets. The average thickness of g-C_3N_4 nanosheets was calculated based on several scans, which were taken from AFM images, and the value was found to be around 4 nm. One of those scans is depicted in Figure 5.6. The formation of thin g-C_3N_4 nanosheets was also inferred from STEM analysis (Figure 5.3), in which transparent nanosheets were observed. The obtained value of 4 nm is in alignment with previous studies, in which similar size thicknesses ranging from 2 to 15 nm were reported for g-C_3N_4 nanosheets [11–13].

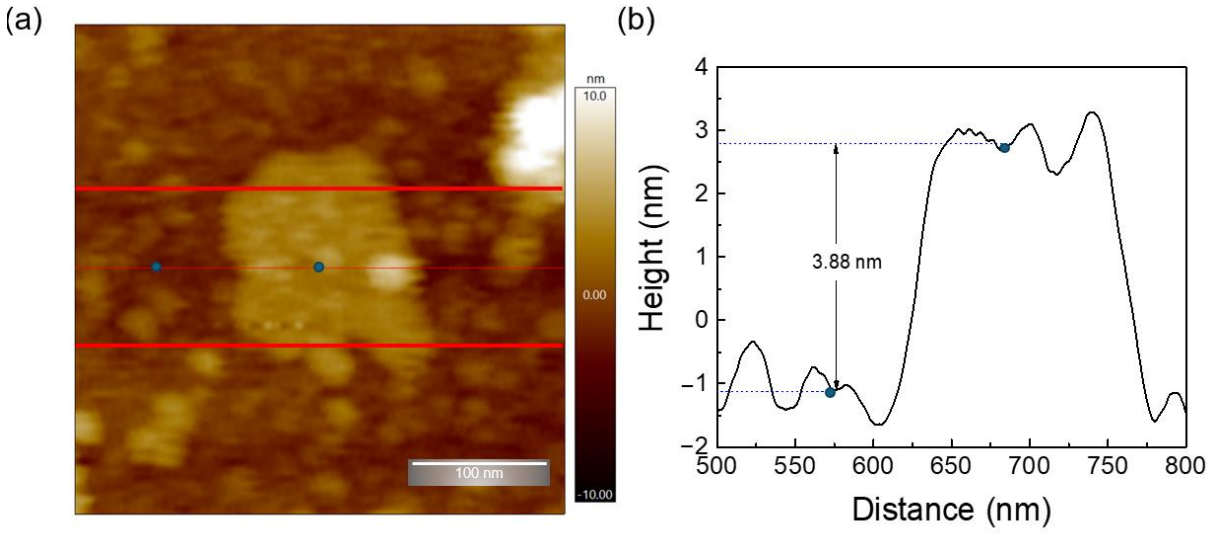

Figure 5.6: (a) AFM image of a g-C_3N_4 nanosheet and (b) corresponding average height values measured between the red lines.

5.2.1.4 XPS

The surface chemical compositions of TiO_2, g-C_3N_4 and 30-GCN-T materials were analyzed by XPS. Figure 5.7 (a) shows the survey spectra of the above mentioned materials, revealing the existence of C and N elements in the g-C_3N_4 nanopowder. Through the analysis of the survey spectra, the characteristic peaks of Ti and O appear in TiO_2 along with Ti, O, N and C elements in 30-GCN-T, which confirms the purity of the produced materials. High-resolution XPS spectra of each element present in the materials (TiO_2, g-C_3N_4 and 30-GCN-T) are presented in Figure 5.7 (b)–(e). Figure 5.7 (b) shows the comparison between the deconvoluted C 1s core level spectra of g-C_3N_4, TiO_2 and 30-GCN-T. The g-C_3N_4 sample was fitted with peaks at 284.8, 286.1 and 288.2 eV of equal full-width at half maximum (FWHM) and a broader peak at 293.5 eV. The peaks at 284.8 eV and 286.1 eV are identified as C–C and C–O bonds of adventitious carbon, respectively. The most intense peak at 288.2 eV corresponds to sp^2 C atoms in the N=C−N aromatic ring of g-C_3N_4, whereas the peak at 293.5 eV is related to the three-coordinate C atoms C−NH_2 [14–16]. The C 1s emission of TiO_2 only presents emissions from adventitious carbon. The 30-GCN-T material presents a mixture of g-C_3N_4 and TiO_2. Since an excellent fit of the 30-GCN-T C 1s emission could be obtained by applying the peak models of both g-C_3N_4 and TiO_2 (with fixed relative binding energies and relative peak areas, respectively), it can be concluded that no significant change occurred in the chemistry of both g-C_3N_4 and TiO_2 when forming the heterostructure. XPS high-resolution O 1s core level spectra for g-C_3N_4, TiO_2 and 30-GCN-T are also shown in Figure 5.7 (c). Only a very small amount of oxygen

is present in g-C_3N_4, in accordance with the C−O bond of adventitious carbon. For TiO_2, a typical set of peaks related to Ti−O bonds, undercoordinated oxygen, hydroxyl groups and surface-adsorbed water are found (in ascending order of binding energy) [14,17]. These peaks do not change significantly in their relative areas when comparing the TiO_2 with the 30-GCN-T material, indicating no chemical change in TiO_2 upon the formation of the heterostructure.

Figure 5.7 (d) shows the high-resolution Ti 2p core level spectra of TiO_2 and 30-GCN-T. For TiO_2, the binding energy values of Ti $2p_{3/2}$ and Ti $2p_{1/2}$ obtained at 458.5 and 464.3 eV can be assigned to Ti^{4+} species in the form of TiO_2 agglomerates [18], and the peak positions are consistent with the reported values for pure TiO_2 nanostructures [19]. The Ti 2p spectrum of 30-GCN-T is similar to the one of TiO_2, both in shape and in peak position. Note that it is not possible to comment on eventual binding energy shifts due to the necessary usage of an electron flood gun during the measurement. Regarding the deconvoluted high-resolution N 1 s spectra of g-C_3N_4 and 30-GCN-T (Figure 5.7 (e)), both materials exhibit five peaks at 398.7, 399.3, 400.0, 401.1, 404.3 eV and 406.6 eV, corresponding to the binding states of sp^2-hybridized aromatic N atoms bonded to carbon atoms (–C–N=C), tertiary nitrogen N–$(C)_3$, C–N–H groups [20], respectively, and two satellite peaks at higher binding energies [21]. No shifts in N 1s spectra were observed. The N/C ratio of g-C_3N_4 was also obtained, and its value was close to the theoretical value of ideal g-C_3N_4 (≈ 1.30). Using the C 1s peak model to determine the carbon of g-C_3N_4 inside the 30-GCN-T material also allows quantifying the N/C ratio in 30-GCN-T, which amounts to 1.4, which is very close to pristine g-C_3N_4.

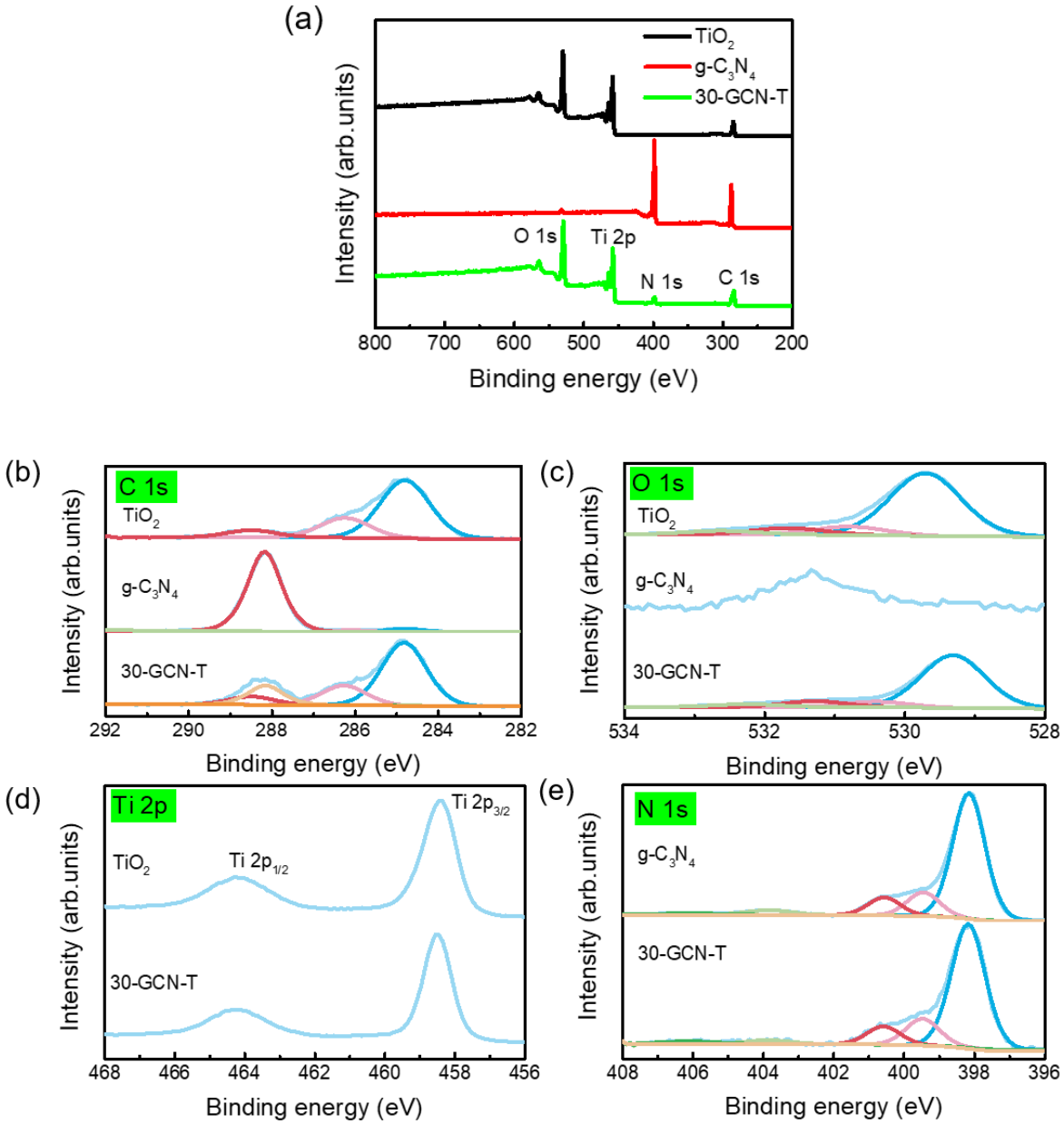

Figure 5.7: (a) XPS survey spectra of TiO_2, g-C_3N_4 and 30-GCN-T materials. (b) Deconvolution of XPS C 1s of TiO_2, g-C_3N_4 and 30-GCN-T spectra. (c) Deconvolution of XPS O 1s spectra of TiO_2, g-C_3N_4 and 30-GCN-T. (d) XPS Ti 2p spectra of TiO_2 and 30-GCN-T. (e) Deconvolution of XPS N 1s spectra of g-C_3N_4 and 30-GCN-T.

5.2.2 Optical characterization

The optical properties of the produced materials were investigated by UV-VIS absorption and PL spectroscopies (Figure 5.8). As observed in Figure 5.8 (a), pure g-C_3N_4 shows an absorption maximum at around 384 nm (3.23 eV), arising from the n $\rightarrow \pi^*$ transitions caused by the electron transfer from a nitrogen non-bonding orbital to an aromatic antibonding orbital [22,23], and an absorption onset at *ca.* 450 nm. Meanwhile, pure anatase TiO_2 exhibits an

absorption maximum in the UV region and an absorption onset at *ca.* 390 nm (3.18 eV). The absorption onsets allow to estimate the optical band gap values of the materials (around 2.8 and 3.2 eV, respectively, for pure g-C_3N_4 and pure TiO_2). These results are in good agreement with the band gap values obtained from DRS spectra by means of the Kubelka–Munk function [24], as depicted in the inset of Figure 5.8 (a), and fairly in line with the reported band gap values for these materials [25–28]. For 30-GCN-T nanostructures, it is visible that two absorption peaks appear: one in the UV region, placed at the same wavelength value as for the absorption maximum of pure TiO_2, and another one with a lower absorption at *ca.* 384 nm, most likely related to the presence of g-C_3N_4. In addition, compared with pure TiO_2, these nanostructures exhibited a red shift in the absorption onset, from 390 nm (pure TiO_2) to around 450 nm, hence suggesting the ability of these materials to absorb photons in the visible region and a possible enhancement of their photocatalytic activity under visible light.

The PL spectra of TiO_2, g-C_3N_4 and 30-GCN-T materials are also presented in Figure 5.8 (b). In the case of pure TiO_2, barely any emission was detected, while pure g-C_3N_4 and 30-GCN-T materials exhibited a similar broad and asymmetric emission band, typical of graphitic carbon nitride [29,30]. The inset of Figure 5.8 (b) reveals a slight shift in the peak position between the two materials, with the band associated with pure g-C_3N_4 peaking at 450 nm (~2.75 eV) while 30-GCN-T exhibiting its maximum at ~446 nm (~2.78 eV).

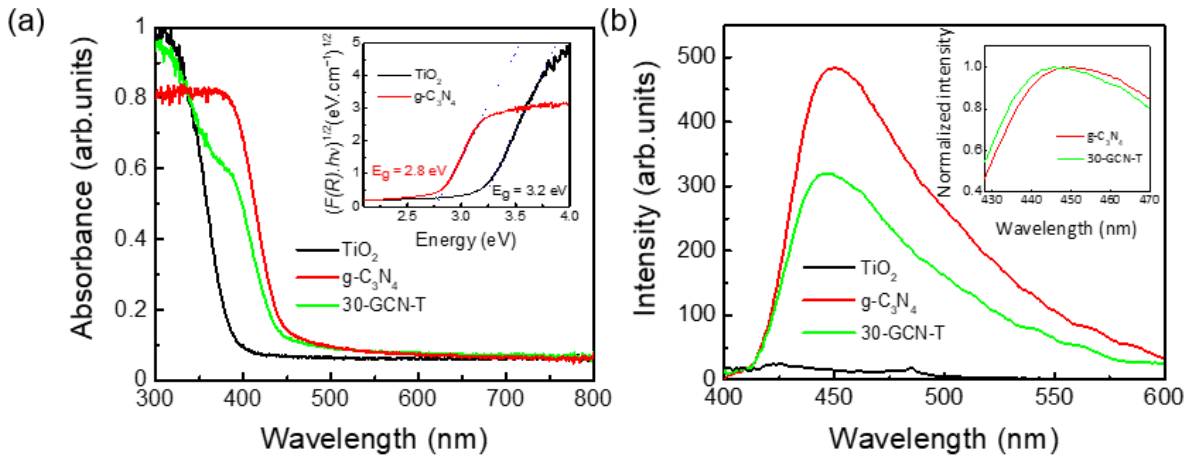

Figure 5.8: (a) RT absorption spectra of TiO_2, g-C_3N_4 and 30-GCN-T nanopowders. The inset shows the Kubelka–Munk plots (from DRS spectra of TiO_2 and g-C_3N_4 nanopowders). For the determination of the optical band gap values, TiO_2 and g-C_3N_4 materials were considered as indirect band gap semiconductors. (b) RT PL spectra of TiO_2, g-C_3N_4 and 30-GCN-T nanostructures from 400 to 600 nm using an excitation wavelength of 350 nm. The inset shows the RT PL spectra (normalized intensity as a function of the wavelength from 428 to 470 nm) of g-C_3N_4 and 30-GCN-T nanostructures.

Figure 5.9 (a) and (b) depict the spectral deconvolution of the broad bands for each material using three Gaussian functions. In both cases, the same bands were identified, peaking at 2.817 eV (~440 nm), 2.709 eV (~458 nm) and 2.494 eV (~497 nm), which indicates the contribution of the same optical centers to the overall PL emission. These findings are in line with reports from Yuan *et al.* and Das *et al.*, who demonstrated that after deconvolution of the g-C_3N_4 PL spectrum, three emission centers could be observed in this material at around 431, 458 and 491 nm, originating from the σ^*— lone pair, π^*–LP and π^*–π transition pathways, respectively [31,32]. The slight shift in the peak position observed in the present materials is due to different relative intensities of the deconvoluted bands, specifically, an increase in the relative intensity of the band peaking at the highest energy, while the bands at lower energies experience a reduction in their relative intensity. Although not shown, the same results were observed for 15-GCN-T and 45-GCN-T, attesting to the reproducibility of this behavior. This change in the relative intensity of the PL components can be related to the interaction between the g-C_3N_4 nanosheets and the TiO_2 particles, namely charge transfer phenomena, as reported in other works [33,34], which will be highly beneficial for photocatalytic applications.

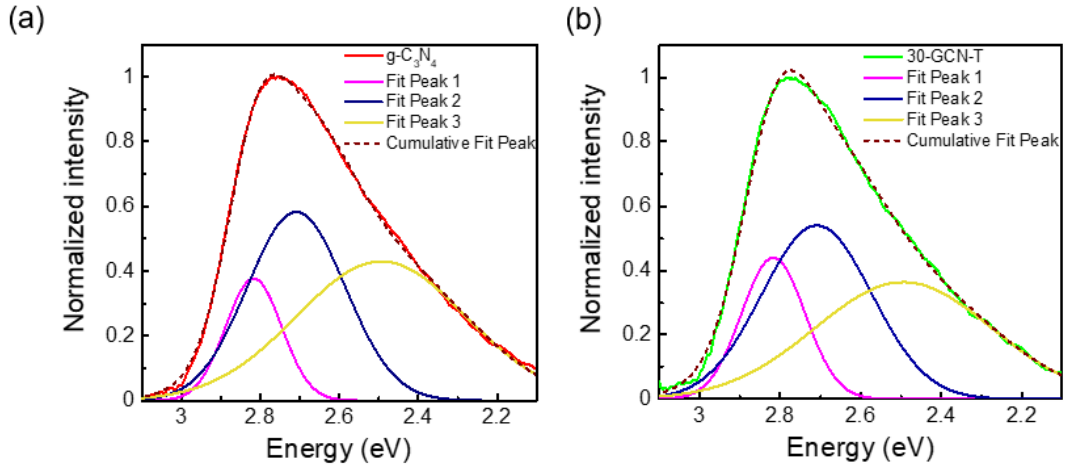

Figure 5.9: Spectral deconvolution of the broad visible bands into three components for (a) g-C_3N_4 and (b) 30-GCN-T materials. An adequate fitting was obtained using three Gaussian functions peaked at ~2.817 eV, ~2.709 eV and ~2.494 eV.

5.2.3 Photocatalytic degradation of MO under simulated solar light

The produced nanomaterials in powder form were tested as photocatalysts for the degradation of MO under a simulated solar light source. The degradation rate was monitored by recording the decay in the absorbance peak intensity at 464 nm [35] by using a UV-VIS

spectrophotometer in intervals of 30 min (during the first 2 h) and after that every 1 h up to 240 min (4 h). After this time, a transparent solution could be observed (inset of Figure 5.10 (a)). The MO degradation ratio (%) was calculated based on equation (3.3) in Chapter 3. Based on the absorbance *vs*. wavelength graphs, it is possible to calculate the ratio between the maximum value of each absorbance spectrum (A) at each exposure time and the initial absorbance of the solution (A_0), as depicted in Figure 5.10 (a). As shown in Figure 5.10 (a), MO degradation without catalyst was insignificant in the dark and under simulated solar light, which indicates that MO solution is highly stable under light exposure cycles. In fact, a slight increase in MO intensity is observed over time, likely associated with the evaporation of the solvent [7].

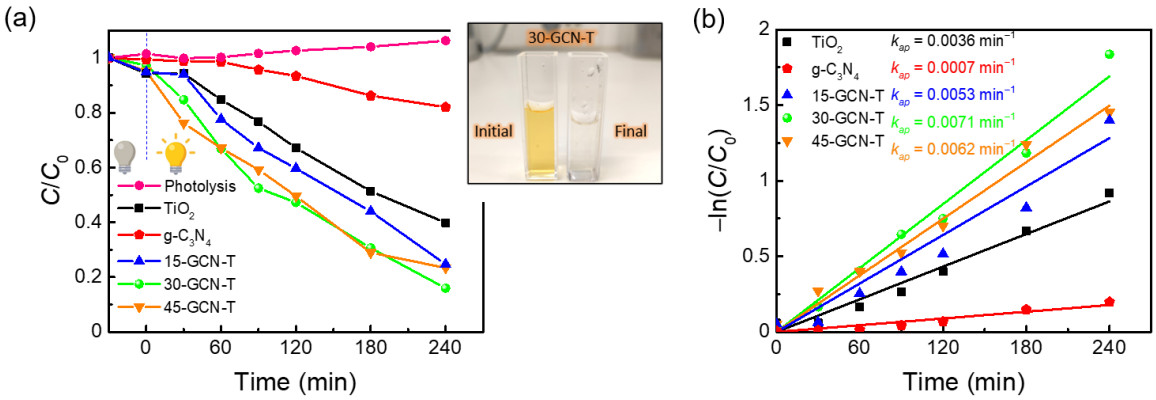

Figure 5.10: Degradation curves (C/C_0) as a function of the exposure time) under simulated solar light up to 4 h without photocatalyst (photolysis) and for TiO_2, g-C_3N_4, 15-GCN-T, 30-GCN-T,45-GCN-T photocatalysts. The lines are for eye guidance only. (b) Pseudo-first-order kinetics for MO degradation in the presence of TiO_2, g-C_3N_4, 15-GCN-T, 30-GCN-T and 45-GCN-T photocatalysts. The lines represent the linear fittings of the pseudo-first-order kinetics equation.

A minimal MO degradation percentage was obtained (18 %) in the presence of pure g-C_3N_4 within 4 h under solar light. This phenomenon can be explained by the fast electron–hole recombination in this material, which lowers its photocatalytic activity [36]. In contrast, a substantial increase to 60 % of MO degradation was achieved with pure TiO_2 for the same exposure time.

Many factors influence TiO_2 photocatalytic behavior, such as crystalline phase, specific surface area, active facets and particle size [37,38]. Regarding the effect of particle size, large TiO_2 aggregates composed of nanocrystals were obtained (with an average size of ~ 543 nm, as confirmed by SEM). It is well known that larger particles possess lower specific surface area and surface-to-volume ratio [7]. Despite that, some hollow spheres were also observed (Figure 5.2 (b), providing more active sites for photocatalytic reactions. In terms of TiO_2 active surfaces,

as revealed by STEM, the (100) surface was exposed in the TiO_2 nanocrystals, which is one of the most active surfaces for photocatalysis [39,40]. This is due to its superior surface atomic structure (100 % five-coordinate Ti atoms (Ti_{5c})), which is highly reactive, enhancing pollutant adsorption and facilitating the photoreactions [39,41,42]. The crystalline phase also plays a key role in photocatalytic activity. Although the synergistic effect of a mixture of TiO_2 phases seems to be beneficial for photocatalysis, among the different TiO_2 polymorphs and when it comes to a single phase, TiO_2 anatase is considered the most photoactive phase [43]. Pure TiO_2 brookite may present superior photocatalytic activity compared to the other two phases. However, it is difficult to synthesize, making it the least studied TiO_2 polymorph in photocatalysis [44]. Comparing TiO_2 rutile and anatase, TiO_2 rutile suffers from low generation and high recombination rate of charge carriers because of deep electron traps, despite having a lower band gap energy value (~3.0 eV) than TiO_2 anatase (~3.2 eV). Studies also indicate that TiO_2 anatase shows a slower charge carrier recombination since it has the lightest average effective mass of photogenerated electrons and holes, hence the lowest recombination rate of charge carriers [43,44]. In addition, TiO_2 anatase is considered an indirect band gap semiconductor, thus exhibiting a longer lifetime of photoexcited electrons and holes since direct transitions of photogenerated electrons from the conduction band to the valence band of anatase are not possible [45].

Notably, all g-C_3N_4/TiO_2 nanostructures exhibited superior photocatalytic performance compared to pure TiO_2 and pure g-C_3N_4 (Figure 5.10 (a)). As observed previously through the HAADF-STEM image in Figure 5.3 (i), an obvious interface was revealed between the TiO_2 nanocrystal and the g-C_3N_4 sheet. Therefore, the enhancement of MO photocatalytic degradation under simulated solar light is expected to be due to an efficient photogenerated charge carriers' separation at the g-C_3N_4–TiO_2 anatase interface. The 15-GCN-T and 45-GCN-T materials exhibited similar MO photocatalytic degradation percentages (75 and 77 %, respectively, in 4 h). The SEM images in Figure 5.2 (a) show the presence of large TiO_2 agglomerates in the 15-GCN-T material, leaving some uncovered areas of the g-C_3N_4 nanostructures by TiO_2. The low content of g-C_3N_4 may also lead to insufficient visible-light absorption to excite the electrons and holes [46]. With the highest g-C_3N_4 content, not all g-C_3N_4 nanosheets were covered by TiO_2 nanoparticles, and thus, this could have induced recombination of photogenerated charges, as previously reported [46]. The material with an intermediate amount of g-C_3N_4 (30-GCN-T) demonstrated the best photocatalytic performance, and in the presence of this

material, MO degradation of 84 % was achieved in 4 h. Therefore, the optimum g-C_3N_4 loading (among the ones explored) in TiO_2 was found to be 30 % in weight.

To determine the MO degradation kinetics, the L–H model was used, and the simplified pseudo-first-order kinetics equation was applied, as represented in equation 1.11 in Chapter 1. The photodegradation apparent rate constants (k_{ap}) were obtained from the plots of $-\ln\left(\frac{C}{C_0}\right)$ *vs.* time (t), as seen in Figure 5.10 (b), where the apparent rate constants correspond to the slopes of the linear regressions. Table 5.1 summarizes the obtained kinetic parameters (rate constants (k_{ap}) and linear regression coefficients R^2) for the degradation of MO under simulated solar light up to 4 h.

Table 5.1: Pseudo-first-order kinetic parameters (rate constants and linear regression coefficients) for the photocatalytic degradation of MO under simulated solar light in 4 h over TiO_2, g-C_3N_4, 15-GCN-T, 30-GCN-T and 45-GCN-T nanostructures.

Nanostructures	k_{ap} (min^{-1})	R^2
TiO_2	0.0036	0.99
g-C_3N_4	0.0007	0.95
15-GCN-T	0.0053	0.97
30-GCN-T	0.0071	0.99
45-GCN-T	0.0062	0.98

Through the analysis of Table 5.1, it can be concluded that the photocatalytic dye degradation follows pseudo-first-order kinetics for all synthesized nanostructures since a good correlation for the fitted lines was obtained ($R^2 > 0.95$) [7,47]. A much higher photocatalytic degradation rate in the presence of g-C_3N_4/TiO_2 nanostructures (15-GCN-T, 30-GCN-T and 45-GCN-T) was exhibited compared to the pure materials of TiO_2 and g-C_3N_4. Comparing the rate constant obtained with the best photocatalyst (30-GCN-T), an enhanced efficiency of almost 1.97 and 10 times greater than that of TiO_2 and g-C_3N_4 nanosheets was achieved, respectively. Considering the present results, the improvement of the visible light utilization (Figure 5.9 (a)), the suppression in the recombination rate of photogenerated charge carriers compared to g-C_3N_4 (Figure 5.9 (b)), and the interaction between g-C_3N_4 and TiO_2 (Figure 5.3 (i) and Figure 5.7) might have helped in boosting the photocatalytic activity in this material. A summary of g-C_3N_4/TiO_2 nanostructures reported in the literature used for the degradation of MO using different preparation methods is presented in Table 5.2. The results obtained in this work are also presented in blue for comparison.

Table 5.2: Summary of g-C_3N_4/TiO_2 nanostructures reported in the literature used for the degradation of MO using different preparation methods. The results obtained in this work are also presented in blue for comparison.

Material	Preparation method	Light source	[MO]	Optimum loading	Degradation efficiency (%)	k_{ap} (min^{-1})	Ref.
g-C_3N_4/seed grown mesoporous TiO_2	Seed induced solvothermal (MW: 105 ºC/ 48 h)	Visible light	10 mg. L^{-1}	Ti:g-C_3N_4 (1 molar ratio)	Around 100 % MO degradation in 60 min (pH = 3)	0.1014	[48]
g-C_3N_4/TiO_2 (brookite)	Calcination (400 ºC/ 1 h)	Visible light	10 mg. L^{-1}	g-C_3N_4:TiO_2 (35 % weight ratio)	55 % MO degradation in 180 min	No data	[49]
g-C_3N_4/TiO_2 nanotube array	Anodic oxidation method/ultrasonic loading	Xe lamp irradiation (intensity 100 mW/cm^2)	15 mg. L^{-1}	No data	84.6 % MO degradation in 120 min	No data	[50]
g-C_3N_4 nanosheets/ mesoporous TiO_2	Hydrothermal synthesis (MW: 180 ºC/ 6 h)	300 W Xe lamp irradiation with a cut-off filter (λ > 420 nm)	32.7 mg. L^{-1} (100 μM)	g-C_3N_4:TiO_2 (2:1weight ratio)	Around 60 % MO degradation in 300 min (pH = 3)	No data	[51]
g-C_3N_4 nanosheets/TiO_2 nanoflakes	*in situ* sol-gel (400 ºC/ 3 h)	UV-VIS light	20 mg. L^{-1}	g-C_3N_4:TiO_2 (1:4 weight ratio)	97 % MO degradation in 80 min	0.0718	[52]
g-C_3N_4/TiO_2	Solvothermal synthesis (MW: 150 ºC/ 60 min)	Simulated solar light	12.5 mg. L^{-1}	g-C_3N_4:TiO_2 (30 % weight ratio)	84 % MO degradation in 240 min	0.0071	This work

A direct comparison of related studies, such as the ones presented in Table 5.2, is not straightforward due to the distinct parameters employed during photocatalytic experiments. Nonetheless, it is noteworthy to mention the simplicity of the method used to prepare g-C_3N_4/TiO_2 heterostructures by using a lower temperature and shorter reaction time. In future studies, to avoid the drawbacks associated with the recovery and recyclability of powder catalysts, this heterostructure should be synthesized or immobilized on low-cost substrates through a simple and fast approach, such as microwave irradiation, and without the need for using toxic reagents, which has proved to be of great interest in photocatalytic applications [7,19].

5.2.3.1 Reusability tests and possible photocatalytic degradation mechanism

Recyclability tests were carried out with the best photocatalyst (30-GCN-T) under simulated solar light along five consecutive cycles of 4 h each. Figure 5.11 (a) shows the C/C_0 photocatalytic MO degradation over 30-GCN-T nanostructures along five cycles. A gradual decrease in the degradation efficiency is observed between cycles, and a degradation loss efficiency of around 20 % is obtained at the end of the fifth cycle. A high percentage of MO molecules or reaction products could have remained adsorbed on the surface of the catalyst, retarding the photocatalytic degradation process [53].

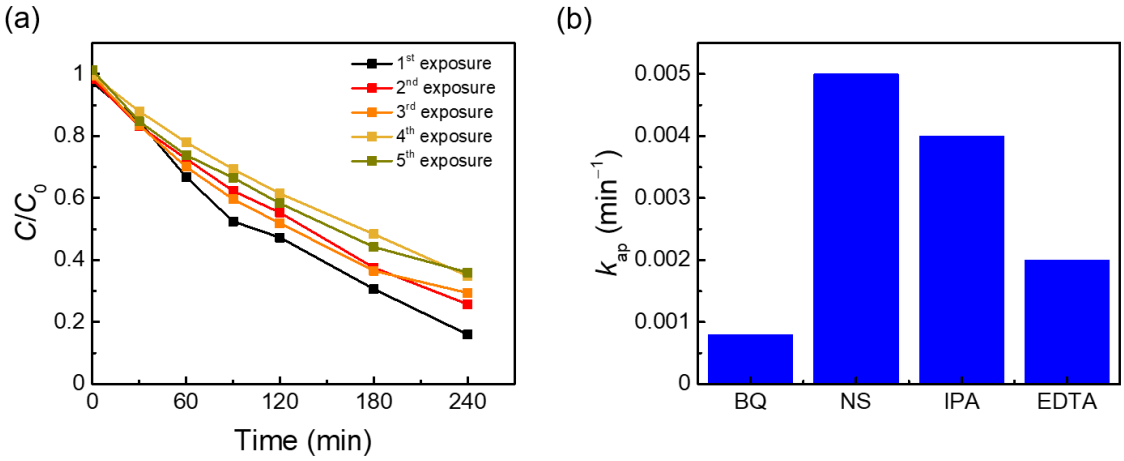

Figure 5.11: (a) MO degradation curves (C/C_0) as a function of the exposure time) in the presence of 30-GCN-T heterostructures up to 4 h under five consecutive cycles. The lines are for eye guidance only. (b) Comparison of the degradation rates of MO under a simulated solar light source using the 30-GCN-T heterostructure, in the presence of trapping reagents (BQ, IPA and EDTA) and with NS and 5 mL of water.

The contribution of different ROS to the degradation rate of MO dye using the 30-GCN-T nanostructures was investigated under simulated solar light for 4 h. Although various ROS

contribute to the photocatalytic degradation process [47,54], studies have shown that MO degradation is mainly driven by holes (h^+), hydroxyl radicals ($^{\bullet}OH$) and superoxide ions ($^{\bullet}O_2^-$) radicals [55,56]. Therefore, in this study, EDTA, IPA and BQ were used as specific scavengers of holes (h^+), hydroxyl radicals ($^{\bullet}OH$) and superoxide ions ($^{\bullet}O_2^-$). Photocatalytic degradation in the absence and presence of the different scavengers is presented as a MO degradation rate constant (Figure 5.11 (b)). As shown in Figure 5.11 (b), all scavengers inhibited MO degradation. The addition of IPA had little effect on the MO degradation rate, revealing negligible participation of ·OH radicals in the degradation process. Unlike IPA, upon the use of BQ, the removal rate of MO dye over 30-GCN-T was significantly suppressed, thus suggesting that superoxide ions are the primary active species involved in the photocatalytic degradation process. This trend was followed by holes, since the addition of EDTA also showed a significant decrease in the reaction rate. Similar results are also reported in the literature, where superoxide radicals were the main active species, and holes acted as complementary species in MO photodegradation [57].

5.2.4 Electrochemical characterization

For a better insight into the charge transfer process and band alignment of the 30-GCN-T material, the flat band potentials (E_{FB}) of TiO_2 and g-C_3N_4 were obtained under 1 kHz from M–S plots, as shown in Figure 5.12. The values were estimated based on the M–S relation (equation (5.1)):

$$\frac{1}{C_{int}^2} = \left(\frac{2}{e\varepsilon_r\varepsilon_0 N_d}\right) \times \left(V - E_{FB} - \frac{KT}{e}\right) \quad (5.1)$$

where C_{int}^2 is the interfacial capacitance; e is the electron charge (1.6×10^{-19} C); ε_r is the dielectric constant of the materials; ε_0 is the vacuum permittivity (8.85×10^{-12} F.m^{-1}); N_d is the electron donor density; V is the applied potential; E_{FB} is the flat band potential; K is the Boltzmann constant ($1.38 \times 10{-}23$ J.K^{-1}); and T is the temperature [58,59]. At RT, $\frac{KT}{e}$ is negligible [58]. Flat band potentials can be estimated by plotting a graph of $1/C_{int}^2$ as a function of V and can thus be estimated from the intercept of the linear portion of these graphs with the potential axis (y-axis = 0) [60].

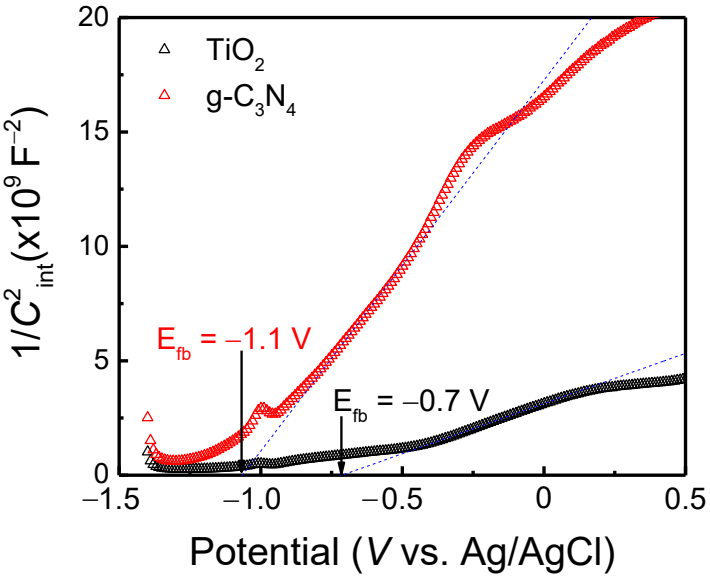

Figure 5.12: M-S analyses performed at 1 kHz in 0.5 M Na_2SO_4 electrolyte for TiO_2 and g-C_3N_4. The potentials were measured against the Ag/AgCl reference. The flat band potentials (E_{FB}) can be estimated from the linear portion of the graphs, represented in blue dashed lines.

As visible in Figure 5.12, the positive slope on M–S plot curves suggests that both TiO_2 and g-C_3N_4 materials exhibit an n-type semiconductor behavior [61–63]. The flat band potential values against Ag/AgCl were also estimated to be −0.7 V for TiO_2 and −1.1 V for g-C_3N_4. These values are close to the previously reported data under 1 kHz [64,65]. The potentials were recalculated against NHE, according to equation (5.1), and values of −0.50 V and −0.90 V were found for TiO_2 and g-C_3N_4, respectively. Moreover, an approximation of the conduction band potential values (E_{CB}) can also be performed, whereby for n-type semiconductors it is often considered that E_{FB} *vs.* NHE values are more positive at 0.1 V than E_{CB} values [65,66]; therefore, E_{CB} values were determined as −0.6 V and −1 V for TiO_2 and g-C_3N_4, respectively. Based on the predicted optical band gap values, as visible in the inset of Figure 5.8 (a), it is possible to estimate the valence band potential values (E_{VB}), which are obtained by adding the E_{CB} values to the optical band gap values [67], resulting in +2.6 V and +1.8 V for TiO_2 and g-C_3N_4, respectively.

Based on the experimental results above, two possible MO degradation mechanisms of the 30-GCN-T material are proposed (Figure 5.13). Under solar light, electrons are excited from the VB of TiO_2 and g-C_3N_4 to the CB and generate electron–hole pairs. Regarding the first mechanism, since the VB potential of g-C_3N_4 (+1.8 V *vs.* NHE) is less positive than the reduction–oxidation potential of $OH^-/{}^{\bullet}OH$ (+1.99 V *vs.* NHE) and $H_2O/{}^{\bullet}OH$(+2.37 V *vs.* NHE), the

holes will not be able to oxidize OH^- or H_2O into $^{\bullet}OH$ radical species. Nevertheless, a small decrease in the photodegradation percentage of MO was observed previously after the addition of IPA (Figure 5.11 (b)). Therefore, hydroxyl radicals participated in the degradation process. This was further supported by the decreased percentage of MO degradation after the addition of EDTA because the presence of holes was detected, which could contribute to the generation of $^{\bullet}OH$ radicals. Therefore, the formation of a Z-scheme mechanism seems possible (Figure 5.13 (a)) [68]. In this scheme, the photogenerated electrons in TiO_2 recombine with the holes in g-C_3N_4 through the built-in electrostatic field, resulting in a more efficient separation of photogenerated charge carriers. Due to the more positive VB potential in TiO_2 (+2.6 V *vs.* NHE) than that in $OH^-/^{\bullet}OH$ (+1.99 V *vs.* NHE) and $H_2O/^{\bullet}OH$ (+2.37 V *vs.* NHE) [69], the holes can form hydroxyl radicals by reacting with adsorbed water molecules or surface hydroxyls at the surface of TiO_2. At the same time, the electrons on the CB of g-C_3N_4 could be captured by O_2 to form $^{\bullet}O_2^-$ radical species due to the more cathodic CB potential (−1 V *vs.* NHE) compared to the redox potential of $O_2/^{\bullet}O_2^-$ (−0.33 V *vs.* NHE) radicals [69,70]. These hydroxyl and superoxide radical species (OH^- and $^{\bullet}O_2^-$, respectively) will further reduce and oxidize MO dye to H_2O and CO_2, with a major contribution from the superoxide radicals, as observed in the photodegradation experiments with ROS (Figure 5.11 (b)) [71,72]. In this case, the good coupling between TiO_2 and g-C_3N_4 leads to stronger reduction and oxidation abilities, which will confer improved efficiency to the heterostructure for MO photocatalytic degradation under sunlight.

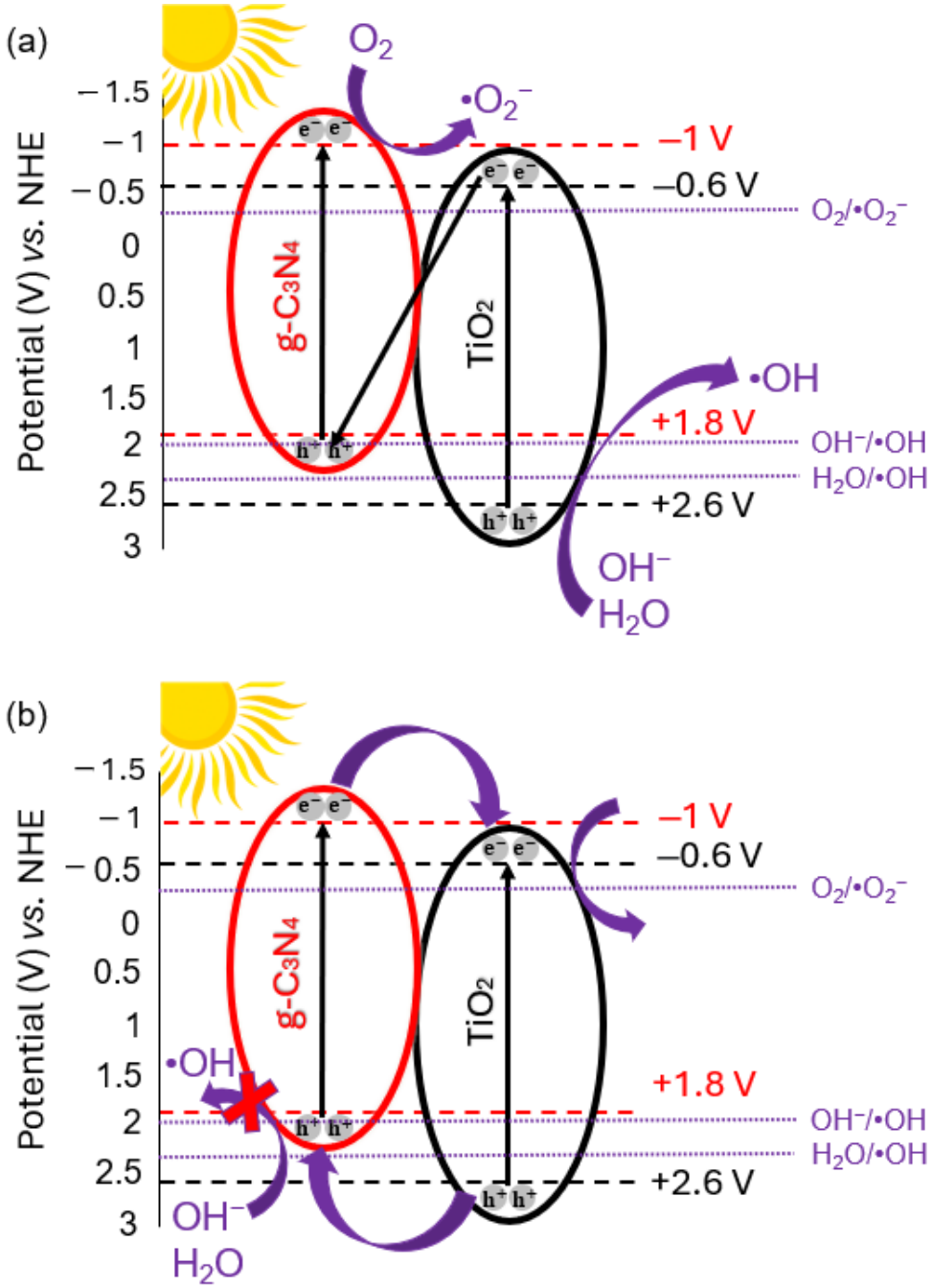

Figure 5.13: Illustrated mechanism of the photocatalytic activity of the 30-GCN-T heterostructure under solar light. The potentials (V) relative to NHE scale are also represented. Black and red dashed lines correspond to the CB/VB potentials of TiO_2 and g-C_3N_4, respectively. Purple dotted lines are related to the redox potentials of the common reactive species in photocatalysis. (a) Represents a possible Z-scheme photocatalytic degradation mechanism of the 30-GCN-T heterostructure, while (b) illustrates a possible type-II photocatalytic degradation mechanism of the 30-GCN-T heterostructure.

In contrast to this mechanism, and as revealed before, only a small fraction of hydroxyl radicals was formed during the photocatalytic reaction due to the slight inhibition with IPA.

These hydroxyl radicals could have been produced by the reaction of remaining TiO_2 holes and hydroxyl groups. In this mechanism (type-II heterostructure), see Figure 5.13 (b), electron–hole pairs are produced and separated in both materials upon light irradiation. Photogenerated holes are transferred from TiO_2 to g-C_3N_4 and do not produce hydroxyl radicals, although they might directly oxidize MO dye. Meanwhile, the electrons in g-C_3N_4 flow to the conduction band of TiO_2 and are subsequently scavenged by oxygen at the surface of the catalyst to generate superoxide radicals [34]. Efficient separation of electron–hole pairs is expected, thereby prolonging the lifetime of photogenerated charge carriers, resulting in improvement of the photocatalytic efficiency of the photocatalyst [73].

5.3 Summary

In conclusion, visible-light-activated photocatalysts based on g-C_3N_4 and TiO_2 were produced through a simple and fast microwave-assisted approach, contrary to the frequently employed time- and energy-consuming fabrication methods reported in the literature. Different g-C_3N_4 amounts in TiO_2 were investigated, and the produced nanopowders (15-GCN-T, 30-GCN-T and 45-GCN-T) were tested for the degradation of MO under a simulated solar light source. XRD data indicated the presence of solely anatase TiO_2 and g-C_3N_4 in 30-GCN-T and 45-GCN-T heterostructures, while only the TiO_2 anatase phase was detected in the 15-GCN-T material, likely due to the low percentage of g-C_3N_4 in the heterostructure. The SEM results showed that the use of ethanol as solvent resulted in irregularly shaped TiO_2 particles, which formed large aggregates. The increase in the amount of g-C_3N_4 in TiO_2 led to the disintegration of these larger particles, and smaller TiO_2 particles were formed, along with the formation of a TiO_2 film, which covered the porous g-C_3N_4 nanosheets. For the 30-GCN-T material, STEM revealed an established interface between a TiO_2 crystal and a g-C_3N_4 sheet, while XPS confirmed both components to be chemically intact in the heterostructure. The ability to use visible light was demonstrated by the red shift in the absorption onset compared with pure TiO_2. The best photocatalytic performance was achieved with the 30-GCN-T heterostructure. This heterostructure can degrade 84 % of MO dye in 4 h under solar light, corresponding to an enhanced efficiency of almost 2 and 10 times greater than that of TiO_2 and g-C_3N_4 nanosheets, respectively. Two photocatalytic degradation mechanisms were proposed: type-II heterostructure and Z-scheme, where the latter seemed more plausible owing to the small fraction of hydroxyl radical species detected, whereas superoxide radicals were the main active species

observed in the ROS scavengers' experiment. An easy strategy was employed in this study, without the need for pre- or post-treatment processes, in which g-C_3N_4/TiO_2 heterostructures were synthesized through a microwave-assisted solvothermal method, demonstrating great potential for water decontamination.

5.4 References

1. Fina, F.; Callear, S. K.; Carins, G. M.; Irvine, J. T. S. Structural investigation of graphitic carbon nitride via XRD and neutron diffraction. *Chemistry of Materials* **2015**, *27(7)*, 2612–2618, doi:10.1021/ACS.CHEMMATER.5B00411.
2. Zhang, H.; Liu, F.; Wu, H.; Cao, X.; Sun, J.; Lei, W. In situ synthesis of g-C_3N_4/TiO_2 heterostructures with enhanced photocatalytic hydrogen evolution under visible light. *RSC Advances* **2017**, *7*, *64*, 40327–40333, doi:10.1039/C7RA06786K.
3. Li, J.; Ma, Y.; Xu, Y.; Li, P.; Guo, J. Enhanced photocatalytic degradation activity of Z-scheme heterojunction $BiVO_4$/Cu/g-C_3N_4 under visible light irradiation. *Water Environment Research* **2021**, *93*, *10*, 2010–2024, doi:10.1002/WER.1572.
4. Mo, Z.; She, X.; Li, Y.; Liu, L.; Huang, L.; Chen, Z.; Zhang, Q.; Xu, H.; Li, H. Synthesis of g-C_3N_4 at different temperatures for superior visible/UV photocatalytic performance and photoelectrochemical sensing of MB solution. *RSC Advances* **2015**, *5(123)*, 101552–101562, doi:10.1039/C5RA19586A.
5. Dong, J.; Zhang, Y.; Hussain, M. I.; Zhou, W.; Chen, Y.; Wang, L. N. g-C_3N_4: Properties, Pore Modifications, and Photocatalytic Applications. *Nanomaterials* **2022**, *12(1)*, 121, doi:10.3390/NANO12010121.
6. Rhimi, B.; Wang, C.; Bahnemann, D. W. Latest progress in g-C_3N_4 based heterojunctions for hydrogen production via photocatalytic water splitting: A mini review. *JPhys Energy* **2020**, *2*, 042003, doi:10.1088/2515-7655/ABB782.
7. Matias, M. L.; Morais, M.; Pimentel, A.; Vasconcelos, F. X.; Reis Machado, A. S.; Rodrigues, J.; Fortunato, E.; Martins, R.; Nunes, D. Floating TiO_2-Cork Nano-Photocatalysts for Water Purification Using Sunlight. *Sustainability* **2022**, *14(15)*,9645, doi:10.3390/SU14159645.
8. Shakeelur Raheman, A. R.; Wilson, H. M.; Momin, B. M.; Annapure, U. S.; Jha, N. TiO_2 nanosheet/ultra-thin layer g-C_3N_4 core-shell structure: Bifunctional visible-light photocatalyst for H_2 evolution and removal of organic pollutants from water. *Applied Surface Science* **2020**, *528*, 146930, doi:10.1016/J.APSUSC.2020.146930.
9. DeRita, L.; Resasco, J.; Dai, S.; Boubnov, A.; Thang, H. V.; Hoffman, A. S.; Ro, I.; Graham, G. W.; Bare, S. R.; Pacchioni, G.; Pan, X.; Christopher, P. Structural evolution of atomically dispersed Pt catalysts dictates reactivity. *Nature Materials* **2019**, *18 (7)*, 746–751, doi:10.1038/S41563-019-0349-9.
10. Yang, H. G.; Sun, C. H.; Qiao, S. Z.; Zou, J.; Liu, G.; Smith, S. C.; Cheng, H. M.; Lu, G. Q. Anatase TiO_2 single crystals with a large percentage of reactive facets. *Nature* **2008**, *453*, 638–641, doi:10.1038/nature06964.
11. Sun, K.; Shen, J.; Liu, Q.; Tang, H.; Zhang, M.; Zulfiqar, S.; Lei, C. Synergistic effect of

Co(II)-hole and Pt-electron cocatalysts for enhanced photocatalytic hydrogen evolution performance of P-doped g-C_3N_4. *Chinese Journal of Catalysis* **2020**, *41(1)*, 72–81, doi:10.1016/S1872-2067(19)63430-3.

12. Zhao, Z.; Sun, Y.; Luo, Q.; Dong, F.; Li, H.; Ho, W. K. Mass-Controlled Direct Synthesis of Graphene-like Carbon Nitride Nanosheets with Exceptional High Visible Light Activity. Less is Better. *Scientific Reports* **2015**, *5(1)*, 14643, doi:10.1038/SREP14643.
13. Zhang, S.; Hang, N. T.; Zhang, Z.; Yue, H.; Yang, W. Preparation of g-C_3N_4 /Graphene Composite for Detecting NO_2 at Room Temperature. *Nanomaterials* **2017**, *7(1)*, 12, doi:10.3390/NANO7010012.
14. Li, K.; Gao, S.; Wang, Q.; Xu, H.; Wang, Z.; Huang, B.; Dai, Y.; Lu, J. In-situ-reduced synthesis of Ti^{3+} self-doped TiO_2/g-C_3N_4 heterojunctions with high photocatalytic performance under LED light irradiation. *ACS Applied Materials and Interfaces* **2015**, *7(17)*, 9023–9030, doi:10.1021/AM508505N.
15. Alcudia-Ramos, M. A.; Fuentez-Torres, M. O.; Ortiz-Chi, F.; Espinosa-González, C. G.; Hernández-Como, N.; García-Zaleta, D. S.; Kesarla, M. K.; Torres-Torres, J. G.; Collins-Martínez, V.; Godavarthi, S. Fabrication of g-C_3N_4/TiO_2 heterojunction composite for enhanced photocatalytic hydrogen production. *Ceramics International* **2020**, *46*, *1*, 38–45, doi:10.1016/J.CERAMINT.2019.08.228.
16. Cao, J.; Qin, C.; Wang, Y.; Zhang, H.; Sun, G.; Zhang, Z. Solid-state method synthesis of SnO_2-decorated g-C_3N_4 nanocomposites with enhanced gas-sensing property to ethanol. *Materials* **2017**, *10(6)*, 604, doi:10.3390/MA10060604.
17. Gong, S.; Jiang, Z.; Zhu, S.; Fan, J.; Xu, Q.; Min, Y. The synthesis of graphene-TiO_2/g-C_3N_4 super-thin heterojunctions with enhanced visible-light photocatalytic activities. *Journal of Nanoparticle Research* **2018**, *20(11)*, 1–13, doi:10.1007/S11051-018-4399-8.
18. Boonprakob, N.; Wetchakun, N.; Phanichphant, S.; Waxler, D.; Sherrell, P.; Nattestad, A.; Chen, J.; Inceesungvorn, B. Enhanced visible-light photocatalytic activity of g-C_3N_4/TiO_2 films. *Journal of Colloid and Interface Science* **2014**, *417*, 402–409, doi:10.1016/J.JCIS.2013.11.072.
19. Matias, M. L.; Pimentel, A.; Reis-Machado, A. S.; Rodrigues, J.; Deuermeier, J.; Fortunato, E.; Martins, R.; Nunes, D. Enhanced Fe-TiO_2 Solar Photocatalysts on Porous Platforms for Water Purification. *Nanomaterials* **2022**, *12*.
20. Shen, L.; Xing, Z.; Zou, J.; Li, Z.; Wu, X.; Zhang, Y.; Zhu, Q.; Yang, S.; Zhou, W. Black TiO_2 nanobelts/g-C_3N_4 nanosheets Laminated Heterojunctions with Efficient Visible-Light-Driven Photocatalytic Performance. *Scientific Reports* **2017**, *7*, *41978*, 1–11, doi:10.1038/srep41978.
21. Hutchings, G. J.; Davies, P. R.; Pattisson, S.; Davies, T. E.; Morgan, D. J.; Dlamini, M. W. Facile synthesis of a porous 3D g-C_3N_4 photocatalyst for the degradation of organics in shale gas brines. *Catalysis Communications* **2022**, *169*, 106480, doi:10.1016/J.CATCOM.2022.106480.
22. Kumar, A.; Kumar, P.; Joshi, C.; Manchanda, M.; Boukherroub, R.; Jain, S. L. Nickel decorated on phosphorous-doped carbon nitride as an efficient photocatalyst for reduction of nitrobenzenes. *Nanomaterials* **2016**, *6(4)*, doi:10.3390/NANO6040059.
23. Chen, J.; Zhang, Y.; Wu, B.; Ning, Z.; Song, M.; Zhang, H.; Sun, X.; Wan, D.; Li, B. Porous g-C_3N_4 with defects for the efficient dye photodegradation under visible light. *Water*

Science and Technology **2021**, *84(6)*, 1354–1365, doi:10.2166/WST.2021.313.
24. Landi, S.; Rocha Segundo, I.; Freitas, E.; Vasilevskiy, M.; Carneiro, J.; Tavares, C. J. Use and misuse of the Kubelka-Munk function to obtain the band gap energy from diffuse reflectance measurements. *Solid State Communications* **2022**, *341*, 1–7.
25. Nunes, D.; Pimentel, A.; Santos, L.; Barquinha, P.; Fortunato, E.; Martins, R. Photocatalytic TiO_2 Nanorod Spheres and Arrays Compatible with Flexible Applications. *Catalysts* **2017**, *7 (2)*, 1–18.
26. Giannakopoulou, T.; Papailias, I.; Todorova, N.; Boukos, N.; Liu, Y.; Yu, J.; Trapalis, C. Tailoring the energy band gap and edges' potentials of g-C_3N_4/TiO_2 composite photocatalysts for NOx removal. *Chemical Engineering Journal* **2017**, *310, Part*, 571–580, doi:10.1016/J.CEJ.2015.12.102.
27. Abdel-Moniem, S. M.; El-Liethy, M. A.; Ibrahim, H. S.; Ali, M. E. M. Innovative green/non-toxic Bi_2S_3@g-C_3N_4 nanosheets for dark antimicrobial activity and photocatalytic depollution: Turnover assessment. *Ecotoxicology and Environmental Safety* **2021**, *226*, 112808, doi:10.1016/J.ECOENV.2021.112808.
28. Dong, F.; Zhao, Z.; Xiong, T.; Ni, Z.; Zhang, W.; Sun, Y.; Ho, W.-K. In Situ Construction of g-C_3N_4/g-C_3N_4 Metal-Free Heterojunction for Enhanced Visible-Light Photocatalysis. *ACS Applied Materials and Interfaces* **2013**, *5*, 11392–11401, doi:10.1021/am403653a.
29. Pattnaik, S. P.; Behera, A.; Martha, S.; Acharya, R.; Parida, K. Facile synthesis of exfoliated graphitic carbon nitride for photocatalytic degradation of ciprofloxacin under solar irradiation. *Journal of Materials Science* **2019**, *54(7)*, 5726–5742, doi:10.1007/S10853-018-03266-X.
30. Jia, T.; Li, J.; Long, F.; Fu, F.; Zhao, J.; Deng, Z.; Wang, X.; Zhang, Y. Ultrathin g-C_3N_4 nanosheet-modified biocl hierarchical flower-like plate heterostructure with enhanced photostability and photocatalytic performance. *Crystals* **2017**, *7(9)*, 266, doi:10.3390/CRYST7090266.
31. Das, D.; Shinde, S. L.; Nanda, K. K. Temperature-Dependent Photoluminescence of g-C_3N_4: Implication for Temperature Sensing. *ACS Applied Materials and Interfaces* **2016**, *8*, *3*, 2181–2186, doi:10.1021/ACSAMI.5B10770.
32. Yuan, Y.; Zhang, L.; Xing, J.; Utama, M. I. B.; Lu, X.; Du, K.; Li, Y.; Hu, X.; Wang, S.; Genç, A.; Dunin-Borkowski, R.; Arbiol, J.; Xiong, Q. High-yield synthesis and optical properties of g-C_3N_4. *Nanoscale* **2015**, *7*, *29*, 12343–12350, doi:10.1039/C5NR02905H.
33. Fu, M.; Liao, J.; Dong, F.; Li, H.; Liu, H. Growth of g-C_3N_4 layer on commercial TiO_2 for enhanced visible light photocatalytic activity. *Journal of Nanomaterials* **2014**, *2014*, 86909, doi:10.1155/2014/869094.
34. Lin, T. H.; Chang, Y. H.; Chiang, K. P.; Wang, J. C.; Wu, M. C. Nanoscale Multidimensional Pd/TiO_2 /g-C_3N_4 Catalyst for Efficient Solar-Driven Photocatalytic Hydrogen Production. *Catalysts 2021, Vol. 11, Page 59* **2021**, *11(1)*, 59, doi:10.3390/CATAL11010059.
35. Farahani, N.; Kelly, P. J.; West, G.; Ratova, M.; Hill, C.; Vishnyakov, V. An investigation into W or Nb or $ZnFe_2O_4$ Doped Titania nanocomposites deposited from Blended powder targets for UV/Visible photocatalysis. *Coatings* **2013**, *3(3)*, 153–165, doi:10.3390/COATINGS3030153.
36. Zhang, T.; Souza, I. P. A. F.; Xu, J.; Almeida, V. C.; Asefa, T. Mesoporous Graphitic

Carbon Nitrides Decorated with Cu Nanoparticles: Efficient Photocatalysts for Degradation of Tartrazine Yellow Dye. *Nanomaterials* **2018**, *8(9)*, 636, doi:10.3390/NANO8090636.

37. Freire, T.; Fragoso, A. R.; Matias, M.; Vaz Pinto, J.; Marques, A. C.; Pimentel, A.; Barquinha, P.; Huertas, R.; Fortunato, E.; Martins, R.; Nunes, D. Enhanced solar photocatalysis of TiO_2 nanoparticles and nanostructured thin films grown on paper. *Nano Express* **2021**, *2,4*, 1–20.
38. Guo, Y.; Li, H.; Chen, J.; Wu, X.; Zhou, L. TiO_2 mesocrystals built of nanocrystals with exposed {001} facets: facile synthesis and superior photocatalytic ability. *Journal of Materials Chemistry A* **2014**, *2*, 19589–19593, doi:10.1039/C4TA05068A.
39. Pan, F.; Wu, K.; Li, H.; Xu, G.; Chen, W. Synthesis of {100} Facet Dominant Anatase TiO_2 Nanobelts and the Origin of Facet-Dependent Photoreactivity. *Chemistry – A European Journal* **2014**, *20*, *46*, 15095–15101, doi:10.1002/CHEM.201403866.
40. Xu, H.; Ouyang, S.; Li, P.; Kako, T.; Ye, J. High-active anatase TiO_2 nanosheets exposed with 95% {100} facets toward efficient H_2 evolution and CO_2 photoreduction. *ACS Applied Materials and Interfaces* **2013**, *5(4)*, 1348–1354, doi:10.1021/AM302631B.
41. Pan, J.; Liu, G.; Qing, G.; Lu, M.; Cheng, H.-M. On the True Photoreactivity Order of {001}, {010}, and {101} Facets of Anatase TiO_2 Crystals. *Angewandte Chemie* **2011**, *123*, 2181–2185, doi:10.1002/ANGE.201006057.
42. Selloni, A. Crystal growth: Anatase shows its reactive side. *Nature Materials* **2008**, *7*, 613–615, doi:10.1038/NMAT2241.
43. Luttrell, T.; Halpegamage, S.; Tao, J.; Kramer, A.; Sutter, E.; Batzill, M. Why is anatase a better photocatalyst than rutile? - Model studies on epitaxial TiO_2 films. *Scientific Reports* **2014**, *4*, *4043*, 1–8, doi:10.1038/srep04043.
44. Zerjav, G.; Zizek, K.; Zavasnik, J.; Pintar, A. Brookite vs. rutile vs. anatase: What`s behind their various photocatalytic activities? *Journal of Environmental Chemical Engineering* **2022**, *10*, 107722, doi:10.1016/J.JECE.2022.107722.
45. Zhang, J.; Zhou, P.; Liu, J.; Yu, J. New understanding of the difference of photocatalytic activity among anatase, rutile and brookite TiO_2. *Physical Chemistry Chemical Physics* **2014**, *16*, *38*, 20382–20386, doi:10.1039/C4CP02201G.
46. Lin, P.; Hu, H.; Lv, H.; Ding, Z.; Xu, L.; Qian, D.; Wang, P.; Pan, J.; Li, C.; Cui, C. Hybrid reduced graphene oxide/TiO_2/graphitic carbon nitride composites with improved photocatalytic activity for organic pollutant degradation. *Applied Physics A: Materials Science and Processing* **2018**, *124(7)*, 1–11, doi:10.1007/S00339-018-1933-6.
47. Hassan, F.; Bonnet, P.; Dangwang Dikdim, J. M.; Gatcha Bandjoun, N.; Caperaa, C.; Dalhatou, S.; Kane, A.; Zeghioud, H. Synthesis and Investigation of TiO_2/g-C_3N_4 Performance for Photocatalytic Degradation of Bromophenol Blue and Eriochrome Black T: Experimental Design Optimization and Reactive Oxygen Species Contribution. *Water* **2022**, *14(20)*, 3331, doi:10.3390/W14203331.
48. Li, Y.; Wang, J.; Yang, Y.; Zhang, Y.; He, D.; An, Q.; Cao, G. Seed-induced growing various TiO_2 nanostructures on g-C_3N_4 nanosheets with much enhanced photocatalytic activity under visible light. *Journal of Hazardous Materials* **2015**, *292*, 79–89, doi:10.1016/J.JHAZMAT.2015.03.006.
49. Zang, Y.; Li, L.; Xu, Y.; Zuo, Y.; Li, G. Hybridization of brookite TiO_2 with g-C_3N_4: a

visible-light-driven photocatalyst for As^{3+} oxidation, MO degradation and water splitting for hydrogen evolution. *Journal of Materials Chemistry A* **2014**, *2*, *38*, 15774–15780, doi:10.1039/C4TA02082K.

50. Zeng, L.; He, Z.; Luo, Y.; Xu, J.; Chen, J.; Wu, L.; Huang, P.; Xu, S. A Simple g-C_3N_4/TNTs Heterojunction for Improving the Photoelectrocatalytic Degradation of Methyl Orange. *Journal of The Electrochemical Society* **2021**, *168*, *11*, 116520, doi:10.1149/1945-7111/AC3ABC.
51. Mohini, R.; Lakshminarasimhan, N. Coupled semiconductor nanocomposite g-C_3N_4/TiO_2 with enhanced visible light photocatalytic activity. *Materials Research Bulletin* **2016**, *76*, 370–375, doi:10.1016/J.MATERRESBULL.2015.12.034.
52. Liu, X.; Chen, N.; Li, Y.; Deng, D.; Xing, X.; Wang, Y. A general nonaqueous sol-gel route to g-C_3N_4-coupling photocatalysts: the case of Z-scheme g-C_3N_4/TiO_2 with enhanced photodegradation toward RhB under visible-light. *Scientific Reports* **2016**, *6*, *39531*, 1–16, doi:10.1038/srep39531.
53. Kobkeatthawin, T.; Trakulmututa, J.; Amornsakchai, T.; Kajitvichyanukul, P.; Smith, S. M. Identification of Active Species in Photodegradation of Aqueous Imidacloprid over g-C_3N_4/TiO_2 Nanocomposites. *Catalysts* **2022**, *12(2)*, 1–16, doi:10.3390/CATAL12020120.
54. Rovisco, A.; Morais, M.; Branquinho, R.; Fortunato, E.; Martins, R.; Barquinha, P. Microwave-Assisted Synthesis of Zn_2SnO_4 Nanostructures for Photodegradation of Rhodamine B under UV and Sunlight. *Nanomaterials* **2022**, *12*, 2119, doi:10.3390/NANO12122119.
55. Li, W.; Li, D.; Lin, Y.; Wang, P.; Chen, W.; Fu, X.; Shao, Y. Evidence for the active species involved in the photodegradation process of methyl Orange on TiO_2. *Journal of Physical Chemistry C* **2012**, *116*, *5*, 3552–3560, doi:10.1021/jp209661d.
56. Mahalakshmi, G.; Rajeswari, M.; Ponnarasi, P. Synthesis of few-layer g-C_3N_4 nanosheets-coated MoS_2/TiO_2 heterojunction photocatalysts for photo-degradation of methyl orange (MO) and 4-nitrophenol (4-NP) pollutants. *Inorganic Chemistry Communications* **2020**, *120*, 108146, doi:10.1016/J.INOCHE.2020.108146.
57. Jiang, D.; Li, J.; Xing, C.; Zhang, Z.; Meng, S.; Chen, M. Two-Dimensional $CaIn_2S_4$/g-C_3N_4 Heterojunction Nanocomposite with Enhanced Visible-Light Photocatalytic Activities: Interfacial Engineering and Mechanism Insight. *ACS Applied Materials and Interfaces* **2015**, *7*, 19234–19242, doi:10.1021/acsami.5b05118.
58. Ma, Y.; Zhang, Z.; Jiang, X.; Sun, R.; Xie, M.; Han, W. Supporting Information: Direct Z-scheme Sn-In_2O_3/In_2S_3 heterojunction nanostructures for enhanced photocatalytic CO_2 reduction activity. *Journal of Materials Chemistry C* **2021**, *9,11*.
59. Hong, S. J.; Lee, S.; Jang, J. S.; Lee, J. S. Heterojunction $BiVO_4$/WO_3 electrodes for enhanced photoactivity of water oxidation. *Energy and Environmental Science* **2011**, *4*, 1781–1787, doi:10.1039/C0EE00743A.
60. Hankin, A.; Bedoya-Lora, F. E.; Alexander, J. C.; Regoutz, A.; Kelsall, G. H. Flat band potential determination: avoiding the pitfalls. *Journal of Materials Chemistry A* **2019**, *7*, *45*, 26162–26176, doi:10.1039/C9TA09569A.
61. Drisya, K. T.; Solís-López, M.; Ríos-Ramírez, J. J.; Durán-Álvarez, J. C.; Rousseau, A.; Velumani, S.; Asomoza, R.; Kassiba, A.; Jantrania, A.; Castaneda, H. Electronic and optical competence of TiO_2/$BiVO_4$ nanocomposites in the photocatalytic processes.

Scientific Reports **2020**, *10*, *13507*, 1–16, doi:10.1038/s41598-020-69032-9.

62. Jing, J.; Chen, Z.; Feng, C.; Sun, M.; Hou, J. Transforming g-C_3N_4 from amphoteric to n-type semiconductor: The important role of p/n type on photoelectrochemical cathodic protection. *Journal of Alloys and Compounds* **2021**, *851*, 156820, doi:10.1016/J.JALLCOM.2020.156820.
63. Nunes, D.; Fragoso, A. R.; Freire, T.; Matias, M.; Marques, A. C.; Martins, R.; Fortunato, E.; Pimentel, A. Ultrafast Microwave Synthesis of WO_3 Nanostructured Films for Solar Photocatalysis. *physica status solidi (RRL) – Rapid Research Letters* **2021**, *15*,*9*, 2100196.
64. Naeem, R.; Ehsan, M. A.; Rehman, A.; Yamani, Z. H.; Hakeem, A. S.; Mazhar, M. Single step aerosol assisted chemical vapor deposition of p-n Sn(II) oxide-Ti(IV) oxide nanocomposite thin film electrodes for investigation of photoelectrochemical properties. *New Journal of Chemistry* **2018**, *42*, *7*, 5256–5266, doi:10.1039/C7NJ04606E.
65. Ismael, M.; Wu, Y. A facile synthesis method for fabrication of $LaFeO_3$/g-C_3N_4 nanocomposite as efficient visible-light-driven photocatalyst for photodegradation of RhB and 4-CP. *New Journal of Chemistry* **2019**, *43*, *35*, 13783–13793, doi:10.1039/c9nj03376a.
66. Tang, Y.; Huang, J.; Jiang, M.; Yu, J.; Wang, Q.; Zhao, J.; Li, J.; Yu, X.; Zhao, J. Photo-induced synthesis of nanostructured Pt-on-Au/g-C_3N_4 composites for visible light photocatalytic hydrogen production. *Journal of Materials Science* **2020**, *55*, *32*, 15574–15587, doi:10.1007/S10853-020-05120-5.
67. Beranek, R. (Photo)electrochemical methods for the determination of the band edge positions of TiO_2-based nanomaterials. *Advances in Physical Chemistry* **2011**, *2011*, 786759, doi:10.1155/2011/786759.
68. Jo, W. K.; Natarajan, T. S. Influence of TiO_2 morphology on the photocatalytic efficiency of direct Z-scheme g-C_3N_4/TiO_2 photocatalysts for isoniazid degradation. *Chemical Engineering Journal* **2015**, *281*, 549–565, doi:10.1016/J.CEJ.2015.06.120.
69. Gao, Y.; Duan, J.; Zhai, X.; Guan, F.; Wang, X.; Zhang, J.; Hou, B. Photocatalytic degradation and antibacterial properties of Fe^{3+}-doped alkalized carbon nitride. *Nanomaterials* **2020**, *10(9)*, 1–17, doi:10.3390/nano10091751.
70. Yu, J.; Wang, S.; Low, J.; Xiao, W. Enhanced photocatalytic performance of direct Z-scheme g-C_3N_4-TiO_2 photocatalysts for the decomposition of formaldehyde in air. *Physical Chemistry Chemical Physics* **2013**, *15(39)*, 16883–16890, doi:10.1039/C3CP53131G.
71. Liu, M.; Wei, S.; Chen, W.; Gao, L.; Li, X.; Mao, L.; Dang, H. Construction of direct Z-scheme g-C_3N_4/TiO_2 nanorod composites for promoting photocatalytic activity. *Journal of the Chinese Chemical Society* **2019**, *67*, *2*, 246–252, doi:10.1002/JCCS.201900135.
72. Sewnet, A.; Abebe, M.; Asaithambi, P.; Alemayehu, E. Visible-Light-Driven g-C_3N_4/TiO_2 Based Heterojunction Nanocomposites for Photocatalytic Degradation of Organic Dyes in Wastewater: A Review. *Air, Soil and Water Research* **2022**, *15*, 1–23, doi:10.1177/11786221221117266.
73. Naveed, A. B.; Javaid, A.; Zia, A.; Ishaq, M. T.; Amin, M.; Farooqi, Z. U. R.; Mahmood, A. TiO_2/g-C_3N_4 Binary Composite as an Efficient Photocatalyst for Biodiesel Production from Jatropha Oil and Dye Degradation. *ACS Omega* **2022**, *8*, *2*, 2173–2182, doi:10.1021/acsomega.2c04841.

6

DEVELOPMENT AND CHARACTERIZATION OF TiO_2 ON 3D PU FOAMS

The next section was adapted from the publication: Matias, M. L.; Pimentel, A.; Reis-Machado, A.; Rodrigues, J. C.; Fernandes, A.; Monteiro, T.; Almeida Carvalho, P.; Neves Amaral, M. N.; Reis, C. P.; Deuermeier, J.; Fortunato, E.; Martins, R.; Nunes, D. Functionalized 3D Polyurethane Foams with Microwave-synthesized TiO_2 Nanostructures for Solar Light-driven Degradation of Tetracycline. *Environmental Science: Advances* **2025**, 4, 713–738 doi:10.1039/D4VA00110A.

6.1 Introduction

Encouraged by the lack of research work regarding the decontamination of wastewater using TiO_2 nano photocatalysts immobilized on reusable PU foams, and considering the potential that floating photocatalysts may bring to replace the conventional TiO_2 photocatalysts, this study reports the adsorption and photocatalytic performance of TiO_2 nanostructures immobilized on PU foams by a simple dip-coating process for the removal and degradation of tetracycline under solar light radiation. To our best knowledge, this has never been reported.

As stated in the first chapter, PU foam is an ideal low-cost substrate for the immobilization of nanostructures and further use in photocatalysis due to its open-skeleton structure, which provides a high surface area, excellent adsorption capacity and low density, making it floatable. Additionally, PU foams can be flexible and have the potential for reusability [1–4].

The effect of ethanol, IPA and water on the formation of TiO_2 nanostructures by a simple and fast MW approach (10 min) is also systematically studied at the atomic level, demonstrating the direct relation between the structural defects and the nanomaterial's photocatalytic performance. The TiO_2 nanostructures synthesized in ethanol, IPA and water will be denoted as TiO_2_EtOH, TiO_2_IPA and TiO_2_H_2O, respectively. The TiO_2 nanopowder that showed the highest effectiveness against tetracycline was used in the chemical quenching experiments (to understand the photocatalytic mechanism) and it was further incorporated into PU foams. Recyclability tests were performed on both TiO_2 nanopowders and 3D TiO_2 PU foams. Moreover, the results of ecotoxicity experiments were reported by assessing the acute toxicity of PU foams (with and without TiO_2 nanostructures) to nauplii of *Artemia salina*. The structural and optical properties of the TiO_2 nanopowders were investigated by XRD, electron microscopy, BET analysis, XPS and PL/PLE spectroscopies. The adsorption mechanisms were studied by using five kinetic models: first−order, the McKay and Ho pseudo−second-order,

Weber−Morris intraparticle diffusion, Elovich, Bangham and Boyd. For the PU foams, their structural characterization was also carried out through SEM/EDS.

6.2 Results and discussion

6.2.1 Structural and optical characterization of the TiO_2 nanopowders

6.2.1.1 XRD

The X-ray diffractograms of the TiO_2 nanopowders (TiO_2_EtOH, TiO_2_IPA and TiO_2_H_2O) are shown in Figure 6.1. In the presence of ethanol, all experimental diffraction maxima can be assigned to the tetragonal TiO_2 anatase crystalline phase (ICDD file number 00-021-1272). An analogous study reported the production of TiO_2 nanostructures by MW irradiation in ethanol under similar conditions of time and temperature, i.e., 10 min and 200 °C. In this study, the XRD also showed a pure TiO_2 anatase phase [5]. However, when isopropanol was used, besides observing the anatase diffraction maxima, another diffraction maximum appears at around 30° (2θ), ascribed to the (121) plane of orthorhombic brookite crystalline phase (ICDD file number 00-029-1360). Despite the experimental difficulties in obtaining pure brookite, previous studies have shown that this phase can appear as a secondary phase in acidic alcohol-based solutions under optimum conditions of acidity, temperature and precursor concentration [6–8]. For the TiO_2_H_2O nanopowder, a clear mixture of rutile (ICDD file number 00-021-1276) and anatase crystalline phases is identified. This result is in accordance with previous reports on TiO_2 synthesis in an acidic medium under a MW-assisted hydrothermal synthesis under the same temperature and time conditions, in which the formation of both anatase and rutile was observed [9].

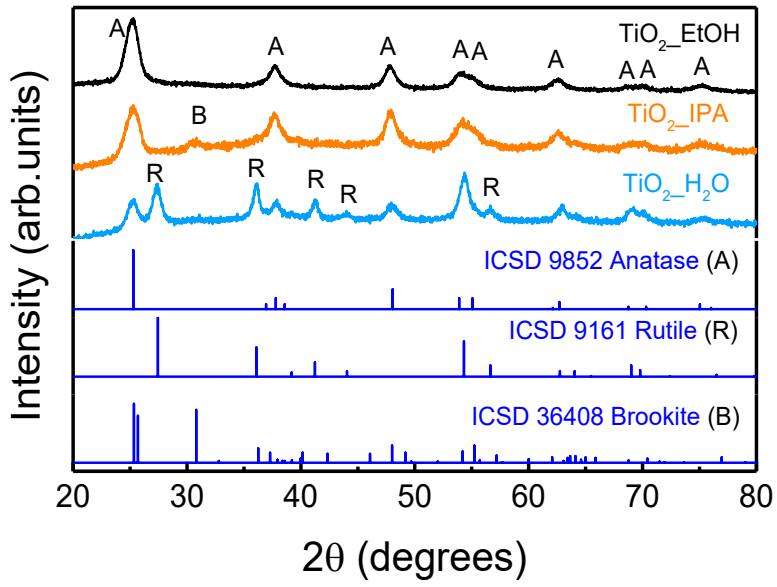

Figure 6.1: X-ray diffractograms of the TiO_2 nanopowders (TiO_2_EtOH, TiO_2_IPA and TiO_2_H_2O) synthesized under MW irradiation at 200 °C for 10 min. The simulations of TiO_2 anatase, rutile and brookite are also presented for comparison.

6.2.1.2 Electron microscopy

6.2.1.2.1 SEM

The effect of different solvents on the morphology of the TiO_2 nanomaterials was investigated using scanning electron microscopy. From Figure 6.2 (a) and (b), it can be seen the formation of micro-sized TiO_2 aggregates. These aggregates tend to have a spherical shape however, elongated aggregates were also observed. From Figure 6.2 (b) and its inset, it can be noted that these larger aggregates are composed of very fine nanocrystals. TiO_2 micrometer spherical aggregates were previously reported with ethanol as a solvent in MW synthesis [5,10]. Moreover, it can also be inferred that these larger aggregates are highly porous (refer to the arrows/dark spots in the inset of Figure 6.2 (b)). When it comes to the TiO_2_IPA nanopowder (Figure 6.2 (c) and (d)), the formation of 1D nanostructures can be detected, with other smaller nanocrystals with an undefined shape (refer to the inset in Figure 6.2 (d)). These very fine TiO_2 nanocrystals tend to aggregate [11], however, no specific larger structure was found for this condition of synthesis. XRD measurements determined that this nanomaterial was mostly composed of anatase with a minor presence of brookite and, for that reason, the heterogeneity observed in this nanomaterial can be related to the mixture of phases. As for the TiO_2_H_2O nanomaterial, the synthesis carried out in water resulted in 1D nanostructures.

However, in this condition, it is clear that the TiO_2 nanorods presented a tetragonal shape, which has been previously reported to be from the rutile phase [12]. This observation corroborates the XRD measurements, in which a mixture of rutile and anatase was identified. Nanocrystals with an undefined shape were also observed, but the 1D nanostructures dominated, as can be seen in Figure 6.2 (e) and (f) and in the inset of Figure 6.2 (f). The nanocrystals synthesized with H_2O also tended to aggregate in larger structures and in this case, it can be observed the formation of quasi-spherical micro-sized aggregates.

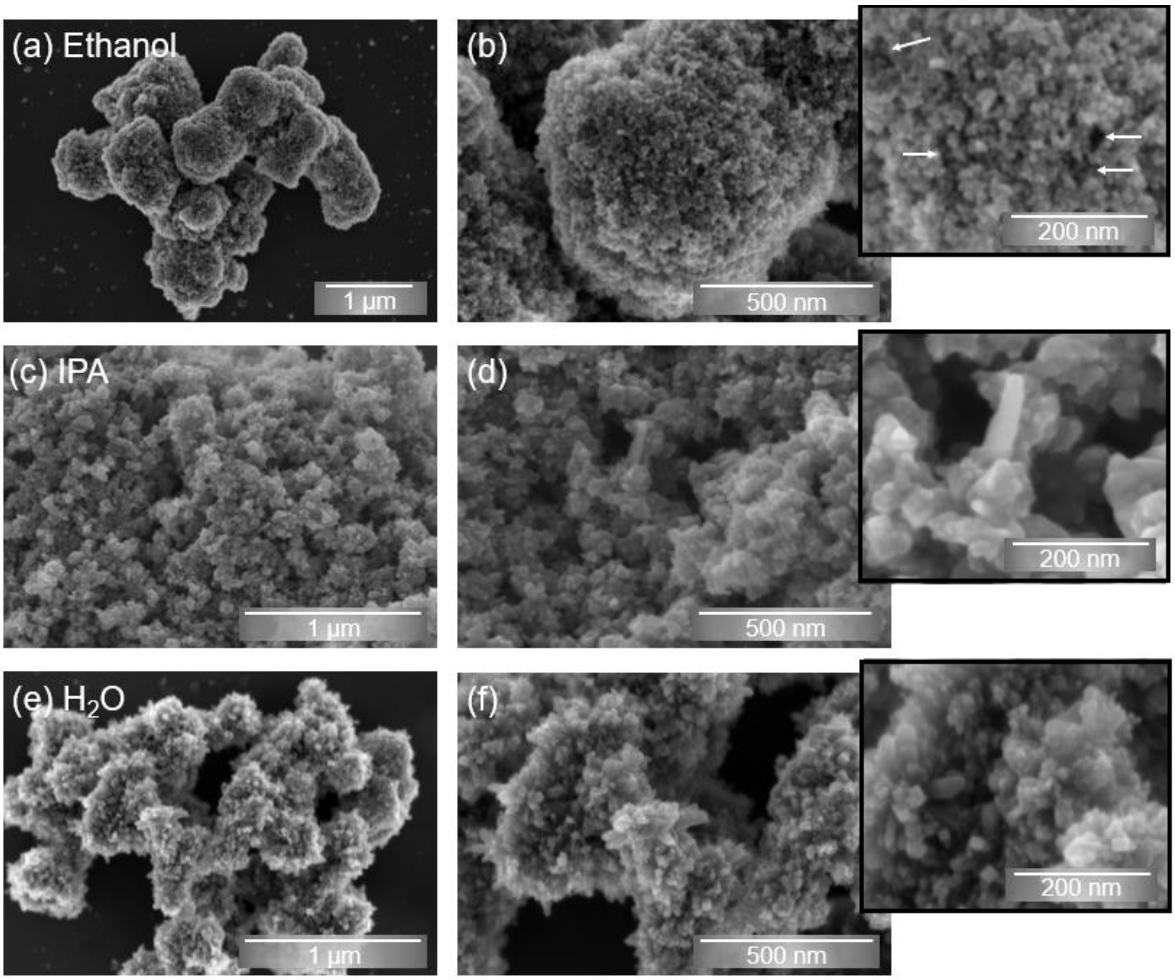

Figure 6.2: SEM images of the TiO_2 nanomaterials, (a) and (b) TiO_2_EtOH, (c) and (d) TiO_2_IPA and (e) and (f) TiO_2_H_2O.

6.2.1.2.2 STEM

The TiO_2_EtOH, TiO_2_IPA and TiO_2_H_2O nanostructures were also investigated using STEM analyses. As demonstrated by the SEM images, the formation of micro-sized TiO_2 nanocrystal aggregates for the material synthesized with ethanol is clear. From the STEM images in Figure 6.3, the presence of porosity is evident even at the nanoscale (arrows in the inset). As

shown in the inset of Figure 6.3, faceted TiO_2 nanocrystals and others with round edges could also be observed. The average TiO_2 nanocrystals' size was found to be 5.93 ± 0.94 nm.

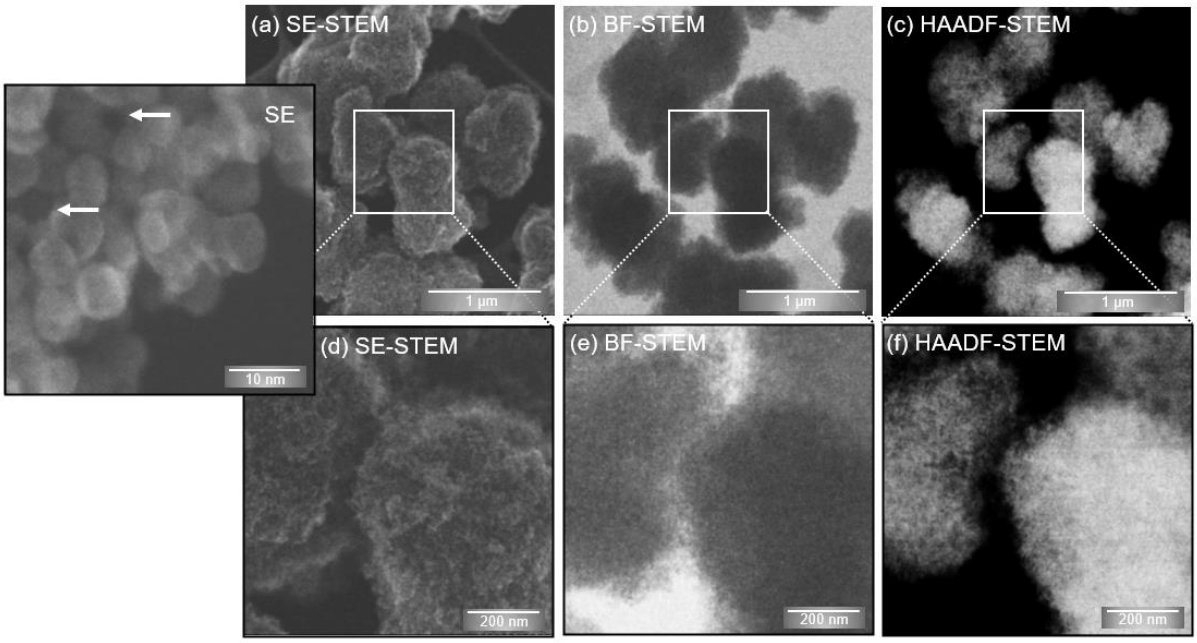

Figure 6.3: (a) and (d) SE-STEM, (b) and (e) BF-STEM, and (c) and (f) HAADF-STEM images of the micro-scaled TiO_2 aggregates of the TiO_2_EtOH nanomaterial highlighting their porous characteristics. The inset shows that the aggregates are composed of TiO_2 nanocrystals. The presence of spaces/voids is also evident between the nanocrystals (arrows), suggesting porosity at the nanoscale.

The TiO_2_EtOH nanocrystals were further investigated using atomic-resolution annular bright-field (ABF) HAADF imaging (Figure 6.4). The SE-STEM images were of great importance since the topographical contrast assisted the interpretation of the ABF and HAADF images [13]. The Ti atomic columns are visible in the ABF and HAADF images, albeit with reverse contrast [14]. The Ti atomic columns correspond to lattice spacings of 0.27 nm and 0.29 nm, which perfectly match the (110) and (102) atomic planes of anatase, respectively. FFT images acquired along the [221] zone axis showed that the angle between $(1\bar{1}0)$ and $(10\bar{2})$ is ~56°, in accordance with the theoretical value reported for pure crystalline TiO_2 anatase (ICDD file number 00-021-1272). The TiO_2 nanocrystals show structural defects in the STEM images, attested by a darker topographical contrast in the SE images (arrows pointing to the absence of Ti atoms). Surface steps can also be observed in Figure 6.4 (e) and (f). The TiO_2 faceted nanocrystal was further investigated (Figure 6.4 (h) and (i)) and high-index {012} and {102} facets can clearly be observed. TiO_2 anatase high-index nanocrystals have been reported to display high photocatalytic activities when compared to low-index faceted crystals due to their unique atomic and electronic structure, with a high density of atomic steps, kinks, ledges, dangling

bonds and abundant unsaturated coordination sites [15]. It has been proposed that higher index planes containing structural steps cause the electrons to be trapped at the low-coordinated Ti cations at the steps, thereby enhancing the separation of charges. Consequently, these additional electrons contribute to surface processes. On the other hand, the trapping of holes at the surfaces of anatase is facet-dependent. Studies have shown that the (001) and (100), and the (105) and (107) surfaces have the strongest affinity to trap holes, favoring the charge separation on anatase crystals and allowing the presence of holes on these surfaces to interact with molecular adsorbates. It has been suggested that hole trapping mainly occurs within the subsurface layers rather than on the surface facets for the (101), (110), (112) and (103) surfaces. This could potentially extend the lifetime of electrons, preventing recombination [16]. In the case of the (102) facets of anatase, the presence of surface defects was demonstrated with terminations of oxygen completely distinct from the predicted stoichiometric structures [17]. Low-index faceted anatase nanocrystals were also observed in the TiO_2_EtOH nanomaterial, however, no topographical contrast was detected in the SE images or the ABF and HAADF images of these nanocrystals, suggesting that they are defect-free. To the authors' knowledge, TiO_2 anatase faceted nanocrystals with sizes in the order of ~6 nm had their atomic structure investigated using STEM experiments for the first time. Such studies were paramount to determine the nanocrystals' surfaces and presence of structural defects, including steps on their high-index {012} facets and the absence of Ti atoms in the bulk (see arrows in Figure 6.4 (b) and (c), and (e) and (f)). Previously, only larger TiO_2 anatase defective crystals like sub-micrometer rods were reported [17]. The present STEM experiments determined that MW synthesis with ethanol as solvent resulted in low- and high-index faceted anatase nanocrystals, the latter with surface structural defects, which, when associated with the porous structure of the micro-sized aggregates, effectively play a key role in the photocatalytic activity of these materials.

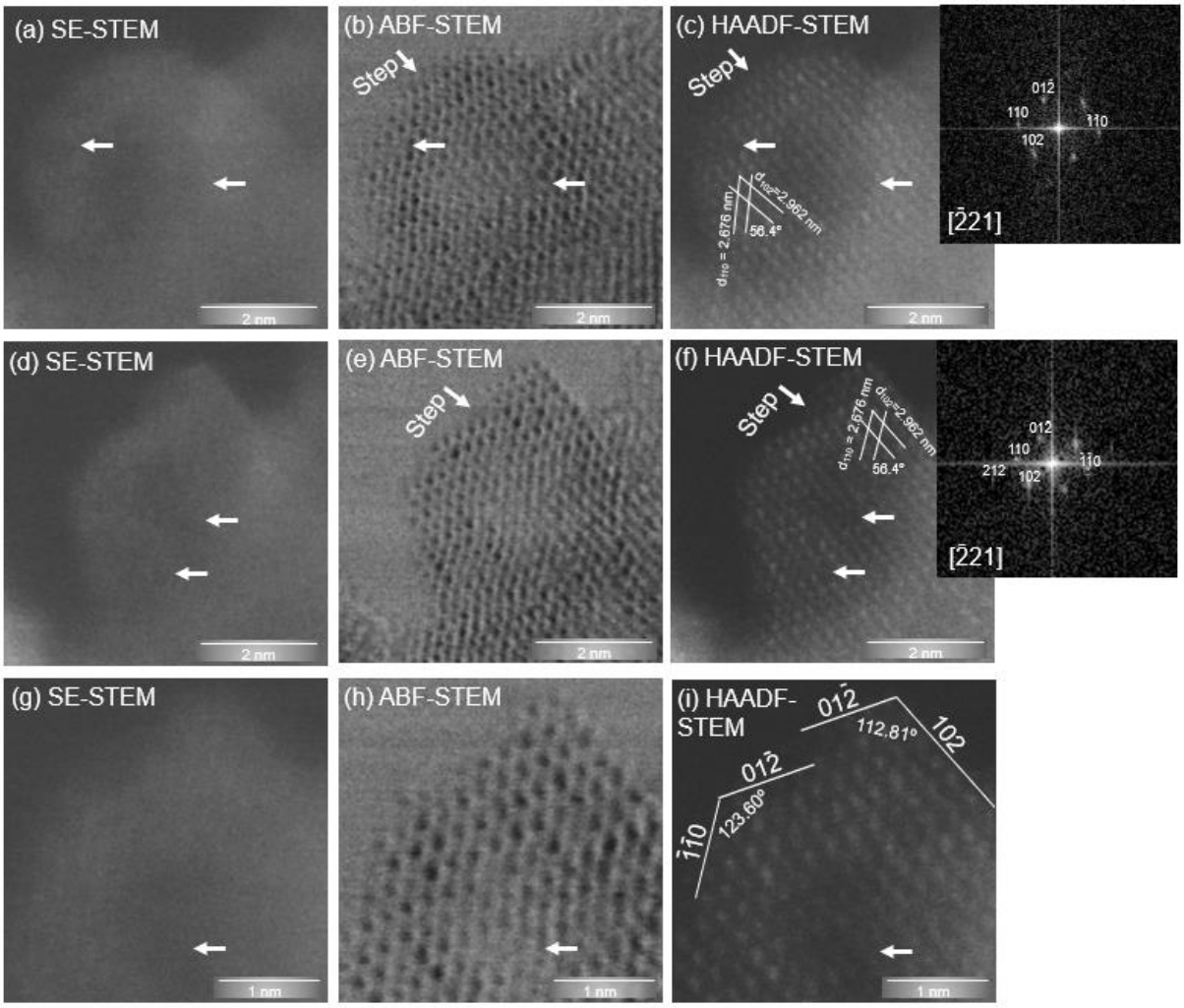

Figure 6.4: (a) SE-STEM, (b) ABF-STEM and (c) HAADF-STEM images acquired simultaneously of a TiO_2 anatase nanocrystal of the TiO_2_EtOH nanomaterial. The inset shows the FFT image obtained from (c). (d) SE-STEM, (e) ABF-STEM and (f) HAADF-STEM images of a TiO_2 faceted nanocrystal with a FFT image of (f) presented in the inset. The facet nanocrystal of images (d) to (f) was further magnified in (g) to (i). The arrows point to the atomic-level surface structural defects.

The TiO_2_IPA nanomaterial was also studied using atomic-resolution STEM (Figure 6.5), and, in accordance with the SEM observations, the nanomaterial is composed of 1D nanostructures and nanoparticles with undefined shapes. XRD analysis demonstrated that this material is mainly based on the TiO_2 anatase phase with a minor presence of brookite. This mixture of phases was confirmed by the electron diffraction pattern on the inset of Figure 6.5 (d). The presence of TiO_2 nanorods is evident in the STEM images (Figure 6.5 (a) to (c)) and in the BF-TEM image (Figure 6.5 (d)), in which 1D nanorods with different sizes are perceptible. Although larger nanorods with ~200 nm in length could be identified, the majority of nanorods

appear with 28.5 ± 4.3 nm in length and width, respectively. One of the larger TiO_2 nanorods was individually investigated (Figure 6.5), and from the atomic-resolution STEM images and the FFT patterns, it can be concluded that the nanorods had the tetragonal TiO_2 anatase phase (Figure 6.5 (f)). Moreover, the nanorod grew along its *c*-axis in the [100] direction, suggesting a fast growth rate along this direction. From Figure 6.5 (e) and (f), it can be observed that Ti atomic columns are perpendicular to each other. A lattice spacing of 0.19 nm perfectly matches the (200) and (020) atomic planes of anatase [18]. The angle between (200) and (020) is 90° and was also observed along the $[00\bar{1}]$ zone axis, which is expected for anatase (ICDD file number 00-021-1272). The facets of the nanorod are {010} surfaces. The surface energy of the major facets of anatase follows the order {001} (0.90 J/m^2) > {010}/{100} (0.53 J/m^2) > {101} (0.44 J/m^2) [15]. The relatively high surface energies of the {001} and {100}/{010} facets are ascribed to the 100 % five-fold coordinated titanium atoms (Ti_{5c}), in contrast to the 50 % Ti_{5c} found on {101} facets [19]. The {101} facets of anatase have been extensively investigated, however, it has been reported that the {010}/{100} facets display higher reactivity than {101} ones due to the higher concentration of low-coordination Ti_{5c} centers, making crystals with these high-energy facets desirable for photocatalysis [19,20]. When it comes to surface energy, it has been reported that high-index facets display higher surface energy. As far as we know, the surface energy associated with the {012}/{102} facets is unknown and cannot be easily measured in the present case, due to the mixed nanocrystal types. However, the {201} facets, with a surface energy of 1.72 $J.m^{-2}$, have been described to have more uncoordinated Ti atoms, promoting the photogeneration of hydroxyl radicals [15]. The {102} and {103} surfaces have undersaturated Ti atoms and high-density step defects, resulting in high photocatalytic activity [21]. The surface energy and atomic structure of crystals are vital for the photocatalytic performance of TiO_2 anatase [15] and the literature suggests that high-index facets have better photocatalytic behavior.

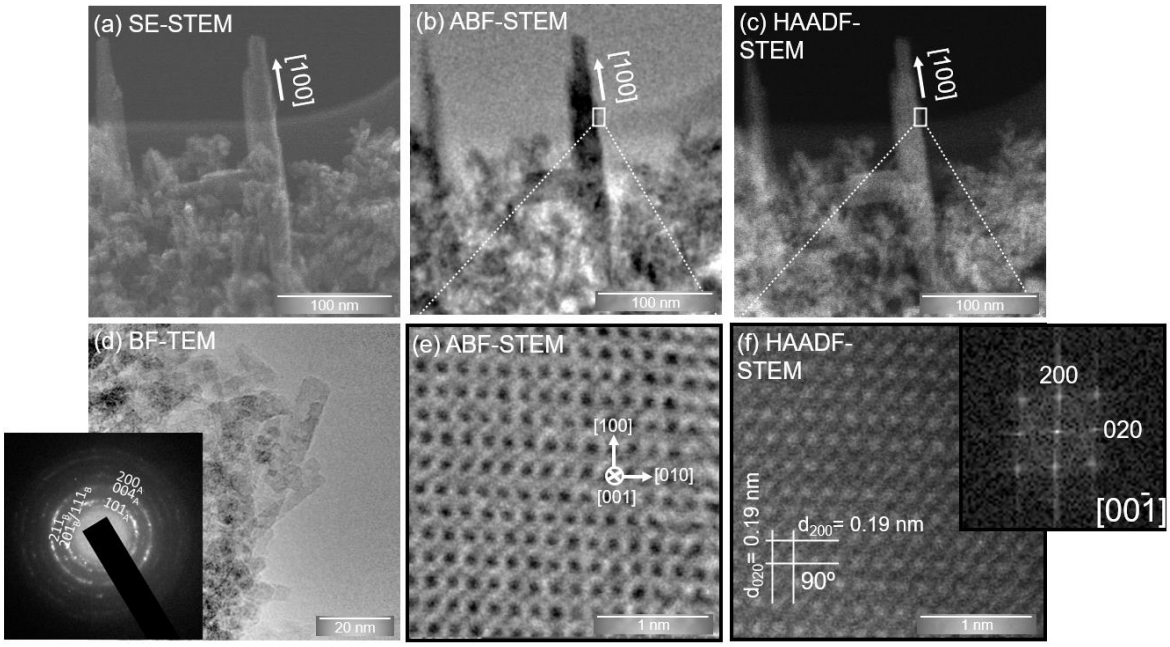

Figure 6.5: (a) SE-STEM, (b) ABF-STEM, (c) HAADF-STEM and (d) BF-TEM images of TiO_2_ IPA nanocrystals. The inset in (d) depicts the electron diffraction pattern of TiO_2 nanocrystals with the anatase (A) and brookite (B) phases. Atomic-resolution (e) ABF-STEM and (f) HAADF-STEM images of an individual TiO_2 nanorod (~200 nm). The inset in (f) shows the FFT image of the area in (f).

Figure 6.6 shows STEM images of the TiO_2_H_2O nanomaterial. XRD analysis showed that the TiO_2 nanostructures are a mixture of TiO_2 rutile and anatase with the presence of tetragonal-shaped nanorods, attributed to the rutile, as confirmed by SEM (Figure 6.2 (e) and (f)). STEM observations corroborated the SEM images, in which the nanostructures are mostly nanorods, with other nanocrystals having an undefined (quasi-spherical) shape. The rutile tetragonal nanorods have a pencil-like tip shape, and the presence of structural defects on the nanorod tip and throughout its length was detected. An individual nanorod (~100 nm) was further investigated (Figure 6.6), and based on the atomic-resolution STEM images and the FFT pattern, it can be proven that the nanorods correspond to the tetragonal rutile (Figure 6.6 (d) to (f)). The axis direction of the nanorod is [001]. The crystal growth along the *c*-axis has been associated with the fastest growth rate [22]. A lattice spacing of 0.30 nm has been ascribed to the (001) atomic planes of rutile [23], while the reported 0.20 nm matches the (120) rutile atomic planes, as seen in Figure 6.6 (f). Along the [210] zone axis, the angle between (001) and (120) is 90°, in accordance with the tetragonal rutile structure (ICDD file number 00-021-1276). Moreover, photocatalysts based on a mixture of rutile and anatase have been largely investigated for their high photocatalytic activity [24–26].

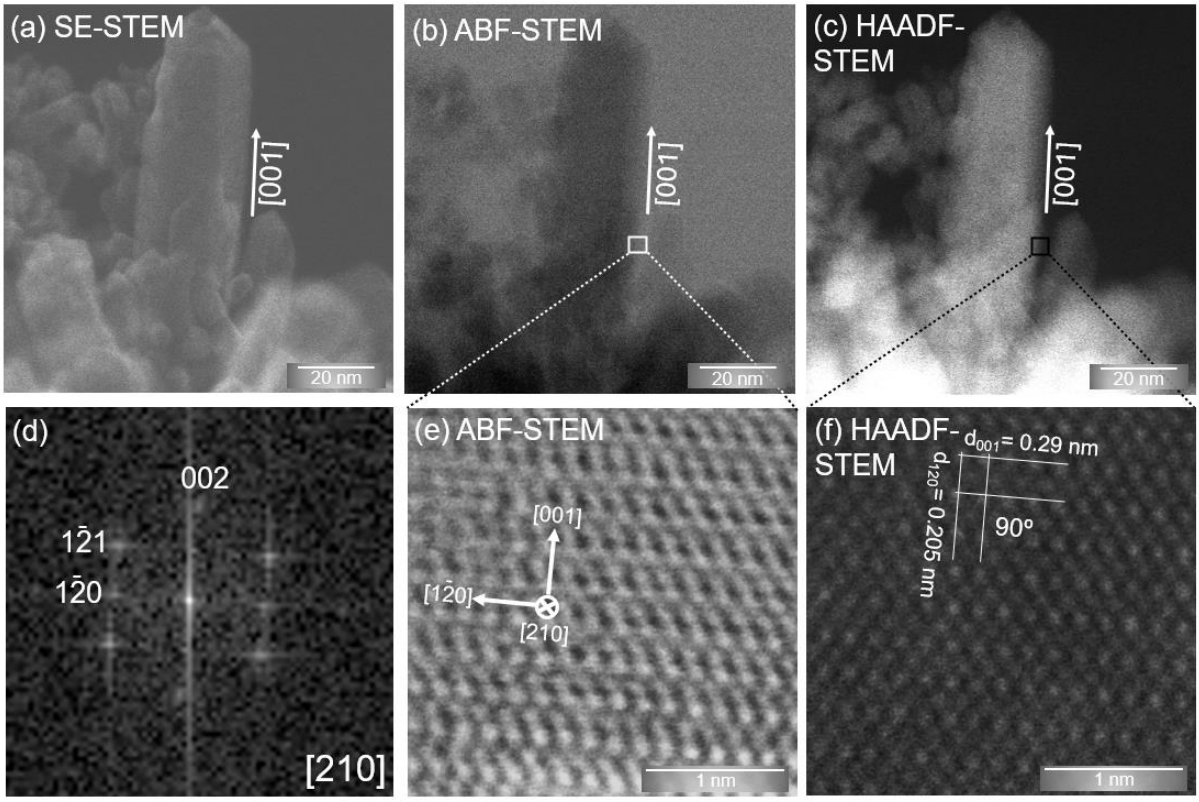

Figure 6.6: (a) SE-STEM, (b) ABF-STEM and (c) HAADF-STEM images of TiO_2_ H_2O nanocrystals. An individual TiO_2 nanorod was magnified and in (d) the FFT image of the area observed in (e) and (f) is presented. (e) Atomic-resolution ABF-STEM and (f) HAADF-STEM images of the nanorod analyzed.

6.2.1.3 Specific surface area

The BET-specific surface area of the TiO_2 nanopowders synthesized with different solvents is presented in Table 6.1.

Table 6.1: BET specific surface area of the TiO_2_EtOH, TiO_2_IPA and TiO_2_H_2O nanopowders synthesized under MW irradiation at 200 °C for 10 min.

TiO_2 nanopowders	Specific surface area ($m^2.g^{-1}$)
TiO_2_EtOH	231
TiO_2_IPA	177
TiO_2_H_2O	121

As seen in Table 6.1, the highest specific surface area was obtained with the TiO_2_EtOH followed by TiO_2_IPA and then TiO_2_H_2O. These different solvents originated TiO_2 nanostructures with various morphologies and, consequently, different specific surface area values were obtained. Moreover, intraparticle pores were observed in the TiO_2_EtOH nanopowder

aggregates by SEM and STEM analyses. Hence, the high density of pores is likely to have a significant influence on the specific surface area value. A larger surface area provides more available sites on the particle surface for the adsorption of pollutant molecules, which, in turn, enhances the photocatalytic process [27]. Although large aggregates were formed when ethanol was used as a solvent, these aggregates were composed of very small TiO_2 nanocrystals (average size of 5.93 nm), see inset of Figure 6.2 (b). Therefore, not only the shape of the particles but also their size is likely to have contributed to the differences observed in Table 6.1. It should also be noted that compared with previous studies [5,28,29], all the MW-synthesized TiO_2 nanopowders exhibited much higher specific surface area values, though of the same order of magnitude.

6.2.1.4 XPS

To study the surface properties of the TiO_2 nanopowders, XPS measurements were conducted. The survey spectra (Figure 6.7) revealed that all synthesized TiO_2 nanopowders are composed of titanium, oxygen and carbon (related to the adventitious carbon [30]).

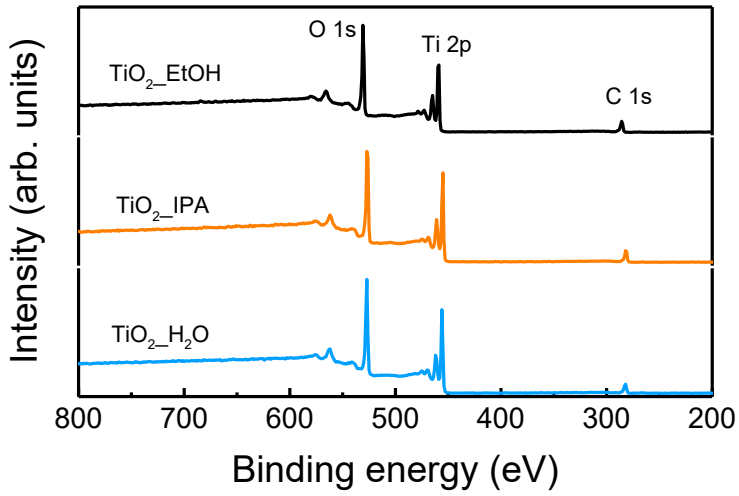

Figure 6.7: Survey spectra of all synthesized TiO_2 nanopowders (TiO_2_EtOH, TiO_2_IPA, TiO_2_H_2O).

The high-resolution XPS spectra of Ti 2p and O 1s (deconvoluted) are visible in Figure 6.8. As seen in Figure 6.8 (a), for all synthesized TiO_2 nanopowders, the Ti 2p core level shows two components: Ti $2p_{1/2}$ and Ti $2p_{3/2}$, which are located at 458.6 eV and 458.6 eV and are both associated with Ti^{4+} oxidation state [31,32]. The Ti 2p peak shapes are identical for all TiO_2 nanopowders and no peak shift could be identified. Regarding O 1s spectra, the deconvolution was fitted with three components according to the literature [33], see Figure 6.8 (b). The first

component at 529.7 eV corresponds to lattice oxygen atoms (O^{-2}) in a fully-coordinated TiO_2 with the Ti^{4+}ions mainly from the bulk, the second component, at 530.2 eV, is usually assigned to oxygen-deficient regions (O^{-},O^{-2}) of the metal oxide and the third component at 531.8 eV is related with surface oxygen, which can be ascribed to loosely adsorbed, dissociated oxygen or OH species from O_2 or H_2O on the surface of TiO_2 [34,35]. These peak positions have been kept fixed during the fitting. Initially, the FWHM have been left free to adjust (within ± 0.1 eV). For the final fitting, an average FWHM was calculated for all components, which was then held constant between each nanopowder. Through the fitting, a clear decrease in surface oxygen was revealed for the TiO_2_H_2O nanopowder, compared to the ones synthesized with alcohol. This difference can be further visualized by plotting the normalized intensity of all O 1s emissions (Figure 6.9). This is also supported by the peak areas of the surface oxygen component (see Figure 6.8 (b)), in which a decrease in the peak area percentages was observed from around 12 % for the TiO_2_EtOH and TiO_2_IPA nanopowders to 9 % for the TiO_2_H_2O nanopowder. This suggests a higher adsorption of oxygen species by the TiO_2 nanopowders synthesized with alcohol, rather than water. As observed previously with the obtained specific surface areas and STEM analysis, the higher porosity and density of structural defects present at the high-index facets of TiO_2 anatase (surface and bulk structural defects) should be the major factors in the enhancement of capacity for surface oxygen adsorption [34,35].

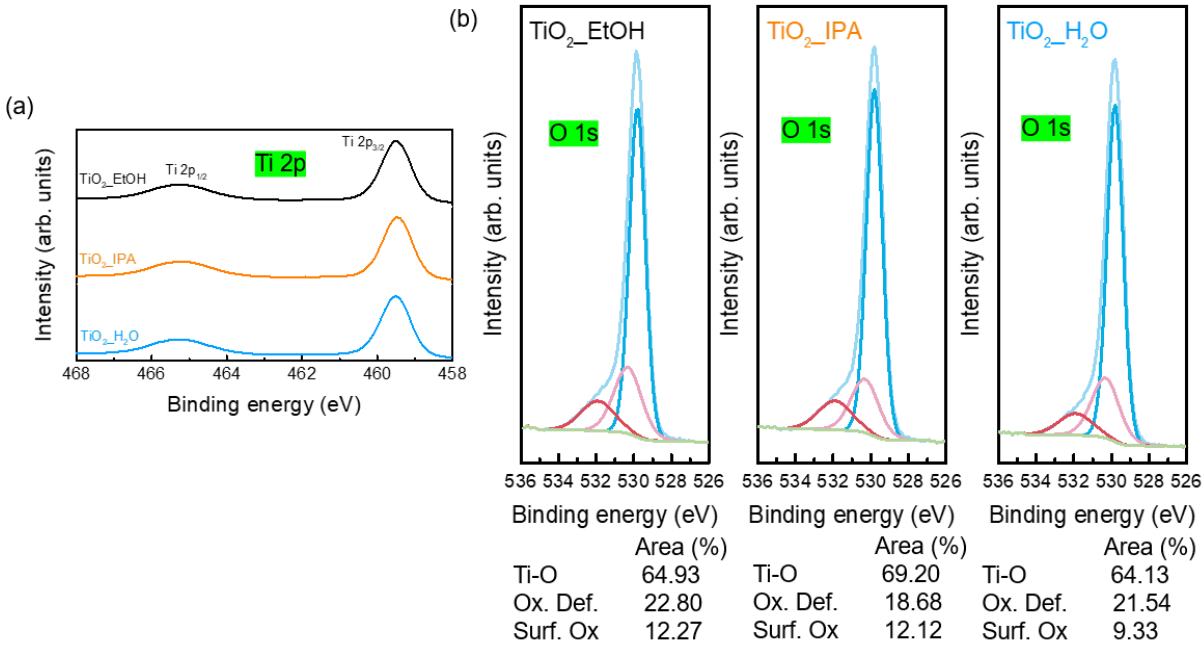

Figure 6.8: (a) XPS high-resolution Ti 2p spectra for the TiO_2_EtOH, TiO_2_IPA and TiO_2_H_2O nanopowders. (b) XPS high-resolution O 1s spectra for the TiO_2_EtOH, TiO_2_IPA and TiO_2_H_2O nanopowders. The peak area of each component (lattice oxygen (Ti-O), oxygen-deficient regions and surface oxygen) is also shown for each synthesis condition.

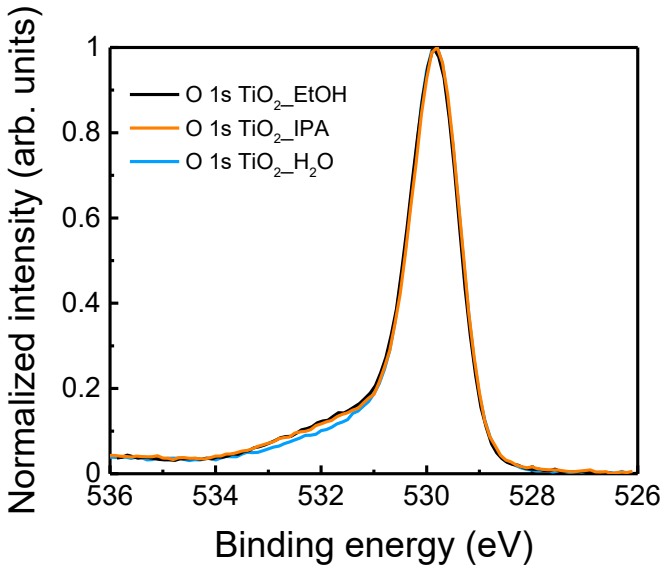

Figure 6.9: Normalized intensity of all XPS O 1s emissions. The O 1s emissions in black, orange, and blue colors represent the TiO_2_EtOH, TiO_2_IPA and TiO_2_H_2O nanopowders, respectively.

6.2.1.5 Photoluminescence

Figure 6.10 displays the PLE and PL spectra obtained for all synthesized TiO_2 nanopowders at RT. The PL spectra were obtained by exciting the nanopowders with 390 nm photons of a Xe lamp (450 W). As can be seen, the spectra are dominated by a broad visible band peaked in the yellow-orange spectral region. The maxima of the PL bands are slightly different depending on the solvent used. The TiO_2_EtOH nanomaterial exhibits its maximum at ~576 nm (~2.15 eV), while the TiO_2_IPA and TiO_2_H_2O nanomaterials display maxima at ~565 nm (~2.19 eV) and ~584 nm (2.12 eV), respectively. Besides, the TiO_2_EtOH nanomaterial evidences a higher PL intensity, ~2.7 times higher than the one recorded for IPA, suggesting a lower contribution from nonradiative processes when compared to the remaining nanopowders and/or a higher contribution from the defect centres that give rise to the observed luminescence. It is also worth noting that the quantity of powder analyzed was similar for all experiments and that all excitation and light collection conditions were kept during the experiments to enable a reliable comparison of the absolute intensities of the PL emission.

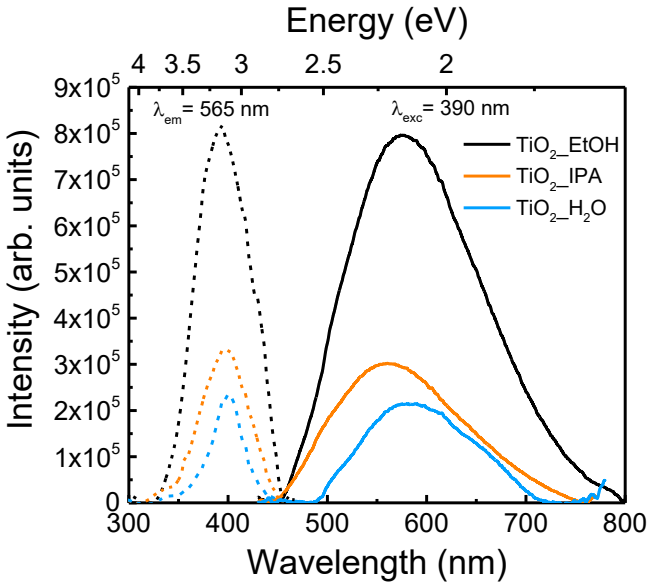

Figure 6.10: RT PLE /PL spectra (represented by dashed lines and solid lines, respectively) of the TiO_2_EtOH, TiO_2_IPA and TiO_2_H_2O nanopowders. PL was acquired under the 390 nm excitation of an Xe lamp, while the PLE spectra were obtained by monitoring at the maxima of the PL bands.

Broad yellow/orange bands have been previously reported in the literature for TiO_2 anatase [36–40]. According to Iijima *et al.* [40], the band that appears at ~2.1 eV is likely related to the presence of oxygen vacancies at the particle's surface since these authors observed that its contribution decreases with increasing annealing in a flowing oxygen atmosphere. It was

also considered that the broad band observed was composed of more than one component overlapping. Indeed, the large FWHM observed for the present nanopowders should also consider this possibility. Another common band present in this spectral region for anatase crystals is the one centered around 2.3-2.5 eV [39,40], which is often attributed to the radiative recombination of self-trapped excitons (STE) localized in TiO_6 octahedra, and which the mentioned authors claimed to be independent of the annealing process [40]. Tang *et al.* analyzed the PL properties of TiO_2 anatase single crystals and argued that the luminescence observed in this region was due to STE and/or impurity-trapped excitons, in line with what is often reported in several titanates containing TiO_6 octahedra [41]. Nevertheless, the peak position and spectral shape of this band are seen to be strongly dependent on the surrounding environment and the excitation conditions, which suggests an overlap with other possible contributions [39]. The presence of other recombination processes involving surface states and trap states has been identified as potential contributors to the broad PL band observed in anatase crystals in this spectral region, which becomes more relevant as the specific surface area of the particles increases [39].

In fact, when one considers the PLE spectra, a broad excitation band is observed in all cases, particularly for the TiO_2_EtOH and TiO_2_IPA nanopowders. In both cases, the bands have a peak at ~395 nm (~3.15 eV), likely corresponding to their optical band gap energies. These results indicate that the emission bands are preferentially populated via photons with energies equal to the band gap one, with an important contribution from shallow sub/below band gap states, likely related to defect states, as mentioned above. For the TiO_2_H_2O nanopowder, the excitation band maximum was found to be at ~401 nm (~3.09 eV), at a slightly lower peak position than the one identified for the other two nanopowders. Indeed, this nanopowder was shown to be composed of both rutile and anatase phases and rutile is known to have a lower band gap energy than that of anatase (~3.0 eV vs ~3.2 eV [42]), hence, the observed PLE band may correspond to an overlap of both contributions.

6.2.1.6 Adsorption kinetics' study of the TiO_2 nanopowders

To understand the effectiveness of pollutant molecules' uptake from the solution by the adsorbent, the adsorption kinetics was studied [43]. The influence of contact time on tetracycline adsorption capacity onto TiO_2 nanopowders is depicted in Figure 6.11. The uptake of tetracycline molecules reaches its maximum value on average after 120 min for TiO_2_IPA, whereas for TiO_2_EtOH 240 min are necessary to reach equilibrium. Since the adsorption

capacity of TiO_2_H_2O was almost null, it cannot be seen in Figure 6.11. Figure 6.11 shows that at the initial moments of the contact period, the adsorption is fast, especially for the TiO_2_EtOH nanopowder, and after that time, it becomes slower near the equilibrium. A larger amount of vacant surface sites may be initially available for the adsorption to occur and then repulsive interactions between the solute molecules and the solid might take place [44]. In fact, the improvement of adsorption efficiency with the TiO_2_EtOH nanopowder compared with the other nanopowders might be related to its high specific surface area (Table 6.1) during the first 120 min (Figure 6.11).

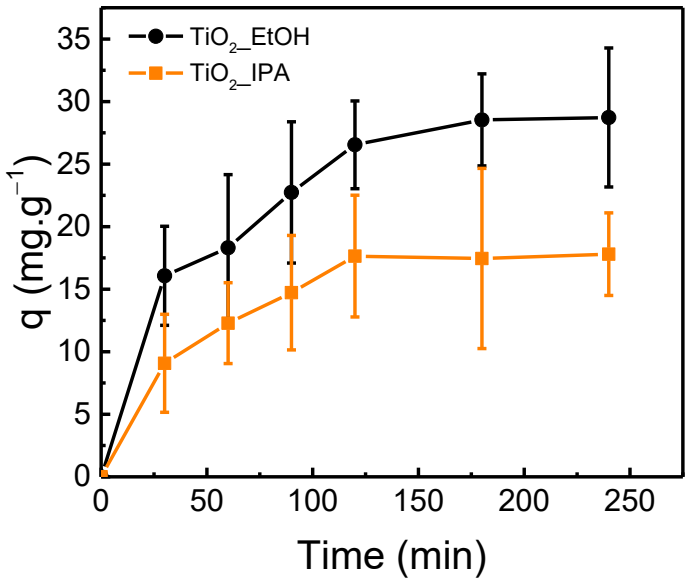

Figure 6.11: Influence of contact time on tetracycline adsorption capacity onto TiO_2 nanopowders. Experimental conditions: q_{max} is 34 mg.g^{-1}, [TC] ~25-30 ppm, $V_{solution}$ = 50 mL, max. adsorption time = 240 min, W = 25 mg. The error bars indicate the standard deviations of triplicate experiments (n = 3).

The average adsorption capacities of the TiO_2 nanopowders decrease in the following order: TiO_2_EtOH (28.73 mg. g^{-1}) > TiO_2_IPA (17.80 mg. g^{-1}) > TiO_2_H_2O (~0 mg. g^{-1}). Since the sorption efficiencies of TiO_2_IPA and TiO_2_H_2O are too low (34.7 % and 0 % after 240 min (4 h)) compared with the sorption efficiency of ethanol (~55 %), see equations (2.5) and (2.6) in Chapter 2, the adsorption mechanisms of tetracycline with both IPA and water nanopowders were not further investigated.

The adsorption process comprises three distinct stages. Initially, solute species are transferred from the bulk solution into the outer surface of the adsorbent (film diffusion). Then, solute molecules migrate from the adsorbent outer surface to the pores of the adsorbent internal surface (intraparticle diffusion). The last step is the adsorptive attachment of the solute

species onto the active sites on the inner and outer surfaces of the adsorbent. Since this step occurs very quickly, it is considered negligible as a rate-controlling step. Hence, the adsorption rate is primarily governed either by outer diffusion, intraparticle diffusion or both [45,46].

To explore the adsorption process of tetracycline on the TiO_2_EtOH nanopowder, several models were employed to fit the experimental data, including pseudo-first-order kinetic, pseudo-second-order kinetic, Elovich, intraparticle diffusion, Bangham and Boyd plot models [47], see equations (2.7), (2.8), (2.9), (2.10), (2.11), (2.12), (2.13) and (2.14) in Chapter 2. Through linear regressions of the kinetic plots, the kinetic parameters for each model were calculated and are listed in Table 6.2 and Table 6.3. For the calculations, only the first cycle of adsorption was considered.

Table 6.2: Adsorption kinetic parameters of TC onto TiO_2_EtOH adsorbent for the pseudo-first-order, pseudo-second-order and Elovich models.

Model	Parameters*						
	q_e^{exp} ($mg.g^{-1}$)	q_e^{cal} ($mg.g^{-1}$)	k_1 (min^{-1})	R^2	k_2 ($g.mg^{-1}.min^{-1}$)	a_e ($mg.g^{-1}.min^{-1}$)	b_e ($g.mg^{-1}$)
Pseudo-first-order	34.2	27.78	0.017	0.97	-	-	-
Pseudo-second-order	34.2	35.88	-	0.98	0.0015	-	-
Elovich	34.2	-	-	0.95	-	3.99	0.14

* q_e^{exp} and q_e^{cal} represent the experimental and calculated quantities of TC adsorbed at the equilibrium time ($mg.g^{-1}$), respectively; k_1 stands for the pseudo-first-order rate constant of TC sorption (min^{-1}); R^2 is the correlation coefficient; k_2 is the pseudo−second-order adsorption rate ($g.mg^{-1}.min^{-1}$); a_e is the initial sorption rate constant ($mg.g^{-1}.min^{-1}$) and b_e is related to the extent of surface coverage and the activation energy for chemisorption ($g.mg^{-1}$) [47].

Table 6.3: Adsorption kinetic parameters of TC onto TiO_2_EtOH adsorbent for the intraparticle diffusion, Bangham and Boyd models.

Model	Parameters*											
	k_{id}^1	C^1	R_1^2	k_{id}^2	C^2	R_2^2	k_{id}^3	C^3	R_3^2	R_B^2	α_B	k_b
Intra-particle diffu-sion	3.70	0	1	2.20	7.65	0.86	0.84	21.31	1	-	-	-
Bang-ham	-	-	-	-	-	-	-	-	-	0.95	0.37	12.09
Boyd	-	-	-	-	-	-	-	-	-	0.98	-	-

*$k_{id}^{1,2,3}$ is the intraparticle diffusion rate constant of the 1st, 2nd and 3rd stages, respectively ($mg.g^{-1}.min^{-0.5}$); $C^{1,2,3}$ are the values of the intercept of the 1st, 2nd and 3rd stages, respectively ($mg.g^{-1}$); α_B and k_b ($mg.g^{-1}.min^{-1}$) are the constants from Bangham's model equation, and R_B^2 is the correlation coefficient for the Bangham or Boyd model [47].

The pseudo-first-order model characterizes the rate at the initial stage of adsorption, but cannot describe the entire adsorption process [48]. The pseudo−second−order kinetic model, on the other hand, presumes that chemisorption governs the adsorption mechanism, with the sorption capacity being proportional to the number of active sites occupied by the adsorbent [49]. Conversely, the Elovich model suggests that the active sites of the adsorbent have different activation energies for chemisorption and so, the rate of solute adsorption decreases exponentially with the accumulation of adsorbed solute [50,51]. Comparing the three models, the experimental data are more closely aligned with the pseudo-second-order model, showing higher correlation coefficient values (R^2 = 0.98). Additionally, the calculated q values (q_e^{cal}) from the pseudo-second-order model are a better approximation of the experimental q values (q_e^{exp}). Hence, the adsorption process is driven by chemisorption. Other studies have already reported a similar behavior by TiO_2 nanomaterials [52,53].

Since the pseudo-second-order model cannot identify the diffusion mechanism and the possible rate-limiting step of the adsorption process, the intraparticle diffusion model was also analyzed [45]. According to equation 2.10 in Chapter 2, a linear relationship between q and $t^{1/2}$ indicates the involvement of intraparticle diffusion in the adsorption process. Furthermore, if a straight line intercepts the origin in the plot, intraparticle diffusion is the rate-controlling step [46]. As visible in Figure 6.12, multi-stage mechanisms are present. The linear regression analysis of the data gives three different regions for the TiO_2_EtOH nanopowder. The three stages are likely related to external diffusion or film diffusion, gradual adsorption

and equilibrium [54]. The absence of intercepts at the origin (value of the intercept C) in the linear plots of the second and third stages is likely attributed to variations in mass transfer rates from the initial to final adsorption stages [55]. This suggests that intraparticle diffusion may not be the only rate-limiting step, with film diffusion also influencing the adsorption process [47].

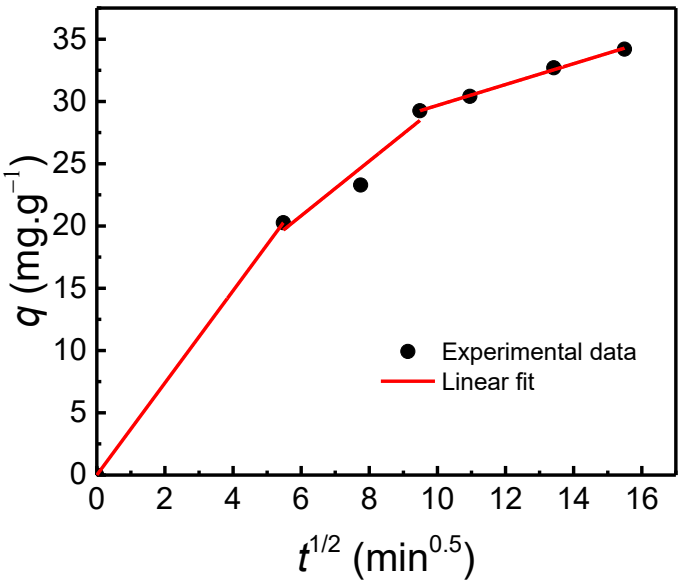

Figure 6.12: Plot of the intraparticle diffusion model for the adsorption of tetracycline (first cycle) onto TiO_2_EtOH nanopowder. The solid red line represents the linear fit, while the black dots are the experimental data.

Bangham's model was also investigated and the value of the obtained regression coefficient was not higher than 0.95. This corroborates the major contribution of film diffusion of tetracycline onto the nanopowder [56]. To determine the rate-limiting step in the adsorption process of TC onto TiO_2_EtOH nanopowder, the Boyd model was employed [46,47]. Through the plot of B_t *vs.* t, if a straight line intercepts the origin, intraparticle diffusion governs the rate of the process. Otherwise, the adsorption process is governed by film diffusion or chemical reaction dominates the adsorption rate. Even though the plot was linear, it did not intercept the origin. Therefore, film diffusion primarily controls the adsorption process [57,58].

6.2.1.7 Photocatalytic degradation of TC over TiO_2 nanopowders

The photocatalytic activity of the TiO_2 nanomaterials synthesized at 200 °C for 10 min with different solvents under MW irradiation was evaluated through the degradation of tetracycline under simulated solar irradiation. Before light exposure, the solutions containing

tetracycline and the photocatalysts were stirred in the dark for 240 min. After that time, the solutions were exposed to a simulated solar light source for 30 min. During the blank experiments (photolysis), no degradation was observed, indicating that tetracycline does not degrade over time (Figure 6.13 (d)). As previously discussed, the TiO_2_EtOH and TiO_2_IPA nanopowders showed a significant TC adsorption percentage after the dark (about 58 % and 30 % during the first cycle, respectively), whereas with the TiO_2_H_2O there was no adsorption. However, after the time in the dark, under 30 min of solar light exposure and for all nanopowders, a clear decrease in C/C_0 is observed (Figure 6.13). Moreover, the total TC removal percentages reach around 88 %, 77 % and 72 % with the TiO_2_EtOH, TiO_2_IPA and TiO_2_H_2O nanopowders (Figure 6.13 (a), (b) and (c)), respectively.

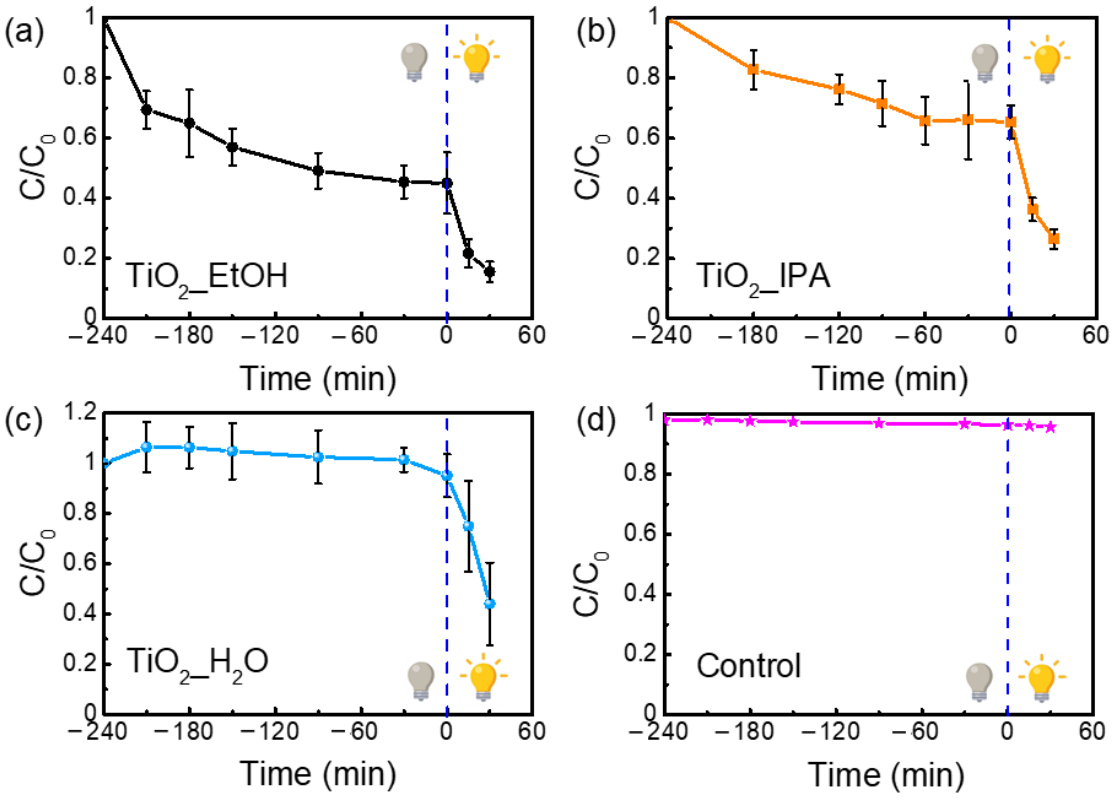

Figure 6.13: Degradation profiles of tetracycline over TiO_2 catalysts (a) TiO_2_EtOH, (b) TiO_2_IPA, (c) TiO_2_H_2O and (d) without photocatalyst, in the dark and under simulated solar light. Error bars indicate the standard deviations of triplicate experiments (n = 3) in (a), (b) and (c).

The photocatalytic performance is highly influenced by the crystalline phase, particle morphology, crystallite size, specific surface area and crystal facets of the photocatalyst [59]. In terms of crystalline phases, mixtures of anatase/brookite, anatase/rutile, and pure anatase phase were obtained, respectively, for the nanopowders synthesized in IPA, H_2O and ethanol.

Many reports state that a mixture of TiO_2 crystalline phases could lead to a synergistic effect that would improve the separation of photogenerated carriers [60,61]. However, this was not verified in the present study, and the findings demonstrated that the nanopowder comprising pure TiO_2 anatase displayed the best photocatalytic performance. As seen from SEM and STEM images, the TiO_2_EtOH powder presented micrometer spherical/elongated aggregates with faceted nanocrystals and displayed porosity even at the nanoscale. In the case of both TiO_2_IPA and TiO_2_H_2O, nanorods and some particles with undefined shapes were observed. For the latter, these nanostructures aggregated in quasi-spherical micro-sized particles. The porous structure of TiO_2_EtOH suggested that this material would have a higher surface area, which was confirmed by the BET measurements. In heterogeneous catalysis, most reactions between the catalysts and reactants occur on the catalyst's surface in a way that a large surface area will not only provide more active sites at the catalyst surface to produce radical species but also anchor the organic pollutant's molecules [62]. Indeed, a larger specific surface area was obtained with the TiO_2_EtOH nanopowder, which provided more adsorption sites, resulting in an enhancement of tetracycline molecules to adsorb onto the surface of TiO_2, as visible with the adsorption kinetics study. The combination of a high adsorption capacity, together with the ability to produce radical species, contributed to enhancing the removal of the pollutant from water. In fact, XPS measurements attested to the ability of both TiO_2_EtOH and TiO_2_IPA nanopowders to adsorb surface oxygen.

At the atomic level, differences were evident between the different solvents used. In the case of the TiO_2_EtOH nanopowder, faceted nanocrystals (~6 nm) with atomic structural surface (steps) and bulk (absence of Ti atoms) defects were observed on the high-index facets. The atomic arrangement of titanium and oxygen on the anatase phase determines the different facets formed, dominating the TiO_2 surface chemistry [15]. It is known that the low-index (101) TiO_2 anatase surface is the most stable, followed by the (001) one. However, the (001) surface has a higher photocatalytic activity than the (101) surface [63]. Therefore, the interest in high-index TiO_2 anatase surfaces has been increasing lately since these nanomaterials exhibit exceptional photocatalytic properties when compared to low-index ones. Indeed, it has been demonstrated that high-index TiO_2 nanomaterials exhibit better adsorption and photooxidation performance than the low-index {001}, {100} and {101} surfaces [15]. Moreover, generally, high-index facets exhibit high surface energy, resulting in a high reactivity [15]. TiO_2 high-index faceted nanocrystals ({012} and {102} facets) were observed through STEM and thus are expected to significantly impact the overall photocatalytic activity of the nanomaterial with an

additional contribution from the presence of structural defects. In fact, the surface defects observed in the high-index facets, and suggested by the photoluminescence results, can contribute to stabilizing these high-index facets and, consequently, enhance the separation of photogenerated charges and ultimately aid in boosting the photocatalytic performance [16,64]. It is noteworthy to mention that most reports on the synthesis of high-index facets of TiO_2 highly depend on the use of toxic chemicals [15]. Unlike these studies, an environmentally benign approach is herein proposed.

Integrating high-index facets with defective TiO_2 nanocrystals is highly desirable to strengthen the response in the visible light region and limit the recombination of photo-generated carriers [15]. Regarding the defects in TiO_2, Kong *et al.* discovered that adjusting the ratio of bulk defects to surface defects in TiO_2 nanocrystals can significantly boost the separation of photogenerated charge carriers and improve the photocatalytic performance [65]. Yet, establishing a direct correlation between surface/bulk defects and photocatalytic activity remains difficult, mainly due to their interaction with other factors that influence photocatalytic performance, such as crystalline phases and exposed crystal facets [66].

Nevertheless, when it comes to surface defects, various reasons are attributed to their improvement in the removal of pollutants. The first is related to changes in the surface properties of TiO_2, which could induce different adsorption/desorption capabilities of reactants, intermediates, or products. Another reason is the light absorption ability. Due to the existence of these surface or sub-surface defects, new intermediate levels could be created within the band gap of TiO_2, leading to enhanced capacity for visible light absorption. The third reason has to do with disorders at the surface that could turn into traps for electrons or holes, limiting the recombination of photogenerated charge carriers and, consequently, increasing the lifetime of charge carriers in the material [67–69].

Therefore, the enhanced photocatalytic activity observed in the TiO_2_EtOH nanopowder can be ascribed to a synergistic effect of factors. These include its high surface area stemming from a porous structure at the micrometer scale, as well as nanometer and atomic level contributions, characterized by pores within the nanocrystals, and the exposure of high-index crystal facets with atomic bulk and surface defects. Additionally, the higher capacity for surface oxygen adsorption further contributes to this enhanced activity.

To quantitatively compare the decomposition efficiency under solar light, the experimental data were fitted according to the pseudo-first-order kinetic model (equation (1.11), Chapter 1). The kinetic parameters (rate constants k_{ap} and linear regression coefficients R^2)

can be found in Table 6.4 (highlighted in blue). These results were compared with those found in the literature, where TiO_2 nanostructures were also used for the degradation of TC (see Table 6.4).

Table 6.4: Kinetic parameters and experimental conditions for the tetracycline degradation under light irradiation over TiO_2 photocatalysts found in several studies from the literature. A comparison is made with the results obtained in this study, including the control (without photocatalyst) and TiO_2 nanopowders synthesized with ethanol, IPA and water (highlighted in blue).

	Kinetic parameters		$[TC]_{after\ dark}$ ($mg.L^{-1}$)	$[TC]_{initial}$ ($mg.L^{-1}$)	$V_{solution}$*** (mL)	W (mg)	[Catalyst] ($g.L^{-1}$)	t* (min)	Light source	Ref.
	k_{ap} (min^{-1})	R^2								
Nano TiO_2	2.4×10^{-2}	1	–	37	–	–	1	120	UV (λ = 254 nm)	[70]
Nano TiO_2	2.1×10^{-2}	–	~20	20	–	–	1	210	UV	[71]
Nano TiO_2 (aeroxide P25)	3.8×10^{-2} (0–30 min); 2.0×10^{-2} (30–120 min)	0.98 (0–30 min); 1 (30–120 min)	~8**	10	100	20	0.2	120	UV (λ = 350 nm)	[72]
	3.6×10^{-2} (0–30 min); 3.9×10^{-3} (30–120 min)	0.97 (0–30 min), 0.84 (30–120 min)	~8**	10	100	20	0.2	120	Visible (λ = 420 nm)	
Nano TiO_2	2.3×10^{-3}	0.97	~8.19**	10	100	20	0.2	240	Visible (λ > 400 nm; 40 $mW.cm^{-2}$)	[73]
Control	2.2×10^{-4}	0.94	12							
TiO_2_EtOH	0.4×10^{-1}	0.90	24	30	50	25	0.5	30	Simulated solar light (100 $mW.cm^{-2}$)	This work
TiO_2_IPA	0.3×10^{-1}	0.97	19							

* Reaction time under light exposure;** Deduced; *** Volume of TC solution

Comparing the rate constant (k_{ap}) values in Table 6.4 with previous studies, Safari *et al.* reported similar rate constant values by nanosized TiO_2 for the photodegradation of TC in aqueous solutions under UV light (k_{ap} = 2.49 × 10^{-2} min^{-1}, $[TC]_{initial}$ = 27 $mg.L^{-1}$) [70]. Bouafia-Chergui *et al.* also reported the photocatalytic degradation of TC in water using TiO_2 as the photocatalyst under UV light. The most concentrated solution had an initial tetracycline concentration of 20 $mg.L^{-1}$ and the obtained apparent rate constant value was 2.1×10^{-2} min^{-1} [71]. Again, this value is in line with the present results for TiO_2 nanopowders. However, in this study, solar radiation was used, which adds significant environmental value, with the incorporation of renewable sunlight energy and not being restricted just to UV radiation. Other studies were found; however, tetracycline hydrochloride was used as the pollutant [74–76] and/or the photocatalytic experiments were conducted under different experimental conditions [72,73,77]. Moreover, it is worth mentioning that this work reports a simple and fast MW synthesis of TiO_2 nanostructures by employing non-toxic reagents, which showed excellent ability for the removal of tetracycline molecules from polluted water.

6.2.1.8 Recyclability tests

To determine the stability of the photocatalysts, reusability tests were performed in the presence of the best photocatalyst (the TiO_2_EtOH nanopowder) under a simulated solar light source. For the second cycle, as seen in Figure 6.14 (a), little adsorption (~ 15 %) occurred within 240 min (4 h) in dark (no regeneration). This result may be due to the fact that tetracycline molecules are blocking all active sites around the photocatalyst. After the completion of the second cycle, the TiO_2 nanopowder without regeneration was observed through SEM (Figure 6.14 (b)). A clear thick layer is wrapping the photocatalyst structures, which is thought to be causing the significant loss of TC adsorption's capability. It also impacted the overall percentage of TC removal, and the material can only reach 40 % of TC degradation, compared to the initial 88 % (Figure 6.13 (a)). To fully recover the adsorption capacity of the photocatalyst, a strategy based on UV exposure was explored, since it is simple to implement in a real production process [78]. After the first cycle (adsorption + photocatalytic activity), the TiO_2_EtOH nanopowder was exposed for 4 h to UV light irradiation in an aqueous solution. A complete recovery is observed in terms of TC adsorption (~ 60 % after 240 min of dark) and overall TC removal (~ 80 % is obtained after 240 min of dark + 30 min of light exposure), see Figure 6.14 (a). In contrast with the TiO_2 nanopowder without regeneration, the SEM image of the nanopowder treated with UV light shows the presence of well-defined particles without a

coating layer (Figure 6.14 (b)), which confirms the recovery of the TiO_2 nanostructures. To the best of our knowledge, there are no other studies in the literature showing similar SEM images of nanostructures encapsulated/coated with TC compounds and/or products from the photodegradation reaction of TC.

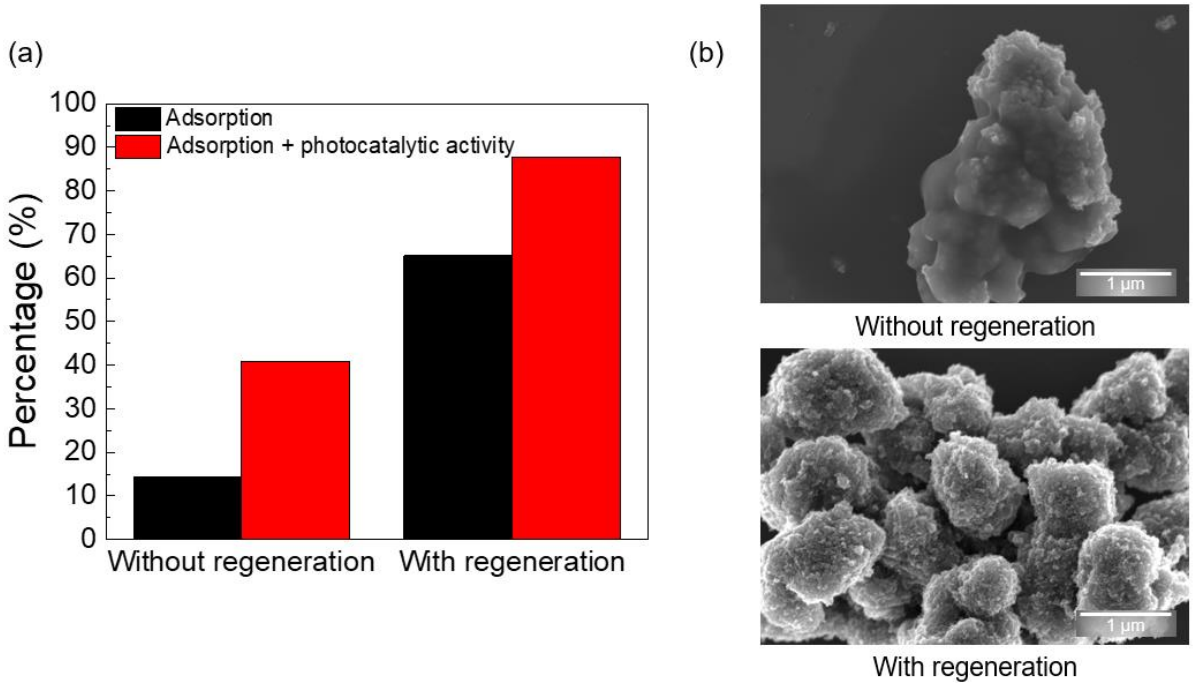

Figure 6.14: (a) Comparison of TC adsorption (240 min in the dark) and adsorption followed by photocatalytic activity (240 min in the dark + 30 min of simulated solar light exposure) without and with a UV exposure regeneration of 240 min (both corresponding to the second cycle of reutilization). (b) SEM images of the TiO_2_EtOH nanopowder without and with regeneration.

6.2.1.9 ROS' scavengers experiments

The influence of different ROS on the degradation rate of TC using the TiO_2_EtOH nanopowder was investigated under simulated solar light and after 240 min in the dark (Figure 6.15). Several ROS contribute to the photocatalytic degradation process, encompassing holes (h^+), hydroxyl ($^{\bullet}OH$), superoxide ions ($^{\bullet}O_2^-$), singlet oxygen ($^1O_2$) radicals and electrons (e^-) [79–81]. As shown in Figure 6.15, it can be observed a reduction in the degradation percentages upon the use of BQ and SA scavengers. This indicates that $^{\bullet}O_2^-$ and $^1O_2$ radicals are the main active species involved in the degradation process of TC. These findings are well aligned with earlier research reporting the presence of superoxide radical species in the degradation process of tetracycline over TiO_2 nanostructures [34,82–84]. Regarding the generation of singlet oxygen radical species, several pathways have been proposed in the literature [85]. Nevertheless, surface defects that can act as both reactive sites and trapping sites might enhance the

photocatalytic performance. Studies indicated that the existence of surface V_O can be further reduced into superoxide anions and then converted into singlet oxygen [86,87]. Although the existence of surface V_O could not be undoubtedly confirmed by XPS and photoluminescence spectroscopy analyses, the surface defects of the photocatalyst, as observed through STEM, may be associated with the origin of these reactive species.

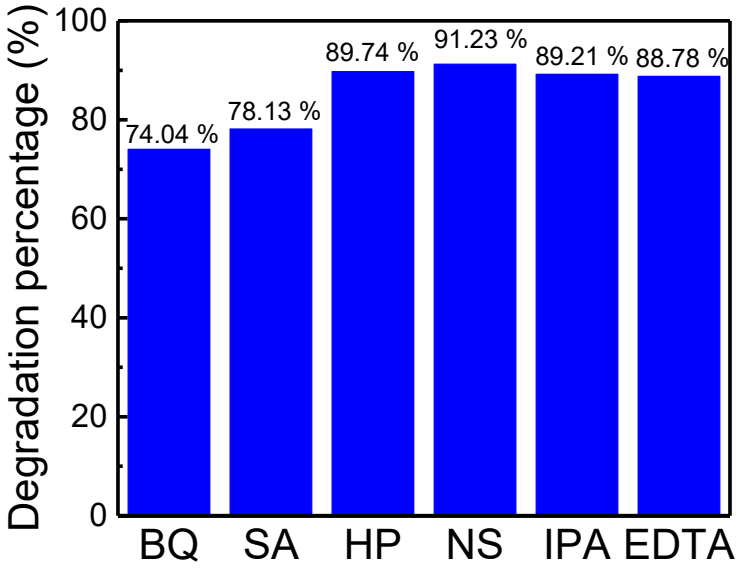

Figure 6.15: Degradation percentages (%) of TC with the TiO_2_EtOH nanopowder under solar simulated light, after 240 min of dark, in the presence of different scavengers (BQ, SA, HP, IPA and EDTA) and with NS.

6.2.2 Structural characterization of the PU foams

The photocatalytic experiments with the TiO_2_EtOH nanopowder showed enhanced overall adsorption and degradation of tetracycline molecules compared with the other solvents (i.e., nanopowders with IPA and water). Therefore, this nanopowder was chosen for further impregnation on PU foams to avoid the costly recovery processes of nanopowders and guarantee the sustainable character of the materials produced. The photodegradation of tetracycline under simulated solar light and ecotoxicity assays against *Artemia salina* were both conducted in the presence of these functionalized TiO_2 PU Foams.

6.2.2.1 SEM/EDS

The PU foams observed by SEM showed the typical cellular structure specific to polyurethane foams (Figure 6.16) [88,89]. The pores of the commercial PU foam were in the millimeter range (Figure 6.16).

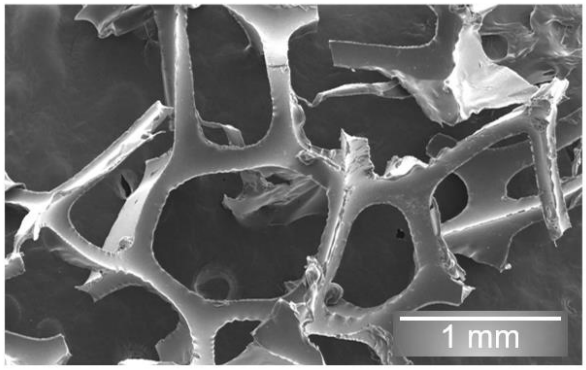

Figure 6.16: SEM image of the pristine PU foam.

From the SEM images, it is possible to observe that the surface of the pristine PU foam is smooth without any macro-sized defects and crack-free but with wrinkling edges (Figure 6.17 (a)). At the micrometer range, it was possible to observe artifacts throughout its surface (Figure 6.17 (b)). The PU foams were also observed after the NaOH treatment (pre-treated) and no clear difference could be inferred when compared to the pristine PU foam (Figure 6.17 (c) and (d)). Nevertheless, when the pre-treated PU foam was observed after the dip-coating process, the differences became evident (Figure 6.17 (e) and (f)), even at the macro-scale, with the presence of some agglomerates on the wrinkling edges of the PU foam resultant from the deposition process (Figure 6.17 (e)). SEM images (Figure 6.2 (a) and (b)) show that the TiO_2 nanomaterials synthesized with ethanol as solvent resulted in micrometer TiO_2 aggregates and, after the dip-coating process, these aggregates are still discernible. The artifacts observed in the pristine and pre-treated PU foams can still be observed after the deposition process, however, other smaller structures were observed, suggesting the presence of dispersed TiO_2 particles or smaller TiO_2 aggregates at the foam surface.

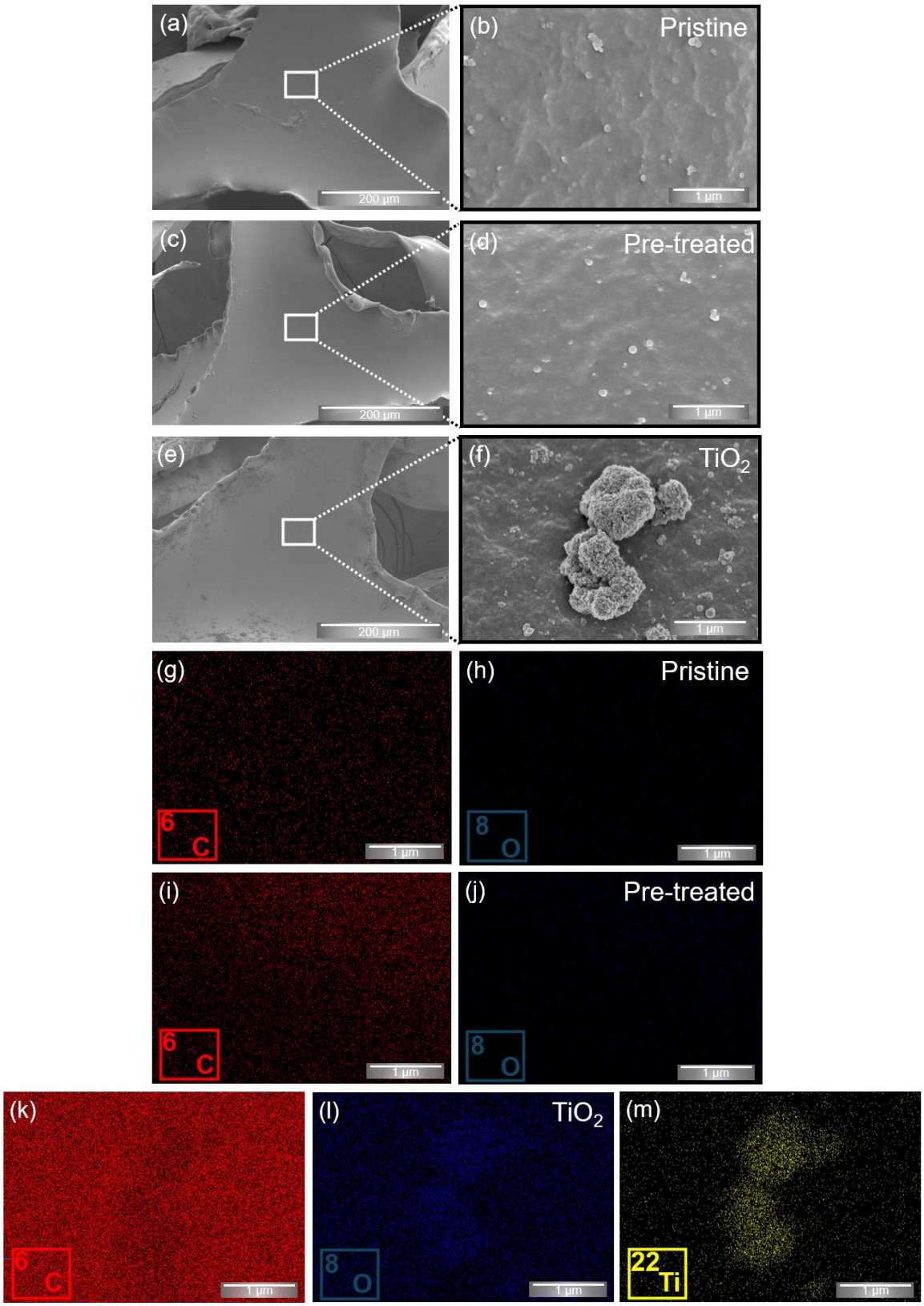

Figure 6.17: SEM images of the PU foams. (a) Pristine PU foam, (b) pre-treated PU foam and (d) pre-treated PU foam after dip-coating of the TiO_2 nanomaterials synthesized with ethanol. The corresponding EDS maps of C (g), (i) and (k); O (h), (j) and (l); and Ti (m) are presented.

Pristine PU foam, pre-treated PU foam and pre-treated PU foam after dip-coating of the TiO_2_EtOH nanomaterial were also analysed using EDS. The analyses were carried out simultaneously in the same areas of the SEM images for all the PU foams. EDS analysis confirmed that the pre-treatment with NaOH did not leave residues at the surface of the foam, since no impurities were detected, i.e., sodium salts. Both pristine and pre-treated PU foams were composed of C and O, which is expected for polyurethane foam substrates [90] (Figure 6.17 (g) to (j)). In Figure 6.17 (k) to (m), C and O are observed from the substrate, but also Ti and O are present on the TiO_2 agglomerates. Ti was also detected throughout the foam surface as can be observed by the Ti EDS map in Figure 6.17 (m). Based on the EDS analyses, it can be inferred that the NaOH surface treatment assisted the immobilization of the TiO_2 nanostructures at the PU surface.

6.2.2.2 Photocatalytic degradation of TC over pre-treated PU foams

The photocatalytic activity of the pre-treated PU foams, with and without the photocatalyst, was determined considering the degradation percentages when exposed to simulated solar light. Two different types of water were investigated with the pre-treated TiO_2 PU foams and under identical experimental conditions: Milli-Q and potable tap water. In both cases, the study in the absence of light was performed for 1 h to achieve adsorption-desorption equilibrium. For the experiment with Milli-Q water, after the dark phase, it can be seen that both pristine (uncoated) and pre-treated TiO_2 PU foam (black curve) did not adsorb TC molecules (Figure 6.18). Despite the microporosity, the foam's surface is flat and smooth (Figure 6.17 (c) and (d)), leading to the low adsorption of tetracycline molecules observed with the pristine PU foam during the dark. Regarding the pre-treated TiO_2 PU foam (experiment with Milli-Q water), as seen previously in Figure 6.13 (a), the TiO_2 nanopowder showed significantly high adsorption towards molecules of tetracycline during the dark phase. Throughout this process, the surface area played an important role. In contrast with the use of nanopowder, upon immobilization on a PU foam (Figure 6.18, black curve), this adsorption was almost null. A possible explanation could be related to the use of polyacrylic acid in the dip-coating process, impacting the adsorption mechanism of the photocatalysts. This polymer may be blocking the available sites at the surface of the photocatalyst. Nevertheless, under light irradiation a notable decay in the concentration of tetracycline is observed in the presence of the TiO_2 PU foam, in comparison with the pristine PU foam, attesting the photocatalytic behavior of the TiO_2

nanostructures, Figure 6.18, by reaching around 80 % of TC degradation in 180 min of light exposure.

The adsorption + photocatalytic performance of the pre-treated TiO_2 PU foam for TC degradation was also evaluated with tap water to simulate conditions closer to practical applications. The presence of mineral content (dissolved inorganic anions and cations [91]) in tap water had little effect on both adsorption and photocatalytic behaviour (Figure 6.18, green curve), with a slight decrease in efficiency (~13 %). This loss of efficiency might be attributed to the competition of inorganic matter for the active sites on the photocatalyst's surface or to its deactivation, ultimately reducing the pollutant degradation rate. Inorganic anions in water can interact with h^+ and •OH, acting as scavengers. Moreover, this interaction can be promoted by the high reactivity and non-selectivity of •OH radical species. This results in inefficient degradation or even complete inhibition of the advanced oxidation process [91,92]. This phenomenon might be occurring, leading to the stabilization of the photodegradation rate after 60 minutes of light exposure. Nonetheless, if trace amounts of TC remain after wastewater treatment, the TiO_2 PU foams can effectively degrade this water pollutant in real water for up to 60 min.

The organic water pollutants' photodegradation in the presence of semiconductors is achieved when the photocatalyst is exposed to light with an energy superior to the one of its band gap. In these conditions, the photons' energy is absorbed, leading to the excitation of electrons from the VB to the CB, thus creating electron-hole pairs. If the recombination of electrons and holes does not occur, electrons and holes can migrate to the surface of the photocatalyst and participate in redox reactions. Holes will oxidize water molecules and form $^{\bullet}O_2^-$ species. Simultaneously, electrons will reduce oxygen molecules and generate •OH species. The superoxide radicals will be protonated afterwards to harvest hydro-peroxyl radicals ($HOO^{\bullet}$) and thereafter H_2O_2 and •OH are formed [93–96]. These hydroxyl radical species will be further responsible for the transformation of TC molecules into different intermediates. Although multiple degradation pathways could be proposed due to these various intermediates that may be formed, the ROS produced would attack the double bonds, aromatic ring and amino group in tetracycline, typically via ring opening and cleavage of the central carbon bond reactions [80,97,98]. Smaller intermediates would be generated and eventually would be mineralized into some tiny molecules, such as CO_2, H_2O [99] and inorganic ions that are gradually formed via oxidation steps [80].

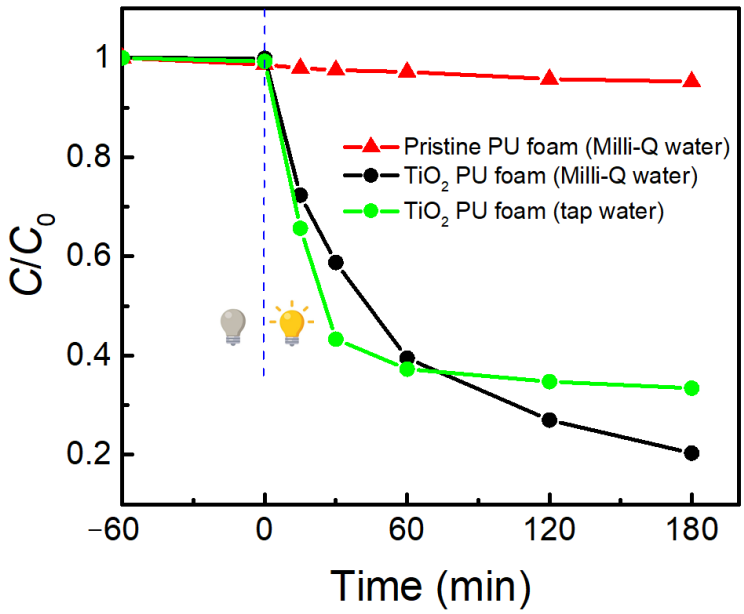

Figure 6.18: Degradation profiles of TC over PU foams (pristine and pre-treated TiO_2 PU foams) in the dark (for 60 min) and under simulated solar light (for 180 min). The red curve represents the C/C_0 over time for the pristine foam (uncoated) in Milli-Q water, while the black and green curves are for the pre-treated TiO_2 PU foams in Milli-Q and tap water, respectively.

6.2.2.3 Proposed degradation pathways of TC

To understand the photocatalytic degradation process of TC in Milli-Q water and in the presence of the TiO_2 PU foams, LC-HRMS was employed to identify the degradation intermediates and help to propose a reaction mechanism. The MS spectra and proposed ionic structure of all products identified, in the dark (for −60 min), and under simulated solar light (for 180 min) are displayed in Figure A.10. For pure TC solution, the spectra 1a) and 2a) (in the dark and 0 min, respectively) show two peaks, one with *m/z* 445.1611 assigned to the protonated molecule of tetracycline, and a smaller one with *m/z* 427.1499 attributed to an anhydrotetracycline structure. The later peak is probably due to an impurity present on the active pharmaceutical ingredients, the anhydrotetracycline (tetracycline European Pharmacopoeia (EP) impurity C) [99].

The TC photodegradation pathways include dealkylation, hydroxylation, ring-opening and mineralization [100]. Several studies have demonstrated that the TC dimethylamine moiety ($(CH_3)_2N$ at the C4 position in TC molecule, see in Figure 6.19 TC 444) is preferentially dealkylated due to the N atom directly attached to the chiral center. This degradation pathway is dependent on the specific reaction conditions and incomplete removal of the methyl group can occur [101]. TC has three types of functional groups with relatively high electron density,

including the double bond, phenolic group and amine group. Among them, the double bond is the most reactive with hydroxyl radicals. In TC, the double bond at the C11a-C12 position (Figure 6.19, see TC 444) has higher electron density than that at the C2-C3 position (Figure 6.19, see TC 444), which is more likely to be attacked with •OH radicals [102]. Upon completion of the demethylation and double bond opening reactions, TC continues to be attacked by reactive groups such as $\bullet O_2^-$, •OH and h^+ holes [77,100]. As a result, the molecular structure of TC undergoes further decomposition and ring-opening reactions, gradually transforming from a tetracyclic to a monocyclic or bicyclic structure.

The photodegradation of TC results in the production of different intermediates due to the different nature of the photocatalysts and reaction conditions. Light conditions, inorganic ions and pH in the system can also influence the adsorption process and the oxidation of reactive radicals, affecting the generation and conversion of intermediates [100].

During the solar-light-driven TiO_2 PU foam photocatalysts process, the intensity peak of TC was decreased and some intermediates with *m*/*z* 477, 461, 447, 431, 413 and 401 appeared after 30 min of irradiation (Figure A.10 (4a-b)). These main intermediates were mainly generated in N-demethylation process and hydroxylation process, and three possible degradation pathways are presented in Figure 6.19. Pathway I is related to the low bond energy of N-C bond (Figure 6.19). Several studies have demonstrated that a N-demethylation process due to $\bullet O_2^-$ or h^+ attack of C4 bond of TC molecule would occur, resulting in the removal of the methyl group conducting to the formation of the transformation product (TP) 430, which subsequently produced other intermediate with *m*/*z* 417 [101,102]. However, in the present study, a TP 412 with *m*/*z* 413.1341 and 32.027 u lower than the protonated molecule of TC (*m*/*z* 445.1611) was found. This intermediate may be due to the loss of the $-CH_2$ group at C4 plus an H_2O molecule at C5a and C6 (Figure 6.19), and is also reported in Ref. [103]. Further continuous $\bullet O_2^-$ or h^+ attacks generated TPs 320, 290 and 276, followed by degradation to small molecules (*m*/*z* 199 and 177) via decarboxylation and dihydroxylation reactions. Pathway II is primarily a hydroxylation process (Figure 6.19). The C11a-C12b double bond of TC was attached molecules by •OH, which first leads to the formation of the major intermediate (TP 460), which is further degraded by •OH producing TP 476 and TP 494 (a very small peak with *m*/*z* 495.1617 assigned to $[C_{22}H_{27}N_2O_{11}]^+$, not included in the Figure 6.19) [101]. Pathway III in Figure 6.19 is associated with the demethylation of the dimethylamine group of intermediate TP460, which leads to the formation of intermediate TP 446. This further loses the remaining methyl group, producing TP 400. These two intermediates are further decomposed by the ring opening

reaction via decarboxylation and H_2O removal reaction, forming smaller products with *m*/*z* 323, 303, 235, 207, 157 and 135. At 180 min of light exposition, the main signals present in both mass spectra (Figure A.10 7a-b) are mainly due to small molecules (*m*/*z* 157, 135 and 199, 177, respectively), indicating that the organic intermediates are gradually mineralized into water, carbon dioxide and other inorganic substances.

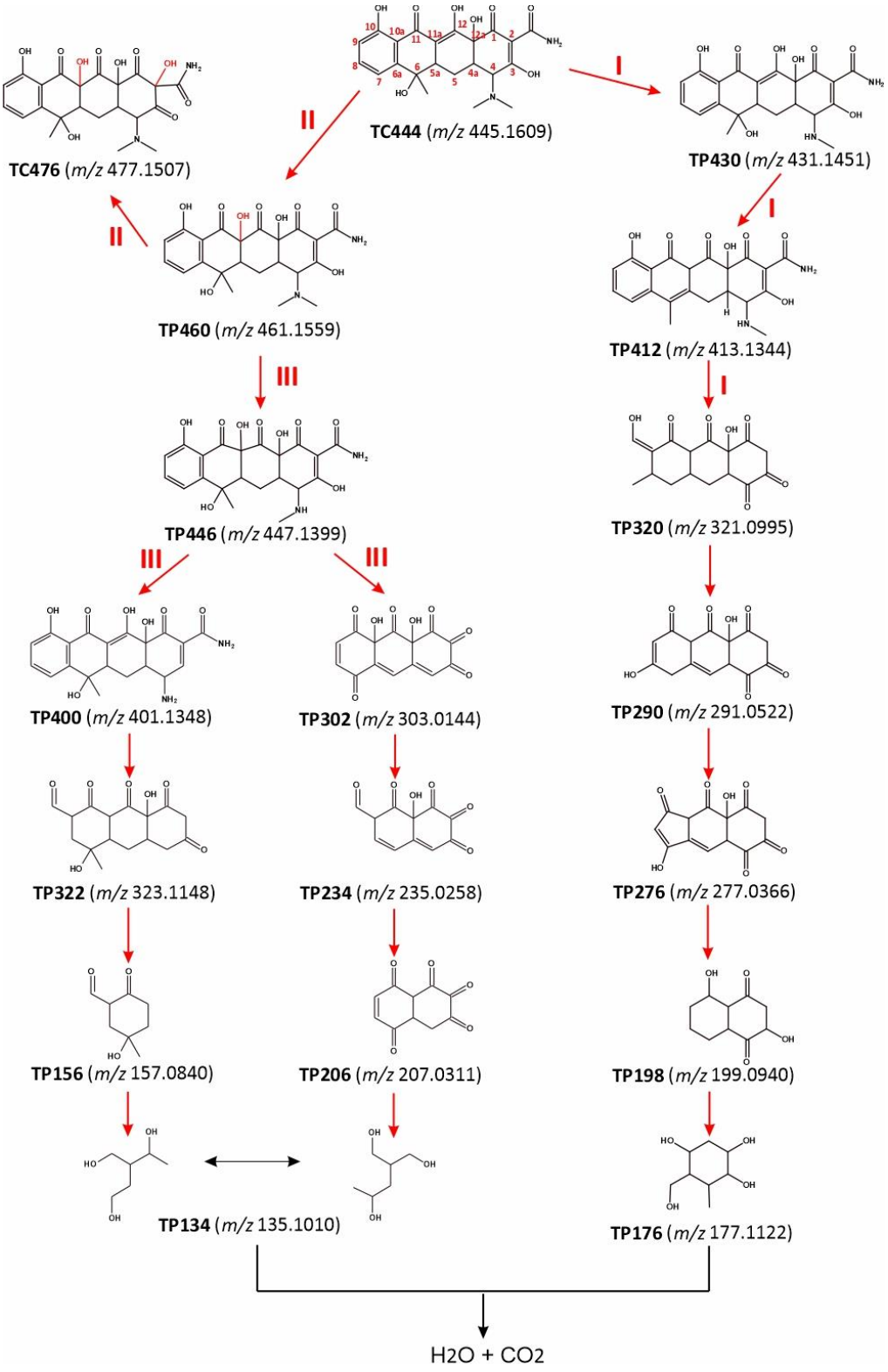

Figure 6.19: Proposed photocatalytic degradation pathways of TC in the TiO_2 PU foam system.

6.2.2.4 Recyclability tests with the pre-treated TiO_2 PU foams

To verify the integrity of the TiO_2 PU foam, reusability tests were conducted under 5 consecutive cycles, Figure 6.20. In each cycle, the foam was exposed to solar light for 180 min. A minimal photocatalytic efficiency loss of around 20 % was obtained upon completion of the fifth cycle. This indicates that the TiO_2 PU foam is stable [104] and can be reused for up to 5 cycles. In fact, the dip-coating method enables a good adhesion of the nanomaterials to different substrates with various compositions and intricate geometrical structures, as previously demonstrated [105]. Moreover, studies have shown that the polymer used for dip-coating (PAA) is compatible with this technique [106,107]. The present results demonstrate that reusable photocatalysts with high degradation efficiency towards water pollutants can be produced effectively and affordably while avoiding the issues associated with the recovery of powdered photocatalysts.

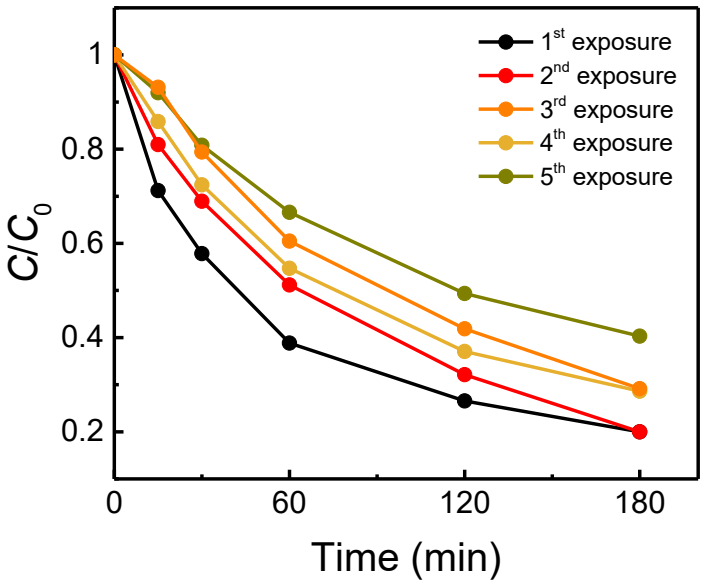

Figure 6.20: Photocatalytic recycling activity of pre-treated TiO_2 PU foam within 5 cycles under simulated solar light for 180 min.

6.2.2.5 Ecotoxicity assays

Exposure studies on *Artemia salina* (nauplii) were conducted in the presence of the pre-treated TiO_2 PU foams to examine their effects on marine ecosystems. The mortality (%) was determined under acute exposure for 24 h with the PU foams, (without photocatalyst, with pre-treatment and photocatalyst), as well as with the negative control (artificial seawater) and positive control (10 % DMSO), see equation (2.15) in Chapter 2. The mortality rate (%) for

Artemia is shown in Table 6.5. As expected, the pre-treated TiO_2 PU foam exhibits a slightly higher mortality percentage compared with the foam without the catalyst. This may be related to the photocatalytic behavior of TiO_2 under light irradiation and the generation of ROS causing oxidative stress on the organisms [108]. However, the aim of the utilization of a polymer (in this case, polyacrylic acid) to coat the TiO_2 nanostructures is not only to promote better adhesion of the nanostructures to the PU foam but also to minimize possible toxic effects on aquatic organisms. According to the literature, polyacrylic acid can hinder the formation of ROS by TiO_2 nanostructures and help mitigate their phototoxicity under sunlight [109]. Most importantly, it should be noted that the TiO_2 PU foams presented very low mortality (< 10 %), and hence, are considered safe for aquatic species [110]. As for current eco-toxicological studies, these often assess the toxicity effects with suspensions of nanoparticles [110–113], rather than determining the acute toxicity of nanoparticles functionalized on substrates to aquatic organisms, as herein investigated.

Table 6.5: Mortality rate (%) for *Artemia Salina* (nauplii) measured for 24 h exposure to pristine (without photocatalyst) and pre-treated PU foam (with TiO_2 photocatalyst). Mean ± SEM, n = 5.

	Mortality (%)	Standard error of the mean (%)
Negative control (*Artemia* salt)	2	1.79
PU foam (without) photocatalyst	2	1.79
Pre-treated PU foam (with photocatalyst)	8	4.92
Positive control (10 % DMSO)	100	0

6.3 Summary

Solar-light-driven TiO_2 photocatalysts on 3D polyurethane foams were developed with the aid of MW irradiation and a dip-coating method. MW synthesis of TiO_2 nanopowders was performed at 200 °C for 10 min in the presence of different solvents (ethanol, IPA and water). Pure anatase was obtained for the synthesis in ethanol, whereas in IPA and H_2O, a mixture of anatase/brookite or anatase/rutile phases was present, respectively, as revealed by XRD. SEM/STEM results revealed highly porous micro-sized spherical/elongated TiO_2 aggregates composed of fine nanocrystals for the TiO_2_EtOH nanomaterial. These TiO_2 nanocrystals had low and high-index facets, while the latter presented bulk/surface structural defects. For the

syntheses using IPA and water, 1D nanostructures were formed together with other smaller nanocrystals with an undefined shape. A higher contribution from the defect states for the TiO_2 ethanol nanopowder was also suggested based on the PL measurements. BET analysis confirmed that the specific surface area of the porous TiO_2 synthesized with ethanol was superior to the nanopowders synthesized with IPA and H_2O, thus conferring it enhanced capacity for surface oxygen adsorption, as observed through XPS. This characteristic enabled a high TC sorption efficiency (~ 58 % in 240 min). Reusability tests demonstrated that UV exposure effectively restored its adsorption capacity and overall performance for the removal of TC. Although TC adsorption was suppressed when TiO_2 nanostructures were incorporated into a PU foam, almost the same percentage of TC removal+degradation from aqueous systems could be obtained (~ 80 % in 180 min of solar light exposure with the TiO_2 PU foam and ~ 88 % with the TiO_2_EtOH nanopowder in 240 min of dark + 30 min of solar light exposure). Photocatalytic experiments using tap water demonstrated the potential of TiO_2-PU foams for degrading TC in real-life aqueous systems. LC-HRMS spectra confirmed the contaminant degradation over the TiO_2 PU foam solution. Moreover, the exposure of TiO_2 PU foams to aquatic organisms had no significant toxic effects after 24 h. In summary, this study highlighted the production of reusable 3D TiO_2 PU foams with a strong ability to remove water pollutants, such as antibiotics, by the combination of a fast MW-assisted approach and a simple dip-coating technique.

6.4 References

1. Gu, R.; Konar, S.; Sain, M. Preparation and characterization of sustainable polyurethane foams from soybean oils. *JAOCS, Journal of the American Oil Chemists' Society* **2012**, *89*, 2103–2111, doi:10.1007/S11746-012-2109-8/.
2. Matias, M. L.; Pimentel, A.; Reis-Machado, A.; Rodrigues, J. C.; Fernandes, A.; Monteiro, T.; Almeida Carvalho, P.; Neves Amaral, M. N.; Reis, C. P.; Deuermeier, J.; Fortunato, E.; Martins, R.; Nunes, D. Functionalized 3D Polyurethane Foams with Microwave-synthesized TiO_2 Nanostructures for Solar Light-driven Degradation of Tetracycline. *Environmental Science: Advances* **2025**, 4, 713–738 doi:10.1039/D4VA00110A.
3. Rossignolo, G.; Malucelli, G.; Lorenzetti, A. Recycling of polyurethanes: where we are and where we are going. *Green Chemistry* **2024**, *26*, 1132–1152, doi:10.1039/D3GC02091F.
4. Kardeş, M.; Yatmaz, H. C.; Öztürk, K. ZnO Nanorods Grown on Flexible Polyurethane Foam Surfaces for Photocatalytic Azo Dye Treatment. *ACS Applied Nano Materials* **2023**, *6*, *8*, 6605–6613, doi:10.1021/acsanm.3c00210.
5. Krishnapriya, R.; Praneetha, S.; Vadivel Murugan, A. Microwave-solvothermal synthesis of different TiO_2 nano-morphologies with enhanced efficiency by

incorporating Ni nanoparticles in an electrolyte for dye-sensitized solar cells. *Inorganic Chemistry Frontiers* **2017**, *4*, 1665–1678, doi:10.1039/C7QI00329C.

6. Morishima, Y.; Kobayashi, M.; Petrykin, V.; Kakihana, M.; Tomita, K. Microwave-assisted hydrothermal synthesis of brookite nanoparticles from a water-soluble titanium complex and their photocatalytic activity. *Journal of the Ceramic Society of Japan* **2007**, *115*, 826–830, doi:10.2109/JCERSJ2.115.826.
7. Di Paola, A.; Bellardita, M.; Palmisano, L. Brookite, the Least Known TiO_2 Photocatalyst. *Catalysts* **2013**, *3*, 36–73, doi:10.3390/catal3010036.
8. Delgado, L. P.; Figueroa-Torres, M. Z.; Ceballos-Chuc, M. C.; García-Rodríguez, R.; Alvarado-Gil, J. J.; Oskam, G.; Rodriguez-Gattorno, G. "Tailoring the TiO_2 phases through microwave-assisted hydrothermal synthesis: Comparative assessment of bactericidal activity." *Materials Science and Engineering: C* **2020**, *117*, 111290, doi:10.1016/J.MSEC.2020.111290.
9. Bandas, C.; Lazau, C.; Dabici, A.; Sfirloaga, P.; Vaszilcsin, N.; Grozescu, I.; Tiponut, V. Microwave-Assisted Hydrothermal Method for Synthesis of Nanocrystalline Anatase TiO_2. *Chemical Bulletin of "Politehnica" University of Timisoara* **2011**, *56(70)*, 81–84.
10. Nunes, D.; Pimentel, A.; Santos, L.; Barquinha, P.; Fortunato, E.; Martins, R. Photocatalytic TiO_2 Nanorod Spheres and Arrays Compatible with Flexible Applications. *Catalysts* **2017**, *7 (2)*, 1–18.
11. Xu, F. Review of analytical studies on TiO_2 nanoparticles and particle aggregation, coagulation, flocculation, sedimentation, stabilization. *Chemosphere* **2018**, *212*, 662–677, doi:10.1016/J.CHEMOSPHERE.2018.08.108.
12. Nunes, D.; Pimentel, A.; Pinto, J. V.; Calmeiro, T. R.; Nandy, S.; Barquinha, P.; Pereira, L.; Carvalho, P. A.; Fortunato, E.; Martins, R. Photocatalytic behavior of TiO_2 films synthesized by microwave irradiation. *Catalysis Today* **2016**, *278*, 262–270.
13. Mitchell, D. R. G.; Casillas, G. Secondary Electron Imaging in an Aberration-Corrected STEM. *Microscopy Today* **2016**, *24*, 22–27, doi:10.1017/S1551929516000705.
14. DeRita, L.; Resasco, J.; Dai, S.; Boubnov, A.; Thang, H. V.; Hoffman, A. S.; Ro, I.; Graham, G. W.; Bare, S. R.; Pacchioni, G.; Pan, X.; Christopher, P. Structural evolution of atomically dispersed Pt catalysts dictates reactivity. *Nature Materials* **2019**, *18 (7)*, 746–751, doi:10.1038/S41563-019-0349-9.
15. Zhou, Z.; Yu, Y.; Ding, Z.; Zuo, M.; Jing, C. Modulating High-Index Facets on Anatase TiO_2. *European Journal of Inorganic Chemistry* **2018**, *2018*, 683–693, doi:10.1002/EJIC.201701027.
16. Carey, J. J.; McKenna, K. P. Does Polaronic Self-Trapping Occur at Anatase TiO_2 Surfaces? *Journal of Physical Chemistry C* **2018**, *122*, 27540–27553, doi:https://doi.org/10.1021/acs.jpcc.8b09437.
17. Yuan, W.; Meng, J.; Zhu, B.; Gao, Y.; Zhang, Z.; Sun, C.; Wang, Y. Unveiling the Atomic Structures of the Minority Surfaces of TiO_2 Nanocrystals. *Chemistry of Materials* **2018**, *30*, 288–295, doi:https://doi.org/10.1021/acs.chemmater.7b04541.
18. Yang, H. G.; Sun, C. H.; Qiao, S. Z.; Zou, J.; Liu, G.; Smith, S. C.; Cheng, H. M.; Lu, G. Q. Anatase TiO_2 single crystals with a large percentage of reactive facets. *Nature* **2008**, *453*, 638–641, doi:10.1038/nature06964.
19. Liu, Z.; Zheng, Y.; Gao, T.; Zhang, J.; Sun, X.; Zhou, G. Fabrication of anatase TiO_2

tapered tetragonal nanorods with designed {100}, {001} and {101} facets for enhanced photocatalytic H_2 evolution. *International Journal of Hydrogen Energy* **2017**, *42,34*, 21775–21785, doi:10.1016/J.IJHYDENE.2017.07.067.

20. Roy, N.; Sohn, Y.; Pradhan, D. Synergy of low-energy {101} and high-energy {001} TiO_2 crystal facets for enhanced photocatalysis. *ACS Nano* **2013**, *7*, *3*, 2532–2540, doi:https://doi.org/10.1021/nn305877v.
21. Han, X.; Zheng, B.; Ouyang, J.; Wang, X.; Kuang, Q.; Jiang, Y.; Xie, Z.; Zheng, L. Control of anatase TiO_2 nanocrystals with a series of high-energy crystal facets via a fuorine-free strategy. *Chemistry, an Asian journal* **2012**, *7(11)*, 2538–2542, doi:10.1002/ASIA.201200474.
22. Lin, J.; Heo, Y. U.; Nattestad, A.; Sun, Z.; Wang, L.; Kim, J. H.; Dou, S. X. 3D Hierarchical Rutile TiO_2 and Metal-free Organic Sensitizer Producing Dye-sensitized Solar Cells 8.6% Conversion Efficiency. *Scientific Reports* **2014**, *4*, 1–8, doi:10.1038/srep05769.
23. Lai, Z.; Peng, F.; Wang, H.; Yu, H.; Zhang, S.; Zhao, H. A new insight into regulating high energy facets of rutile TiO_2. *Journal of Materials Chemistry A* **2013**, *1*, *13*, 4182–4185, doi:10.1039/C3TA00188A.
24. Holm, A.; Hamandi, M.; Simonet, F.; Jouguet, B.; Dappozze, F.; Guillard, C. Impact of rutile and anatase phase on the photocatalytic decomposition of lactic acid. *Applied Catalysis B: Environmental* **2019**, *253*, 96–104, doi:10.1016/J.APCATB.2019.04.042.
25. He, J.; Du, Y. en; Bai, Y.; An, J.; Cai, X.; Chen, Y.; Wang, P.; Yang, X.; Feng, Q. Facile Formation of Anatase/Rutile TiO_2 Nanocomposites with Enhanced Photocatalytic Activity. *Molecules* **2019**, *24(16)*, 2996, doi:10.3390/MOLECULES24162996.
26. Ma, R.; Chen, T. Checking the Synergetic Effect between Anatase and Rutile. *Journal of Physical Chemistry C* **2019**, *123*, *32*, 19479–19485, doi:https://doi.org/10.1021/acs.jpcc.9b03381.
27. Wei, X.; Zhu, G.; Fang, J.; Chen, J. Synthesis, characterization, and photocatalysis of well-dispersible phase-pure anatase TiO_2 nanoparticles. *International Journal of Photoenergy* **2013**, *2013(7268)*, 1–6, doi:10.1155/2013/726872.
28. Jalawkhan, R. S.; Ouda, A. A.; Abdul-Lettif, A. M.; Mohamad Alosfur, F. K. Effect of solvents on the morphology of TiO_2 nanoparticles prepared by microwave method. *IOP Conference Series: Materials Science and Engineering* **2020**, *928*, *7*, 072159, doi:10.1088/1757-899X/928/7/072159.
29. Andrade-Guel, M.; Diáz-Jiménez, L.; Cortés-Hernández, D.; Cabello-Alvarado, C.; Ávila-Orta, C.; Bartolo-Pérez, P.; Gamero-Melo, P. Microwave assisted sol–gel synthesis of titanium dioxide using hydrochloric and acetic acid as catalysts. *Boletín de la Sociedad Española de Cerámica y Vidrio* **2019**, *58*, *4*, 171–177, doi:10.1016/J.BSECV.2018.10.005.
30. Zhang, E.; Pan, Y.; Lu, T.; Zhu, Y.; Dai, W. Novel synthesis of S-doped anatase TiO_2 via hydrothermal reaction of Cu–Ti amorphous alloy. *Applied Physics A: Materials Science and Processing* **2020**, *126*, 1–8, doi:10.1007/S00339-020-03790-1.
31. Zhu, L.; Lu, Q.; Lv, L.; Wang, Y.; Hu, Y.; Deng, Z.; Lou, Z.; Hou, Y.; Teng, F. Ligand-free rutile and anatase TiO_2 nanocrystals as electron extraction layers for high performance inverted polymer solar cells. *RSC Advances* **2017**, *7*, 20084–20092.
32. Matias, M. L.; Pimentel, A.; Reis-Machado, A. S.; Rodrigues, J.; Deuermeier, J.; Fortunato, E.; Martins, R.; Nunes, D. Enhanced Fe-TiO_2 Solar Photocatalysts on Porous Platforms for Water Purification. *Nanomaterials* **2022**, *12*.

33. Hiji, A.; Hanawa, T.; Yokoi, T.; Chen, P.; Ashida, M.; Kawashita, M. Time Transient of Calcium and Phosphate Ion Adsorption by Rutile Crystal Facets in Hanks' Solution Characterized by XPS. *Langmuir* **2021**, *37*, 3597–3604, doi:10.1021/ACS.LANGMUIR.0C03540.
34. Wang, F.; Sun, L.; Li, Y.; Zhan, W.; Wang, X.; Han, X. Hollow Anatase TiO_2 Octahedrons with Exposed High-Index {102} Facets for Improved Dye-Sensitized Photoredox Catalysis Activity. *Inorganic Chemistry* **2018**, *57*, *8*, 4550–4555, doi:https://doi.org/10.1021/acs.inorgchem.8b00307.
35. Ghobadi, A.; Ulusoy, T. G.; Garifullin, R.; Guler, M. O.; Okyay, A. K. A Heterojunction Design of Single Layer Hole Tunneling ZnO Passivation Wrapping around TiO_2 Nanowires for Superior Photocatalytic Performance. *Scientific Reports* **2016**, *6(30587)*, 1–15, doi:10.1038/SREP30587.
36. Zhang, W. F.; Zhang, M. S.; Yin, Z. Microstructures and visible photoluminescence of TiO_2 nanocrystals. *Physica status solidi. A. Applied research* **2000**, *179*, *2*, 319–327.
37. Mercado, C.; Seeley, Z.; Bandyopadhyay, A.; Bose, S.; McHale, J. L. Photoluminescence of dense nanocrystalline titanium dioxide thin films: Effect of doping and thickness and relation to gas sensing. *ACS Applied Materials and Interfaces* **2011**, *3*, *7*, 2281–2288, doi:https://doi.org/10.1021/am2006433.
38. Graça, M. P. F.; Nico, C.; Peres, M.; Valente, M. A.; Monteiro, T. Study of the optical and dielectric properties of TiO_2 nanocrystals prepared by the Pechini method. *Journal of nanoscience and nanotechnology* **2012**, *12(11)*, 8600–8606, doi:10.1166/JNN.2012.6819.
39. Pallotti, D. K.; Passoni, L.; Maddalena, P.; Di Fonzo, F.; Lettieri, S. Photoluminescence Mechanisms in Anatase and Rutile TiO_2. *Journal of Physical Chemistry C* **2017**, *121*, *16*, 9011–9021, doi:10.1021/acs.jpcc.7b00321.
40. Iijima, K.; Goto, M.; Enomoto, S.; Kunugita, H.; Ema, K.; Tsukamoto, M.; Ichikawa, N.; Sakama, H. Influence of oxygen vacancies on optical properties of anatase TiO_2 thin films. *Journal of Luminescence* **2008**, *128*, 911–913, doi:10.1016/J.JLUMIN.2007.11.071.
41. Tang, H.; Berger, H.; Schmid, P. E.; Lévy, F.; Burri, G. Photoluminescence in TiO_2 anatase single crystals. *Solid State Communications* **1993**, *87*, *9*, 847–850, doi:10.1016/0038-1098(93)90427-O.
42. Scanlon, D. O.; Dunnill, C. W.; Buckeridge, J.; Shevlin, S. A.; Logsdail, A. J.; Woodley, S. M.; Catlow, C. R. A.; Powell, M. J.; Palgrave, R. G.; Parkin, I. P.; Watson, G. W.; Keal, T. W.; Sherwood, P.; Walsh, A.; Sokol, A. A. Band alignment of rutile and anatase TiO_2. *Nature Materials* **2013**, *12*, 798–801, doi:10.1038/nmat3697.
43. Garcia, R. M.; Carleer, R.; Pérez, M. A.; Torres, J. P.; Gu, Y.; Samyn, P.; Yperman, J. Fe-TiO_2/AC and Co-TiO_2/AC composites: Novel photocatalysts prepared from waste streams for the efficient removal and photocatalytic degradation of cibacron yellow F-4G dye. *Catalysts* **2021**, *11(10)*, 1–24, doi:10.3390/CATAL11101137.
44. Tan, I. A. W.; Ahmad, A. L.; Hameed, B. H. Adsorption isotherms, kinetics, thermodynamics and desorption studies of 2,4,6-trichlorophenol on oil palm empty fruit bunch-based activated carbon. *Journal of Hazardous Materials* **2009**, *164(2–3)*, 473–482, doi:10.1016/J.JHAZMAT.2008.08.025.
45. Yu, F.; Ma, J.; Han, S. Adsorption of tetracycline from aqueous solutions onto multi-walled carbon nanotubes with different oxygen contents. *Scientific Reports* **2014**, *4*, *5326*,

1–8, doi:10.1038/srep05326.
46. Ghanim, B.; Leahy, J. J.; O'Dwyer, T. F.; Kwapinski, W.; Pembroke, J. T.; Murnane, J. G. Removal of hexavalent chromium (Cr(VI)) from aqueous solution using acid-modified poultry litter-derived hydrochar: adsorption, regeneration and reuse. *Journal of Chemical Technology & Biotechnology* **2022**, *97*, 55–66, doi:10.1002/JCTB.6904.
47. Matos, R.; Kuźniarska-Biernacka, I.; Rocha, M.; Belo, J. H.; Araújo, J. P.; Estrada, A. C.; Lopes, J. L.; Shah, T.; Korgel, B. A.; Pereira, C.; Trindade, T.; Freire, C. Design and photo-Fenton performance of Graphene/CuS/Fe_3O_4 tertiary nanocomposites for Rhodamine B degradation. *Catalysis Today* **2023**, *418*, 114132, doi:10.1016/J.CATTOD.2023.114132.
48. Zhang, L.; Ai, T.; Tian, X.; Dai, S. An efficient removal mechanism for different hydrophilic antibiotics from aquatic environments by Cu–Al–Fe–Cr quasicrystals. *RSC Advances* **2022**, *12*, 9995, doi:10.1039/D1RA08095D.
49. de Sousa, D. N. R.; Insa, S.; Mozeto, A. A.; Petrovic, M.; Chaves, T. F.; Fadini, P. S. Equilibrium and kinetic studies of the adsorption of antibiotics from aqueous solutions onto powdered zeolites. *Chemosphere* **2018**, *205*, 137–146, doi:10.1016/J.CHEMOSPHERE.2018.04.085.
50. Kajjumba, G. W.; Emik, S.; Öngen, A.; Aydın, H. K. Ö.; Serdar, A.; Kajjumba, G. W.; Emik, S.; Öngen, A.; Aydın, H. K. Ö.; Serdar, A. Modelling of Adsorption Kinetic Processes—Errors, Theory and Application. In *Advanced Sorption Process Applications*; IntechOpen, 2018 ISBN 978-1-78984-819-9.
51. Álvarez-Torrellas, S.; Ribeiro, R. S.; Gomes, H. T.; Ovejero, G.; García, J. Removal of antibiotic compounds by adsorption using glycerol-based carbon materials. *Chemical Engineering Journal* **2016**, *296*, 277–288, doi:10.1016/J.CEJ.2016.03.112.
52. Ezati, F.; Sepehr, E.; Ahmadi, F. The efficiency of nano-TiO_2 and γ-Al_2O_3 in copper removal from aqueous solution by characterization and adsorption study. *Scientific Reports* **2021**, *11*, *1*, 1–14, doi:10.1038/s41598-021-98051-3.
53. Tio, R.; Priyadarshini, B.; Rath, P. P.; Behera, S. S.; Panda, S. R.; Sahoo, T. R.; Parhi, P. K. Kinetics, Thermodynamics and Isotherm studies on Adsorption of Eriochrome Black-T from aqueous solution using. *IOP Conference Series: Materials Science and Engineering* **2018**, *310*, 012051, doi:10.1088/1757-899X/310/1/012051.
54. Wang, H.; Fang, C.; Wang, Q.; Chu, Y.; Song, Y.; Chen, Y.; Xue, X. Sorption of tetracycline on biochar derived from rice straw and swine manure. *RSC Advances* **2018**, *8*, 16260–16268, doi:10.1039/C8RA01454J.
55. Eltaweil, A. S.; Abd El-Monaem, E. M.; Omer, A. M.; Khalifa, R. E.; Abd El-Latif, M. M.; El-Subruiti, G. M. Efficient removal of toxic methylene blue (Mb) dye from aqueous solution using a metal-organic framework (mof) mil-101(fe): Isotherms, kinetics, and thermodynamic studies. *Desalination and Water Treatment* **2020**, *189*, 395–407, doi:10.5004/DWT.2020.25599.
56. Mishra, V. Modeling of batch sorber system: kinetic, mechanistic, and thermodynamic modeling. *Applied Water Science* **2017**, *7*, *6*, 3173–3180, doi:10.1007/S13201-016-0463-7.
57. Srivastava, P.; Goyal, S.; Tayade, R. Ultrasound-assisted adsorption of reactive blue 21 dye on TiO_2 in the presence of some rare earths (La, Ce, Pr & Gd). *Canadian Journal of Chemical Engineering* **2014**, *92*, 41–51, doi:10.1002/CJCE.21799.
58. Roy, K.; Khan, I. A.; Rizkallah, B. M.; Galal, M. M.; Matta, M. E.; Alami, K.

Characteristics of Tetracycline Adsorption on Commercial Biochar from Synthetic and Real Wastewater in Batch and Continuous Operations: Study of Removal Mechanisms, Isotherms, Kinetics, Thermodynamics, and Desorption. *Sustainability* **2023**, *15(10)*, 8249, doi:10.3390/SU15108249.

59. Du, Y. E.; Niu, X.; Li, W.; An, J.; Liu, Y.; Chen, Y.; Wang, P.; Yang, X.; Feng, Q. Microwave-Assisted Synthesis of High-Energy Faceted TiO_2 Nanocrystals Derived from Exfoliated Porous Metatitanic Acid Nanosheets with Improved Photocatalytic and Photovoltaic Performance. *Materials* **2019**, *12(21)*, 3614, doi:10.3390/MA12213614.
60. Chen, H.; Hsu, H.-F.; Wu -, H.-Y.; Segal, G.; Parkinson, D.; Ruu Siah, W.; Lintang, H. O.; Shamsuddin, M.; Yuliati, L.; Johor Bahru, U. High photocatalytic activity of mixed anatase-rutile phases on commercial TiO_2 nanoparticles. *IOP Conference Series: Materials Science and Engineering* **2016**, *107*, 012005, doi:10.1088/1757-899X/107/1/012005.
61. Zerjav, G.; Zizek, K.; Zavasnik, J.; Pintar, A. Brookite vs. rutile vs. anatase: What's behind their various photocatalytic activities? *Journal of Environmental Chemical Engineering* **2022**, *10(3)*, 107722, doi:10.1016/J.JECE.2022.107722.
62. Cheng, H.; Wang, J.; Zhao, Y.; Han, X. Effect of phase composition, morphology, and specific surface area on the photocatalytic activity of TiO_2 nanomaterials. *RSC Advances* **2014**, *4(87)*, 47031–47038, doi:10.1039/C4RA05509H.
63. Zhao, Z.; Li, Z.; Zou, Z. A Theoretical study of water adsorption and decomposition on the low-index stoichiometric anatase TiO_2 surfaces. *Journal of Physical Chemistry C* **2012**, *116*, *13*, 7430–7441, doi:https://doi.org/10.1021/jp212407s.
64. Shen, M.; Han, A.; Wang, X.; Ro, Y. G.; Kargar, A.; Lin, Y.; Guo, H.; Du, P.; Jiang, J.; Zhang, J.; Dayeh, S. A.; Xiang, B. Atomic Scale Analysis of the Enhanced Electro- and Photo-Catalytic Activity in High-Index Faceted Porous NiO Nanowires. *Scientific Reports* **2015**, *5*, *1*, 1–6, doi:10.1038/srep08557.
65. Kong, M.; Li, Y.; Chen, X.; Tian, T.; Fang, P.; Zheng, F.; Zhao, X. Tuning the relative concentration ratio of bulk defects to surface defects in TiO_2 nanocrystals leads to high photocatalytic efficiency. *Journal of the American Chemical Society* **2011**, *133*, *41*, 16414–16417, doi:https://doi.org/10.1021/ja207826q.
66. Yan, J.; Wu, G.; Guan, N.; Li, L.; Li, Z.; Cao, X. Understanding the effect of surface/bulk defects on the photocatalytic activity of TiO_2: anatase versus rutile. *Physical Chemistry Chemical Physics* **2013**, *15*, 10978–10988, doi:10.1039/C3CP50927C.
67. Zhao, H.; Pan, F.; Li, Y. A review on the effects of TiO_2 surface point defects on CO_2 photoreduction with H_2O. *Journal of Materiomics* **2017**, *3*, *1*, 17–32, doi:10.1016/J.JMAT.2016.12.001.
68. Zhang, H.; Cai, J.; Wang, Y.; Wu, M.; Meng, M.; Tian, Y.; Li, X.; Zhang, J.; Zheng, L.; Jiang, Z.; Gong, J. Insights into the effects of surface/bulk defects on photocatalytic hydrogen evolution over TiO_2 with exposed {001} facets. *Applied Catalysis B: Environmental* **2018**, *220*, 126–136, doi:10.1016/J.APCATB.2017.08.046.
69. Piler, K.; Bahrim, C.; Twagirayezu, S.; Benson, T. J. Lattice disorders of TiO_2 and their significance in the photocatalytic conversion of CO_2. In *Advances in Catalysis*; Song, C., Ed.; Academic Press Inc., 2020; Vol. 66, pp. 109–233 ISBN 9780128203699.
70. Safari, G. H.; Hoseini, M.; Seyedsalehi, M.; Kamani, H.; Jaafari, J.; Mahvi, A. H. Photocatalytic degradation of tetracycline using nanosized titanium dioxide in aqueous

solution. *International Journal of Environmental Science and Technology* **2015**, *12(2)*, 603–616, doi:10.1007/S13762-014-0706-9.

71. Bouafıa-Chergui, S.; Zemmouri, H.; Chabani, M.; Bensmaili, A. TiO_2-photocatalyzed degradation of tetracycline: kinetic study, adsorption isotherms, mineralization and toxicity reduction. *Desalination and Water Treatment* **2016**, *57*, *35*, 16670–16677, doi:10.1080/19443994.2015.1082507.
72. Wu, S.; Hu, H.; Lin, Y.; Zhang, J.; Hu, Y. H. Visible light photocatalytic degradation of tetracycline over TiO_2. *Chemical Engineering Journal* **2020**, *382*, 1–10, doi:10.1016/J.CEJ.2019.122842.
73. Wu, S.; Li, X.; Tian, Y.; Lin, Y.; Hu, Y. H. Excellent photocatalytic degradation of tetracycline over black anatase-TiO_2 under visible light. *Chemical Engineering Journal* **2021**, *406*, 1–10, doi:10.1016/J.CEJ.2020.126747.
74. Lian, P.; Qin, A.; Liu, Z.; Ma, H.; Liao, L.; Zhang, K.; Li, N. Facile Synthesis to Porous TiO_2 Nanostructures at Low Temperature for Efficient Visible-Light Degradation of Tetracycline. *Nanomaterials* **2024**, *14*, 943, doi:10.3390/NANO1411094.
75. Hu, L.; Xing, M.; He, X.; Yang, K.; Zhu, J.; Wang, J.; He, J.; Shi, J. Photocatalytic degradation of tetracycline hydrochloride by ZnO/TiO_2 composite photocatalyst. *Journal of Materials Science: Materials in Electronics* **2023**, *34*, 1–19, doi:10.1007/S10854-023-11690-2.
76. Huang, Z.; Wang, J.; Yang, M. Q.; Qian, Q.; Liu, X. P.; Xiao, L.; Xue, H. Construction of TiO_2-Eggshell for Efficient Degradation of Tetracycline Hydrochloride: Sunlight Induced In-Situ Formation of Carbonate Radical. *Materials* **2021**, *14*, 1–16, doi:10.3390/MA14071598.
77. Hasham Firooz, M.; Naderi, A.; Moradi, M.; Roshanak, &; Kalantary, R. Enhanced tetracycline degradation with TiO_2/natural pyrite S-scheme photocatalyst. *Scientific Reports* **123AD**, *14*, 1–20, doi:10.1038/s41598-024-54549-0.
78. Dalto, F.; Kuźniarska-Biernacka, I.; Pereira, C.; Mesquita, E.; Soares, O. S. G. P.; Pereira, M. F. R.; Rosa, M. J.; Mestre, A. S.; Carvalho, A. P.; Freire, C. Solar light-induced methylene blue removal over TiO_2/AC composites and photocatalytic regeneration. *Nanomaterials* **2021**, *11(11)*, 1–24, doi:10.3390/NANO11113016.
79. Ma, Y.; Peng, Q.; Sun, M.; Zuo, N.; Mominou, N.; Li, S.; Jing, C.; Wang, L. Photocatalytic oxidation degradation of tetracycline over La/Co@TiO_2 nanospheres under visible light. *Environmental Research* **2022**, *215*, 114297, doi:10.1016/J.ENVRES.2022.114297.
80. Zhu, X. D.; Wang, Y. J.; Sun, R. J.; Zhou, D. M. Photocatalytic degradation of tetracycline in aqueous solution by nanosized TiO_2. *Chemosphere* **2013**, *92*, *8*, 925–932, doi:10.1016/J.CHEMOSPHERE.2013.02.066.
81. Rovisco, A.; Morais, M.; Branquinho, R.; Fortunato, E.; Martins, R.; Barquinha, P. Microwave-Assisted Synthesis of Zn_2SnO_4 Nanostructures for Photodegradation of Rhodamine B under UV and Sunlight. *Nanomaterials* **2022**, *12*, 2119, doi:10.3390/NANO12122119.
82. Divakaran, K.; Baishnisha, A.; Balakumar, V.; Perumal, K. N.; Meenakshi, C.; Kannan, R. S. Photocatalytic degradation of tetracycline under visible light using TiO_2@sulfur doped carbon nitride nanocomposite synthesized via in-situ method. *Journal of Environmental Chemical Engineering* **2021**, *9*, *4*, 105560, doi:10.1016/J.JECE.2021.105560.

83. Salmanzadeh-Jamadi, Z.; Habibi-Yangjeh, A.; Pouran, S. R.; Xu, X.; Wang, C. Facile fabrication of TiO_2/Bi_5O_7Br photocatalysts for visible-light-assisted removal of tetracycline and dye wastewaters. *Journal of Physics D: Applied Physics* **2022**, *55*, 165105, doi:10.1088/1361-6463/AC48AF.
84. Sharma, M.; Mandal, M. K.; Pandey, S.; Kumar, R.; Dubey, K. K. Visible-Light-Driven Photocatalytic Degradation of Tetracycline Using Heterostructured Cu_2O-TiO_2 Nanotubes, Kinetics, and Toxicity Evaluation of Degraded Products on Cell Lines. *ACS Omega* **2022**, *7*, *37*, 33572–33586, doi:10.1021/acsomega.2c04576.
85. Dvoranová, D.; Barbieriková, Z.; Brezová, V. Radical Intermediates in Photoinduced Reactions on TiO_2 (An EPR Spin Trapping Study). *Molecules* **2014**, *19(11)*, 17279, doi:10.3390/MOLECULES191117279.
86. Chen, Q.; Wang, K.; Gao, G.; Ren, J.; Duan, R.; Fang, Y.; Hu, X. Singlet oxygen generation boosted by Ag–Pt nanoalloy combined with disordered surface layer over TiO_2 nanosheet for improving the photocatalytic activity. *Applied Surface Science* **2021**, *538*, 147944, doi:10.1016/J.APSUSC.2020.147944.
87. Chen, Q.; Wang, H.; Wang, C.; Guan, R.; Duan, R.; Fang, Y.; Hu, X. Activation of molecular oxygen in selectively photocatalytic organic conversion upon defective TiO_2 nanosheets with boosted separation of charge carriers. *Applied Catalysis B: Environmental* **2020**, *262*, 118258, doi:10.1016/J.APCATB.2019.118258.
88. Peyrton, J.; Avérous, L. Structure-properties relationships of cellular materials from biobased polyurethane foams. *Materials Science and Engineering: R: Reports* **2021**, *145*, 100608, doi:10.1016/J.MSER.2021.100608.
89. Tewari, A.; Gandla, S.; Bohm, S.; McNeill, C. R.; Gupta, D. Highly Exfoliated MWNT-rGO Ink-Wrapped Polyurethane Foam for Piezoresistive Pressure Sensor Applications. *ACS Applied Materials and Interfaces* **2018**, *10*, *6*, 5185–5195, doi:https://doi.org/10.1021/acsami.7b15252.
90. Mârșolea (Cristea), A. C.; Mocanu, A.; Stănescu, P. O.; Brincoveanu, O.; Orbeci, C.; Irodia, R.; Pîrvu, C.; Dinescu, A.; Bobirica, C.; Rusen, E. Synthesis and characterization of polyurethane flexible foams provided from PET derivatives, fly ash, and glass wastes. *Heliyon* **2023**, *9*, *12*, e23097, doi:10.1016/J.HELIYON.2023.E23097.
91. Ahmad, S.; Almehmadi, M.; Janjuhah, H. T.; Kontakiotis, G.; Abdulaziz, O.; Saeed, K.; Ahmad, H.; Allahyani, M.; Aljuaid, A.; Alsaiari, A. A.; Muhammad, J.; Khan, I. The Effect of Mineral Ions Present in Tap Water on Photodegradation of Organic Pollutants: Future Perspectives. *Water* **2023**, *15*, 175, doi:10.3390/W15010175.
92. Mahmoodi, N. M.; Arami, M.; Limaee, N. Y.; Gharanjig, K. Photocatalytic degradation of agricultural N-heterocyclic organic pollutants using immobilized nanoparticles of titania. *Journal of Hazardous Materials* **2007**, *145*, 65–71, doi:10.1016/J.JHAZMAT.2006.10.089.
93. Ameta, R.; Solanki, M. S.; Benjamin, S.; Ameta, S. C. Chapter 6 - Photocatalysis. In *Advanced Oxidation Processes for Wastewater Treatment: Emerging Green Chemical Technology*; Ameta, Suresh C.; Ameta, R., Ed.; Elsevier Inc., 2018; pp. 135–175 ISBN 9780128105252.
94. Nunes, D.; Pimentel, A.; Branquinho, R.; Fortunato, E.; Martins, R. Metal oxide-based photocatalytic paper: A green alternative for environmental remediation. *Catalysts* **2021**,

11(4), 1–30, doi:10.3390/catal11040504.

95. Orege, J. I.; Oderinde, O.; Kifle, G. A.; Ibikunle, A. A.; Raheem, S. A.; Ejeromedoghene, O.; Okeke, E. S.; Olukowi, O. M.; Orege, O. B.; Fagbohun, E. O.; Ogundipe, T. O.; Avor, E. P.; Ajayi, O. O.; Daramola, M. O. Recent advances in heterogeneous catalysis for green biodiesel production by transesterification. *Energy Conversion and Management* **2022**, *258*, 115406, doi:10.1016/J.ENCONMAN.2022.115406.
96. Al-Mamun, M. R.; Kader, S.; Islam, M. S.; Khan, M. Z. H. Photocatalytic activity improvement and application of UV-TiO_2 photocatalysis in textile wastewater treatment: A review. *Journal of Environmental Chemical Engineering* **2019**, *7*, *5*, 103248, doi:10.1016/J.JECE.2019.103248.
97. Guo, J.; Jiang, L.; Liang, J.; Xu, W.; Yu, H.; Zhang, J.; Ye, S.; Xing, W.; Yuan, X. Photocatalytic degradation of tetracycline antibiotics using delafossite silver ferrite-based Z-scheme photocatalyst: Pathways and mechanism insight. *Chemosphere* **2021**, *270*, 128651, doi:10.1016/J.CHEMOSPHERE.2020.128651.
98. Wang, B.; Guo, Y.; Li, Q.; Xin, C.; Tian, Y.; Zhang, W.; Yu, X. Design of porous ZrO_2 with well-tuned band structures and strong visible-light harvesting via Zn doping for enhanced visible-light photocatalysis. *Chemical Engineering Journal* **2024**, *481*, 148489, doi:10.1016/J.CEJ.2023.148489.
99. Hermansson, J.; Andersson, M. Reversed-phase ion-pair chromatography of tetracycline, tetracycline analogs, and their potential impurities. *Journal of Pharmaceutical Sciences* **1982**, *71*, 222–229, doi:10.1002/jps.2600710221.
100. Huang, Z.; Liu, H. Insights into the pathways, intermediates, influence factors and toxicological properties in the degradation of tetracycline by TiO_2-based photocatalysts. *Journal of Environmental Chemical Engineering* **2023**, *11*, 110587, doi:10.1016/J.JECE.2023.110587.
101. Deng, Y.; Tang, L.; Zeng, G.; Wang, J.; Zhou, Y.; Wang, J.; Tang, J.; Wang, L.; Feng, C. Facile fabrication of mediator-free Z-scheme photocatalyst of phosphorous-doped ultrathin graphitic carbon nitride nanosheets and bismuth vanadate composites with enhanced tetracycline degradation under visible light. *Journal of Colloid and Interface Science* **2018**, *509*, 219–234, doi:10.1016/J.JCIS.2017.09.016.
102. He, D.; Sun, Y.; Xin, L.; Feng, J. Aqueous tetracycline degradation by non-thermal plasma combined with nano-TiO_2. *Chemical Engineering Journal* **2014**, *258*, 18–25, doi:10.1016/J.CEJ.2014.07.089.
103. Li, S.; Hu, J. Photolytic and photocatalytic degradation of tetracycline: Effect of humic acid on degradation kinetics and mechanisms. *Journal of Hazardous Materials* **2016**, *318*, 134–144, doi:10.1016/J.JHAZMAT.2016.05.100.
104. Phanichphant, S.; Nakaruk, A.; Chansaenpak, K.; Channei, D. Evaluating the photocatalytic efficiency of the $BiVO_4$/rGO photocatalyst. *Scientific Reports* **2019**, *9*, *16091*, 1–9, doi:10.1038/s41598-019-52589-5.
105. Dell'Edera, M.; Lo Porto, C.; De Pasquale, I.; Petronella, F.; Curri, M. L.; Agostiano, A.; Comparelli, R. Photocatalytic TiO_2-based coatings for environmental applications. *Catalysis Today* **2021**, *380*, 62–83, doi:10.1016/J.CATTOD.2021.04.023.
106. Turkoglu, S.; Zhang, J.; Dodiuk, H.; Kenig, S.; Ratto, J. A.; Mead, J. Dynamic Wetting Properties of Silica-Poly (Acrylic Acid) Superhydrophilic Coatings. *Polymers* **2023**, *15(5)*,

1242, doi:10.3390/POLYM15051242.
107. Nguyen, H. T.; Guo, S. Y.; You, S. J.; Wang, Y. F. Visible light driven photocatalytic coating of PAA plasma-grafted PVDF membrane by TiO_2 doped with lanthanum recovered from waste fluorescent powder. *Environmental Engineering Research* **2022**, *27(3)*, 210144, doi:10.4491/EER.2021.144.
108. Anaya-Esparza, L. M.; González-Silva, N.; Yahia, E. M.; González-Vargas, O. A.; Montalvo-González, E.; Pérez-Larios, A. Effect of TiO_2-ZnO-MgO Mixed Oxide on Microbial Growth and Toxicity against *Artemia salina*. *Nanomaterials* **2019**, *9(7)*, 992, doi:10.3390/NANO9070992.
109. Felix, L. C.; Folkerts, E. J.; He, Y.; Goss, G. G. Poly(acrylic acid)-coated titanium dioxide nanoparticle and ultraviolet light co-exposure has minimal effect on developing zebrafish (*Danio rerio*). *Environmental Science: Nano* **2017**, *4*, *3*, 658–669, doi:10.1039/C6EN00436A.
110. Rekulapally, R.; Chavali, L. N. M.; Idris, M. M.; Singh, S. Toxicity of TiO_2, SiO_2, ZnO, CuO, Au and Ag engineered nanoparticles on hatching and early nauplii of *Artemia sp. PeerJ* **2019**, *6*, e6138, doi:10.7717/peerj.6138.
111. Khoshnood, R.; Jaafarzadeh, N.; Jamili, Sh.; Farshchi, P;Taghavi, L. Acute toxicity of TiO_2, CuO and ZnO nanoparticles in brine shrimp, *Artemia franciscana*. *Iranian Journal of Fisheries Sciences* **2017**, *16(4)*, 1287–1296.
112. Ozkan, Y.; Altinok, I.; Ilhan, H.; Sokmen, M. Determination of TiO_2 and $AgTiO_2$ Nanoparticles in Artemia salina: Toxicity, Morphological Changes, Uptake and Depuration. *Bulletin of Environmental Contamination and Toxicology* **2016**, *96*, *1*, 36–42, doi:https://doi.org/10.1007/s00128-015-1634-1.
113. Dağlioğlu, Y.; Altinok, İ.; İlhan, H.; Sökmen, M. Determination of the acute toxic effect of ZnO-TiO_2 nanoparticles in brine shrimp (*Artemia salina*). *Acta biologica turcica* **2016**, *29(1)*, 6–13.

7

DEVELOPMENT AND CHARACTERIZATION OF FE:TiO_2 ON MCE FILTERS

7.1 Introduction

In this study, surfactant-modified TiO_2 nanopowders were prepared using a fast solvothermal method (1 h) under microwave irradiation and without any further calcination processes. The surface modification of the nanopowders with PEG (PEG 400) as a surfactant was explored to produce porous materials with a high surface area and enhanced photocatalytic activity.

These nanopowders were impregnated on porous platforms (MCE membrane filters) by a drop-casting technique. The effect of incorporating different molar ratios (1, 2, and 5 %) of iron precursor and the effectiveness of the impregnation method were systematically studied. The characterization of the produced materials was carried out in terms of structural and morphological properties by SEM, EDS, XRD, XPS, and Raman spectroscopy. Optical characterization was also carried out for the nanostructures via UV–VIS absorption measurements. Finally, their efficiency as photocatalysts on water filters was investigated for the degradation of the organic model pollutant, RhB, under solar radiation. Reusability tests within three repeated cycles were also performed. The nanopowders will be referred to as pure TiO_2, 1-Fe:TiO_2, 2-Fe:TiO_2 and 5-Fe:TiO_2 for the materials synthesized with 0, 1, 2 and 5 mol. % of iron precursor, respectively.

7.2 Results and discussion

7.2.1 Characterization of the TiO_2 nanopowders

7.2.1.1 XRD

The as-synthesized nanopowders were also investigated using XRD and the results are depicted in Figure 7.1. All peaks in the experimental diffractograms indicate the presence of the TiO_2 anatase phase, which has Ti^{-6} (octahedral) and O^{-3} (trigonal planar) coordination geometry [1,2]. The peaks detected correspond to the planes (101), (004), (200), (105), (211), (204), (116), (220), and (215) at 2θ = 25.3, 37.8, 48.0, 53.8, 54.9, 62.8, 68.9, and 75.0°, respectively. No peaks associated with rutile or brookite were detected. For the Fe-rich nanostructures, no additional peaks assignable to a metal oxide phase (Fe_2O_3 (hematite) or Fe_2TiO_5) were detected. As such, the quantity/percentage of these oxides could be too low to be detected, could be amorphous or, since Fe^{3+} and Ti^{4+} have similar ionic radii, Fe^{3+} ions could have successfully

substituted Ti^{4+} ions. No changes in peak intensity as a function of iron loading, or shifts could be observed [3–5]. No peaks coming from impurities such as $Ti(OH)_4$ were detected, and the XRD results demonstrate that the materials were well-crystallized (high intensity and well-defined peaks that match well with a known structure [6]) and highly nanostructured (the reflections are broader/larger FWHM compared to bulk crystalline materials [7,8]) [4,9].

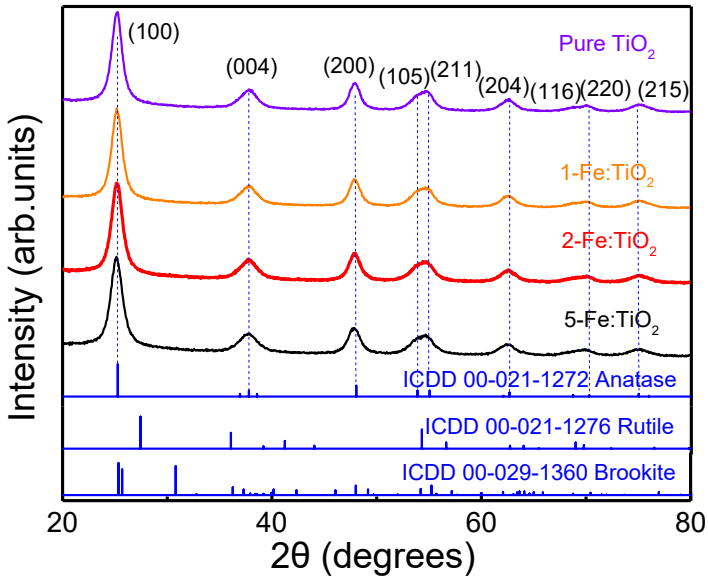

Figure 7.1: XRD diffractograms of pure TiO_2 and 1-Fe:TiO_2, 2-Fe:TiO_2 and 5-Fe:TiO_2 nanostructures with PEG synthesized by microwave irradiation. The simulated TiO_2 anatase, rutile, and brookite structures are also presented for comparison.

The average crystallite sizes of the synthesized nanomaterials were calculated using the X-pert highscore plus software. The estimated crystallite sizes for each powder are summarized in Table 7.1.

Table 7.1: Estimated crystallite sizes (nm) for pure TiO_2, 1-Fe:TiO_2,2-Fe:TiO_2 and 5-Fe:TiO_2 materials with PEG synthesized by microwave irradiation.

	Pure TiO_2	1-Fe:TiO_2	2-Fe:TiO_2	5-Fe:TiO_2
Sizes (nm)	6	5.7	5.2	4.9

The increase in iron content led to a decrease in the crystallite size. As reported, doping with Fe ions could inhibit the growth of TiO_2 anatase crystals [5,10,11]. Hence, it can be suggested that this effect is more pronounced for higher iron contents.

7.2.1.2 Electron microscopy

7.2.1.2.1 SEM

Figure 7.2 depicts the SEM morphology of pure TiO_2 (Figure 7.2 (a)) and 1-Fe:TiO_2, 2-Fe:TiO_2 and 5- Fe:TiO_2 nanoparticles (Figure 7.2 (b)-(d), respectively). PEG was used as a surfactant for all microwave syntheses. It can be observed that all conditions resulted in nanosized TiO_2 particles with a spherical shape. These nanoparticles form agglomerates as they aggregate into larger particles, reaching the micrometer range during the drying process. The insets in Figure 7.2 also show the grain size histograms and the Gaussian model with an acceptable fitting for all particle size distributions. The estimated average particle sizes were 18.58 ± 2.73 nm, 18.40 ± 2.26 nm, 17.00 ± 2.57 nm, and 16.54 ± 3.02 nm for pure TiO_2, 1-Fe:TiO_2, 2-Fe:TiO_2 and 5-Fe:TiO_2 materials, respectively. A decrease in diameter was observed with the increase in iron content, which has been previously reported [10–12]. As expected, the obtained values for the particle sizes are superior to the crystallite sizes (Table 7.1) since particles are agglomerates of grains, and the grains are composed of several crystallites. A more pronounced decrease in the nanoparticle size was achieved when the Fe concentration was above 2 mol. %.

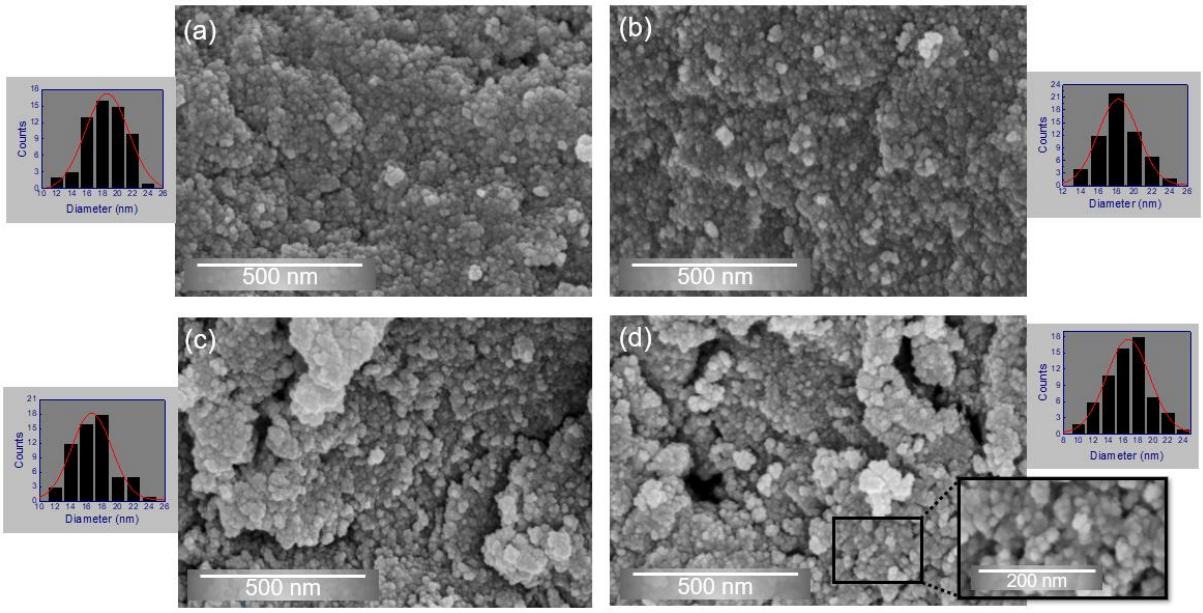

Figure 7.2: SEM images and insets showing the Gaussian model (in red) for fitting the histograms of (a) pure TiO_2, (b) 1-Fe:TiO_2, (c) 2-Fe:TiO_2, and (d) 5-Fe:TiO_2 nanoparticles prepared by microwave irradiation using PEG.

7.2.1.3 XPS

The chemical composition of pure TiO_2 and the Fe:TiO_2 nanostructures with PEG was analyzed by XPS. The conditions of 1 and 2 mol. % of Fe showed a weak iron signal; therefore, these data were not included in this study; hence, only the composition of 5 mol. % (corresponding to 1.4 at. %, as estimated by XPS) is presented. Survey spectra of pure TiO_2 and 5-Fe:TiO_2 are shown in Figure 7.3. XPS results showed that Ti and O were clearly identified for pure TiO_2, whereas for the Fe:TiO_2 nanostructures, Fe could also be detected. A carbon peak was also visible, related to adventitious carbon at the surface. Figure 7.4 shows the high-resolution XPS spectra of O 1s (deconvoluted) and Ti 2p core levels of pure TiO_2 nanostructures with PEG and of 5-Fe:TiO_2.

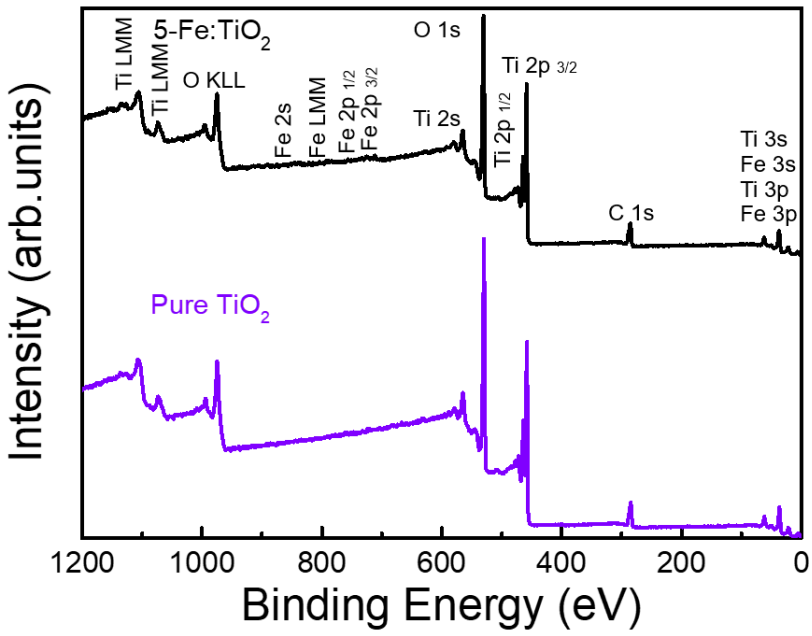

Figure 7.3: Survey spectra of pure TiO_2 spectra and 5-Fe:TiO_2 nanostructures synthesized with PEG.

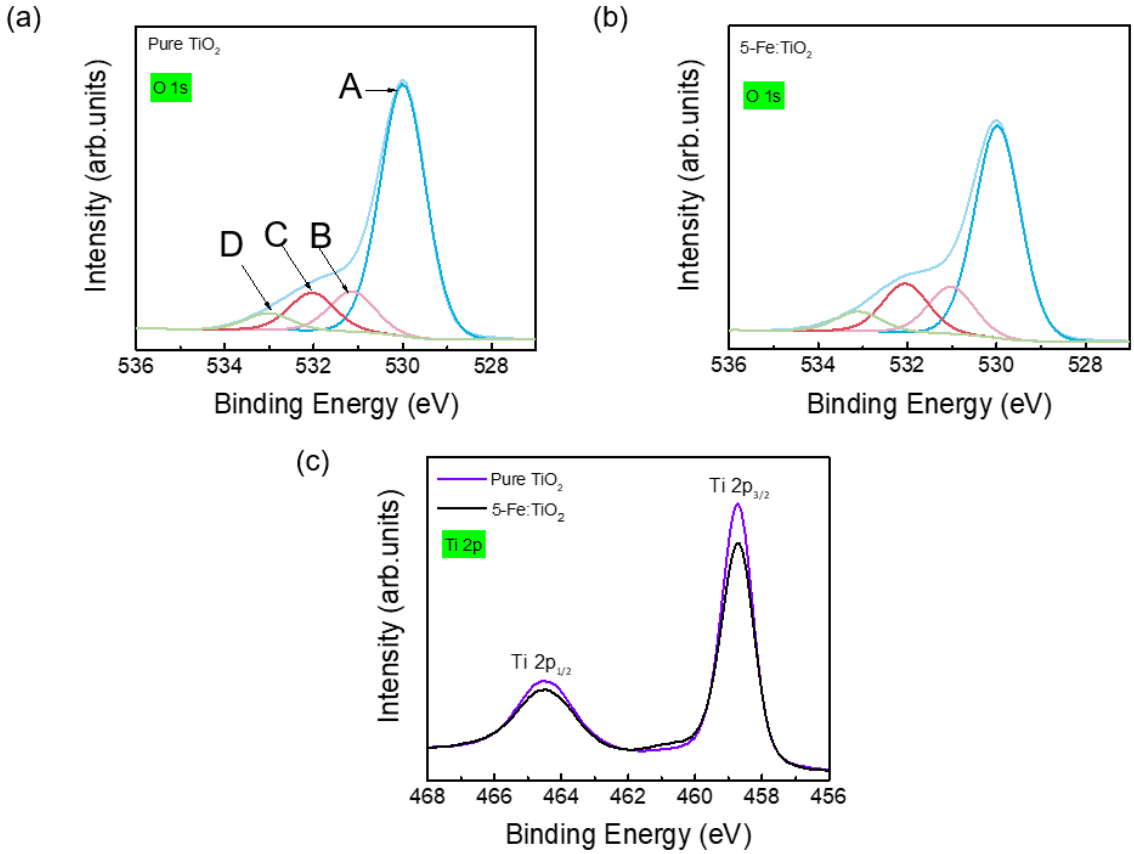

Figure 7.4: Deconvolution of XPS O 1s spectra of (a) pure TiO_2, where features A, B, C and D are visible and correspond to lattice oxygen, undercoordinated oxygen either at the surface or close to oxygen vacancies and adsorbed water and organic species, respectively, and (b) 5-Fe:TiO_2 nanostructure with PEG. Ti 2p peak is also shown in (c) for pure TiO_2 and 5-Fe:TiO_2 nanostructures with PEG.

In Figure 7.4, four peaks can be observed that correspond to lattice oxygen (A), under-coordinated oxygen either at the surface or close to oxygen vacancies (B), and adsorbed water and organic species (C, D) [13]. An increase of the peaks B–D with respect to peak A is observed in the 5-Fe:TiO_2 material, compared to TiO_2. Part of this increase may be ascribed to a higher oxygen vacancy concentration due to doping. Due to charge neutrality, the substitution of titanium ions by iron of a lower oxidation state may lead to the formation of compensating defects, such as oxygen vacancies. In both cases, the O 1s core level is centered at around 530 eV, which corresponds to the binding energy of the metal oxide (TiO_2). A shoulder is observed at around 533 eV and is related to the OH groups at the surface [14]. Regarding Figure 7.4 (c), the two components of the Ti 2p core level that arise from spin orbit-splitting [15] can be observed for pure TiO_2 and 5-Fe:TiO_2 nanostructures, both associated with the Ti^{4+}oxidation state. The peak positions and the peak separation of the Ti 2p doublet are in good agreement with previous studies of pure TiO_2 nanostructures [16]. A detailed scan of Fe 2p from 5-Fe:TiO_2 is shown in

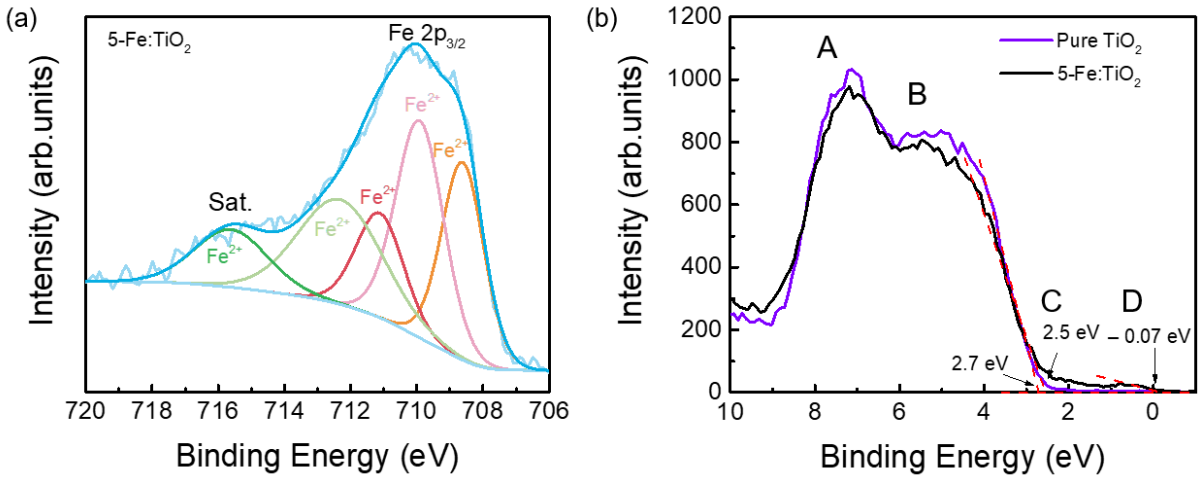

Figure 7.5 (a). The pronounced peak around 708.6 eV indicates the presence of Fe^{2+}, and a set of fitting parameters accounting for the rich satellite structure of oxidized iron is available in the literature [17]. The deconvolution did not converge using the exact relative constraints for the peak parameter of Fe^{2+}(FeO) in ref [87]. However, freeing the area of the peak at the highest binding energy led to convergence and a satisfactory fit quality. The intensity of this satellite peak at 5.9 eV from the center of gravity of the main peaks (another indication for Fe^{2+} [18]) is sensitive to the polarizability of the environment of the Fe atoms via the extra-atomic relaxation, one of the relaxation processes related to the photoemission event [19,20]. In contrast to FeO, Fe atoms in the 5-Fe:TiO_2 sample were surrounded by TiO_2, which has about 40 times higher permittivity than FeO [21,22]. This justifies the different relative intensity of the

satellite peak compared to FeO [17] and identifies the iron oxidation state as pure Fe^{2+}. Photocatalytic reduction of Fe^{3+} to Fe^{2+} in a TiO_2 matrix was speculated to occur in vacuum under X-ray irradiation [23], which made the quantification of the iron oxidation state in the original sample unreliable. Since the reduction of iron is the first part of the photocatalytic mechanism explained below, the detection of only Fe^{2+} by XPS corroborates the high photocatalytic activity of the sample.

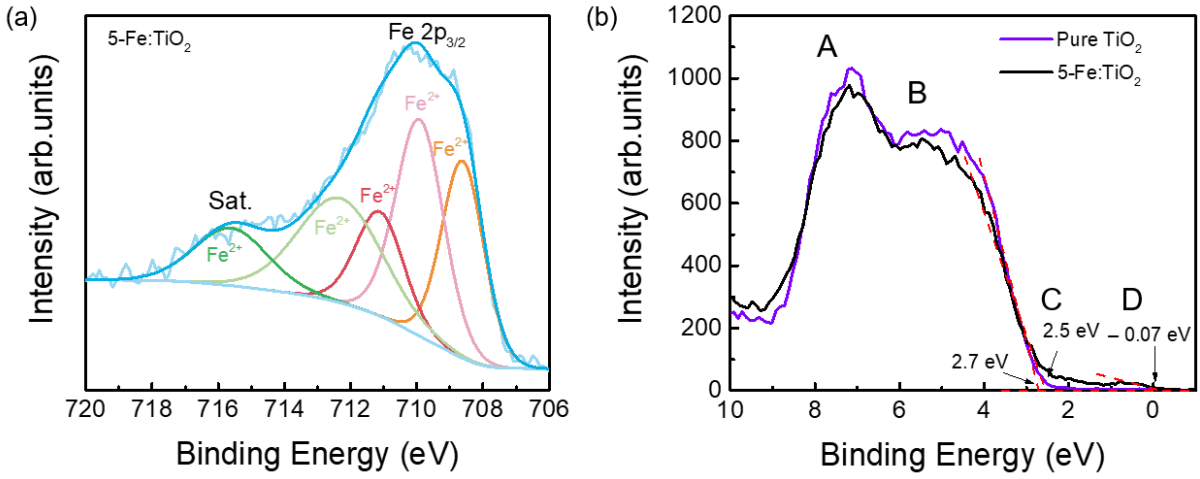

Figure 7.5: (a) XPS spectrum of Fe 2p for 5-Fe:TiO_2 with PEG (in which green, light green, red, pink and orange colors represent the Gaussian–Lorentzian components that best fitted Fe 2p spectrum (GL 30), and (b) VB XPS spectra of pure TiO_2 and 5-Fe:TiO_2 with PEG.

In

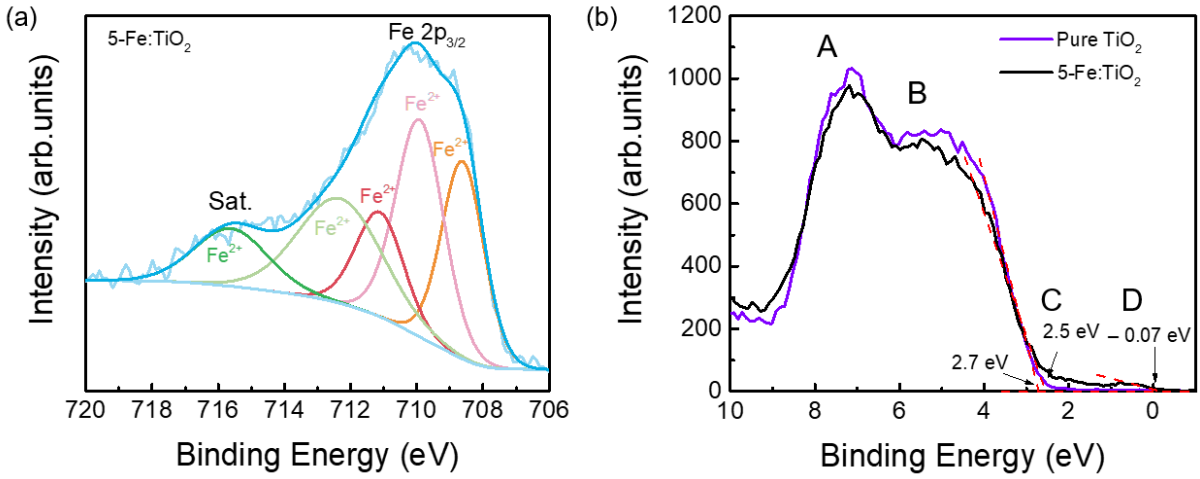

Figure 7.5 (b), the XPS valence bands of pure TiO_2 and 5-Fe:TiO_2 nanostructures are represented. No binding energy reference was applied to these spectra (C 1s was measured at

285.8 eV). For 5-Fe:TiO_2 nanostructures, four features (A, B, C, and D) are visible at binding energy positions of ~7, 5, 2.5, and 1 eV, whereas pure TiO_2 only shows features A and B. These values are consistent with the ones found in the literature [24]. Both A and B features are related to O 2p derived states and correspond, respectively, to the 'bonding' and 'non-bonding orbital emissions' of TiO_2. Feature D is potentially related to the defect state of Ti^{3+} 3d. This would support the conclusion above of a photocatalytic reduction in the XPS chamber [23]. At around 2.5 eV, another feature starts to appear with Fe doping (feature C), related to mixed Fe 3d and Ti 3d derived states very close to the Fermi level [14,24,25]. As seen in

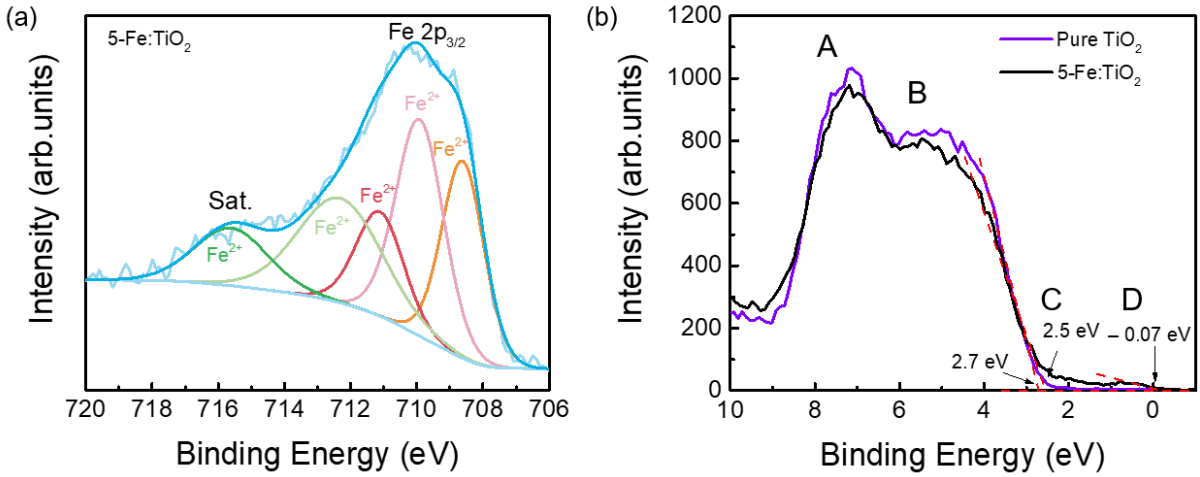

Figure 7.5 (b), pure TiO_2 has a valence band maximum of ~2.5 eV, while for 5-Fe:TiO_2, a new state was formed within the band gap, with an edge of maximum energy at ~−0.07 eV. Additionally, Fe addition led to a shift towards lower binding energies for the maximum edge of the original valence band of TiO_2 (from 2.7 eV for pure TiO_2 to 2.5 eV for 5-Fe:TiO_2) [26]. A similar shift was previously reported [24].

7.2.1.4 UV-VIS absorption measurements

To investigate the optical absorption characteristics of pure TiO_2 and 5-Fe:TiO_2 nanostructures with PEG, UV-VIS absorption spectra were recorded (

Figure 7.6). Pure TiO_2 shows an absorption peak at 354 nm (~3.5 eV), with an onset around 400 nm (~3.1 eV), which is fairly in line with the value expected for the anatase band gap [27,28]. Moreover, intrinsic TiO_2 also did not show any absorption beyond 400 nm. Meanwhile, for Fe:TiO_2 nanopowders, even though the absorption maximum is placed at the same value obtained for pure TiO_2 (which has also been previously reported [29]), the onset absorption is seen to shift towards higher wavelengths due to the increasing contribution from a tail of states that extends from the absorption maximum. This observation is likely related to a

higher density of defect states present in these materials and contributing to the visible light absorption. Such an increase accompanies the increase in the Fe %. This could effectively indicate that the visible light absorption of TiO_2 has been enhanced by the introduction of Fe. Moreover, a small band can be distinguished at around 476 nm, becoming more pronounced with higher concentrations of iron. According to the literature, this visible light absorption can be attributed to two factors. One is the formation of a dopant energy level (Fe^{3+}/Fe^{4+}) within the band gap of TiO_2, which is related to the excitation of 3d electrons of Fe^{3+} from the dopant energy level to the TiO_2 conduction band at 415 nm. The second one can be ascribed to the d–d transition of Fe(III) or the charge transfer transition between interacting iron ions (broad band at around 500 nm) [30,31]. Considering the XPS result discussed above, the introduction of new intermediate levels at the nanoparticles surface may be a likely explanation for the emergence of this new absorption band. These levels can act as traps and reduce the rate of recombination [5,32]. Besides that, a further reduction of the nanoparticles size could accentuate their contribution from surface defects due to the increase in the surface/volume ratio. The enhancement of the visible light absorption can also be seen from the inset of

Figure 7.6. The powder color changed from white (pure TiO_2 on the left side) to yellow (5-Fe:TiO_2 on the right side). All of these reasons may thus contribute to an improvement in the photocatalytic efficiency of the nanomaterials under visible light.

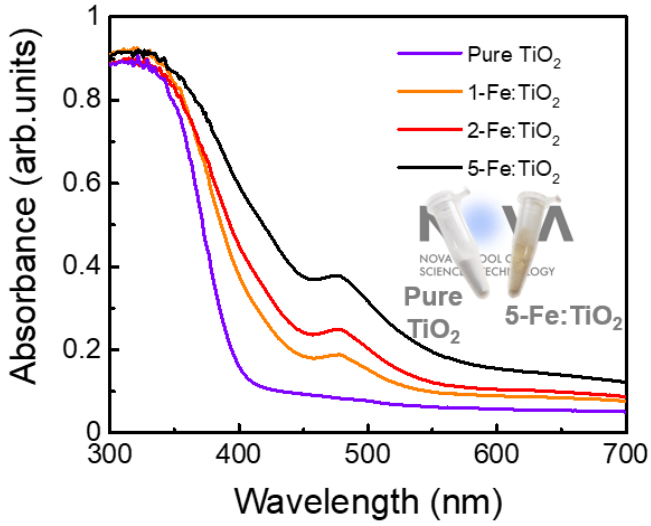

Figure 7.6: Absorption curves of pure TiO_2 and 1-Fe:TiO_2, 2-Fe:TiO_2, and 5-Fe:TiO_2 catalysts with PEG synthesized by microwave irradiation.

7.2.2 Characterization of the impregnated substrates

7.2.2.1 Electron microscopy

7.2.2.1.1 SEM

As previously mentioned, the as-synthesized nanopowders were impregnated on porous water filters to aid in the recovery of the nanosized photocatalysts. Pure TiO_2 and 5-Fe:TiO_2 nanopowders were incorporated on the substrates for further photocatalytic experiments. Figure 7.7 shows the SEM images of the pristine porous substrates, together with the impregnated ones. From Figure 7.7, it is possible to compare the differences between the substrates, without (Figure 7.7 (a)) and with the nanopowders (Figure 7.7 (b) and (c)). The substrate presents a micro-sized porosity, which remained after impregnation. Regarding the impregnated substrates, the nanopowders of pure TiO_2 (Figure 7.7 (b)) and 5-Fe:TiO_2 (Figure 7.7 (c)) formed, by using the drop-casting technique, uniform films of nanoparticles that entirely and uniformly covered the substrates. Some micrometer-sized agglomerates were also observed on the substrate's surfaces. In terms of morphology, and as expected from the SEM analysis of nanopowders, similar nanosized and spherical particles were obtained on the investigated porous substrates in both conditions.

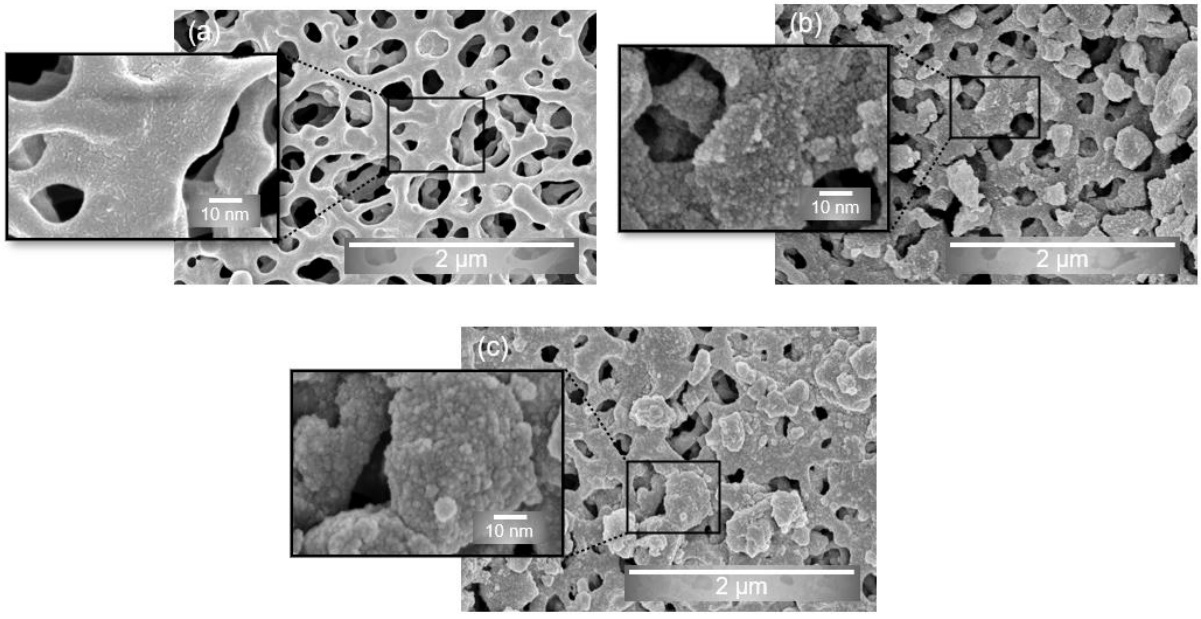

Figure 7.7: SEM images of the pristine porous polymeric substrates, together with the impregnated ones. (a) Pristine substrate (without nanopowders), (b) impregnated with pure TiO_2 and (c) with 5-Fe:TiO_2 nanopowders with the addition of PEG.

EDS analyses were also carried out on these substrates (Figure 7.8 and Figure 7.9). The pristine substrates were only composed of C and O (Figure 7.8 (b) and (c)), consistent with a substrate made of mixed cellulose esters [33,34]. For the impregnated substrates with pure TiO_2 nanoparticles, a strong presence of Ti was observed, together with C and O (Figure 7.8 (e),(f) and Figure 7.9 (b)).

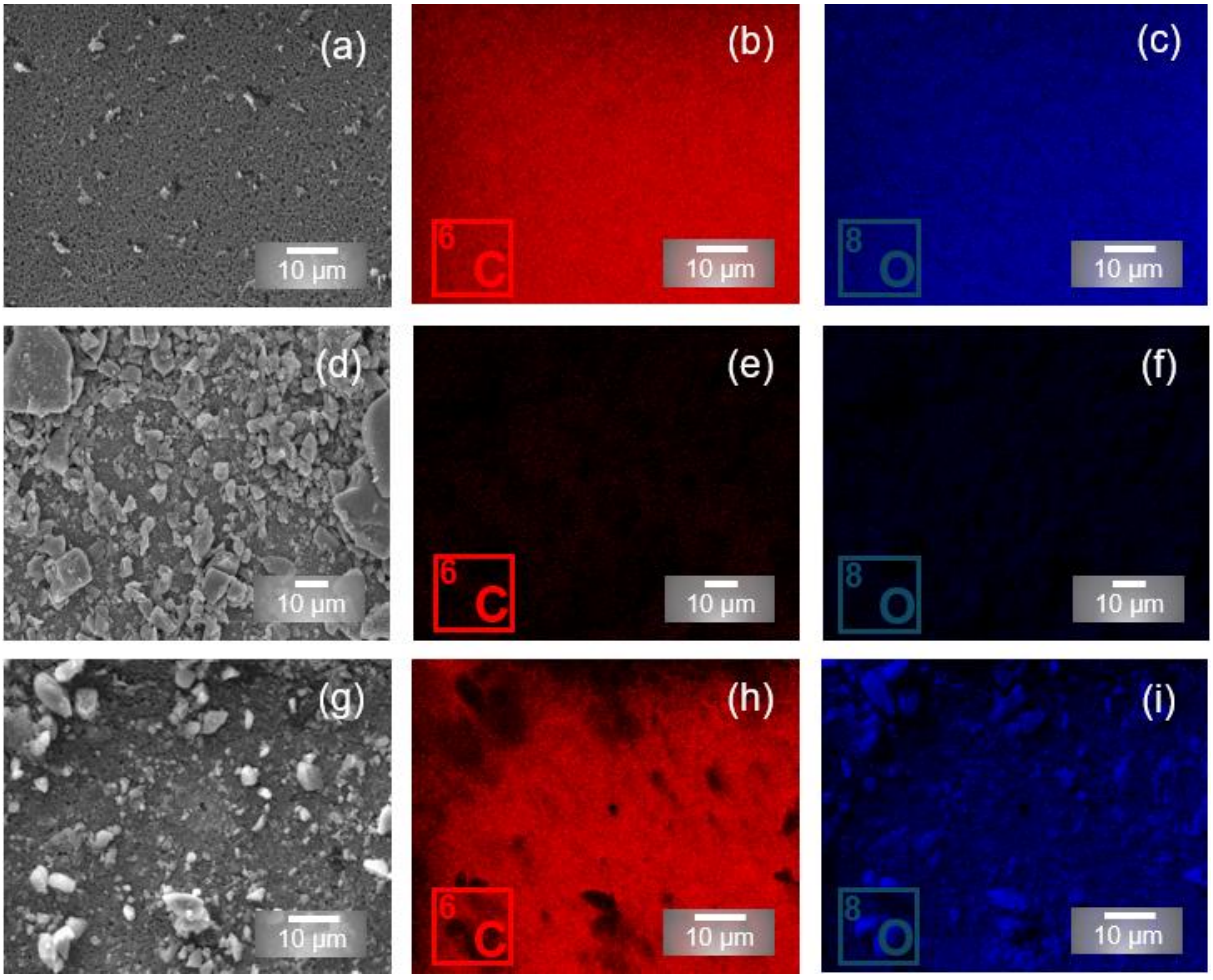

Figure 7.8: SEM images of the polymeric substrates (a) pristine (without nanopowders), (d) with pure TiO_2 + PEG and (h) with 5-Fe:TiO_2+ PEG. The corresponding EDS maps of C ((b),(e),(h)) and O ((c),(f),(i)) are also visible.

In the case of impregnated substrates with 5-Fe:TiO_2 nanostructures, the presence of Ti along with Fe was visible, as well as C and O (Figure 7.8 (h),(i) and Figure 7.9 (d),(e)), which confirms the successful impregnation of the substrates. In EDS analyses, the presence of some micrometer-sized agglomerates on the impregnated substrates was visible, as well as the homogeneous distribution of all elements.

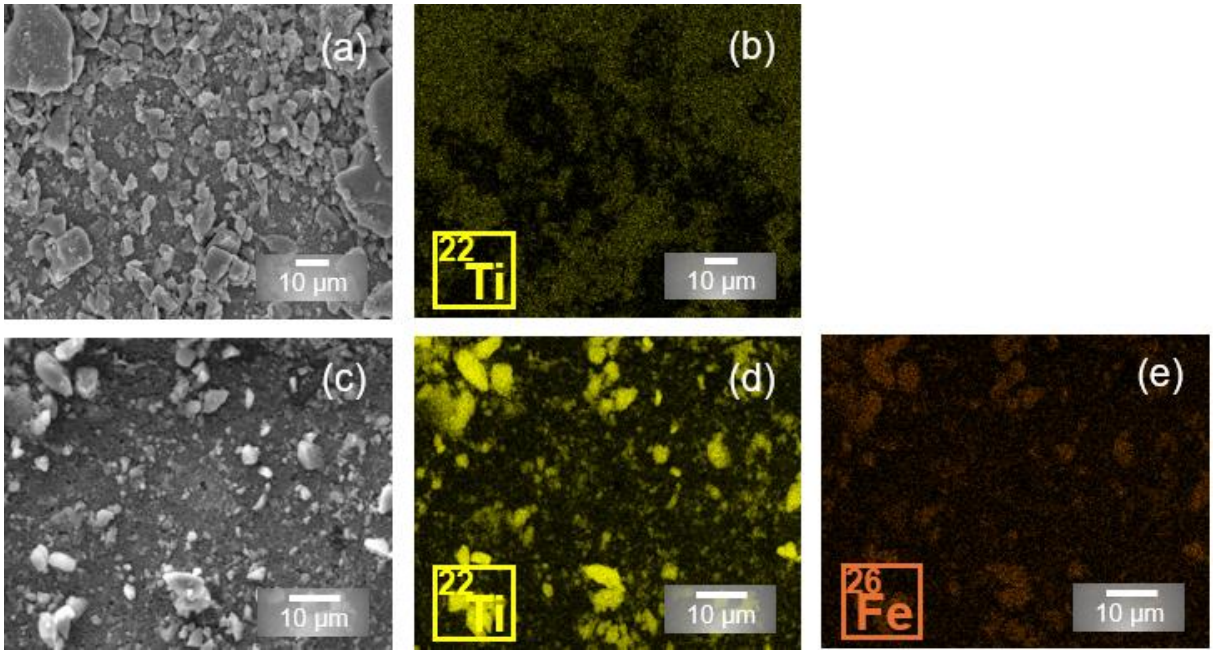

Figure 7.9: SEM images of the impregnated polymeric substrates (a) with pure TiO_2 + PEG and (c) with 5-Fe:TiO_2+ PEG. The corresponding EDS maps of Ti ((b),(d)) and Fe (e) are also visible.

Table 7.2 summarizes the EDS chemical analysis of the 5-Fe:TiO_2 and pure TiO_2 nanopowders impregnated on the porous substrates.

Table 7.2: EDS chemical analysis (at. %) of the 5-Fe:TiO_2 nanopowder after impregnation on the porous substrate (a). The atomic percentages of the different elements with the pure TiO_2 water filter are also shown for comparison (b).

	(a)	(b)
Elements	At. %	At. %
C	32.8	20.6
Ti	26.8	14.0
O	39.0	65.4
Fe	1.40	0
Total	100	100

The EDS Fe:Ti atomic ratio obtained was 0.05 (Table 7.2 (a)). This value is in line with the ratio obtained by XPS (0.06).

7.2.2.2 Raman spectroscopy

Raman measurements were also carried out, as this technique allows to clearly distinguish between TiO_2 phases [35] and evaluate the purity of TiO_2 and 5-Fe:TiO_2 nanostructures impregnated on polymeric substrates. The results obtained are shown in Figure 7.10.

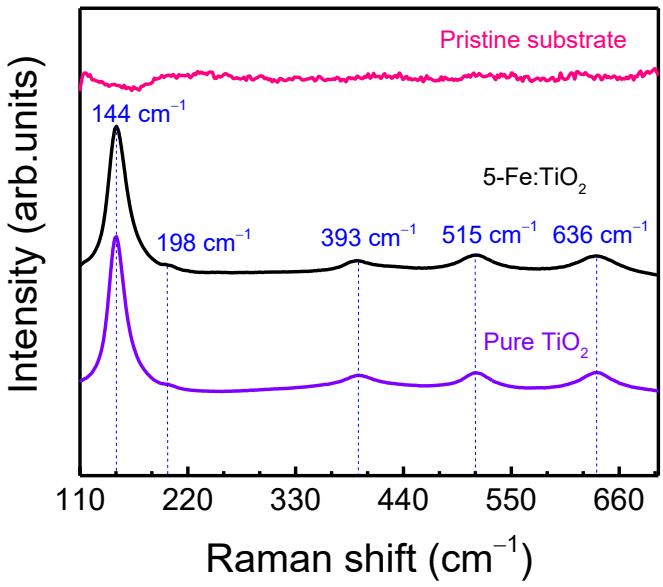

Figure 7.10: Raman spectra of the pristine polymeric substrate, pure TiO_2 and 5-Fe:TiO_2 nanopowders impregnated on the polymeric substrates. Vertical dash lines represent anatase TiO_2.

The Raman spectrum of the pristine substrate is also shown for comparison, demonstrating that there was no contribution associated with the substrate. In the impregnated substrates, five bands corresponding to six active modes of the tetragonal anatase phase can be observed in Figure 7.10, i.e., 144 cm^{-1} (E_g), 198 cm^{-1} (E_g), 393 cm^{-1} (B_{1g}), 515 cm^{-1} (B_{1g} + A_{1g}), and 636 cm^{-1} (E_g) [9,36,37]. The E_g mode is ascribed to symmetric stretching vibration in octahedral TiO_6 clusters, while the B_{1g} mode is related to symmetric bending vibration in the same clusters. The A_{1g} mode is assigned to anti-symmetric bending vibration and it is reported that the E_g mode at 636 cm^{-1} is attributed to the displacement of symmetric oxygen atoms in Ti-O bonds in the x,y-plane [38,39]. No additional peaks related to iron or iron oxides were detected in the 5-Fe:TiO_2 substrate, which corroborates the XRD results.

7.2.2.3 Photocatalytic degradation of RhB under simulated solar light

Absorbance spectra were acquired to evaluate the photocatalytic activity of the impregnated substrates in the degradation of RhB under solar radiation at RT (Figure 7.11). The absorption peak intensity of RhB (occurring at 554 nm [40]) was measured at different irradiation times to estimate the decrease of RhB content. The photodegradation rate of the RhB can be calculated using the equation (3.3) in Chapter 3.

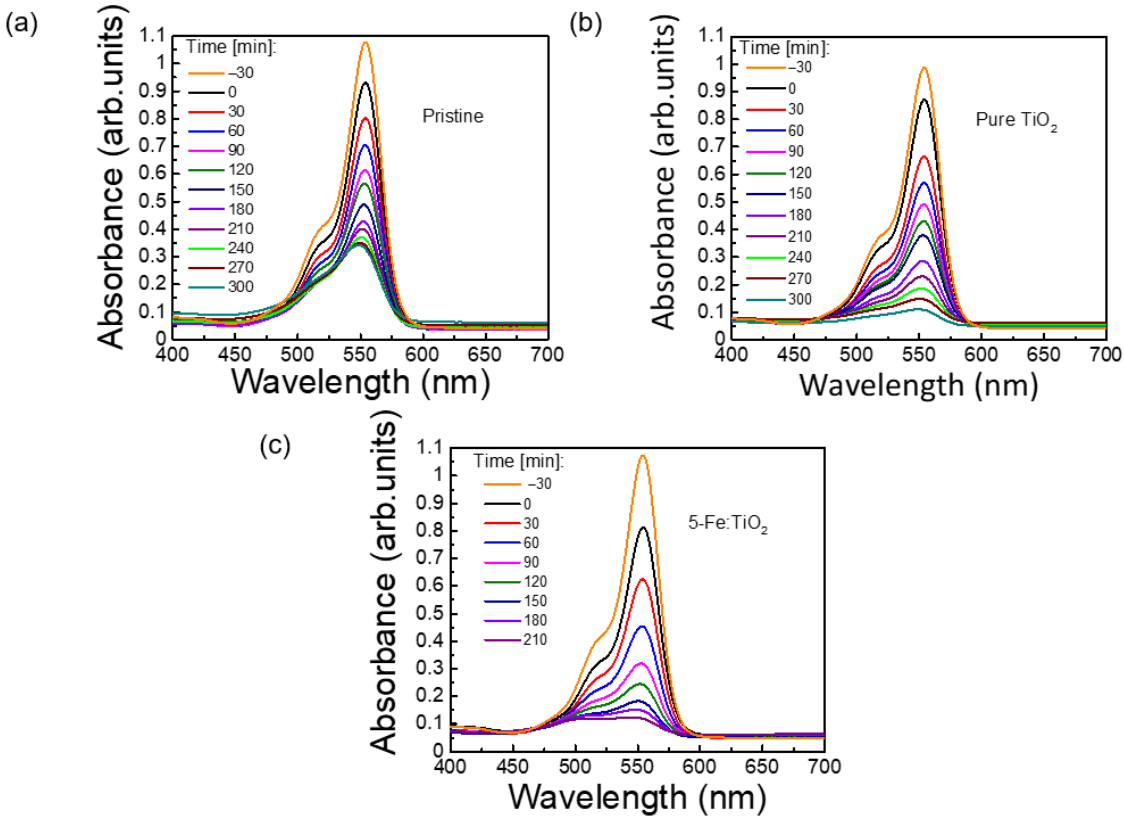

Figure 7.11: RhB absorbance spectra under simulated solar light radiation (LED simulator with AM 1.5 spectrum) up to 5 h for the polymeric substrates (a) without nanopowders, (b) with pure TiO_2 and (c) with 5-Fe:TiO_2 nanopowders with the addition of PEG.

According to Figure 7.11 (a), without the catalyst on the surface of the polymeric substrates, some removal of the dye was observed either in the absence or presence of light. As reported in the product description, these polymeric membranes can also be used in aqueous solutions as filters. They possess a high porosity percentage and thus act like hydrophilic "sponges" that can easily capture the RhB dye molecules on the pore sites in some hours (63 % of degradation was achieved in 5 h). This retention of RhB dye molecules was also clearly observed (Figure 7.12) with the color change of the substrate before (from white) and after photocatalysis (to fuchsia pink).

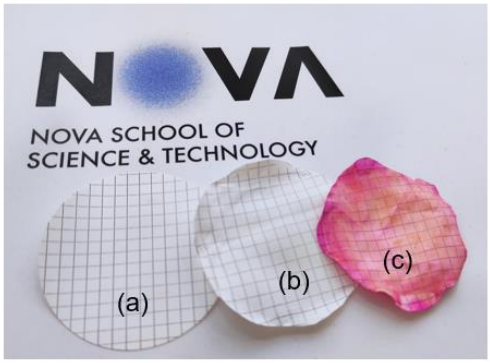

Figure 7.12: Water filters used in this study, (a) pristine, (b) impregnated substrate before photocatalysis and (c) impregnated substrate after photocatalysis.

Nevertheless, since all experiments were conducted with the same substrate, this contribution will be equal for all the materials studied [9]. In the presence of pure TiO_2 (Figure 7.11 (b)), a higher degradation percentage of 87 % was achieved for the same time exposure as the substrate without catalyst. On the other hand, the addition of 5 mol. % of Fe drastically improved the photocatalytic activity of TiO_2. In 3.5 h, a RhB degradation of 85 % was obtained, whereas for pure TiO_2, the RhB degradation was 74 % for the same exposure time.

As mentioned before, various factors can influence photocatalytic activity, such as the crystalline structure, morphology, porosity, particle size, iron content and the presence of surface defects [41,42]. Regarding the contribution of particles' shape and size to the enhanced photocatalytic behavior observed, as assessed by the SEM images in Figure 7.2 and estimated from the XRD results, all conditions resulted in spherical nanoparticles in the same size range (around ~18 nm from SEM measurements). Since both size and shape are comparable, similar contributions are expected for both materials, thus it does not justify the observed behavior for the 5-Fe:TiO_2 material.

Moreover, in terms of the TiO_2 phase present, it is well known that anatase TiO_2 shows superior photocatalytic activity than rutile or brookite [43,44]. It has been reported that anatase exhibits a longer lifetime of photogenerated electrons and holes than rutile and brookite [45]. Additionally, the average effective mass of electrons and holes in anatase is smaller than that of rutile and brookite, which favors a faster migration of photogenerated charge carriers from the interior to the surface of anatase, thus reducing the recombination rate and improving the photocatalytic activity [45]. As revealed by the XRD and Raman spectroscopy results, all synthesized materials have the anatase TiO_2 phase, hence the photocatalytic degradation enhancement of the 5-Fe:TiO_2 substrate must be owed to the incorporation of iron ions into the TiO_2 lattice.

The enhanced photocatalytic behavior observed with the Fe addition may be ascribed to the mechanism of the photocatalytic processes in 5-Fe:TiO_2 material. It is reported that there are two energy levels: the reduction level, which is located below the TiO_2 conduction band (Fe^{3+}/ Fe^{2+}) and another one, the oxidation level, above the TiO_2 valence band (Fe^{3+}/Fe^{4+}). First, the formation of Fe^{2+} species occurs due to the migration of photogenerated electrons from TiO_2 to Fe^{3+}. These Fe^{2+} species are unstable, owing to the loss of the d^5 electronic configuration, and easily oxidize to Fe^{3+} by transferring electrons to absorbed O_2 and forming reactive superoxide anions (0_2^-). Meanwhile, Fe^{3+} ions can act as a hole trap, since Fe^{3+}/Fe^{4+} energy level is above the TiO_2 valence band and oxidize to Fe^{4+}. Fe^{4+} then reduces to Fe^{3+} by reacting with an OH^- group and hydroxyl radicals (•OH) are formed. These hydroxyl radicals are powerful oxidizing species that attack the chemical bonds of surface-adsorbed organic materials. Therefore, Fe^{3+} ions can act as trap sites for the photogenerated electrons and holes, thus suppressing the recombination of those photogenerated charges and ultimately enhancing the photocatalytic activity under visible light [12,46].

However, an important note should be taken regarding the amount of iron content that plays an important role in photocatalytic activity [47]. Some studies report a reduction in photocatalytic activity when the dopant concentration increases. For example, the photodegradation rate of phenol decreases when La^{3+} concentration in TiO_2 is between 1.5 and 5 mol. % [48]. Similarly, the photocatalytic activity for the degradation of Acid Yellow 29 dye decreases when the Ce^{3+} percursor exceeds 2 (w/v) % and the Nd^{3+} precursor is superior to 1.5 (w/v) % in TiO_2 [49]). In another study, no improvement in RhB degradation was observed with dopant concentrations up to 10 at. % of Mo^{5+} and Cr^{3+} in TiO_2, compared to the undoped TiO_2 [50]. It is stated that multiple trapping of charge carriers can take place, which in consequence increases the electron-hole recombination. Thus, fewer charge carriers will be able to reach the surface to degrade the pollutant. Moreover, an excessive concentration of dopant may accumulate on the surface of the catalyst, reducing the penetration depth of light and consequently the number of active sites [46]. Nevertheless, this excessive dopant trend does not seem to occur in this study, since improved photocatalytic activity was demonstrated relative to pure TiO_2.

The generation of intermediate energy levels as a result of the presence of Fe ions was also confirmed by XPS, which could have served as trapping centers for the photogenerated carriers. As also revealed by XPS, the valence state of Fe ions is lower than that of lattice Ti ions. Considering charge balance, oxygen vacancies are likely to exist in the 5-Fe:TiO_2 sample

and are also expected to play important roles in enhanced photocatalysis, since they can act as photoinduced charge traps and adsorption sites, thus contributing to increase the lifetime of photogenerated charge carriers and resulting in an improvement of the photocatalytic performance [51–53].

Comparing the curves in Figure 7.13 (a), it can also be confirmed that the photodegradation was much faster with the 5-Fe:TiO_2 substrate. The reaction kinetics was also investigated using the Langmuir–Hinshelwood kinetic model (equation (1.11), Chapter 1). According to the Lambert–Beer law, the concentration is proportional to the absorbance; thus, it can be assumed that $\ln\left(\frac{C}{C_0}\right) \propto \ln\left(\frac{A}{A_0}\right)$ [54], where C_0 is the initial concentration and C is the concentration at a certain time.

Based on (equation (1.11), Chapter 1), the rate constants k_{ap} (min^{-1}) can be determined by plotting $-\ln\left(\frac{C}{C_0}\right)$ or $-\ln\left(\frac{A}{A_0}\right)$ versus time [54]. From the slope of the linear regressions, the rate constants can be obtained. The obtained kinetic parameters (rate constants, linear regression coefficients and half-life times) are summarized in Table 7.3. From Figure 7.13 (b) and Table 7.3, it can be concluded that the photocatalytic dye degradation follows the first-order kinetics for both pure TiO_2 and 5-Fe:TiO_2 samples, as the correlation constant (R^2) for the fitted lines is above 0.95 [55].

The obtained photodegradation apparent rate constants were found to be 0.007 min^{-1} and 0.01 min^{-1} for the substrates with pure TiO_2 and 5-Fe:TiO_2 nanostructures, respectively. The obtained k_{ap} values indicate that the RhB photodegradation with the 5-Fe:TiO_2 material was 1.5 times faster than pure TiO_2. Half-life times were also calculated (see Table 7.3) and they are defined by the time it takes for the concentration of a reactant to reach half of its initial value [56], and can be determined by using equations (7.1) and (7.2).

$$t_{1/2} = \frac{2^{n_{\text{a}}-1}-1}{(n_a-1)k_{\text{ap}}[A_0]^{n_{\text{a}}-1}} \tag{7.1}$$

For n_{a} = 1 (pseudo-first order):

$$t_{1/2,}n_{\text{a}=1} = \frac{\ln(2)}{k_{\text{ap}}} \tag{7.2}$$

where n_{a} is the apparent or pseudo-reaction order [56,57].

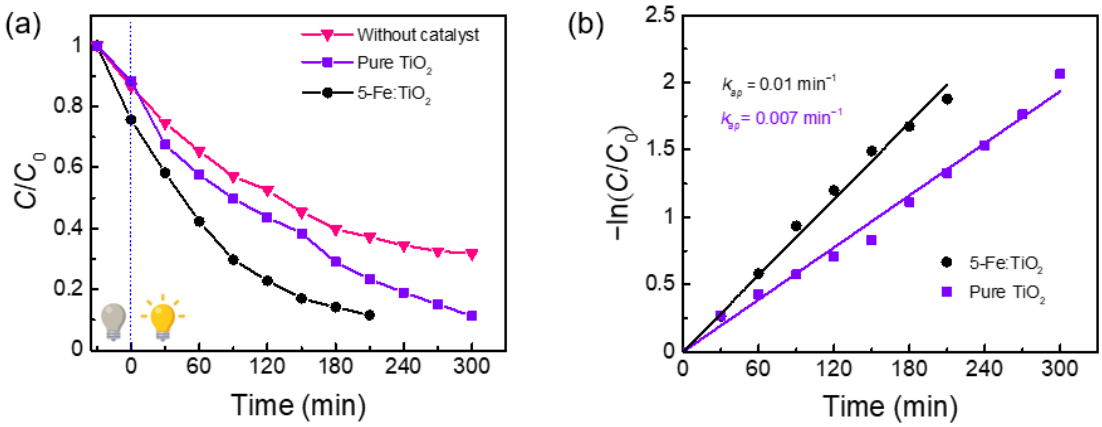

Figure 7.13: (a) RhB degradation ratio (C/C_0) *vs.* exposure time for the impregnated substrates (with pure TiO_2 and 5-Fe:TiO_2 photocatalysts) and the pristine (without catalyst) under simulated solar light. (b) Pseudo-first order kinetics for RhB photocatalytic degradation of the investigated impregnated substrates.

Table 7.3: Kinetic parameters (rate constants k_{ap}, linear regression coefficients R^2, and half-life times $t_{1/2}$) for RhB photocatalytic degradation under solar radiation with the impregnated materials (with pure TiO_2 and 5-Fe:TiO_2 photocatalysts).

	Kinetic parameters		
	k_{ap} (min^{-1})	R^2	$t_{1/2}$ (min)
Pure TiO_2	0.007	0.99	99
5-Fe:TiO_2	0.01	0.98	69

As expected, the kinetic studies confirm that the 5-Fe:TiO_2 substrate exhibited the highest photocatalytic degradation of RhB, compared to the pure TiO_2 substrate under the same experimental conditions, since it achieved the lowest half-life time.

7.2.2.4 Recyclability tests

Reusability tests of photocatalytic materials are of great importance to examine their applicability in real wastewater treatments. To evaluate the possibility of reuse, the best photocatalyst, i.e. 5-Fe:TiO_2 photocatalyst on the porous substrate, was chosen for the experiments. An the end of each cycle, the water filter was recovered, and the RhB solution was discarded. Afterwards, the photocatalyst was dried in air and exposed to the next cycle with a fresh solution of RhB. No washing steps were carried out between cycles. Five consecutive cycles of RhB removal and photocatalytic degradation were performed under the same experimental conditions and up to 210 min (3.5 h). In Figure 7.14 (a) and (b) a decrease in photocatalytic

activity was observed. The reaction rate decreased with the number of uses from 0.01 min^{-1} in the first cycle, to 0.004 min^{-1} in the fifth cycle.

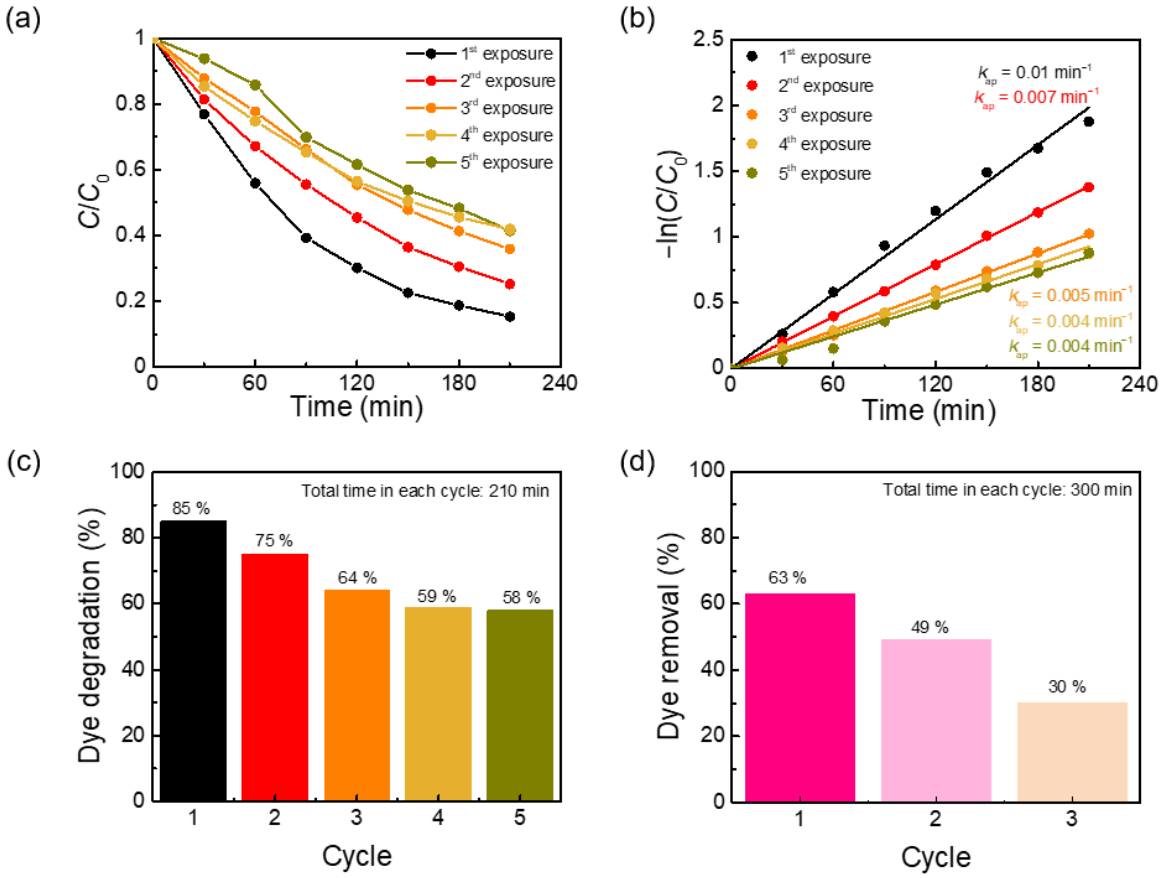

Figure 7.14: (a) Different cycles of RhB degradation ratio (C/C_0) *vs.* exposure time for 5-Fe:TiO_2 material on the porous substrate, (b) pseudo-first-order kinetics for RhB photocatalytic degradation of the impregnated investigated substrate (5-Fe:TiO_2), (c) reusability of the 5-Fe:TiO_2 substrate under 5 dye degradation cycles within 210 min each and under solar radiation and (d) reusability of the pristine substrate under 3 dye removal cycles within 300 min each and under solar radiation.

The reusability results can also be seen in Figure 7.14 (c). The impregnated substrate lost approximately 27 % of degradation efficiency after performing 5 repeated cycles since in the first cycle a dye degradation of 85 % was achieved, while in the fifth cycle, it was 58 %. Despite the considerable loss of efficiency after 3 cycles (of around 21 %), a much smaller efficiency loss is observed during the next cycles. This loss could be attributed to the high adsorption phenomenon of RhB, where RhB molecules remain adsorbed on the photocatalyst surface, hindering the available pore sites of the substrate with the nanostructures for reaction [58,59]. The reusability tests of the pristine substrate also confirmed that a significant contribution to this degradation efficiency loss comes from the substrate, with the adsorption of RhB molecules (see Figure 7.14 (d)). This phenomenon is also occurring on the 5-Fe:TiO_2 substrate,

decreasing its overall cycling efficiency. Moreover, the possibility of some nanoparticles detaching from the water filter to the solution after each cycle cannot be excluded, which may reduce the performance in the subsequent cycle.

7.3 Summary

Pure TiO_2 and TiO_2 nanostructures with Fe were successfully synthesized by a fast surfactant-assisted microwave irradiation (1 h), without a calcination step, and impregnated by drop-casting on porous water filters. The approach used in this study enabled the total covering of the porous substrates and the evaluation of their photocatalytic activity in the degradation of RhB under solar radiation. SEM confirmed the formation of fine particles with a sphere-like appearance and films that uniformly coated the substrates. XRD revealed the presence of pure TiO_2 anatase in all nanostructures, which was further confirmed by Raman spectroscopy on the impregnated substrates. The 5-Fe:TiO_2 substrate exhibited an enhanced RhB photodegradation when compared to pure TiO_2. The highest photodegradation under solar radiation was 85 % with the 5-Fe:TiO_2 material after 3.5 h, compared to 74 % with pure TiO_2. The photodegradation rate of RhB dye with the 5-Fe:TiO_2 substrate was 1.5 times faster than pure TiO_2. The XPS and UV-VIS results support that the presence of Fe ions led to the introduction of new energy levels, as well as defects, such as oxygen vacancies, that played an important role as traps for the photogenerated carriers, leading to a reduction in the recombination rate, followed by a visible enhancement in the photocatalytic activity. In summary, this study demonstrated that the synergy between the micro-porosity of the substrates and the surface-modified Fe:TiO_2 nanostructures enhanced the substrates photocatalytic properties. Flexible and eco-friendly photocatalytic functionalized substrates were produced with the potential for wastewater removal.

7.4 References

1. Ahmad, M. M.; Mushtaq, S.; Al Qahtani, H. S.; Sedky, A.; Alam, M. W. Investigation of TiO_2 Nanoparticles Synthesized by Sol-Gel Method for Effectual Photodegradation, Oxidation and Reduction Reaction. *Crystals* **2021**, *11*, 1–16.
2. Tesfaye, L.; Bekele, B.; Saka, A.; Ramaswamy, K.; Nagaprasad, N.; Sivaramasundaram, K. Investigating Spectroscopic and Structural Properties of Cr doped TiO_2 NPs Synthesized through Sol gel Deposition Technique. *Tierärztliche Praxis* **2021**, *41*, 860–872.
3. Ochoa Rodríguez, P. A.; Pecchi, G. A.; Casuscelli, S. G.; Elías, V. R.; Eimer, G. A. A

simple synthesis way to obtain iron-doped TiO_2 nanoparticles as photocatalytic surfaces. *Chemical Physics Letters* **2019**, *732*, 1–6.
4. Nunes, D.; Pimentel, A.; Santos, L.; Barquinha, P.; Fortunato, E.; Martins, R. Photocatalytic TiO_2 Nanorod Spheres and Arrays Compatible with Flexible Applications. *Catalysts* **2017**, *7 (2)*, 1–18.
5. Vijayalakshmi, K.; Jereil, S. D. Influence of Fe catalytic doping on the properties of TiO_2 nanoparticles synthesized by microwave method. *Journal of Materials Science: Materials in Electronics* **2014**, *25*, 5089–5094.
6. Cullity, B. D.; Stock, S. R. *Elements of X-Ray Diffraction*; 3rd ed.; Pearson: USA, 2014; ISBN 1269374508.
7. Wang, Z.; Zhao, Y.; Schiferl, D.; Zha, C. S.; Downs, R. T. Pressure induced increase of particle size and resulting weakening of elastic stiffness of CeO_2 nanocrystals. *Applied Physics Letters* **2004**, *85*, 124–126, doi:10.1063/1.1768298.
8. Pal, K.; Madhu Mohan, M. L. N.; Regius, F.; Luo, B.; Wang, G. Investigations of CdS nanostructures encapsulated in soft self-assembled thermotropic liquid crystals matrix. *Science of Advanced Materials* **2016**, *8*, 1331–1344, doi:10.1166/SAM.2016.2742.
9. Freire, T.; Fragoso, A. R.; Matias, M.; Vaz Pinto, J.; Marques, A. C.; Pimentel, A.; Barquinha, P.; Huertas, R.; Fortunato, E.; Martins, R.; Nunes, D. Enhanced solar photocatalysis of TiO_2 nanoparticles and nanostructured thin films grown on paper. *Nano Express* **2021**, *2,4*, 1–20.
10. Bharti, B.; Barman, P. B.; Kumar, R. XRD analysis of undoped and Fe doped TiO_2 nanoparticles by Williamson Hall method. *AIP Conference Proceedings* **2015**, *1675*, 1–4.
11. Luu, L.; Nguyen, Q. T.; Ho, S. T. Synthesis and characterization of Fe-doped TiO_2 photocatalyst by the sol–gel method. *Advances in Natural Sciences: Nanoscience and Nanotechnology* **2010**, *1*, 015008.
12. Moradi, H.; Eshaghi, A.; Hosseini, S. R.; Ghani, K. Fabrication of Fe-doped TiO_2 nanoparticles and investigation of photocatalytic decolorization of reactive red 198 under visible light irradiation. *Ultrasonics Sonochemistry* **2016**, *32*, 314–319.
13. Fernandes, C.; Santa, A.; Santos, Â.; Bahubalindruni, P.; Deuermeier, J.; Martins, R.; Fortunato, E.; Barquinha, P. A Sustainable Approach to Flexible Electronics with Zinc-Tin Oxide Thin-Film Transistors. *Advanced Electronic Materials* **2018**, *4*, 1800032.
14. Abidov, A.; Allabergenov, B.; Lee, J.; Jeon, H.-W.; Kim, S. X-Ray Photoelectron Spectroscopy Characterization of Fe Doped TiO_2 Photocatalyst. *International Journal of Materials, Mechanics and Manufacturing* **2013**, *1*, 294–296.
15. Bharti, B.; Kumar, S.; Lee, H. N.; Kumar, R. Formation of oxygen vacancies and Ti^{3+} state in TiO_2 thin film and enhanced optical properties by air plasma treatment. *Scientific Reports* **2016**, *6*, 1–12.
16. Zhu, L.; Lu, Q.; Lv, L.; Wang, Y.; Hu, Y.; Deng, Z.; Lou, Z.; Hou, Y.; Teng, F. Ligand-free rutile and anatase TiO_2 nanocrystals as electron extraction layers for high performance inverted polymer solar cells. *RSC Advances* **2017**, *7*, 20084–20092.
17. Biesinger, M. C.; Payne, B. P.; Grosvenor, A. P.; Lau, L. W. M.; Gerson, A. R.; Smart, R. S. C. Resolving surface chemical states in XPS analysis of first row transition metals, oxides and hydroxides: Cr, Mn, Fe, Co and Ni. *Applied Surface Science* **2011**, *257*, 2717–2730.

18. Grosvenor, A. P.; Kobe, B. A.; Biesinger, M. C.; McIntyre, N. S. Investigation of multiplet splitting of Fe 2p XPS spectra and bonding in iron compounds. *Surface and Interface Analysis* **2004**, *36*, 1564–1574.
19. Bagus, P. S.; Nelin, C. J.; Brundle, C. R.; Vincent Crist, B.; Lahiri, N.; Rosso, K. M. Covalency in Fe_2O_3 and FeO: Consequences for XPS satellite intensity. *The Journal of Chemical Physics* **2020**, *153*, 194702.
20. Deuermeier, J.; Fortunato, E.; Martins, R.; Klein, A. Energy band alignment at the nanoscale. *Applied Physics Letters* **2017**, *110*, 051603.
21. Bonkerud, J.; Zimmermann, C.; Weiser, P. M.; Vines, L.; Monakhov, E. V. On the permittivity of titanium dioxide. *Scientific Reports* **2021**, *11*, 1–5.
22. Liu, P.; Franchini, C.; Marsman, M.; Kresse, G. Assessing model-dielectric-dependent hybrid functionals on the antiferromagnetic transition-metal monoxides MnO, FeO, CoO, and NiO. *Journal of physics: Condensed matter* **2019**, *32*.
23. Morikawa, T.; Ohwaki, T.; Suzuki, K. ichi; Moribe, S.; Tero-Kubota, S. Visible-light-induced photocatalytic oxidation of carboxylic acids and aldehydes over N-doped TiO_2 loaded with Fe, Cu or Pt. *Applied Catalysis B: Environmental* **2008**, *83*, 56–62.
24. Ismail, M. A.; Hedhili, M. N.; Anjum, D. H.; Singaravelu, V.; Chung, S. H. Synthesis and Characterization of Iron-Doped TiO_2 Nanoparticles Using Ferrocene from Flame Spray Pyrolysis. *Catalysts* **2021**, *11*, 438.
25. Bapna, K.; Phase, D. M.; Choudhary, R. J. Study of valence band structure of Fe doped anatase TiO_2 thin films. *Journal of Applied Physics* **2011**, *110*, 043910.
26. Feng, N.; Liu, F.; Huang, M.; Zheng, A.; Wang, Q.; Chen, T.; Cao, G.; Xu, J.; Fan, J.; Deng, F. Unravelling the Efficient Photocatalytic Activity of Boron-induced Ti^{3+} Species in the Surface Layer of TiO_2. *Scientific Reports* **2016**, *6*, 1–9.
27. Li, K.; Wang, H.; Pan, C.; Wei, J.; Xiong, R.; Shi, J. Enhanced photoactivity of Fe + N Codoped anatase-rutile TiO_2 nanowire film under visible light irradiation. *International Journal of Photoenergy* **2012**, *1,398508*, 1–8.
28. Mansour, H.; Omri, K.; Bargougui, R.; Ammar, S. Novel α-Fe_2O_3/TiO_2 nanocomposites with enhanced photocatalytic activity. *Applied Physics A: Materials Science and Processing* **2020**, *126*, 1–10.
29. Ganesh, I.; Kumar, P. P.; Gupta, A. K.; Sekhar, P. S. C.; Radha, K.; Padmanabham, G.; Sundararajan, G. Preparation and characterization of Fe-doped TiO_2 powders for solar light response and photocatalytic applications. *Processing and Application of Ceramics* **2012**, *6*, 21–36.
30. Niu, Y.; Xing, M.; Zhang, J.; Tian, B. Visible light activated sulfur and iron co-doped TiO_2 photocatalyst for the photocatalytic degradation of phenol. *Catalysis Today* **2013**, *201*, 159–166.
31. Zhu, J.; Chen, F.; Zhang, J.; Chen, H.; Anpo, M. Fe^{3+}-TiO_2 photocatalysts prepared by combining sol-gel method with hydrothermal treatment and their characterization. *Journal of Photochemistry and Photobiology A: Chemistry* **2006**, *180*, 196–204.
32. Yehezkiel Gintinga, L.; Agusta, M. K.; Nugraha; H.Lubis, A.; Kresno Dipojono, H. Cr, Fe – Doped Anatase TiO_2 Photocatalyst: DFT+U Investigation on Band Gap. *Advanced Materials Research* **2014**, *893*, 31–34.
33. Dias, F.; Duarte, C. Cellulose and Its Derivatives Use in the Pharmaceutical

Compounding Practice. In *Cellulose - Medical, Pharmaceutical and Electronic Applications*; Theo G.M. Van De Ven, Ed.; InTech, 2013; pp. 141–162.
34. Heinze, T.; El Seoud, O. A.; Koschella, A. Cellulose Esters. In *Cellulose Derivatives*; Springer Cham, 2018; pp. 293–427 ISBN 978-3-319-73168-1.
35. Wang, Y.; Li, L.; Huang, X.; Li, Q.; Li, G. New insights into fluorinated TiO_2 (brookite, anatase and rutile) nanoparticles as efficient photocatalytic redox catalysts. *RSC Advances* **2015**, *5*, 34302–34313.
36. Ohsaka, T.; Fujiki, I.; Fujiki, Y. Raman Spectrum of Anatase, TiO_2. *Journal of Raman Spectroscopy* **1978**, *7,6*, 321–324.
37. Yu, S.; Yun, H. J.; Lee, D. M.; Yi, J. Preparation and characterization of Fe-doped TiO_2 nanoparticles as a support for a high performance CO oxidation catalyst. *Journal of Materials Chemistry* **2012**, *22*, 12629–12635.
38. Ekoi, E. J.; Gowen, A.; Dorrepaal, R.; Dowling, D. P. Characterisation of titanium oxide layers using Raman spectroscopy and optical profilometry: Influence of oxide properties. *Results in Physics* **2019**, *12*, 1574–1585.
39. Araújo, M. M.; Silva, L. K. R.; Sczancoski, J. C.; Orlandi, M. O.; Longo, E.; Santos, A. G. D.; Sá, J. L. S.; Santos, R. S.; Luz, G. E.; Cavalcante, L. S. Anatase TiO_2 nanocrystals anchored at inside of SBA-15 mesopores and their optical behavior. *Applied Surface Science* **2016**, *389*, 1137–1147.
40. Zhao, J.; Wu, T.; Wu, K.; Oikawa, K.; Hidaka, H.; Serpone, N. Photoassisted degradation of dye pollutants.3.Degradation of the cationic dye rhodamine B in aqueous anionic surfactant/TiO_2 dispersions under visible light irradiation: Evidence for the Need of Substrate Adsorption on TiO_2 Particles. *Environ. Sci. Technol.* **1998**, *32,16*, 2394–2400.
41. El Mragui, A.; Logvina, Y.; Pinto da Silva, L.; Zegaoui, O.; C G Esteves da Silva, J. Synthesis of Fe- and Co-Doped TiO_2 with Improved Photocatalytic Activity Under Visible Irradiation Toward Carbamazepine Degradation. *Materials (Basel)* **2019**, *12(23):387*, 1–14.
42. Romero, V. M. J.; Santaclara, J. G.; Oar-Arteta, L.; van Koppen, L.; Osadchii, D. Y.; Gascon, J.; Kapteijn, F. Photocatalytic properties of TiO_2 and Fe-doped TiO_2 prepared by metal organic framework-mediated synthesis. *Chemical Engineering Journal* **2019**, *360*, 75–88.
43. Fu, W.; Li, G.; Wang, Y.; Zeng, S.; Yan, Z.; Wang, J.; Xin, S.; Zhang, L.; Wu, S.; Zhang, Z. Facile formation of mesoporous structured mixed-phase (anatase/rutile) TiO_2 with enhanced visible light photocatalytic activity. *Chemical Communications* **2017**, *54*, 58–61, doi:10.1039/C7CC05750D.
44. Han, G.; Kim, J. Y.; Kim, K. J.; Lee, H.; Kim, Y. M. Controlling surface oxygen vacancies in Fe-doped TiO_2 anatase nanoparticles for superior photocatalytic activities. *Applied Surface Science* **2020**, *507*, 144916.
45. Zhang, J.; Zhou, P.; Liu, J.; Yu, J. New understanding of the difference of photocatalytic activity among anatase, rutile and brookite TiO_2. *Physical Chemistry Chemical Physics* **2014**, *16*, *38*, 20382–20386, doi:10.1039/C4CP02201G.
46. Ali, T.; Tripathi, P.; Azam, A.; Raza, W.; Ahmed, A. S.; Ahmed, A.; Muneer, M. Photocatalytic performance of Fe-doped TiO_2 nanoparticles under visible-light irradiation. *Materials Research Express* **2017**, *4*, 1–12.

47. Shyniya, C. R.; Bhabu, K. A.; Rajasekaran, T. R. Enhanced electrochemical behavior of novel acceptor doped titanium dioxide catalysts for photocatalytic applications. *Journal of Materials Science: Materials in Electronics* **2017**, *28,9*, 6959–6970.
48. Liqiang, J.; Xiaojun, S.; Baifu, X.; Baiqi, W.; Weimin, C.; Honggang, F. The preparation and characterization of La doped TiO_2 nanoparticles and their photocatalytic activity. *Journal of Solid State Chemistry* **2004**, *177*, 3375–3382, doi:10.1016/J.JSSC.2004.05.064.
49. Raza, W.; Haque, M. M.; Muneer, M.; Harada, T.; Matsumura, M. Synthesis, characterization and photocatalytic performance of visible light induced bismuth oxide nanoparticle. *Journal of Alloys and Compounds* **2015**, *648*, 641–650, doi:10.1016/J.JALLCOM.2015.06.245.
50. Wilke, K.; Breuer, H. D. The influence of transition metal doping on the physical and photocatalytic properties of titania. *Journal of Photochemistry and Photobiology A: Chemistry* **1999**, *121*, 49–53, doi:10.1016/S1010-6030(98)00452-3.
51. Tan, H.; Zhao, Z.; Zhu, W. Bin; Coker, E. N.; Li, B.; Zheng, M.; Yu, W.; Fan, H.; Sun, Z. Oxygen vacancy enhanced photocatalytic activity of pervoskite $SrTiO_3$. *ACS Applied Materials and Interfaces* **2014**, *6*, 19184–19190.
52. Zhao, Y.; Zhao, Y.; Shi, R.; Wang, B.; N Waterhouse, G. I.; Wu, L.-Z.; Tung, C.-H.; Zhang, T. Tuning Oxygen Vacancies in Ultrathin TiO_2 Nanosheets to Boost Photocatalytic Nitrogen Fixation up to 700 nm. *Advanced Materials* **2019**, *31*, 1806482.
53. Hu, J.; Li, S.; Chu, J.; Niu, S.; Wang, J.; Du, Y.; Li, Z.; Han, X.; Xu, P. Understanding the Phase-Induced Electrocatalytic Oxygen Evolution Reaction Activity on FeOOH Nanostructures. *ACS Catalysis* **2019**, *9*, 10705–10711.
54. Colina-Márquez, J.; Machuca-Martínez, F.; Puma, G. L.; Mueses, M. . Photocatalysis: Fundamentals, Materials and Potential. In *Molecules*; Pierre Pichat, Ed.; MDPI: Basel: Switzerland, 2016; pp. 1–664.
55. Alkaykh, S.; Mbarek, A.; Ali-Shattle, E. E. Photocatalytic degradation of methylene blue dye in aqueous solution by $MnTiO_3$ nanoparticles under sunlight irradiation. *Heliyon* **2020**, *6,4*, e03663,1-6, doi:10.1016/j.heliyon.2020.e03663.
56. Rytwo, G.; Zelkind, A. L. Evaluation of Kinetic Pseudo-Order in the Photocatalytic Degradation of Ofloxacin. *Catalysts* **2022**, *12*.
57. De Araujo Scharnberg, A. R.; Loreto, A. C. De; Wermuth, T. B.; Alves, A. K.; Arcaro, S.; Santos, P. A. M. Dos; Rodriguez, A. D. A. L. Porous ceramic supported TiO_2 nanoparticles: Enhanced photocatalytic activity for Rhodamine B degradation. *Boletín de la Sociedad Española de Cerámica y Vidrio* **2020**, *59*, 230–238.
58. Nunes, D.; Fragoso, A. R.; Freire, T.; Matias, M.; Marques, A. C.; Martins, R.; Fortunato, E.; Pimentel, A. Ultrafast Microwave Synthesis of WO_3 Nanostructured Films for Solar Photocatalysis. *physica status solidi (RRL) – Rapid Research Letters* **2021**, *15,9*, 2100196.
59. Moulai, F.; Fellahi, O.; Messaoudi, B.; Hadjersi, T.; Zerroual, L. Electrodeposition of nanostructured γ-MnO_2 film for photodegradation of Rhodamine B. *Ionics* **2018**, *24,7*, 2099–2109.

8

DEVELOPMENT AND CHARACTERIZATION OF CA:TiO_2 CELLULOSE MEMBRANES

The present study is under submission: Matias, M. L.; Gaspar D.; Carvalho, D.; Pimentel, A.; Pereira, L.; Machado, A. S. Reis; Rodrigues, J.; Monteiro, T.; Deuermeier, D.; Martins, R.; Fortunato, E.; Nunes, D. Defect-Engineered Ca-TiO_2 Nanomaterials for Enhanced Adsorption and Photocatalytic Degradation of Water Pollutants on Sustainable Cellulose Membranes. *Advanced Sustainable Systems* **2025**, e00675. https://doi.org/10.1002/adsu.202500675.

8.1 Introduction

In this study, cellulose-based membranes embedded with Ca-modified TiO_2 nanomaterials were synthesized using a rapid solvothermal-assisted microwave method (30 min). Nanopowders containing 5 and 10 mol.% Ca in TiO_2 (designated as 5-Ca:TiO_2 and 10-Ca:TiO_2, respectively) were produced, along with intrinsic TiO_2 (designated as TiO_2), for comparison. The nanopowders' structural, optical, and electrical properties were analyzed using XRD, STEM/EDS, BET analysis, XPS, UV-VIS absorption measurements, and conductivity tests. Additionally, DFT computational calculations were performed to gain deeper insights into the impact of calcium on the TiO_2 lattice.

The structural and morphological characterization of the membranes was conducted via SEM/EDS. The effectiveness of these membranes in removing and degrading TC was evaluated under both simulated solar light and natural sunlight. Scavenger experiments were carried out to identify the ROS involved in the TC photocatalytic degradation process. Furthermore, the reusability of the best-performing photocatalytic membrane was assessed over five consecutive cycles under simulated solar light.

The novelty of this work lies in harnessing cellulose, a biodegradable and abundantly available biopolymer, as a robust support. Unlike previous studies by other authors that rely on unsustainable methods and powdered photocatalysts, our approach utilizes eco-friendly micro-sized cellulose derived from wood to create membranes with enhanced adsorptive and photocatalytic properties. The integration of the nanostructures during membrane fabrication is intended to minimize the risk of potential release into the environment and facilitate future large-scale applications. Another highlight of this study is the fine-tuning of structural defects, resulting from calcium addition and microwave irradiation.

8.2 Results and discussion

8.2.1 Characterization of the TiO_2 nanopowders

8.2.1.1 XRD

The diffractograms of the TiO_2-based powders (Figure 8.1) show that the materials can be fully ascribed to anatase, with the broadness of the diffraction maxima reflecting the nanocrystalline nature. No impurity phases could be detected, indicating that the Ca^{2+} ions integrate the TiO_2 structure. Given that oxygen has a much higher electronegativity than calcium (3.44 *vs.* 1 [1]), the substitution of oxygen for calcium is improbable. It is also unlikely for Ca^{2+} to occupy interstitial sites due to its significantly larger ionic radius than Ti^{4+} (1 *vs.* 0.61 Å [2,3]). Most likely calcium substitutes titanium [4], and the difference in radius justifies the structural distortion summarized in Table 8.1. An increase in the amount of calcium had a negligible effect on the lattice parameter a, while a marginal decrease of the c value was observed, as shown in Table 8.1. The corresponding shifts toward higher 2θ values are observed for the (004) and (101) planes of anatase for the 5-Ca:TiO_2 and 10-Ca:TiO_2 materials in Figure 8.1.

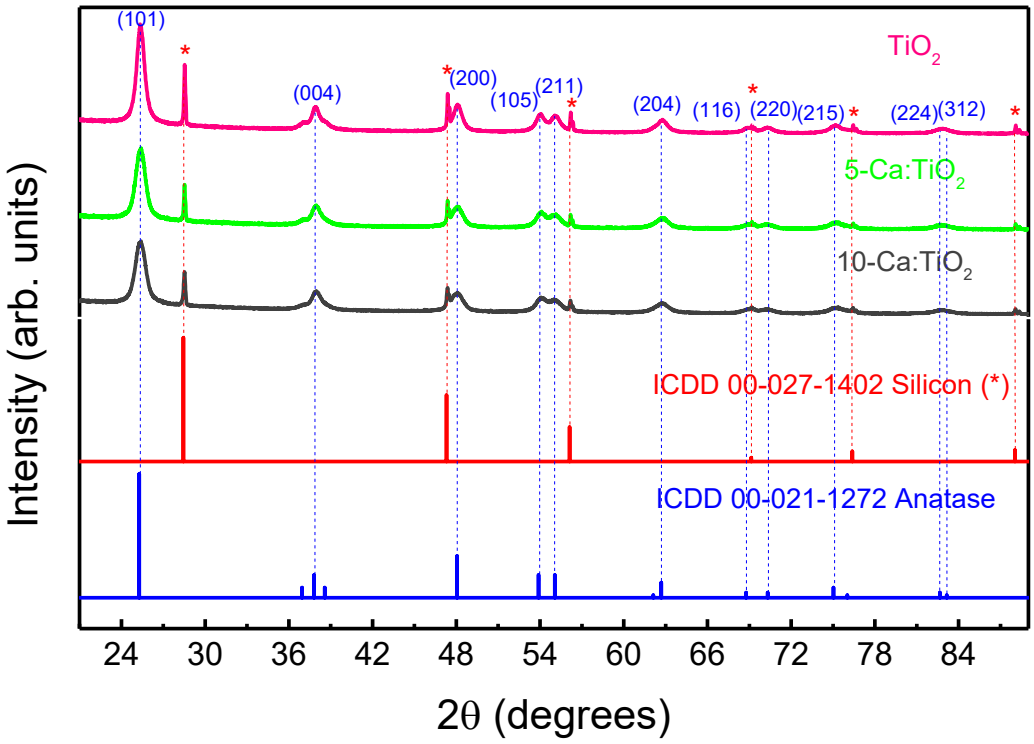

Figure 8.1: XRD diffractograms of the synthesized nanopowders (TiO_2, 5-Ca:TiO_2 and 10-Ca:TiO_2). The simulated cards for TiO_2 anatase and silicon (intern XRD pattern represented by *) are also shown.

Table 8.1: Estimated lattice parameters of the nanomaterials (TiO_2, 5-Ca:TiO_2, 10-Ca:TiO_2).

	Lattice parameters (Å)		
	a=b	c	a/c ratio
TiO_2	3.779	9.502	0.3977
5-Ca:TiO_2	3.780	9.492	0.3982
10-Ca:TiO_2	3.781	9.492	0.3983

In most cases, substituting a smaller ion for a larger one causes a lattice expansion, while the opposite shrinks it [5,6]. However, factors beyond the cationic size can govern the lattice expansion or shrinkage [7]. For instance, Vaisakhan *et al.* studied the influence of alio-valent cation substitution on the structural and electrical properties of $Gd_2(Zr_{1-x}M_x)_2O_{7-\delta}$ (M = Sc^{3+} and Y^{3+}; x = 0, 0.1,0.2, 0.3, 0.4). The reported ionic radii of Gd^{3+}, Zr^{4+}, Sc^{3+}, and Y^{3+} in an eight-coordinated fluorite-type lattice are 1.053 Å, 0.84 Å, 0.87 Å, and 1.019 Å, respectively [6]. Although both Sc^{3+} and Y^{3+} possess larger radii than Zr^{4+}, Sc^{3+} substitution reduced the lattice parameter, causing the lattice to contract, whereas substitution with Y^{3+} increased it and

resulted in a lattice expansion [6]. In the first case, this effect was attributed to Schottky defects in the anionic sublattice resulting from aliovalent substitution. The replacement of tetravalent Zr with trivalent Sc was suggested to create oxygen vacancies in the lattice to maintain electrostatic balance [6]. A similar explanation was proposed in another study on tungsten bronze ceramics ($Sr_5SmTi_{3+2x}Nb_{7-2x}O_{30-x}$), where lattice contraction was attributed to an increased deficiency of oxygen [8]. Other factors may contribute to shifts such as stacking faults, point and extended defects, stresses or strain [9]. Another explanation is phase transformation or the formation of secondary phases [10,11] like CaO or $CaTiO_3$; however, additional phases were not identified in the present XRD results.

8.2.1.2 Electron microscopy

8.2.1.2.1 STEM

STEM observations showed that calcium introduction has a significant impact on the shape, size and local crystal structure of the TiO_2 nanocrystals. Microwave synthesis in the absence of calcium resulted in the formation of nanocrystals with quasi-equiaxed and square shapes as well as rod-like morphologies with rounded edges, as illustrated in Figure 8.2 (a) and (b). The nanoparticles exhibited well-defined steps and atomically flat facets as indicated by the arrows in Figure 8.2 (c), a feature previously reported for microwave-assisted synthesis of TiO_2 nanoparticles [12]. The average particle size was 12.6 ± 4.3 nm. The size heterogeneity reflected in the histogram of Figure 8.2 (b) resulted from the presence of a relatively small population of rods, whose average diameter and length were 11.9 ± 3.1 nm and 19.0 ± 6.2 nm, respectively. All particles consisted of well-crystallized anatase (Figure 8.2 (c) and (d)). The fast growth direction of the anatase rod-like structures is one of the <110> directions, as reported earlier [13]. This overruling of symmetry attests to the influence of kinetics during the growth process in microwave-assisted synthesis due to the high-temperature gradients across the hot spots [14,15].

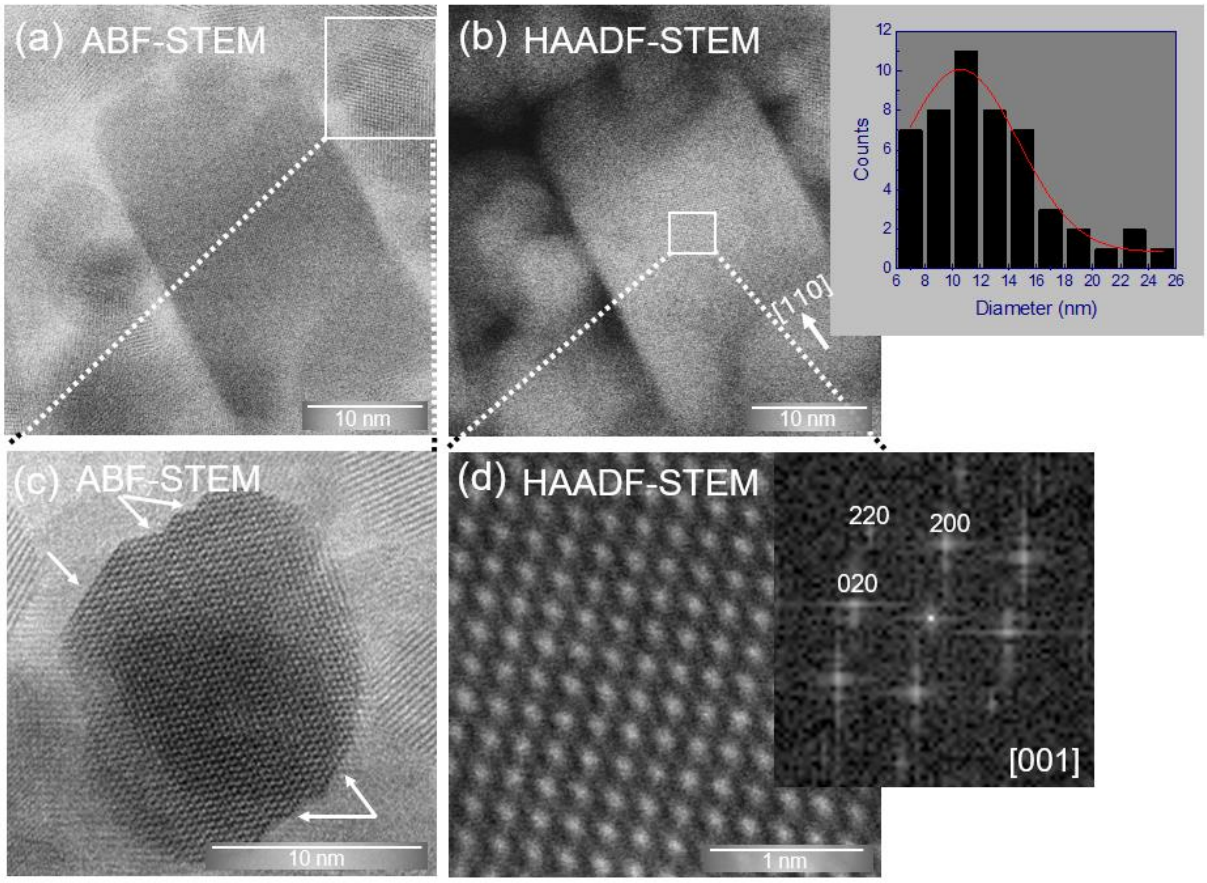

Figure 8.2: (a) ABF-STEM and (b) HAADF-STEM images of quasi-equiaxed and rod-like TiO_2 nanocrystals synthesized in the absence of Ca. The inset in (b) shows the nanoparticles' size distribution. (c) The quasi-equiaxed particles evidenced atomically flat facets and surface steps (arrows). (d) Magnified detail of the rod-like nanocrystal demonstrating that the fast growth direction of these morphologies is one of the <110> directions. The FFT image of the image is presented in the inset.

Adding 5 mol. % of Ca (Figure 8.3) induced a slight decrease in the average size of the nanocrystals (10.5 ± 3.1 nm). Square-shaped and rod-like particles (10.6 ± 2.2 nm and 15.0 ± 1.7 nm in diameter and length, respectively) were also observed for this condition. The presence of Ca atoms was not detected from contrast differences in HAADF STEM images due to the close atomic numbers of Ca and Ti. Nevertheless, lattice distortions and surface defects were detected in these particles (see arrows in Figure 8.3 (c) and (d) and the lines in (f)). In addition, the presence of Ti vacancies along the atomic columns could be inferred from the noticeable lower contrast (see arrow in Figure 8.3 (f)). Structural defects are known to occur in metal oxides synthesized under microwave irradiation [16–21] with significant enhancement in the presence of dopant/impurity elements [22]. Microwave irradiation activates non-thermal microwave-field-induced diffusion processes at the surfaces [16,23–25]. This interaction enhances mass transfer within the crystal, causing structural defects and impurity

accumulation near boundaries [16,23,26]. Rosa *et al.* demonstrated that adding different concentrations of Ca to ZrO_2 led to the formation of surface steps and lattice distortions and disarrangements in the ZrO_2 nanocrystals [16]. A similar behaviour may justify the distortions and defects observed in the 5-Ca:TiO_2 nanomaterial. Figure 8.3 (f) shows that the investigated nanocrystal exhibits both ordered and disordered atomic columns, with lattice spacings varying by approximately 10 %. The lattice disarrangements observed in Figure 8.3 (f) are consistent with the XRD results (Table 8.1) that suggested lattice distortion in the anatase lattice induced by Ca^{2+} ions. A similar effect, with lattice distortion, was also observed with the insertion of chloride ions into TiO_2, which prevented the recombination of electron–hole pairs and increased the photocatalytic activity of the material under visible light [27]. By adding Hf into anatase, lattice distortions were also imaged, confirming that Hf^{4+} substitutes in the Ti^{4+} sites. This substitution resulted in a more open crystal structure, which was achieved via the difference in ionic radius [28].

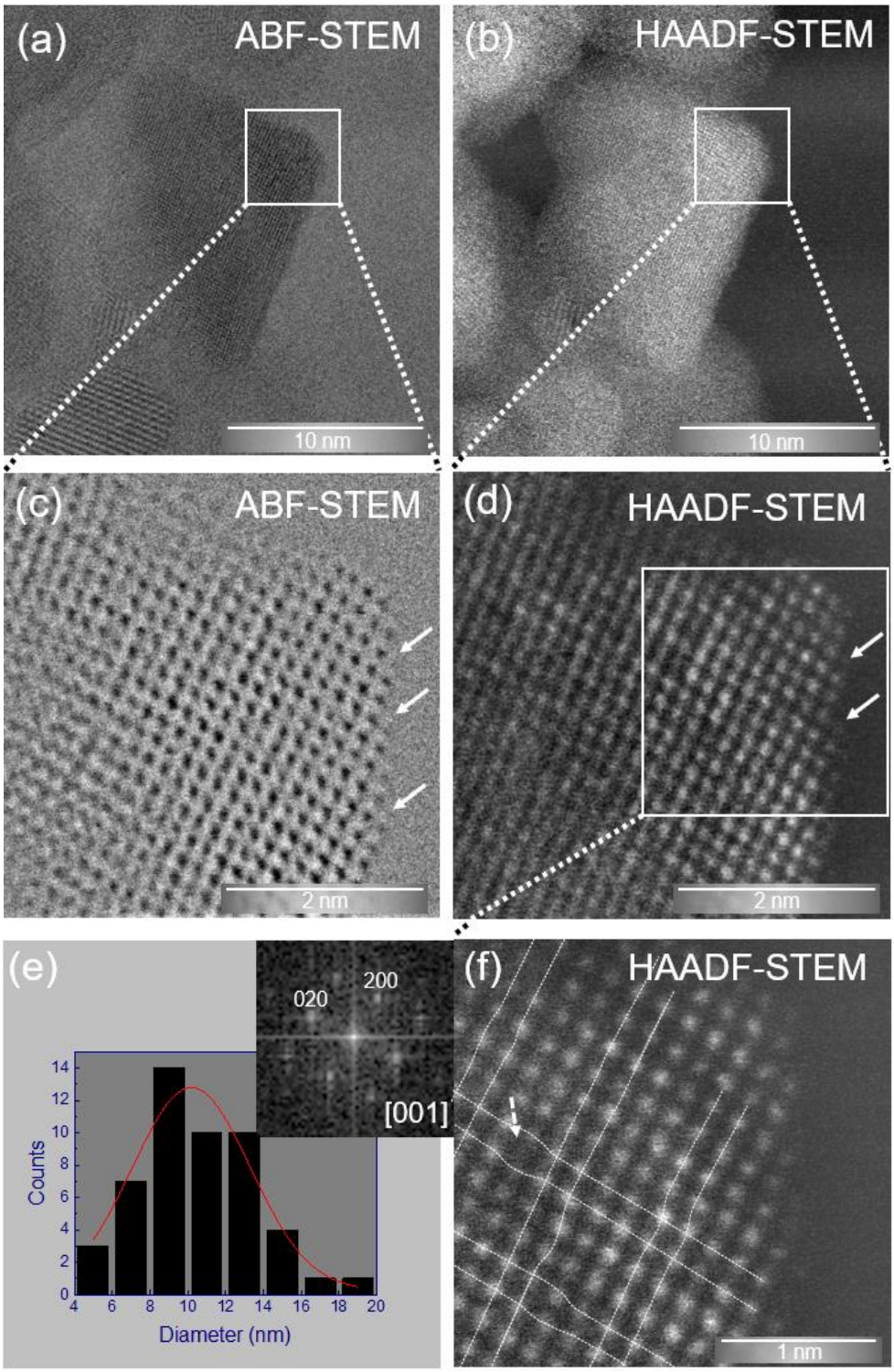

Figure 8.3: (a) ABF-STEM and (b) HAADF-STEM images of TiO_2 nanocrystals synthesized with 5 mol. % of Ca. (c) and (d) Magnified details where the solid arrows point to surface defects. (e) Nanoparticle size distribution for the 5-Ca:TiO_2 nanopowder. (f) Magnified detail of (d) and corresponding FFT (inset in (e)). The dashed arrow in (f) points to a lower contrast region likely resulting from the presence of Ti vacancies across the atomic columns.

With an increase in Ca concentration to 10 mol. %, a slight reduction in nanocrystal size was observed, with an average particle size of 9.7 ± 3.0 nm. Additionally, the particles' morphology tended to become more rounded and irregular, without atomically flat facets. Moreover, a notable increase in surface defects compared to the 5-Ca:TiO_2 nanomaterial was observed (see Figure 8.4 and arrows in Figure 8.5 and Figure 8.6).Various types of structural defects were identified in this material. For instance, Figure 8.4 presents a stacking fault, a 1D crystallographic defect.

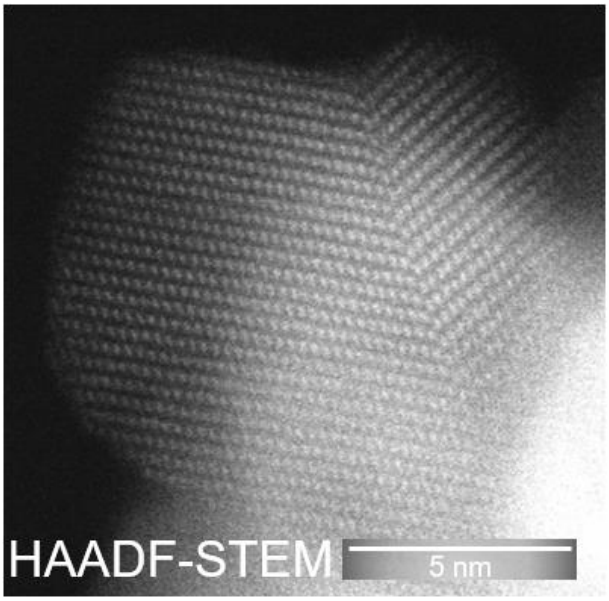

Figure 8.4: A 10-Ca:TiO_2 nanocrystal with a stacking fault.

Furthermore, in the inset of Figure 8.5 (b), a clear and coherent interface with different crystallographic orientations is evident. This type of grain boundary (2D defect) becomes increasingly prevalent with higher Ca concentrations, favoring a non-epitaxial growth between the adjacent grains. The Ti atom columns within the inner structure of the nanocrystal (denoted as region A) were identified by the characteristic dumbbell-like arrangement with lattice spacings of 3.8 Å and 2.4 Å. These values correspond precisely to the (200) and (004) crystallographic planes of anatase, respectively, defining a [010] zone axis. In the surface, designated as B, the FFT pattern obtained along the [001] zone axis (right inset in Figure 8.5 (d)) exhibited a deviation from the expected 90° angle between the (200) and (020) planes of pure anatase. Such a deviation is associated with the lattice disarrangements induced by Ca^{2+} ions, as observed for the 5-Ca:TiO_2 nanomaterial, which is in line with a previous study on doped ZrO_2 [16]. During synthesis, dopants can influence the nucleation and growth mechanisms of

materials, either by inhibiting or promoting specific crystallographic orientations. This process can lead to the development of irregular surface structures, including steps and kinks [29–32].

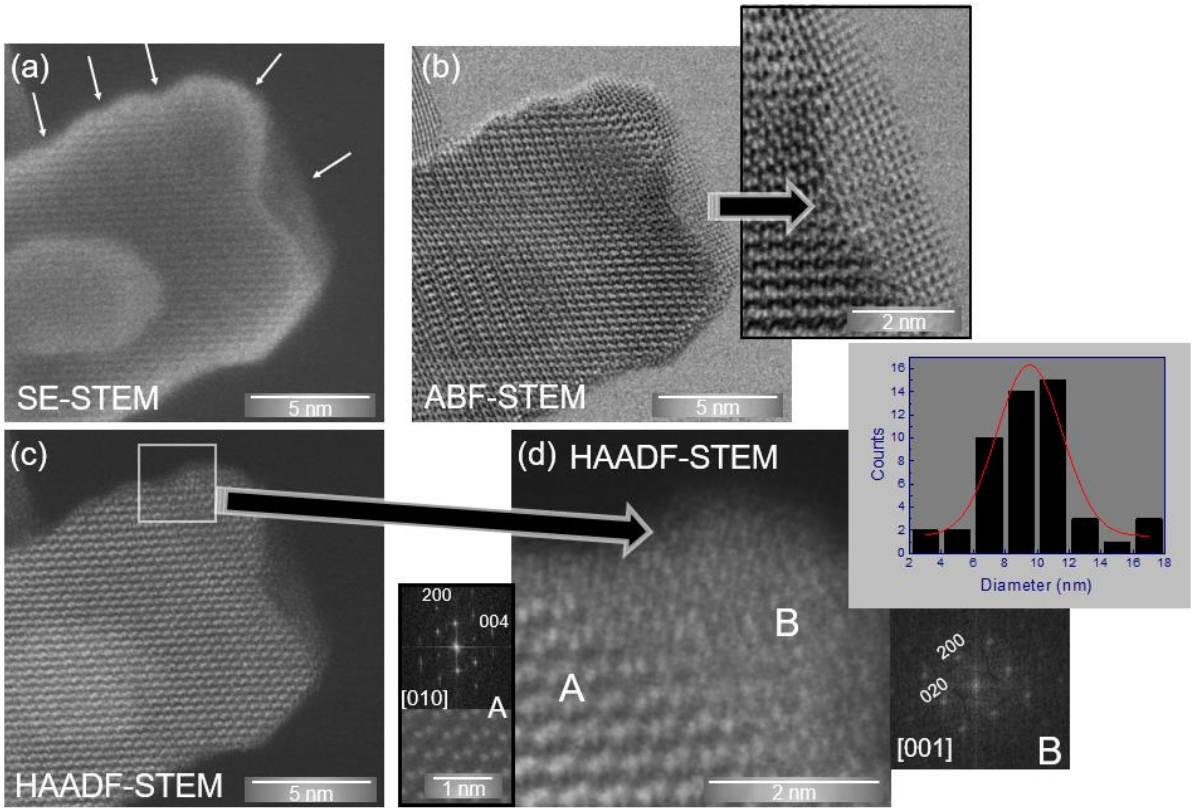

Figure 8.5: (a) SE-STEM, (b) ABF-STEM, and (c) HAADF-STEM images of a synthesized TiO_2 nanocrystal with 10 mol. % of Ca. The arrows point to the surface defects observed within the nanocrystal. (d) The defective area of the nanocrystal was further investigated using atomic-resolution ABF-STEM (inset in (b)) and HAADF-STEM images (d), where it is clear the grain boundary defect. The FFT images of both areas (A and B) are presented in the insets of (d). The nanocrystals' size distribution was also estimated for the 10-Ca:TiO_2 nanopowder and is presented in (d).

Another 10-Ca:TiO_2 nanocrystal was further investigated, as shown in Figure 8.6. The extensive presence of surface defects can be observed in Figure 8.6 (a), (b) and (e). Grain boundaries were also observed in both inner and surface regions, however, in this specific nanocrystal, voids were also observed in the defective area (Figure 8.6 (e)). EDS analysis was also performed to evaluate the distribution of Ca within the 10-Ca:TiO_2 nanocrystals. From Figure 8.6 (h), it can be seen that Ca is uniformly distributed alongside Ti and O. Additionally, no impurities were detected in the EDS measurements.

It is known that structural defects are fundamental to the reactivity of ionic solids, as the defect-induced disorder within the surface layer primarily governs their chemical reactivity [33]. It has also been demonstrated that a high density of surface steps significantly

enhances molecular adsorption and lowers the energy barriers for chemical reactions [34]. Numerous studies have explored the influence of structural defects on the adsorption properties and photocatalytic performance of TiO_2 nanomaterials [12,35,36]. Fu *et al.* demonstrated that the synergy between bulk and surface defects on TiO_2 can effectively address its rapid charge recombination and limited O_2 adsorption capacity [37]. Bulk defects can act as hole acceptors, facilitating directional hole transfer and significantly improving electron–hole separation [37]. Simultaneously, surface defects enhance adsorption, further contributing to the material's overall photocatalytic performance. In Ref. [38], the authors synthesized both rutile and anatase TiO_2 phases using a hydrothermal method and controlled defect formation through calcination. The study revealed that bulk defects in TiO_2 tend to confine photogenerated holes, making them unavailable for reactions. As a result, these trapped holes may act as recombination centers for photogenerated charges, thereby reducing photocatalytic efficiency. In contrast, surface defects can trap photogenerated holes, promoting charge separation and consequently enhancing photocatalytic activity. Liu *et al.* [39] showed that TiO_2 nanosheets with predominant surface defects have significantly higher activity in photocatalytic water reduction to hydrogen compared to those with dominant bulk defects. This enhanced activity is attributed to surface defects that can trap electrons at the surface and facilitate the adsorption and activation of water molecules. It was shown that TiO_{2-x} particles with surface and bulk defects with more grain boundary oxygen vacancies exhibited an improved charge separation, leading to a remarkable degradation efficiency of gaseous isopropanol [40]. Han *et al.* [41] attributed the enhancement in photocatalytic activity of TiO_2 Degussa P25 to the structural modification of this material under microwave irradiation with the formation of surface defects, such as Ti^{3+} and Ti-OH, and the reaggregation of the anatase/rutile phases. An analogous study with TiO_2 anatase nanocrystals synthesized under microwave irradiation revealed the presence of surface steps within the high-index {012}/{102} facets and bulk defects (absence of Ti atoms) [12]. The surface defects contributed to the significant TC adsorption capacity of the nanomaterial (about 58 % in 240 min) and the removal of ~90 % after 30 min of simulated solar light exposure.

In the present study, the addition of 10 mol. % of Ca led to the extensive formation of point and 2D defects, accompanied by 1D defects, lattice disarrangements and voids. This indicates that increasing the Ca concentration significantly influenced the formation of structural defects, with a higher density of surface defects observed at higher Ca concentrations. Therefore, this is expected to increase reactivity, with surface defects acting as adsorption sites for

the reaction, facilitating charge transfer and enhancing charge separation within the photocatalyst, thereby improving its catalytic performance [39,42]. Bulk defects also play a role in the overall photocatalytic activity since they typically act as recombination sites for photogenerated electron–hole pairs and hinder the diffusion of charge carriers, which can result in reduced photocatalytic activity [42].

To the best of the authors' knowledge, this study is the first to provide direct imaging evidence of the correlation between Ca concentration and the formation of structural defects, including point defects (vacancies), 1D defects (stacking faults), 2D defects (grain boundaries), and 3D defects (voids), ultimately resulting in the formation of highly distorted anatase nanocrystals. Hence, it was hypothesized that the synergistic effect of microwave irradiation and Ca incorporation significantly contributes to the pronounced formation of both surface and bulk defects.

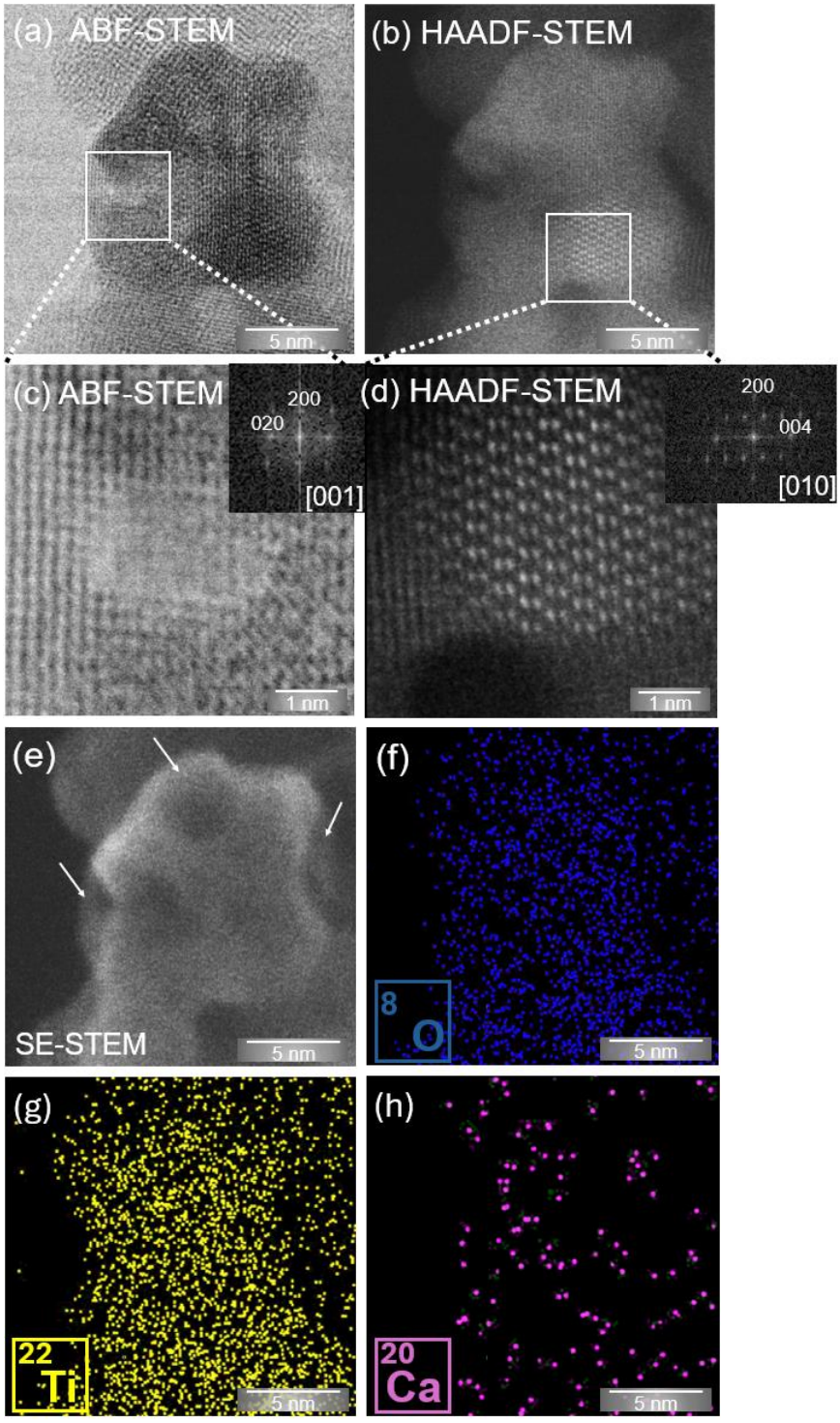

Figure 8.6: (a) ABF-STEM and (b) HAADF-STEM images of a defective 10-Ca:TiO_2 nanocrystal. The defective nanocrystal presents voids (c) and grain boundary defects (d). The FFT images of the investigated areas are presented in the insets of (c) and (d). (e) SE-STEM image of the defective nanocrystal with arrows pointing to the surface defects, together with its EDS maps of oxygen (f), titanium (g) and calcium (h).

8.2.1.3 Specific surface area

The nanopowders were further investigated by BET measurements. Figure 8.7 shows the isotherm curve obtained for the 10-Ca:TiO_2 material. The hysteresis loop observed corresponds to a type IV isotherm, as classified by the International Union of Pure and Applied Chemistry (IUPAC), indicating the presence of a mesoporous structure with pore sizes ranging from 2 to 50 nm [43,44]. The same type of isotherm was observed for the other synthesized nanopowders (data not shown).

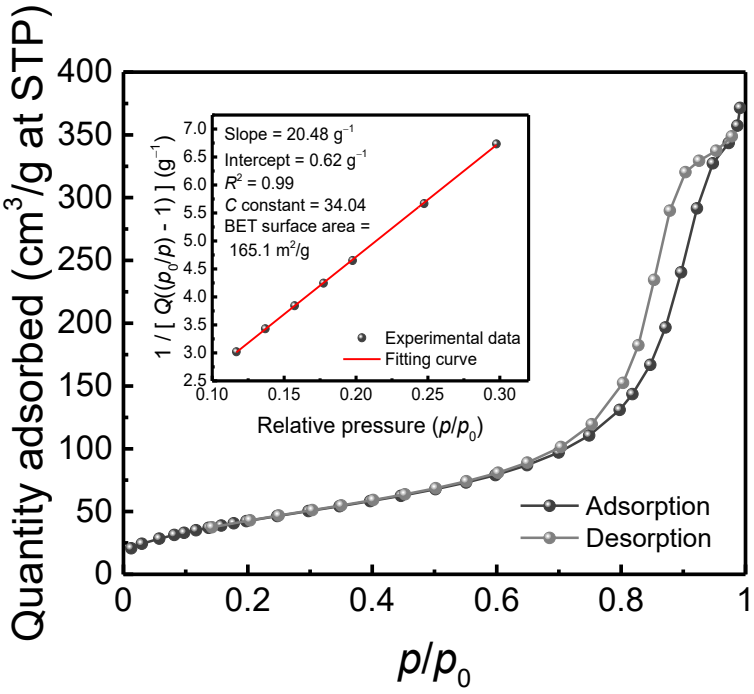

Figure 8.7: N_2 adsorption/desorption isotherm (quantity adsorbed *vs.* p/p_0) at standard temperature and pressure (STP)) for the 10-Ca:TiO_2. The inset shows the fitting curve of the BET surface area for the 10-Ca:TiO_2 material.

Based on these results, it was possible to calculate the surface area by the BET equation [45]. The BET surface areas of TiO_2 and Ca:TiO_2 nanopowders are shown in Table 8.2 and also in the inset of Figure 8.7 (only for the 10-Ca:TiO_2 nanopowder). Table 8.2 shows an increase in the specific surface area with higher calcium content, suggesting that the defective regions (extensive presence of surface defects and bulk defects, i.e. voids in the case of the 10-Ca:TiO_2 material) and the smaller particle size may contribute to this increase. The 10-Ca:TiO_2 material is thus anticipated to provide a wider contact surface for the adsorption of pollutant molecules, thereby accelerating the removal process of pollutants [46–48].

Table 8.2: Specific surface areas for the synthesized nanomaterials estimated by the BET method.

	Specific surface area ($m^2.g^{-1}$)
TiO_2	134.4
5-Ca:TiO_2	137.6
10-Ca:TiO_2	165.1

8.2.1.4 XPS

To understand the effect of the addition of calcium in TiO_2, XPS measurements were conducted for TiO_2 and 10-Ca:TiO_2 nanopowders. Although the survey spectrum for 10-Ca:TiO_2 was not recorded, Figure A.11 confirms the presence of Ti and O in the TiO_2 material. Additionally, Ca was detected in the 7 mol. % Ca:TiO_2 nanopowder (7-Ca:TiO_2). The observed C 1s peak is attributed to adventitious carbon adsorbed on the TiO_2 surface [49]. The 10-Ca:TiO_2 material is expected to exhibit a spectrum comparable to that of 7-Ca:TiO_2. The binding energy varies from 286 eV in the case of 10-Ca:TiO_2 to 287.8 eV for TiO_2. While 286 eV is an average value for oxide [50], 287.8 eV is a clear indication of charge accumulation during the measurement. Consequently, the Ti 2p and O 1s binding energies of TiO_2 spectra are also significantly higher than the ones of 10-Ca:TiO_2 (Figure 8.8 (a) and (c)). A similar shift of 0.35 eV to higher binding energies was also reported for 3 at. % Sb-doped SnO_2 compared to undoped SnO_2 and it was attributed to the occupation of conduction-band states in degenerately doped SnO_2 [51]. The presence of structural surface defects may have also affected the binding energies of the nanopowder with calcium. For instance, Mahatha *et al.* [52] reported a similar shift of Mo 3d and S 2p core levels between different regions on molybdenum disulfide (MoS_2) (0001). In this case, the binding energy shift was attributed to band bending effects due to surface defects, such as steps. Upon the overlap of the Ti 2p spectrum of TiO_2 with the one of 10-Ca:TiO_2, it becomes visible that the peak shapes and peak separation are identical (Figure 8.8 (b)) [27,53]. The overlapped O 1s emissions of the two samples (Figure 8.8 (d)) reveal a slight increase in the shoulder at 533 eV. This might be attributed to the additional adsorption of hydroxyl groups at the surface of the metal oxide, possibly indicating a higher chemical reactivity of the surface [54]. It was reported that more negative surface charges lead to more efficient adsorption of pollutant molecules by the metal oxide through the formation of hydrogen bonds [54–56]. The presence of oxygen vacancies can not be directly inferred from the XPS results, as the analysis of materials exposed to the atmosphere is generally influenced by hydrocarbons and moisture at the surface [57].

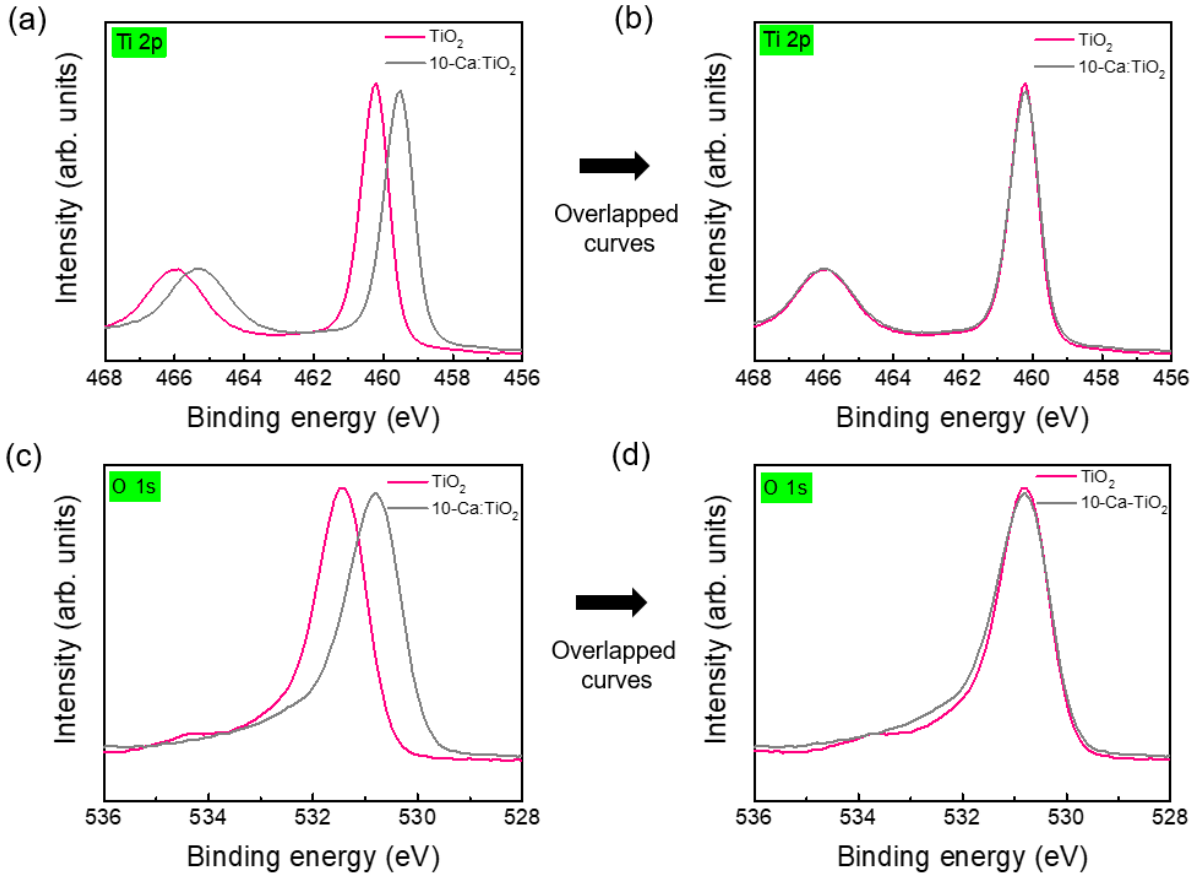

Figure 8.8: (a) Ti 2p XPS high-resolution spectra of TiO_2 and 10-Ca:TiO_2 nanopowders. (b) The TiO_2 curve in (a) was shifted to overlap with the 10-Ca:TiO_2 curve in (a), due to charging effects in the TiO_2 material. (c) O 1s XPS high-resolution spectra of TiO_2 and 10-Ca:TiO_2 nanopowders. (d) The TiO_2 curve in (c) was shifted to overlap with the 10-Ca:TiO_2 curve in (c), due to charging effects in theTiO_2 material.

For a better understanding of TiO_2 doping by Ca, XPS of the valence band region of the 10-Ca:TiO_2 nanopowder was obtained, as displayed in Figure 8.10. The results for TiO_2 were not presented due to its low conductivity. Nevertheless, studies have shown that the valence band maximum values for intrinsic TiO_2 anatase range between 2.94-3.23 eV (measured as the energy difference between the Fermi level (E_F) and the valence band maximum) [49,58]. For 10-Ca:TiO_2, this energy difference was found to be 3.6 eV. This suggests the presence of a downward band bending at the surface (as visible in Figure 8.9) and an associated accumulation layer of electrons or an increased bulk electron concentration due to doping of this n-type material [59–61].

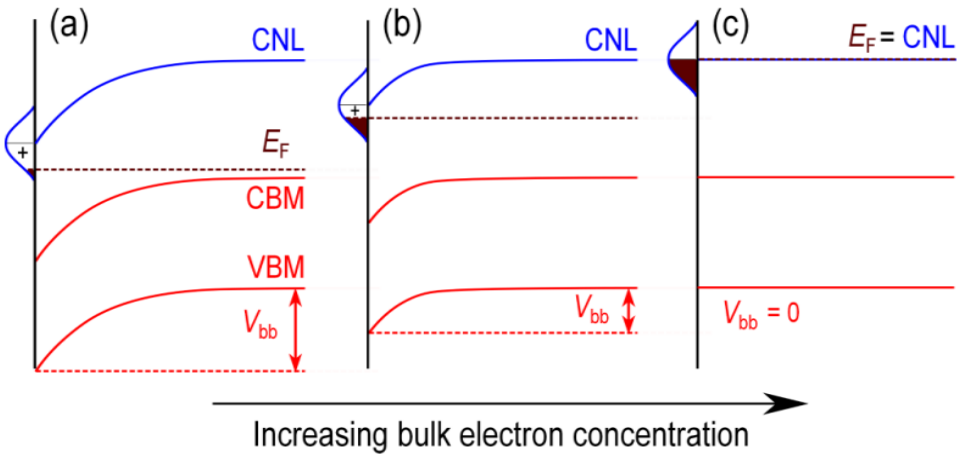

Figure 8.9: Schematic representation of a downward band bending, V_{bb}, in an n-type semiconductor, as the Fermi energy level (E_F) moves up towards the charge neutrality level (CNL) (a)–(c). As the electron concentration increases on the bulk material, a reduction in the density of unoccupied surface states is observed until the bulk and surface Fermi levels stabilize at the CNL (c). VBM and CBM represent the valence band maximum and conduction band minimum levels, respectively. The surface is represented by the vertical black line. Reproduced from Ref. [62].

Similarly to [63], it can also be deduced from Figure 8.10 that the Fermi-level position of the 10-Ca:TiO_2 material is probably above the conduction band minimum by 0.47 eV since the estimated band gap for TiO_2 anatase is 3.13 eV (see section 8.2.1.7) and the obtained energy difference between E_F and the valence band maximum is 3.6 eV. Doping is expected to modify the electrical properties of TiO_2 [53]. In fact, it has been demonstrated that V_O content is increased when a lower-valence cation (e.g. Ca^{2+}) replaces Ti^{4+}, preventing Ti^{3+} formation. In contrast, higher-valence cation doping stabilizes Ti^{3+} without generating V_O, as Ti^{4+} sites are occupied by higher-valence cations, suppressing vacancy formation [64]. The formation of oxygen vacancies will increase the electronic conductivity of TiO_2 [28,65]. Therefore, the 10-Ca:TiO_2 nanopowder should exhibit a higher electron conductivity [64,66].

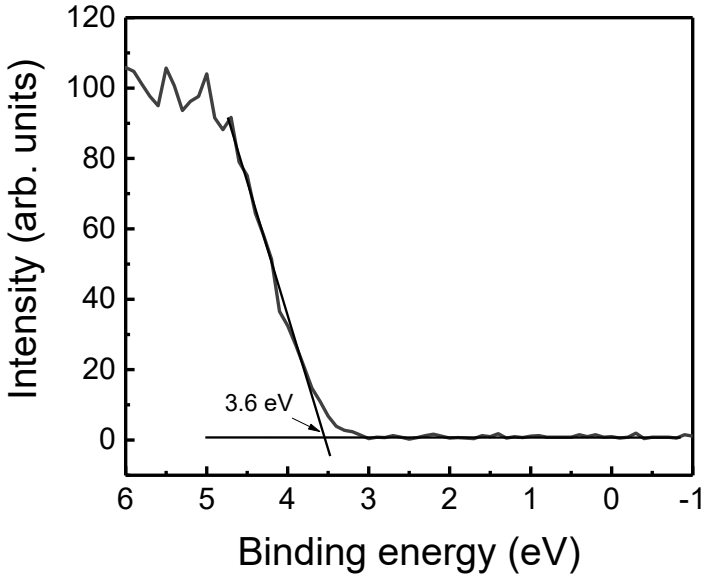

Figure 8.10: XPS valence band spectrum of the 10-Ca:TiO_2 nanopowder.

8.2.1.5 Conductivity measurements

The conductive nature of both TiO_2 and 10-Ca:TiO_2 nanopowders was further probed by recording the current (*I*)–*V* curves from −10 to 10 V (Figure 8.11). Both materials displayed a linear *I-V* behaviour, indicating ohmic contact between the electrodes and the nanoparticles, characteristic of semiconducting materials [67,68]. However, it can be observed from the semi-logarithmic graph in the inset of Figure 8.11 that calcium strongly influenced the electrical properties of TiO_2, showing an increase in the current of around 2 orders of magnitude for the whole range of voltages, compared to TiO_2. This is in line with the degenerate Fermi level position in 10-Ca:TiO_2 found by XPS, which implies a high carrier concentration. Lin *et al.* recently reported an improvement in the electric conductivity in 1D Na-TiO_2(B) nanobelts with a high lattice distortion of 2 orders of magnitude higher than that of pristine TiO_2 (B), which was attributed to the increased content of V_O that could promote a high electron concentration [69]. Al-Salim *et al.* also reported that in TiO_2 films doped with Ca^{2+}, the Ca^{2+} ions promoted the formation of V_O or interstitial Ti^{3+}. This, in turn, contributed to a reduction in the recombination rate of charge carriers [70]. This explanation suggests the enhancement of the photocatalytic and photoelectrochemical performances [71], and it remains the most plausible explanation for the high conductivity [4]. Indeed, the dopant characteristics (such as radii, electronegativity, atomic number, and energy level of the valence shell) strongly influence the electrical conductivity and resistivity [72].

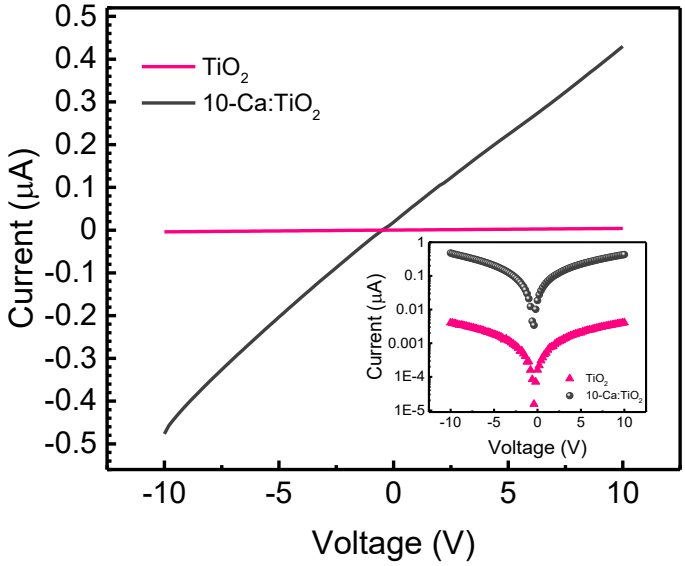

Figure 8.11: *I-V* curves of TiO_2 and 10-Ca:TiO_2 nanomaterials between −10 to 10 V. The corresponding *I-V* curves plotted on a semi-logarithmic scale can be seen in the inset.

8.2.1.6 DFT calculations

The anatase phase of TiO_2 has D_{4h} symmetry and all atoms of the same chemical element are equivalent to each other. The calculated lattice parameters are $a = b = 3.77$ Å and $c = 9.56$ Å, which deviate from the experimental values by 0.1% and 0.6 %, respectively. The calculated band gap of the pristine material is 3.07 eV, in line with the one found in Ref. [73] using a very similar level of theory, and agreeing with our measured band gap.

Concerning Ca-related defects in this material, it has been suggested in previous works that Ca atoms favour a Ti-substitutional position. For example, in the calculations in Ref. [58], it was assumed that interstitial Ca (Ca_{int}) or O-substitutional Ca (Ca_O) cannot occur due to the relatively large radius of Ca atoms, so only Ti-substitutional Ca (Ca_{Ti}) was considered. In turn, after the experimental measurements in Ref. [4], the authors of this study suggested that the conductivity of anatase TiO_2 can be increased by increasing the Ca substitution into Ti. In the present work, we modelled the three possibilities mentioned above, Ca_{int}, Ca_O and Ca_{Ti}, by adding a Ca atom in the corresponding location, relaxing the atomic positions, and calculating their respective formation energies, E_{form}, given by

$$E_{form} = E_{defect} - E_{pristine} + E_{removed} - E_{added}. \quad (8.1)$$

Here, E_{defect} and $E_{pristine}$ are the total energies of a supercell of defective and pristine TiO_2, respectively, whereas $E_{removed}$ and E_{added} correspond to the energies of the atoms removed or

added to form the defect, respectively. With this definition, defects with lower formation energies are more stable and more easily created in the material. We considered O-rich conditions, so that the energy of an O atom is half the energy of an O_2 molecule, and the energy of a Ti atom is $E(\mathrm{Ti}) = E(\mathrm{TiO_2}) - E(\mathrm{O_2})$, the difference between the energy per formula unit of a TiO_2 unit cell and an O_2 molecule. The energy of a Ca atom is the energy per atom of a face-centred cubic Ca unit cell.

Table 8.3 contains the calculated formation energies and local symmetries of Ca_{int}, Ca_O and Ca_{Ti}, which shows that there is a clear preference for Ca atoms to occupy Ti-substitutional sites when incorporated into anatase TiO_2. The Ca atom takes up more space in the lattice than a Ti one. Indeed, the average Ti-O bond length is 1.95 Å, while for Ca-O it is 2.17 Å, which is 11 % longer.

Table 8.3: Calculated formation energies and local symmetries of interstitial calcium (Ca_{int}), oxygen-substitutional calcium (Ca_O) and titanium-substitutional calcium (Ca_{Ti}) defects in anatase TiO_2.

Defect	E_{form} (eV)	Symmetry
None	---	D_{4h}
Ca_{int}	-0.58	C_{2v}
Ca_O	-0.11	C_{2v}
Ca_{Ti}	-3.19	D_{2d}

In Ref. [58], a non-hybrid DFT method was used to predict that the introduction of substitutional Ca in anatase TiO_2 slightly increases the band gap energy of the material but does not add any localized states due to Ca within the band gap. Here, we calculated the band energies at the Γ point of bulk TiO_2 and Ca_{Ti}-defective TiO_2, which are shown in Figure 8.12. The calculated band gap of pristine anatase TiO_2 is 3.07 eV, in agreement with the calculations in Ref. [73] and the value estimated by the absorption measurements presented in section 8.2.1.7. This value increases marginally by 0.02 eV with the introduction of a Ca_{Ti} defect, an effect predicted in the work in Ref. [58]. However, our band gap value is significantly more accurate due to the more refined method of calculation. The minimal difference of 0.02 eV is below the accuracy of DFT calculations, often considered to be around 50 meV. Nevertheless, we can state that the band gap remains practically unchanged in the presence of Ca_{Ti}, and that this defect alone does not add energy states inside the TiO_2 band gap. The increased conductivity of Ca-modified TiO_2 cannot be explained by substitutional Ca alone.

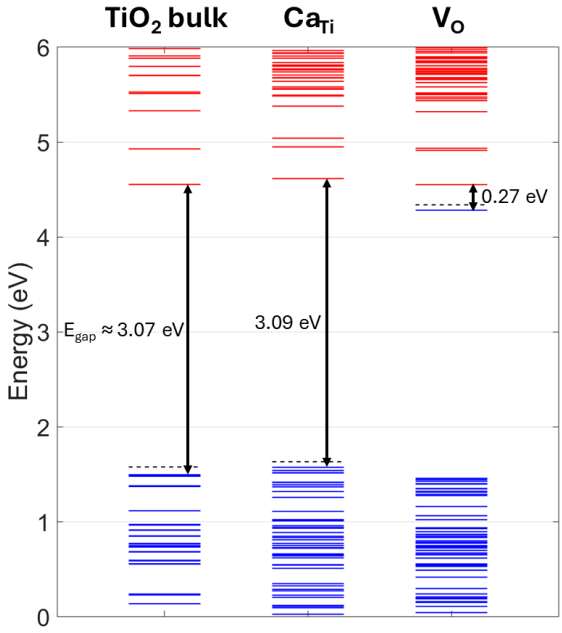

Figure 8.12: Band energies at the Γ point of anatase TiO_2 bulk (leftmost diagram), with Ca_{Ti} (middle diagram), or with an oxygen vacancy (rightmost diagram). Blue (red) lines denote occupied (unoccupied) levels.

Oxygen vacancies famously promote an increase in n-type conductivity in materials. In a previous DFT work [74], it was predicted that V_O defects in anatase TiO_2 have a high formation energy, above 4 eV. In fact, we calculated the formation energy of V_O and obtained 4.20 eV. However, the calculations of Ref. [74] also showed that, when the material was doped with Ti-substitutional cations (Y, Zr, Nb, Mo, Ag, Sn, Au or Ce) the formation energy was reduced by almost 5 eV. This motivated our investigation of the formation of O vacancies in the vicinity of a substitutional Ca atom (V_O-Ca_{Ti}) in the anatase TiO_2 model, which yielded a formation energy of −1.71 eV, that is, a decrease of almost 6 eV with respect to the 4.20 eV found on the intrinsic material. The resulting relaxed structure is shown in Figure 8.13, where it can be seen that both the Ca atom and a nearby O atom are attracted towards the vacancy. In fact, this nearby O atom is closer to the vacant site than to its initial position. Figure 8.12 reveals that an oxygen vacancy within the anatase TiO_2 model alters the band structure of the latter by adding an electronic state of just 0.27 eV below the conduction band bottom, which can lead to an increase in the conductivity. This was observed both with V_O and with V_O-Ca_{Ti}.

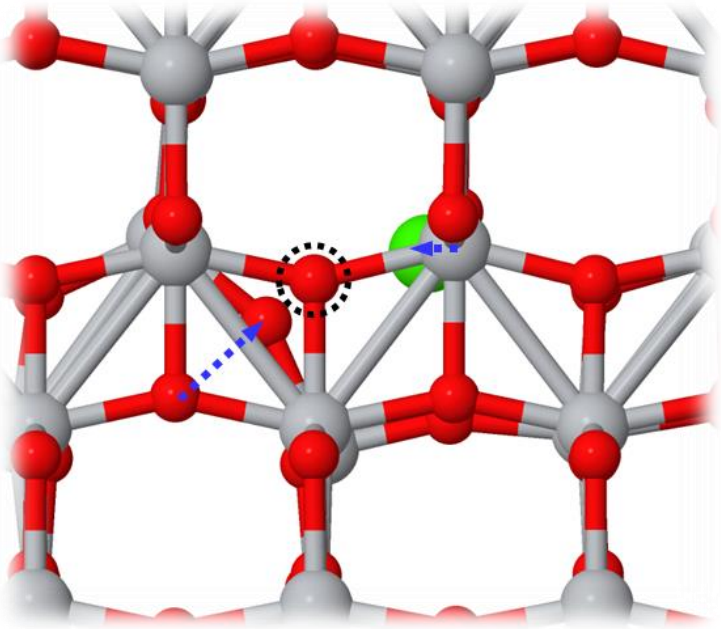

Figure 8.13: Side view, along the *b* lattice vector, of the relaxed structure of an O vacancy in the vicinity of a substitutional Ca atom. The spheres represent atoms of titanium (grey), oxygen (red) or calcium (green). The dotted circle is the location of the oxygen vacancy, and the blue arrows connect the initial positions of the Ca atom and a nearby O atom to their final positions.

Lastly, let us look into the effect of the occurrence of Ca_{Ti} or V_O defects on the lattice parameters of anatase TiO_2, with the aid of Table 8.4. The values in this Table indicate that the presence of substitutional Ca increases both the a and c lattice parameters relative to intrinsic TiO_2, while O vacancies have the opposite effect. The composite defect, V_O-Ca_{Ti}, leaves a unchanged but causes c to increase, albeit by less than 1 % (see Table 8.4). Both experimental and calculated results indicate that the two lattice parameters change by less than 0.1 Å and by less than 1 % with the inclusion of Ca in the lattice.

Table 8.4: Calculated lattice parameters of anatase TiO_2 models, both pristine and defective.

System	$a = b$ (Å)	c (Å)
Bulk TiO_2	3.77	9.56
Ca_{Ti}	3.79	9.63
V_O	3.76	9.55
V_O-Ca_{Ti}	3.77	9.62

8.2.1.7 UV-VIS absorption measurements

Figure 8.14 presents the RT UV-VIS normalized absorption spectra of the produced nanopowders from 250 to 800 nm. To better compare the different materials, the inset in Figure 8.14 presents a magnification between 320 to 450 nm. Even though all nanopowders have the same absorption maxima related to the excitation of electrons from the valence band to the conduction band in the UV region ~312 nm (3.97 eV) [75], a slight difference in the absorption onset is visible on the inset. The introduction of dopant results in a slight blue shift. The optical band gap of the materials was estimated from the onset of absorption, and values of 3.13 eV, 3.10 eV and 3.07 eV were obtained for the 10-Ca:TiO_2, 5-Ca:TiO_2 and TiO_2, respectively. These were compared to the values obtained using the Tauc method, which provided 3.13 eV, 3.11 eV, and 3.07 eV for the same materials. As expected, the values are close considering the observed step absorption indicated by the arrow in the inset. Moreover, a minor increase in the optical band gap is observed with higher calcium concentrations. However, it is important to note that the true band gap values remain uncertain due to estimation errors [76,77]. The minor blue shift can be due either to the differences in the density of surface states that are responsible for changes in the tail of states or to the presence of defect levels near the band edges [78,79]. Indeed, as estimated by the DFT calculations, the introduction of Ca can promote the formation of a higher number of V_O, which subsequently creates energy levels near the bottom of the conduction band. This hypothesis was further corroborated by the experimental results, as an increase in conductivity was observed with the Ca introduction.

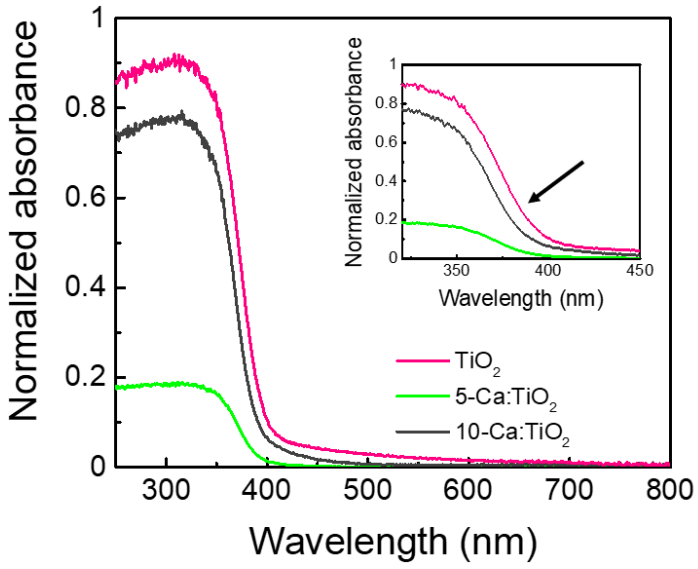

Figure 8.14: UV-VIS normalized absorption spectra of TiO_2, 5-Ca:TiO_2 and 10-Ca:TiO_2 nanopowders between 250-800 nm. The inset represents a magnification between 320-450 nm. The arrow points to the slight deviation that is observed between the nanopowders.

8.2.2 Characterization of the membranes

The 10 mol. % Ca nanopowder exhibited a higher specific surface area and a predominance of structural defects due to the increased Ca concentration. For that reason, it was selected for incorporation into cellulose matrices to produce sustainable adsorptive and photocatalytic membranes activated by solar radiation. For comparison, cellulose membranes were also prepared with TiO_2 but without calcium.

8.2.2.1 Electron microscopy

8.2.2.1.1 SEM/EDS

Figure 8.15 presents the surface morphology of the nanocellulose membranes (pristine (a), with TiO_2 (b) and 10-Ca:TiO_2 (c) nanopowders). As seen in the low magnification image, the pristine membrane (Figure 8.15 (a)) exhibits a highly compact surface structure, without pores, due to the small fibril dimension with a diameter of tens of micrometers in length, and nanometer range (~50 nm) in width, as previously reported [80,81]. The network of fibrils is also randomly oriented, as observed in an analogous study [82]. It was also reported that the small fibril size leads to a large surface area [81], which may increase the number of contact sites for a good dispersion of nanoparticles. Some irregularities at the surface are also

perceptible due to the entanglement of fibers forming lumps (in the order of nanometers [83]), which are randomly distributed throughout the membrane (Figure 8.15 (a)). After incorporating TiO_2 nanoparticles into the solution for membrane preparation, no visible damage to the fibers was observed, and the anatomical characteristics of the cellulose fibers, including their lengths, were maintained (Figure 8.15 (b)). However, the surface became rougher (Figure 8.15 (b)) compared with the pristine (Figure 8.15 (a)). The nanoparticles are also clearly perceptible at the surface and appear to be well distributed. The same morphological characteristics are preserved with the addition of the 10-Ca:TiO_2 nanopowder (Figure 8.15 (c)).

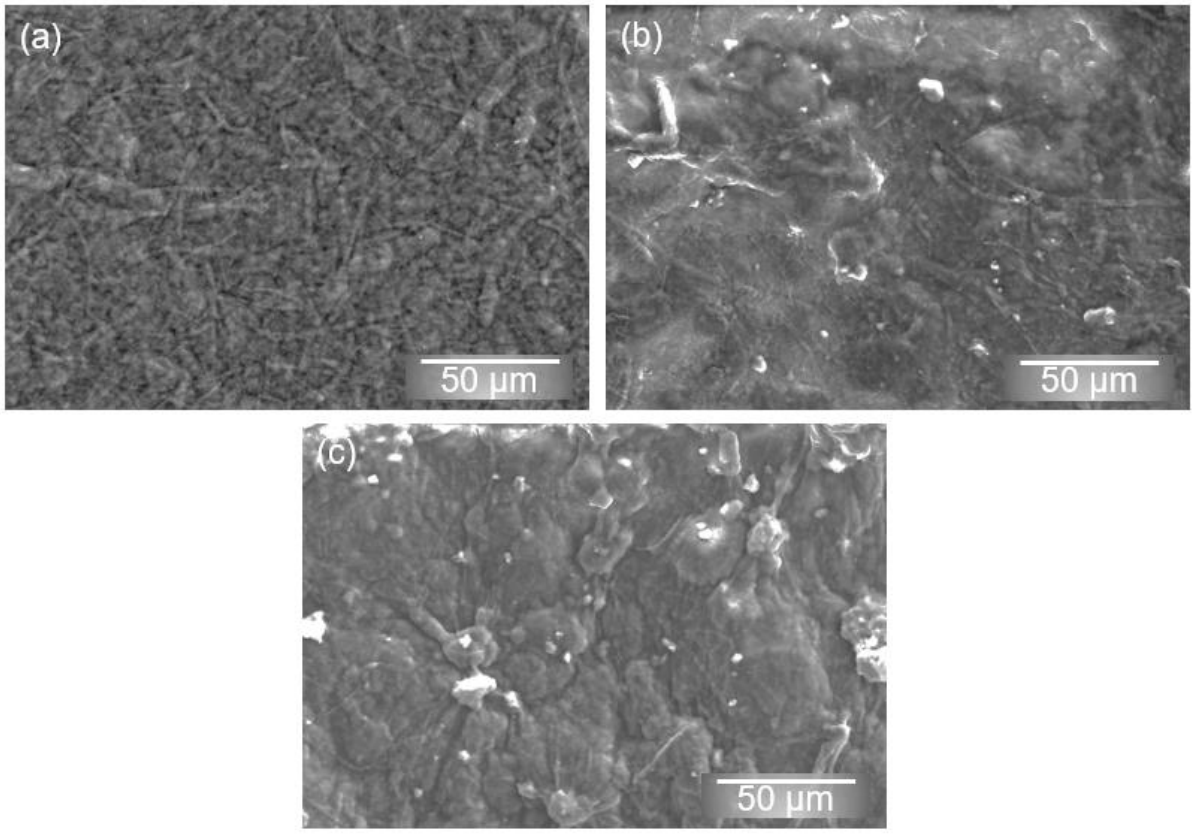

Figure 8.15: SEM images of the cellulose membranes: (a) pristine membrane, (b) membrane with TiO_2 and, (c) membrane with 10-Ca:TiO_2.

EDS analyses of the membranes were also performed (Figure 8.16). The pristine membrane was mainly composed of C and O. The analyses also revealed that Ti was uniformly distributed throughout the surface (for TiO_2 and 10-Ca:TiO_2 membranes), and present within the agglomerates. For the 10-Ca:TiO_2 membrane, Ca was also evident with the dark purple spots (Figure 8.16 (l)), composing the randomly distributed agglomerates at the surface.

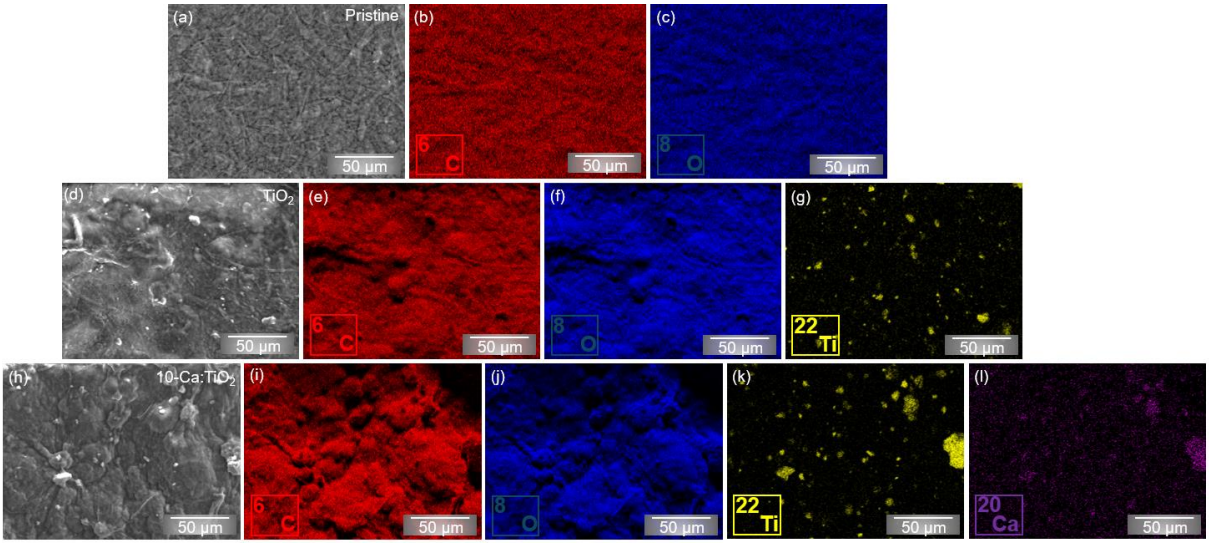

Figure 8.16: EDS maps of the pristine cellulose membrane, TiO_2 and 10-Ca:TiO_2 membranes. EDS maps show the corresponding elemental mapping images of carbon ((b), (e), (i)) – represented in red; oxygen ((c), (f), (j)) – blue; titanium ((g), (k)) – yellow; and calcium (l) – purple.

Figure 8.17 presents SEM cross-section images of the membranes. The pristine membrane exhibits a dense and compact structure, characterized by the closely packed fiber arrangement typical of nanopaper membranes [84,85]. The addition of nanopowders results in a noticeable change in morphology, characterized by a more open structure and the formation of channels within the membrane. As shown in Figure 8.17, both TiO_2 and 10-Ca:TiO_2 membranes exhibit an expressive increase in surface roughness. This higher roughness is highly desirable for the removal of pollutants as these surfaces are more susceptible to fouling than membranes with smoother textures (more attachment sites for pollutant molecules) [86]. The average thicknesses of the membranes were also determined, with values of 44.6 $\pm$ 4.6 µm, 36.2 $\pm$1.3 µm; 33.2 $\pm$ 4.5 µm for the pristine, TiO_2 and 10-Ca:TiO_2 membranes, respectively (n = 5). The significant morphological changes resulting from the addition of nanopowders can explain the observed variations in membrane thicknesses. Furthermore, from EDS measurements, it was confirmed that the nanoparticles of TiO_2 and 10-Ca:TiO_2 formed agglomerates completely embedded within the cellulose fiber matrix (Figure 8.17 (g), (k), (l) and see the arrows indication in Figure 8.17 (c), (k) and (l)). Additionally, it is evident that the TiO_2 agglomerates were not confined to the surface but well distributed throughout the membrane structure. In agreement with the previously obtained EDS results (Figure 8.16), no impurities were detected in the membranes (Figure 8.17 (d)-(l)).

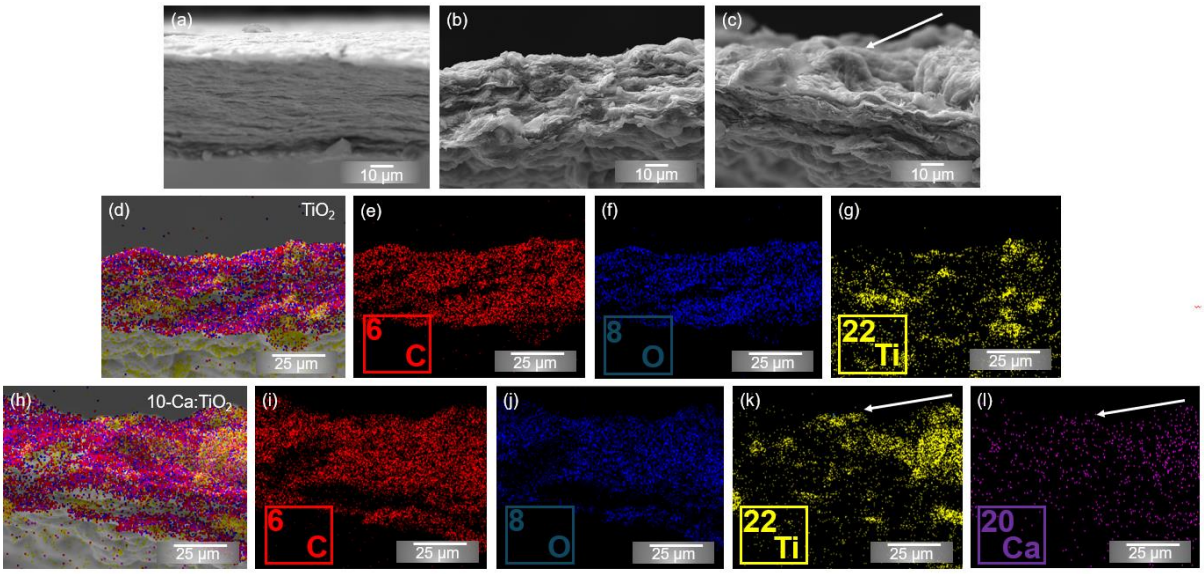

Figure 8.17: (a)-(c) SEM flat cross-section images of the pristine, TiO_2 and 10-Ca:TiO_2 membranes. The arrows indicate the presence of agglomerates embedded within the membranes. (d)-(l) The respective EDS maps of TiO_2 and 10-Ca:TiO_2 membranes are also visible. EDS maps show the corresponding elemental mapping images of carbon ((e), (i)) – represented in red; oxygen ((f), (j)) – blue; titanium ((g), (k)) – yellow; and calcium (l) – purple.

8.2.2.2 Adsorption and photodegradation of TC under simulated solar light and natural sunlight

The adsorption capacity of TC over different materials (pristine, TiO_2 and 10-Ca:TiO_2 cellulose-based membranes) is shown in Figure 8.18. Before performing the visible light degradation experiments, the adsorption properties of these materials were evaluated in the dark at RT for 120 min. Initially, the adsorption rate with all membranes was rapid during the first hour (Figure 8.18), owing to the abundance of available binding sites. Afterwards, the adsorption rate gradually slowed as the binding sites became saturated, in line with the reports of reference [87]. Several experimental conditions can influence the adsorption capacity and the mechanism of interaction between the adsorbate and adsorbent such as pH, temperature, adsorbent dosage, contact time, initial pollutant concentration, and adsorbent nature (e.g. adsorbent shape) [88]. In this study, pH, temperature, adsorbent dosage, contact time, and initial pollutant concentration were kept constant. Therefore, only the adsorbent nature is expected to influence the adsorption. Compared to the adsorption percentage of 25.5 % (adsorption capacity of ~11.8 mg. g^{-1}) with the TiO_2 membrane, the 10-Ca:TiO_2 membrane achieved a value of 55.9 % (adsorption capacity of ~25.8 mg. g^{-1}).

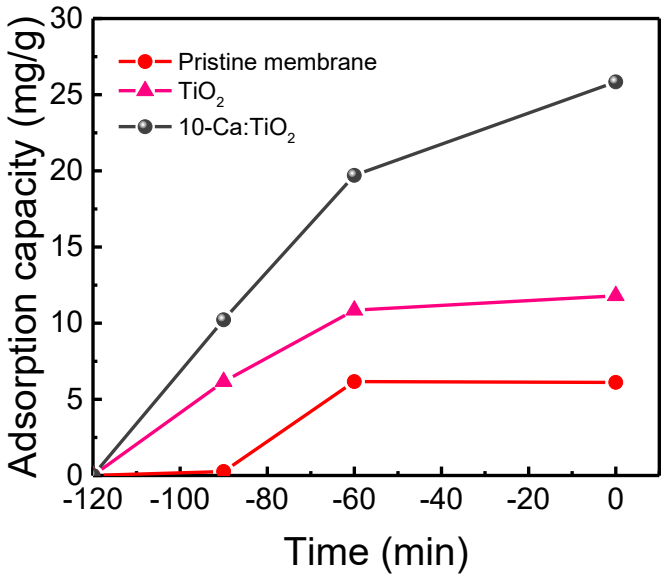

Figure 8.18: Effect of contact time on TC adsorption capacity onto pristine, TiO_2 and 10-Ca:TiO_2 membranes. Experimental conditions: q_{max}= 25.8 mg.g^{-1}, $[TC]_{initial}$= 23.11 ppm, $V_{solution}$= 12.5 mL, maximum adsorption time = 120 min, W = 6.25 mg.

The membrane with calcium demonstrated improved adsorption capability toward pollutant molecules. In fact, the rapid microwave heating combined with the addition of dopant atoms/impurities favored the formation of more defects in the materials, thereby extensively modifying the surface of the TiO_2, as revealed from the STEM images in Figure 8.3, Figure 8.5 and Figure 8.6. As indicated by the XPS results, the hydroxyl species in the calcium membranes might have also enhanced the binding of organic pollutant molecules [89].

To further understand the adsorption mechanism, kinetic studies were conducted by adjusting the experimental data to four adsorption models: the pseudo-first-order (Lagergren 1898), pseudo-second-order (Ho & McKay 1998), Elovich (Aharoni & Tompkins 1970), and intra-particle (Weber Jr. & Morris 1963) models [90–92]. The kinetic studies of the pristine and TiO_2 membranes were not further investigated due to their significantly lower adsorption capacity compared with the calcium-containing membrane. The obtained kinetic parameters for the 10-Ca:TiO_2 membrane are summarized in Table 8.5 and Table 8.6.

Table 8.5: Adsorption kinetic parameters of TC onto 10-Ca:TiO_2 adsorbent for the pseudo-first-order, pseudo-second-order and Elovich models.

Model	Parameters*						
	q_e^{exp}	q_e^{cal}	k_1	R^2	k_2	a_e	b_e
Pseudo-first-order**	25.8	316	0.13	0.75	-	-	-
Pseudo-second-order**	25.8	29.14	-	0.74	0.0015	-	-
Elovich**	25.8	-	-	0.97	-	0.975	0.089

* q_e^{exp} and q_e^{cal} are the experimental and calculated amounts of TC adsorbed at the equilibrium time ($mg.g^{-1}$), respectively; k_1 is the pseudo-first-order rate constant of TC adsorption (min^{-1}); k_2 is the pseudo−second-order adsorption rate ($g.mg^{-1}.min^{-1}$); a_e is the initial adsorption rate constant ($mg.g^{-1}.min^{-1}$); b_e is the extent of surface coverage and the activation energy for chemisorption ($g.mg^{-1}$); R^2 is the correlation coefficient

**To see the equations used, check Chapter 2 (equations (2.7), (2.8) and (2.9)).

Table 8.6: Adsorption kinetic parameters of TC onto 10-Ca:TiO_2 adsorbent for the intra-particle model.

Model	Parameters*								
	k_{id}^1	C^1	R_1^2	k_{id}^2	C^2	R_2^2	k_{id}^3	C^3	R_3^2
Intra-particle model**	1.87	2.83	1	4.18	-12.7	1	1.91	4.88	1

*$k_{id}^{1,2,3}$ are the intraparticle diffusion rate constants of the 1st, 2nd and 3rd stages, respectively ($mg.g^{-1}.min^{-0.5}$); $C^{1,2,3}$ are the values of the intercept of the 1st, 2nd and 3rd stages, respectively ($mg.g^{-1}$); $R_{1,2,3}^2$ are the correlation coefficients of the 1st, 2nd and 3rd stages, respectively.

**To see the equations used, check Chapter 2 (equation (2.10)).

Even though the correlation coefficients (R^2) for the pseudo-first-order and pseudo-second-order models were too low (below 0.80), the Elovich model is the one that could better describe the experimental data, showing an R^2 of 0.97 (Table 8.5). This model assumes that

adsorption occurs on localized sites and that the rate of adsorption of solute decreases exponentially as the amount of adsorbed solute increases, without the desorption of products. This suggests that the rate-limiting step in the process is chemisorption through bond sharing and interactions between the TC molecules and the active sites of the photocatalyst. These interactions are likely mediated by the functional groups in the pollutant (e.g., −OH, −C=O) and those on the photocatalyst surface (e.g., −Ti–OH). In this case, two types of adsorption probably exist [93]. First, the adsorption might occur at the lower energy surface sites of the photocatalyst, and then at the higher energy surface sites, resulting in a decrease in the adsorption rate [90,94–96]. Similar findings were observed for the adsorption of TC onto TiO_2 photocatalysts [93,97,98].

The intra-particle diffusion model was applied to understand the diffusion rate-controlling procedure, and the obtained parameters were included in Table 8.6. This model is based on the following assumptions: diffusion occurs in a radial direction; the external resistance to mass transfer of adsorbate molecules is negligible, and intraparticle or pore diffusivity remains constant over time and with position. Typically liquid–solid adsorption processes can be divided into three steps: in the first one, the mass transfer takes place from the bulk solution to the solid external surface (film diffusion); then, mass transfer into the pores of the adsorbent occurs (intraparticle diffusion), and finally, adsorbate molecules are adsorbed by physical or chemical mechanisms on the active sites of the solid [90,99]. Three linear regions can be identified in Figure 8.19, indicating that the intraparticle diffusion is not the only rate-controlling step. In the first stage (stage I), the adsorbate molecules are transferred from the bulk liquid to the external surface of the adsorbent, while in the second stage (stage II), the intraparticle diffusion becomes the rate-controlling step, involving the penetration of adsorbate molecules into the porous structure of the photocatalyst. In the final stage (stage III), the slope decreases (k_{id}^3) compared to stage II (Table 8.6), indicating a slowdown in intraparticle diffusion as the process approaches equilibrium and reaches maximum adsorption. Nevertheless, it is important to note that these results do not enable the identification of which process serves as the overall rate-limiting step in the adsorption mechanism [90,92,100].

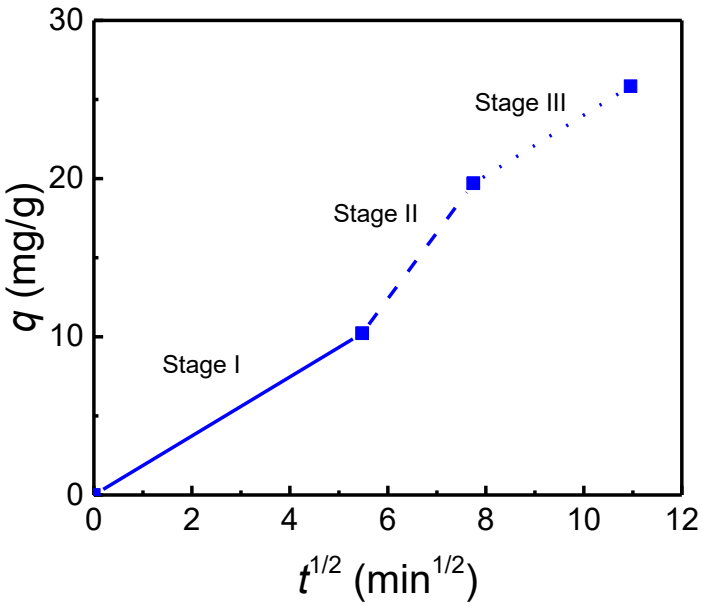

Figure 8.19: Intra-particle diffusion model plot for TC adsorption onto the 10-Ca:TiO_2 membrane. Stage I is represented by a solid blue line, while stages II and III are illustrated with dashed and dotted blue lines, respectively.

Photocatalytic experiments under simulated solar light were also conducted for the degradation of TC in the presence of the membranes, either pristine or with the photocatalysts (TiO_2 and 10-Ca:TiO_2), as presented in Figure 8.20. The real image of the membranes is shown in Figure 8.21. After mixing cellulose with the nanopowders, the membranes became less transparent and exhibited a more whitish appearance (Figure 8.21). During the black experiment (photolysis), the degradation of the TC solution without photocatalyst was minimal before and after light exposure (Figure 8.20), confirming the stability of the solution. Similarly, in the presence of the pristine membrane, only an overall small degradation value of 18 % was observed after light exposure.

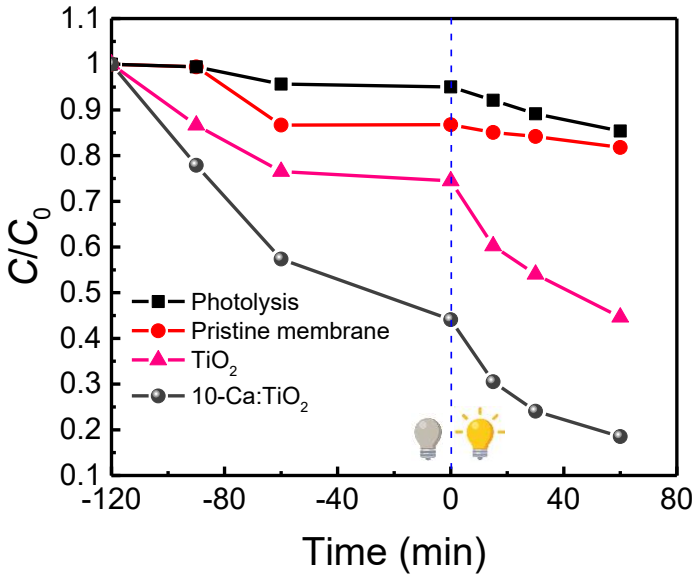

Figure 8.20: C/C_0 over time without (photolysis) and with the produced membranes for the TC removal and photodegradation in the dark conditions (for 120 min) and under simulated solar light (for 60 min). $[TC]_{Initial}$ = 23.11 ppm, W = 6.25 mg, $V_{solution}$ = 12. 5 mL.

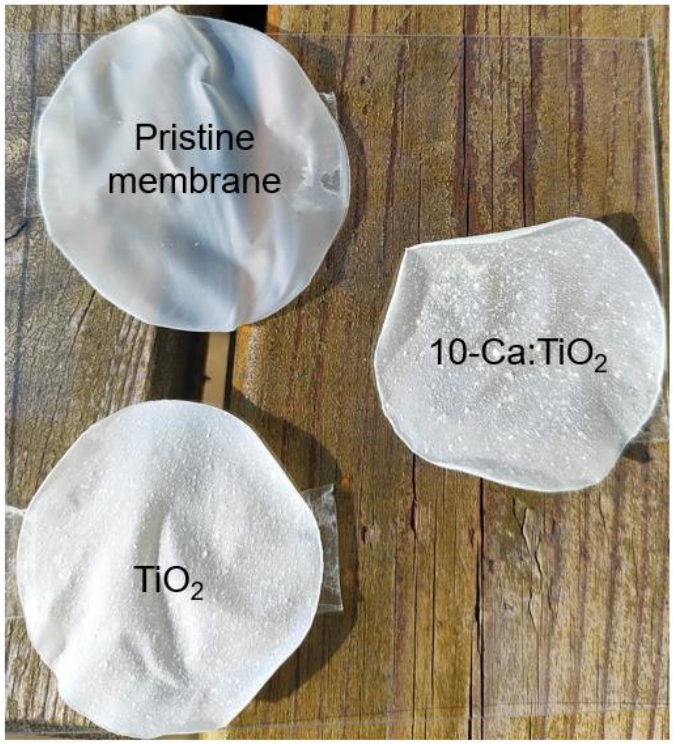

Figure 8.21: Real image of the cellulose-based membranes: pristine, with TiO_2 and 10-Ca:TiO_2 nanopowders.

After irradiation for 60 min, the overall percentage of adsorption + photocatalytic degradation of TC was 81 % in the presence of the 10-Ca:TiO_2 membrane. In contrast, it was 55 % with the TiO_2 membrane under the same conditions.

It is well known that the different synthesis parameters will determine the final material characteristics [101]. STEM analyses confirmed that microwave irradiation and calcium incorporation effectively induced several defects, namely lattice distortion, surface defects (irregularities at the surface, such as steps) and voids, as observed in the 10-Ca:TiO_2 material. As reported by Nishikawa *et al.*, lattice distortions of TiO_2 induced by doping can lead to the formation of potential slopes of the valence band maximum and conduction band minimum [102]. These potential slopes facilitate the separation of the photogenerated electron-hole pairs, improving the photocatalytic performance.

Bulk defects typically improve light absorption while acting as both charge carrier traps and recombination centers. In contrast, surface defects serve mostly as charge carrier traps and adsorption sites, promoting charge transfer to adsorbed species and photocatalytic reactions [39]. Nevertheless, by adjusting the concentration of metal ions, the surface-to-bulk defect ratio modifies, and an optimal ratio can enhance the efficiency of electron–hole separation [101].

Additionally, it has been reported that surface hydroxyl groups (Ti-OH) facilitate the transfer of carriers from the interior to the surface of the metal oxide by the formation of a high electron density to trap the photogenerated holes [103–105]. Not only is the charge separation process affected [106], but the formation of hydroxyl radicals can also be promoted upon the reaction of the terminated hydroxyl groups on the TiO_2 surface with the photoinduced holes [103,107].

In terms of specific surface area, the 10-TiO_2:Ca nanopowder had the highest surface area value (see Table 8.2), with a mesoporous character, which is anticipated to enhance the photocatalytic performance of the membrane, as the increased surface area provides more active sites, facilitating the generation of radical species and improving pollutant molecule adsorption, thereby boosting overall photocatalytic activity [108,109].

Part of the C/C_0 decay can be attributed to the adsorption of pollutants directly onto the membrane, as observed in the pristine membrane (Figure 8.20). Due to the distinct structural differences between the pristine and TiO_2-based membranes it is expected that the latter have a higher surface adsorption, since they exhibiting a more open and channeled

morphology. However, the membrane's structural contribution between TiO_2 and Ca-modified TiO_2 cannot be considered, given their similar surface roughness and thickness.

The kinetic parameters of TC photodegradation over TiO_2 and 10-Ca:TiO_2 membranes were determined, and the experimental data were fitted to the pseudo-first-order kinetic model (Table 8.7). Since this model did not fit the data well ($R^2 < 0.9$), the applicability of the pseudo-second-order model was examined [110,111], and the obtained kinetic parameters are also shown in Table 8.7.

Table 8.7: Kinetic parameters (rate constants and linear regression coefficients) for the TC degradation under simulated solar light with TiO_2 and 10-Ca:TiO_2 membranes.

	Kinetic parameters for each model[a]			
	Pseudo-first-order*		Pseudo-second-order*	
	k_{ap} (min^{-1})	R^2	k_{ap} ($L.mg^{-1}min^{-1}$)	R^2
TiO_2 membrane	0.016	0.81	2.94×10^{-4}	0.90
10-Ca:TiO_2 membrane	0.034	0.73	9.4×10^{-4}	0.99

[a] Reaction conditions: [TC] after dark = 17.2, 10.2 mg L^{-1} for the solutions with TiO_2 and 10-Ca:TiO_2 membranes. $V_{solution}$ = 12.5 mL, W = 6.25 mg, reaction time = 60 min, source of light: simulated solar light.

*To see the equations used, check Chapter 1 (equation 1.11) and Chapter 3 (equation 3.4).

For both TiO_2 and 10-Ca:TiO_2 membranes, a better fit was found for the pseudo-second-order model ($R^2 \geq 0.90$). This could be related to the formation of a low concentration of hydroxyl radical species in the degradation process [111]. This model assumes that the degradation process occurs in multiple stages involving the formation of various intermediate species. Unlike the pseudo-first-order model, which presumes that the degradation reaction rate is directly proportional to the concentration, the pseudo-second-order model suggests that the reaction is primarily governed by chemisorption interactions between adsorbent and adsorbate involving valence forces through sharing or exchanging electrons. This process creates a non-equilibrium of adsorption-desorption. Degradation processes exhibiting this type of kinetic behaviour have been previously reported, particularly when composites or combined systems are employed [111,112].

Photocatalytic experiments were also conducted under natural sunlight, maintaining the same experimental conditions as those used with simulated solar light, i.e. 120 min in the dark, except the light exposure duration, which was reduced to 30 min instead of 60 min, as the concentration of the solution tended to stabilize beyond this point (Figure 8.22).

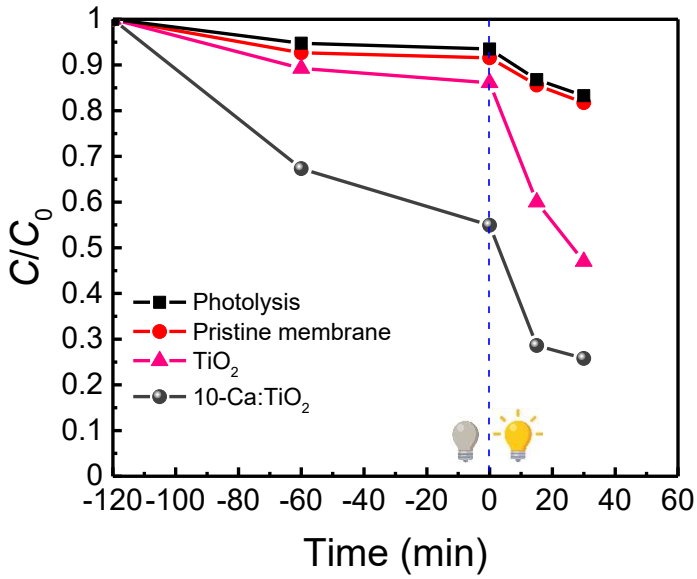

Figure 8.22: C/C_0 over time without (photolysis) and with the produced membranes for the TC removal and photocatalytic degradation in dark conditions (for 120 min) and under natural sunlight (for 30 min). [TC] = 23.11 ppm, W = 6.25 mg, $V_{solution}$= 12. 5 mL.

A similar adsorption + photocatalytic behaviour was observed across all samples compared to the exposure under simulated solar light. The 10-Ca:TiO_2 membrane demonstrated the best overall performance in terms of adsorption and photocatalytic activity, reaching a removal + degradation percentage of 74 %.

Cellulose-based materials have been widely studied for photocatalysis [113–117]. These materials are commonly used to form cellulosic fiber matrixes with metal oxide nanomaterials (composite materials) or as support to be immobilized with nanostructures and thin films, hence facilitating their reutilization [117,118]. Regarding the utilization of TiO_2/cellulose-based composites for the removal and degradation of tetracycline, only a limited number of studies were found. Zhang *et al.* produced an aerogel by freeze-drying based on cellulose and titanium dioxide materials which removed 86.48 % within 180 min under visible light (simulated solar light source). Almost the same percentage was obtained in the present study, though in 60 min of light exposure and without needing complex and multi-step experimental approaches [119]. Additionally, the fabricated Ca:TiO_2 membranes demonstrated the ability to remove TC even

in the absence of light, making them particularly promising for applications in light-deprived environments. The other research study by Kanmaz *et al.* reported the synthesis of a TiO_2-ethyl cellulose biocomposite by a solvent-free mechanochemical synthesis. The best adsorptive composite reached an adsorption capacity of 23.26 mg. g^{-1} in 480 min [92]. In contrast, in the present study, a similar adsorption capacity (25.8 mg. g^{-1}) of TC was obtained, but in just 120 min.

8.2.2.3 Recyclability tests

For practical uses, it is essential to have a stable photocatalyst with reusable characteristics. For that reason, the reusability of the best-performing 10-Ca:TiO_2 photocatalyst was investigated over 5 consecutive cycles under simulated solar light. Prior to the following cycle, the membrane was rinsed with deionized water and allowed to dry at RT before starting a new cycle with a fresh solution. The results presented in Figure 8.23 show a decrease of around 20 % in the performance of the catalyst after the fifth cycle (a reduction in membrane performance of 5.86 %, 7.34 %, 3.25 %, and 5.44 % was observed between the first and second, second and thrid, third and forth, and forth and fifth cycles, respectively). Only five cycles were performed, as the decrease in efficiency remained relatively consistent, ranging between 5 % and 7 %. TC molecules from previous cycles may remain adsorbed, blocking the active sites of the photocatalyst and reducing its overall cycling efficiency [12].

Regarding the disposal of photocatalytic platforms after use, cellulose offers a sustainable solution by enabling a second life for these platforms through recycling. This recycling process involves separating the cellulose fibers from the photocatalytic powder, recovering the fibers, and producing new recycled membranes [82].

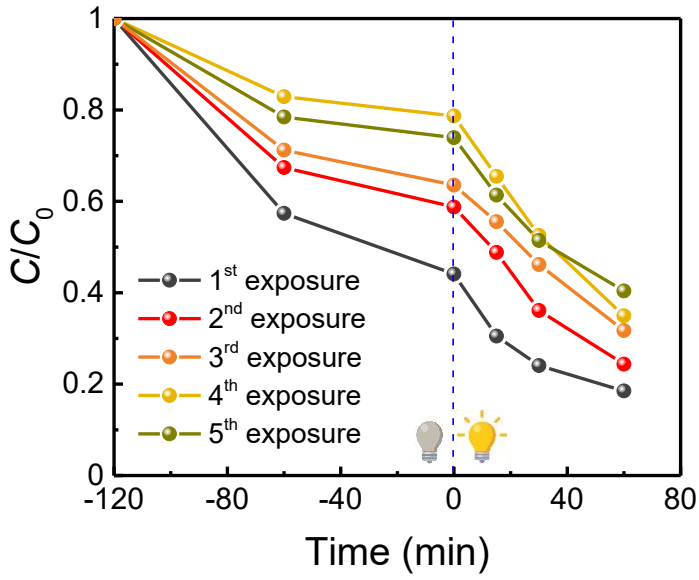

Figure 8.23: C/C_0 over time for the removal and degradation of TC under dark (for 120 min) and under simulated solar light (for 60 min) with the 10-Ca:TiO_2 membrane in 5 consecutive cycles.

8.2.2.4 ROS' scavengers experiments

Scavenger experiments were conducted to identify the ROS involved in the TC photocatalytic degradation process over the 10-Ca:TiO_2 membrane. Figure 8.24 shows a slight decrease in the degradation percentage upon the addition of the BQ scavenger, indicating that $^{\bullet}O_2^-$ radicals may be the major species that participate in the photocatalytic degradation process. These findings align with prior research demonstrating that superoxide radicals play a major role in the photocatalytic degradation of TC over TiO_2-based materials [120–122]. This trend was followed by holes, which have been indicated in other studies as key radical species involved in the photocatalytic degradation process under simulated solar light (Figure 8.24) [123,124]. Simultaneously, the results indicate that electrons, hydroxyl radicals and singlet oxygen species were the least important reactive species in the degradation process (Figure 8.24).

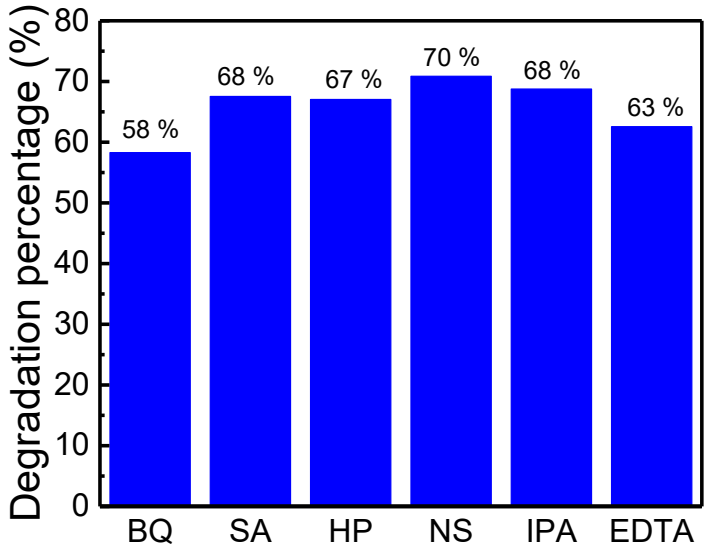

Figure 8.24: Effect of several scavengers (BQ, SA, HP, IPA and EDTA) on TC photocatalytic degradation over the 10-Ca:TiO_2 membrane under simulated solar light. For comparison, the photocatalytic degradation percentage of a solution without a scavenger (no scavenger (NS)) is also shown.

8.3 Summary

Ca-modified TiO_2 nanomaterials were developed by a microwave-assisted approach followed by a simple method to produce sustainable cellulose membranes for the degradation of TC under simulated solar light and natural sunlight. All produced nanomaterials (TiO_2, 5-Ca:TiO_2 and 10-Ca:TiO_2) exhibited a pure anatase phase, as confirmed by XRD measurements. A higher amount of calcium in the nanomaterials led to an increase in the specific surface area values, together with a higher density of structural defects, 0D, 1D, 2D and 3D defects. The formation of these structural defects was proved to be due to a synergetic effect of Ca concentration and microwave irradiation. XPS results indicated enhanced adsorption efficiency of hydroxyl groups, reflecting greater chemical reactivity on the surface of the 10-Ca:TiO_2 nanomaterial. DFT calculations predicted that substitutional Ca significantly facilitates the creation of O vacancies, introducing additional electronic states near the conduction band edge, namely by increasing the density of the oxygen vacancies, and thus enhancing electrical conductivity. The 10-Ca:TiO_2 cellulose membrane achieved an adsorption percentage of 55.9 % compared to 25.5 % with TiO_2 in 120 min. The best performance was achieved with the 10 mol. % Ca:TiO_2 membrane with an overall TC adsorption and degradation percentage of 81 % in 180 min under simulated solar light. These enhanced adsorptive and photocatalytic properties of the

developed membranes are a combination of the high surface area of Ca:TiO_2 agglomerates, the possible presence of oxygen vacancies, other structural defects, and surface hydroxyl groups. The approach developed in this study provides a sustainable solution for wastewater treatment and pollutant degradation, even in low-light conditions. This makes the membranes particularly promising for applications in environments with limited or no light. Furthermore, the membranes demonstrated reusability and recyclability, while the adopted approaches align with sustainability principles and circular economy and enable efficient scaling for practical applications.

8.4 References

1. Stöwe, K.; Weber, M. Niobium, Tantalum, and Tungsten Doped Tin Dioxides as Potential Support Materials for Fuel Cell Catalyst Applications. *Zeitschrift fur Anorganische und Allgemeine Chemie* **2020**, *646*, 1470–1480, doi:10.1002/ZAAC.201900345.
2. Yadav, V.; Verma, P.; Sharma, H.; Tripathy, S.; Saini, V. K. Photodegradation of 4-nitrophenol over B-doped TiO_2 nanostructure: effect of dopant concentration, kinetics, and mechanism. *Environmental Science and Pollution Research* **2020**, *27*, 10966–10980, doi:10.1007/S11356-019-06674-X.
3. Mahal, H. S.; Singh, B. P.; Kant, R. The effect of Co doping on structural, optical and dielectric behaviour of TiO_2 nanoparticles. *Defence Science Journal* **2021**, *71*, 390–394, doi:10.14429/DSJ.71.16720.
4. Arshad, Z.; Shakir, S.; Khoja, A. H.; Javed, A. H.; Anwar, M.; Rehman, A.; Javaid, R.; Qazi, U. Y.; Farrukh, S. Performance Analysis of Calcium-Doped Titania (TiO_2) as an Effective Electron Transport Layer (ETL) for Perovskite Solar Cells. *Energies* **2022**, *15*, 1408, doi:10.3390/EN15041408.
5. Kamal Yadav, R.; Chauhan, P. Estimation of lattice strain in Mn-doped ZnO nanoparticles and its effect on structural and optical properties. *Indian Journal of Pure & Applied Physics* **2019**, *57*, 881–890.
6. Vaisakhan Thampi, D. S.; Padala, P. R.; Renju, U. A. Influence of aliovalent cation substitution on structural and electrical properties of $Gd_2(Zr_{1-x}M_x)_2O_{7-\delta}$ (M = Sc, Y) systems. *RSC Advances* **2015**, *5*, 88675–88685, doi:10.1039/C5RA17203A.
7. Jiang, P.; Neuefeind, J. C.; Avdeev, M.; Huang, Q.; Yue, M.; Yang, X.; Cong, R.; Yang, T. Unprecedented lattice volume expansion on doping stereochemically active Pb^{2+} into uniaxially strained structure of $CaBa_{1-x}Pb_xZn_2Ga_2O_7$. *Nature Communications* **2020**, *11*, 1–7, doi:10.1038/s41467-020-14759-2.
8. Deng, B. L.; Zhu, X. L.; Liu, X. Q.; Chen, X. M. Effects of oxygen-deficiency on crystal structure, dielectric and ferroelectric properties in $Sr_5SmTi_{3+2x}Nb_{7-2x}O_{30-x}$ with tungsten bronze structure. *RSC Advances* **2017**, *7*, 27370–27376, doi:10.1039/C7RA03870D.
9. Phillips, R.; Jolley, K.; Zhou, Y.; Smith, R. Influence of temperature and point defects on the X-ray diffraction pattern of graphite. *Carbon Trends* **2021**, *5*, 100124, doi:10.1016/J.CARTRE.2021.100124.

10. Singh, J. P.; Lim, W. C.; Won, S. O.; Song, J.; Chae, K. H. Synthesis and Characterization of Some Alkaline-Earth-Oxide Nanoparticles. *Journal of the Korean Physical Society* **2018**, *72*, 890–899, doi:10.3938/JKPS.72.890.
11. Ali, A.; Chiang, Y. W.; Santos, R. M. X-ray Diffraction Techniques for Mineral Characterization: A Review for Engineers of the Fundamentals, Applications, and Research Directions. *Minerals* **2022**, *12*, 205, doi:10.3390/MIN12020205.
12. Matias, M. L.; Pimentel, A.; Reis-Machado, A.; Rodrigues, J. C.; Fernandes, A.; Monteiro, T.; Almeida Carvalho, P.; Neves Amaral, M. N.; Reis, C. P.; Deuermeier, J.; Fortunato, E.; Martins, R.; Nunes, D. Functionalized 3D Polyurethane Foams with Microwave-synthesized TiO_2 Nanostructures for Solar Light-driven Degradation of Tetracycline. *Environmental Science: Advances* **2025**, 4, 713–738 doi:10.1039/D4VA00110A.
13. Chen, R. S.; Liu, Y. L.; Chan, C. H.; Huang, Y. S. Photoconductivities in anatase TiO_2 nanorods. *Applied Physics Letters* **2014**, *105*, doi:10.1063/1.4898004/385079.
14. Wang, X.; Tian, J.; Fei, C.; Lv, L.; Wang, Y.; Cao, G. Rapid construction of TiO_2 aggregates using microwave assisted synthesis and its application for dye-sensitized solar cells. *RSC Advances* **2015**, *5*, 8622–8629, doi:10.1039/C4RA11266K.
15. Carlucci, C.; Xu, H.; Scremin, B. F.; Giannini, C.; Sibillano, T.; Carlino, E.; Videtta, V.; Gigli, G.; Ciccarella, G. Controllable one-pot synthesis of anatase TiO_2 nanorods with the microwave-solvothermal method. *Science of Advanced Materials* **2014**, *6*, 1668–1675, doi:10.1166/SAM.2014.1928.
16. Rosa, M. T.; Matias, M. L.; Bento, D.; Morais, M.; Pimentel, A.; Deuermeier, J.; Rodrigues, J.; Monteiro, T.; Martins, R.; Almeida, H.; Fortunato, E.; Nunes, D. Defective Cubic-ZrO_2 Nanomaterials Stabilized with Calcium Under Microwave Irradiation. *Materials Characterization* **2025**, 228, 115359, doi: 10.1016/j.matchar.2025.115359.
17. Prado-Gonjal, J.; Gutiérrez-Seijas, J.; Ansorregui, I. H.; Morán, E.; Terry, I.; Schmidt, R. The role of defects in microwave and conventionally synthesized $LaCoO_3$ perovskite. *Journal of the European Ceramic Society* **2016**, *36*, 1197–1206, doi:10.1016/J.JEURCERAMSOC.2015.12.014.
18. Gu, W.; Wang, W.; Li, G.; Xie, H.; Wong, P. K.; An, T. Microwave-assisted synthesis of defective tungsten trioxide for photocatalytic bacterial inactivation: Role of the oxygen vacancy. *Chinese Journal of Catalysis* **2020**, *41*, 1488, doi:10.1016/S1872-2067(19)63409-1.
19. Kabongo, G.; G, N.; K, O.; S, D. Microwave Irradiation Induces Oxygen Vacancy in Metal Oxides based Materials and Devices: A Review. *Journal of Nanosciences: Current Research* **2018**, *03*, doi:10.4172/2572-0813.1000125.
20. Yoshida, K.; Sonobe, T.; Zen, H.; Hachiya, K.; Okumura, K.; Mishima, K.; Inukai, M.; Negm, H.; Torgasin, K.; Omer, M.; Kinjo, R.; Kii, T.; Masuda, K.; Ohgaki, H. Effect of microwave irradiation on the electronic structure of ZnO. *Journal of Physics and Chemistry of Solids* **2015**, *83*, 47–51, doi:10.1016/J.JPCS.2015.03.013.
21. Thundiyil, R.; Poornesh, P.; Ozga, K.; Jedryka, J. An insight in to microwave induced defects and its impact on nonlinear process in NiO nanostructures under femtosecond and continuous wave laser excitation. *RSC Advances* **2024**, *14*, 30011–30036, doi:10.1039/D4RA06056C.
22. Ortega, P. P.; Amoresi, R. A. C.; Teodoro, M. D.; Merízio, L. G.; Ramirez, M. A.; Aldao, C. M.; Malagù, C.; Ponce, M. A.; Longo, E.; Simões, A. Z. Insights into the Morphology

and Structural Defects of Eu-Doped Ceria Nanostructures for Optoelectronic Applications in Red-Emitting Devices. *ACS Applied Nano Materials* **2024**, *7*, 12466–12479, doi:10.1021/ACSANM.4C00875.

23. Zayats, N. S.; Konakova, R. V.; Milenin, V. V.; Milenin, G. V.; Red'ko, R. A.; Red'ko, S. N. Microwave-radiation-induced structural transformations in homo- and heterogeneous GaAs-based systems. *Technical Physics* **2015**, *60*, 432–436, doi:10.1134/S1063784215030299.
24. Semenov, V. E.; Rybakov, K. I. Enhanced mass and charge transfer in solids exposed to microwave fields. In *Advances in Microwave and Radio Frequency Processing*; Willert-Porada, M., Ed.; Springer Verlag, 2006; pp. 472–481 ISBN 3540432523.
25. Horikoshi, S.; Minatodani, Y.; Tsutsumi, H.; Uchida, H.; Abe, M.; Serpone, N. Influence of lattice distortion and oxygen vacancies on the UV-driven/microwave-assisted TiO_2 photocatalysis. *Journal of Photochemistry and Photobiology A: Chemistry* **2013**, *265*, 20–28, doi:10.1016/J.JPHOTOCHEM.2013.05.010.
26. M., S. K.; Manamel, L. T.; Das, B. C.; M., S. K.; Manamel, L. T.; Das, B. C. Doping of Semiconductors at Nanoscale with Microwave Heating (Overview). In *Microwave Heating - Electromagnetic Fields Causing Thermal and Non-Thermal Effects*; Churyumov, G. I., Ed.; IntechOpen, 2021 ISBN 978-1-83968-227-8.
27. Xu, Y.; Wu, S.; Wan, P.; Sun, J.; Hood, Z. D. Introducing Ti^{3+} defects based on lattice distortion for enhanced visible light photoreactivity in TiO_2 microspheres. *RSC Advances* **2017**, *7*, 32461–32467, doi:10.1039/C7RA04885H.
28. Gnedenkov, S. V.; Sinebryukhov, S. L.; Zheleznov, V. V.; Opra, D. P.; Voit, E. I.; Modin, E. B.; Sokolov, A. A.; Ustinov, A. Y.; Sergienko, V. I. Effect of Hf-doping on electrochemical performance of anatase TiO_2 as an anode material for lithium storage. *Royal Society Open Science* **2018**, *5*, 1–14, doi:10.1098/RSOS.171811.
29. Chung, S.; Revia, R. A.; Zhang, M. Graphene Quantum Dots and Their Applications in Bioimaging, Biosensing, and Therapy. *Advanced materials* **2021**, *33*, 1–26, doi:10.1002/ADMA.201904362.
30. Pişkin, F.; Bliem, R.; Yildiz, B. Effect of crystal orientation on the segregation of aliovalent dopants at the surface of $La_{0.6}Sr_{0.4}CoO_3$. *Journal of Materials Chemistry A* **2018**, *6*, 14136–14145, doi:10.1039/C8TA01293H.
31. Tuschel, D. Effect of Dopants or Impurities on the Raman Spectrum of the Host Crystal. *Spectroscopy* **2017**, *32*, 13–18.
32. Diebold, U. The surface science of titanium dioxide. *Surface Science Reports* **2003**, *48*, 53–229, doi:10.1016/S0167-5729(02)00100-0.
33. Bak, T.; St, D.; Gannon, P.; Gür, T. M.; Jasiuk, I.; Sherif, S. A.; Sigmund, W. M.; Nowotny, J. *In situ* surface monitoring of energy materials during processing: impact of defect disorder on surface versus bulk semiconducting properties of photocatalytic hematite (Fe_2O_3). *Energy Advances* **2024**, *3*, 614–624, doi:10.1039/D3YA00482A.
34. Xu, J.; Xue, X. X.; Shao, G.; Jing, C.; Dai, S.; He, K.; Jia, P.; Wang, S.; Yuan, Y.; Luo, J.; Lu, J. Atomic-level polarization in electric fields of defects for electrocatalysis. *Nature Communications* **2023**, *14*, 1–9, doi:10.1038/s41467-023-43689-y.
35. Maarisetty, D.; Baral, S. S. Defect engineering in photocatalysis: formation, chemistry, optoelectronics, and interface studies. *Journal of Materials Chemistry A* **2020**, *8*, 18560–

18604, doi:10.1039/D0TA04297H.
36. Daskalakis, I.; Vamvasakis, I.; Papadas, I. T.; Tsatsos, S.; Choulis, S. A.; Kennou, S.; Armatas, G. S.; Armatas, G. S. Surface defect engineering of mesoporous Cu/ZnS nanocrystal-linked networks for improved visible-light photocatalytic hydrogen production. *Inorganic Chemistry Frontiers* **2020**, *7*, 4687–4700, doi:10.1039/D0QI01013H.
37. Fu, C.; Liu, L.; Li, Z.; Wei, Y.; Huang, W.; Zhang, X. Synergy of Bulk Defects and Surface Defects on TiO_2 for Highly Efficient Photocatalytic Production of H_2O_2. *Journal of Physical Chemistry Letters* **2023**, *14*, 7690–7696, doi:10.1021/ACS.JPCLETT.3C01865.
38. Yan, J.; Wu, G.; Guan, N.; Li, L.; Li, Z.; Cao, X. Understanding the effect of surface/bulk defects on the photocatalytic activity of TiO_2: anatase versus rutile. *Physical Chemistry Chemical Physics* **2013**, *15*, 10978–10988, doi:10.1039/C3CP50927C.
39. Liu, Y.; Wang, M.; Li, D.; Fang, F.; Huang, W. Engineering self-doped surface defects of anatase TiO_2 nanosheets for enhanced photocatalytic efficiency. *Applied Surface Science* **2021**, *540*, 148330, doi:10.1016/J.APSUSC.2020.148330.
40. Wu, S.; Ishisone, K.; Sheng, Y.; Manuputty, M. Y.; Kraft, M.; Xu, R. TiO_2 with controllable oxygen vacancies for efficient isopropanol degradation: photoactivity and reaction mechanism. *Catalysis Science & Technology* **2021**, *11*, 4060–4071, doi:10.1039/D1CY00417D.
41. Han, E.; Vijayarangamuthu, K.; Youn, J. sang; Park, Y. K.; Jung, S. C.; Jeon, K. J. Degussa P25 TiO_2 modified with H_2O_2 under microwave treatment to enhance photocatalytic properties. *Catalysis Today* **2018**, *303*, 305–312, doi:10.1016/J.CATTOD.2017.08.057.
42. Sharma, M.; Sajwan, D.; Gouda, A.; Sharma, A.; Krishnan, V. Recent progress in defect-engineered metal oxides for photocatalytic environmental remediation. *Photochemistry and Photobiology* **2024**, *100*, 830–896, doi:10.1111/PHP.13959.
43. Athithya, S.; Harish, S.; IKeda, H.; Shimomura, M.; Hayakawa, Y.; Archana, J.; Navaneethan, M. Hierarchically ordered macroporous TiO_2 architecture via self-assembled strategy for environmental remediation. *Chemosphere* **2022**, *288*, 132236, doi:10.1016/J.CHEMOSPHERE.2021.132236.
44. Thommes, M.; Kaneko, K.; Neimark, A. V.; Olivier, J. P.; Rodriguez-Reinoso, F.; Rouquerol, J.; Sing, K. S. W. Physisorption of gases, with special reference to the evaluation of surface area and pore size distribution (IUPAC Technical Report). *Pure and Applied Chemistry* **2015**, *87*, 1051–1069, doi:10.1515/PAC-2014-1117.
45. Dollimore, D.; Spooner, P.; Turner, A. The bet method of analysis of gas adsorption data and its relevance to the calculation of surface areas. *Surface Technology* **1976**, *4*, 121–160, doi:10.1016/0376-4583(76)90024-8.
46. Mohtar, S. S.; Aziz, F.; Ismail, A. F.; Sambudi, N. S.; Abdullah, H.; Rosli, A. N.; Ohtani, B. Impact of Doping and Additive Applications on Photocatalyst Textural Properties in Removing Organic Pollutants: A Review. *Catalysts* **2021**, *11*, 1160, doi:10.3390/CATAL11101160.
47. Sihotang, A.; Is Heriyanti, S.; Djangkung Sumbogo Murti, S.; Mirda Yanti, F.; Farizt Ichsan, A.; Adiningtyas Putri, A.; Riski Gusti, D. The Effect of Metal Impregnation Of Fe Cu And Co on Surface Area of ZSM-5 Catalyst Analyzed Using Surface Area Analyzer (AAS). *Al-Kimia* **2022**, *10*, doi:10.24252/AL-KIMIA.V10I2.32912.
48. Wajid Shah, M.; Zhu, Y.; Fan, X.; Zhao, J.; Li, Y.; Asim, S.; Wang, C. Facile Synthesis of

Defective TiO_{2-x} Nanocrystals with High Surface Area and Tailoring Bandgap for Visible-light Photocatalysis. *Scientific Reports* **2015**, *5*, 1–8, doi:10.1038/srep15804.
49. Matias, M. L.; Pimentel, A.; Reis-Machado, A. S.; Rodrigues, J.; Deuermeier, J.; Fortunato, E.; Martins, R.; Nunes, D. Enhanced Fe-TiO_2 Solar Photocatalysts on Porous Platforms for Water Purification. *Nanomaterials* **2022**, *12*.
50. Greczynski, G.; Hultman, L. Compromising Science by Ignorant Instrument Calibration—Need to Revisit Half a Century of Published XPS Data. *Angewandte Chemie International Edition* **2020**, *59*, 5002–5006, doi:10.1002/ANIE.201916000.
51. Egdell, R. G.; Rebane, J.; Walker, T. J. Competition between initial- and final-state effects in valence- and core-level x-ray photoemission of sb-doped SnO2. *Physical Review B - Condensed Matter and Materials Physics* **1999**, *59*, 1792–1799, doi:10.1103/PHYSREVB.59.1792.
52. Mahatha, S. K.; Menon, K. S. R. Inhomogeneous band bending on MoS_2 (0001) arising from surface steps and dislocations. *Journal of Physics: Condensed Matter* **2012**, *24*, 305502, doi:10.1088/0953-8984/24/30/305502.
53. Bharti, B.; Kumar, S.; Lee, H. N.; Kumar, R. Formation of oxygen vacancies and Ti^{3+} state in TiO_2 thin film and enhanced optical properties by air plasma treatment. *Scientific Reports* **2016**, *6*, 1–12, doi:10.1038/srep32355.
54. Zhang, W.; Wang, L.; Su, Y.; Liu, Z.; Du, C. Indium oxide/Halloysite composite as highly efficient adsorbent for tetracycline Removal: Key roles of hydroxyl groups and interfacial interaction. *Applied Surface Science* **2021**, *566*, 150708, doi:10.1016/J.APSUSC.2021.150708.
55. Cui, T.; Su, Y.; Fu, X.; Zhu, Y.; Zhang, Y. The key role of surface hydroxyls on the activity and selectivity in photocatalytic degradation of organic pollutants and NO removal. *Journal of Alloys and Compounds* **2022**, *921*, 165931, doi:10.1016/J.JALLCOM.2022.165931.
56. Hao, R.; Jiang, B.; Li, M.; Xie, Y.; Fu, H. Fabrication of mixed-crystalline-phase spindle-like TiO_2 for enhanced photocatalytic hydrogen production. *Science China Materials* **2015**, *58*, 363–369, doi:10.1007/S40843-015-0052-3.
57. Krishna, D. N. G.; Philip, J. Review on surface-characterization applications of X-ray photoelectron spectroscopy (XPS): Recent developments and challenges. *Applied Surface Science Advances* **2022**, *12*, 1–30, doi:10.1016/J.APSADV.2022.100332.
58. Sahnoun, R. Density functional theory of Ca/F co-doped anatase TiO_2. *Experimental and Theoretical NANOTECHNOLOGY* **2023**, *7*, 78–86, doi:10.56053/7.2.78.
59. Zhang, Z.; Li, B.; Qian, Q.; Tang, X.; Hua, M.; Huang, B.; Chen, K. J. Revealing the Nitridation Effects on GaN Surface by First-Principles Calculation and X-Ray/Ultraviolet Photoemission Spectroscopy. *IEEE Transactions on Electron Devices* **2017**, *64*, 4036–4043, doi:10.1109/TED.2017.2733547.
60. Mocatta, D.; Cohen, G.; Schattner, J.; Millo, O.; Rabani, E.; Banin, U. Heavily doped semiconductor nanocrystal quantum dots. *Science* **2011**, *332*, 77–81, doi:10.1126/SCIENCE.1196321.
61. Heinhold, R.; Allen, M. W. Polarity-dependent photoemission of in situ cleaved zinc oxide single crystals. *Journal of Materials Research* **2012**, *27*, 2214–2219, doi:10.1557/JMR.2012.181.
62. Vasheghani Farahani, S. K.; Veal, T. D.; Mudd, J. J.; Scanlon, D. O.; Watson, G. W.;

Bierwagen, O.; White, M. E.; Speck, J. S.; McConville, C. F. Valence-band density of states and surface electron accumulation in epitaxial SnO_2 films. *Physical Review B - Condensed Matter and Materials Physics* **2014**, *90*, 1–9, doi:10.1103/PHYSREVB.90.155413.

63. Veal, T. D.; Jefferson, P. H.; Piper, L. F. J.; McConville, C. F.; Joyce, T. B.; Chalker, P. R.; Considine, L.; Lu, H.; Schaff, W. J. Transition from electron accumulation to depletion at InGaN surfaces. *Applied Physics Letters* **2006**, *89*, 1–4, doi:10.1063/1.2387976.
64. Khan, J.; Han, L.; Khan, J.; Han, L. Oxygen Vacancy in TiO_2: Production Methods and Properties. In *Updates on Titanium Dioxide*; Bejaoui, B., Ed.; IntechOpen, 2023 ISBN 978-1-80355-673-4.
65. Ge, J.; Du, G.; Kalam, A.; Bi, X.; Ding, S.; Su, Q.; Xu, B.; Al-Sehemi, A. G. Oxygen vacancy-rich black TiO_2 nanoparticles as a highly efficient catalyst for Li–O_2 batteries. *Ceramics International* **2021**, *47*, 6965–6971, doi:10.1016/J.CERAMINT.2020.11.045.
66. Vijay, A.; Charan Prasanth, S.; Jose, R.; Saravanan K, V. Enhancement in the electrical transport properties of $CaMnO_3$ via La/Dy co-doping for improved thermoelectric performance. *RSC Advances* **2023**, *13*, 19651, doi:10.1039/D3RA03053A.
67. Mohamad Saad, P. S.; Sutan, H. B.; Shariffudin, S. S.; Hashim, H.; Mohd Noor, U. TiO_2 Thin Film via Sol-Gel Method: Investigation on Molarity Effect. *IOP Conference Series: Materials Science and Engineering* **2015**, *99*, doi:10.1088/1757-899X/99/1/012006.
68. Bhat, S.; Sandeep, K. M.; Kumar, P.; Venu, M. P.; Dharmaprakash, S. M.; Bhat, J. S. Effect of Al doping on the carrier transport characteristics of TiO_2 thin films anchored on glass substrates. *Applied Physics A: Materials Science and Processing* **2019**, *125*, 1–11, doi:10.1007/S00339-019-2464-5.
69. Lin, G.; Ju, Q.; Liu, L.; Guo, X.; Zhu, Y.; Zhang, Z.; Zhao, C.; Wan, Y.; Yang, M.; Huang, F.; Wang, J. Caged-Cation-Induced Lattice Distortion in Bronze TiO_2 for Cohering Nanoparticulate Hydrogen Evolution Electrocatalysts. *ACS Nano* **2022**, *16*, 9920–9928, doi:10.1021/ACSNANO.2C04513.
70. Al-Salim, N. I.; Bagshaw, S. A.; Bittar, A.; Kemmitt, T.; McQuillan, A. J.; Mills, A. M.; Ryan, M. J. Characterisation and activity of sol–gel-prepared TiO_2 photocatalysts modified with Ca, Sr or Ba ion additives. *Journal of Materials Chemistry* **2000**, *10*, 2358–2363, doi:10.1039/B004384M.
71. Liu, X.; Bi, Y. Synergistic effect of Ti^{3+} doping and facet regulation over Ti^{3+}-doped TiO_2 nanosheets with enhanced photoreactivity. *Catalysis Science and Technology* **2018**, *8*, 3876–3882, doi:10.1039/C8CY01016A.
72. Kumari, S.; Suthar, D.; Kumari, N.; Dhaka, M. Understanding Grain Growth Mechanism in Vacuum Evaporated CdTe Thin Films by Different Halide Treatments: An Evolution of Ion Size Impact on Physical Properties for Solar Cell Applications. *Comments on Inorganic Chemistry* **2022**, *43*, 429–464, doi:10.1080/02603594.2022.2142938.
73. S B, S. L.; Murali, M. D.; Posselt, M.; Sasikala Devi, A. A.; Sharan, A. Modified HSE06 functional applied to anatase TiO_2: influence of exchange fraction on the quasiparticle electronic structure and optical response. *Electronic Structure* **2022**, *4*, 045001, doi:10.1088/2516-1075/AC8F03.
74. Esfandfard, S. M.; Elahifard, M. R.; Behjatmanesh-Ardakanii, R.; Kargar, H. DFT study on oxygen-vacancy stability in rutile/anatase TiO_2: Effect of cationic substitutions. *Physical Chemistry Research* **2018**, *6*, 547–563, doi:10.22036/PCR.2018.128713.1481.

75. Perumal, R. N.; Subalakshmi, G. Near-infrared down-conversion in Yb^{3+}:TiO_2 for solar cell applications. *Journal of Materials Science: Materials in Electronics* **2017**, *28*, 1837–1843, doi:10.1007/S10854-016-5734-4.
76. Gibbs, Z. M. Band Engineering in Thermoelectric Materials Using Optical, Electronic, and Ab-Initio Computed Properties, PhD thesis, California Institute of Technology, 2015.
77. Makuła, P.; Pacia, M.; Macyk, W. How To Correctly Determine the Band Gap Energy of Modified Semiconductor Photocatalysts Based on UV-Vis Spectra. *Journal of Physical Chemistry Letters* **2018**, *9*, 6814–6817.
78. Hansson, G. V.; Uhrberg, R. I. G. Surface States on Semiconductors. In *Studies in Surface Science and Catalysis*; Kevan, S. D., Ed.; Elsevier, 1992; Vol. 74, pp. 145–212.
79. Xu, J.; Teng, Y.; Teng, F. Effect of Surface Defect States on Valence Band and Charge Separation and Transfer Efficiency. *Scientific Reports* **2016**, *6*, 1–9, doi:10.1038/srep32457.
80. Fauzi, A.; Hapidin, D. A.; Munir, M. M.; Iskandar, F.; Khairurrijal, K. A superhydrophilic bilayer structure of a nylon 6 nanofiber/cellulose membrane and its characterization as potential water filtration media. *RSC Advances* **2020**, *10*, 17205–17216, doi:10.1039/D0RA01077D.
81. Pereira, L.; Gaspar, D.; Guerin, D.; Delattre, A.; Fortunato, E.; Martins, R. The influence of fibril composition and dimension on the performance of paper gated oxide transistors. *Nanotechnology* **2014**, *25*, 094007, doi:10.1088/0957-4484/25/9/094007.
82. Gaspar, D.; Martins, J.; Carvalho, J. T.; Grey, P.; Simões, R.; Fortunato, E.; Martins, R.; Pereira, L. Alkali-Doped Nanopaper Membranes Applied as a Gate Dielectric in FETs and Logic Gates with an Enhanced Dynamic Response. *ACS Applied Materials and Interfaces* **2023**, *15*, 8319–8326, doi:10.1021/ACSAMI.2C20486/.
83. Vicente, A. T.; Araújo, A.; Gaspar, D.; Santos, L.; Marques, A. C.; Mendes, M. J.; Pereira, L.; Fortunato, E.; Martins, R. Optoelectronics and Bio Devices on Paper Powered by Solar Cells. In *Nanostructured Solar Cells*; Narottam, D., Ed.; InTech, 2017; p. 35.
84. Nunes, D.; Pimentel, A.; Araujo, A.; Calmeiro, T. R.; Panigrahi, S.; Pinto, J. V.; Barquinha, P.; Gama, M.; Fortunato, E.; Martins, R. Enhanced UV Flexible Photodetectors and Photocatalysts Based on TiO_2 Nanoplatforms. *Springer Nature* **2018**, *61*, 1591–1606.
85. Grey, P.; Fernandes, S. N.; Gaspar, D.; Fortunato, E.; Martins, R.; Godinho, M. H.; Pereira, L.; Grey, P.; Fernandes, S. N.; Gaspar, D.; Fortunato, E.; Martins, R.; Godinho, M. H.; Pereira, L. Field-Effect Transistors on Photonic Cellulose Nanocrystal Solid Electrolyte for Circular Polarized Light Sensing. *Advanced Functional Materials* **2019**, *29*, 1805279, doi:10.1002/ADFM.201805279.
86. Chen, W.; Ye, T.; Xu, H.; Chen, T.; Geng, N.; Gao, X. An ultrafiltration membrane with enhanced photocatalytic performance from grafted N–TiO_2/graphene oxide. *RSC Advances* **2017**, *7*, 9880–9887, doi:10.1039/C6RA27666K.
87. Ezati, F.; Sepehr, E.; Ahmadi, F. The efficiency of nano-TiO_2 and γ-Al_2O_3 in copper removal from aqueous solution by characterization and adsorption study. *Scientific Reports* **2021**, *11*, 1–14, doi:10.1038/s41598-021-98051-3.
88. Iftekhar, S.; Ramasamy, D. L.; Srivastava, V.; Asif, M. B.; Sillanpää, M. Understanding the factors affecting the adsorption of Lanthanum using different adsorbents: A critical

review. *Chemosphere* **2018**, *204*, 413–430, doi:10.1016/J.CHEMOSPHERE.2018.04.053.
89. Vasić, V.; Kukić, D.; Šćiban, M.; Đurišić-Mladenović, N.; Velić, N.; Pajin, B.; Crespo, J.; Farre, M.; Šereš, Z. Lignocellulose-Based Biosorbents for the Removal of Contaminants of Emerging Concern (CECs) from Water: A Review. *Water* **2023**, *15*, 1853, doi:10.3390/W15101853.
90. Dalto, F.; Kuźniarska-Biernacka, I.; Pereira, C.; Mesquita, E.; Soares, O. S. G. P.; Pereira, M. F. R.; Rosa, M. J.; Mestre, A. S.; Carvalho, A. P.; Freire, C. Solar light-induced methylene blue removal over TiO_2/AC composites and photocatalytic regeneration. *Nanomaterials* **2021**, *11(11)*, 1–24, doi:10.3390/NANO11113016.
91. Nippes, R. P.; Macruz, P. D.; Coslop, T. F.; Molinari, D.; Scaliante, M. H. N. O. Removal of ivermectin from aqueous media using commercial, bentonite-based organophilic clay as an adsorbent. *Clay Minerals* **2022**, *57*, 21–30, doi:10.1180/CLM.2022.16.
92. Kanmaz, N.; Buğdaycı, M.; Demirçivi, P. Solvent-free mechanochemical synthesis of TiO_2-ethyl cellulose biocomposite for adsorption of tetracycline and organic dyes. *Journal of Molecular Liquids* **2023**, *378*, 121643, doi:10.1016/J.MOLLIQ.2023.121643.
93. Adesina, M. O.; Block, I.; Günter, C.; Unuabonah, E. I.; Taubert, A. Efficient Removal of Tetracycline and Bisphenol A from Water with a New Hybrid Clay/TiO_2 Composite. *ACS Omega* **2023**, *8*, 21594–21604, doi:10.1021/acsomega.3c00184.
94. Kajjumba, G. W.; Emik, S.; Öngen, A.; Aydın, H. K. Ö.; Serdar, A.; Kajjumba, G. W.; Emik, S.; Öngen, A.; Aydın, H. K. Ö.; Serdar, A. Modelling of Adsorption Kinetic Processes—Errors, Theory and Application. In *Advanced Sorption Process Applications*; IntechOpen, 2018 ISBN 978-1-78984-819-9.
95. Álvarez-Torrellas, S.; Ribeiro, R. S.; Gomes, H. T.; Ovejero, G.; García, J. Removal of antibiotic compounds by adsorption using glycerol-based carbon materials. *Chemical Engineering Journal* **2016**, *296*, 277–288, doi:10.1016/J.CEJ.2016.03.112.
96. Largitte, L.; Pasquier, R. A review of the kinetics adsorption models and their application to the adsorption of lead by an activated carbon. *Chemical Engineering Research and Design* **2016**, *109*, 495–504, doi:10.1016/J.CHERD.2016.02.006.
97. Pete, K. Y.; Kabuba, J.; Otieno, B.; Ochieng, A. Modeling adsorption and photocatalytic treatment of recalcitrant contaminant on multi-walled carbon/TiO_2 nanocomposite. *Environmental Science and Pollution Research* **2023**, *30*, 94154–94165, doi:10.1007/S11356-023-28852-8.
98. Fu, D.; Huang, Y.; Zhang, X.; Kurniawan, T. A.; Ouyang, T. Uncovering potentials of integrated TiO_2(B) nanosheets and H_2O_2 for removal of tetracycline from aqueous solution. *Journal of Molecular Liquids* **2017**, *248*, 112–120, doi:10.1016/J.MOLLIQ.2017.10.020.
99. Inglezakis, V. J.; Balsamo, M.; Montagnaro, F. Liquid-Solid Mass Transfer in Adsorption Systems - An Overlooked Resistance? *Industrial and Engineering Chemistry Research* **2020**, *59*, 22007–22016, doi:10.1021/ACS.IECR.0C05032.
100. Ojedokun, A. T.; Bello, O. S. Kinetic modeling of liquid-phase adsorption of Congo red dye using guava leaf-based activated carbon. *Applied Water Science* **2017**, *7*, 1965–1977, doi:10.1007/S13201-015-0375-Y.
101. Piler, K.; Bahrim, C.; Twagirayezu, S.; Benson, T. J. Lattice disorders of TiO_2 and their significance in the photocatalytic conversion of CO_2. In *Advances in Catalysis*; Song, C.,

Ed.; Academic Press, 2020; Vol. 66, pp. 109–233 ISBN 9780128203699.
102. Nishikawa, M.; Yuto, S.; Nakajima, T.; Tsuchiya, T.; Saito, N. Effect of Lattice Distortion on Photocatalytic Performance of TiO_2. *Catalysis Letters* **2017**, *147*, 292–300, doi:10.1007/S10562-016-1928-X.
103. Xiao, S. T.; Wu, S. M.; Dong, Y.; Liu, J. W.; Wang, L. Y.; Wu, L.; Zhang, Y. X.; Tian, G.; Janiak, C.; Shalom, M.; Wang, Y. T.; Li, Y. Z.; Jia, R. K.; Bahnemann, D. W.; Yang, X. Y. Rich surface hydroxyl design for nanostructured TiO_2 and its hole-trapping effect. *Chemical Engineering Journal* **2020**, *400*, 125909, doi:10.1016/J.CEJ.2020.125909.
104. Zhu, K.; Frehan, S. K.; Mul, G.; Huijser, A. Dual Role of Surface Hydroxyl Groups in the Photodynamics and Performance of NiO-Based Photocathodes. *Journal of the American Chemical Society* **2022**, *144*, 11010–11018, doi:10.1021/jacs.2c04301.
105. Huang, J.; Liu, S.; Long, W.; Wang, Q.; Yu, X.; Li, S. Highly enhanced photodegradation of emerging pollutants by Ag/AgCl/Ta_2O_{5-x} mesocrystals. *Separation and Purification Technology* **2021**, *279*, 119733, doi:10.1016/J.SEPPUR.2021.119733.
106. Pan, X.; Yang, M. Q.; Fu, X.; Zhang, N.; Xu, Y. J. Defective TiO_2 with oxygen vacancies: Synthesis, properties and photocatalytic applications. *Nanoscale* **2013**, *5*, 3601–3614, doi:10.1039/C3NR00476G.
107. Rychtowski, P.; Tryba, B.; Skrzypska, A.; Felczak, P.; Sreńscek-Nazzal, J.; Wróbel, R. J.; Nishiguchi, H.; Toyoda, M. Role of the Hydroxyl Groups Coordinated to TiO_2 Surface on the Photocatalytic Decomposition of Ethylene at Different Ambient Conditions. *Catalysts* **2022**, *12*, 386, doi:10.3390/CATAL12040386.
108. Bento, D. H.; Matias, M. L.; Magalhães, M.; Quitério, C.; Pimentel, A.; Sousa, D.; Amaral, P.; Galhano, C.; Fortunato, E.; Martins, R.; Nunes, D. Self-cleaning stone Façades using TiO_2 Microwave-Synthesised Coatings. *Cleaner Materials* **2025**, *15*, 100294, doi:10.1016/J.CLEMA.2025.100294.
109. Wei, X.; Zhu, G.; Fang, J.; Chen, J. Synthesis, characterization, and photocatalysis of well-dispersible phase-pure anatase TiO_2 nanoparticles. *International Journal of Photoenergy* **2013**, *2013(7268)*, 1–6, doi:10.1155/2013/726872.
110. Foroutan, R.; Peighambardoust, S. J.; Boffito, D. C.; Ramavandi, B. Sono-Photocatalytic Activity of Cloisite 30B/ZnO/Ag_2O Nanocomposite for the Simultaneous Degradation of Crystal Violet and Methylene Blue Dyes in Aqueous Media. *Nanomaterials* **2022**, *12*, doi:10.3390/NANO12183103.
111. Argote-Fuentes, S.; Feria-Reyes, R.; Ramos-Ramírez, E.; Gutiérrez-Ortega, N.; Cruz-Jiménez, G. Photoelectrocatalytic Degradation of Congo Red Dye with Activated Hydrotalcites and Copper Anode. *Catalysts* **2021**, *11*, 211, doi:10.3390/CATAL11020211.
112. Tran, H. D.; Nguyen, D. Q.; Do, P. T.; Tran, U. N. P. Kinetics of photocatalytic degradation of organic compounds: a mini-review and new approach. *RSC Advances* **2023**, *13*, 16915–16925, doi:10.1039/D3RA01970E.
113. Sudhaik, A.; Raizada, P.; Ahamad, T.; Alshehri, S. M.; Nguyen, V. H.; Van Le, Q.; Thakur, S.; Thakur, V. K.; Selvasembian, R.; Singh, P. Recent advances in cellulose supported photocatalysis for pollutant mitigation: A review. *International Journal of Biological Macromolecules* **2023**, *226*, 1284–1308, doi:10.1016/J.IJBIOMAC.2022.11.241.
114. Mafra, G.; Brognoli, R.; Carasek, E.; López-Lorente, Á. I.; Luque, R.; Lucena, R.; Cárdenas, S. Photocatalytic Cellulose-Paper: Deepening in the Sustainable and Synergic

Combination of Sorption and Photodegradation. *ACS Omega* **2021**, *6*, 9577–9586, doi:10.1021/ACSOMEGA.1C00128.

115. Matias, M. L.; Nunes, D.; Pimentel, A.; Ferreira, S. H.; Borda D'Agua, R.; Duarte, M. P.; Fortunato, E.; Martins, R. Paper-based nanoplatforms for multifunctional applications. *Journal of Nanomaterials* **2019**, *2019*, doi:10.1155/2019/6501923.
116. Pimentel, A.; Samouco, A.; Nunes, D.; Araújo, A.; Martins, R.; Fortunato, E. Ultra-Fast Microwave Synthesis of ZnO Nanorods on Cellulose Substrates for UV Sensor Applications. *Materials* **2017**, *10(11)*, 1308, doi:10.3390/MA10111308.
117. Nunes, D.; Pimentel, A.; Branquinho, R.; Fortunato, E.; Martins, R. Metal oxide-based photocatalytic paper: A green alternative for environmental remediation. *Catalysts* **2021**, *11(4)*, 1–30, doi:10.3390/catal11040504.
118. Zhang, J.; Liu, W.; Wang, P.; Qian, K. Photocatalytic behavior of cellulose-based paper with TiO_2 loaded on carbon fibers. *Journal of Environmental Chemical Engineering* **2013**, *1*, 175–182, doi:10.1016/J.JECE.2013.04.022.
119. Zhang, Y.; Liu, F.; Zhong, L.; Dong, Z.; Chen, C.; Xu, Z. Reusable and environmentally friendly cellulose nanofiber/titanium dioxide/chitosan aerogel photocatalyst for efficient degradation of tetracycline. *Applied Surface Science* **2023**, *641*, 158425, doi:10.1016/J.APSUSC.2023.158425.
120. Wu, F. Di; Chen, J. C.; Hu, J. P. Synthesis of $TiO_2/Ti_3C_2T_X$/AgI Z-scheme photocatalyst for tetracycline hydrochloride photocatalytic degradation. *Journal of Environmental Chemical Engineering* **2022**, *10*, 107117, doi:10.1016/J.JECE.2021.107117.
121. Divakaran, K.; Baishnisha, A.; Balakumar, V.; Perumal, K. N.; Meenakshi, C.; Kannan, R. S. Photocatalytic degradation of tetracycline under visible light using TiO_2@sulfur doped carbon nitride nanocomposite synthesized via in-situ method. *Journal of Environmental Chemical Engineering* **2021**, *9*, *4*, 105560, doi:10.1016/J.JECE.2021.105560.
122. Salmanzadeh-Jamadi, Z.; Habibi-Yangjeh, A.; Pouran, S. R.; Xu, X.; Wang, C. Facile fabrication of TiO_2/Bi_5O_7Br photocatalysts for visible-light-assisted removal of tetracycline and dye wastewaters. *Journal of Physics D: Applied Physics* **2022**, *55*, 165105, doi:10.1088/1361-6463/AC48AF.
123. Liu, Y.; Zhang, H.; Zhu, D.; Duan, J.; Clement Miruka, A.; Tang, L.; Li, P.; Cai, L. Enhanced degradation of tetracycline by TiO_2@MXene with peroxydisulfate under visible light irradiation. *Separation and Purification Technology* **2024**, *343*, 127122, doi:10.1016/J.SEPPUR.2024.127122.
124. Palominos, R. A.; Mondaca, M. A.; Giraldo, A.; Peñuela, G.; Pérez-Moya, M.; Mansilla, H. D. Photocatalytic oxidation of the antibiotic tetracycline on TiO_2 and ZnO suspensions. *Catalysis Today* **2009**, *144*, 100–105, doi:10.1016/J.CATTOD.2008.12.031.
125. Nunes, D.; Pimentel, A.; Barquinha, P.; Mendes, M.; Coelho, J.; Almeida, H.; Fortunato, E.; Martins, R. Metal–oxide-based flexible photocatalysts. In *Flexible Devices Based on Metal Oxides*; Nunes, D., Pimentel, A., Barquinha, P., Mendes, M., Coelho, J., Almeida, H., Fortunato, E., Martins, R., Eds.; Elsevier, 2025; pp. 533–579 ISBN 978-0-443-21656-5.

9

FUTURE PERSPECTIVES AND FINAL REMARKS

This PhD thesis highlighted the potential of sustainable solutions to treat polluted water using TiO_2-based nanopowders/platforms. Therefore, several fabrication processes and the systematic characterization of the produced materials were presented. Eco-friendly and simple microwave-assisted methods were conducted to develop solar-light-driven TiO_2-based nanostructures, demonstrating high efficiency in removing and degrading various water pollutants. The degradation was evaluated under solar radiation (simulated solar light and natural sunlight). To address the challenges of recovery and recyclability of nanopowders, the TiO_2-based nanostructures were incorporated or directly synthesized onto various inexpensive and eco-friendly substrates, either floating or non-floating, namely cork, cellulose-based materials (mixed cellulose esters and pristine cellulose), resin, and polyurethane foams. Microwave irradiation followed by several impregnation techniques (direct synthesis, drop-casting and dip-coating) was suitable for producing TiO_2-based platforms with great adsorptive and photocatalytic properties. These properties were enhanced by employing several strategies to modify TiO_2, which included the fabrication of a heterostructure (g-C_3N_4/TiO_2), the creation of surface defects, and doping with two different abundant metal ions: Fe^{3+} and Ca^{2+}. Therefore, all proposed objectives were accomplished.

9.1 Floating photocatalysts *vs.* non-floating photocatalysts

Floating photocatalysts, such as cork and PU foams, remain on the water surface and offer several advantages over non-floating alternatives: (i) maximization in the utilization of solar energy and good surface oxygenation, (ii) easy recovery and recyclability from water solutions, reducing time and costs with subsequent water treatments; (iii) lower energy consumption, since they revealed good photocatalytic performance without magnetic stirring, thus making them highly suitable for lakes and other low-agitation water bodies. Moreover, they provide future potential for integration with solar cells, maximizing solar energy utilization for simultaneous energy generation and water treatment.

However, studies involving non-floating platforms (in this case, impregnated cork, resin, and cellulose-based substrates) demonstrated comparable effectiveness in pollutant removal and degradation in aqueous systems. The selection between floating and non-floating substrates depends on the final application: floating catalysts are advantageous for outdoor large-scale water treatment systems due to their ease of recovery and sunlight accessibility, while non-floating ones exhibit enhanced stability in fixed systems and versatile applicability

(e.g., self-cleaning surfaces, immobilized configurations). The latter are particularly suited for gas-phase reactions and scenarios requiring precise control over the reaction parameters (e.g., flow rate, light intensity) in controlled industrial environments, such as continuous flow reactors where immobilization on reactor walls is essential.

9.2 Experimental conditions of photocatalytic tests

Both anionic (i.e., MO) and cationic (i.e., RhB) model dyes, as well as TC (an antibiotic), were tested in the photocatalytic experiments. Since real effluents typically contain multiple pollutants, investigating potential interactions between different chromophores is crucial for developing effective water treatment strategies. Although using the same TiO_2-based substrate for degrading multiple pollutants posed challenges due to the complexity of the involved reactions, these studies demonstrated the successful degradation of various water contaminants, including dyes (RhB and MO) and antibiotics (tetracycline) using sustainable TiO_2-based platforms. Other pollutants, such as phenol and caffeine, were also tested in the photocatalytic experiments; however, since the investigated materials were unable to degrade them, these results were not included. To bridge the gap between laboratory and real-world conditions, experiments were conducted with tap water, revealing promising potential for practical implementation. The experiments with TiO_2 PU foams revealed that tap water had little effect on both TC adsorption and photocatalytic performance compared to Milli-Q water, with only a slight efficiency reduction (~13%).

Detailed investigations on removal efficiency, degradation kinetics, and optimization of key process parameters, including pH, temperature, and pollutant/photocatalyst concentration are essential, as these factors contribute to the performance of the photocatalysts. The impact of these last parameters should be explored in more detail in future studies. Moreover, integrating photocatalysis with other advanced oxidation processes could further boost efficiency and cost-effectiveness.

9.3 Adsorption and photocatalytic degradation of different pollutants over TiO_2-based platforms

Among all the impregnated substrates developed, the highest efficiency in RhB removal and degradation was achieved under simulated solar light using TiO_2 nanostructures containing 5 mol. % iron on water filters, reaching a combined adsorption and degradation rate of

85 %, compared to 74 % with pure TiO_2, after 3.5 hours of light exposure. This enhanced performance was attributed to the interaction between the substrates' microporosity and the surface-modified Fe:TiO_2 nanostructures, greatly improving their photocatalytic activity. The 3D-printed TiO_2 architectures after the impregnation and microwave synthesis also demonstrated the ability to degrade RhB under the same solar light conditions, achieving a degradation rate of 72 % with the larger structure, in contrast to 44 % with the thinner structure. The architectural design was crucial in defining the final photocatalytic behavior. Finally, the TiO_2 cork substrates, particularly those exposed to natural sunlight, exhibited the highest RhB decolorization efficiency, reaching 67 % after 4 h of light exposure, compared to 39 % with the pristine substrate. When considering powder photocatalysts, they are expected to have higher efficiency compared to impregnated platforms due to their superior surface-to-volume ratios [1]. Nevertheless, for the degradation of the MO dye, the 30 wt. % g-C_3N_4/TiO_2 heterostructure exhibited the best performance, achieving 85 % degradation in 4 h. Although the immobilization of this photocatalyst on a substrate was not explored in the current study, subsequent research should prioritize its incorporation into sustainable substrates, such as those examined in this thesis. This integration should employ environmentally friendly processes while adopting a lifecycle perspective, including the recycling of these platforms after their end-of-life, in alignment with circular economy principles. In terms of TC adsorption and degradation, both defective TiO_2 nanostructures on PU foams and TiO_2 membranes with 10 mol. % Ca exhibited a comparable overall efficiency, achieving approximately 80 % adsorption and degradation under simulated solar light within 240 min (60 min dark + 180 light exposure) and 180 min (120 min dark + 60 min light exposure), respectively. However, the Ca-modified TiO_2 membrane achieved this degradation percentage value in a shorter time than the PU foam. These findings underscore that doping, heterostructure formation, and defect engineering of TiO_2 are effective strategies for enhancing photocatalytic performance.

As demonstrated in some cases in this thesis, scavenger agents were insufficient for identifying the ROS involved in the photocatalytic degradation process. An alternative approach could be the use of electron paramagnetic resonance spectroscopy (EPR). In this technique, upon exposure to a magnetic field, the species that have unpaired electrons (e.g. ROS), absorb electromagnetic radiation at specific frequencies, causing the electron spins to align in different orientations (paramagnetism). From this interaction, the EPR spectrum can give detailed information about the type, concentration, and nature of the ROS [2,3]. *In situ* (mimics local environments) and *operando* (under operation) studies could also provide valuable insights

into the reaction mechanisms and facilitate the design of high-performance catalysts. By allowing the monitoring of catalysts during photocatalytic reactions, species and intermediates that are often undetectable under ex-situ conditions can be detected. This real-time data is crucial for elucidating reaction pathways and identifying active sites. Moreover, structural, bonding, and reactivity changes of the catalysts can be revealed during reactions, thus enabling researchers to get a more comprehensive understanding of the relationship between catalyst properties and performance under reaction conditions, enabling the development of materials tailored to specific applications [4–6].

In addition, tracking the levels of TOC, which reflects the amount of organic material in water, is crucial for assessing how well drinking water treatment systems are performing. Reducing TOC is essential for meeting regulatory standards, as elevated levels can promote the formation of harmful byproducts that may persist in the environment and pose significant health risks. The standard approach for measuring TOC involves oxidizing the organic matter present in the water and transforming it into quantifiable forms. Therefore, the degree of mineralization in the photocatalytic processes should be studied in the future using TOC analysers [9].

The TiO_2 platforms investigated were reusable for the tested number of cycles; however, further research should ensure that nanostructures are not released during longer cycling tests (even months or years), for instance with an inductively coupled plasma technique, to facilitate the transition from laboratory studies to real-world applications.

Before implementing these TiO_2 platforms in practical applications, it is important to assess their impact on aquatic organisms, as shown with TiO_2 PU foams, which were environmentally safe for aquatic systems, thus contributing to sustainability. However, further research is required to identify the physicochemical properties of the nanomaterials that could potentiate adverse effects on the species and explore the interactions between nanomaterials and cells.

9.4 Adsorption and photocatalytic degradation of contaminants with real polluted water samples

To better evaluate the real-life applicability of the photocatalytic degradation process, experiments should first be conducted using tap water. This assessment will also facilitate the application of the process to real contaminated water samples, ultimately enabling its

implementation in industrial wastewater treatment systems. Assessing the individual impact of organic and inorganic ions present in the water, the physicochemical properties of water (e.g. pH and conductivity), as well as the photocatalyst's properties such as surface charge are vital for comprehending the photodegradation process of organic pollutants. The study of toxicity from the by-products formed after the photocatalytic degradation process in these systems is equally important.

9.5 Combining photocatalysis and 3D printing technologies

SLA 3D printing technology was explored to construct 3D porous and photocatalytic architectures of resin-based TiO_2 nanostructures. The freedom of design allowed the construction of porous architectures, significantly influencing the final photocatalytic performance. Despite showing great potential for fabricating catalysts and reactors, the successful implementation of 3D printing technologies requires interdisciplinary expertise to address several challenges. These include optimizing the printing slurry with well-dispersed, stable, and cost-effective photoactive nanomaterials, refining the structural design while ensuring high catalytic performance of the 3D structures, and improving scalable printing methods.

9.6 Integration of computational methods for further advances in photocatalysis

As demonstrated for the work of Ca-modified TiO_2 membranes, DFT calculations played a key role in studying the impact of calcium addition on the TiO_2 properties. Therefore, it is predicted that not only the optimization of the photocatalyst properties (including the exploration of various strategies to turn the catalysts active under the whole spectrum of solar radiation) but also finding the best photocatalytic conditions can be significantly accelerated by integrating computational predictions before experimental implementation.

9.7 Final remarks

This PhD thesis demonstrated that efficient and sustainable platforms of TiO_2-based nanostructures with adsorptive and photocatalytic properties can be developed through fast, non-toxic, simple microwave-assisted methods, even at low temperatures. As water scarcity and water pollution continue to pose global challenges, the combination of photocatalysis with

other advanced oxidation processes and novel nanomaterials may offer sustainable solutions to ensure clean and safe water for future generations. This synergy lays the foundation for a healthier society by ensuring universal access to safe water, sanitation, and hygiene, improving water quality, and protecting/restoring water-related ecosystems. This PhD research contributes specifically to achieving the latter two goals. Nevertheless, the scope of this thesis extends beyond this specific application, as the advanced nanomaterials developed can also be integrated into sensing, energy harvesting, conversion and storage, and various other technological domains. Their versatility, sustainability, and abundance make them highly promising for a wide range of applications. Moreover, their photoactive properties under solar radiation, the most abundant energy source on Earth, further enhance their potential for environmentally friendly and energy-efficient solutions.

9.8 References

1. Thakur, S.; Ojha, A.; Kansal, S. K.; Gupta, N. K.; Swart, H. C.; Cho, J.; Kuznetsov, A.; Sun, S.; Prakash, J. Advances in powder nano-photocatalysts as pollutant removal and as emerging contaminants in water: Analysis of pros and cons on health and environment. *Advanced Powder Materials* **2024**, *3*, 100233, doi:10.1016/J.APMATE.2024.100233.
2. Al-Madanat, O.; Nunes, B. N.; Alsalka, Y.; Hakki, A.; Curti, M.; Patrocinio, A. O. T.; Bahnemann, D. W. Application of EPR Spectroscopy in TiO_2 and Nb_2O_5 Photocatalysis. *Catalysts* **2021**, *11*, 1514, doi:10.3390/CATAL11121514.
3. Villamena, F. A.; Zweier, J. L. Detection of reactive oxygen and nitrogen species by EPR spin trapping. *Antioxidants & redox signaling* **2004**, *6*, 619–629, doi:10.1089/152308604773934387.
4. Roldán Cuenya, B.; Bañares, M. A. Introduction: Operando and In Situ Studies in Catalysis and Electrocatalysis. *Chemical Reviews* **2024**, *124*, 8011–8013, doi:10.1021/ACS.CHEMREV.4C00184.
5. Chen, L.; Ding, X.; Wang, Z.; Xu, S.; Jiang, Q.; Dun, C.; Urban, J. J. Advances in in situ/operando techniques for catalysis research: enhancing insights and discoveries. *Surface Science and Technology* **2024**, *2*, 1–23, doi:10.1007/S44251-024-00038-5.
6. Zaera, F. *In-situ* and *operando* spectroscopies for the characterization of catalysts and of mechanisms of catalytic reactions. *Journal of Catalysis* **2021**, *404*, 900–910, doi:10.1016/J.JCAT.2021.08.013.

10 OUTPUTS

10.1 Publications

Published scientific papers/book chapters related to this PhD thesis (5):

- **Matias, M. L.**; Pimentel, A.; Reis-Machado, A. S.; Rodrigues, J.; Deuermeier, J.; Fortunato, E.; Martins, R.; Nunes, D. Enhanced Fe-TiO_2 Solar Photocatalysts on Porous Platforms for Water Purification. *Nanomaterials* **2022**, *12*.
- **Matias, M. L.**; Morais, M.; Pimentel, A.; Vasconcelos, F. X.; Reis Machado, A. S.; Rodrigues, J.; Fortunato, E.; Martins, R.; Nunes, D. Floating TiO_2-Cork Nano-Photocatalysts for Water Purification Using Sunlight. *Sustainability* **2022**, *14(15)*, 9645, doi:10.3390/SU14159645/S1.
- **Matias, M. L.**; Reis-Machado, A. S.; Rodrigues, J.; Calmeiro, T.; Deuermeier, J.; Pimentel, A.; Fortunato, E.; Martins, R.; Nunes, D. Microwave Synthesis of Visible-Light-Activated g-C_3N_4/TiO_2 Photocatalysts. *Nanomaterials* **2023**, *13(6)*, doi:10.3390/NANO13061090/S1.
- **Matias, M. L.**; Pimentel, A.; Reis-Machado, A.; Rodrigues, J. C.; Fernandes, A.; Monteiro, T.; Almeida Carvalho, P.; Neves Amaral, M. N.; Reis, C. P.; Deuermeier, J.; Fortunato, E.; Martins, R.; Nunes, D. Functionalized 3D Polyurethane Foams with Microwave-synthesized TiO_2 Nanostructures for Solar Light-driven Degradation of Tetracycline. *Environmental Science: Advances* **2025**, 4, 713–738 doi:10.1039/D4VA00110A.
- Xue, R.; **Matias, M. L.**; Pimentel, A.; Pinto, J. V.; Fortunato, E.; Martins, R. Photocatalytic Activity of 3D Printed TiO_2 Architectures Under Solar Radiation. In *Photocatalysis for Environmental Remediation and Energy Production*; Green Chemistry and Sustainable Technology; Springer International Publishing, 2023; pp. 79–100 ISBN 978-3-031-27706-1.

List of scientific articles under revision/accepted related to this PhD thesis (2):

- **Matias**, M. L.; Gaspar D.; Carvalho, D.; Pimentel, A.; Pereira, L.; Machado, A. S. Reis; Rodrigues, J.; Monteiro, T.; Deuermeier, D.; Martins, R.; Fortunato, E.; Nunes, D. Defect-Engineered Ca-TiO_2 Nanomaterials for Enhanced Adsorption and Photocatalytic Degradation of Water Pollutants on Sustainable Cellulose Membranes. *Advanced Sustainable Systems* **2025**, e00675. https://doi.org/10.1002/adsu.202500675.

- **Matias**, M. L., Pimentel, A., Fortunato, E., Martins, R.; Nunes, D. Advanced Cellulose-Based Photocatalysts for Environmental Remediation. In *Chapter 7: Advanced Cellulose-Based Photocatalysts for Environmental Remediation, vol. 3* - Handbook of Paper based sensors and devices, Springer.

Other relevant scientific studies published during the development of this PhD thesis (4):

- **Matias, M. L.**; Carlos, E.; Branquinho, R.; do Valle, H.; Marcelino, J.; Morais, M.; Pimentel, A.; Rodrigues, J.; Monteiro, T.; Fortunato, E.; Martins, R.; Nunes, D. A Comparison between Solution-Based Synthesis Methods of ZrO_2 Nanomaterials for Energy Storage Applications. *Energies* **2022**, *15(17)*, 6452, doi:10.3390/EN15176452/S1.
- Rosa, M. T.; **Matias, M. L.**; Bento, D.; Morais, M.; Pimentel, A.; Deuermeier, J.; Rodrigues, J.; Monteiro, T.; Martins, R.; Almeida, H.; Fortunato, E.; Nunes, D. Defective Cubic-ZrO_2 Nanomaterials Stabilized with Calcium Under Microwave Irradiation. *Materials Characterization* **2025**, 228, 115359, doi: 10.1016/j.matchar.2025.115359.
- **Matias, M. L.**; Pereira, C.; Almeida, H. V.; Jana, S.; Panigrahi, S.; Menda, U. D.; Nunes, D.; Fortunato, E.; Martins, R.; Nandy, S. 3D printed MXene architectures for a plethora of smart applications. *Materials Today Advances* **2024**, *23*, 100512, doi:10.1016/J.MTADV.2024.100512.
- Bento, D. H.; **Matias, M. L.**; Magalhães, M.; Quitério, C.; Pimentel, A.; Sousa, D.; Amaral, P.; Galhano, C.; Fortunato, E.; Martins, R.; Nunes, D. Self-cleaning stone Façades using TiO_2 Microwave-Synthesised Coatings. *Cleaner Materials* **2025**, *15*, 100294, doi:10.1016/J.CLEMA.2025.100294.

10.2 Scientific conferences/meetings

Oral communications (7):

- **Matias, M. L.**; Pimentel, A.; Reis-Machado, A. S.; Rodrigues, J.; Deuermeier, J.; Fortunato, E.; Martins, R.; Nunes, D. Enhanced Fe-TiO_2 solar photocatalysts on porous platforms for water purification. Materiais 2022 – April 10-13, 2022, Marinha Grande, Portugal.

The abstract from the conference is available in the following reference: Matias, M. L.; Pimentel, A.; Reis Machado, A. S.; Rodrigues, J.; Deuermeier, J.; Fortunato, E.; Martins, R.; Nunes, D. The Effect of Iron on TiO_2 Nanostructures Deposited on Porous Platforms for Water Purification. *Materials Proceedings* **2022**, *8*, 146, doi:10.3390/MATERPROC2022008146.

- **Matias, M. L.**; Morais, M.; Pimentel, A.; Vasconcelos, F. X.; Reis Machado, A. S.; Rodrigues, J.; Fortunato, E.; Martins, R.; Nunes, D. Floating catalysts activated under solar light based on nano-TiO_2 materials grown on cork for water purification. EMRS Spring 2022 – May 30-June 03, 2022, online.

  The oral presentation was on May 31 in the section of Functional films II (session chair: Tanaka Hidekazu) N 6.1.

- **Matias, M. L.**; Morais, M.; Pimentel, A.; Vasconcelos, F. X.; Reis Machado, A. S.; Rodrigues, J.; Fortunato, E.; Martins, R.; Nunes, D. TiO_2 nano-floating photocatalysts grown on cork for water purification using natural sunlight. 11th European School for Young Materials Scientists 2022 – September 27-28, 2022, FCT-UNL, Portugal.

  The oral presentation was on September 28 in the section of Oxide materials and thin-films session (chairperson: prof. Pedro Barquinha), talk 15.

- **Matias, M. L.**; Reis-Machado, A. S.; Rodrigues, J.; Calmeiro, T.; Deuermeier, J.; Pimentel, A.; Fortunato, E.; Martins, R.; Nunes, D. Photocatalytic behaviour of visible-light activated g-C_3N_4/TiO_2 heterojunctions. AdvPhotoCat-EE2023 (invited speaker) – July 25-28, 2023, online.

  The oral presentation was on July 27 in section 3 (chairs D. McCormack and Y. Mahmoud).

- **Matias, M. L.**; Reis-Machado, A. S.; Rodrigues, J.; Calmeiro, T.; Deuermeier, J.; Pimentel, A.; Fortunato, E.; Martins, R.; Nunes, D. Solar light-driven activated g-

C_3N_4/TiO_2 photocatalysts synthesized by microwave irradiation. FEMS EUROMAT 2023 – September 03-07, 2023, Frankfurt Am Main, Germany.

The oral presentation was on September 06 in section A05.02: Functional Catalytic and Nanoporous Materials-2, lecture #1244 (session chair Prof. Sixto Giménez).

- **Matias, M. L.**; Morais, M.; Pimentel, A.; Vasconcelos, F. X.; Reis Machado, A. S.; Rodrigues, J.; Fortunato, E.; Martins, R.; Nunes, D. Microwave-assisted synthesis of photocatalysts based on nano TiO_2 materials for water remediation. 12th European School for Young Materials Scientists 2023 – November 07-08, 2023, Brno, Czech Republic.

  The oral presentation was on November 8 in the section of Advanced materials.

- **Matias, M. L.**; Pimentel, A.; Reis-Machado, A.; Rodrigues, J. C.; Fernandes, A.; Monteiro, T.; Almeida Carvalho, P.; Neves Amaral, M. N.; Reis, C. P.; Deuermeier, J.; Fortunato, E.; Martins, R.; Nunes, D. Microwave-assisted synthesis of 3D TiO_2-polyurethane foams for the degradation of antibiotics under solar radiation. MSE 2024 – September 24-26, 2024, Darmstadt, Germany.

  The oral presentation was on September 26 In the F10.02: Session 2 (F10: 3D Structural Design of Functional Materials for Smart Applications), lecture #1028 (session chair Prof. João Mano).

Poster communications (3):

- **Matias, M. L.**; Reis Machado, A. S.; Rodrigues, J.; Fortunato, E.; Martins, R.; Nunes, D. Eco-friendly TiO_2-based platforms produced by microwave-assisted approaches to treat wastewater. IX Annual Meeting i3N – May 02-03, 2024, Leiria, Portugal. P17
- **Matias, M. L.**; Morais, M.; Pimentel, A.; Reis Machado, A. S.; Rodrigues, J.; Deuermeier, J.; Calmeiro, T.; Fortunato, E.; Martins, R.; Nunes, D. Microwave-assisted synthesis of TiO_2-based nanostructures activated by solar energy for water purification. SPMicros Conference 2024 – September 13, 2024, Braga (INL), Portugal.

- **Matias, M. L.;** Morais, M.; Pimentel, A.; Reis Machado, A. S.; Rodrigues, J.; Deuermeier, J.; Calmeiro, T.; Fortunato, E.; Martins, R.; Nunes, D. Sustainable TiO_2 platforms produced with the aid of microwave with potential for the degradation of water contaminants. EurASc Annual Symposium & Ceremony 2024 – October 29-30, 2024, Academia das Ciências, Portugal. P14

10.3 Workshops/courses

- **Project Management I** course from NOVA Doctoral School – May 05, 15, 22 and 29, 2023, online, Portugal.
- **3rd FIT4NANO workshop** – July 17-19, 2023, Faculty of Pharmacy, University of Lisbon.
- **Correlative Materials Characterization Workshop 2023** – November 09-10, 2023, Brno, Czech Republic.

10.4 Projects

This PhD thesis is integrated in the project "Sustainable Stone by Portugal" with the ref. a110405010101, approved and financed by Portugal's Recovery and Resilience Plan (cf. Aviso N-o-02/C05-i01/2022). The development of functionalized stone surfaces is proposed with self-cleaning abilities to be applied as facade claddings, protecting building walls while contributing to environmental remediation. Titanium dioxide (TiO_2) will cover the second-life stone materials using the easily up-scaling and green microwave synthesis technique. These functionalized materials will be directly installed on building facades originating photocatalytic stone surfaces, capable of removing dirt while purifying air. FCT NOVA has already developed the process, providing the Industrial Partners with all the technology behind the deposition of the TiO_2 photoactive layers and assisting the implementation of industrial microwave equipment for large-scale production. Hence, the integration of TiO_2 nanostructures on sustainable substrates, such as stone, through microwave irradiation is necessary to achieve the task of functionalized stone. This task is related to the research aims of this PhD thesis.

10.5 Invitations

Invitation to submit cover artwork for issue no. 5 of *Environmental Science: Advances* related to the publication of the paper: "Functionalized 3D Polyurethane Foams with Microwave-synthesized TiO_2 Nanostructures for Solar Light-driven Degradation of Tetracycline."

A

Appendix

Figure A.1 shows the Raman spectroscopy measurements of the cork substrates (pristine and with TiO_2).

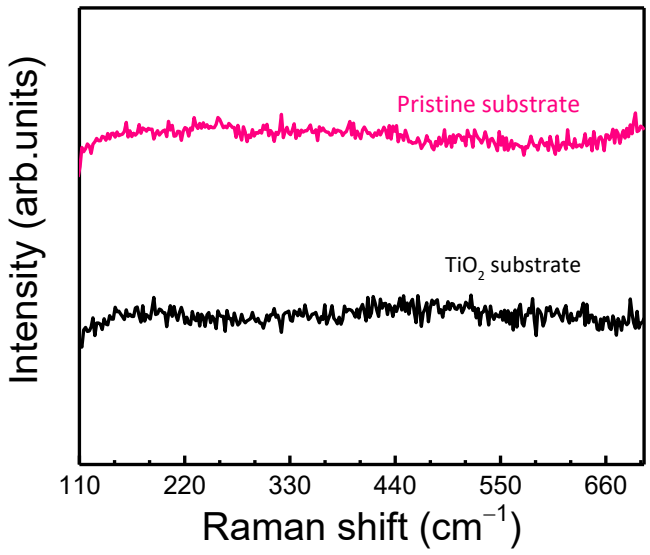

Figure A.1: Raman spectra of the cork substrates (pristine and with TiO_2).

Figure A.2 reveals the presence of very fine particles highly agglomerated for the TiO_2 nanopowder synthesized in the absence of the cork substrates.

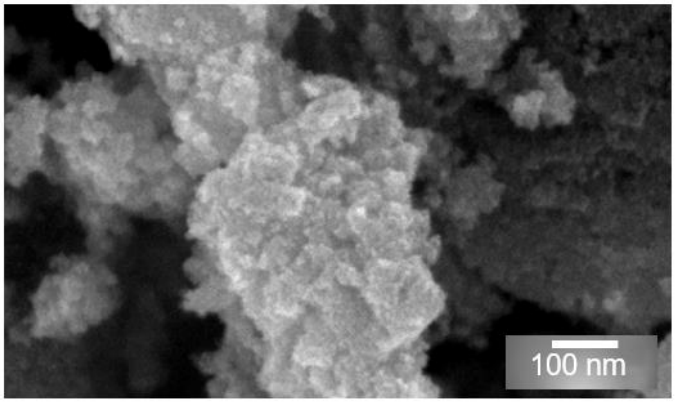

Figure A.2: SEM image of the TiO_2 nanopowder.

Figure A.3 shows the EDS analysis of the cork substrates (pristine and with TiO_2).

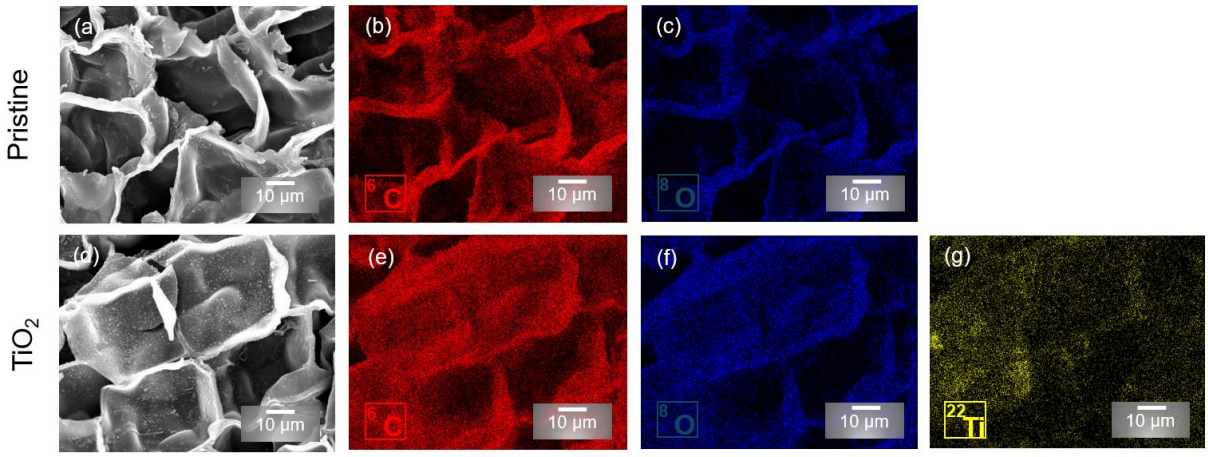

Figure A.3: SEM images of the cork substrates: (a) pristine substrate and (d) TiO_2 substrate. The corresponding EDS maps of C ((b) and (e)), O ((c) and (f)) and Ti (g) are also visible.

Figure A.4 shows the prepared RhB dye solutions with the pristine and TiO_2 cork substrates during the photocatalytic experiments under natural sunlight. No-stirring or oxygenation were needed during the reactions. As visible, due to the floating characteristic of cork, the substrates can be easily collected from the solution without the need of complex experimental equipment.

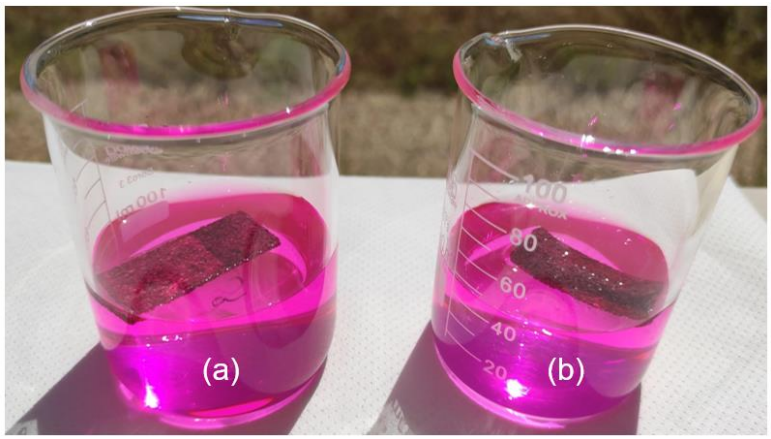

Figure A.4: Photocatalytic experiments with the cork substrates under natural sunlight: (a) pristine substrate and (b) TiO_2 substrate.

Figure A.5 shows the comparison between the solar irradiance spectrum of the MiniSol model LSH-7320 and the reference AM1.5.

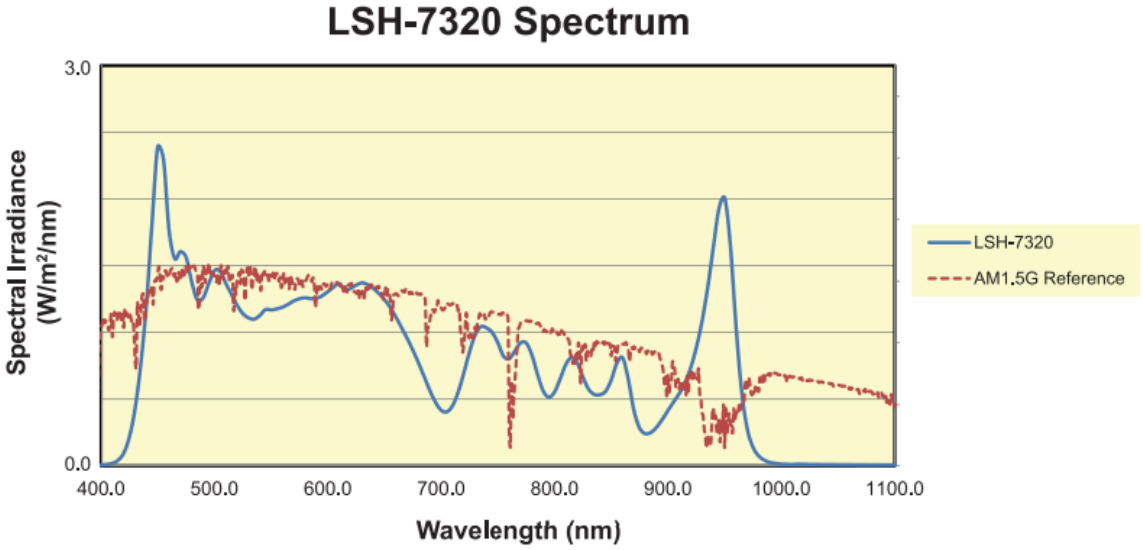

Figure A.5: Spectral irradiance *vs.* wavelength (from 400 to 1100 nm) of the MiniSol model LSH-7320 and the reference AM1.5.

Figure A.6, Figure A.7, Figure A.8 and Figure A.9 present the tandem mass spectra of TC and three TPs. The proposed fragmentation paths of the precursor ions *m*/*z* 445.1609, *m*/*z* 461.1567 and *m*/*z* 235.0256 are also depicted.

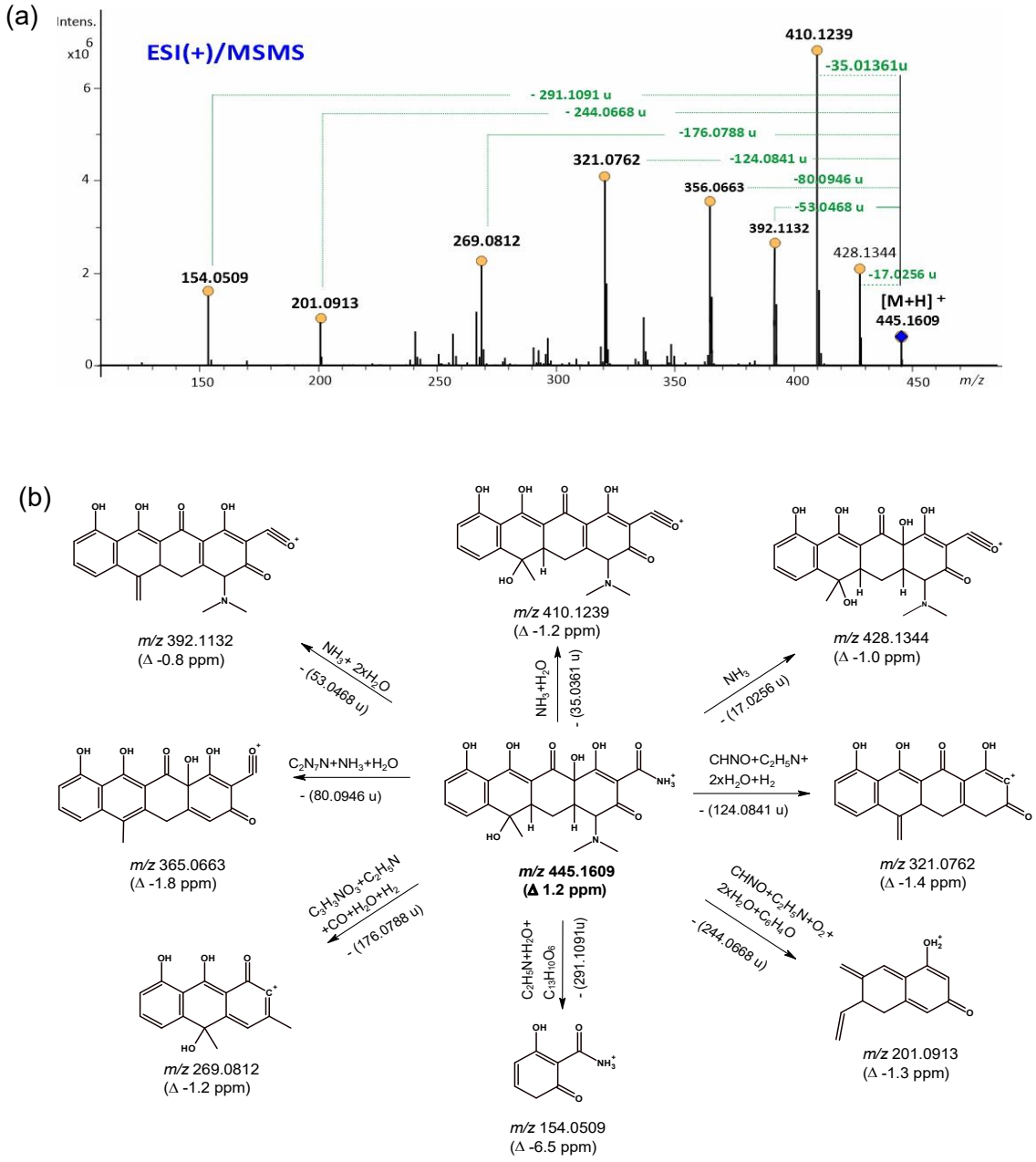

Figure A.6: (a) High-resolution tandem mass spectrum in the ESI positive of the precursor ion *m*/*z* 445.1609 assigned to the protonated molecule of tetracycline. (b) Proposed fragmentation path for the precursor ion *m*/*z* 445.1609 assigned to the protonated molecule of tetracycline with the molecular formula [$C_{22}H_{24}N_2O_8$].

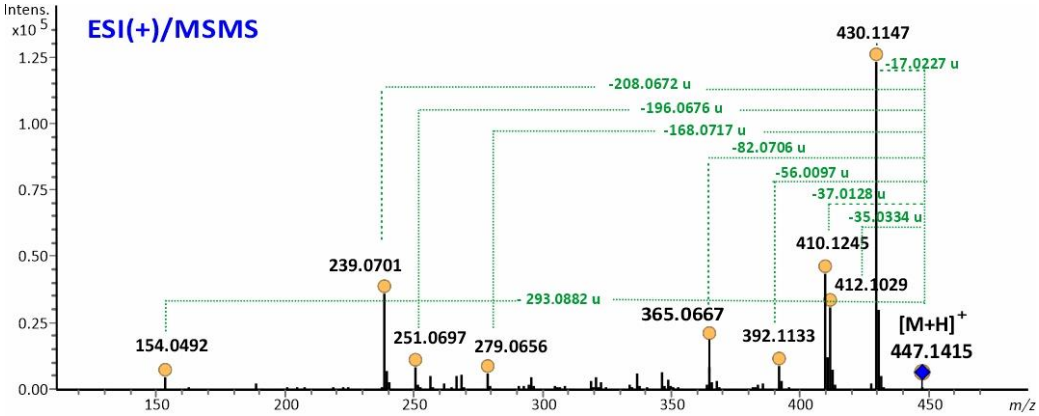

Spectrum Data

Meas. m/z	#	Ion Formula	m/z	err [ppm]	mSigma	# mSigma	Score	rdb	e¯ Conf	N-Rule
154.0492	1	$C_7H_8NO_3$	154.0499	4.7	26.3	1	100.00	5.0	even	ok
239.0701	1	$C_{15}H_{11}O_3$	239.0703	0.6	39.4	1	100.00	11.0	even	ok
251.0697	1	$C_{16}H_{11}O_3$	251.0703	2.2	87.0	1	100.00	12.0	even	ok
279.0656	1	$C_{17}H_{11}O_4$	279.0652	-1.4	65.7	1	100.00	13.0	even	ok
365.0667	1	$C_{20}H_{13}O_7$	365.0656	-3.2	82.2	3	100.00	15.0	even	ok
392.1133	1	$C_{22}H_{18}NO_6$	392.1129	-1.1	87.5	1	100.00	15.0	even	ok
410.1245	1	$C_{22}H_{20}NO_7$	410.1234	-2.7	34.3	1	100.00	14.0	even	ok
412.1039	1	$C_{21}H_{18}NO_8$	412.1027	-2.9	19.1	1	100.00	14.0	even	ok
430.1147	1	$C_{21}H_{20}NO_9$	430.1133	-3.3	4.2	1	100.00	13.0	even	ok
447.1373	1	$C_{21}H_{23}N_2O_9$	447.1398	5.6	'2.2	1	100.00	12.0	even	ok

Figure A.7: Tandem mass spectrum acquired in the ESI positive mode for the precursor ion assigned to the protonated molecule of TP 446, ionic formula $[C_{21}H_{22}N_2O_9+H^+]^+$. The Table "Spectrum data" denotes the accurate mass measurement values for the fragment ions identified in the MS/MS spectrum.

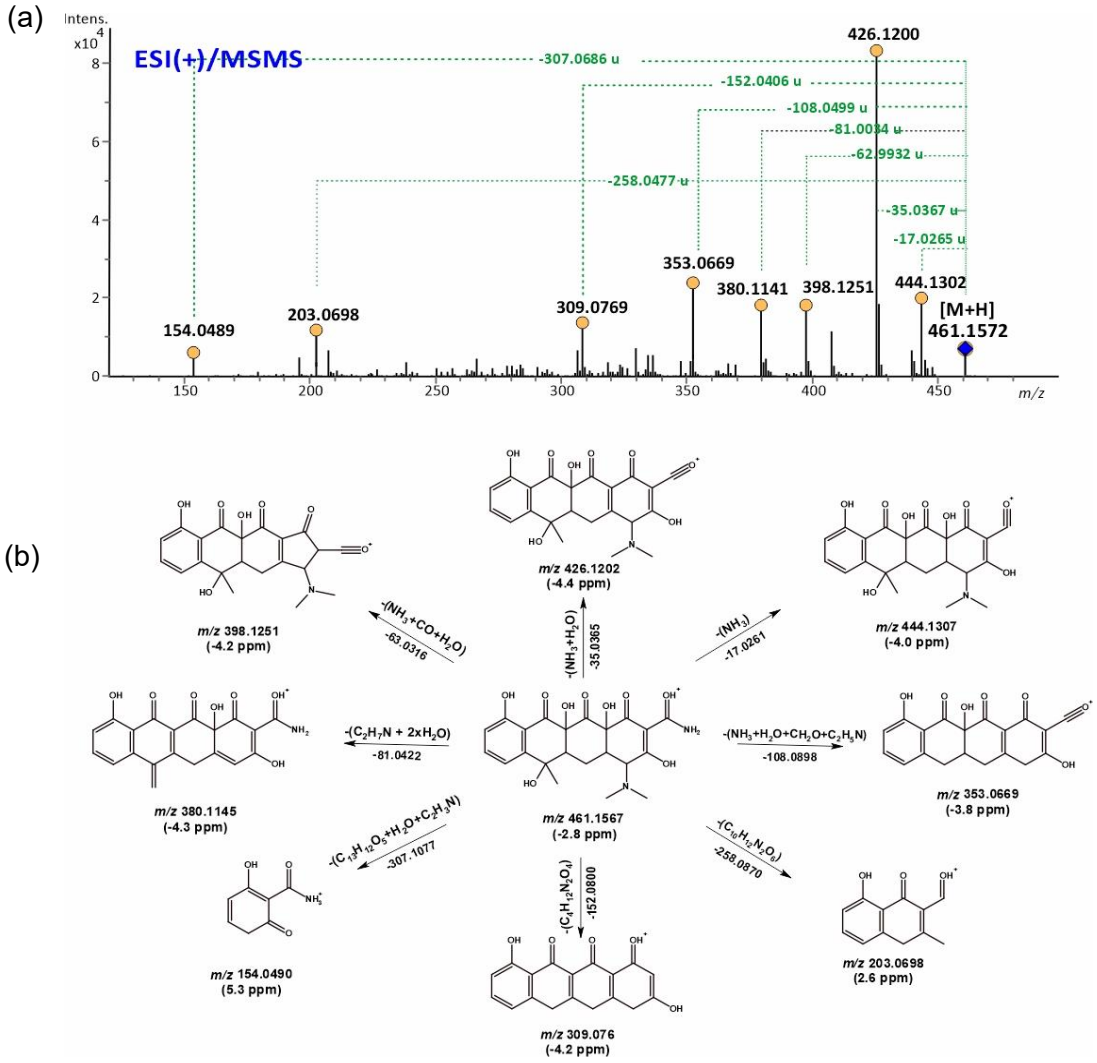

Figure A.8: (a) Tandem mass spectrum of the precursor ion *m/z* 461.1567 attributed to the protonated molecule of TP 460 with the ionic formula $[C_{22}H_{24}N_2O_9+H^+]^+$. (b) A proposed fragment path is described in the scheme.

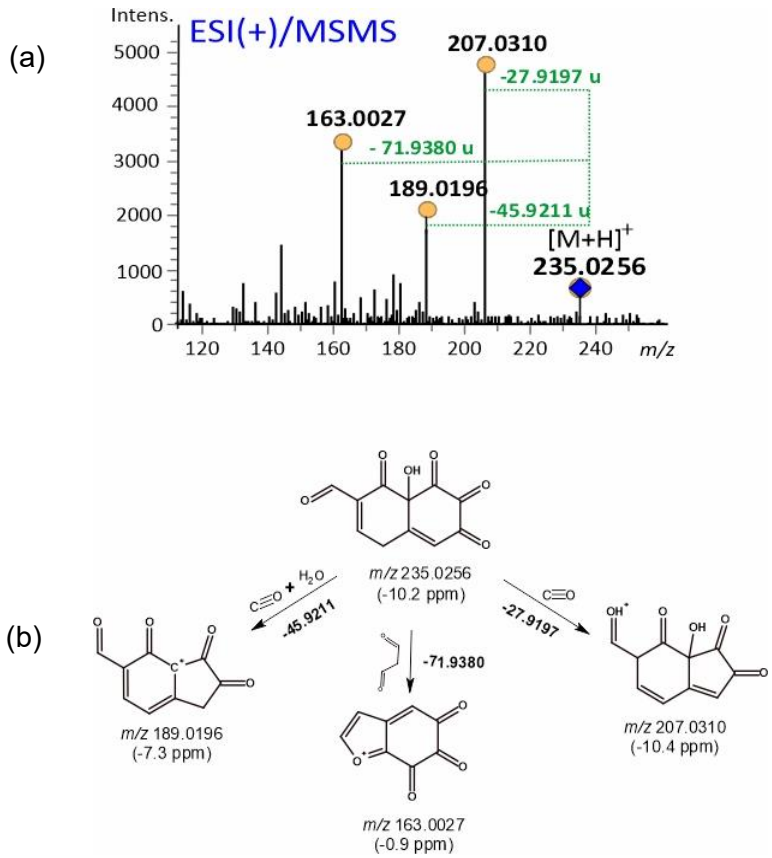

Figure A.9: (a) Tandem mass spectrum of the precursor ion *m/z* 235.0256 assigned to the protonated molecule of TP 234 with ionic molecular formula $[C_{11}H_6O_6+H^+]^+$. (b) The proposed fragmentation path is described in the scheme.

Figure A.10 displays the UHPLC-HRMS analysis in the ESI positive mode of TC in the presence of a pre-treated TiO_2 PU foam.

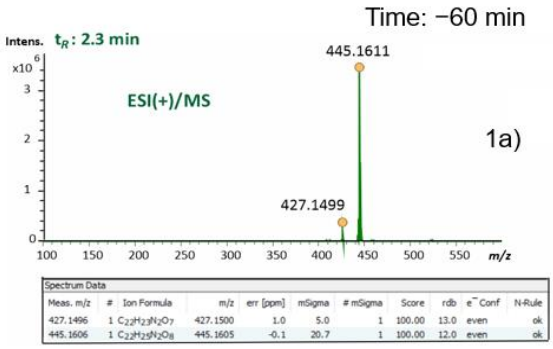

Spectrum Data

Meas. m/z	#	Ion Formula	m/z	err [ppm]	mSigma	# mSigma	Score	rdb	e⁻ Conf	N-Rule
427.1496	1	$C_{22}H_{23}N_2O_7$	427.1500	1.0	5.0	1	100.00	13.0	even	ok
445.1606	1	$C_{22}H_{25}N_2O_8$	445.1605	-0.1	20.7	1	100.00	12.0	even	ok

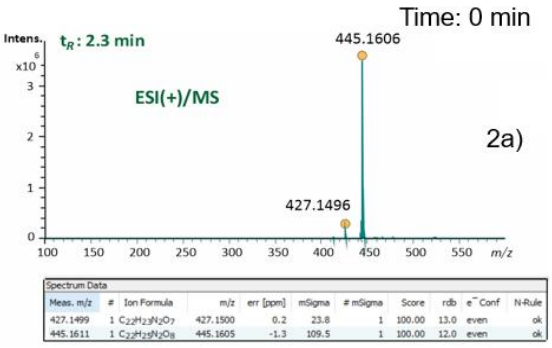

Spectrum Data

Meas. m/z	#	Ion Formula	m/z	err [ppm]	mSigma	# mSigma	Score	rdb	e⁻ Conf	N-Rule
427.1499	1	$C_{22}H_{23}N_2O_7$	427.1500	0.2	23.8	1	100.00	13.0	even	ok
445.1611	1	$C_{22}H_{25}N_2O_8$	445.1605	-1.3	109.5	1	100.00	12.0	even	ok

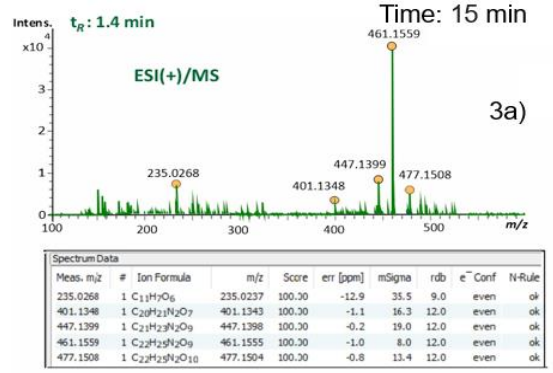

Spectrum Data

Meas. m/z	#	Ion Formula	m/z	Score	err [ppm]	mSigma	rdb	e⁻ Conf	N-Rule
235.0268	1	$C_{11}H_7O_6$	235.0237	100.00	-12.9	35.5	9.0	even	ok
401.1348	1	$C_{20}H_{21}N_2O_7$	401.1343	100.00	-1.1	16.3	12.0	even	ok
447.1399	1	$C_{21}H_{23}N_2O_9$	447.1398	100.00	-0.2	19.0	12.0	even	ok
461.1559	1	$C_{22}H_{25}N_2O_9$	461.1555	100.00	-1.0	8.0	12.0	even	ok
477.1508	1	$C_{22}H_{25}N_2O_{10}$	477.1504	100.00	-0.8	13.4	12.0	even	ok

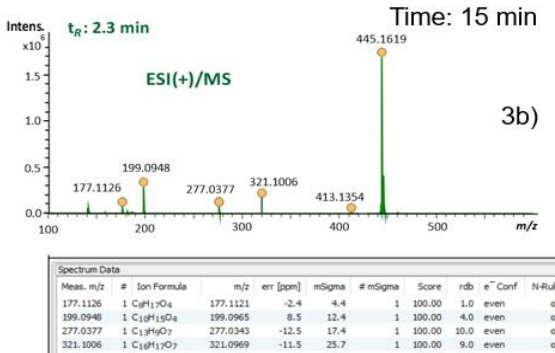

Spectrum Data

Meas. m/z	#	Ion Formula	m/z	err [ppm]	mSigma	# mSigma	Score	rdb	e⁻ Conf	N-Rule
177.1126	1	$C_9H_{17}O_4$	177.1121	-2.4	4.4	1	100.00	1.0	even	ok
199.0948	1	$C_{10}H_{15}O_4$	199.0965	8.5	12.4	1	100.00	4.0	even	ok
277.0377	1	$C_{13}H_9O_7$	277.0343	-12.5	17.4	1	100.00	10.0	even	ok
321.1006	1	$C_{16}H_{17}O_7$	321.0969	-11.5	25.7	1	100.00	9.0	even	ok
413.1354	1	$C_{21}H_{21}N_2O_7$	413.1343	-2.6	38.8	1	100.00	13.0	even	ok
445.1620	1	$C_{22}H_{25}N_2O_8$	445.1605	-3.3	0.7	1	100.00	12.0	even	ok

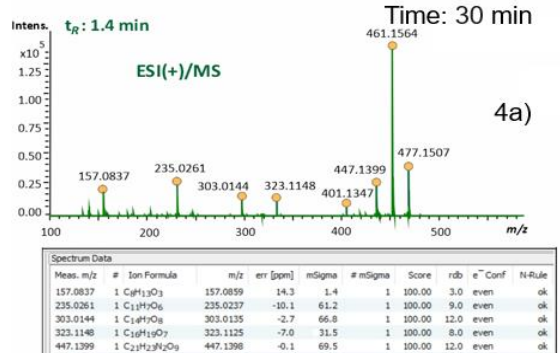

Spectrum Data

Meas. m/z	#	Ion Formula	m/z	err [ppm]	mSigma	# mSigma	Score	rdb	e⁻ Conf	N-Rule
157.0837	1	$C_8H_{13}O_3$	157.0859	14.3	1.4	1	100.00	3.0	even	ok
235.0261	1	$C_{11}H_7O_6$	235.0237	-10.1	61.2	1	100.00	9.0	even	ok
303.0144	1	$C_{14}H_7O_8$	303.0135	-2.7	66.8	1	100.00	12.0	even	ok
323.1148	1	$C_{16}H_{19}O_7$	323.1125	-7.0	31.5	1	100.00	8.0	even	ok
447.1399	1	$C_{21}H_{23}N_2O_9$	447.1398	-0.1	69.5	1	100.00	12.0	even	ok
461.1564	1	$C_{22}H_{25}N_2O_9$	461.1555	-2.0	7.9	1	100.00	12.0	even	ok
477.1507	1	$C_{22}H_{25}N_2O_{10}$	477.1504	-0.8	28.7	1	100.00	12.0	even	ok

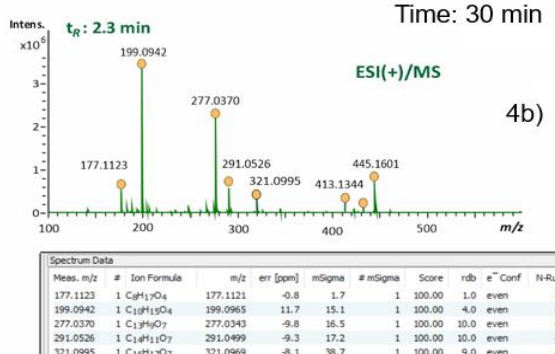

Spectrum Data

Meas. m/z	#	Ion Formula	m/z	err [ppm]	mSigma	# mSigma	Score	rdb	e⁻ Conf	N-Rule
177.1123	1	$C_9H_{17}O_4$	177.1121	-0.8	1.7	1	100.00	1.0	even	ok
199.0942	1	$C_{10}H_{15}O_4$	199.0965	11.7	15.1	1	100.00	4.0	even	ok
277.0370	1	$C_{13}H_9O_7$	277.0343	-9.8	16.5	1	100.00	10.0	even	ok
291.0526	1	$C_{14}H_{11}O_7$	291.0499	-9.3	17.2	1	100.00	10.0	even	ok
321.0995	1	$C_{16}H_{17}O_7$	321.0969	-8.1	38.7	1	100.00	9.0	even	ok
413.1344	1	$C_{21}H_{21}N_2O_7$	413.1343	-0.2	20.3	1	100.00	13.0	even	ok
431.1451	1	$C_{21}H_{23}N_2O_8$	431.1449	-0.4	21.9	2	100.00	12.0	even	ok
445.1608	1	$C_{22}H_{25}N_2O_8$	445.1605	-0.6	0.9	1	100.00	12.0	even	ok

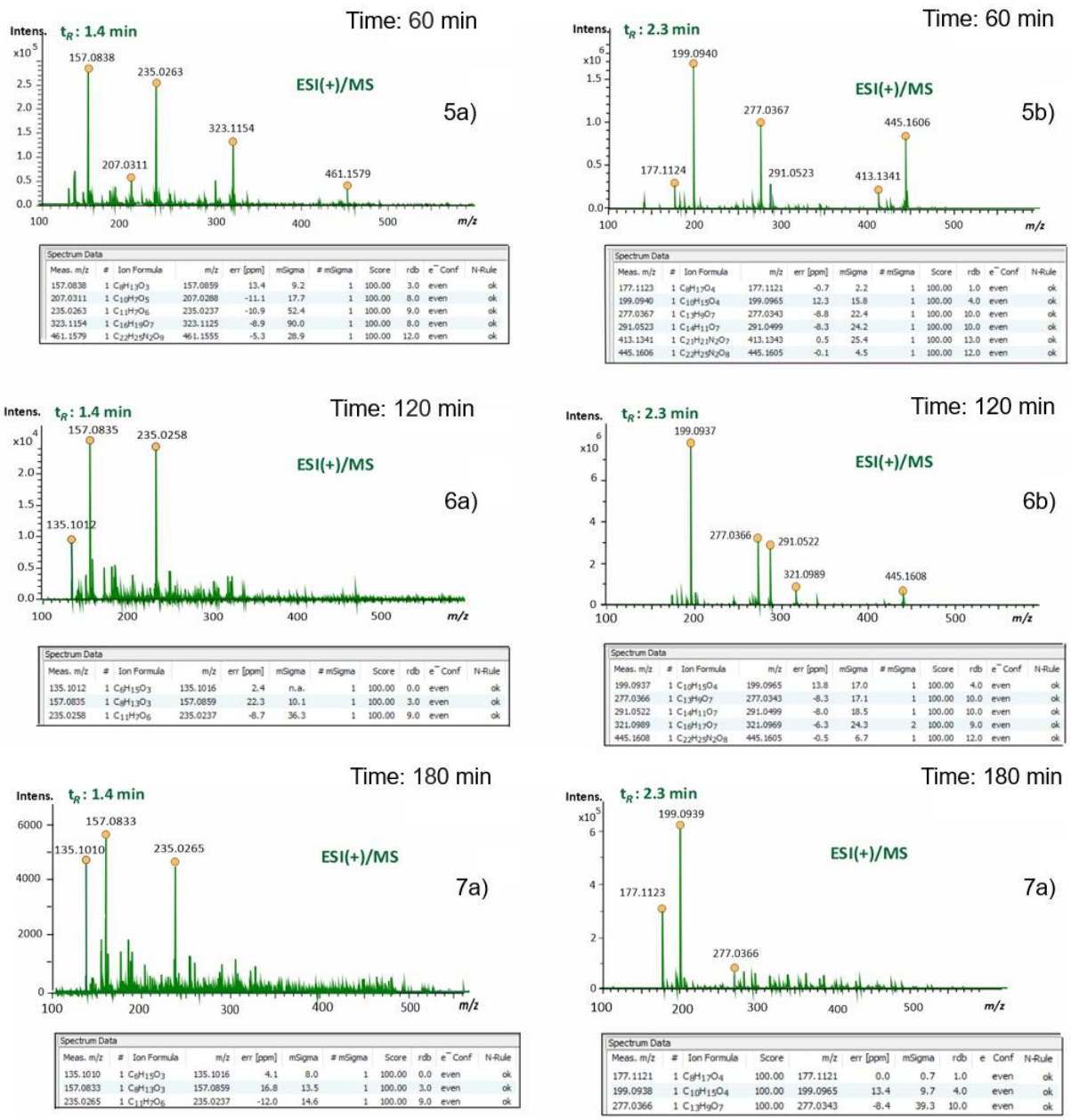

Figure A.10: UHPLC-HRMS analysis in the ESI positive mode of TC in the presence of a pre-treated TiO_2 PU foam. Figures show the mass spectra of TC intermediates in the absence of light 1a) −60 min and when exposed to solar light at different reaction times: 2a) 0 min; 3a-b) 15 min; 4a-b) 30 min; 5 a-b) 60 min, 6 a-b) 120 min, 7a-b) 180 min. Transformation products were identified based on their accurate *m/z* values released as protonated molecules $[M+H]^+$. The elemental composition of each peak was predicted using the algorithm Smart Formula 3D, and values with mass deviation (Δ) lower than 5 Da and mSigma <50 were considered acceptable (see spectra table).

Figure A.11 shows the XPS survey spectra for TiO_2 and 7 mol. % Ca:TiO_2 (7-Ca:TiO_2) nanopowders.

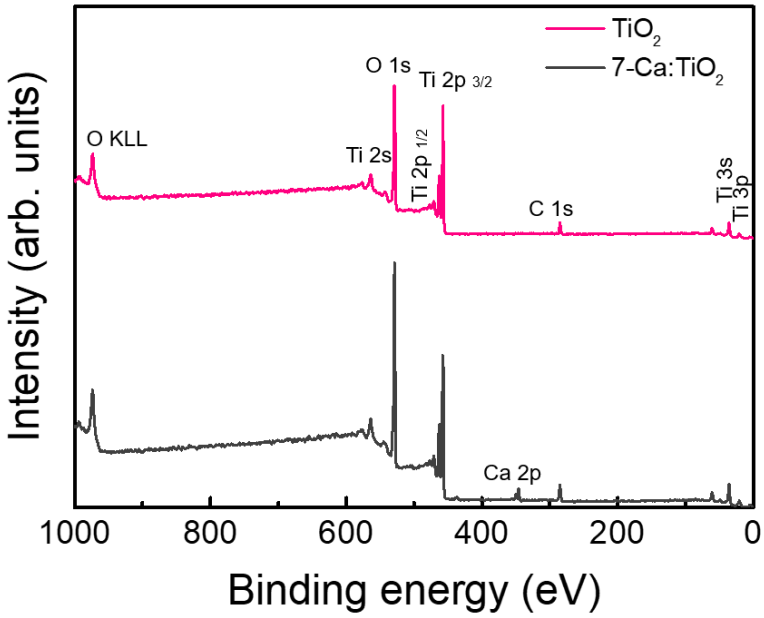

Figure A.11: XPS survey spectra for TiO_2 and 7-Ca:TiO_2 nanopowders.

2025

MARIA LEONOR MATIAS

MICROWAVE-ASSISTED SYNTHESES OF SUSTAINABLE TiO_2-BASED PLATFORMS FOR WATER REMEDIATION